UNIVERSITÀ
DEGLI STUDI
DI PADOVA

UNIVERSITY OF PADUA

Department of Mechanical Engineering

Doctoral School in Industrial Engineering
Section of Mechanical Design and Motorcycle Engineering

XXIII Ph.D. Cycle

Ph.D. Thesis

Study, design and test of the Target - Ion Source system for the INFN SPES facility

Doctoral School Director: **Ch.mo Prof. Paolo Bariani**

Program of study coordinator: **Ch.mo Prof. Vittore Cossalter**

Supervisors: **Dr. Eng. Giovanni Meneghetti** and **Dr. Alberto Andrighetto**

Ph.D. student: **Eng. Mattia Manzolaro**

This work is dedicated to my wife Valentina and to my Family for their fundamental and indispensable support.

Special thanks to Dr. Andrighetto and to Dr. Meneghetti: they have been constantly a reference and a guide for me during the last three years, teaching me a lot of very important things. They gave me the opportunity to do scientific research, the work I like: thanks a lot another time.

I want to thank also my colleagues, in particular my precious friends Lisa Biasetto and Michele Lollo.

Great thanks to Eng. Marzari and to Dr. Stracener: during my internships at CERN and at ORNL, respectively, they supervised me in a professional and friendly way, giving me the opportunity to live two important experiences for my work and for my life.

CONTENTS

List of abbreviations

CERN	Conseil Europèen pour la Recherche Nuclèaire
FEM	Finite Element Method
HRIBF	Holifield Radioactive Ion Beam Facility
INFN	Istituto Nazionale di Fisica Nucleare
ISOL	Isotope Separation On-Line
LNL	Laboratori Nazionali di Legnaro
ORNL	Oak Ridge National Laboratory
PET	Positron Emission Tomography
RIBs	Radioactive Ion Beams
SPES	Selective Production of Exotic Species

Introduction

Since the beginning of the twentieth century nuclear physics explores the behaviour and the stability of nuclei, each time facing new scientific and technological challenges. The complex technologies specifically developed to support research in the field of nuclear physics have often led to important applications in medicine, industry, applied physics, influencing sometimes in a deep way the society: the birth of the “web” at CERN is an emblematic example.

Over the years Europe has become a leader in the field of nuclear physics research: CERN is the world's largest particle physics laboratory, situated in the Northwest suburbs of Geneva on the Franco–Swiss border, and Italy, with INFN (Istituto Nazionale di Fisica Nucleare), is one of its main members. In Italy, one of the most important projects supported by INFN is the so-called SPES (Selective Production of Exotic Species) project that is intended to develop a facility for the production of radioactive ion beams at Legnaro National Laboratories (Padua, Italy). In particular the SPES facility will produce neutron rich nuclei with mass in the range 80-160, to use for forefront research in nuclear physics and for many applications in different fields of science. The core of the project is constituted by the target – ion source system and in this work its study, design and test are presented.

Chapter 1 gives a general overview of the SPES project and its scientific context whereas chapter 2 presents some details of the SPES production area that is composed of the target – ion source system and all the experimental apparatus needed for its functioning. Chapters 3 and 4 describe in detail the study, the design and the experimental tests performed for the SPES target and for the SPES ion sources, respectively. Once described separately the target and the ion source, they are studied together in chapter 5, observing with particular attention their reciprocal effects. In the final part of the thesis chapter 6 reports the description of the on-line test of the uranium carbide SPES target prototype carried on at the HRIBF facility (ORNL, USA).

Introduzione

Sin dagli inizi del ventesimo secolo la fisica nucleare esplora il comportamento e la stabilità dei nuclei atomici, affrontando di volta in volta nuove sfide scientifiche e tecnologiche. Le complesse tecnologie sviluppate appositamente per supportare la ricerca nel campo della fisica nucleare hanno spesso condotto ad importanti applicazioni in medicina, a livello industriale, in fisica applicata, influenzando talvolta in modo profondo gli usi e i costumi della società: la nascita del "web" presso il CERN di Ginevra costituisce un esempio emblematico.

Nel corso degli ultimi anni l'Europa è diventata leader nel campo della fisica nucleare: il CERN è il più grande laboratorio di fisica delle particelle al mondo, situato nella periferia a Nordovest di Ginevra in prossimità del confine Franco-Svizzero, e l'Italia, con l'INFN (Istituto Nazionale di Fisica Nucleare), è uno dei suoi membri principali. In Italia, uno dei più importanti progetti supportati dall'INFN è il progetto SPES (Selective Production of Exotic Species) che prevede la costruzione di una facility per la produzione di fasci radioattivi presso i Laboratori Nazionali di Legnaro (Padova). In particolare la facility SPES produrrà nuclei ricchi di neutroni con masse comprese nel range 80-160, da impiegare per la ricerca di base in fisica nucleare e per numerose altre applicazioni in ambito scientifico. Il cuore del progetto è costituito dal sistema target – sorgente di ionizzazione ed in questo lavoro ne vengono presentati lo studio, la progettazione ed i corrispettivi test sperimentali.

Il capitolo 1 fornisce una presentazione generale del progetto SPES e del contesto scientifico ad esso legato mentre il capitolo 2 presenta alcuni dettagli dell'area di produzione SPES composta dal sistema target – sorgente di ionizzazione e da tutti gli apparati sperimentali necessari al suo funzionamento. I capitoli 3 e 4 descrivono in dettaglio lo studio, la progettazione ed i test sperimentali svolti rispettivamente per il target SPES e per le sorgenti di ionizzazione SPES. Una volta presentati separatamente il target e la sorgente di ionizzazione, tali componenti vengono studiati in modo accoppiato a livello del capitolo 5, prestando particolare attenzione agli effetti reciproci. Nella parte finale della tesi il capitolo 6 riporta la descrizione dei test on-line sul prototipo del target SPES in carburo di uranio svolti presso l' HRIBF facility dei Laboratori Nazionali di Oak Ridge (USA).

Chapter 1

The SPES project at Legnaro National Laboratories: production of Radioactive Ion Beams

1.1. Introduction

Most of the atom's mass (more than 99,9%) is concentrated in the nucleus; the atomic nucleus is positioned in the centre of the atom and is composed of protons (positively charged particles) and neutrons (neutral particles). Protons and neutrons are both called nucleons and their mass (~1.66×10^{-27}kg) is approximately 1800 times bigger than electron's one (~9.11×10^{-31}kg). The stability of the atomic nucleus is guaranteed by the strong interaction: it is one of the four fundamental interactions of nature, along with electromagnetic force, weak interaction and gravitation; it permits to bind protons and neutrons together contrasting the electrostatic repulsions between positively charged protons. The strong interaction is a very intense force and because of it a lot of energy is requested to break the atomic nucleus.

Nuclear physics is the field of physics that studies the behaviour and the stability of nuclei: they are not simple agglomerates of protons and neutrons but rather ordered and well balanced combinations of this two kinds of nucleons. Sometimes the word "nuclide" is used instead of the word "nucleus" even if they don't mean exactly the same thing: in words "nuclide" is an umbrella term for all nuclei with one or more electrons orbiting.

Stable (not radioactive) nuclei own approximately the same number of protons and neutrons (this is true only for light nuclei), and constitute the "valley of stability" in the chart of the nuclides (see the black squares in figure 1.1); the stability of nuclei with number of protons equal to the number of neutrons is explained by the fact that the neutron-proton strong interaction is slightly stronger respect to the proton-proton and neutron-neutron ones. When nuclei have mass number (also called atomic mass number or nucleon number) $A \geq 40$ (where $A = Z+N$, Z = proton number or atomic number and N = neutron number), the electrostatic forces move the stability line far from the straight line $N = Z$, toward the group of nuclei characterized by $N > Z$, since neutrons are not charged and don't feed the electrostatic repulsive forces that act against the nuclear stability. Respect to the strong interactions, the electrostatic forces preserve their efficacy with the increasing of the nuclear radius and limit the existence of Super Heavy Elements (SHE).

Nuclei with excess or shortage of neutrons, and consequently far from the "valley of stability", are unstable, radioactive and decay emitting particles (α and β) and γ rays. Unstable nuclei are

commonly called “exotic nuclei” and at present approximately 3600 of them can be produced in dedicated facilities distributed all over the world. Anyway theoretical calculations predict the existence of more than 6000 unstable nuclei and a great amount of them is still unknown.

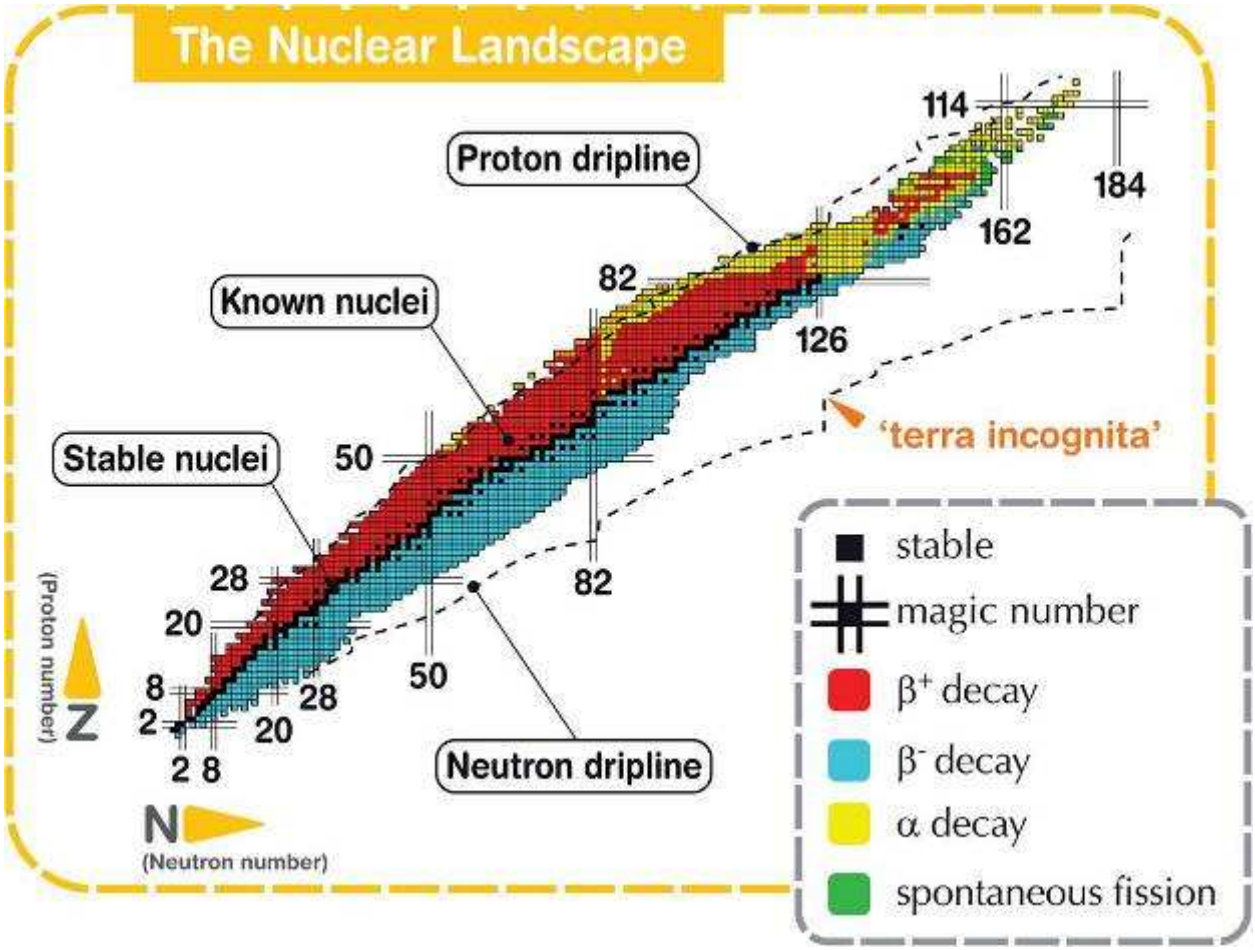

Fig. 1.1. Chart of nuclides [1].

Figure 1.1 shows the chart of nuclides that identify and classify the nuclei on the basis of their proton (Z) and neutron (N) numbers; in particular, the 6000 nuclei that are believed to exist are represented within the borderlines defined by the proton and neutron driplines. The already known and studied nuclei are indicated in red, blue, yellow, green and most of the unknown nuclei do lie in the neutron rich side, on the white area. Theoretical calculations demonstrated that beyond the driplines nuclei have a so high level of instability that start to emit nucleons very quickly in order to reach a sufficient level of stability, entering another time within the aforementioned borderlines (the proton and neutron driplines).

The so-called SPES (Selective Production of Exotic Species) project is intended to develop a radioactive ion beam facility at National Institute of Nuclear Physics (Legnaro, Padua, Italy). In particular the SPES facility will produce neutron rich nuclei with mass in the range 80-160 [2, 3], to use for forefront research in nuclear physics and for many applications in different fields of science.

In the next paragraph some details about the research fields related to RIBs (radioactive ion beams) will be furnished; paragraph 1.3 will describe the techniques needed to produce RIBs and at the end of the chapter a general overview of the SPES project will be presented.

1.2. The Why of Radioactive Ion Beam research [4, 5]

The main goal of the facilities dedicated to the production of radioactive ion beams is to provide an accelerator system to perform forefront research in nuclear physics by studying nuclei far from stability. Most of the present-day knowledge of the structure of the atomic nucleus is based on the properties of nuclei that in the chart of nuclides are positioned very close to the "valley of stability" or in the neutron-deficient side, where the proton-to-neutron ratio is not so different to that of stable nuclei. Extrapolating the models at present adopted to describe the atomic nucleus to the regions far from stability is quite dangerous and it's now evident that some of the "basic truths" of nuclear physics have to be revised and modified. An example is surely the "liquid drop model" developed by Niels Bohr and John Archibald Wheeler that allows to describe the radius R of the atomic nucleus according to the formula $R = R_o A^{1/3}$, where R_o is a constant equal to 1.2 fm (1 fm = 10^{-15} m). Nowadays we know that the nuclear radii of some nuclei do not scale with a $A^{1/3}$ dependence and are appreciably larger than that predicted by the liquid drop model: they are called Halo nuclei and their study is recent and ongoing.

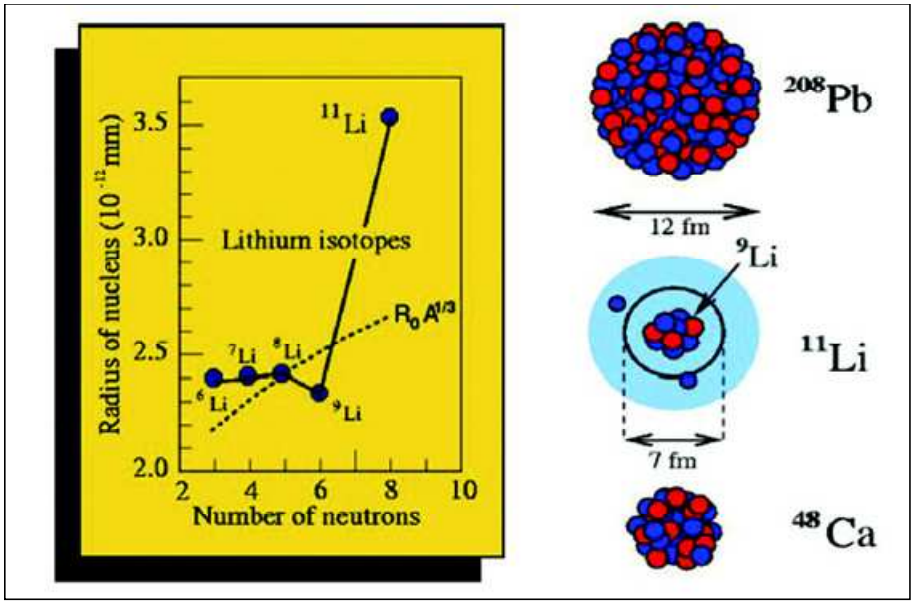

Fig. 1.2. Lithium isotopes nuclear radii and size comparison between ^{11}Li, ^{48}Ca and ^{208}Pb nuclei.

The discovery of the Halo nuclei was done in the mid-1980s at Lawrence Berkeley Laboratory's Bevelac accelerator facility, during some experiments performed to measure the probability of interaction (called cross section) between a beam of Lithium isotopes and a particular

target. The Halo is an effect related to the atomic nucleus according to which one, two or more external nucleons, (usually neutrons) called valence nucleons, orbit around a well defined inert "core" containing all the other nucleons. The most famous Halo nucleus is surely ^{11}Li, composed of two valence neutrons orbiting around a ^{9}Li nucleus. The graph of figure 1.2 clearly shows the trend of the nuclear radii of Lithium isotopes as a function of the neutron number: the discontinuity of size between ^{11}Li and the other lighter isotopes is evident. In figure 1.2 the ^{11}Li nucleus is compared with other heavier nuclei: ^{48}Ca and ^{208}Pb. The mass-weighted average between the radius of the ^{11}Li external valence neutron's orbit and the radius of the ^{11}Li core (^{9}Li nucleus) is comparable to ^{48}Ca nuclear radius whereas the total space wrapped inside the ^{11}Li external valence neutron's orbit is equivalent to ^{208}Pb size.

The two-neutron Halo nuclei are ^{6}He, ^{11}Li, ^{17}B, ^{19}B and ^{22}C: they break into three fragments (the two valence neutrons and the core) and are called Borromean because of this behaviour (in mathematics, the Borromean rings consist of three topological circles which are linked and form a Brunnian link, i.e., removing any ring results in two unlinked rings).

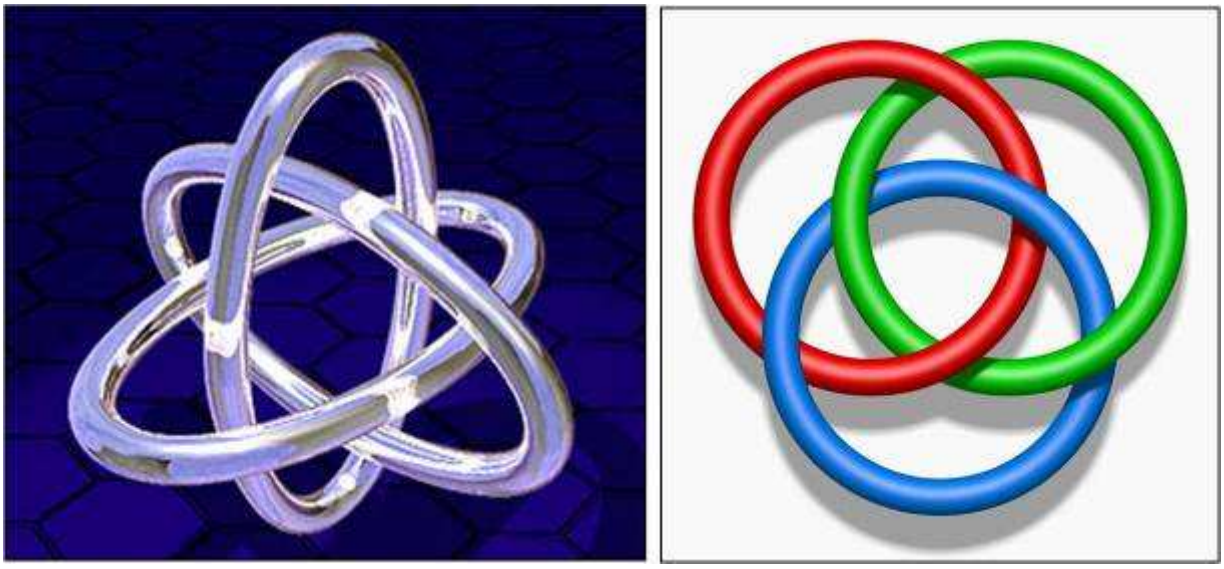

Fig. 1.3. The three Borromean rings.

Single neutron Halo nuclei are ^{11}Be and ^{19}C whereas ^{8}He and ^{14}Be exhibit a four-neutron Halo behaviour. In the context of Halo nuclei valence nucleons can be also protons: in this case nuclei are expected to be more rare and unstable because of the proton-proton electrostatic repulsive force. Single proton Halo nuclei include ^{8}B and ^{26}P; a two-proton Halo behaviour is exhibited by ^{17}Ne and ^{27}S.

In the context of forefront research in nuclear physics, the aforementioned argument is only an example of the numerous topics that can be studied and deeply understood by means of radioactive ion beams. Moreover having strong and pure RIBs can be extremely useful also in other fields such

as nuclear astrophysics, solid-state physics and nuclear medicine. In the following some particular applications in the fields cited above are furnished.

Nuclear Astrophysics. Nuclear astrophysics plays a fundamental role in understanding the structure and composition of the Universe and its constituents. Stars produce energy through nuclear reactions between stable as well as unstable nuclei: these processes can last for billions of years or be explosive involving a timescale of seconds. A typical example of burning cycle involving unstable nuclei is the so-called CNO cycle (CNO stands for Carbon-Nitrogen-Oxygen), one of the two sets of fusion reactions by which stars convert Hydrogen to Helium (the other is the proton-proton chain). To model some steps of these processes nuclear astrophysics must rely on a number of specific characteristics of exotic nuclei. When available, experimental information is used but otherwise scientists must rely on extrapolating nuclear models. In this context radioactive ion beams can provide this experimental information or can severely test the applicability of the current nuclear models.

Solid State Physics. Radioactive ion beams can be used as a powerful diagnostic tool to furnish detailed information on the environment in which they are implanted. An important application is represented by the Emission Channeling technique, used to study the structure and properties of impurity-defect complexes in solids, particularly in semiconductors whose functioning is deeply influenced by defects.

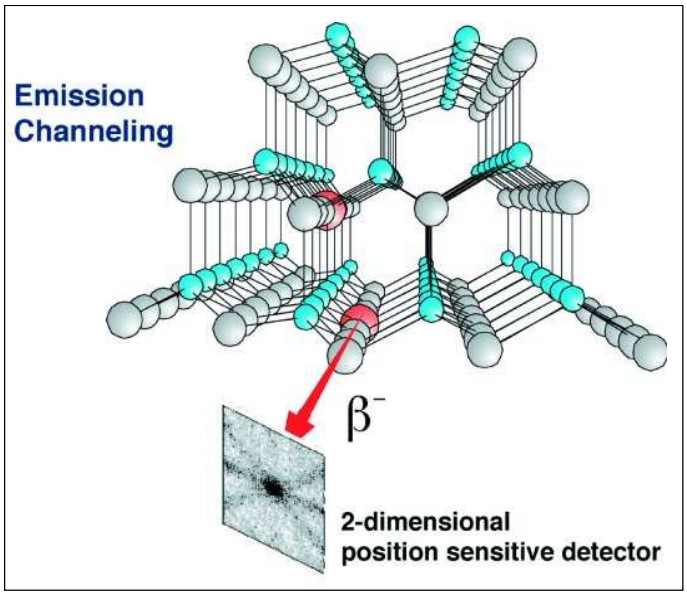

Fig. 1.4. The Emission Channeling technique.

The idea for Emission Channeling was born at CERN in the 1970's and can be described as the emission and movement of charged particles through a single crystal subsequent to radioactive decays coming from radioactive ions previously implanted into the crystal. The aforementioned

charged particles can be α or β particles and their intensity is registered by a 2-dimensional position sensitive detector. The working principle of this technique is based on the angle dependence of the intensity of the emitted radiation as a function of the orientation of the host crystal (different crystal axes and planes): from the measured anisotropic intensity distributions the lattice sites of the emitting radioactive ions can be determined with a great accuracy. This kind of technique can be very useful to study diffusion phenomena and doping in semiconductors.

Nuclear Medicine. Since the early days of nuclear physics, it was realized that nuclear radiation could be used in medicine for diagnostic and therapy operations. Nuclear medicine is a branch of medicine that uses radioactive isotopes (isotopes are different types of atoms of the same chemical element, so with the same number of protons and electrons, each having a different number of neutrons) and relies on the process of radioactive decay in the diagnosis and treatment of disease. An important application of radioactive ion beams in nuclear medicine is the production of radioactive isotopes (or radionuclides) to utilise for Positron Emission Tomography (PET). PET is a nuclear medicine imaging technique able to generate a three-dimensional image or picture of functional processes in the body: it is mainly used in clinical oncology (medical imaging of tumours and the search for metastases) and for clinical diagnosis of some diffuse brain diseases.

Fig. 1.5. Image of a typical facility used for Positron Emission Tomography.

Radionuclides used for PET are typically isotopes with short half lives such as ^{11}C (~20 min), ^{13}N (~10 min), ^{15}O (~2 min), and ^{18}F (~110 min). These radionuclides are incorporated either into compounds normally used by the body such as glucose (or glucose analogues), water, ammonia, or into molecules that are able to bind to the sites where the functional process of interest acts;

incorporated radionuclides undergo positive β decay emitting a positron (the positron or antielectron is the antiparticle or the antimatter counterpart of the electron, characterized by the electric charge +1e and the same mass of the electron) that after travelling up to a few millimetres encounters an electron with opposite charge. When positron and electron collide annihilation occurs producing two or more gamma ray photons moving in opposite directions.

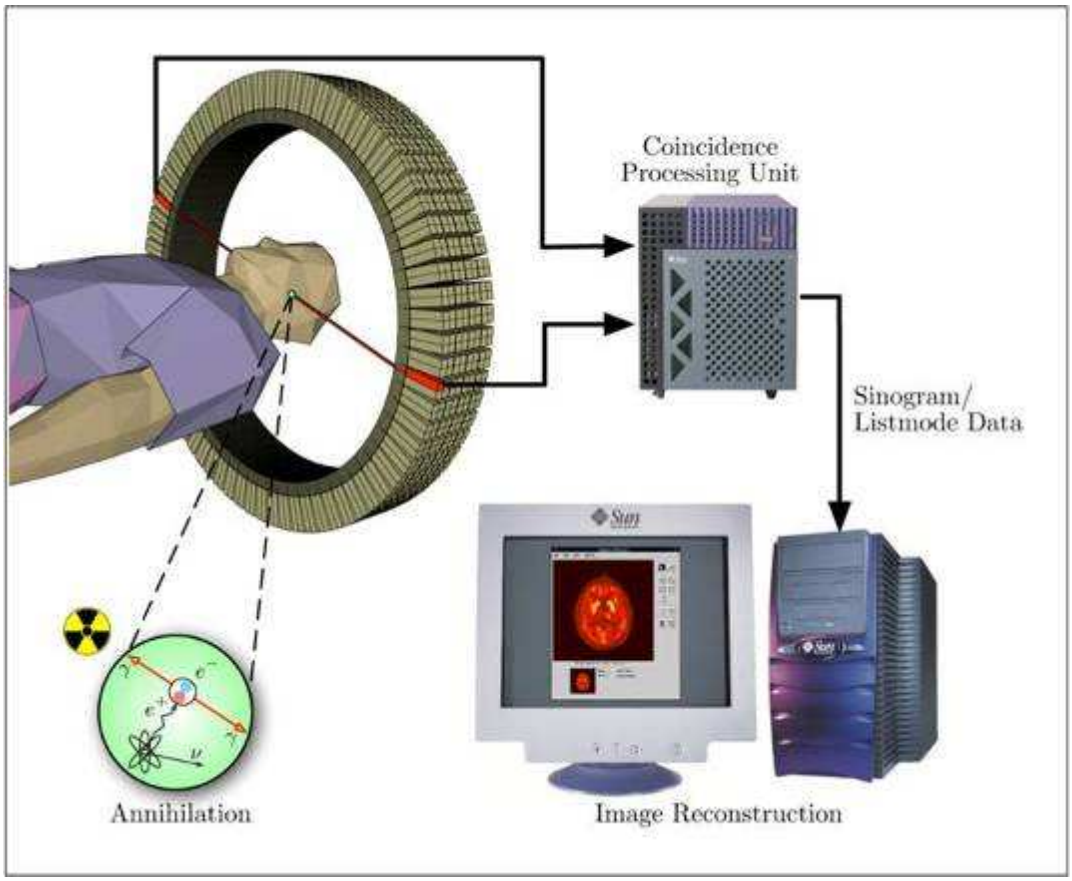

Fig. 1.6. Schematic representation of the PET functioning.

When the photons reach the scintillator (material which exhibits scintillation when excited by ionizing radiation) of the scanning device, they create a burst of light which is detected by photomultiplier tubes or silicon avalanche photodiodes (Si APD). Signals are then opportunely elaborated to reconstruct a digital image of the zone of interest.

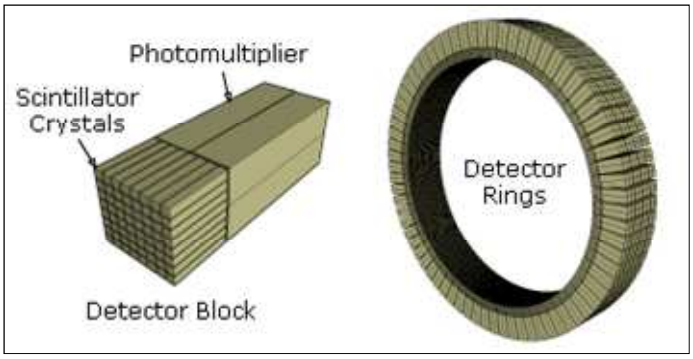

Fig. 1.7. The PET detector system.

One of the main applications of PET is surely in clinical oncology: in this case the tracer fluorodeoxyglucose (FDG) containing the radioactive isotope ^{18}F is taken up by glucose-using cells and phosphorylated (addition of a phosphate PO_4 group) by hexokinase, an enzyme whose presence is greatly elevated in rapidly growing malignant tumours. Most tissues cannot remove the phosphate group added by hexokinase and consequently FDG is trapped in any cell which takes it up, until it decays. This results in intense radiolabeling of tissues with high glucose uptake, such as the brain, the liver, and most cancers. As a result, FDG-PET can be used for diagnosis, staging, and monitoring treatment of cancers, particularly in Hodgkin's lymphoma, non-Hodgkin lymphoma, and lung cancer.

Because of the short half lives of most radioactive isotopes, the radiotracers (tracers containing radioactive isotopes) must be produced using a cyclotron and a radiochemistry laboratory that are in close proximity to the PET imaging facility. The half life of ^{18}F (~110 min) is long enough such that Fluorine-18 labeled radiotracers can be manufactured commercially at an offsite location.

1.3. RIB production

Nowadays mature techniques for the production of radioactive ion beams make it possible to study nuclei and their properties in an unprecedented way, allowing important improvements in fundamental nuclear physics research and in many applications in various fields of science. Moving away from the valley of stability the production of exotic nuclei is influenced by the following difficulties:

- very low production cross sections (see appendix A)
- very intense production of unwanted species in the same target
- very short half lives (see appendix A) of the nuclei of interest

There are two complementary ways to make good quality beams of exotic nuclei: the “in-flight separation technique” and the “isotope separation on line (ISOL) technique”. Both methods transport the nuclei of interest away from the place where they are produced (characterized by a large background due to nuclear reactions) to a well-shielded experimental set-up, where the nuclear properties can be explored. Nuclei transport serves not only to create low background conditions but also to purify the beam and to prepare it in the necessary conditions with respect to energy, time and ion optical properties for the experiments.

In the following sections the two aforementioned methods for the production of radioactive ion beams are illustrated, with a particular emphasis on the ISOL technique adopted in the context of the SPES project.

1.3.1. The In-Flight Separation technique [6]

In the in-flight separation technique the nuclear reactions in a “primary” or “production” target are used to convert an intense primary beam of heavy ions into the desired radioactive, secondary beam (see figure 1.8). In other words a primary heavy ion beam of several tens of mega-electron-volts per nucleon (MeV/u, u = atomic mass unit = mass of a nucleon ~ 1.66×10^{-27}kg) is fragmented in a primary target and the resulting fragments, following electro-magnetic selection, are then directly used for experiments.

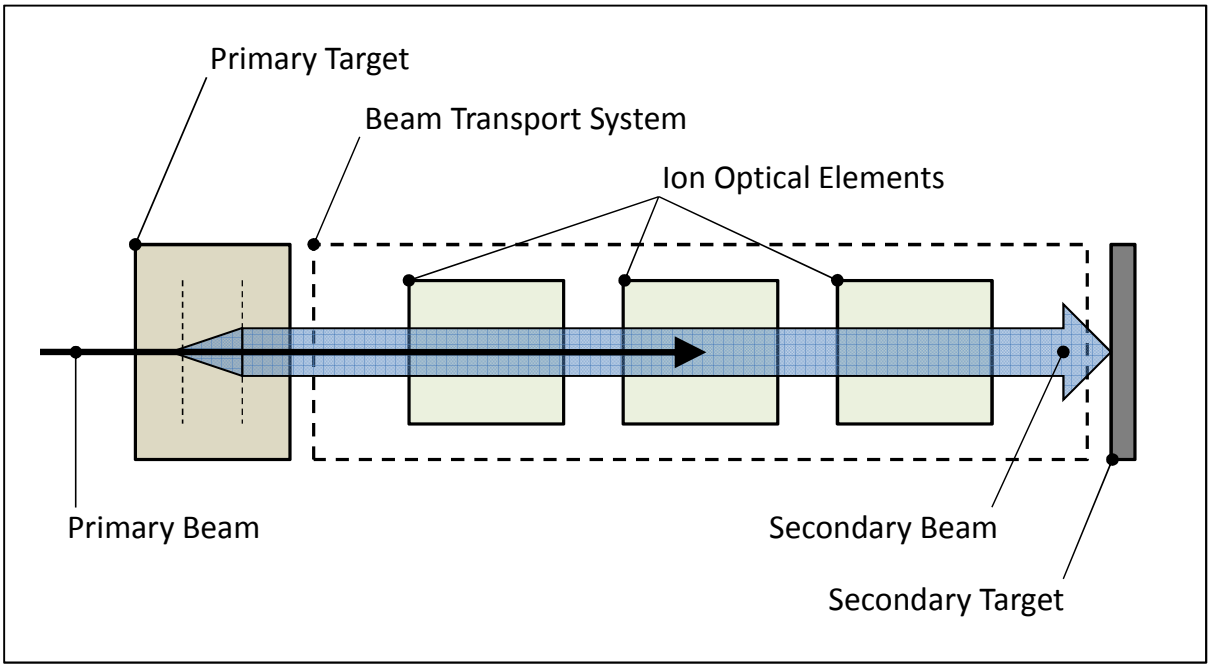

Fig. 1.8. Schematic representation of the in-flight separation technique.

When the primary beam of heavy ions impinges a low-mass target, the energies of the reaction products and of the incident ions are usually comparable. In this kind of facility the beam transport system represent a fundamental element: it has to provide an efficient mechanism for suppressing the intense primary beam transmitted through the primary target and in the same time to guarantee an high quality secondary beam transportation. An example of secondary radioactive ion beam obtained using the in-flight separation technique is ^{17}F: it can be produced starting from ^{16}O or ^{17}O beams; in this case the principal contaminants of the ^{17}F beam (to be suppressed by the beam transport system) are energy-degraded primary beam particles, i.e., ^{16}O or ^{17}O ions. The in-flight separation technique is able to provide isotopes close to stability without limitations due to lifetimes or chemical properties; it allows also for an easy variation of the energy of the reaction products within a certain range and can be implemented in existing heavy-ion accelerators. On the other side the main disadvantages are the low beam quality and the low number of ion species that can be produced.

1.3.2. The isotope separation on line (ISOL) technique [7]

According to the ISOL technique the radioactive isotopes are produced in a target and thermalized in a catcher consisting of solid, liquid or gas material (often the target and the catcher are the same object). These radioactive isotopes are then transported from the target/catcher to the ion source and ionized; once ionized they can be extracted, selected/analysed using a dipole magnet and subsequently accelerated to the required energy. The whole production sequence must be:

- **Efficient.** The production of the very exotic nuclei in the target is always marginal; to avoid to lose these few precious nuclei, any manipulation step (ionization, purification, acceleration, transport to the detection system) has to be very efficient.
- **Fast.** If the species of interest are short lived exotic nuclei, the losses due to radioactive decay between the moment of production and the arrival at the experimental set-up should be kept to a minimum.
- **Selective.** In the nuclear reaction process the unwanted – in general more stable – nuclei are produced much more abundantly; moreover ISOL systems often produce beams of isotopes from the target material itself or from other components of the target – ion source system. As a consequence the separation process should distinguish between the wanted and the unwanted species with efficacy. One defines the unwanted species as contaminants which, if they are characterized by the same mass-over-charge ratio respect to the ions of interest, are called isobaric.

Moreover an high production rate has to be guaranteed; once chosen the target material, the type and the energy of the primary beam in order to determine the production of the desired isotopes, to improve the production rate the highest primary beam intensities have to be delivered, compatibly with the capability of the target to dissipate the power due to the primary beam action.

In figure 1.9 the basic ingredients of an ISOL facility are presented; they represent the following fundamental and characteristic steps of the ISOL technique: production, thermalization, ionization, extraction, mass separation, cooling, charge-state breeding and acceleration. These steps are governed by physical and chemical processes, as a consequence both physical (production cross section, decay – half life, ionization potential, …) and chemical (molecular formation probability, volatility, …) properties of the nuclei of interest and of the target materials adopted are important. It will be discussed in the following paragraphs and chapters how these properties are used to obtain the necessary efficiency and selectivity, and to reduce the delay time. The “delay time” is defined as the average time the radioactive atoms spend from the moment of production to the moment of arrival at the experimental position. Even if all items represented in figure 1 are shown separately, it does not mean that every item represents one mechanical unit: some of the ingredients are

embedded in a single unit but for the clarity of the discussion the items of interest are presented and described as follows.

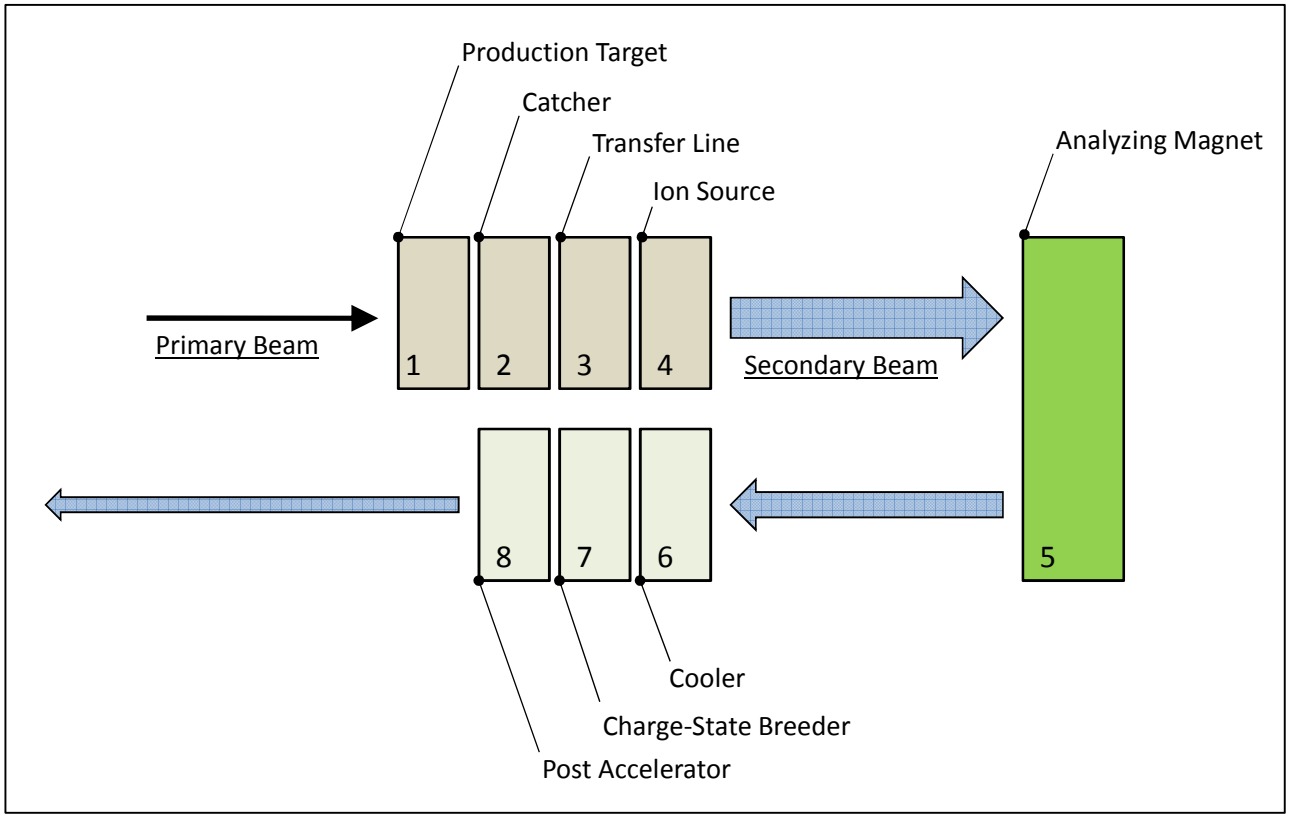

Fig. 1.9. Schematic representation of an ISOL facility.

1. PRODUCTION TARGET. A beam of light (for example *protons*) or heavy (for example ^{58}Ni) ions, electrons or neutrons hits a target to produce the desired radioactive ion beams according to different reaction mechanism (see chapter 3 for more details). In order to be clear we denote the former beam as **primary beam** and the latter as **secondary beam** (see figure 1.9). In some cases a converter is used to transform for instance a primary beam of protons or electrons into a flux of neutrons or γ rays, respectively. This flux is then sent onto the target inducing the nuclear reactions of interest. In choosing the target it is fundamental to optimize the beam-target combination with respect to the highest production cross-section and the lowest amount of contaminants, and to use target material that is able to stand the highest possible beam currents.

2. CATCHER. In some cases the target and the catcher are the same thing; the catcher can be solid or gaseous and is used to stop the exotic nuclei once they are produced by nuclear reactions. The word “thermalized” is often used instead of “stopped” to indicate that the radioactive atoms are cooled down from about 200 MeV , the kinetic energy in case of a fission reaction, to ~300 meV, that is the average kinetic energy corresponding to a catcher temperature of 2000°C. After thermalization a part of the radioactive nuclei of interest is able to escape from the catcher and to

reach the ion source passing through the transfer line (see the following paragraphs). In case of a solid catcher , the diffusion of the radioactive atoms from the target/catcher material is followed by effusion towards the ion source. The diffusion process is governed by the diffusion properties of the atoms of interest and of the target/catcher matrix. In the case of target/catcher constituted by carbide materials, the effusion process starts when the radioactive atoms reach the external surfaces of the material grains and continues inside the pores of the target/catcher material and among the external walls of the target/catcher, the internal walls of the target/catcher's container and the internal surfaces of the transfer line, until the radioactive atoms reach the ion source. The effusion process depends essentially by the following parameters:

- the average number of collisions "ω"
- the average time the atom stops on the wall during a collision (sticking time) "τ_s"
- the average time of flight between two collisions (flight time) "τ_f".

If the sticking time is long compared to the diffusion time of the atom inside the wall material, it will diffuse and eventually disappear in the walls. To reduce the loss of nuclei the speed of the aforementioned processes is often increased by heating the target/catcher system, the transfer line and the ion source to a suitable (usually very high) temperature. In case of a gaseous catcher the radioactive atoms of interest stay in the gas phase and there is no need for high temperature systems.

3. TRANSFER LINE. Through the transfer line the radioactive atoms are transported from the target/catcher to the ion source by effusion. The transfer line is kept generally at high temperatures to avoid loss of radioactive atoms on its walls.

4. ION SOURCE. Depending on the particular requirements, several different ionization mechanisms are used to transform the radioactive atoms into radioactive ions. In general singly charged positive or negative ions are produced. In a few cases multiply charged ions are produced as well. In literature all the above mentioned parts (**production target**, **catcher**, **transfer line** and **ion source**) are commonly named as the **target - ion source system**. To allow the acceleration/extraction of the radioactive ions the ion source is put on a positive (in case of beams of positively charged ions) or negative (negatively charged ions) high voltage of typical values between 40 and 60 kV.

5. ANALYZING MAGNET. Once extracted from the ion source the low energy ion beam is mass separated by an analyzing magnet and transported to the focal plan where it can be opportunely focalized. An important property that express the quality of the system is the mass resolving power, defined as $R = M/\Delta M$, where ΔM is the *full width at half maximum* (in a function that describes a

peak, it is the difference between the two extreme values of the independent variable at which the function is equal to half of its maximum value) of a beam of ions with mass M in the focal plane of the separator. High resolution indicates better peak separation. The resolving power depends on the properties of the magnet and on the ion optical properties of the ion beam. Typical values for ISOL systems vary from a few hundred to a few thousand.

6. COOLER. A "cooler" is used to improve the optical properties of the ion beam and to bunch it. The bunching of the ion beam is often required to increase the peak to background ratio of certain experiments like laser spectroscopy experiments or to inject the beam into a charge-state breeder. In general two kinds of machine are used for cooling and bunching: "Penning traps" and "radio frequency (RF) coolers". The former is based on the storage of ions using a combination of magnetic and electrical fields, the latter using electrical DC (Direct Current) and RF (Radio Frequency) fields. Efficiencies, defined as the beam intensity of the cooled beam versus that of the injected beam, over 50% have been reached.

7. CHARGE-STATE BREEDER. The simplicity, efficiency and cost of the post-accelerator are directly related to the charge-state of the ions: in this context it is useful to produce a multiple charge state ion beam before the injection into the post-accelerator. To do it a charge-state breeder is used: it performs the transformation from a singly charged ion beam into a multiple charged one. Two types of charge-state breeding ion sources are used: the Electron Beam Ion Source (EBIS) and the Electron Cyclotron Resonance (ECR) ion source. Both rely on the principle of intense bombardment of the ions with energetic electrons, with electron impact ionization yielding ions in higher charge states. The plasma of ions and electrons is confined through electrical and strong magnetic fields.

8. POST ACCELERATOR. The highly charged ion beam from the charge-state breeder or the beam of singly charged ions is then injected into the post-accelerator. After the post-acceleration step the beam is sent to the experimental areas where the aforementioned topics are studied.

Once presented the fundamental components of an ISOL facility, it is important to introduce some general notions about its functioning. The intensity ($I_{\text{reaction-products}}$) of the reaction products synthesized in the target is calculated using the following equation,

$$I_{\text{reaction-products}} = \sigma N_{\text{target}} \Phi \quad (1)$$

where,

- σ is the cross-section (cm^2), often expressed in units of barns, mbarns or μbarns, with 1 barn = $10^{-24} cm^2$

- N_{target} is the number of target atoms per surface area (cm^{-2})
- Φ is the primary beam intensity.

Since the cross section is energy dependent and the primary beam looses energy while passing through the target, the intensity has to be calculated by integrating over the target thickness taking into account the energy loss of the beam.

Because of all the aforementioned steps needed to produce radioactive ion beams, the final intensity of the secondary beam (I) will be reduced respect to $I_{reaction\text{-}products}$ as follows:

$$I = I_{reaction\text{-}products}\, \varepsilon = \sigma\, N_{target}\, \Phi\, \varepsilon \qquad (2)$$

with ε being the efficiency of the whole process; it is defined as the ratio of the final secondary beam intensity that arrives at the experimental set-up (I) versus the intensity of the reaction products ($I_{reaction\text{-}products}$). It is a product of a series of partial efficiencies,

$$\varepsilon = \varepsilon_{delay}\, \varepsilon_{ion}\, \varepsilon_{trans}\, \varepsilon_{cool\text{-}bunch}\, \varepsilon_{breeding}\, \varepsilon_{post\text{-}acceleration} \qquad (2)$$

where,

- ε_{delay} is the probability of survival against radioactive decay during the time needed to extract the ion from the target-ion source system
- ε_{ion} is the ionization efficiency
- ε_{trans} is the efficiency of mass analysis and transport to the experimental set-up
- $\varepsilon_{cool\text{-}bunch}$ is the cooling and bunching efficiency
- $\varepsilon_{breeding}$ is the charge-state breeding efficiency
- $\varepsilon_{post\text{-}acceleration}$ is the efficiency of the post-accelerator.

The component ε_{delay} expresses the relative amount of ions that survive, in spite of their radioactive decay, the time elapsed from the moment of their production to the moment of their extraction from the ion source. This amount of time is often called **release time** since in case of solid and liquid catcher systems it is determined by the diffusion from the target/catcher material and the effusion to the ion source exit hole. In case of gaseous catcher the term “release time” is replaced by “**delay time**”; it is determined by the gas flow and, in case electrical fields are used to obtain a faster evacuation of the gas cell, the mobility of the ions. Once the radioactive isotopes become radioactive ions in the ion source, they are extracted by means of electrostatic fields, forming a radioactive ion beam; at this point mass separation and transport goes fast compared to the delay time and half life of the nuclei and no significant losses are expected. If cooling and bunching are involved an extra loss factor due to radioactive decay might occur. It is thus clear that ε_{delay} will strongly depend on the half life of the exotic nucleus of interest.

1.4. The SPES project at LNL: Selective Production of Exotic Species [8]

The facility proposed for the SPES project has two main goals: to provide a radioactive ion beam accelerator system to perform forefront research in nuclear physics by studying nuclei far from stability and to develop an accelerator based interdisciplinary research centre. The SPES project is concentrating on the production of neutron-rich radioactive nuclei with mass in the range 80-160 by the ^{238}U fission at a rate of 10^{13} fission/s. The emphasis to neutron-rich isotopes was explained and justified in the previous paragraphs. Radioactive ion beams will be produced according to the ISOL technique, using the proton induced fission on a direct target of UCx (Uranium Carbide). The primary beam (proton beam) is furnished by a Cyclotron with variable energy (15-70MeV) and a maximum current of 0.750 mA upgradeable to 1.5 mA and splitted on two exit ports.

The SPES facility is designed to supply a second generation of exotic beams able to perform a step toward EURISOL (European ISOL Facility) and to offer a powerful accelerator based system for research in applied physics, nuclear astrophysics, solid-state physics and nuclear medicine (see paragraph 1.2). An overview of the SPES facility is presented in figure 1.10.

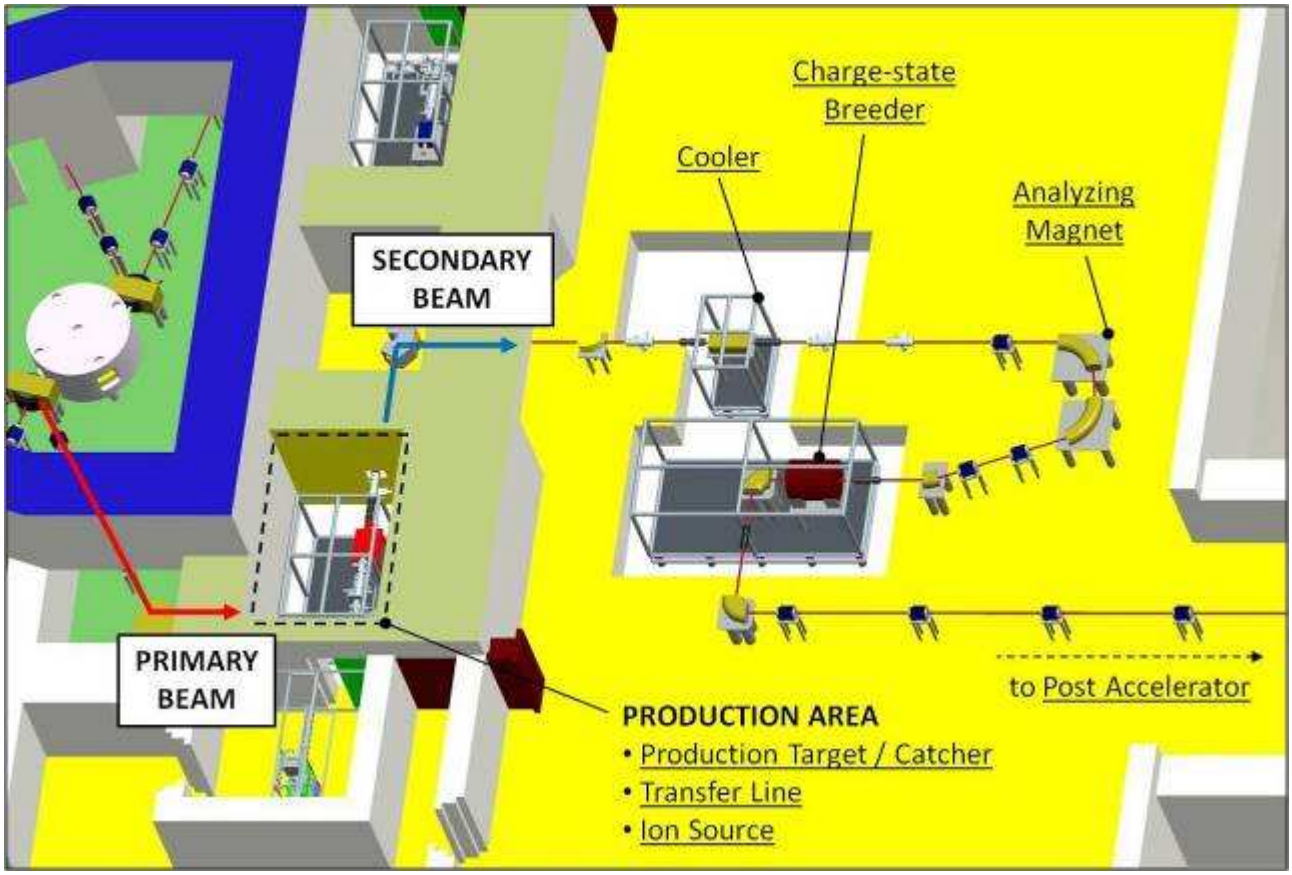

Fig. 1.10. General overview of the SPES facility.

The most critical element of the SPES project is the production target; it represents an innovation in terms of capability to sustain the primary beam power. The design is carefully oriented to optimise cooling by thermal radiation taking advantage of the high operating temperature of approximately 2000°C. An extensive simulation activity has been performed to study the target thermal behaviour [9] and its release properties. Experimental work to benchmark simulations was carried out at HRIBF, the Oak Ridge National Laboratory ISOL facility (USA) [10]. The production target and all the experimental apparatus needed to guarantee its functioning will be designed following the ISOLDE (CERN, Switzerland), the HRIBF (ORNL, USA) and the EXCYT (INFN, LNS, Italy) projects and special care will be devoted to the safety and radioprotection of the system. According to the estimated level of activation in the production area a special infrastructure will be designed; the use of up-to-date techniques of nuclear engineering will result in a high safety level of the installation.

The isotopes will be extracted and ionized at +1 charge state with an ion source connected with the production target by means of an opportunely designed transfer line. Different kinds of ion sources will be used to obtain all the radioactive ion beams of interest. Laser ionization will be implemented in collaboration with the INFN section of Pavia with the aim to produce extremely pure beams.

The transport and the selection of the exotic beam at low energy and low intensity is a challenging task. A cooler and an high resolution analyzing magnet will be placed in series along the beam line after the extraction of the ions from the ion source to improve the optical quality of the beam and to perform an accurate mass selection, respectively. To optimize the post acceleration, a charge breeder will be introduced: it will increase the charge state to +N before injecting the exotic beam in the PIAVE Superconductive RFQ which represents the first reacceleration stage before the injection into the linear accelerator ALPI (see figure 1.11). The proper velocity matching needed to enter PIAVE will be furnished by High Voltage platforms operating approximately at 250kV. The expected beam on experimental target will have a rate on the order of 10^8-10^9 pps (particles per second) for ^{132}Sn, ^{90}Kr, ^{94}Kr and 10^7-10^8 pps for ^{134}Sn, ^{95}Kr with energies of 9-13 MeV/u.

An important aspect of the SPES project is surely its network of collaborations with regional, national and international institutes. Taking as reference figure 1.12 we underline the important R&D activities developed in collaboration with the Universities of Padua, Vicenza, Trento and Pavia.

Fig. 1.11. Some details of the linear accelerator ALPI.

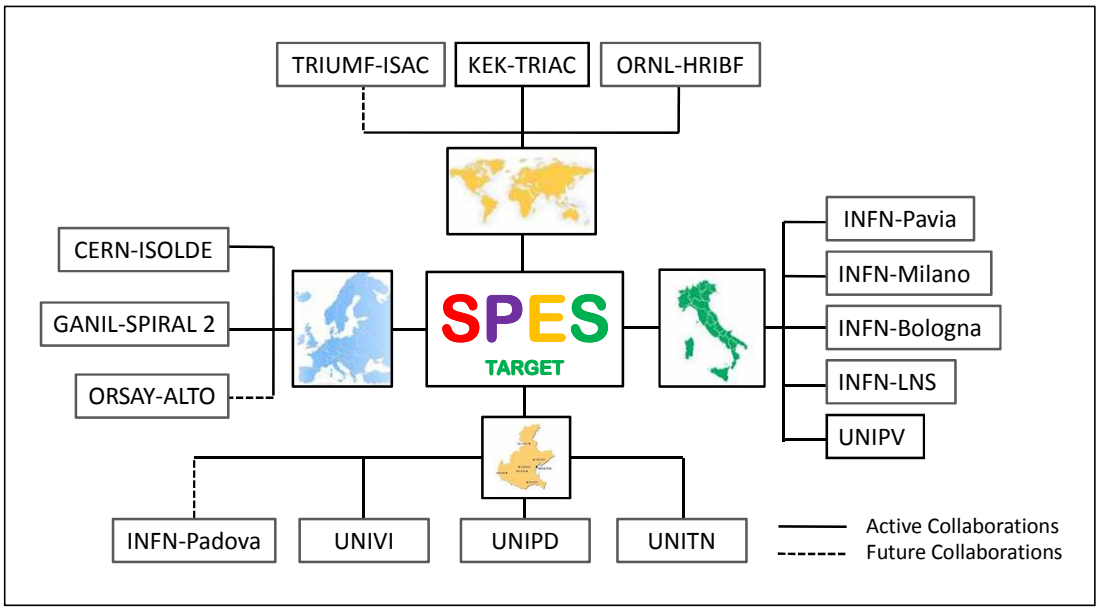

Fig. 1.12. The collaboration networks of the SPES project.

Contributions for the construction of the experimental apparatus needed for the off-line (without primary beam) tests of the SPES production target and ion sources are given by the INFN sections of Pavia, Milano and Bologna. The official international collaboration with the ISOLDE facility at CERN (Switzerland) is fundamental for the design and construction of the SPES

production target, ion sources and all the auxiliary experimental apparatus: the ISOLDE experience in the production of RIBs is well known all over the world. Another important network to evidence is the collaboration with the Oak Ridge National Laboratories (ORNL, USA): at ORNL two prototypes of the SPES target were tested on-line with a primary proton beam in 2007 and in 2010.

1.5. Conclusions

In this chapter a general overview of the SPES project and its scientific context was presented. Some aspects of research in nuclear physics with RIBs were illustrated, together with some important applications of exotic beams in solid-state physics and nuclear medicine. A detailed description of the main components constituting an ISOL facility was furnished in the sub-paragraph 1.3.2 and a parallel general presentation of the main components of the SPES facility was reported at the end of the chapter. In the next chapter the production area of the SPES facility (see figure 1.10) will be described in detail.

REFERENCES

[1] http://www.eurisol.org

[2] A. Andrighetto, C.M. Antonucci, S. Cevolani, C. Petrovich, M. Santana Leitner, Multifoil UCx target for the SPES project – An update, Eur. Phys. J. A 30 (2006) 591-601.

[3] A. Andrighetto, S. Cevolani, C. Petrovich, Fission fragment production from uranium carbide disc targets, Eur. Phys. J. A 25 (2005) 41-47.

[4] J. Al-Khalili, E. Roeckl, The Euroschool Lectures on Physics with Exotic Beams, vol.1, Springer, Berlin, 2006.

[5] http://www.wikipedia.org/

[6] B. Harss et al., Production of radioactive ion beam using the in-flight technique, Rev. Sci. Instrum. 71 (2000) 380-387.

[7] J. Al-Khalili, E. Roeckl, The Euroschool Lectures on Physics with Exotic Beams, vol.2, Springer, Berlin, 2006.

[8] http://www.lnl.infn.it/

[9] M. Manzolaro, Master's Degree Thesis, University of Padua, Department of Mechanical Engineering, Italy, 2007, unpublished.

[10] M. Barbui et al., Calculations and first results obtained with a SiC prototype of the SPES direct target, Nucl. Instrum. Methods Phys. Res., Sect. B 266 (2008) 4289-4293.

Chapter 2

The SPES production area

2.1. Introduction

In the previous chapter a brief presentation of the SPES facility was given; its more critical part is surely the production area, where the primary proton beam (PPB) is converted into a radioactive ion beam (RIB). The SPES production area is constituted by the production target (that with the transfer line composes the target block), the ion source (in this chapter we will take into consideration the surface ion source or hot-cavity ion source, see chapter 4 for more details) and all the experimental apparatus needed for their functioning that is the target chamber and the front end (see figure 2.1).

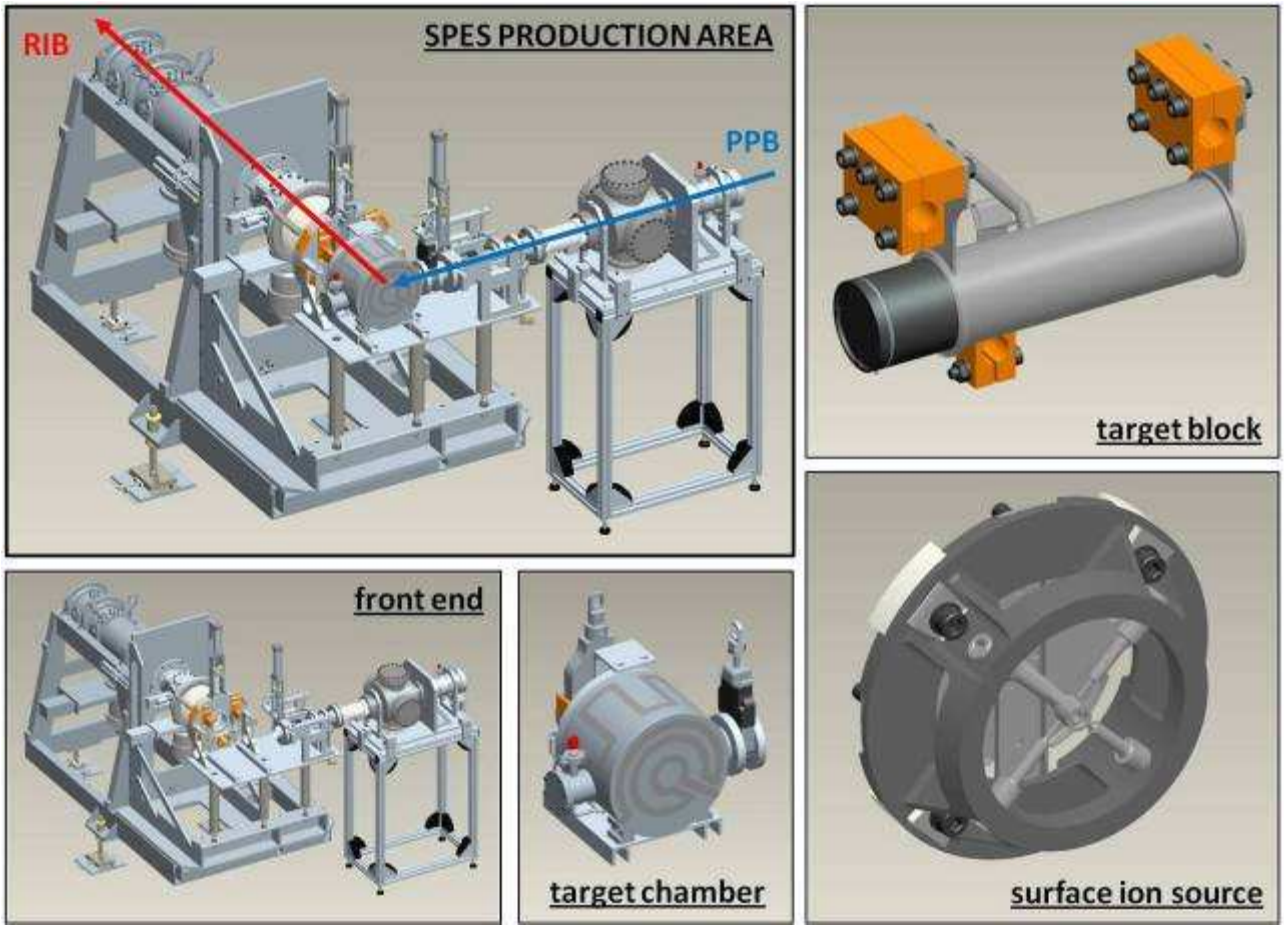

Fig. 2.1. The SPES production area and its main components.

In the following the macro-components composing the SPES production area will be presented; we clarify that a macro-component is a mechanical assembly characterized by a well-defined function in the context of the SPES facility. The front end and the target chamber, that will not be

studied with dedicated sections in the next chapters, will be described in detail in the next paragraphs.

2.2. The macro-component “front end”

The SPES front end is a sophisticated experimental apparatus whose construction was based on the experience of important European ISOL facilities; its main functions are:

- to guarantee a stable positioning of the target chamber containing both the target block and the surface ion source (see figure 2.1)
- to provide high vacuum inside the target chamber, water to cool it down and electrical power to heat by Joule effect both the target block and the surface ion source
- to allow the entrance of the primary proton beam (PPB) directed to the target block
- to extract the radioactive ion beam (RIB) from the “target block – surface ion source” complex and accelerate it to the subsequent areas of the facility
- to provide high vacuum both in the primary proton beam and in the radioactive ion beam channels

The front end used in the context of the SPES project is an evolution of the front end 6 (see figure 2.2) developed at ISOLDE (CERN) [1]. Respect to its precursor in the SPES front end a channel kept under high vacuum was added to allow the entrance of the primary proton beam: in fact respect to the ISOLDE facility in the SPES one the energy of the proton beam is sensibly lower (40 MeV respect to the energy level of approximately 1 GeV that characterizes the ISOLDE proton beam) and consequently it cannot impinge the target passing through air.

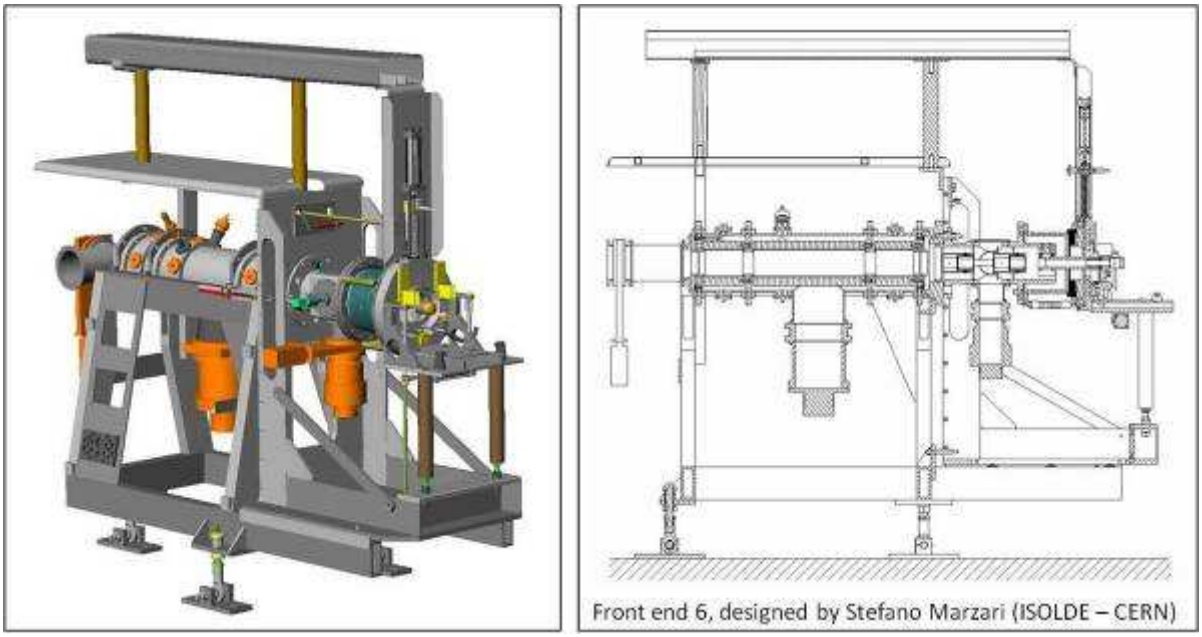

Fig. 2.2. The front end 6 developed at ISOLDE (CERN).

The first thing that is important to notice in the front end architecture is that it is composed of two big channels kept under vacuum: the channel for the primary proton beam entrance (PPB channel) and the channel for the radioactive ion beam extraction (RIB channel) (see figure 2.3).

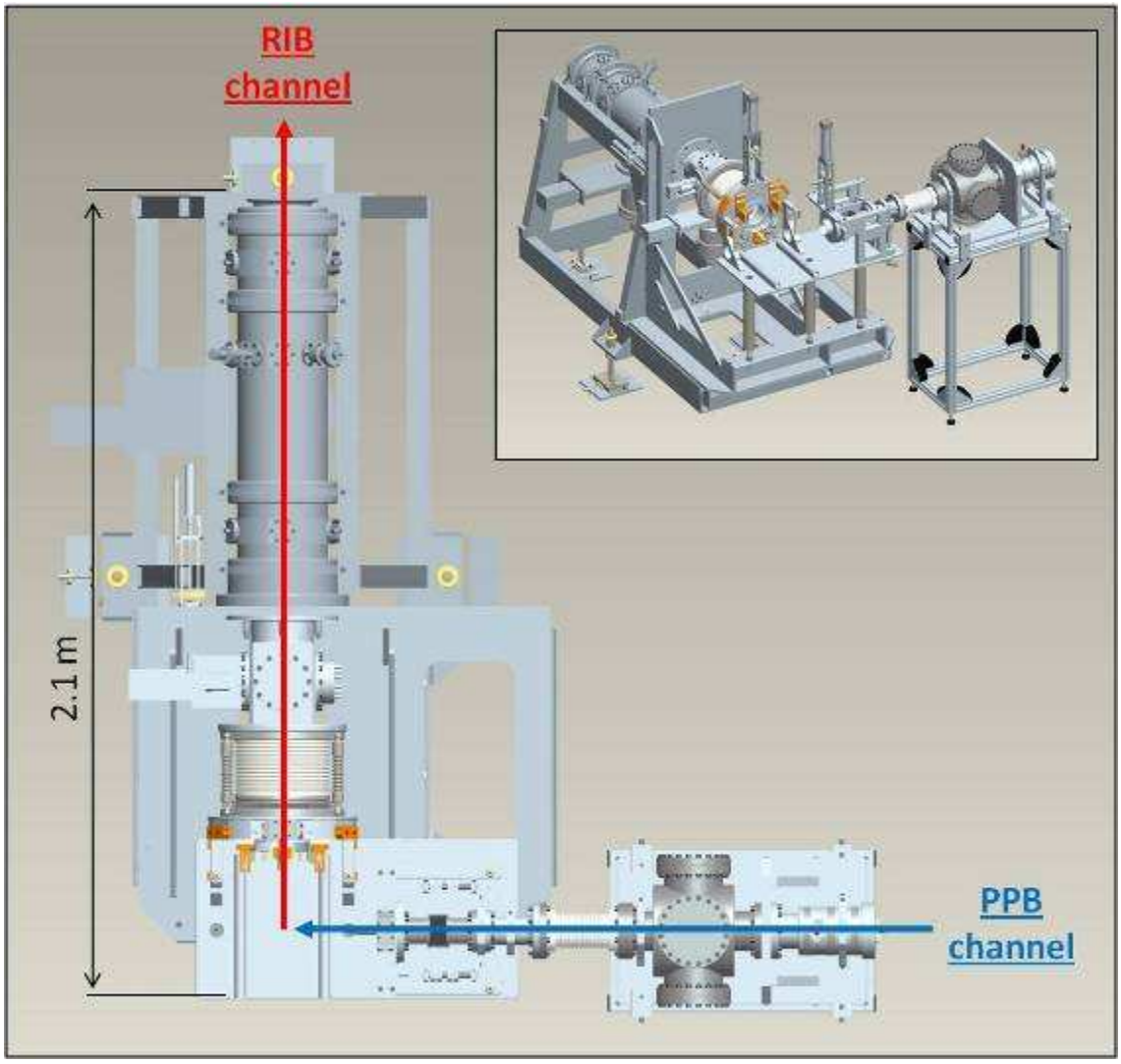

Fig. 2.3. The primary proton beam (PPB) channel and the radioactive ion beam (RIB) channel of the SPES front end.

Then, with the aim to support maintenance operations, the front end general assembly, indicated by the code *ST_FE000* (according to the codification scheme defined for the SPES project), was divided in two portions: the removable part (subassembly *ST_FE200*) and the fixed part (subassemblies *ST_FE100* and *ST_FE300*) (see figure 2.4). The former, lying close to the target block, receives a big dose of radiation whereas the latter is more distant and its absorbed dose is sensibly lower; as a consequence subassembly *ST_FE200* needs to be removed approximately every seven years because of material degradation while the subassemblies *ST_FE100* and *ST_FE300* (constituting the fixed part of the front end) are not subjected to important damages due to radiations and can last much more time. The front end was accurately designed in order to allow an easy and fast removal of subassembly *ST_FE200*.

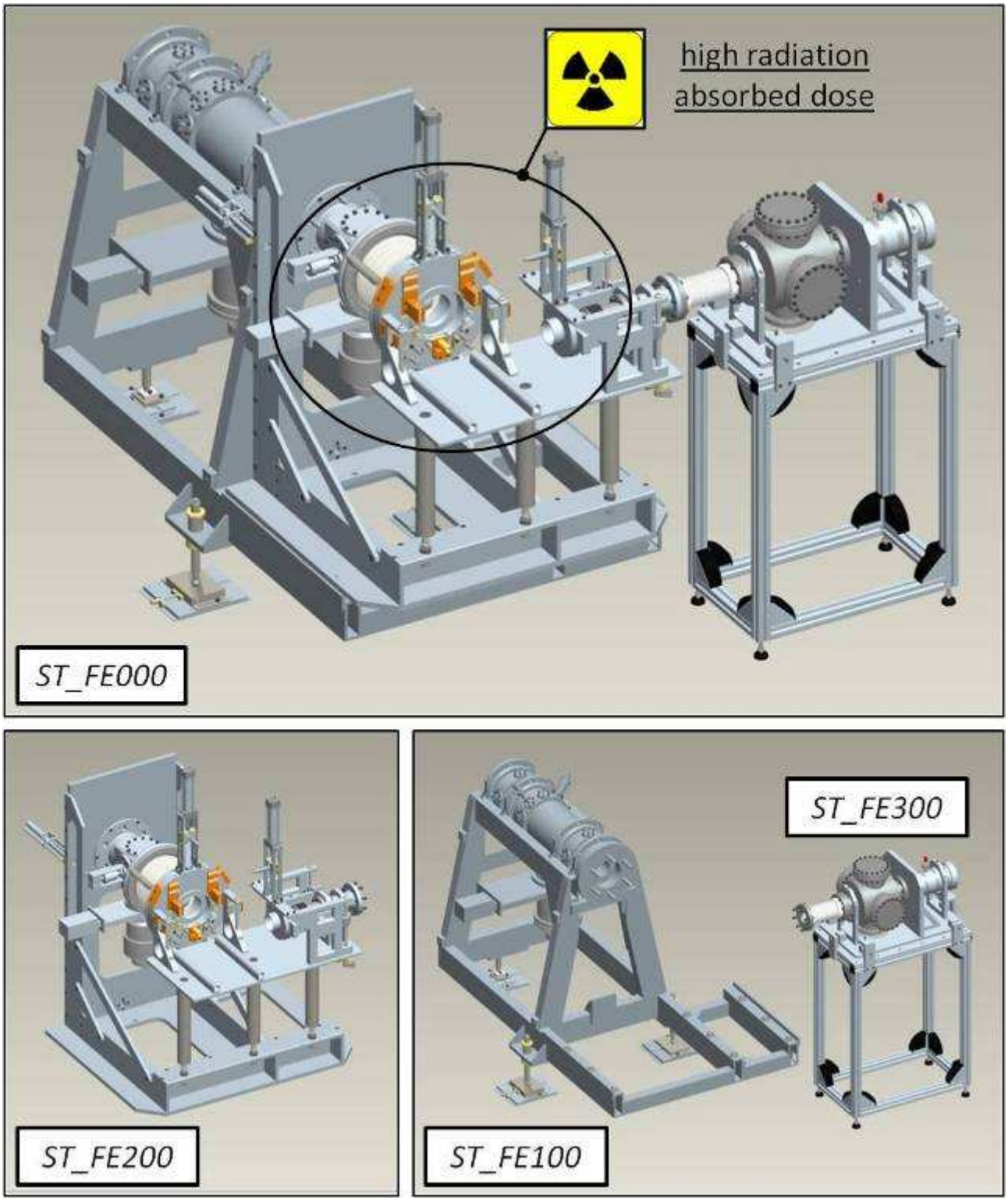

Fig. 2.4. The removable part (subassembly *ST_FE200*) and the fixed part (subassemblies *ST_FE100* and *ST_FE300*) of the SPES front end (*ST_FE000*).

The codes of the subassemblies composing the SPES front end are reported in figure 2.5. The following subparagraphs will be dedicated to present with detailed illustrations the subassemblies belonging to sublevels 1 and 2, remarking the correspondent specific functions.

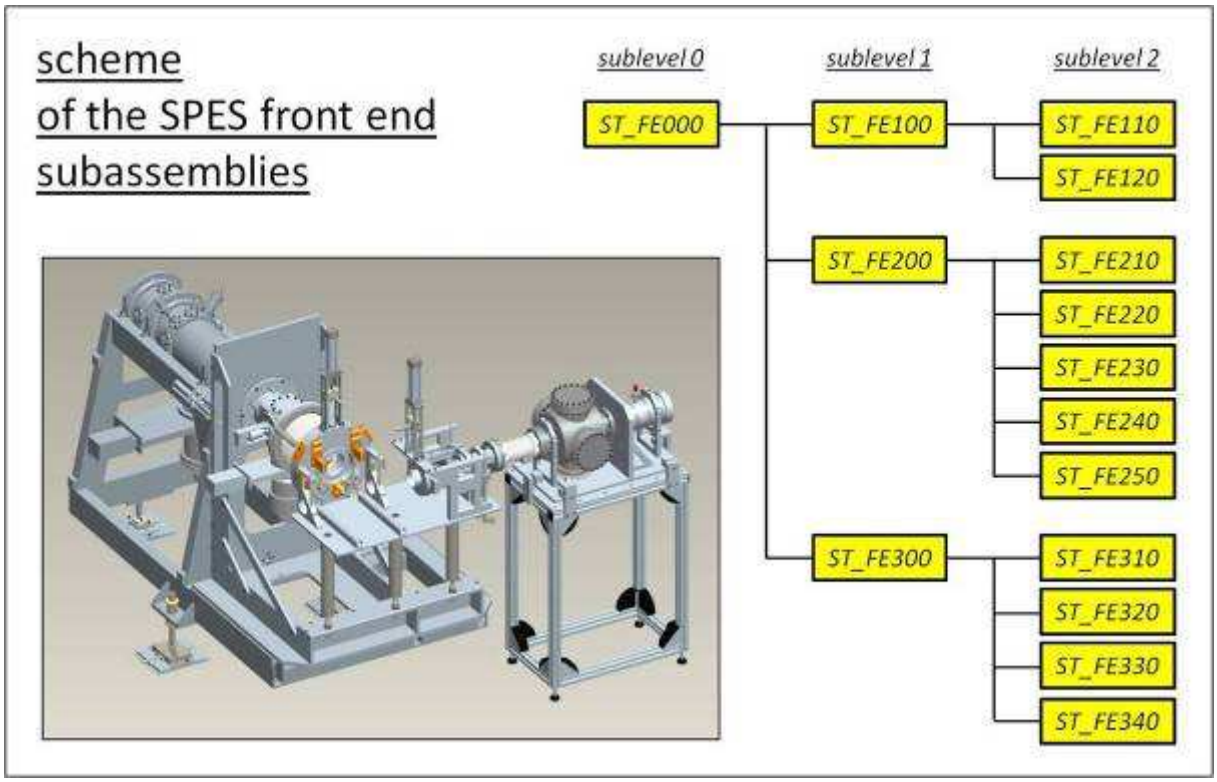

Fig. 2.5. The scheme of the SPES front end subassemblies according to the codification scheme defined for the SPES project.

2.2.1. The removable part of the SPES front end: the subassembly *ST_FE200* [2]

The removable part of the SPES front end is reported in figure 2.6; as explained in the previous paragraph this part of the front end lies very close to the production target and is subjected to an high radiation absorbed dose.

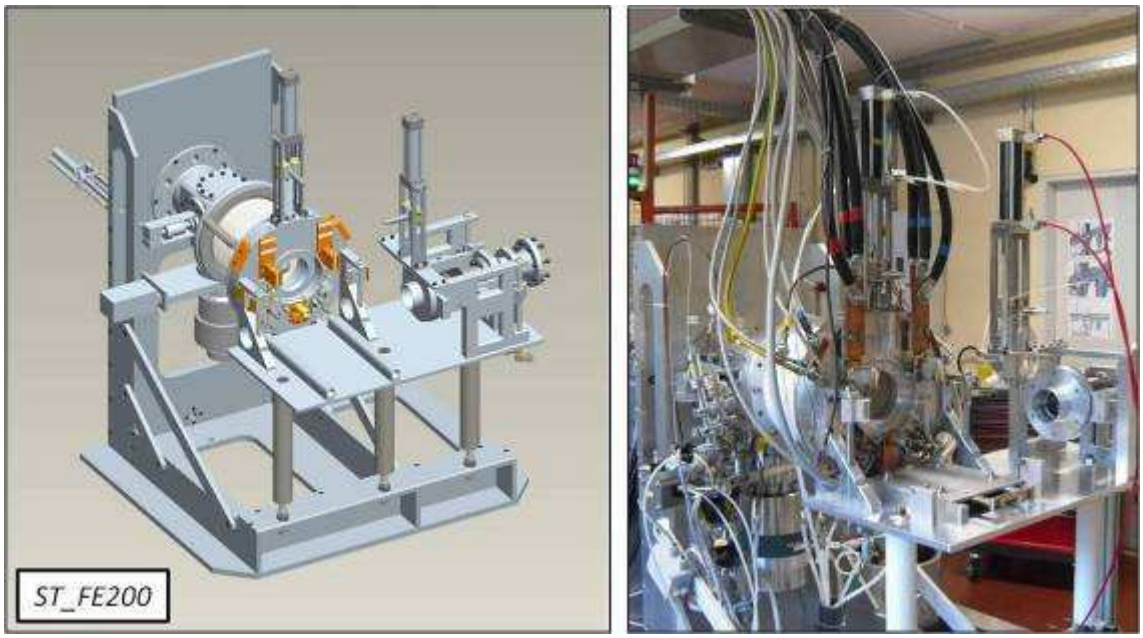

Fig. 2.6. The removable part (subassembly *ST_FE200*) of the SPES front end with a picture of the real object installed at Legnaro National Laboratories.

The subassemblies that compose the removable part of the front end (*ST_FE200*) are clearly reported in figure 2.5; the first in the list is the removable frame (*ST_FE210*): it is made of aluminium alloy and supports the entire removable part of the front end interfacing it with the fixed part of the experimental apparatus (see figure 2.7).

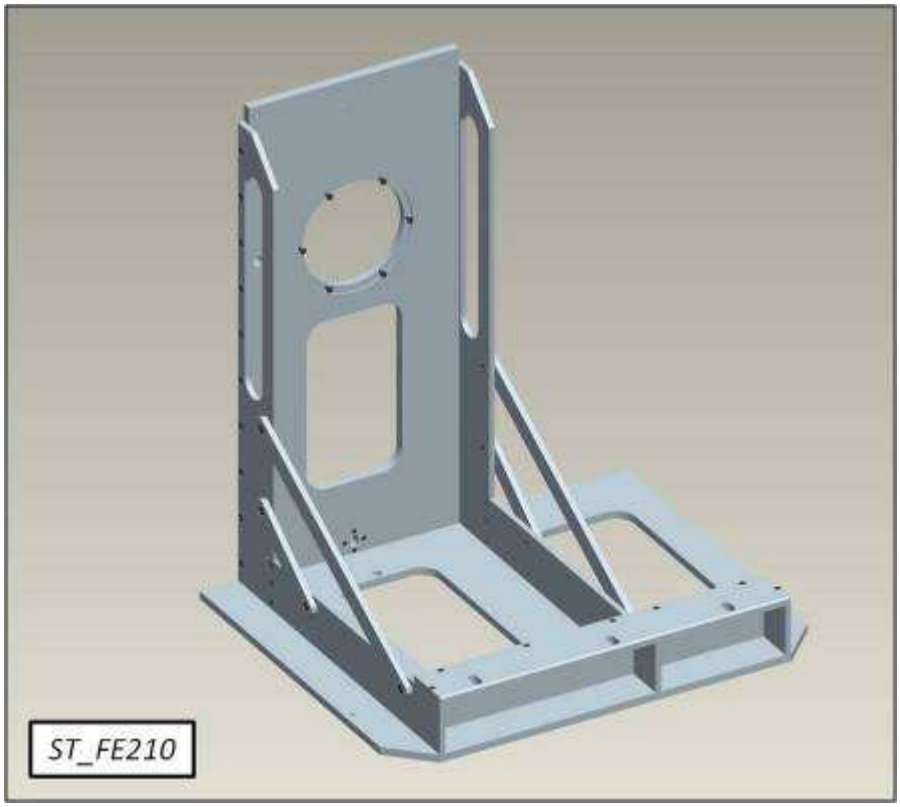

Fig. 2.7. The removable frame (*ST_FE210*).

The core of the front end's removable part is constituted by the extraction system (*ST_FE220*) shown in figure 2.8. The titanium alloy extraction electrode, moved by a dedicated handling system and characterized by a potential difference of -60 kV respect to the ion source, is used to extract the radioactive ion beam from the target – ion source complex. Taking as reference figure 2.9, when the experimental apparatus is ready for the beam extraction the shutter is lifted and the extraction electrode is translated close to the ion source; the electrical field due to the potential difference between the electrode and the ion source allows the acceleration of the positive ions from the ion source (characterized by a potential difference of +60 kV respect to the electrode) to the extraction electrode, generating in this way the positive ion beam. After the extraction electrode, the ion beam can be translated in the x and y directions (maximum translation equal to +/- 1.5 mm) thanks to a group of steerers (see figure 2.10): in particular using two pairs of metallic plates (the steerers) kept at a precise voltage level it is possible to correct electrostatically the beam trajectory in the x direction whereas other two pairs of plates are used correct in the same way (using calibrated voltage levels) the trajectory of the beam in the y direction.

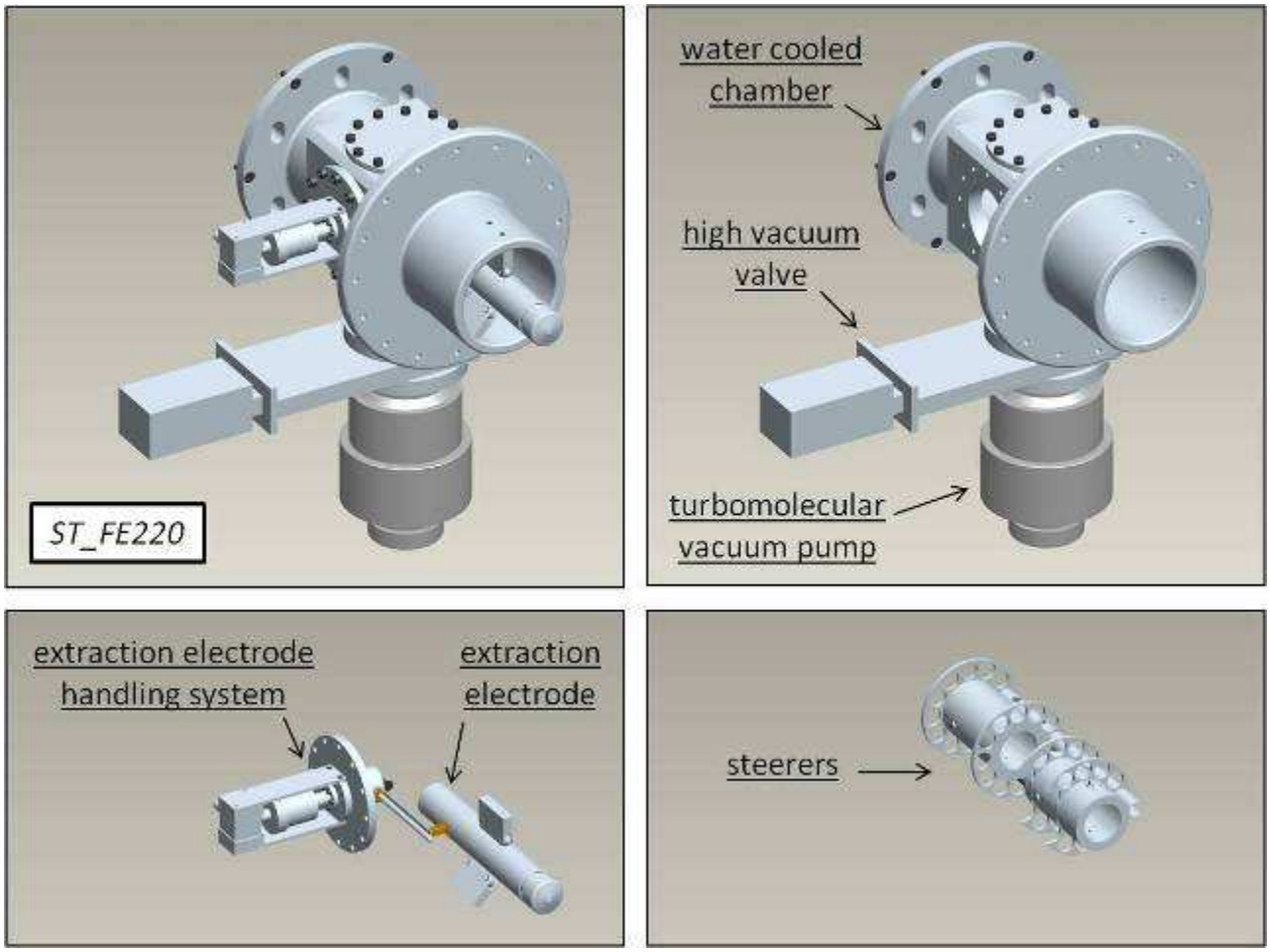

Fig. 2.8. The extraction system (*ST_FE220*).

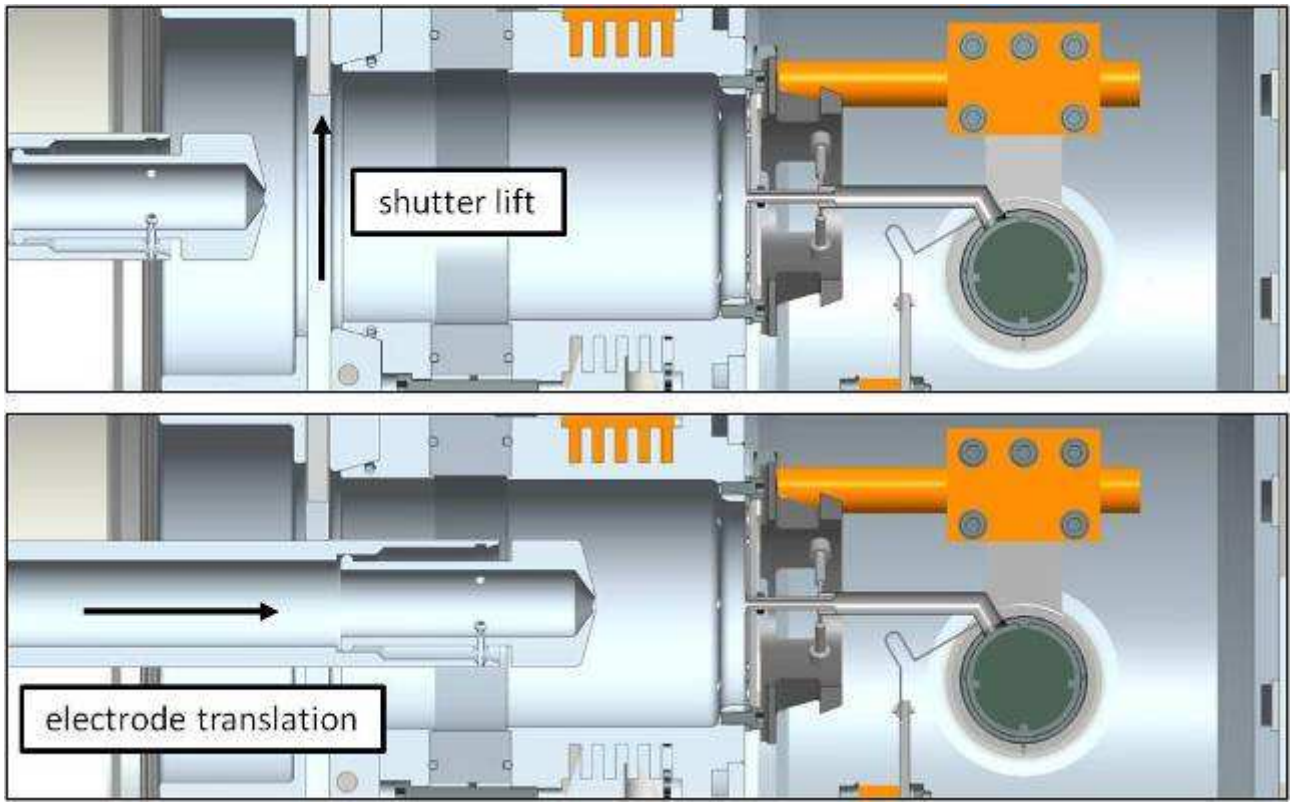

Fig. 2.9. Positioning of the electrode for the extraction of the positive ion beam.

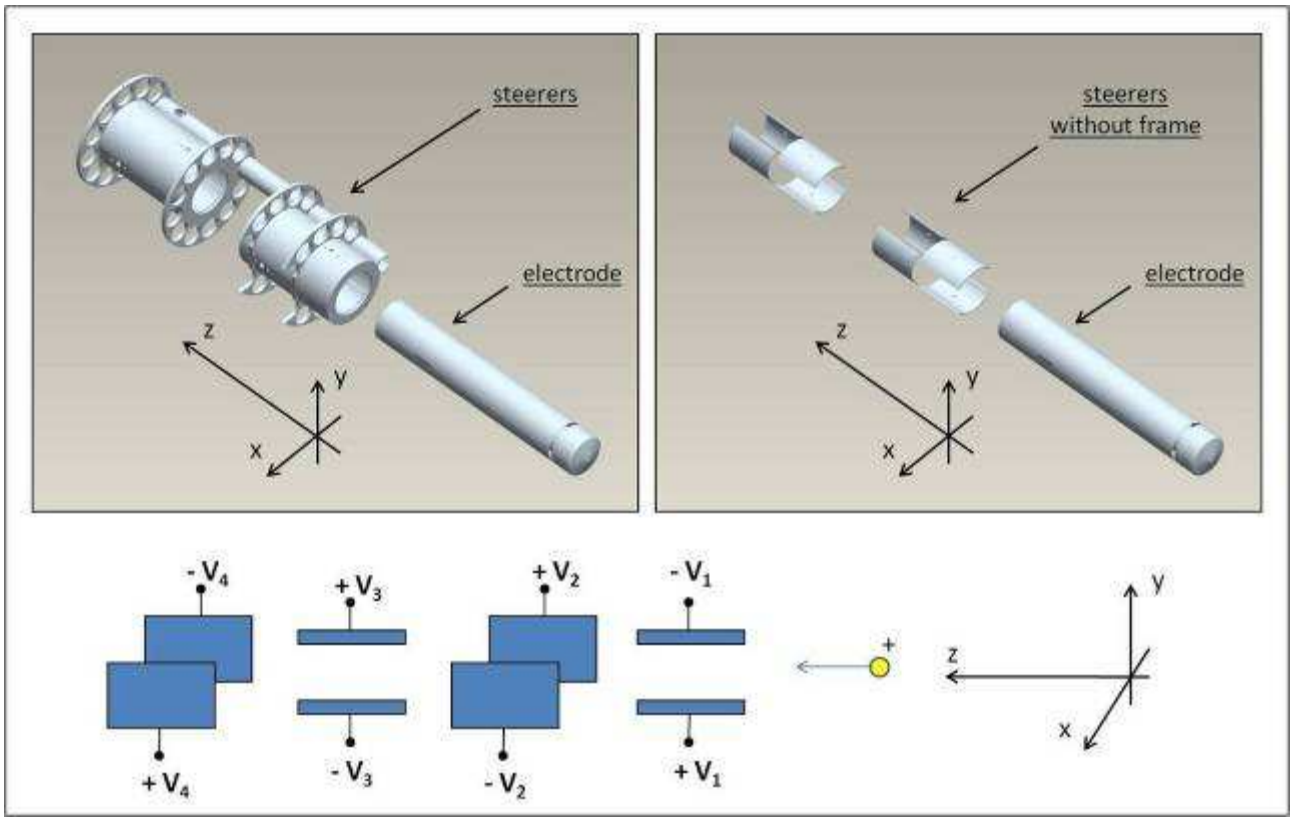

Fig. 2.10. The group of steerers positioned after the extraction electrode.

The steerers, the extraction electrode and a part of the electrode's handling system are positioned inside the water cooled chamber shown in figure 2.8: they are all kept under high vacuum thanks to a turbomolecular pump, a dedicated set of vacuum valves, o-rings and gaskets.

The pneumatic engine system (*ST_FE230*) used to move the extraction electrode is another important subassembly of the removable part of the SPES front end (see figure 2.5): the pneumatic engine and all the accessories needed for its functioning are presented in figure 2.11.

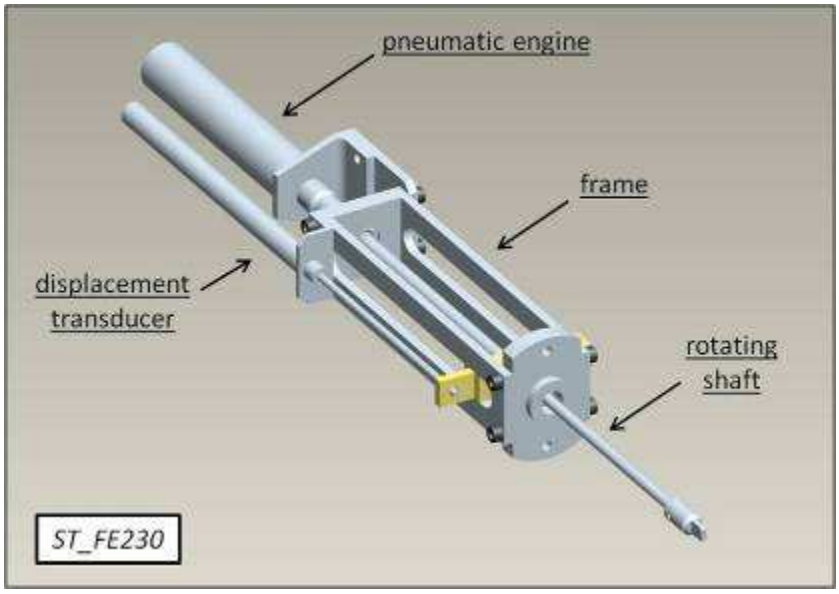

Fig. 2.11. The pneumatic engine system (*ST_FE230*).

The extremity of the rotating shaft represented in figure 2.11 is directly connected to the external part of the extraction electrode handling system (see figure 2.8): the rotation of the shaft is able to produce the translation of the electrode by means of the coupling between the threaded shaft (rotating) and the block with threaded hole (translating) reported in figure 2.12. The pneumatic engine was chosen for its high reliability in radioactive environments respect to the traditional electric engines.

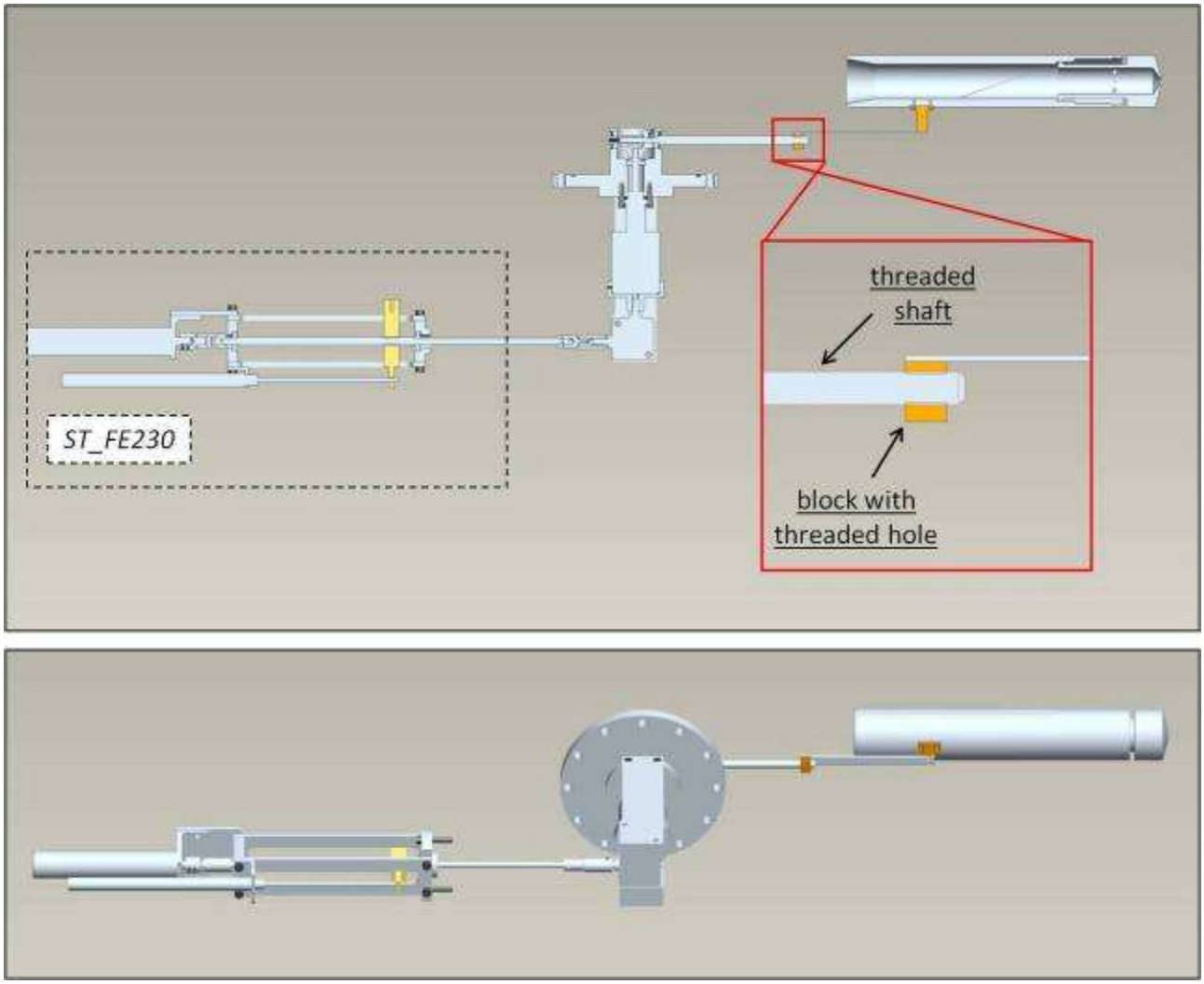

Fig. 2.12. The pneumatic engine system (*ST_FE230*) connected to the electrode handling system.

Figure 2.13 illustrates the main insulator (*ST_FE240*), used to keep the potential difference of 60 kV between the ion source and the extracting electrode; it is a very expensive component mainly because of the cost of the materials that compose it: in fact they have to resist in a radioactive environment preserving their mechanical properties and electrical insulation capabilities. The Al_2O_3 central insulator is brazed to a metallic bellow: the latter absorbs the vibrations and the shocks that could seriously damage the brittle Al_2O_3 part. Four peripheral PEEK insulators contribute to improve the strength and the stiffness of the system. The spherical articulations at the extremities of the peripheral PEEK insulators are used for fine mechanical adjustments during alignment

operations. The main insulator installed in the front end (with the electrode positioned to extract the radioactive ion beam) is shown in figure 2.14.

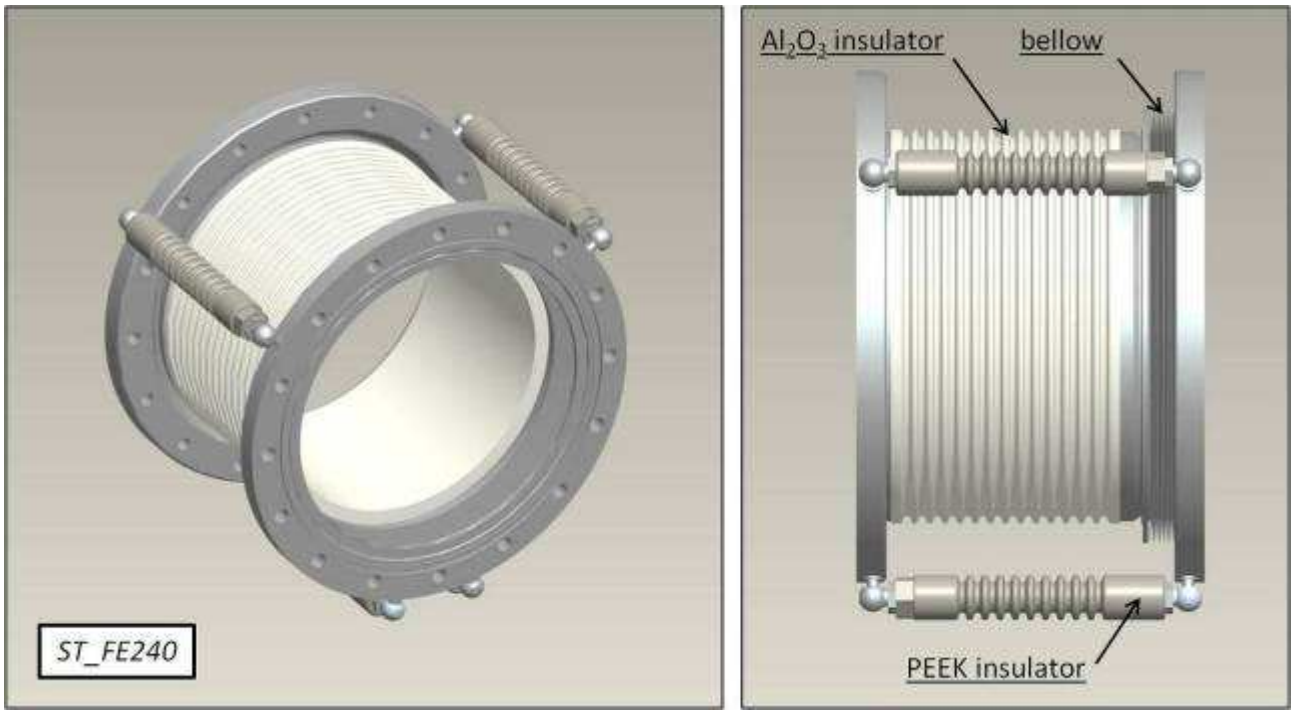

Fig. 2.13. The main insulator (*ST_FE240*) and its most important components.

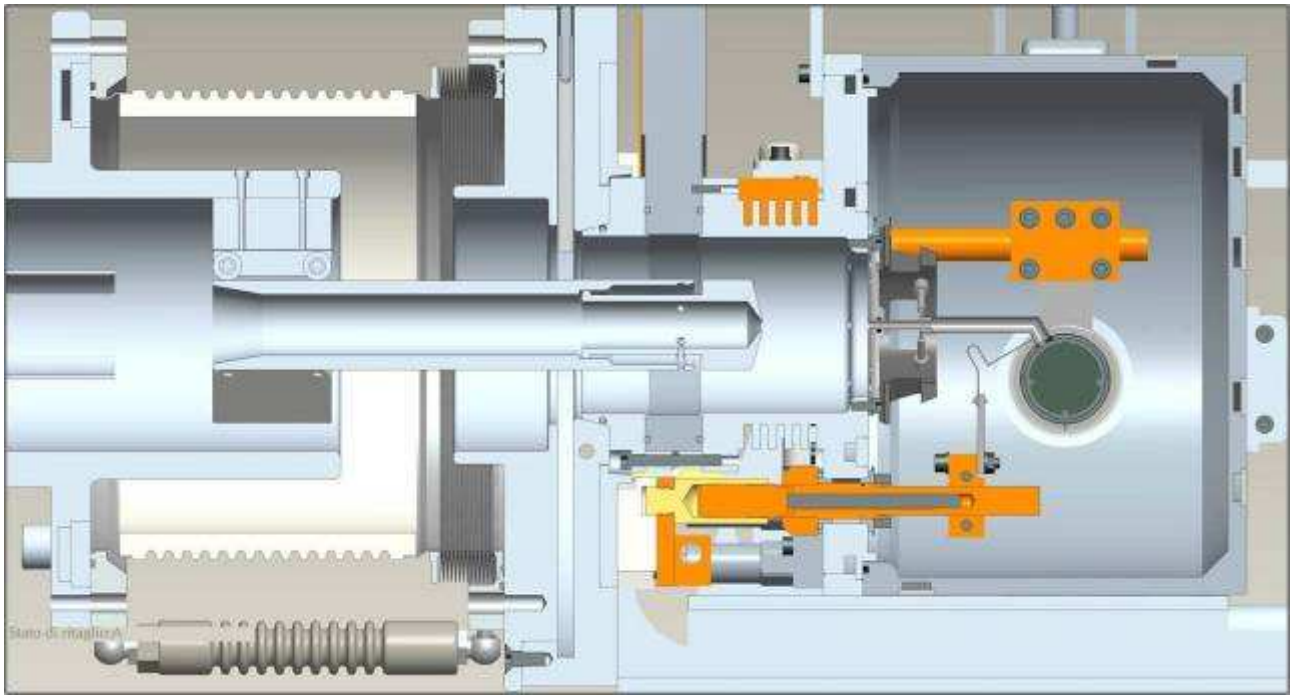

Fig. 2.14. The main insulator (*ST_FE240*) installed in the front end: it is used to insulate electrically the ion source and all the metallic components directly connected to it, respect to the extraction electrode and its frame.

Another fundamental subassembly of the front end's removable part is surely the coupling table (*ST_FE250*) presented in figure 2.15; this important object guarantees a stable positioning of the target chamber (containing both the target block and the ion source, see figure 2.1), connects it with

the PPB and the RIB channels, providing in the same time water for the target chamber's cooling system and the electrical power needed to heat by Joule effect the target block and the ion source. With the aim to keep at high voltage (60 kV) the target block – ion source system (and consequently the target chamber containing them) the coupling table (*ST_FE250*) is rested on the removable frame (*ST_FE210*) by means of three cylindrical PEEK insulators.

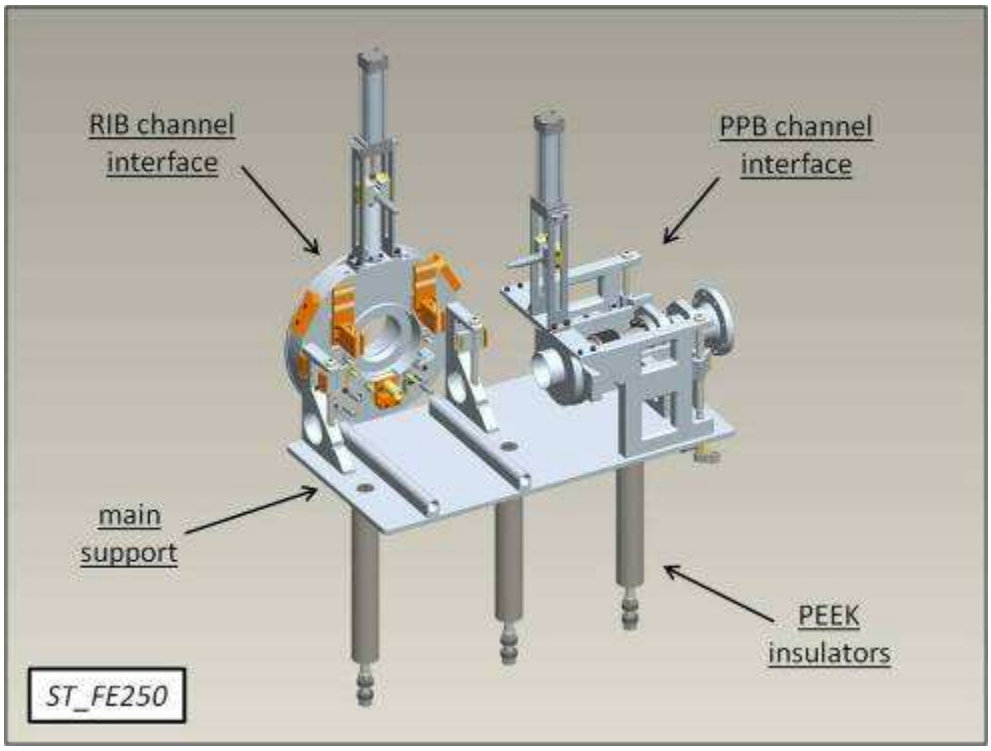

Fig. 2.15. The coupling table (*ST_FE250*) of the SPES front end.

During normal working conditions the primary proton beam will impinge the SPES target for approximately 15 days; once stopped the PPB it will be necessary to wait more or less other 15 days in order to reach acceptable radioactivity levels for the uranium carbide target and for the vacuum chamber containing it. At this point a remote handling system (the radioactivity level does not allow human activity in proximity of the production area) will substitute the old target chamber with a new one, containing a new target and a new ion source. In particular the SPES facility will be equipped with two different handling systems (one of them is redundant, introduced for safety reasons): the first will position the target chamber automatically on the coupling table moving horizontally whereas the second will move along the vertical direction. In both cases the target chamber will be placed on the coupling table as reported in figure 2.16. From this initial position the target chamber will be pushed to the RIB channel interface thanks to pneumatic actuators, allowing the coupling of both the electrical and the hydraulic connectors (see figure 2.17); then the PPB channel interface will be pressed in the same way to the target chamber's correspondent flange as proposed in figure 2.18.

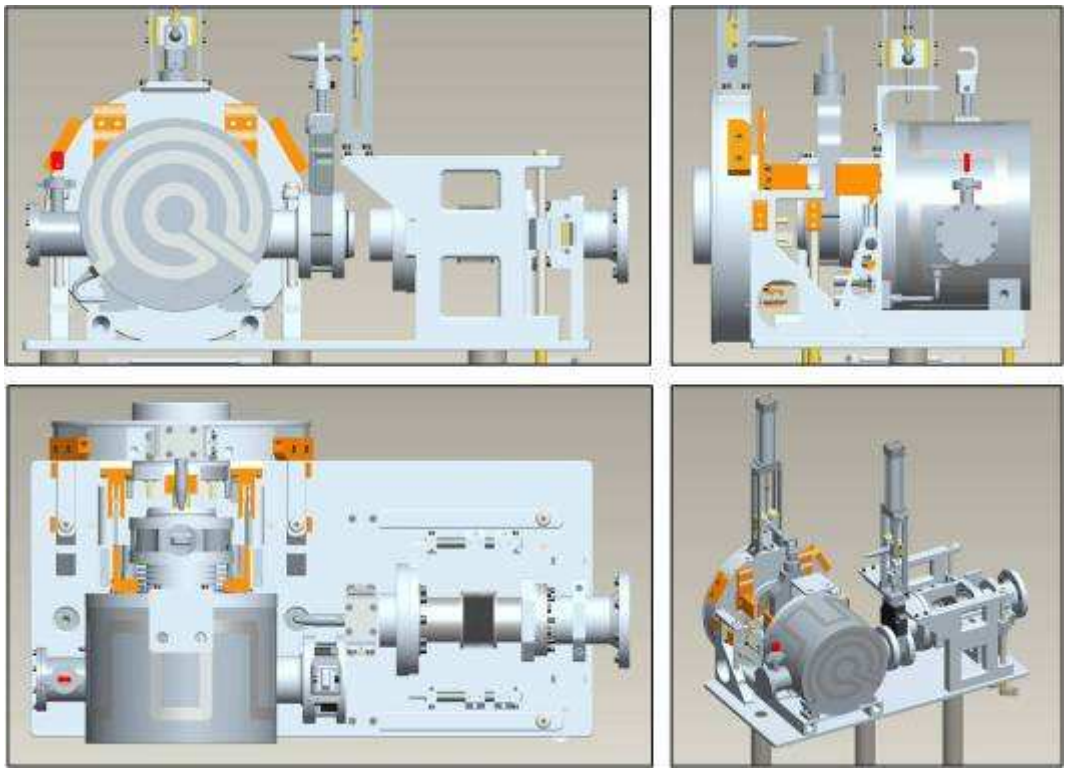

Fig. 2.16. The new target chamber positioned on the coupling table by the handling system.

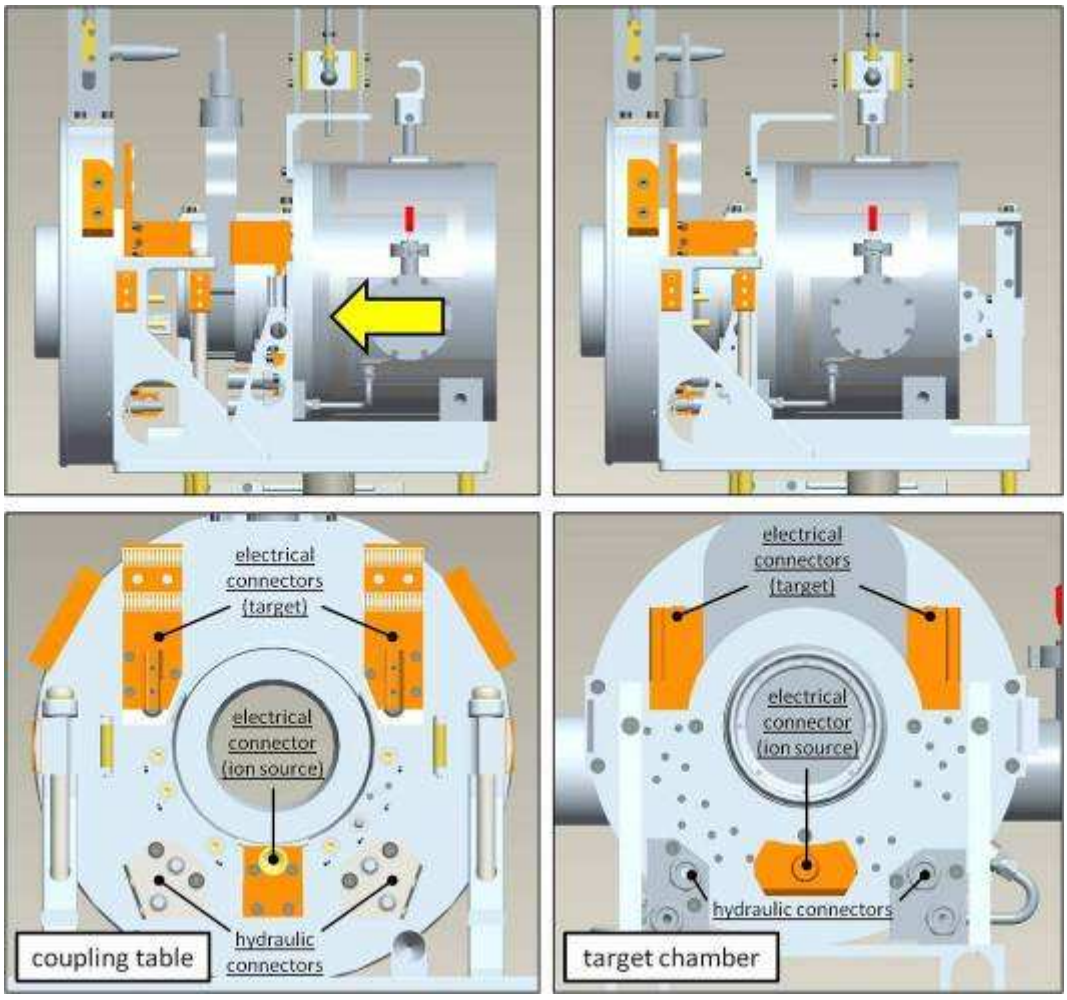

Fig. 2.17. The new target chamber pressed to the RIB channel interface.

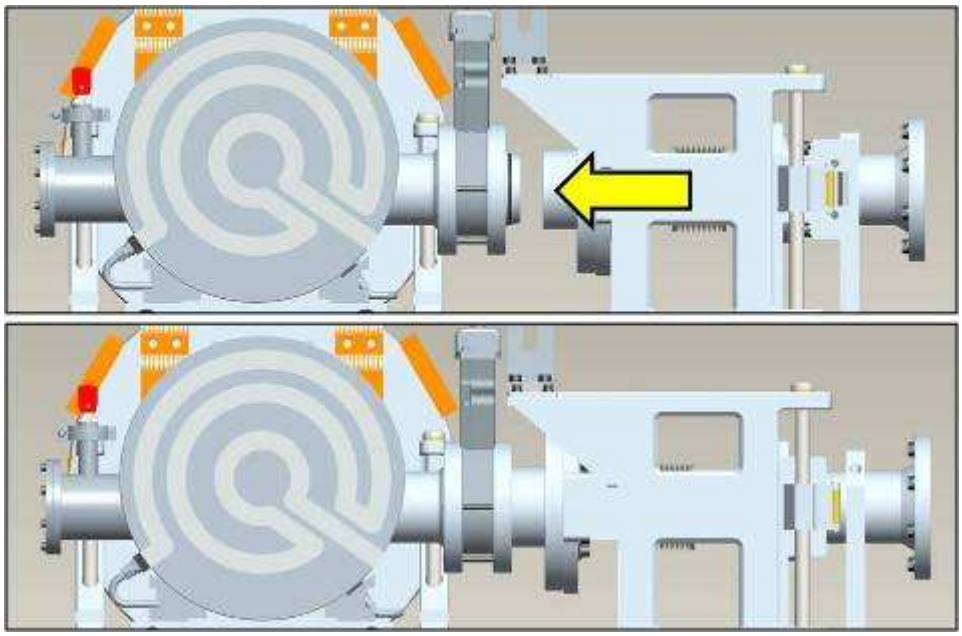

Fig. 2.18. The PPB channel interface pressed to the target chamber's correspondent flange.

The target chamber's vacuum valves will be then opportunely opened thanks to the pneumatic actuators positioned on the top of both the PPB and the RIB channel interfaces (see figure 2.19).

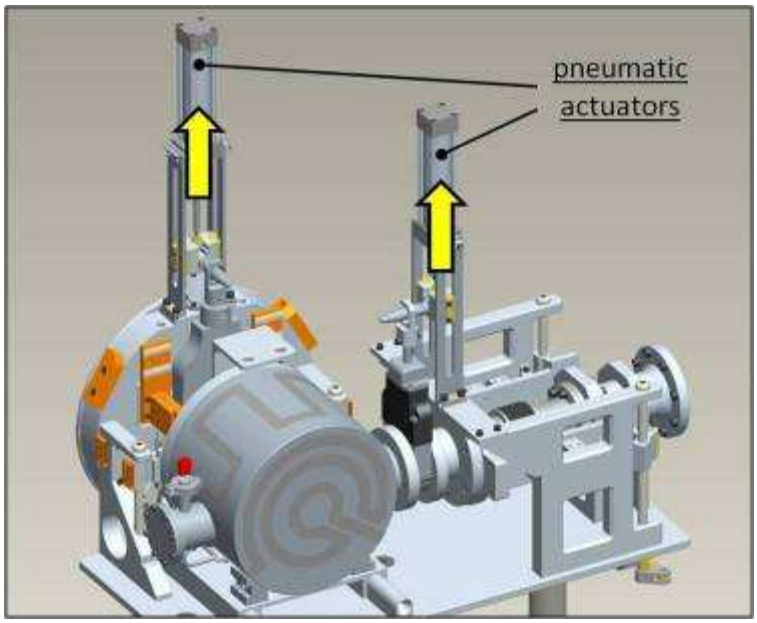

Fig. 2.19. Aperture of the target chamber's vacuum valves.

An analogous procedure will be adopted to remove the target chamber from the front end.

2.2.2. The fixed part of the SPES front end: the subassembly *ST_FE100* and the RIB channel

In figure 2.20 it is possible to appreciate a virtual CAD representation of the SPES front end's fixed part associated to the RIB channel and a picture of the correspondent real object assembled and installed at Legnaro National Laboratories. It constitutes the main part of the channel that receives the radioactive ion beam after the passage through the steerers above described.

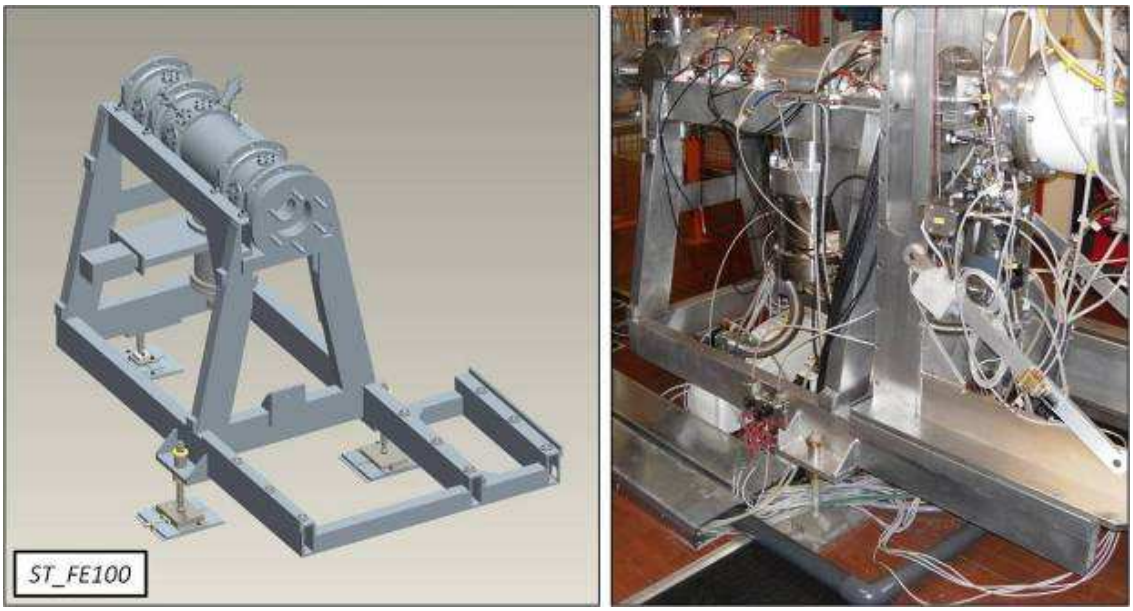

Fig. 2.20. The fixed part (subassembly *ST_FE100*) of the SPES front end associated to the RIB channel with a picture of the real object installed at Legnaro National Laboratories.

As reported in figure 2.5 the subassemblies that compose the fixed part of the SPES front end (*ST_FE100*) are two: the fixed frame (*ST_FE110*) and the triplet of quadrupoles (*ST_FE120*). The former supports both the triplet of quadrupoles (the *ST_FE120* subassembly) and all the removable part of the front end (the *ST_FE200* subassembly) whereas the latter is used to modify the RIB's shape electrostatically after the passage through the steerers: they are presented in figures 2.21 and 2.22, respectively.

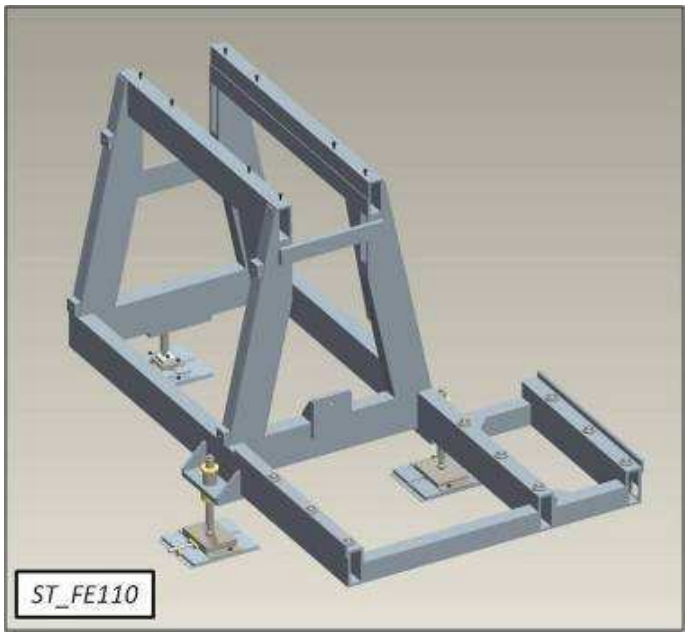

Fig. 2.21. The fixed frame (*ST_FE110*).

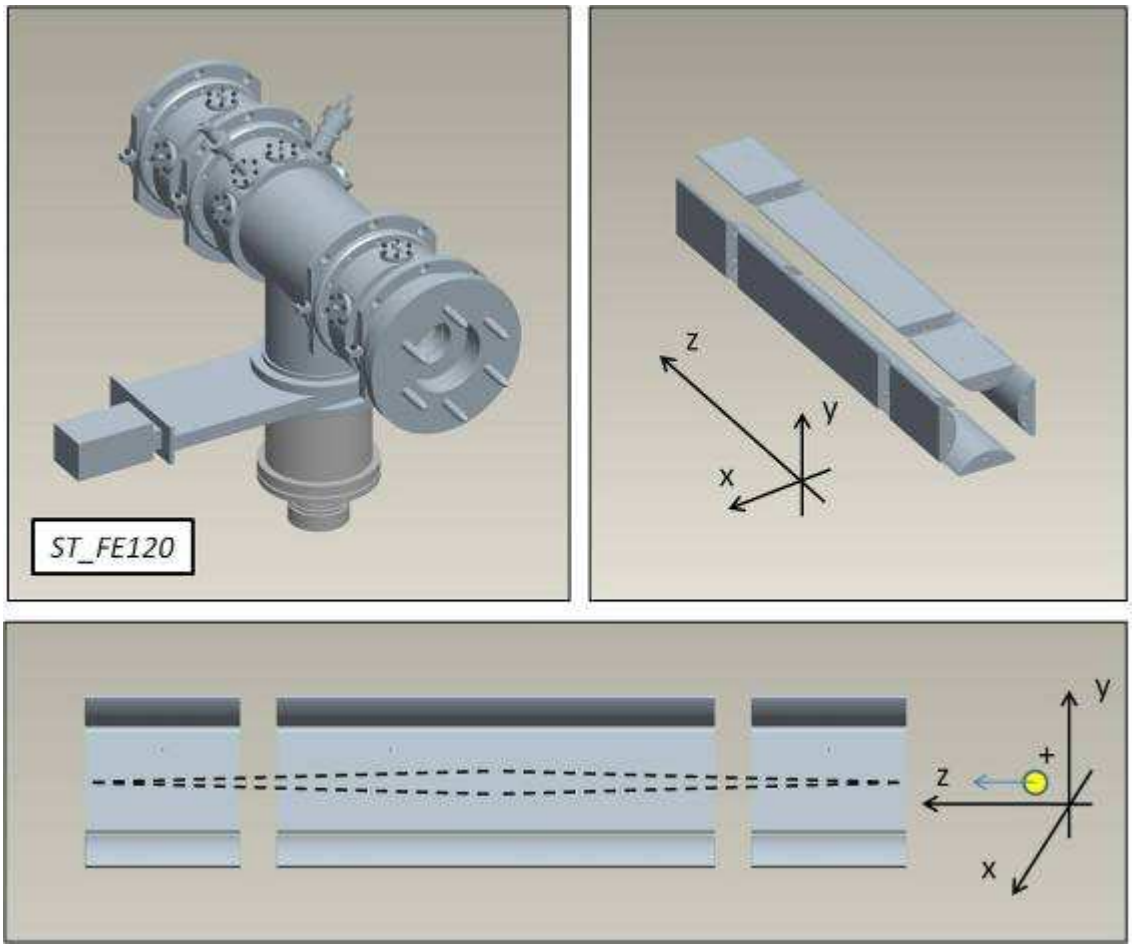

Fig. 2.22. The triplet of quadrupoles (*ST_FE120*).

Similarly respect to the steerers, also the quadrupoles are closed inside a cylindrical vacuum chamber, kept under high vacuum thanks to a turbomolecular pump, a dedicated set of vacuum valves, o-rings and gaskets.

2.2.3. The fixed part of the SPES front end: the subassembly *ST_FE300* and the PPB channel [3]

Figure 2.23 shows the fixed part of the SPES front end associated to the primary proton beam channel (subassembly *ST_FE300*); this important part of the apparatus allows the 40 MeV proton beam coming from the cyclotron to reach the target zone; it is composed of four subassemblies (see figure 2.5): the protonic fame (*ST_FE310*), the collimator (*ST_FE320*), the diagnostic block (*ST_FE330*) and the protonic insulator (*ST_FE340*) (see figure 2.24). The collimator is constituted by a series of coaxial cylindrical blocks of graphite (closed inside a cylindrical water-cooled chamber) with internal diameter decreasing from 70 to 40 mm, that is the value of the external diameter of the uranium carbide disks composing the SPES target (see the following paragraphs): its function is to circumscribe the target volume impinged by the proton beam, even if the PPB is not well focused or correctly aligned (see figure 2.25).

Fig. 2.23. The fixed part (subassembly *ST_FE300*) of the SPES front end associated to the PPB channel with a picture of the real object installed at Legnaro National Laboratories.

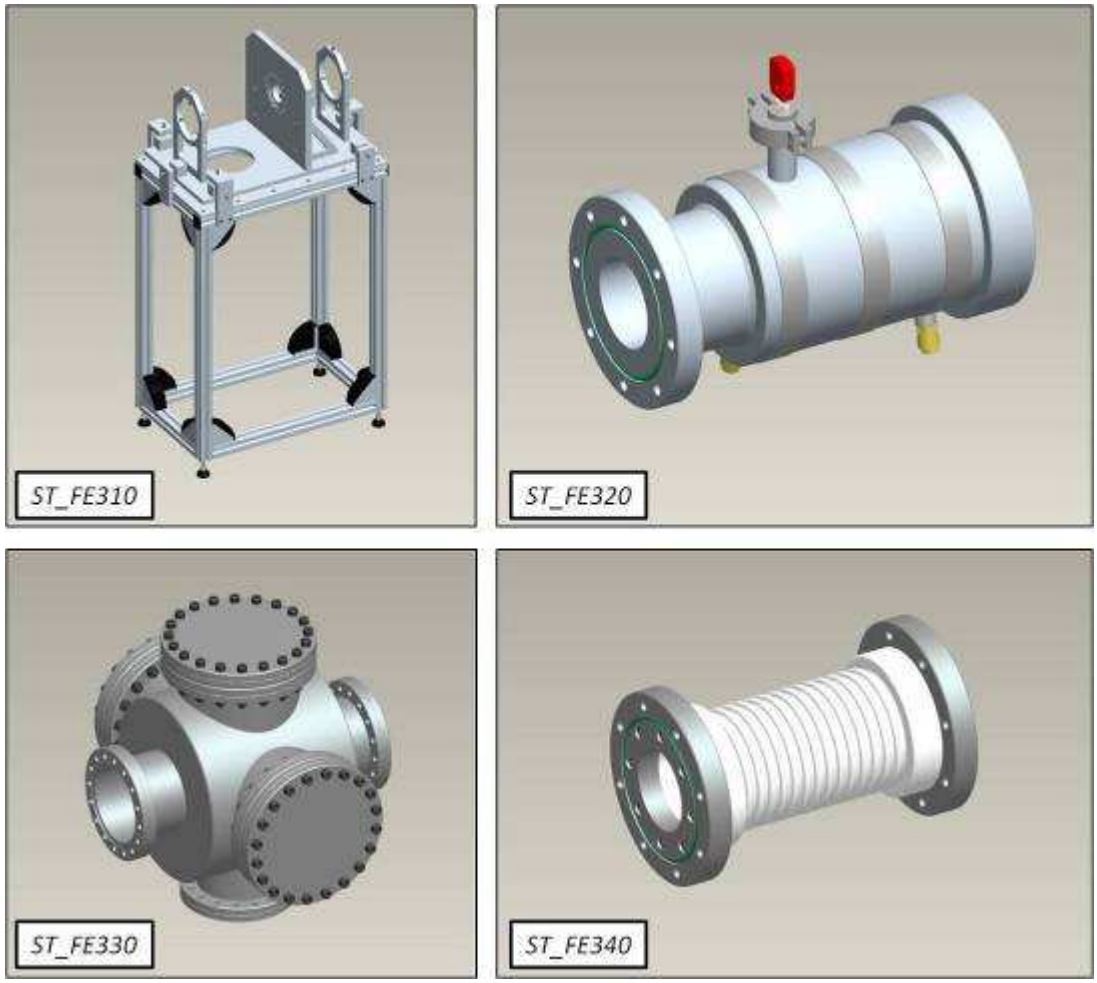

Fig. 2.24. The subassemblies composing the fixed part of the SPES front end associated to the PPB channel: the protonic fame (*ST_FE310*), the collimator (*ST_FE320*), the diagnostic block (*ST_FE330*) and the protonic insulator (*ST_FE340*).

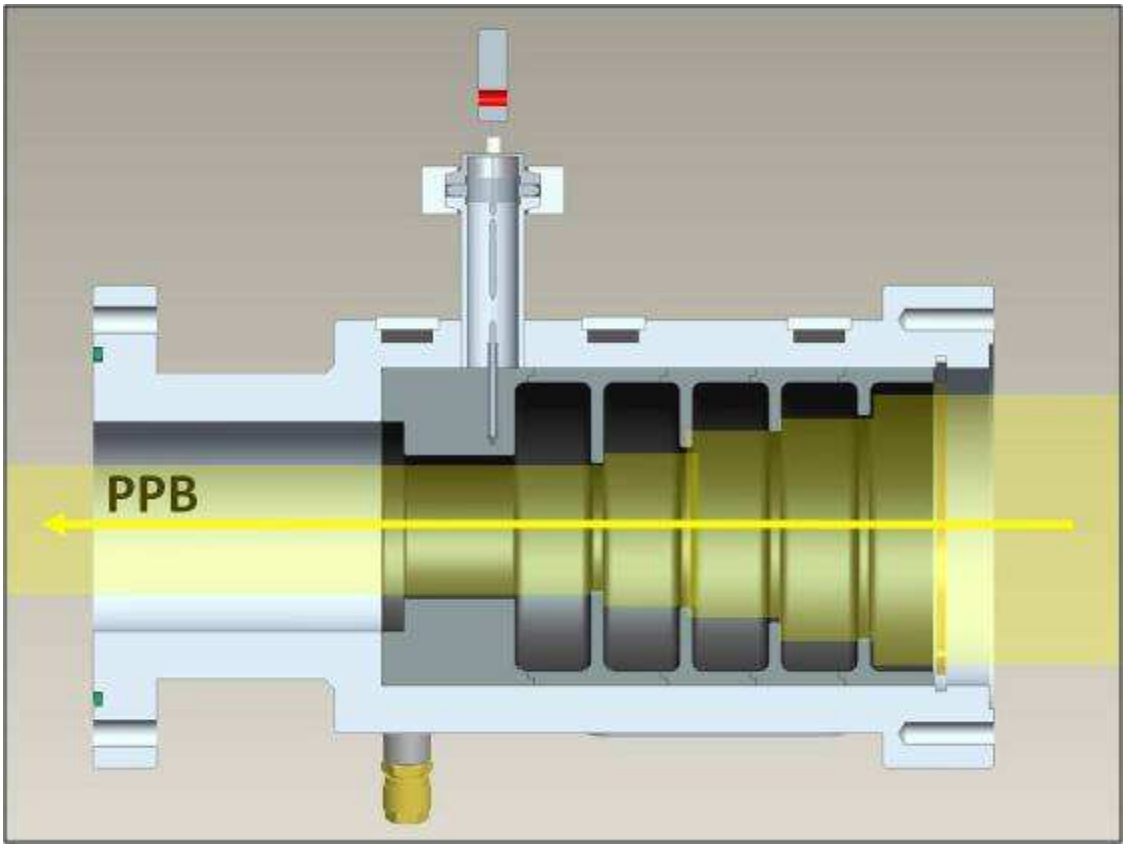

Fig. 2.25. Section view of the collimator (*ST_FE320*).

The diagnostic block (subassembly *ST_FE330*) will be used for the installation of an high power Faraday cup (at present under development at Legnaro National Laboratories) with the aim to monitor the current level of the primary proton beam; moreover a turbomolecular pump will be installed on the lower flange of the diagnostic block to produce an high vacuum level inside the proton beam channel.

The protonic insulator (subassembly *ST_FE340*) presented in figure 2.24 will be used to insulate the high voltage section of the front end respect to the rest of the PPB channel; in particular the illustration reported in figure 2.24 shows a prototype made of Teflon reinforced with glass fibers used recently at Legnaro National Laboratories during high voltage off-line tests: for the on-line version of the SPES front end it will be surely substituted with an insulator made of radiation hard materials (Al_2O_3 and PEEK) and characterized by the same architecture proposed for the main insulator (see figure 2.13).

2.3. The macro-component “target chamber” [2]

In the context of the SPES facility the target chamber is used to contain and support the target – ion source complex in an high vacuum environment, providing both the water for the cooling system and the electrical current needed to heat by Joule effect the production target and the ion source; we

recall that the target – ion source complex constitutes the core of the facility and is used to convert the stable primary proton beam (PPB) into a radioactive ion beam (RIB) (see figure 2.26): to understand in detail its functioning see the following chapters 3 and 4.

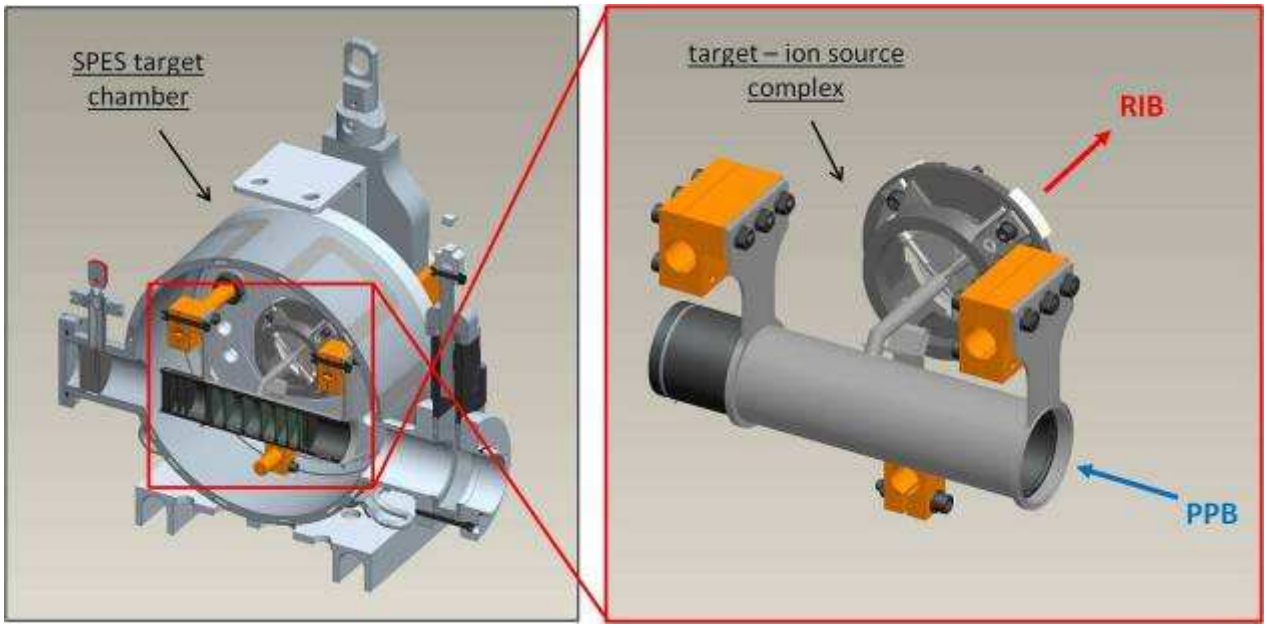

Fig. 2.26. The SPES target chamber and the target – ion source complex.

Similarly to the case of the front end, the SPES target chamber (*ST_CR000A*) is an evolution of the target chamber used at the ISOLDE facility (CERN) (*ST_CR000*); respect to the ISOLDE one the design of the SPES chamber introduced a new water-cooled cover to compensate the higher power deposited in the target by the proton beam, the connection with the primary proton beam channel (respect to the ISOLDE facility the energy of the SPES primary beam is lower, close to 40 MeV, and consequently it has to be kept under vacuum) and the target alarm system that communicates the possible breaks or damages of the UC_x disks. Sometimes the standard ISOLDE chamber is still used at Legnaro National Laboratories during off-line tests: as a consequence it was coded (*ST_CR000*) using the codification scheme created for the SPES project (see figure 2.27).

All the subassemblies composing the SPES target chamber are reported in figure 2.28. The main plate (*ST_CR100*) represents the frame of the chamber: it supports the cover, the electrical clamps and all the target chamber's secondary components, in particular the RIB channel vacuum valve. The main plate is water-cooled and some of its construction details can be appreciated in figure 2.29. The ion source electrical clamp (*ST_CR200*) and the target electrical clamps (*ST_CR300* and *ST_CR400*) are used to provide the high electrical currents needed to heat (by Joule effect) the ion source and the target, respectively. Since they are made of copper (a metal that is not able to sustain very high temperatures) and directly connected to the ion source and to the target

(both working at approximately 2000°C), the electrical clamps are all water cooled (see figure 2.30).

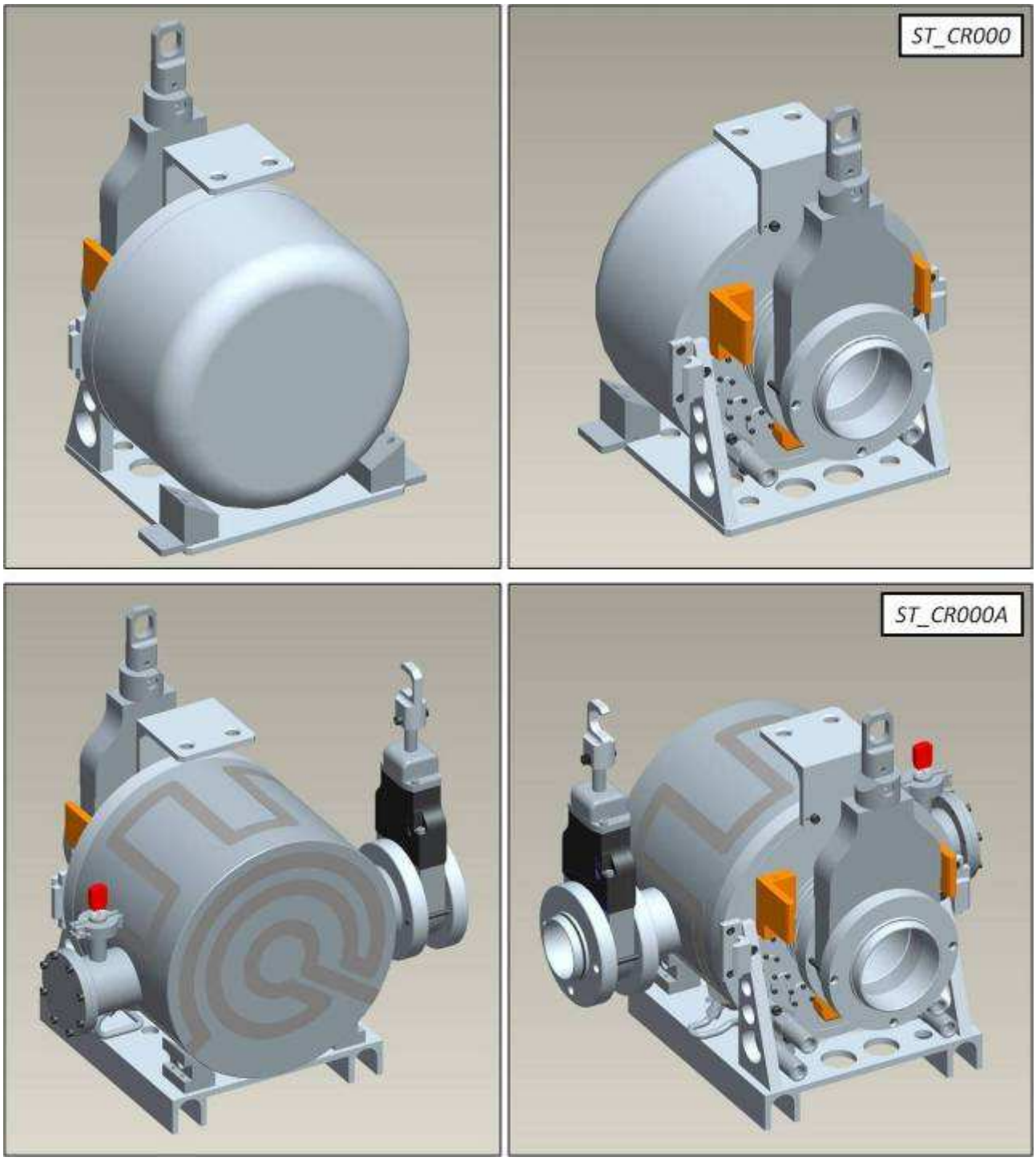

Fig. 2.27. The ISOLDE target chamber (*ST_CR000*) and the SPES target chamber (*ST_CR000A*).

Another fundamental subassembly of the SPES target chamber is surely the cover (*ST_CR500A*); as shown in figure 2.31 it is water cooled in order to dissipate the considerable amount of heat coming from the target – ion source block.

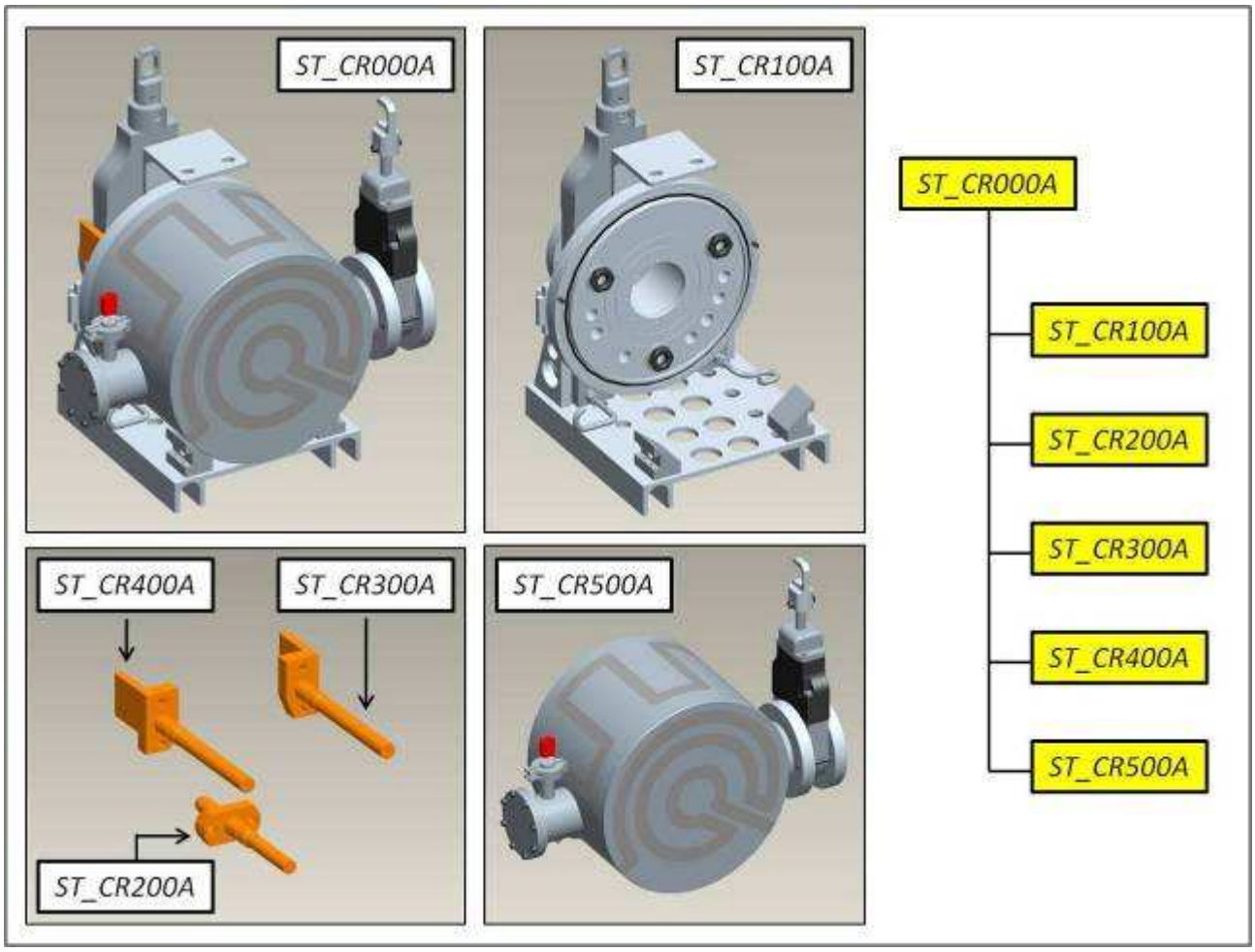

Fig. 2.28. The subassemblies composing the SPES target chamber (*ST_CR000A*): the main plate (*ST_CR100A*), the ion source electrical clamp (*ST_CR200A*), the target electrical clamps (*ST_CR300A* and *ST_CR400A*) and the cover (*ST_CR500A*).

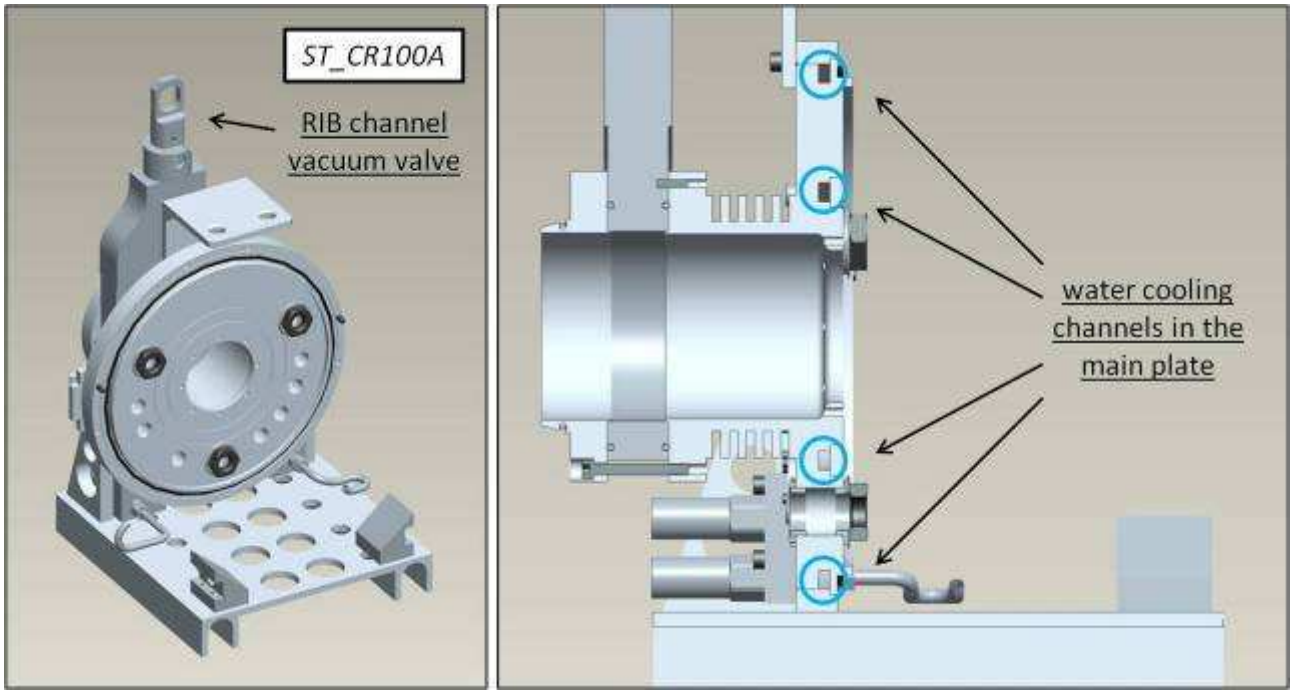

Fig. 2.29. The main plate (*ST_CR100A*) of the SPES target chamber.

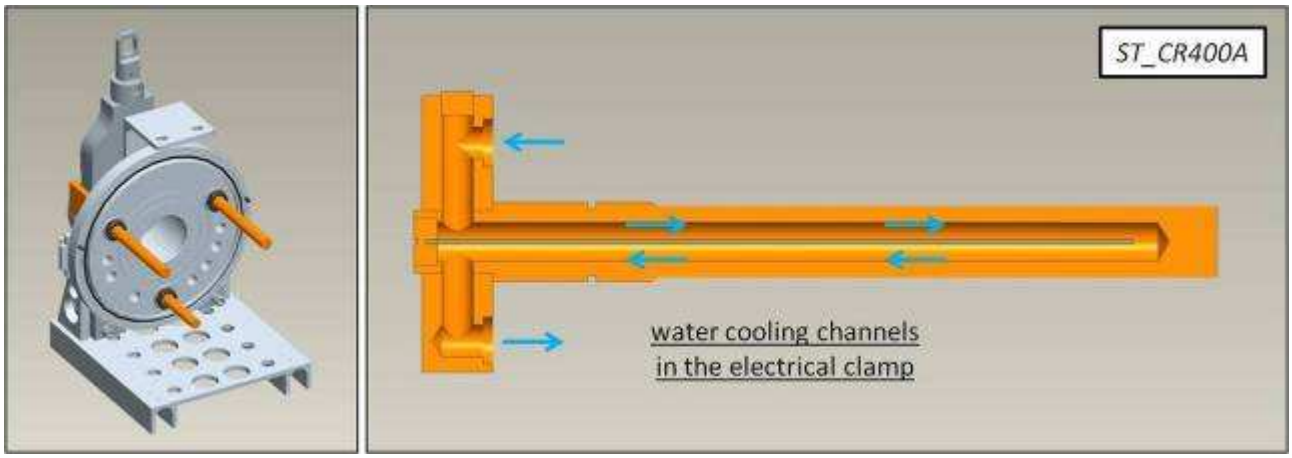

Fig. 2.30. Illustration of the ion source / target electrical clamps installed in the main plate, and section view of subassembly *ST_CR400A*.

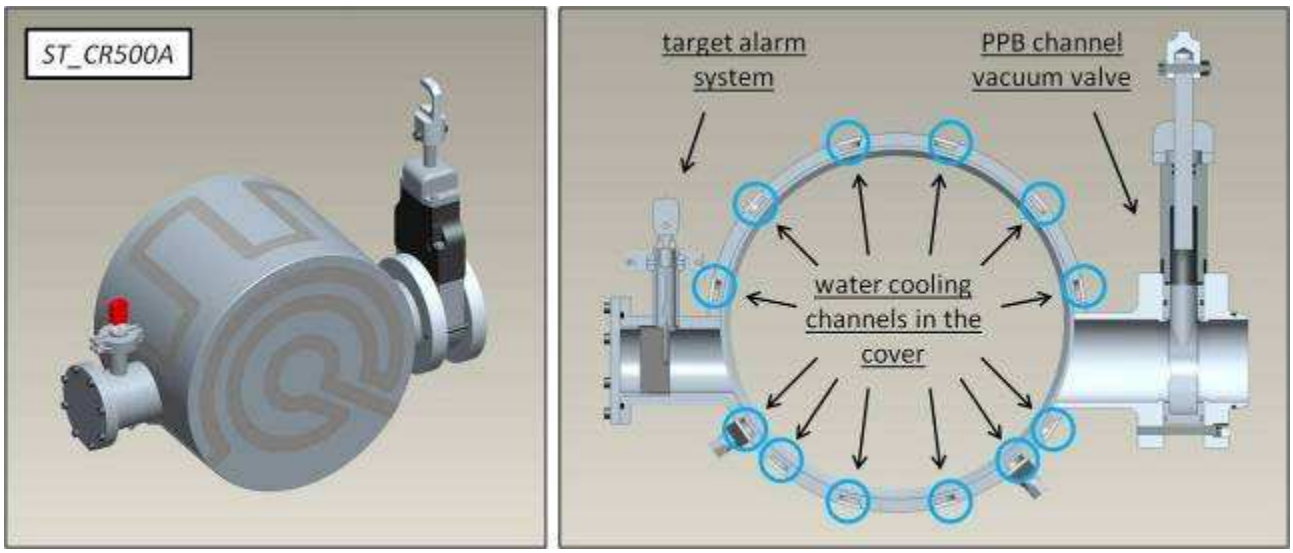

Fig. 2.31. The cover *ST_CR500A*.

A flange and a vacuum valve allow to connect the cover, and so the target chamber, to the primary proton beam channel, whereas at the opposite cover's extremity an alarm system for the target is installed; it is constituted by a cylindrical block of graphite with a thermocouple accurately inserted in the radial direction: if one of the disks composing the target broke, the correspondent power deposited by the proton beam would transfer to the aforementioned block of graphite, increasing its temperature level. In this way the signal of the increased temperature coming from the thermocouple would be addressed to the facility control system in order to start with corrective actions.

At the end of this paragraph we report the illustration of another target chamber version: the SPES target chamber equipped with the magnet needed to make the plasma ion source work properly (see figure 2.32). The SPES target chamber with magnet (*ST_CR000B*) is used only when the plasma ion source is installed: it is a particular kind of ion source whose illustration is reported

in paragraph 2.5. For further details about this kind of ion source and its functioning the reader can consult chapter 4.

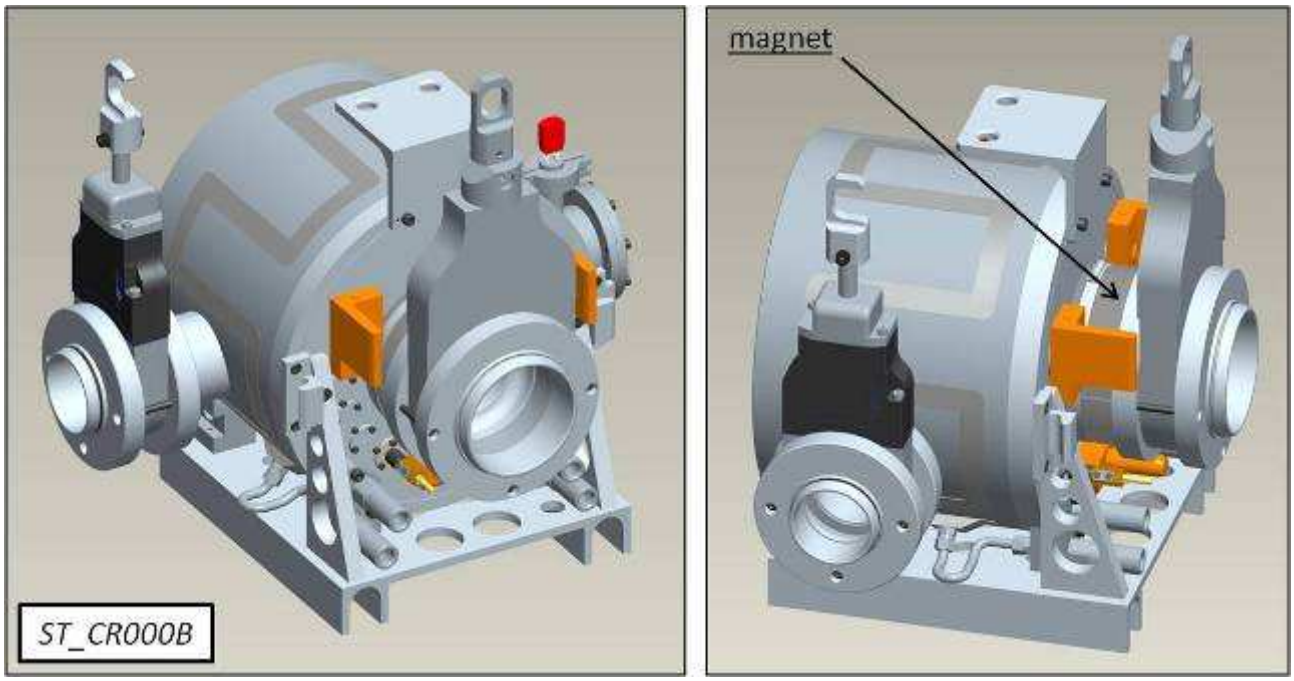

Fig. 2.32. The SPES target chamber with magnet (*ST_CR000B*).

2.4. The macro-component "target block"

The target block at present adopted for the SPES project (*ST_TB000A*) is represented in figure 2.33 together with the subassemblies composing it. The most important one is surely the production target (*ST_TB100A*); it is composed of 7 co-axial disks made of uranium carbide characterized by an external diameter and a thickness equal to 40 and 1.3 mm, respectively: they are spaced in the axial direction in order to promote the dissipation (by thermal radiation) of the heat deposited by the primary proton beam. The uranium carbide disks are contained inside a cylindrical graphite box, closed at its extremities by means of other disks made of graphite (see chapter 3 for further details). The production target is positioned inside the target heating system (*ST_TB200A*): it is composed of a tantalum tube and two tantalum wings welded at its extremities, and is used to heat the production target at high temperatures (when the PPB is not irradiating the target) thanks to the high electrical currents passing through it. Another important component of the target block is the transfer line (*ST_TB300A*); as mentioned in the previous chapter, through the transfer line the radioactive atoms are transported from the production target to the ion source by effusion. It is generally kept at high temperatures to increase the mobility of the atoms but in some cases it can be water-cooled with the aim to improve the selectivity of the system (see chapter 4, figure 4.66). When the transfer line works at high temperatures it is heated by Joule effect making use of the same electrical circuit adopted to heat the ion source (see chapter 4, figure 4.11).

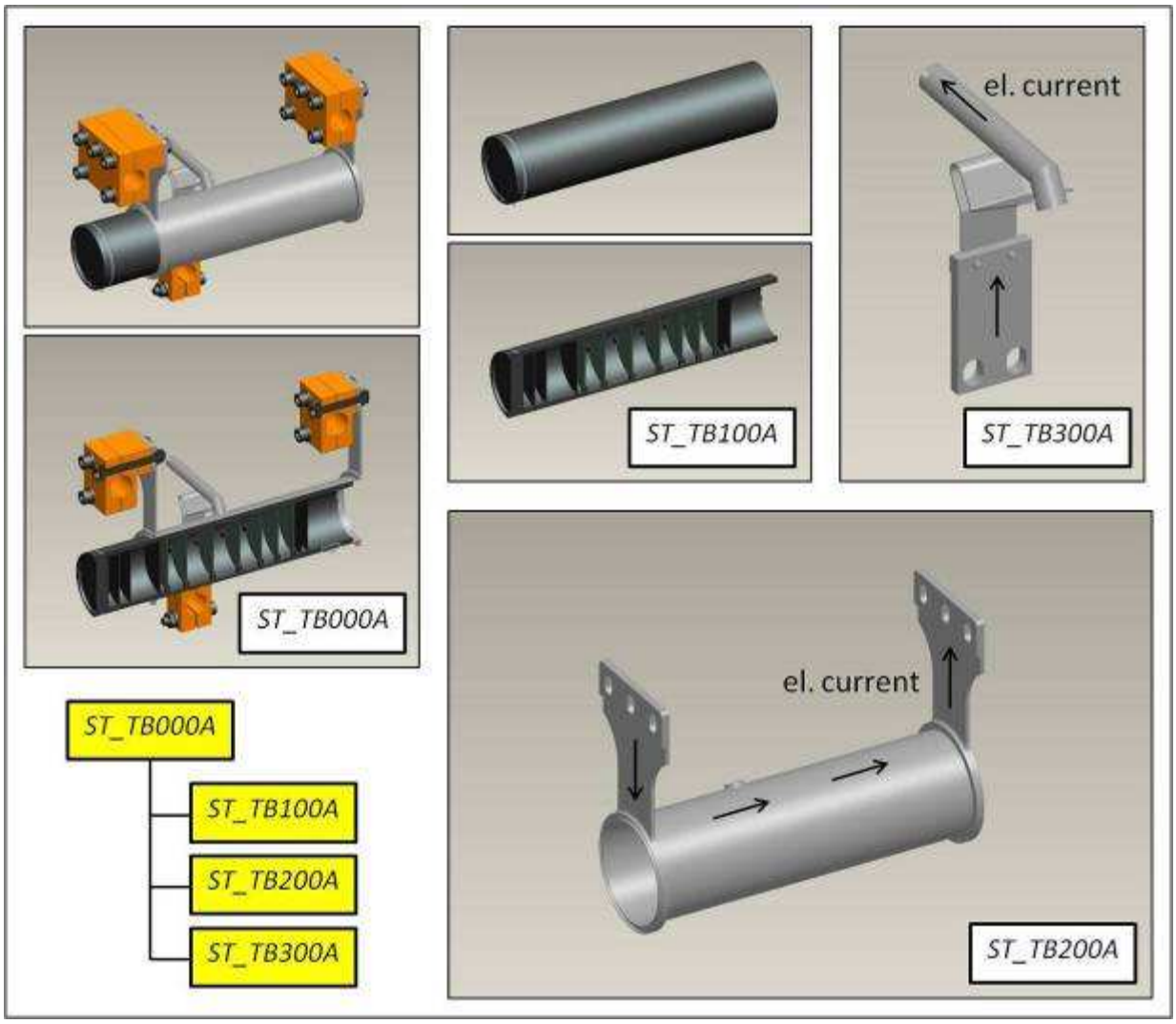

Fig. 2.33. The SPES target block (*ST_TB000A*) and its main subassemblies: the production target (*ST_TB100A*), the target heating system (*ST_TB200A*) and the transfer line (*ST_TB300A*).

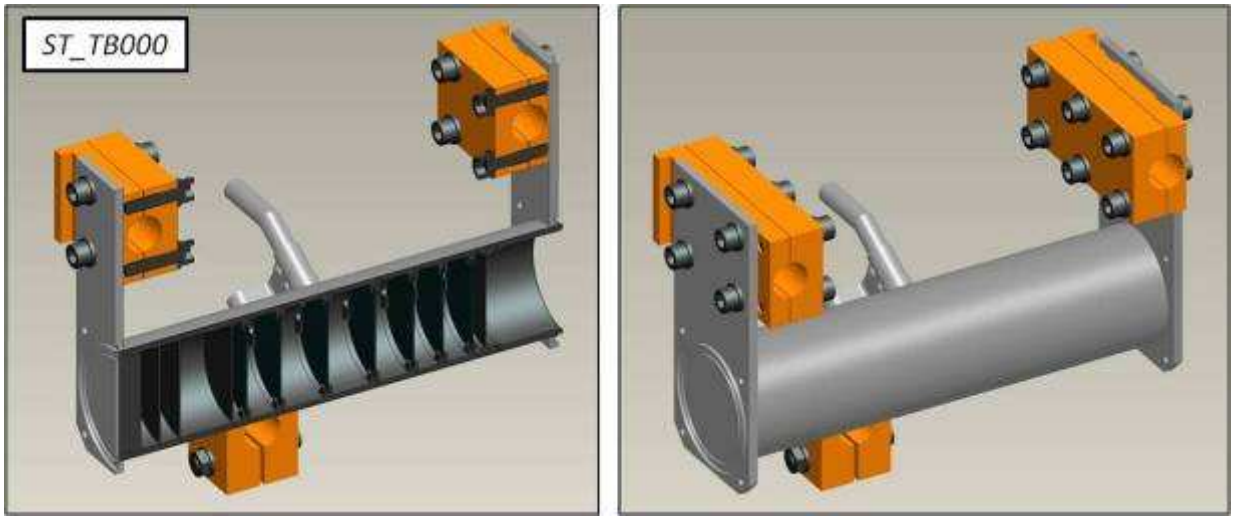

Fig. 2.34. The first prototype of the SPES target block (*ST_TB000*).

Figure 2.34 shows the first prototype of the SPES target block (*ST_TB000*). It was developed in collaboration with a private company and was tested at high temperature (with some small

modifications) at Legnaro National Laboratories, giving a fundamental contribute for the development of the current SPES target block (*ST_TB000A*).

2.5. The macro-component “ion source”

At the beginning of this chapter (paragraph 2.1) the SPES production area was presented taking as reference a particular type of ion source, that is the surface ion source or hot-cavity ion source (*ST_SI000*). It is now illustrated in figure 2.35 together with its main components: the ionizer (*ST_SI100*) and the alignment system (*ST_SI200*). The former is substantially the standard MK1 surface ion source developed and used at the ISOLDE facility (CERN) (see chapter 4) whereas the latter is an additional accessory used to keep aligned the ionizer at high temperatures: the alignment is particularly important, especially when using the hot-cavity ion source to produce ions by means of the laser ionization mechanism (see chapter 4, paragraph 4.4.2).

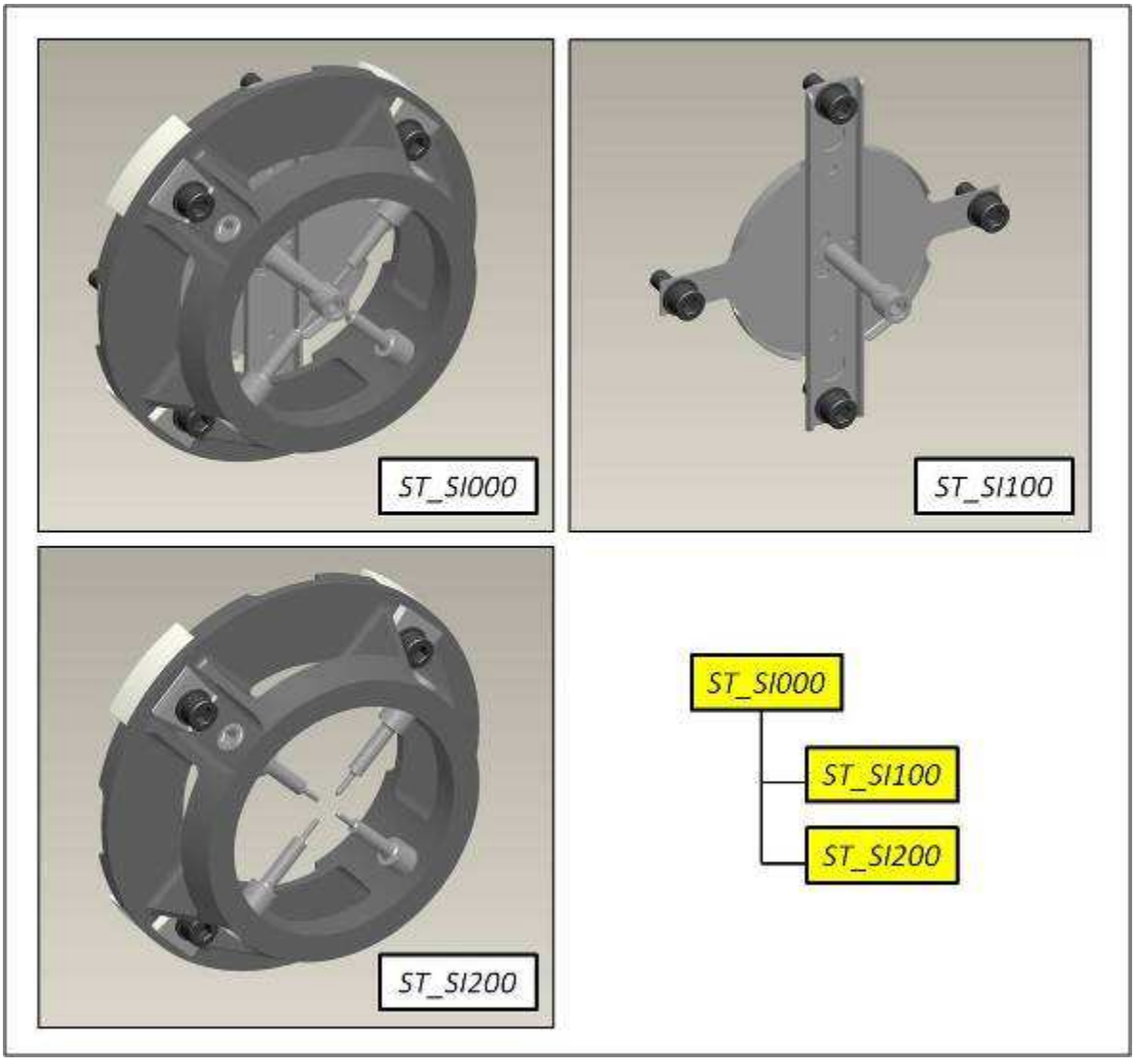

Fig. 2.35. The SPES surface ion source / hot-cavity ion source (*ST_SI000*) and its main subassemblies: the ionizer (*ST_SI100*) and the alignment system (*ST_SI200*).

As it will be clarified in chapter 4, the SPES facility will make use of another kind of ion source: the high temperature plasma ion source. The plasma ion sources developed at the ISOLDE facility (CERN) and at the HRIBF facility (ORNL) are briefly presented in figure 2.36: more details related to their functioning will be presented in chapter 4.

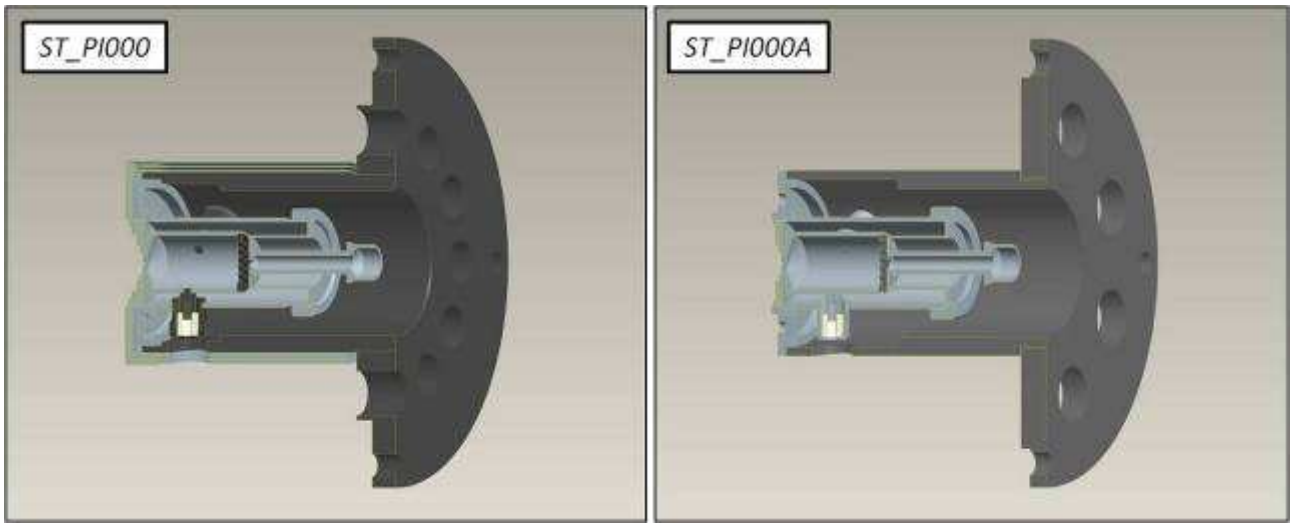

Fig. 2.36. The standard ISOLDE plasma ion source (*ST_PI000*) and the standard HRIBF one (*ST_PI000A*): section views.

2.6. Conclusions

In this chapter the macro-components belonging to the SPES production area were presented; in particular the front end and the target chamber were described including a large number of details since in the next chapters, mainly dedicated to the target and to the ion sources, they will be not reconsidered for detailed discussions. In table 2.1 the complete list of the macro-components composing the SPES production area is reported.

code	macro-component description
ST_FE000	SPES front end
ST_CR000	standard ISOLDE target chamber
ST_CR000A	SPES target chamber
ST_CR000B	SPES target chamber with magnet
ST_TB000	SPES target block: first prototype
ST_TB000A	SPES target block: second prototype
ST_SI000	SPES surface ion source / hot-cavity ion source
ST_PI000	standard ISOLDE plasma ion source
ST_PI000A	standard HRIBF plasma ion source

TABLE 2.1. The macro-components composing the SPES production area.

In figure 2.37 a picture of the SPES font end realized and installed at Legnaro National Laboratories is proposed; it was recently completed and will allow to perform important off-line tests, mainly on the SPES ion sources (ionization efficiency tests, emittance measurements, see chapter 4).

Fig. 2.37. The SPES front end installed at Legnaro National Laboratories and used for the off-line tests.

In the next chapters a detailed study of the target – ion source system is presented, at first analyzing the target and the ion sources separately (see chapter 3 for the target and chapter 4 for the ion sources) and then considering them in a unique assembly (see chapter 5).

REFERENCES

[1] S. Marzari, Front End 6 mechanical development, internal report, AB-ATB-IF section, ISOLDE (CERN).

[2] C. Gobbi, Modellazione solida, progettazione e misure termiche su sistemi meccanici appartenenti alla facility SPES, Degree Thesis in Mechanical Engineering, University of Padua, Italy.

[3] A. Cavazza, Progettazione termica e meccanica dell'apparato di produzione di ioni del progetto SPES, Master Degree Thesis in Mechanical Engineering, University of Padua, Italy.

Chapter 3

The SPES Production Target: design and test at LNL

3.1. Introduction

In the context of ISOL facilities a wide variety of reactions and beam-target combinations are implemented in order to produce the radioactive isotopes of interest [1].

Different kinds of projectile with a large variety of energies are used to induce nuclear reactions in the target: low energy protons and neutrons of 30 to 100 MeV, high-energy protons of 500 to 1500 MeV, heavy ions of 4 to 100 MeV/u, thermal neutrons and electron beams of 50 MeV. Then, as a function of the particular beam-target combination, different nuclear reactions can be produced: light and heavy-ion fusion evaporation, fission, spallation and fragmentation. In the context of the aforementioned reactions the key parameter is the reaction cross-section; it is important to recall that the intensity ($I_{reaction\text{-}products}$) of the reaction products synthesized in the target is calculated using the following equation,

$$I_{reaction\text{-}products} = \sigma N_{target} \Phi \quad (1)$$

where,

- σ is the cross-section (cm^2), often expressed in units of barns, mbarns or μbarns, with 1 barn = $10^{-24} cm^2$
- N_{target} is the number of target atoms per surface area (cm^{-2})
- Φ is the primary beam intensity.

The cross section σ is an energy dependent quantity and in nuclear and particle physics it is used to express the probability of interaction between particles; when the particles forming the beam impinge a foil made of a certain substance, the cross section σ is the hypothetical area measure around the target particles of the substance (usually its atoms) that represents a surface. If a particle of the beam crosses this surface, there will be some kind of interaction. While σ is often unknown experimentally, it can be reliably calculated for many different reactions by means of dedicated calculation codes.

A comprehensive and brief description (the physics behind the different reaction mechanisms will not be discussed here) of the reactions used at ISOL facilities will be given in the following, together with some examples of typical intensities available at today's accelerators or reactors [1].

Light and Heavy-ion Fusion Evaporation Reactions. With light-ion induced fusion reactions nuclei close to the line of stability on the neutron-deficient side are produced. The main advantages of this kind of reaction are the high cross-section and the high intensity of the primary beam available. An example is the $^{13}C(p,n)^{13}N$ reaction (production of ^{13}N isotopes and neutrons using a ^{13}C target and a primary proton beam) that has a peak cross-section of 224 mbarn at an energy level of 6.6 MeV. On the other hand heavy-ion fusion evaporation reactions have typically a much lower cross section but produce neutron-deficient nuclei very far from the line of stability.

It should be noted that these reactions produce on average a limited number of different isotopes while the reaction mechanisms discussed below produce hundreds of different isotopes, putting much more constraints on the selectivity of the target-ion source system [1].

Fission. To produce neutron-rich nuclei in a wide range of masses, fission of ^{238}U, ^{235}U, ^{232}Th and other actinides is used. The different particles to induce fission are low and high energy protons, heavy ions, fast or thermal neutrons and electrons, with photo-fission being used in the latter case. Thermal neutrons are produced in a reactor while fast neutrons are obtained using a converter: in words a high power and high energy primary proton beam is dumped in a well-cooled neutron production target while the neutrons whose power deposition is much smaller than that of protons create the radioactive isotopes of interest. In this way problems related to high power deposition can be decoupled from the target used to produce radioactive isotopes.

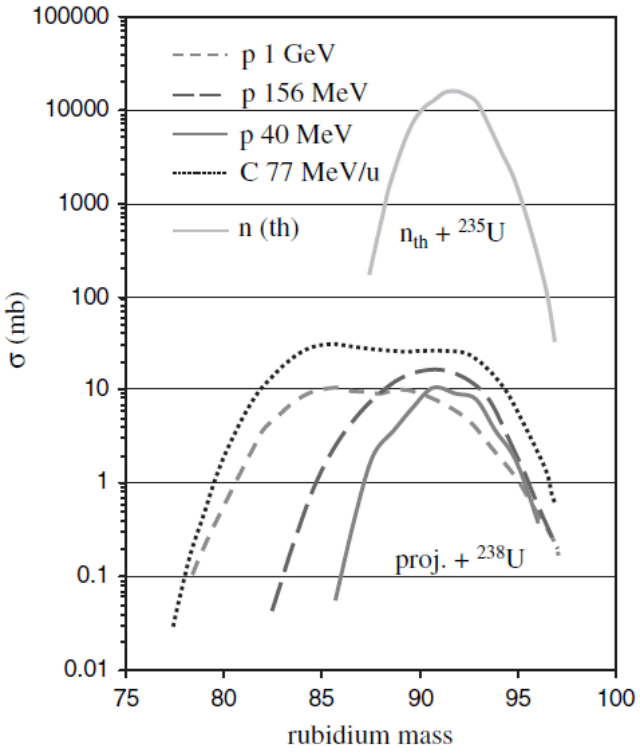

Fig. 3.1. Cross-sections for the production of rubidium isotopes from fission of ^{238}U using different kinds of projectiles. For comparison cross sections from thermal neutron induced fission of ^{235}U are shown [1].

Figure 3.1 shows the cross-sections for the production of rubidium isotopes from fission of ^{238}U using different projectiles; for comparison the cross-section from thermal neutron induced fission of ^{235}U is shown as well; it is very interesting to notice that the primary beam energy doesn't influence in a deep way the cross-section of the fission reaction [1].

Spallation. When a high energy proton beam hits a target, three different types of reaction can occur: fission, spallation and fragmentation. In a spallation reaction a large number of protons, neutrons and α particles (two protons and two neutrons bound together into a particle identical to a helium nucleus) are expelled from the target nucleus. For instance a 1 GeV proton beam that impinges a ^{238}U target produces ^{200}Fr, thereby ablating 5 protons and 23 neutrons. Spallation products can span a large part of the nuclear chart on its neutron-deficient side. The production cross-sections for nuclei very far from stability are modest, but the high proton energy allows the usage of thick targets (of the order of 100 g/cm^2) [1].

Fragmentation. For ISOL systems both target fragmentation, whereby a heavy target is bombarded with a high energy proton beam, and projectile fragmentation, whereby a high energy (energy > 50 MeV/u) heavy ion beam is sent onto e.g., a ^{12}C target, are used. These reactions produce again a wide variety of isotopes, close to the initial target or projectile nucleus as well as very light nuclei. The very short-lived ^{11}Li ($T_{1/2}$ = 8.6 ms, where $T_{1/2}$ is the half life, the time taken for half the radionuclide's atoms to decay) is produced in this way [1].

At this point it is important to remark the fundamental role of the production target in ISOL facilities: its main aim is to produce as much isotopes as possible and to get them released in gaseous form from the target matrix in the fastest and in the most efficient way. The diffusion of radioactive isotopes in the target material (bulk diffusion) and their release from the target's surface (part of the effusion process) depend strongly on their chemical properties: for short-lived isotopes of elements like titanium, vanadium, zirconium, niobium, molybdenum, hafnium, tantalum and tungsten, for example, the efficiencies for surface release are small. This means on the one hand that the radioactive ion beams will not be contaminated with isotopes of those elements, but on the other hand that beams of short-lived isotopes of these elements must be produced by other means.

In ISOL facilities thick targets are mainly used in combination with high-energy proton beams; they have thicknesses typically of a few 100 g/cm^2 and consist of foils (e.g., tantalum), fibres, liquids (e.g., mercury) or powders (e.g., uranium carbide). The target container is usually heated by Joule effect reaching temperatures around 2000°C. Figure 3.2 shows a picture of the ISOLDE uranium carbide target: in particular the top photo shows the target before proton irradiation while

the bottom one displays the same target unit after having received $2.5 \cdot 10^{18}$ protons from a focused beam of $3 \cdot 10^{13}$ protons per pulse.

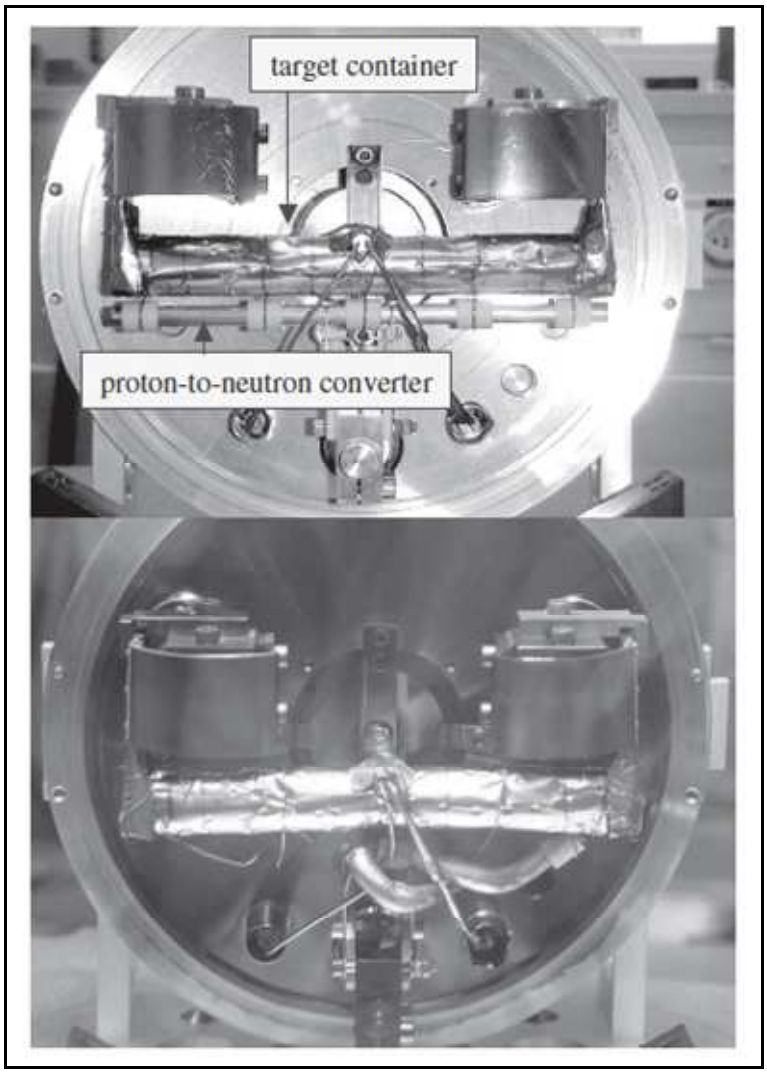

Fig. 3.2. The ISOLDE uranium carbide target: the top picture shows the target before the action of the primary beam while the bottom one displays the same target unit after proton beam irradiation [1].

The tantalum target container, that is wrapped by heat shields, is shown in figure 3.2 together with the clamps to supply the high electrical current that heats the target. The proton beam comes from the left while the reaction products escape from the target material and container through a narrow tube installed on the top of the container. The ion source, in this case a hot-cavity ion source (see chapter 4), is placed behind the target container, followed by the extraction system and the beam line. Below the target container a tantalum rod is shown that serves as proton to neutron converter. When the proton beam impinges this rod, neutrons are produced which hit the uranium carbide target inducing fission. Because of the high instantaneous power deposition in the converter, the latter was twisted during the primary proton beam irradiation.

At this point, after this brief and general presentation on ISOL target systems, the SPES production target is presented and described in detail.

3.2. The SPES Production Target

As exposed in the previous chapters, the so-called SPES (Selective Production of Exotic Species) project is intended to develop a radioactive ion beam (RIB) facility at National Institute of Nuclear Physics (Padua, Italy). In particular, the SPES facility will produce intense neutron-rich RIBs according to the isotope separation on line (ISOL) technique (see chapter 1). The SPES production target (see figure 3.3) is composed of 7 co-axial disks made of uranium carbide (UC_x) (diameter and thickness of 40 and 1.3 mm, respectively), appropriately spaced in the axial direction in order to dissipate by thermal radiation the average power of 8 kW due to the proton beam passing through them.

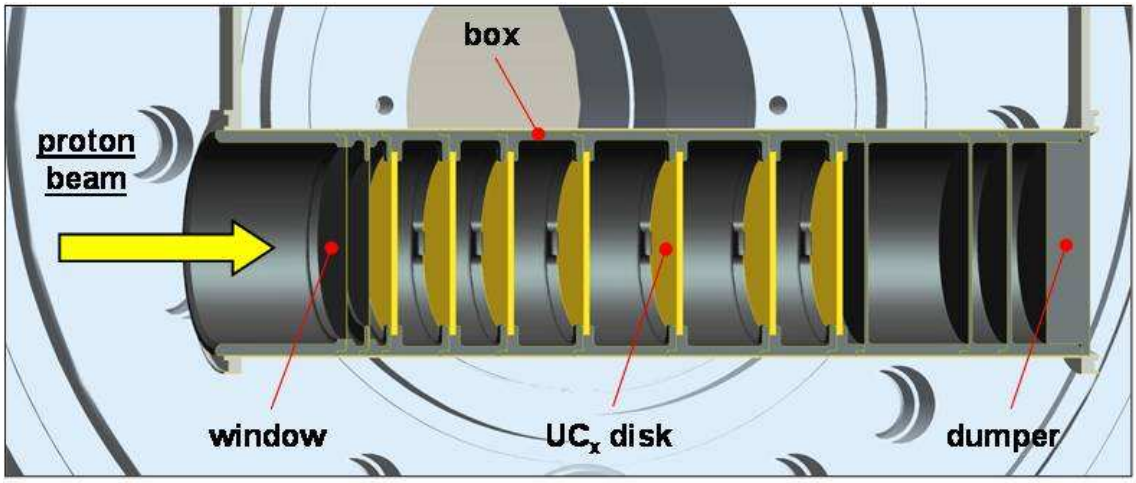

Fig. 3.3. CAD representation of the SPES production target and its main components (UCx disks, windows, dumpers and box).

Two thin (0.2 mm) circular windows made of graphite are located at the proton beam entrance to prevent the undesired emission of the nuclear fragments, while four circular graphite dumpers, with thickness ranging from 0.8 mm up to 10 mm, stop the proton beam at the rear side of the target [2]. All disks, windows, and dumpers are located inside a tubular hollow box made of graphite, having an external diameter and an average length of 49 and 200 mm, respectively. The box is located under vacuum inside a water-cooled chamber and has to maintain the average temperature of 2000°C: vacuum and high temperature are essential to enhance the radioactive isotopes extraction.

The energy and the intensity of the primary proton beam are 40 MeV and 200 μA, respectively, leading to a power level of approximately 8 kW deposited in the target; the correspondent in-target calculated isotope production is reported in figure 3.4.

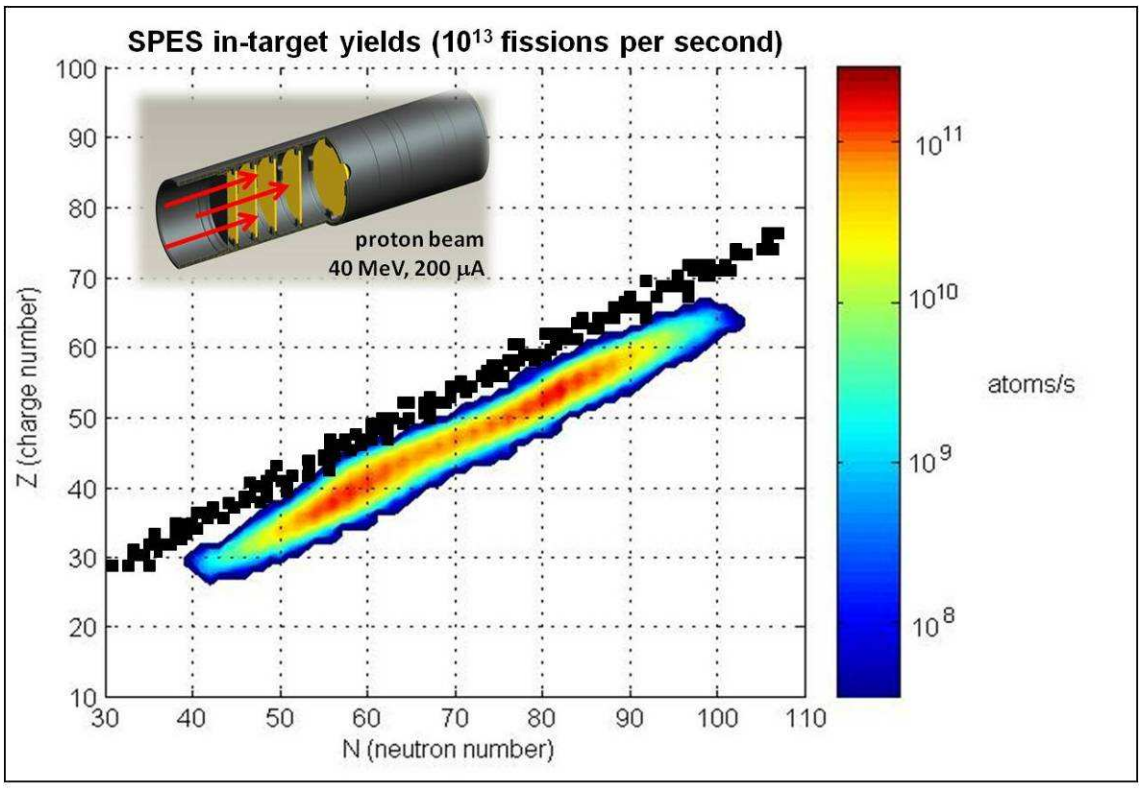

Fig. 3.4. Representation of the in-target isotope production [2].

As we will see in detail later, the aforementioned proton beam power is not sufficient to heat the box up to the required temperature level because of the intense radiative heat exchange from the graphite box to the water-cooled chamber [2]. As a consequence, it is crucial to introduce an additional and independent heating and screening system. It is important to underline that such heating device is completely independent from the proton beam and, additionally, allows for a better thermal control of the target when the proton beam power is not stabilized, i.e. during the start-up and the shut-down procedures. The target heating system (see figure 3.5) consists of a thin tantalum (Ta) tube, with an average length of 200 mm, an external diameter and a thickness of 50 and 0.35 mm, respectively. It is welded at its edges to two tantalum wings, which are directly connected to copper clamps, through which an electric current delivered by a 10 kW power supply (maximum current I_{MAX} = 1000 A and maximum potential ΔV_{MAX} = 10 V) heats by Joule effect the Ta tube. Tantalum was chosen to build the heating system because it is an highly corrosion resistant transition metal, able to conduct heat and electricity (thermal conductivity and electrical resistivity at room temperature equal to 57 W/(m°C) and $1.34 \cdot 10^{-7}$ (ohm·m), respectively, both increasing with temperature increase) and able to operate at very high temperatures: for the pressure of 10^{-4} Pa (that is the pressure level inside the chamber during the working conditions) Ta starts to sublimate at approximately 2200°C [3]. Moreover thanks to its low emissivity (0.15 at 1000°C and 0.26 at

2000°C), tantalum is able to screen efficiently the target box, limiting the cooling effect by thermal radiation.

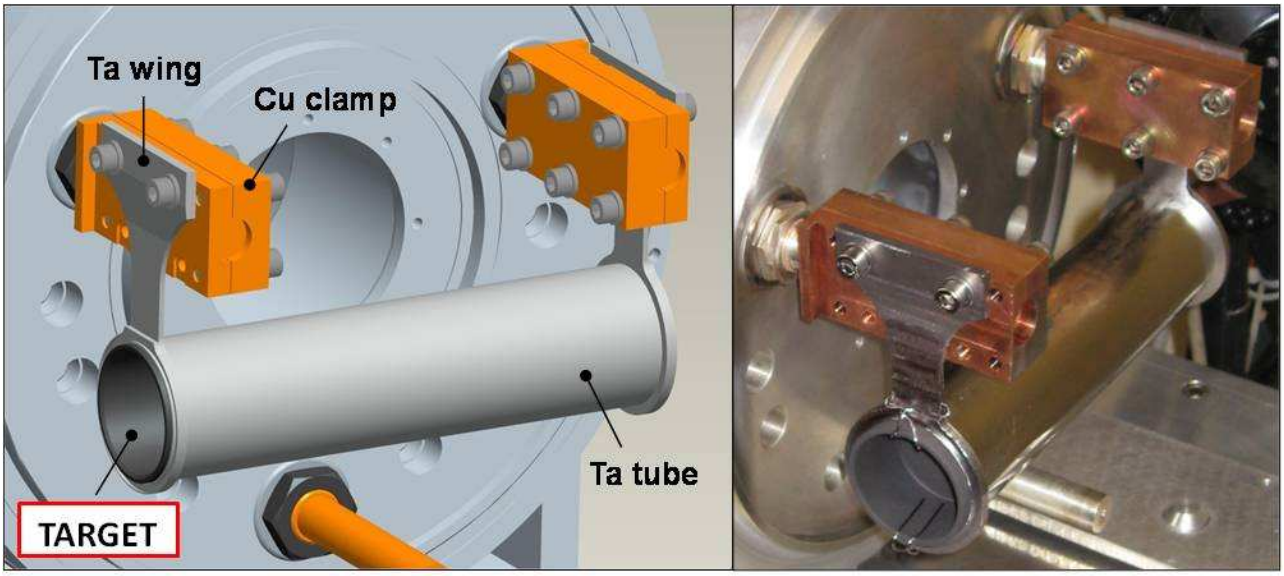

Fig. 3.5. CAD representation and picture of the target heating system and its main components (tube, wings and clamps).

Once described the SPES target and its heating system, the following remarks should be mentioned: a) to guarantee an efficient RIB production rate the SPES target has to work at very high temperatures, close to 2000°C; as a consequence it is important to know the target temperature distribution in detail, especially in the zones where it is not possible to perform temperature measurements, b) the target is heated by two thermal load components, the first one generated by the proton beam, the second one due to the independent heating system, c) the thermal and electrical problems are coupled, since the thermal load due to the heating system is produced by Joule Effect and the electrical resistivity of tantalum is temperature dependent.

For all the aforementioned reasons, a theoretical and experimental study of the target's thermal-electric behaviour was performed and is now reported in the following paragraphs.

3.3. The first SPES Target prototype: thermal-electric study

Once presented the SPES target and the way it works, a detailed study of its thermal-electric behaviour is presented in this paragraph. In particular, a coupled thermal-electric Finite Element (FE) model was defined in the ANSYS® environment, in order to support the design and the optimization process of the target and its heating system. The aforementioned model solves the coupled thermal-electric conductive problem thanks to the ANSYS® coupled-field element type SOLID69, which handles the two-way coupling between the thermal and the electrical problems (thermal loads are produced by Joule Effect and the electrical resistivity is temperature-dependent).

Thermal radiation (the dominant heat transfer mode at high temperatures) was implemented according to the ANSYS® Radiosity Solver method, which enables one to introduce temperature-dependent emissivity values. Temperature dependence of all relevant material properties was taken into account.

Fully coupled thermal-electric FE or analytical simulations are well documented in the literature dealing with various fields of the industry or of the material science (see for example [4,5,6,7,8,9] and references quoted therein), but as far as the authors are aware, FE-based design and simulation of geometrically complex structures operating at temperature on the order of 2000°C, where thermal radiation is the prevailing heat transfer mode, have still little spread in the technical literature [10,11]. In particular, the facility which has been designed and manufactured in the context of the SPES project presents some interesting novelties; one of the most significant is the multi-disk configuration of the target which allows to increase the power of the primary beam and consequently to improve the production rate of the radioactive isotopes. Only recently attention has been devoted to such target configuration in the technical literature [2].

As a first step, only the heating effect of the independent heating system was considered during the first set of FE calculations. Once validated such model against experimental data, the effect of the proton beam was implemented.

Then, aims of simulations described in the present section were as follows:

- to calculate the heat dissipation by Joule effect in the tantalum tube;
- to calculate the target block (i.e. the target and the heating system assembly) temperature distribution;
- to estimate the effect of some design variables and construction details characteristic of the water-cooled chamber (such as the presence of the channel for the proton beam entrance, the chamber's temperature level and the internal surface finish) on the target temperature distribution;
- to study the influence of the proton beam on the target thermal behaviour.

Before running the first set of numerical simulations, a simple, analytical, one-dimensional model was defined to estimate the Ta tube temperature related to Joule heating. All theoretical results (both analytical and numerical) obtained with the first set of analyses (only the Joule heating thermal load is considered) were then compared with thermal and electrical experimental measurements. In order to facilitate the experimental activity the uranium carbide disks were substituted by silicon carbide (SiC) disks; SiC has emissivity values similar to UC_x, but it does not involve the radiological problems that make the use of UC_x more complicated in terms of authorization and safety.

Once validated experimentally the FE model in presence of the Joule heating thermal load, the heating effect of the primary proton beam was virtually estimated by means of a new dedicated set of FE simulations; in this case uranium carbide disks were considered.

3.3.1. Analytic one-dimensional model

In order to support with a simple tool the target block design and optimization, a simple one-dimensional analytical model was considered (see figure 3.6).

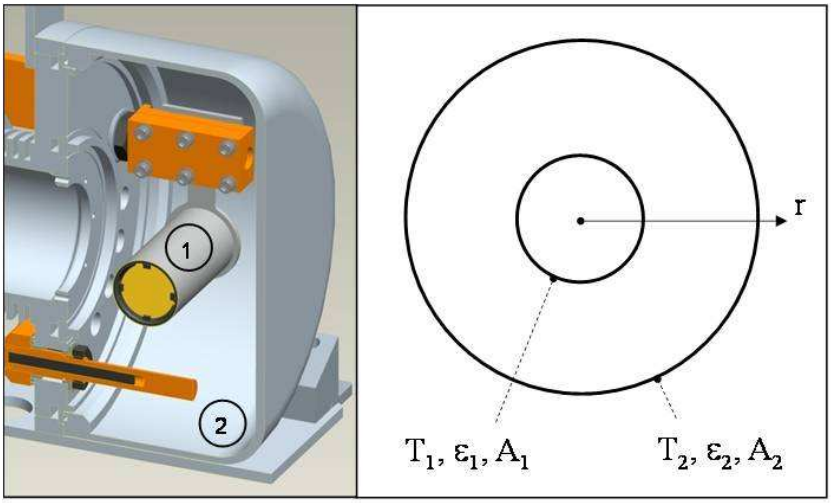

Fig. 3.6. Analytic thermal model; the external cylindrical surface of the Ta tube (A_1) and the internal surface of the vacuum chamber (A_2) are modelled as equivalent concentric spheres.

In particular this model delivers one single temperature value for the whole Ta tube surrounding the graphite box (indeed the Ta tube is characterized by significant temperature gradients, particularly close to the connections with the Ta wings). Even if the geometry was drastically simplified, on the other hand the model takes into account the variability of tantalum electrical resistivity and emissivity with temperature (see figures 3.7 and 3.8).

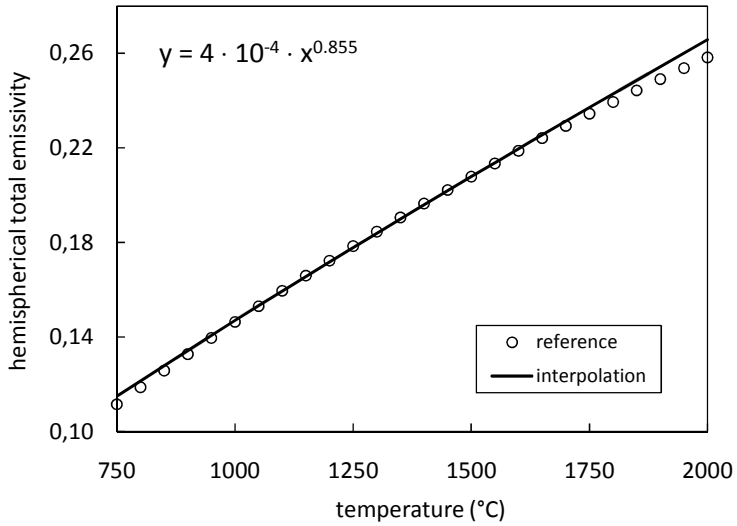

Fig. 3.7. Temperature dependence of the hemispherical total emissivity of tantalum [12] and interpolating function adopted in the analytic model.

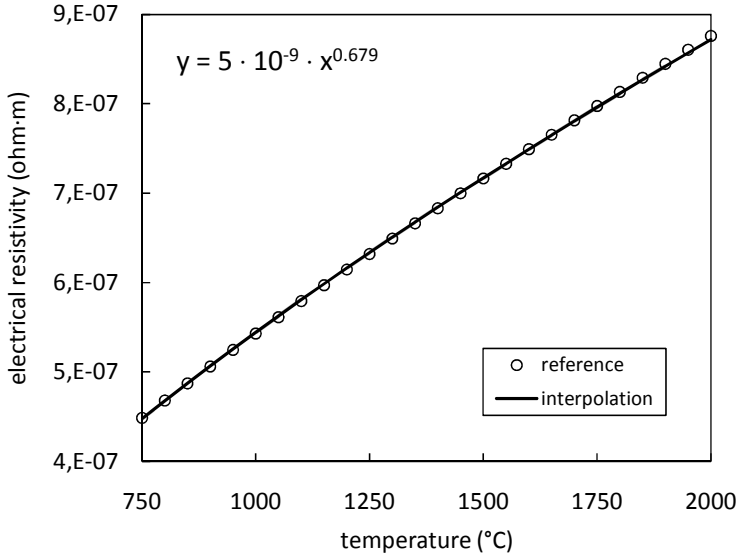

Fig. 3.8. Temperature dependence of the electrical resistivity of tantalum [13] and interpolating function adopted in the analytic model.

Since the target block is kept under vacuum and its working temperature is close to 2000°C, then thermal radiation is dominant with respect to the other heat transfer mechanisms. If we take into consideration only the external lateral surface of the Ta tube (area A_1), the internal surface of the vacuum chamber (total area A_2) and approximate them with equivalent concentric spherical surfaces having same areas A_1 and A_2 (see again figure 3.6), the radiative heat flux $q_{1\text{-}2}$ between the target block and the chamber can be expressed as (in the hypothesis of gray-diffuse surfaces) [14]:

$$q_{1-2} = \frac{A_1 \cdot \sigma_n \cdot (T_1^4 - T_2^4)}{\frac{1}{\varepsilon_1} + \left(\frac{A_1}{A_2}\right) \cdot \left(\frac{1}{\varepsilon_2} - 1\right)} \tag{1}$$

where σ_n is the Stefan-Boltzmann constant, T_1 and T_2 are the absolute temperatures of the two concentric spherical surfaces, ε_1 and ε_2 are the hemispherical total emissivities of surfaces 1 and 2, respectively.

If we consider the heat dissipation produced by the electrical current I that flows through the thin Ta heater (it is a conductor of uniform cross section S, length L and electrical resistivity ρ), and suppose that it is totally dissipated by thermal radiation, then we have [15]:

$$q_{1-2} = \frac{\rho \cdot L}{S} \cdot I^2 \tag{2}$$

As a consequence, combining equations (1) and (2), the temperature of the Ta tube can be estimated by means of the following expression:

$$T_1 = \sqrt[4]{T_2^4 + (\sigma_n \cdot A_1)^{-1} \cdot \left[\frac{1}{\varepsilon_1} + \frac{A_1}{A_2} \cdot \left(\frac{1}{\varepsilon_2} - 1\right)\right] \cdot \frac{\rho \cdot L}{S} \cdot I^2} \qquad (3)$$

Eq. (3) can be used to study the Ta tube temperature dependence on the heating electrical current I. It has to be solved numerically, since Ta electrical resistivity ρ and emissivity ε_1 are temperature T_1 dependent.

In the next paragraph the fundamental thermal and electric equations governing the actual three dimensional temperature field will be presented and discussed.

3.3.2. Theoretical frame

Dealing with the description of heat transfer phenomena, it is possible to observe that coupled conduction/radiation problems are usually solved by means of a sequential method [16], which considers iteratively the thermal diffusion and the radiation equations: radiative heat fluxes deliver boundary conditions for the diffusion problem whereas surface temperature distributions provide boundary data for thermal radiation. Figure 3.9 sketches the coupled conduction/radiation problem, characterized by heat diffusion within the solid region D (conductive problem) and by the radiative heat transfer between the surfaces forming the radiation enclosure S_{enc} (radiative problem).

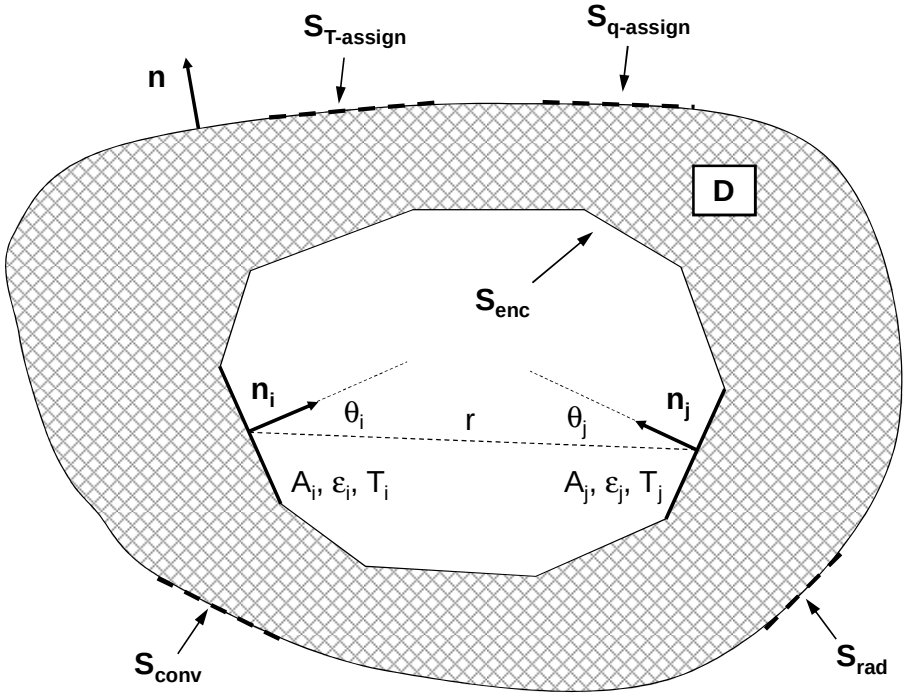

Fig. 3.9. Schematic representation of a coupled conduction/radiation problem and specification of the related boundary conditions.

The conductive problem is described in its general form by the heat diffusion equation (in Cartesian coordinates) [17]:

$$\frac{\partial}{\partial x}\left(k\frac{\partial T}{\partial x}\right)+\frac{\partial}{\partial y}\left(k\frac{\partial T}{\partial y}\right)+\frac{\partial}{\partial z}\left(k\frac{\partial T}{\partial z}\right)+h=\delta c\frac{\partial T}{\partial t} \tag{4}$$

where T(x,y,z) is the temperature field, t is time, δ is the density of the material, c is the specific heat, k is the thermal conductivity and h is the volumetric heat source. To obtain the solution from equation (4), definition of both initial and boundary conditions is necessary.

Initial conditions specify the temperature field T(x,y,z,t) within the whole solid region D at the initial time:

$$T(x,y,z,0)=T_i(x,y,z) \qquad \forall(x,y,z)\in D \tag{5}$$

Boundary conditions describe the status on the surface S that wraps the domain D; in general they can be expressed in the following way:

$$T(x,y,z,t)=T_{assign}(x,y,z,t) \qquad \forall(x,y,z)\in S_{T-assign} \tag{6}$$

$$-k\frac{\partial T}{\partial n}(x,y,z,t)=q_{assign}+q_{conv}+q_{rad} \qquad \forall(x,y,z)\in(S_{q-assign}\cup S_{conv}\cup S_{rad}) \tag{7}$$

$$-k\frac{\partial T}{\partial n}(x,y,z,t)=q_{enc} \qquad \forall(x,y,z)\in S_{enc} \tag{8}$$

where eq. (6) represents an explicit temperature constraint, the normal derivatives in equations (7) and (8) are computed with respect to the external versor **n** normal to the boundary S and $S = S_{T\text{-}assign} \cup S_{q\text{-}assign} \cup S_{conv} \cup S_{rad} \cup S_{enc}$. The terms q_{assign}, q_{conv}, q_{rad} and q_{enc} in the previous expressions are positive when directed along the positive **n**-direction. In particular q_{conv} and q_{rad} indicate the convective and the far-field radiative components of the heat flux on the portion of boundary S_{conv} and S_{rad}, respectively; they are described by the following expressions [16]:

$$q_{conv}=\alpha\cdot(T-T_c) \tag{9}$$

$$q_{rad}=\varepsilon\cdot\sigma\cdot(T^4-T_r^4) \tag{10}$$

In equations (9) and (10) α is the convection heat transfer coefficient, T_c is the temperature of the fluid surrounding the boundary surface S_{conv}, ε is the hemispherical total emissivity of the supposed gray diffuse boundary surface S_{rad}, σ is the Stefan-Boltzmann constant and T_r is the environment absolute temperature or the reference absolute temperature of the isothermal surface (much larger than S) that completely surrounds the external boundary of the domain sketched in figure 3.9. On the surfaces A_i belonging to the enclosure S_{enc}, boundary conditions are governed by eq. (8), where q_{enc} is the net radiative loss from A_i. As eq. (8) shows, since convective heat transfer is absent on S_{enc}, q_{enc} is equal to the conductive heat flux through the boundary surface S_{enc} inside the domain D [18].

The solution of the radiative problem, i.e. the determination of q_{enc} , is obtained by considering the following expression [18] and assuming that the N surfaces involved in the radiative heat transfer are gray and diffuse and that each one is characterized by a uniform value both for the temperature and the net radiative heat flux:

$$\sum_{i=1}^{N}\left[\frac{\delta_{ji}}{\varepsilon_i}-F_{j-i}\left(\frac{1-\varepsilon_i}{\varepsilon_i}\right)\right]\cdot q_{enc,i}=\sum_{i=1}^{N}(\delta_{ji}-F_{j-i})\cdot\sigma\cdot T_i^4 \tag{11}$$

where δ_{ji} is the Kronecker delta (δ_{ji}=1 if i=j, δ_{ji}=0 otherwise), ε_i is the hemispherical total emissivity of surface i, F_{j-i} is the radiation view factor, $q_{enc,\,i}$ is the net rate of radiative energy loss per unit area (net flux) of surface i, σ is the Stefan-Boltzmann constant and T_i is the absolute temperature of surface i. The view factor F_{j-i} is defined as the fraction of the total radiant energy leaving surface j which impacts directly on surface i; it can be expressed as [18]:

$$F_{j-i}=\frac{1}{A_j}\int_{A_j}\int_{A_i}\frac{\cos\theta_j\cdot\cos\theta_i}{\pi\cdot r^2}dA_i\,dA_j \tag{12}$$

where geometric quantities in equation (12) are defined in figure 3.9.

Concerning the electrical problem, the field of current density, **j**(x,y,z), depends on the gradient of the electric potential field, V(x,y,z), according to Ohm's equation:

$$\mathbf{j}=-\frac{1}{\rho(T)}\nabla V \tag{13}$$

where $\rho(T)$ is the temperature dependent electrical resistivity. Moreover, continuity equation for field **j** holds true, since steady state conditions are considered:

$$\nabla\cdot\mathbf{j}=0 \tag{14}$$

According to the Joule effect, heat power dissipation in a unit volume of material, h(x,y,z) in eq. (4), can be calculated as follows:

$$h=-\nabla V\cdot\mathbf{j} \tag{15}$$

where symbol "·" indicates scalar product between the two vectors.

3.3.3. Numerical FE model

The geometry of the target block and the surrounding vacuum chamber is reported in figure 3.10, which summarises also the applied thermal and electric boundary conditions. A perfect electrical and thermal contact was considered between the tantalum wings and the copper clamps (in the real system they are connected by means of screws), whereas a small radial gap (0.2 mm) was introduced between the Ta tube and the external cylindrical surface of the graphite box (in the real system both the graphite box and the Ta tube are positioned horizontally and the box leans against

the Ta tube because of the gravity): as a consequence in our numerical model the heating system and the target can exchange heat only by thermal radiation.

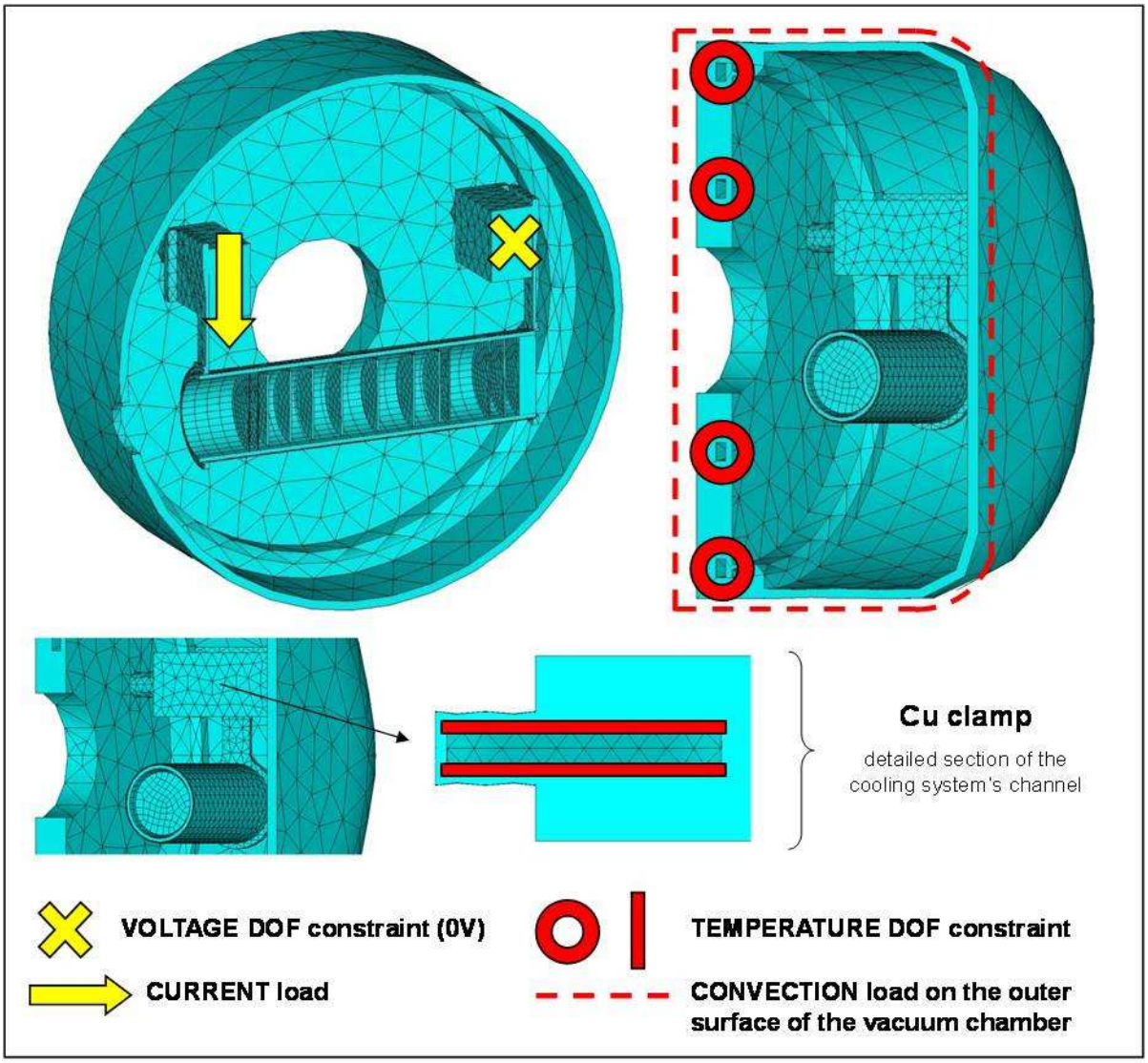

Fig. 3.10. Section views of the FE numerical model used to simulate the thermal-electric behaviour of the target heating system and representation of the applied boundary conditions.

To simulate the thermal behaviour of the production target and its heating system, a three-dimensional FE model was defined in the ANSYS® 11.0 environment. In particular, to model the heating system, the coupled thermal-electric element SOLID69 was used, which is able to consider both the thermal and the electrical problem described by eqs. (4), (9-11), and (13-15). Each node of this element has two degrees of freedom, that is temperature and voltage: with respect to other numerical approaches used to solve coupled thermal-electric problems [19], the adopted element type allows the simulation of heat generation due to the Joule Effect. On the other hand, the single degree of freedom thermal element SOLID70 was adopted to model the target and the vacuum chamber, since only the thermal problem, eqs. (4) and (9-11), has to be solved here.

According to the ANSYS® Radiosity Solver method, that restricts radiation exchange to gray-diffuse surfaces, equation (11) (governing heat radiation) is solved in conjunction with equation (4) (governing heat diffusion). After determining the temperatures T_i on the surfaces forming the radiative enclosure from the conductive problem solution, a system of N explicit equations (11) delivers the net flux at each surface $q_{enc,\,i}$, which can be applied again to the conductive problem as a known boundary condition. In such a sequential solution method, radiative heat fluxes (the radiative problem's output) generate boundary conditions for the conductive problem, whereas superficial temperature distributions (the conductive problem's output) provide boundary data for the radiative one [16]. To calculate the view factors, eq. (12), the code uses the Hemicube method [20]. Six different enclosures (i.e. set of surfaces radiating to one another) were defined: five were needed to compute the radiative heat transfer among windows, disks, dumpers and the internal surfaces of the graphite box, while one was defined to compute thermal radiation between the external surfaces of the graphite box, the heating system and the internal surfaces of the vacuum chamber (see figure 3.11).

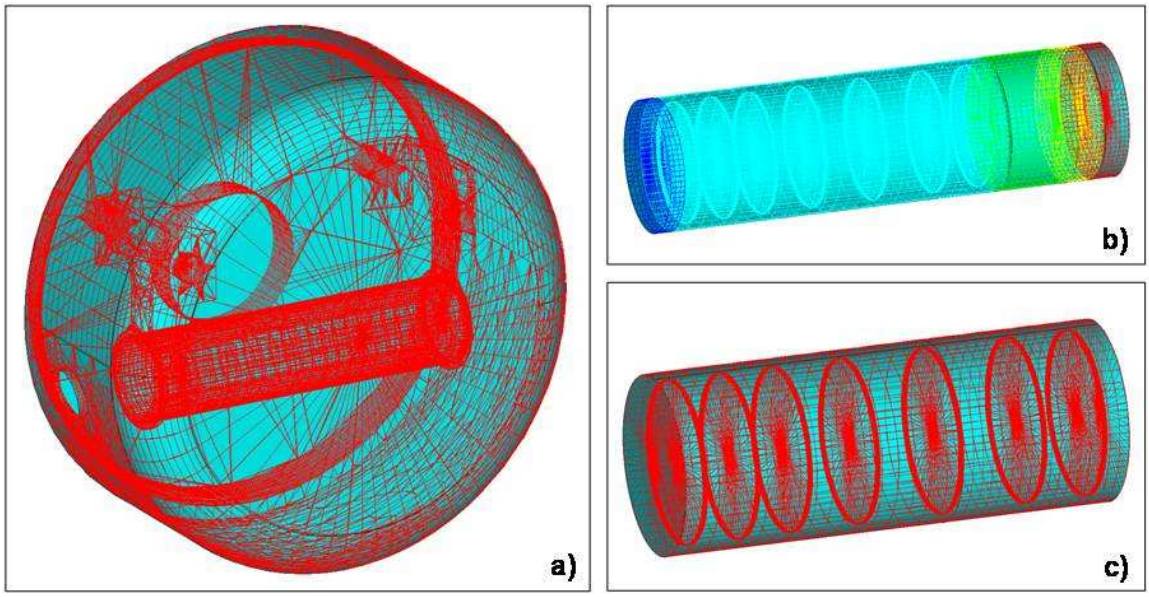

Fig. 3.11. Enclosures defined to calculate radiative heat transfer among the external surfaces of the graphite box, the heating system and the internal surfaces of the vacuum chamber (a), among windows, disks, dumpers and the internal surfaces of the graphite box (b), among disks and the graphite box (c).

Concerning the electrical problem, a constraint of 0 Volt was assigned to one of the copper clamps, whereas an electric current was forced on the other one. Concerning the thermal problem, a temperature constraint of 25°C was assigned to the surfaces of the cooling system's channels, which cross the chamber's base plate and the copper clamps. Since the chamber is kept in atmosphere at room temperature during laboratory tests, then natural convection was applied to the external surface of the chamber, eq. (9), with convection film coefficient α equal to 6 W/m^2K [17] and

reference temperature of the air surrounding the chamber equal to 25°C. Thermal radiation from the external surfaces of the chamber to the surrounding environment, eq. (10), was not considered since the chamber's temperature is too low to produce significant radiative heat fluxes.

To promote convergence of the Radiosity Solver method, transient analyses were performed [21] instead of steady state ones; in particular, a step-wise time-dependent current value was assigned starting from 400A up to the maximum value of 1000A, with steps of 50A. At each step, the simulation covered a sufficient period of time to let temperatures stabilise.

3.3.4. Material properties

The components involved in the coupled thermal-electric problem are the clamps and the heater (tube and wings assembly) made of copper and tantalum, respectively; to calculate their steady state temperature and voltage distributions, it was necessary to consider their temperature dependent properties in terms of electrical resistivity [13,22], emissivity (hemispherical total emissivity) [12] and thermal conductivity [23]. The components involved only in the thermal problem were the graphite (isotropic 2114 type, supplied by Carbon-Lorraine) windows, dumpers and box, the silicon carbide (Hexoloy SA type, supplied by Saint-Gobain) disks and the Al alloy vacuum chamber. Temperature dependent emissivity and thermal conductivity values were considered both for graphite [24,25] and silicon carbide [24,26]. For the Al alloy 5083, which the vacuum chamber is made of, thermal conductivity was assigned as a function of temperature [27] whereas the emissivity was set equal to 0.1. A list of the references, where temperature-dependent material properties implemented in the FE model were taken from, is reported in table 3.1.

Temperature-dependent material property	Temperature range	Reference
Cu electrical resistivity	0°C ($1.5\cdot10^{-8}$ ohm m) ÷ 1085°C ($1.02\cdot10^{-7}$ ohm m)	[22]
Cu emissivity	0°C (0.03) ÷ 900°C (0.05)	[12]
Cu thermal conductivity	0°C (402 W/m°C) ÷ 1085°C (329 W/m°C)	[23]
Ta electrical resistivity	0°C ($1.2\cdot10^{-7}$ ohm m) ÷ 2600°C ($1.1\cdot10^{-6}$ ohm m)	[13]
Ta emissivity	727°C (0.11) ÷ 2600°C (0.3)	[12]
Ta thermal conductivity	0°C (57 W/m°C) ÷ 2600°C (66 W/m°C)	[23]
C (graphite) emissivity	1270°C (0.81) ÷ 1970°C (0.85)	[24]
C (graphite) thermal conductivity	1227°C (56 W/m°C) ÷ 2127°C (43 W/m°C)	[25]
SiC emissivity	1000°C (0.8) ÷ 2000°C (0.85)	[24]
SiC thermal conductivity	0°C (120 W/m°C) ÷ 1000°C (60 W/m°C)	[26]
Al5083 thermal conductivity	-19°C (111 W/m°C) ÷ 576°C (147 W/m°C)	[27]

Table 3.1. Temperature-dependent material properties implemented in the FE model.

For all previous materials, the specific heat and density values were considered independent from temperature, since they do not control the steady state temperature distributions, which have been considered in the present work.

Concerning the emissivity value of 0.1 assigned to the chamber's internal surfaces, we recall that for opaque materials it depends exclusively on the status of a very thin surface layer. Then, it is heavily influenced by the surface finish and, for metallic materials, also by oxidation, which increases the emissivity. Oxidized surfaces of metals are generally characterized by values ranging from 0.25 to 0.7; the surfaces of polished metals may have emissivity values variable between 0.04 and 0.14 and in some particular cases highly polished metals, foils and films can achieve emissivity values as low as 0.02 [17]. For the Al alloys 7075T and 2024T, the average emissivity values found in literature for non oxidised surfaces at room temperature are 0.11 and 0.09, respectively [28]. In our case, being the internal surfaces of the chamber non oxidised and without particular surface treatment to improve surface finishing, an emissivity value equal to 0.1 was assumed, both for the FE and for the analytic models.

3.3.5. Experimental tests at LNL

To perform the off-line (i.e. without the effect of the proton beam) tests on the SPES target block, the experimental apparatus presented in figure 3.12 was adopted.

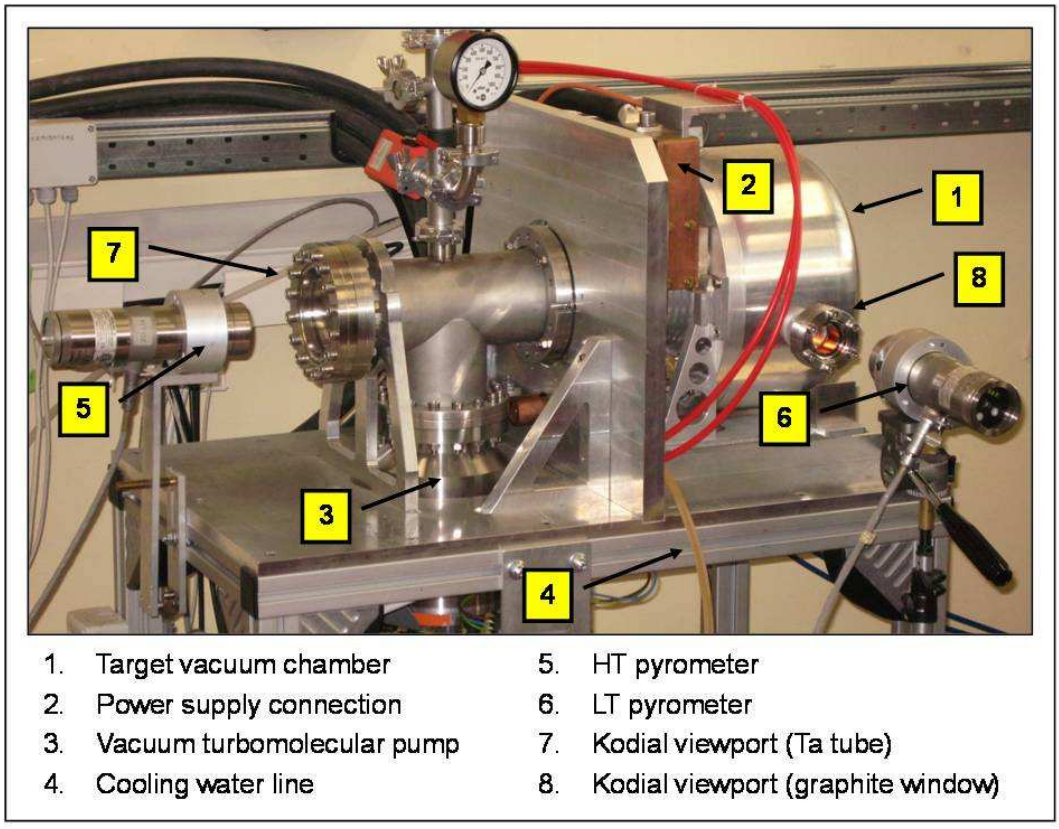

Fig. 3.12. Picture of the experimental apparatus used to measure the temperatures of the Ta tube and of the graphite window.

A power supply unit, delivering the maximum value of 10 kW, was electrically connected to the Ta tube through the Cu clamps thus causing heat dissipation by Joule effect. Vacuum inside the target chamber was supplied by means of a rotary and a turbomolecular pump installed in series, able to provide a vacuum level of 10^{-6} mbar. The chamber's base plate and the copper clamps were water cooled (water temperature and flow rate equal to 20°C and 400 litres per hour, respectively) in order to avoid over-temperature problems and damages on the chamber's vacuum gaskets. The experimental apparatus was arranged to allow the simultaneous measurement of both the Ta tube and the first graphite window (i.e. the first window that the proton beam would impinge) temperatures. Two infrared two-color pyrometers were used: one of them had a temperature range of 600-1400°C (Low Temperature pyrometer) and was used to measure the temperature at the centre of the first graphite window, the other one was fit for temperatures between 1000 and 3000°C (High Temperature pyrometer) and was used to monitor the Ta tube temperature on its lateral external surface, at the mid-point along its axial extension. Both pyrometers were characterized by an accuracy within 0.5% of reading plus 2°C and by a repeatability within 0.1% of full-scale temperature. To measure the temperatures of the graphite window and of the Ta tube closed inside the vacuum chamber, two boro-silicate glass view ports (Kodial view port, supplied by Torr Scientific Ltd, East Sussex-UK) almost completely transparent to infrared radiation were installed (see figure 9). Compressed air flows were used to prevent their local overheating.

Experiments were conduced by raising the heating current with steps of 50A, starting from 600A up to 950A, and keeping the current constant for about 30 minutes at each step, in order to let the system temperature distribution stabilize and then temperature measurements been performed.

When using pyrometers, it is important to limit and to evaluate the reflectance effects, which can lead to significant measurement errors. Fortunately, concerning the temperature measurement of the external graphite window, reflectance effects were limited by the high emissivity of graphite, approximately equal to 0.8 for the temperature range observed during experiments. By simply exchanging the attachments of the tantalum wing to the copper clamps, temperature measurements were performed also on the last graphite dumper (see again fig. 3.3). Concerning temperature measurements on the Ta tube, reflectance problems might have arisen because of the low emissivity of such material (see figure 3.7). Fortunately, the surfaces surrounding the measurement point, namely the surfaces of the vacuum chamber, were characterized by low temperature levels (on the order of 50°C) and then reflectance effects resulted again negligible.

Electrical potential difference values were measured between the external sides of the copper clamps by using a digital voltmeter characterized by a measurement range 0-1000V and an accuracy equal to 0.1% of reading.

It is important to remark that each experimental value reported in this work is the mean of three repeated measurements, that in general proved to maintain a very stable behaviour: in particular the difference between one single measurement and the corresponding mean value was always below 1.6% (in most cases below 1%).

3.3.6. Comparison between theoretical and experimental data

Temperature values calculated by means of both the analytic and the FE models were compared with experimental data. Figures 3.13.a and 3.13.b show a picture of the Ta tube and of the target's first window, respectively, when the temperature has stabilised for a current of 950A. Figure 3.13.c illustrates the corresponding temperature distribution calculated by the FE model. A local overheating of the Ta wing, close to the ring connection with the Ta tube, observed during the experimental tests (see figure 3.13.b), was well predicted also by the FE model (see figure 3.13.c).

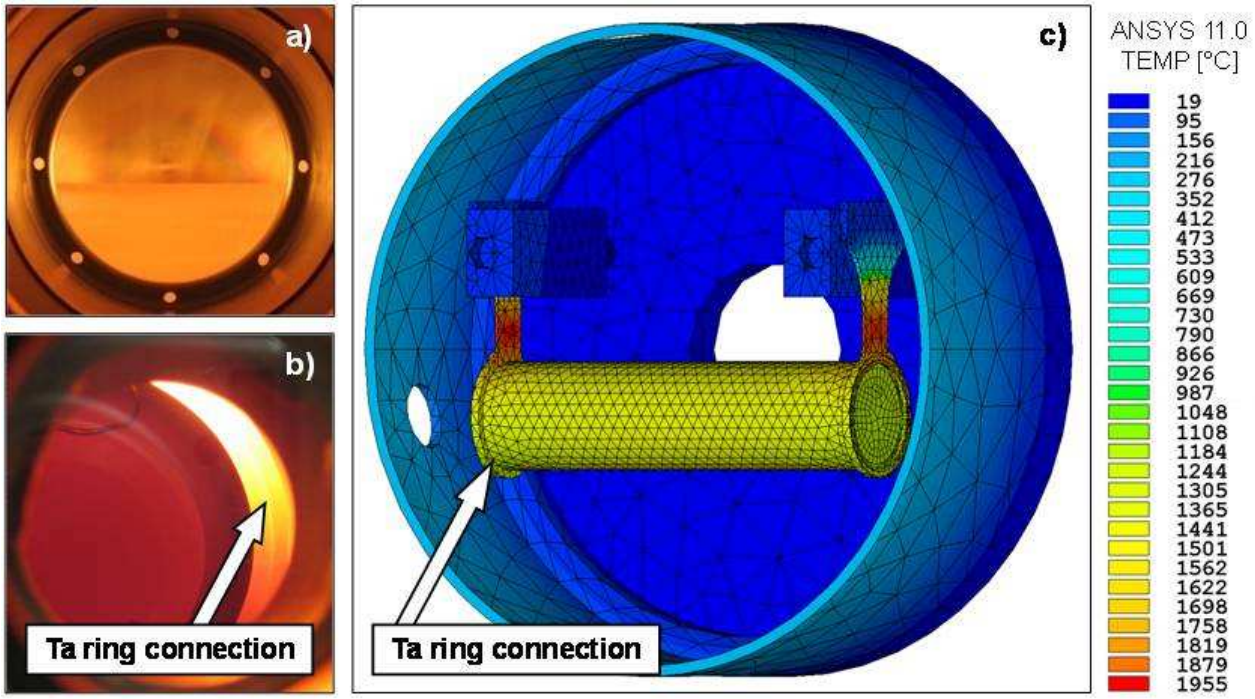

Fig. 3.13. Ta tube at high temperature seen from the Kodial viewport (a); graphite window at high temperature seen from the Kodial viewport (b); FE model temperature distribution (c).

Figure 3.14 reports a comparison among the analytic, the FE and the experimental temperatures of the Ta tube, for different values of the electric current. All data are in agreement, especially at high temperatures. Figure 3.14 shows in particular that FE temperatures are always slightly lower than analytic ones. In fact the analytic model does not consider the additional conductive heat flux from the Ta tube towards the water-cooled Cu clamps. This effect becomes weaker and weaker as temperature increases, because the conductive heat transfer mode is more and more reduced with respect to thermal radiation. We recall that the analytic model is one-dimensional so that it delivers

a single temperature value of the whole external surface of the Ta tube, differently from the FE and experimental results, which are point-related quantities and refer to the Ta tube's external surface, in the middle of its axial extension. The maximum difference between the analytic and the experimental temperatures shown by figure 3.14 is 16°C at 950 A of electric current, while the difference between numerical and experimental temperature ranges from 22°C (heating current equal to 950 A) to 40°C (heating current equal to 600 A).

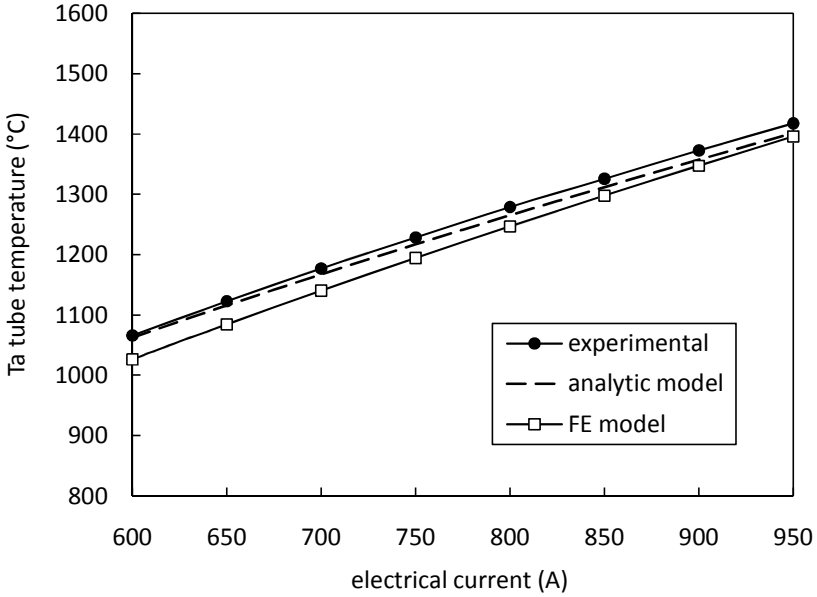

Fig. 3.14. Comparison between theoretical and experimental Ta tube temperatures. FE and experimental data refer to the midpoint along the tube axis on the outer surface.

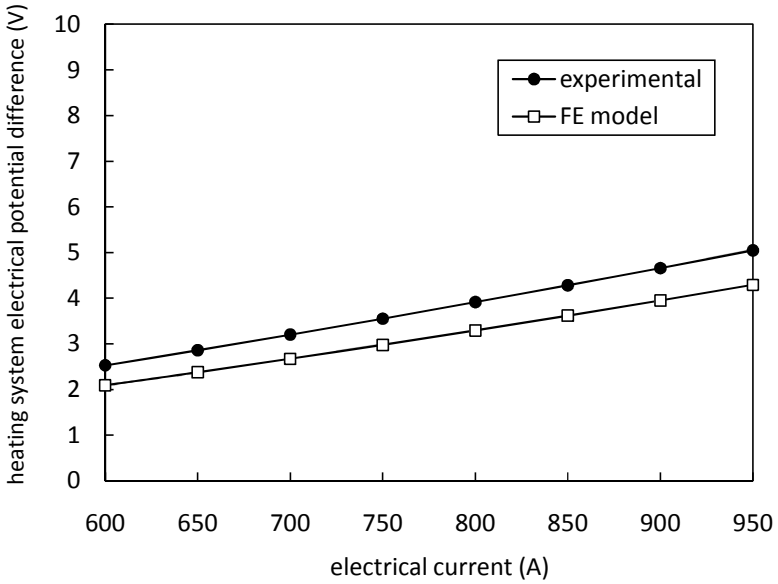

Fig. 3.15. Comparison between theoretical and experimental heating system potential difference values.

The electric potential values detected between the external tips of the Cu clamps are reported in figure 3.15. The difference between theory and experiment shown by the figure is probably due to

the ideal contacts between the Ta wings and the Cu clamps which were implemented in the FE model, while some electric contact resistances are to be expected from real connections, due to the rough mating surfaces, the screw joints and the mechanical deformations caused by thermal expansions. In fact the potential difference values calculated by the FE model are always lower than the measured ones; the differences with respect to the experimental data range from 0.4V for 600A to 0.8V for 950A. In the light of figure 3.15, it is seen that an higher electric power dissipation occurs in laboratory tests than in the FE simulation for the same electric current. This fact explains the higher experimental temperatures shown in figure 3.14 with respect to theoretical values.

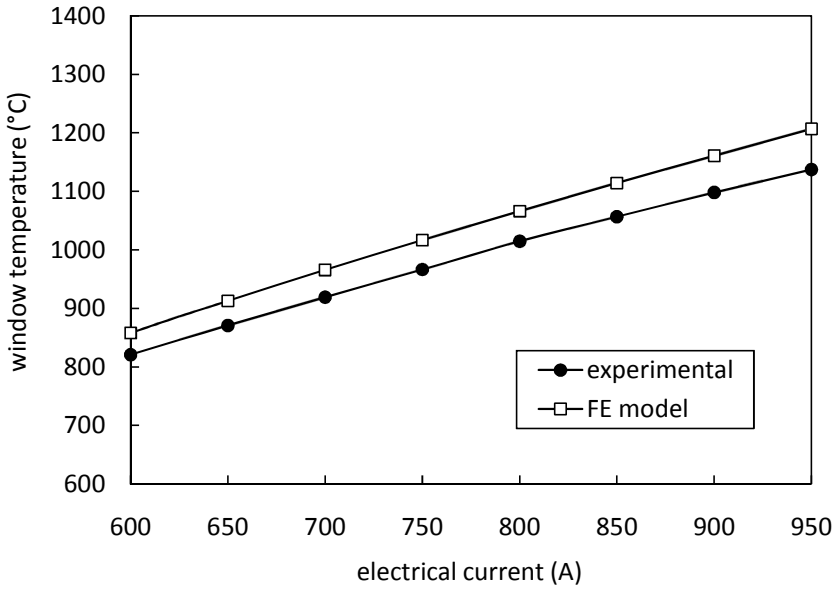

Fig. 3.16. Comparison between theoretical and experimental window temperatures. Data refer to the central point.

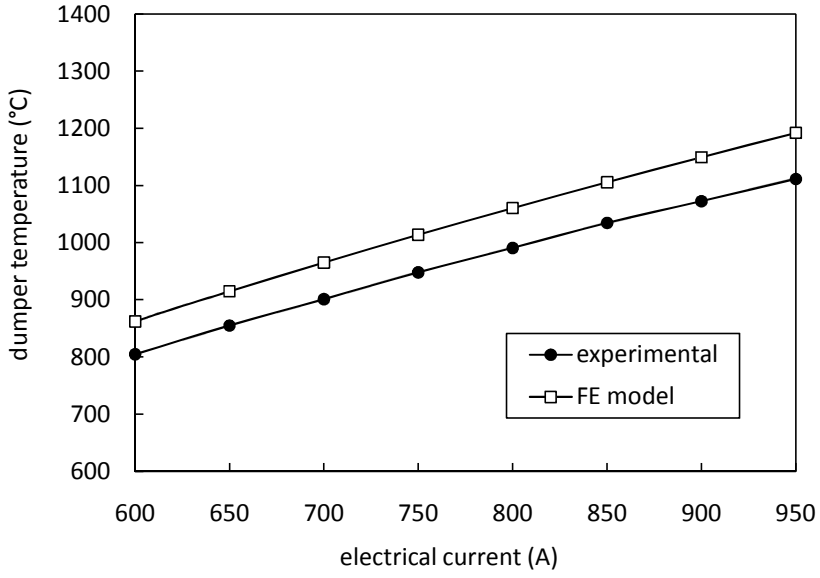

Fig. 3.17. Comparison between theoretical and experimental dumper temperatures. Data refer to the central point.

Figure 3.16 and 3.17 show the comparison between numerical and experimental temperatures on the first window and on the last dumper, respectively. The maximum difference is seen in both

cases when the electrical current is equal to 950 A, in particular it is 69°C for the window and 81°C for the dumper. Such differences could be probably due to the welded joint of the flange installed on the vacuum chamber to measure window's and dumper's temperatures. Such welded zone is shown in figure 3.18. By a thermal point of view it constitutes a ring of material with higher emissivity (worse surface finish) with respect to the surrounding zone; a higher emissivity in this zone (facing the window or the dumper) implies a higher cooling rate by thermal radiation, which was not considered by the FE model.

Fig. 3.18. The welded joint of the measurement flange.

3.3.7. Sensitivity analysis using the FE model

Once the FE model has been validated by means of experimental data, the sensitivity of the target block's temperature distribution to some design variables and construction details was studied. In particular the following topics were investigated: a) the effect of the holes introduced in the vacuum chamber to allow for temperature measurements, b) the effect of the chamber's temperature, c) the effect of the emissivity (i.e. surface finishing) of the chamber's internal surfaces.

Influence of the chamber's holes. The holes made on the vacuum chamber were used to measure the Ta tube and the window temperatures by means of the pyrometers, as shown in figures 3.12 and 3.13. It is very important to take into account their effects on the target block's temperature distribution since a similar and even bigger hole will be introduced in the on-line prototype (i.e. with the presence of the proton beam) to allow the proton beam crossing. To estimate the hole's effect, the FE model results were compared with those obtained from a new FE model that does not consider the holes, i.e. the chamber is completely closed without geometrical discontinuities. Figure 3.19 shows the results and put in evidence the cooling effect of the holes, especially for the first

graphite window: the two holes eliminates locally the reflections of the chamber's internal surfaces, which send back to the target block the incident radiation according to their low emissivity.

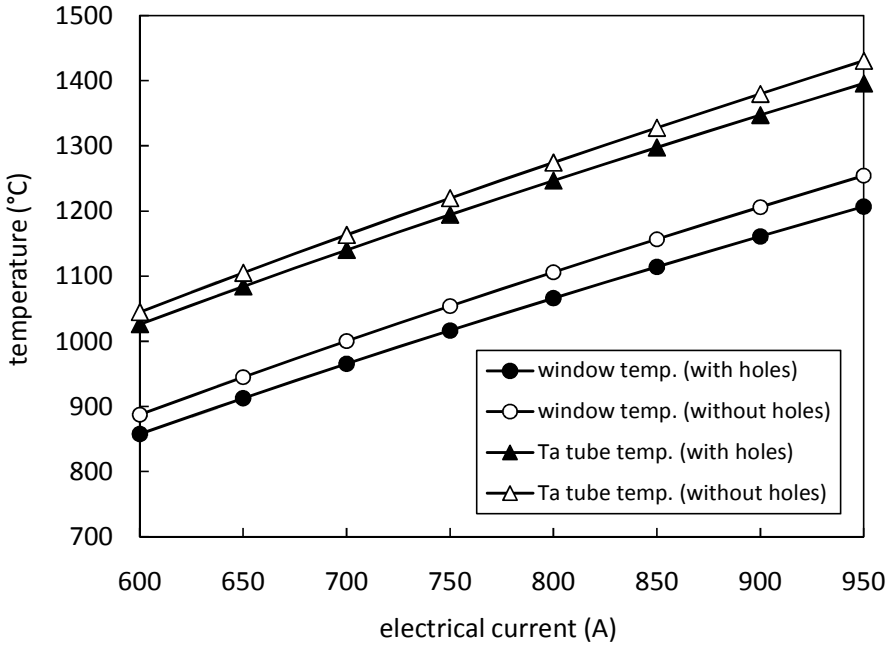

Fig. 3.19. Influence of the measurement holes on the temperature levels of the window and of the Ta tube.

This effect is particularly important in light of eq. (3) since the ratio between the chamber's internal area and the Ta tube's external area is limited. The maximum temperature drop due to the presence of the holes is seen at 950A, both for the first window (48°C) and for the Ta tube (35°C).

Influence of the chamber's temperature. The FE model described in the previous paragraphs did not take into account the effect of the compressed air flows adopted to cool the Kodial view ports and the zones surrounding them. Rather, a simple boundary condition of natural convection was imposed to the external surfaces of the vacuum-chamber. In the present paragraph, the sensitivity of numerical results to different thermal boundary conditions assigned to the chamber's external surface is investigated. The boundary conditions of the FE model were changed, substituting the convective thermal load (boundary condition set A) with a temperature constraint (boundary condition set B) equal to 25°C. We recall that the same temperature value is assigned to the internal surfaces of the cooling system's channels passing through the chamber's base plate and through the copper clamps (see figure 3.10); we will call this reference temperature $T_{BOUNDARY}$. The temperature distributions on the chamber obtained with the two different boundary conditions (sets A and B) are shown in figure 3.20: it was seen that with natural convection (boundary condition set A), the vacuum chamber reaches the maximum temperature of 332°C at its frontal side (i.e. at the maximum distance from the water cooled base plate), which is very different from the value assigned by boundary set B. Nonetheless, figure 3.21 clearly shows that both the Ta tube and the

graphite window do not change their temperature level while changing the boundary condition applied to the chamber.

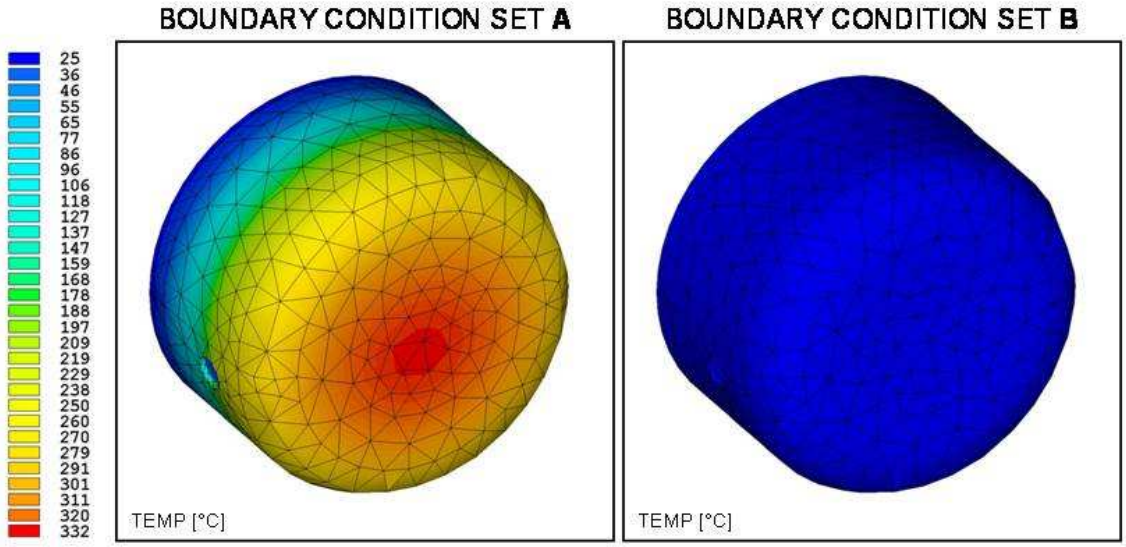

Fig. 3.20. Chamber's temperature distribution resulting from boundary condition set A and B.

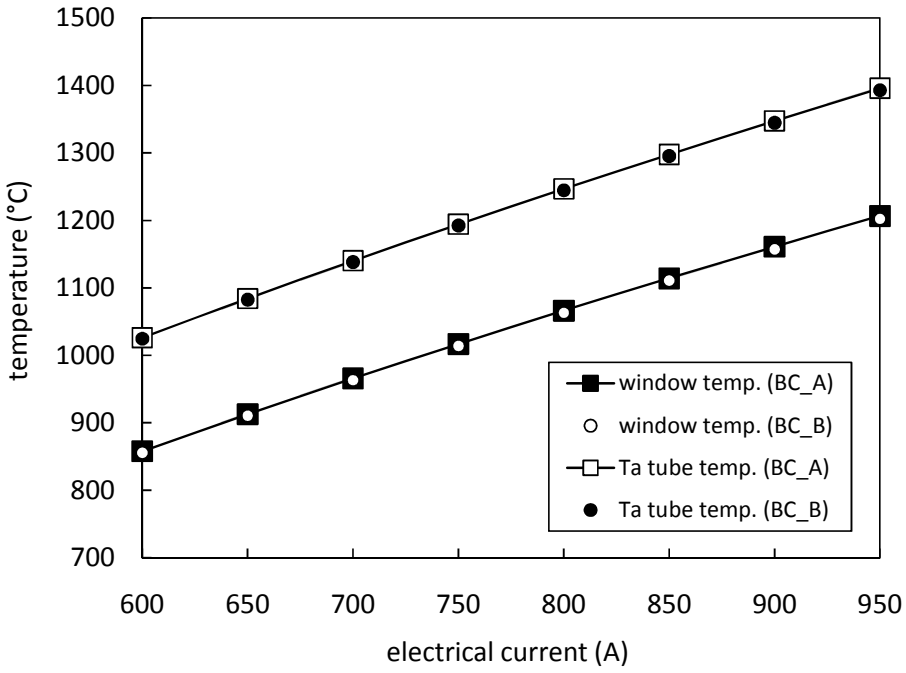

Fig. 3.21. Influence of boundary conditions (set A and set B) applied to the vacuum chamber on the target block's temperature.

The independence of the target block's temperature from the chamber's temperature was analysed in a wider range using the analytic model (eq. (3)). Results are reported in figure 3.22, where it is possible to appreciate that only if the chamber's temperature is beyond approximately 350°C, then the Ta tube's temperature increases significantly, otherwise the target's thermal behaviour remains unchanged. As a consequence, since for practical reasons the chamber temperature will be kept

below 100°C in the final design stage, the FE simulation can be run without paying too much attention to the thermal boundary conditions applied to the chamber itself, at least in the range 25÷100°C.

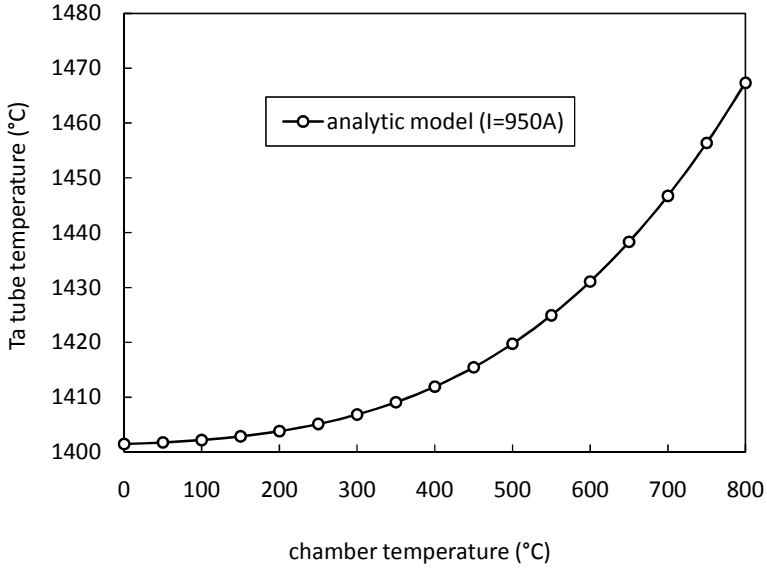

Fig. 3.22. Influence of the chamber's temperature on the Ta tube temperature (results from the analytic model).

In order to derive additional indications about the influence of the copper clamps temperature on the target thermal behaviour, $T_{BOUNDARY}$ was successively varied from 25°C (boundary condition set B) to 100°C. Results are summarized in figure 3.23, which shows that also in this case the influence on the target temperature is negligible.

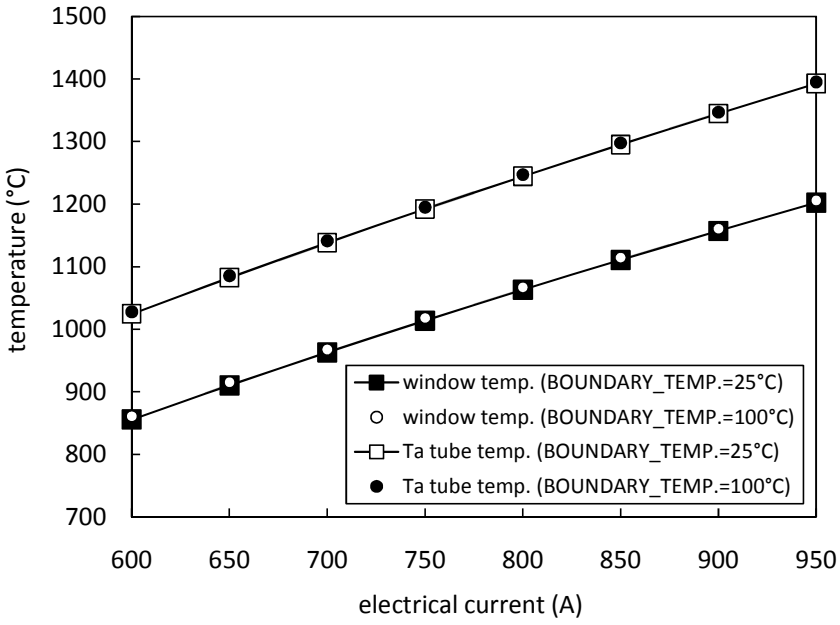

Fig. 3.23. Effect of $T_{BOUNDARY}$ on the target block's temperature distribution (results from the FE model).

Influence of the emissivity of the chamber's surfaces. In this paragraph the sensitivity of the numerical model to the chamber's emissivity is presented. The emissivity value was increased with

steps of size 0.02, starting from 0.06 up to 0.14: by so doing it is possible to estimate the effects of an accurate polishing treatment on the internal surfaces of the chamber and of a slight degradation of the surface finish, respectively; in fact at high temperatures the target releases gassy impurities that condense on the cold internal surfaces of the chamber, affecting their initial state and increasing in general their emissivity. This kind of phenomena were frequently observed during the off-line tests. Figures 3.24 and 3.25 show the influence of chamber's emissivity on the Ta tube temperature as predicted by the FE and by the analytic model, respectively.

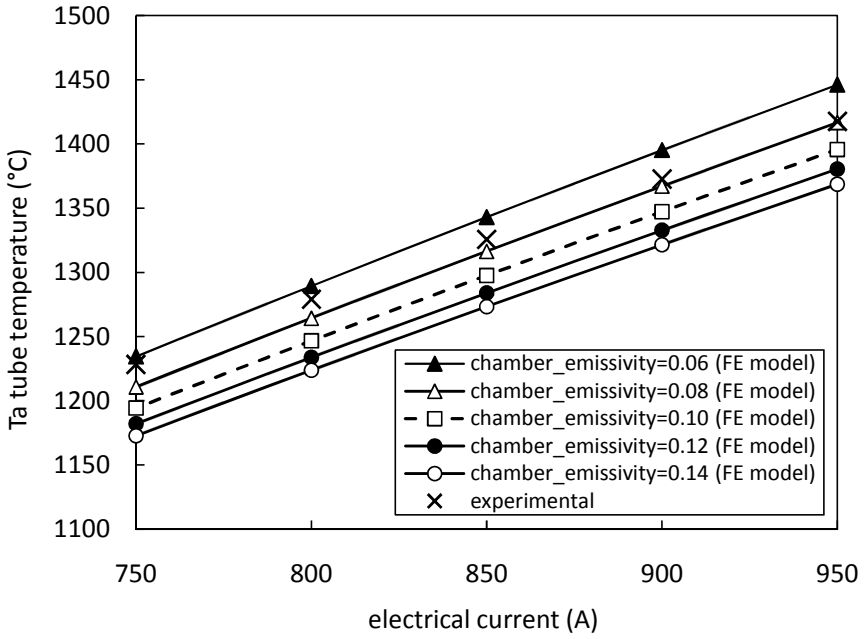

Fig. 3.24. Influence of chamber's emissivity on the Ta tube temperature (results from the FE model).

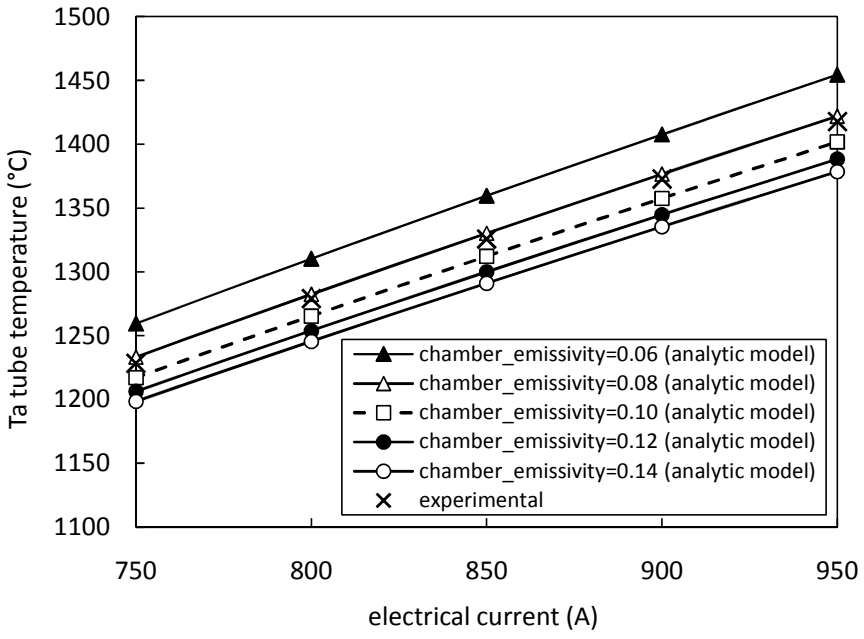

Fig. 3.25. Influence of chamber's emissivity on the Ta tube temperature (results from the analytic model).

The two different approaches deliver similar results, i.e. increasing the emissivity of the chamber results in decreasing the Ta tube temperature. This effect, as shown by equation (3), would be enhanced by increasing the A_1/A_2 ratio, that is the ratio between the external area of the Ta tube (A_1) and the internal area of the chamber (A_2).

The influence of the chamber emissivity on the window temperature as predicted by the FE model is presented in figure 3.26: also in this case decreasing the emissivity leads to increasing temperature levels.

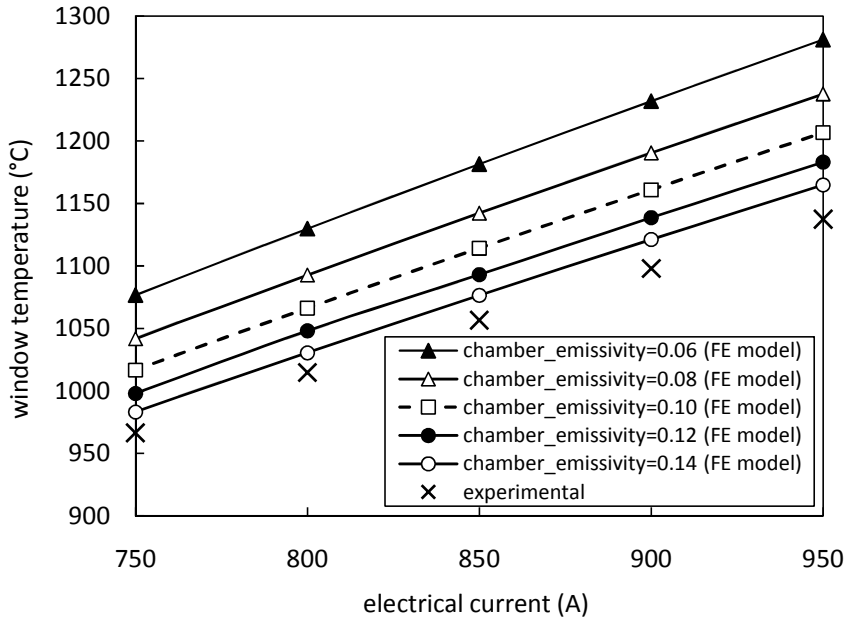

Fig. 3.26. Influence of the chamber emissivity on the window temperature (results from the FE model).

For all cases presented so far, it is interesting to observe that, for the same current value, the effects of the chamber's emissivity are non linear: for low emissivity values, Ta tube and window temperatures vary more rapidly than for high emissivity values.

Determination of the maximum current value sustainable by the target heating system. The maximum electrical current value imposed to the target heating system during the experimental tests was approximately equal to 950A; it was not possible to increase it more because of the limitations of the power supply adopted for this experimental session at INFN-SPES laboratories. In order to determine the maximum current value sustainable by the target heating system, a dedicated set of FE analyses was performed; in particular the FE model was slightly modified, considering UC_x disks instead of SiC ones. An emissivity value and a thermal conductivity of 0.8 (directly measured according to the method described in [24]) and 6 W/m°C [29], respectively, were assumed for uranium carbide; as mentioned before these are the thermal material properties needed to compute a steady state temperature field. $T_{BOUNDARY}$ was imposed equal to 25°C and the emissivity of the chamber's internal surfaces was fixed at 0.1; the same FE model was used to study

the effect of the proton beam on the target temperature distribution (see the next paragraph). Figure 3.27 presents a comparison among the Ta tube temperature, the maximum temperature of the target heating system and the graphite window temperature (see figures 3.3 and 3.5), considering current values ranging from 600 to 1300A.

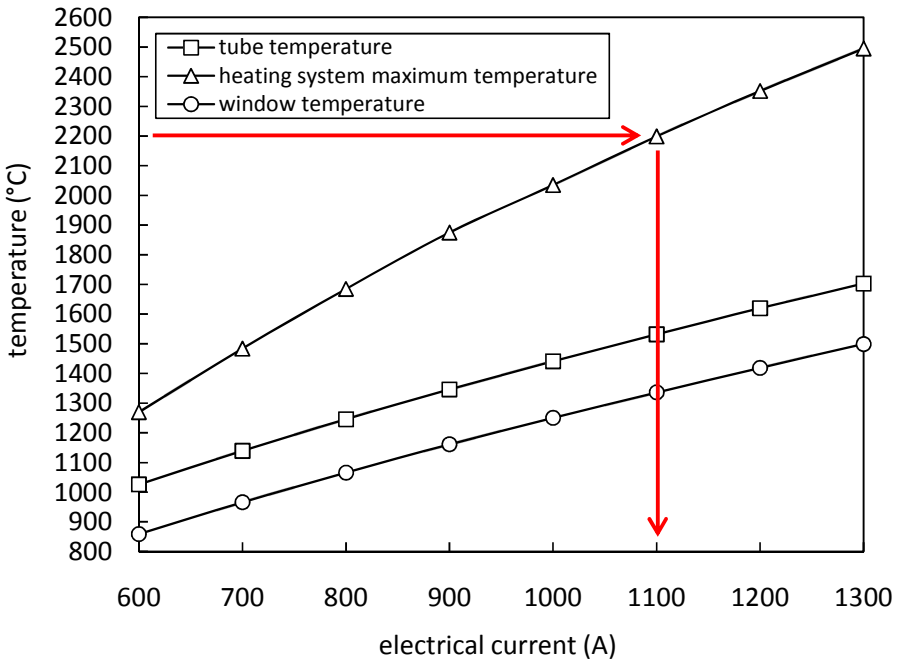

Fig. 3.27. Comparison among the Ta tube temperature, the maximum temperature of the target heating system and the graphite window temperature (results from the FE model).

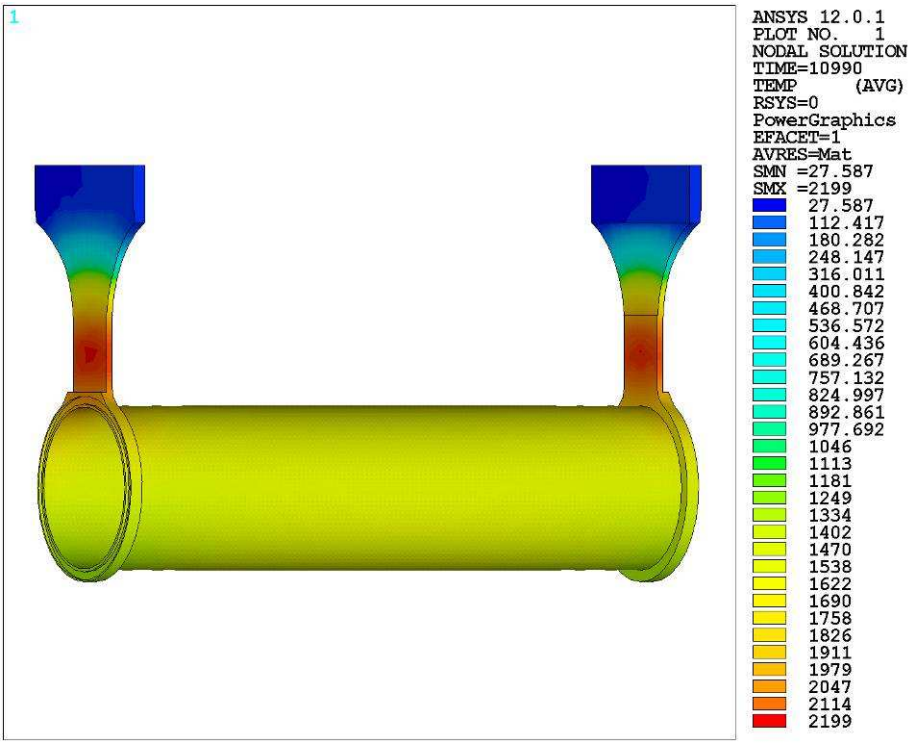

Fig. 3.28. Temperature plot [°C] of the target heating system correspondent to 1100A of heating current (results from the FE model).

The temperature distribution of the heating system is not well balanced: a hot spot is clearly visible on its wings that are notably hotter than its tube (tube temperature) (see figures 3.27 and 3.28). This temperature imbalance limits the possibility to increase the heating current, in particular, considering that the temperature limit for Ta (see paragraph 3.2) is approximately equal to 2200°C, the current limit was fixed at 1100A: according to FE calculations, for this current value the maximum temperature reached by the target heating system is equal to 2199°C (see figures 3.27 and 3.28).

Once discussed the temperature field of the most critical component (the heating system is the hottest object when the electrical current is the only thermal load), some information on the target's temperature distribution is presented. The author reminds that the target is composed of seven uranium carbide disks, two windows, four dumpers and a box made of graphite (see figure 3.3). Looking at the maximum temperatures of the target disks (see figures 3.29 and 3.30), it is possible to appreciate how they are sensibly below 2390°C, that is the minimum literature value of the UC_x melting point reported in [2]. Also the target's components made of graphite (windows, box and dumpers) are sensibly below the melting point of graphite (>3000°C [2]).

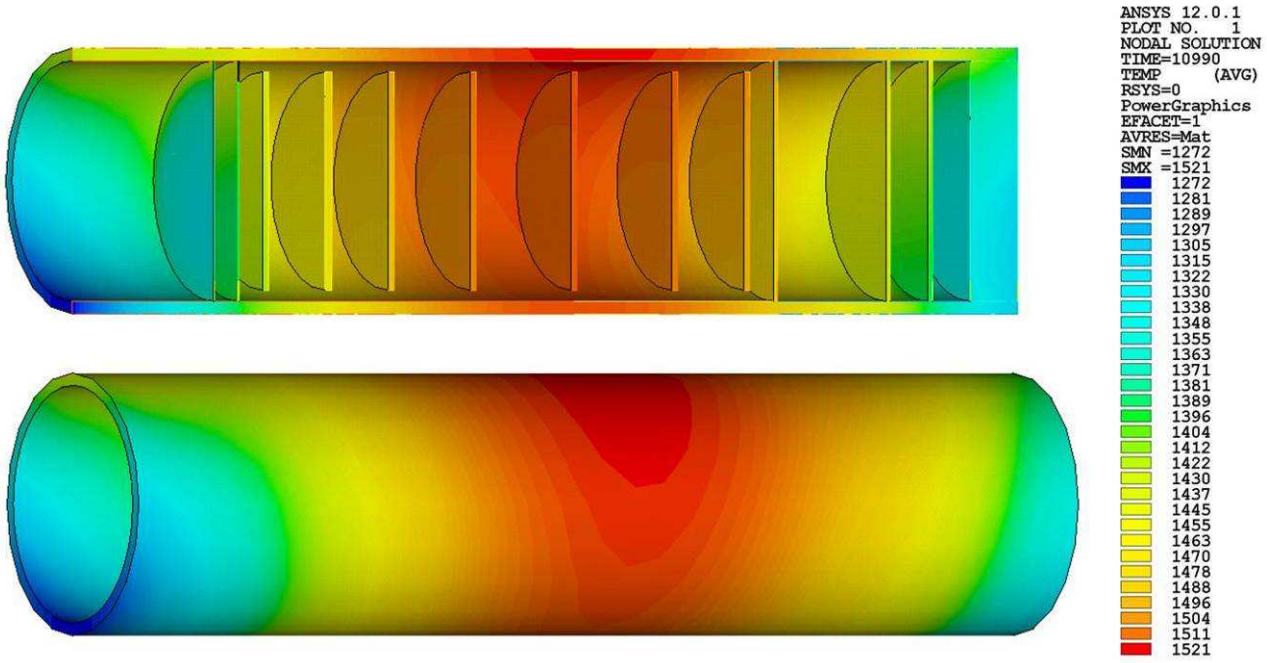

Fig. 3.29. Temperature plot [°C] of the production target (see figure 3.3) correspondent to 1100A of heating current (results from the FE model).

The minimum, the average and the maximum temperatures of the seven uranium carbide disks are reported in figure 3.30; observing this figure it is interesting to notice the general temperature increment moving from the disk facing the internal window (disk 1) to the disks positioned in the central zone of the target; another important aspect is the temperature homogeneity of the single disks: the more internal their position, the more homogeneous their temperature distribution.

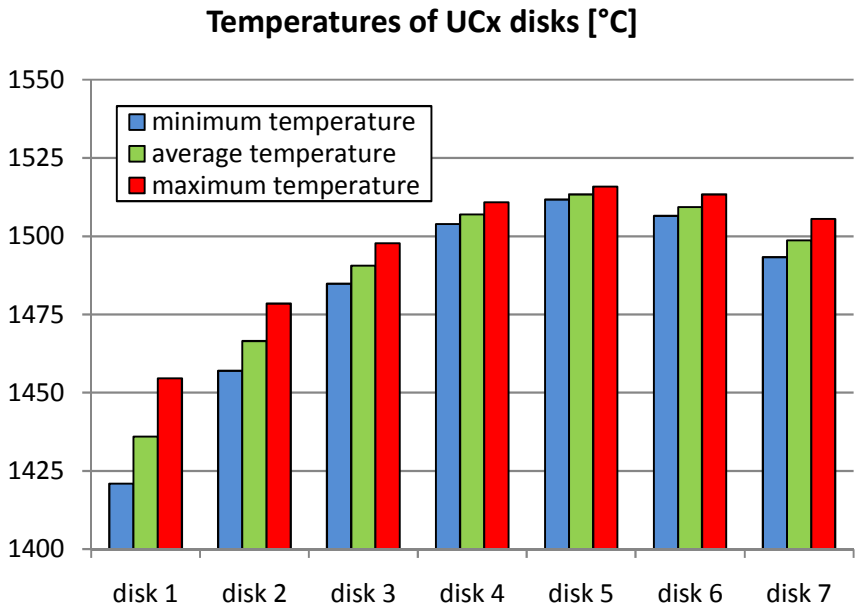

Fig. 3.30. Average, maximum and minimum temperatures of the UC_x disks correspondent to 1100A of heating current (results from the FE model).

Once described the thermal behaviour of the target due to Joule heating, the effect of the primary proton beam is presented in the next paragraph.

3.3.8. Study of the proton beam effect using the FE model

By means of the MCNPX code [2] it was possible to calculate the fission rate for the uranium carbide disks and the amount of power deposited by the proton beam for everyone of the components composing the production target (see table 3.1 and figure 3.31). The power data obtained in this way were then opportunely introduced in the FE model as thermal loads, allowing to estimate the effect of the proton beam on the target temperature distribution.

Component	**Fission rate** [f/s]	**Power** [W]	**Component**	**Power** [W]
- disk 1 -	1.40E+12	538	**- window 1 -**	94
- disk 2 -	1.29E+12	538	**- window 2 -**	94
- disk 3 -	1.22E+12	548	**- dumper 1 -**	518
- disk 4 -	1.15E+12	556	**- dumper 2 -**	532
- disk 5 -	9.80E+11	564	**- dumper 3 -**	738
- disk 6 -	8.22E+11	574	**- dumper 4 -**	920
- disk 7 -	6.19E+11	589	**- box 1 -**	230
/	/	/	**- box 2 -**	1100

TABLE 3.1. Power and fission rate data produced by the MCNPX code.

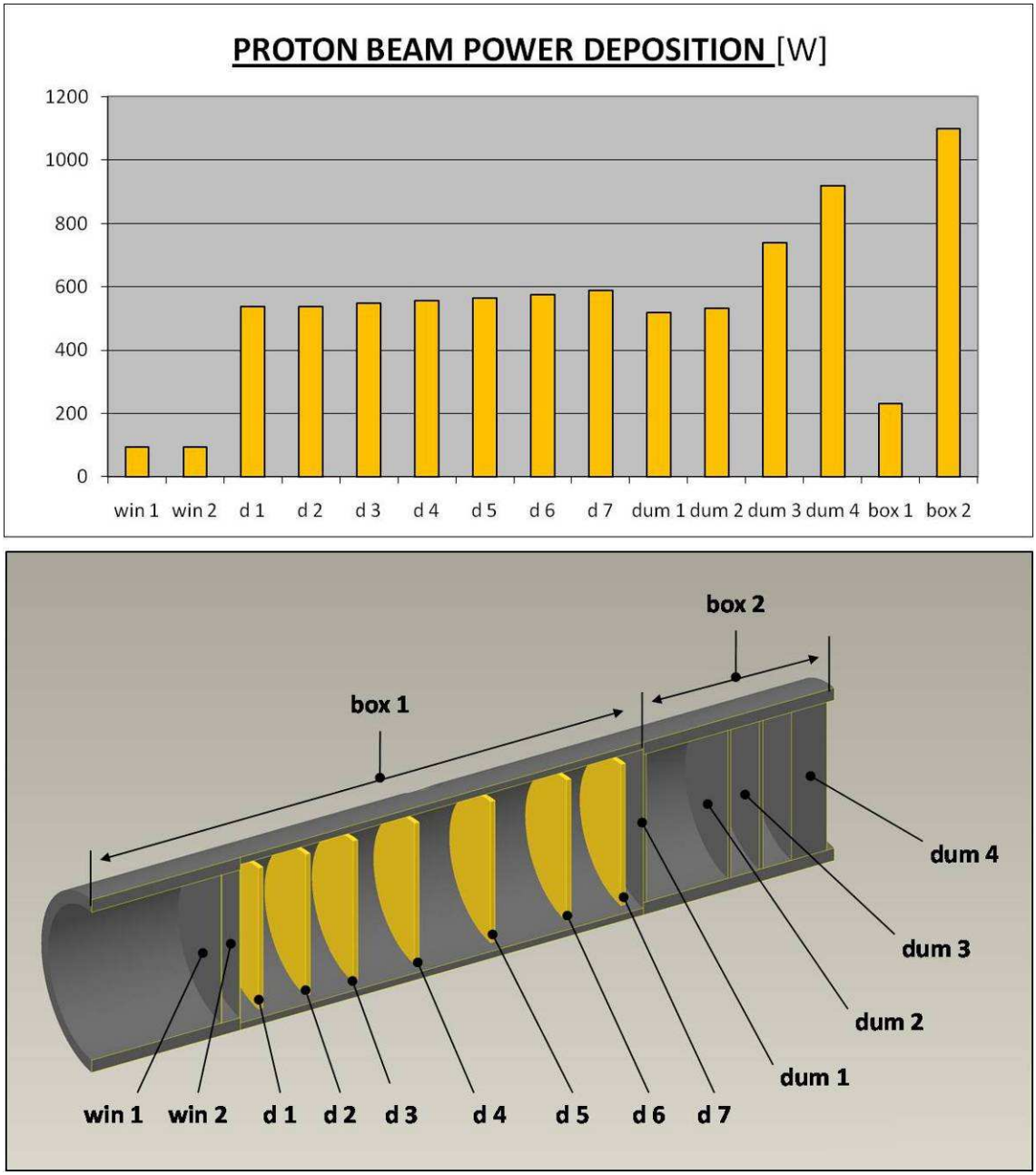

Fig. 3.31. Power deposited by the proton beam in the components composing the production target.

Figure 3.32 shows the temperature distribution of the target heating system due to the proton beam thermal load; it is interesting to observe how the tube's temperature is now higher respect to the wing's one; the heating system's maximum temperature is registered in proximity of the dumping zone and it is abundantly below the limit of 2200°C previously specified for tantalum. In fact in the dumping zone (the zone of the production target enveloped by box 2, see figure 3.31) the primary beam deposits a considerable amount of its power in a relatively small volume. In figure 3.33 the temperature plot of the SPES production target due to the 40 MeV and 200 μA primary proton beam is reported; the dumping zone is particularly hot respect to the rest of the target and the temperature imbalance between the target's extremities is evident. The maximum temperatures are

registered in the seventh disk and in the first dumper and are close to 2450°C; if on one hand this temperature level is not a problem for the graphite dumper, on the other hand it is very dangerous for the aforementioned disk made of uranium carbide, whose melting point is approximately equal to 2390°C.

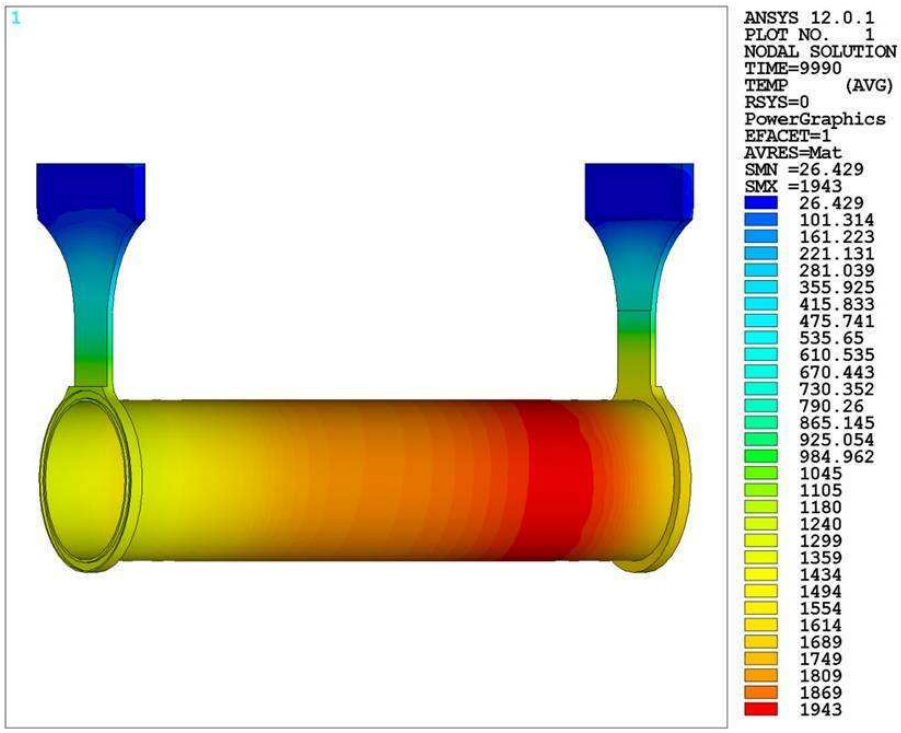

Fig. 3.32. Temperature plot [°C] of the target heating system correspondent to the proton beam thermal load (results from the FE model).

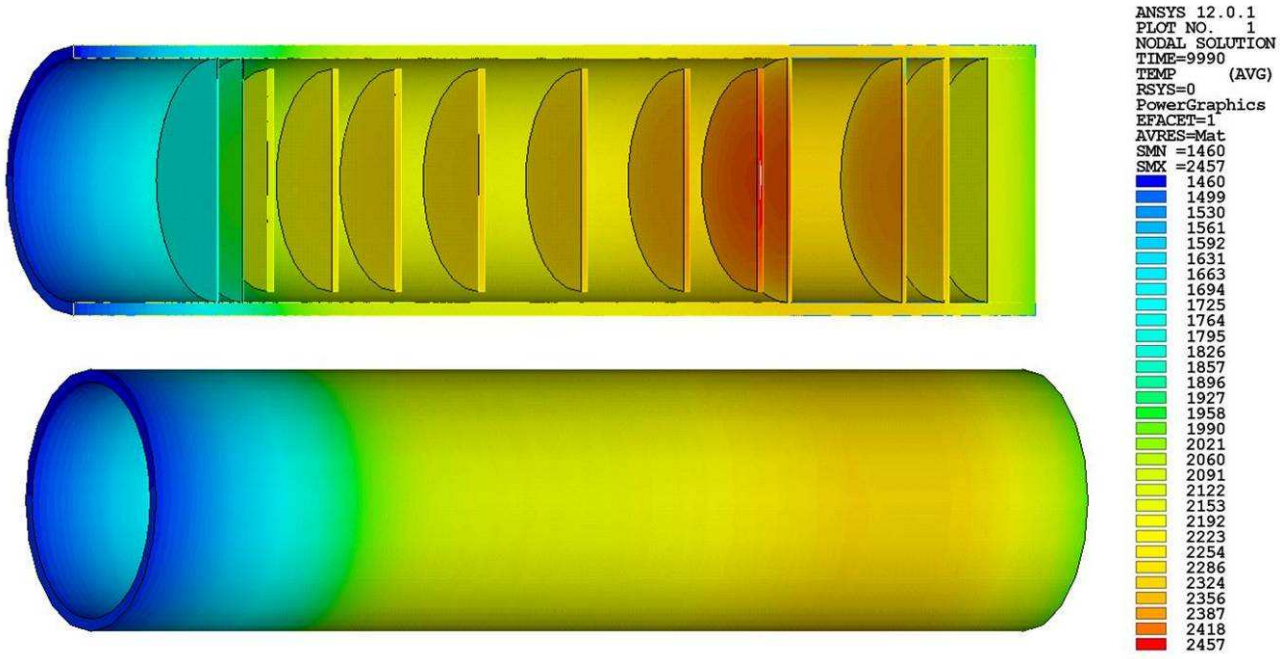

Fig. 3.33. Temperature plot [°C] of the production target correspondent to the proton beam thermal load (results from the FE model).

In order to have more information about the temperature levels of the uranium carbide disks the following figure has been introduced.

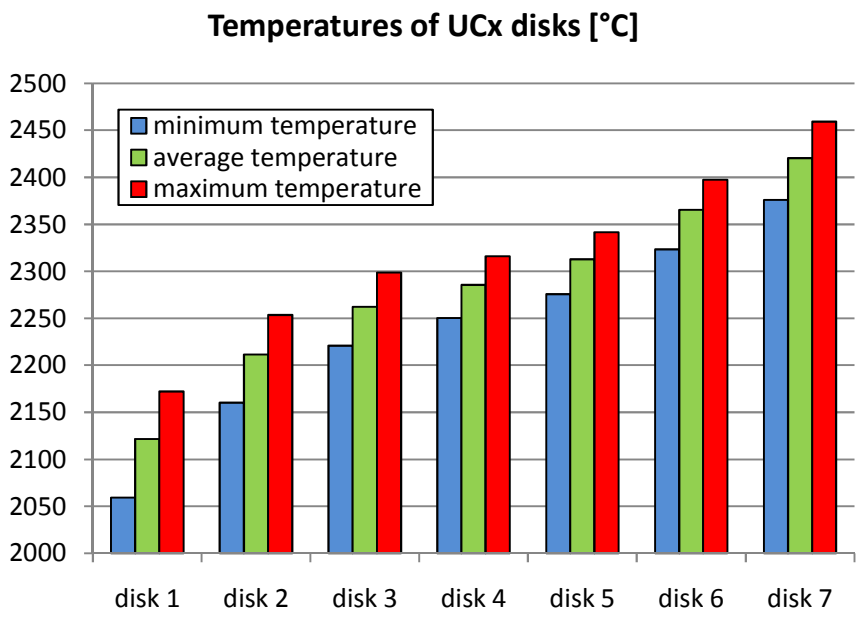

Fig. 3.34. Average, maximum and minimum temperatures of the UCx disks correspondent to the proton beam thermal load (results from the FE model).

The temperature level of the disks increases gradually passing from the first disk (the disk facing the internal window) to the last one (the disk facing the most internal dumper) which registers the maximum temperature of 2457°C at its centre; both the sixth and the seventh disks exceed the uranium carbide temperature limit of 2390°C. Temperature gradients are also considerable: the maximum T_{MAX} - T_{MIN} value is registered at the first disk and is equal to 113°C (see figure 3.35).

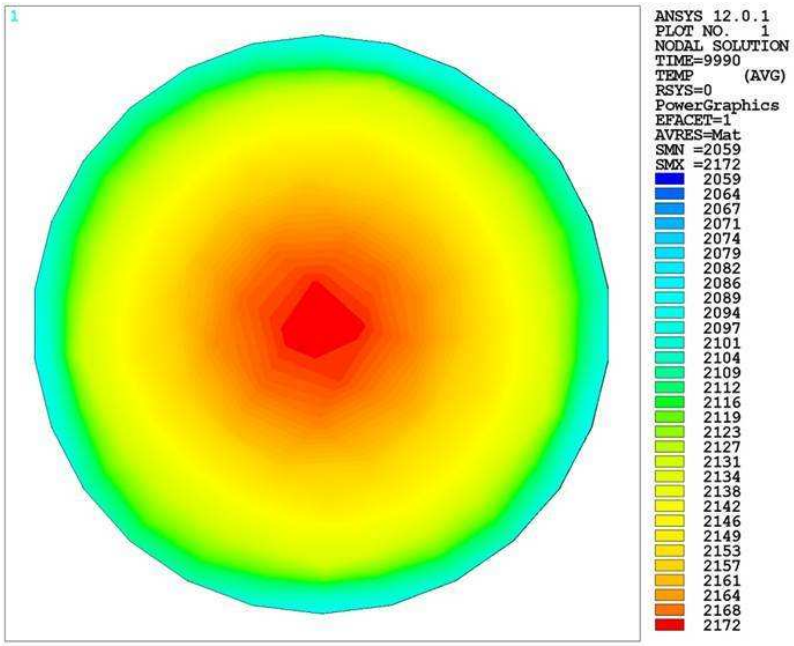

Fig. 3.35. FE temperature plot [°C] of the first disk correspondent to the proton beam thermal load.

Observing figure 3.36 it is possible to evaluate the influence of the heating system when the proton beam thermal load is active: with 1000 A of heating current the average temperature of the disks increases of approximately 100°C. With lower current values the influence of the heating system becomes progressively lower, practically negligible when the heating current is less than 400 A.

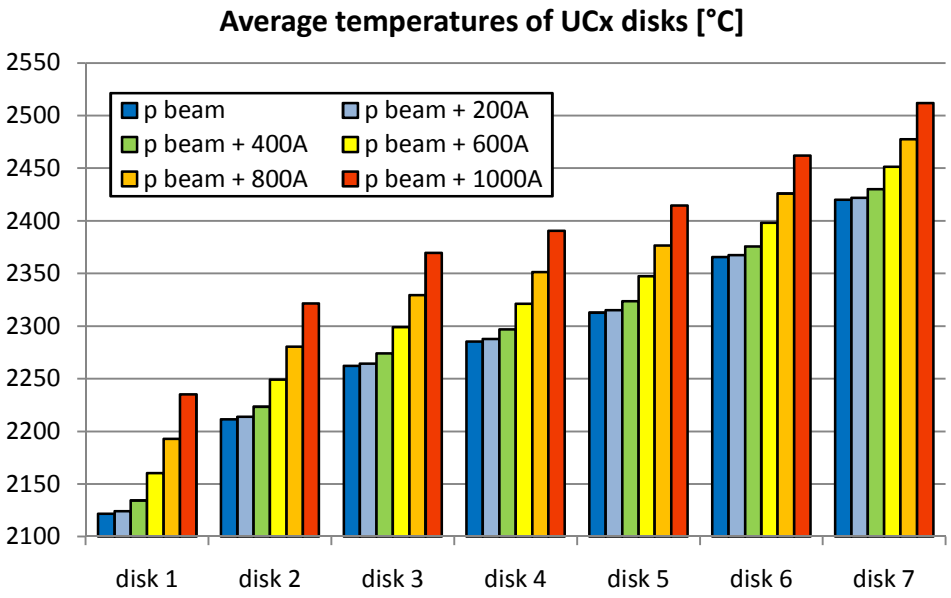

Fig. 3.36. Average temperatures of the UCx disks correspondent to the proton beam thermal load and to different additional current values applied to the target heating system (results from the FE model).

At this point it is important to remark that with the presence of the proton beam and 1000 A of electric current also the heating system reaches a critical condition, in particular its tantalum wings reach the tantalum temperature limit of 2200°C (see figure 3.37).

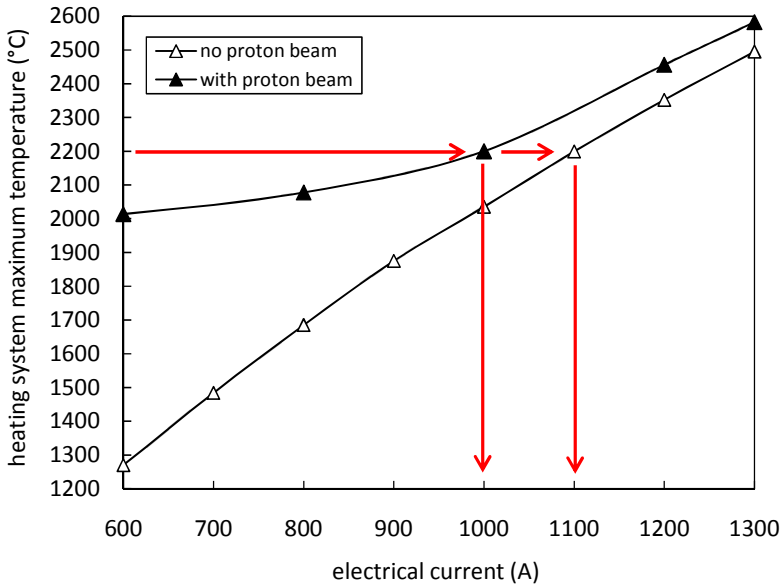

Fig. 3.37. Comparison between the maximum temperature of the target heating system with and without the presence of the proton beam thermal load, considering different values of the heating current (results from the FE model).

3.3.9. The limitations of the first SPES Target prototype

Once presented the thermal study of the first target prototype an accurate analysis of the limitations related to its functioning with and without the presence of the proton beam thermal load is now proposed.

When the proton beam is the only thermal load, the most evident problem is the important overheating of the uranium carbide disks: in particular the sixth and the seventh disks exceed the uranium carbide temperature limit of 2390°C and put in evidence the need to cool them down (see figure 3.34).

Then, taking into consideration only the Joule heating thermal load, the following observations can be stated:

- the heating system temperature distribution is not well balanced and its maximum temperature, localized in proximity of the wings, is much higher respect to the tube's temperature level (see figures 3.5 and 3.27);
- the temperature level of the uranium carbide disks is relatively low (see figure 3.30), approximately equal to 1500°C (a bit lower for the first disk facing the internal window) when the heating current is equal to the maximum value sustainable by the heating system (1100 A).

With the aim to solve the aforementioned limitations, the design of a new target prototype was defined and the steps needed for its formulation are proposed in the following.

3.4. The new Target prototype

The representation of the new target prototype and of its main new features is shown in figure 3.38.

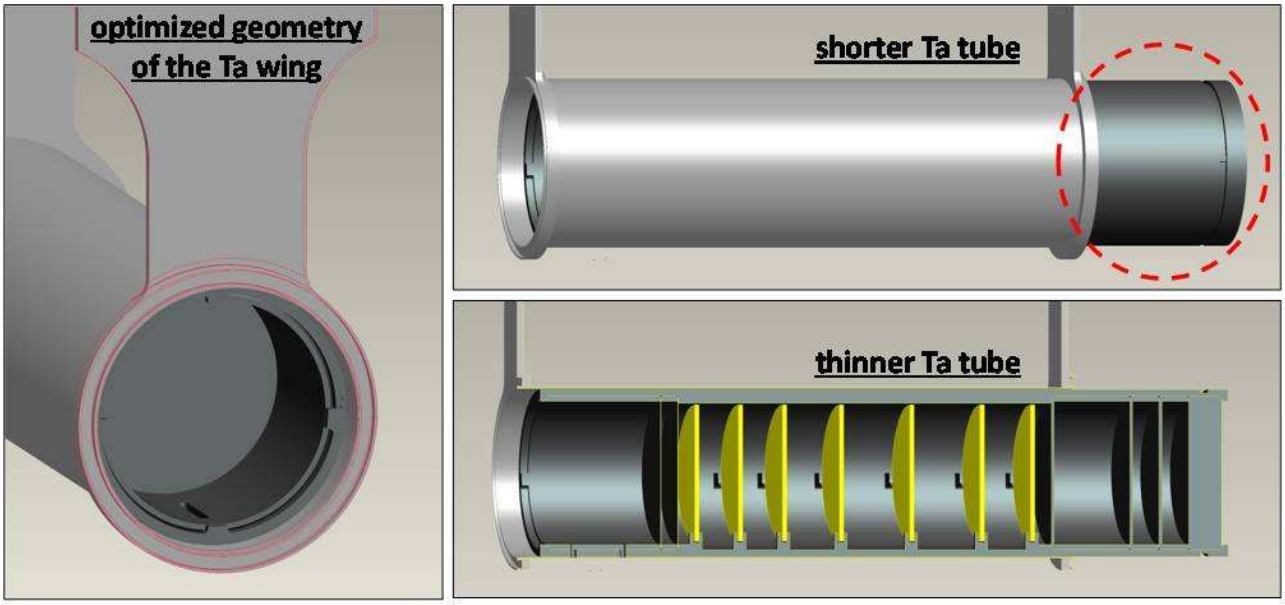

Fig. 3.38. The new target prototype.

The heating system's Ta tube was shortened in order to cool down the rear part of the target: respect to the first prototype (with the graphite box completely covered by the Ta tube) a portion of the graphite box exchanges heat by thermal radiation directly with the internal surfaces of the vacuum chamber taking advantage of the high emissivity of graphite to decrease locally (in the rear part) the target temperature. The Ta tube's thickness was reduced to increase its electrical resistance (see equation (2)) and so the power deposited by Joule effect: this relatively simple modification improved consistently the performances of the target heating system. Another important aspect to mention is the optimization of the Ta wing's shape which reduced importantly the temperature imbalance between the tube and the wings themselves.

The sets of analyses performed to produce the aforementioned improvements are opportunely described in the following.

3.4.1. FE optimization of the heating system

The three main features introduced with the new target prototype are:

1. the reduced length of the Ta tube;
2. the reduced thickness of the Ta tube;
3. the modification of the Ta wing's shape.

The tube's length was reduced in order to leave the box's section called "box 2" (see figure 3.31) completely uncovered and free to exchange heat (by thermal radiation) directly with the vacuum chamber: the effect of this modification can be appreciated mainly when the proton beam thermal load is active, and will be discussed in detail later. Contrarily the other two modifications are exclusively related to the Joule heating thermal load and are clearly described in the following.

Before starting to illustrate the optimization process that led to the definition of the new tube thickness and of the new wing's shape (so of the new heating system), it is important to underline the availability of a new power supply, able to deliver the maximum current and the maximum potential difference value equal to 1300 A and 10 V, respectively. In this context the optimization goal was the maximization of the target's temperature level (so the temperature level of the uranium carbide disks), considering only the Joule heating thermal load (I_{DESIGN}=1300A) and observing the following constraints:

- the heating system's maximum potential difference has to be less than 10 V
- the heating system's maximum temperature has to be less than 2200°C (Ta temperature limit)

The design variables were the tube thickness "t" and the wing's shape, in particular the wing's width "w". A particular range of values was chosen both for "t" and "w", and a set of analyses was performed in order to investigate their influence on the target temperature level (see figure 3.39). Some details of the FE model used for the optimization process are reported in figure 3.40.

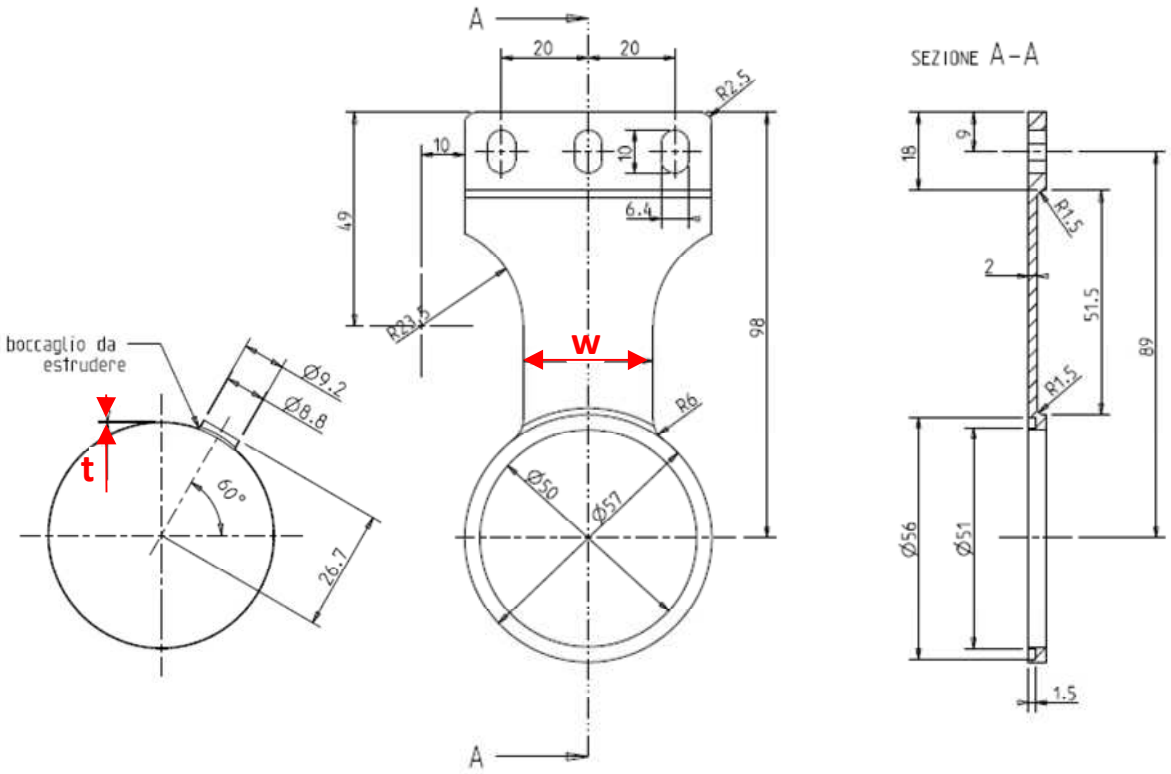

	t = 0.30mm	t = 0.25mm	t = 0.20mm
w = 25mm	analysis $_{1-1}$	analysis $_{1-2}$	analysis $_{1-3}$
w = 30mm	analysis $_{2-1}$	analysis $_{2-2}$	analysis $_{2-3}$
w = 35mm	analysis $_{3-1}$	analysis $_{3-2}$	analysis $_{3-3}$

Fig. 3.39. The design variables: the tube's thickness "t" and the wing's width "w".

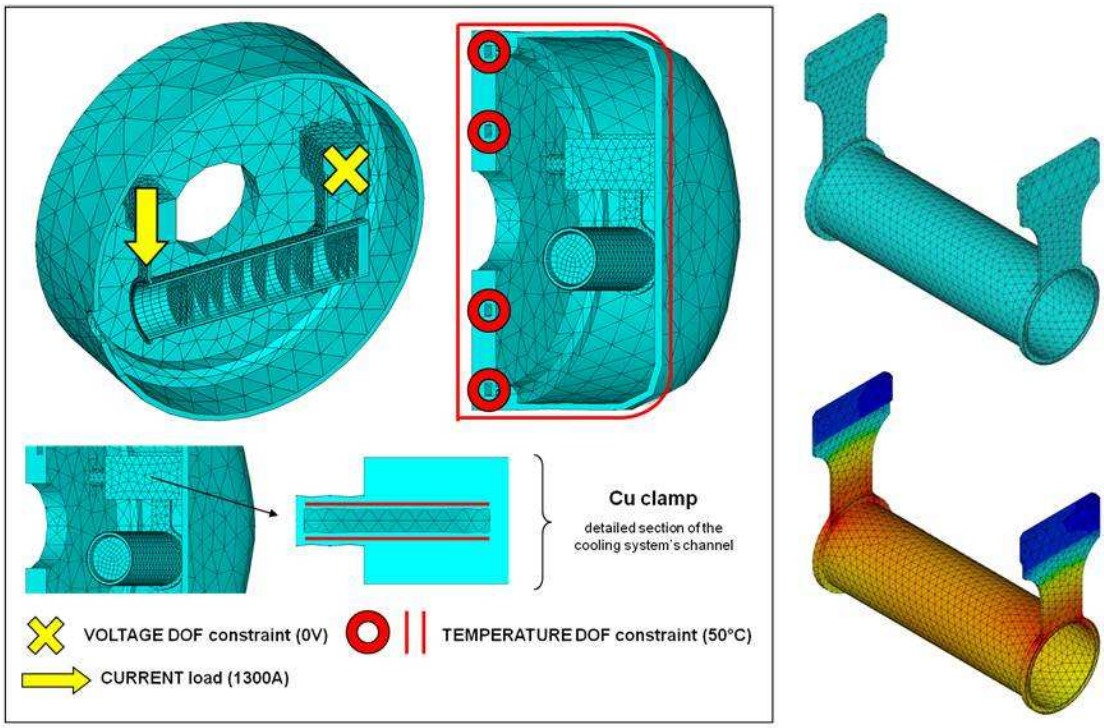

Fig. 3.40. Representation of the FE model used for the optimization of the new target prototype.

In order to interpret in a clear and brief way the results coming from the set of FE analyses the following parameters were defined:

- T_{max_h}, the maximum temperature of the target heating system;
- $T_{average\_disks} = \left(\sum_{i=1}^{7} T_{average\_disk\_i}\right)/7$, the average temperature of the 7 uranium carbide disks (being $T_{average\_disk\_i}$ the average temperature of the single disk i);
- $\Delta T_{local\_disks} = \max (T_{max\_disk\_i} - T_{min\_disk\_i})$, the maximum difference ($T_{max\_disk\_i} - T_{min\_disk\_i}$) among the 7 uranium carbide disks (being $T_{max\_disk\_i}$ and $T_{min\_disk\_i}$ the maximum and the minimum temperature of the single disk i, respectively);
- $\Delta T_{global\_disks} = (T_{max\_disks} - T_{min\_disks})$, the difference between the maximum and the minimum temperature of the 7 uranium carbide disks.

Observing figures 3.41 and 3.42 it is possible to observe that for all the tube thickness values, 30 mm is the wing's width that guarantees the maximum temperature level for the uranium carbide disks, keeping in the same time the heating system's maximum temperature below the Ta temperature limit of 2200°C.

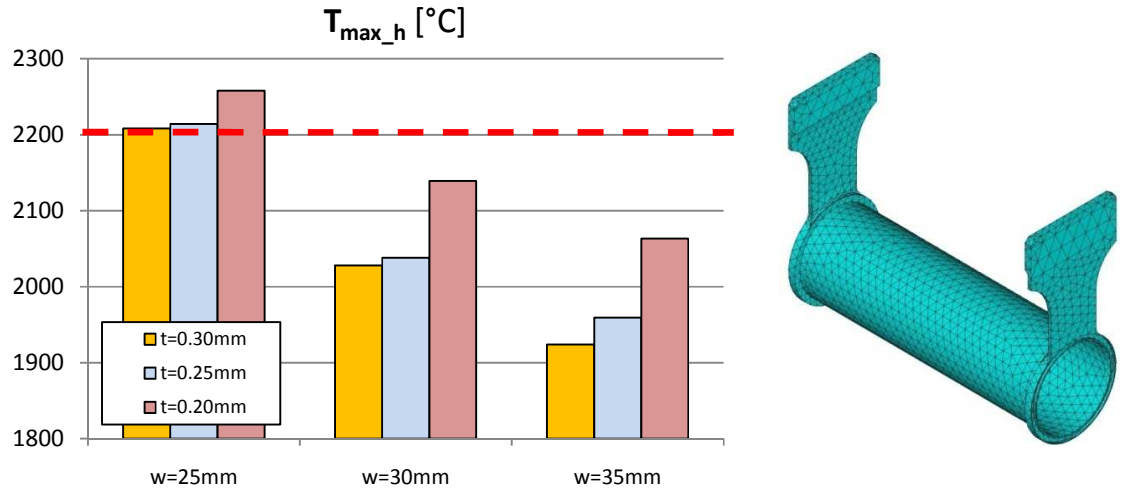

Fig. 3.41. Dependence of T_{max_h} from the parameters "t" and "w".

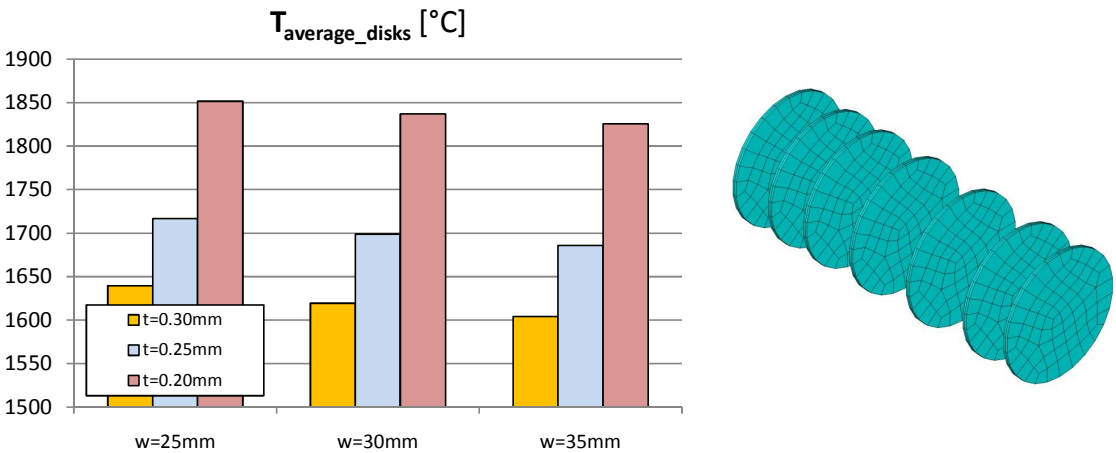

Fig. 3.42. Dependence of $T_{average\_disks}$ from the parameters "t" and "w".

Figure 3.42 puts in evidence the important dependence of $T_{average\_disks}$ from the tube thickness and the low influence of the wing's width on the same parameter; in general the smaller the tube thickness, the higher the temperature level of the disks; on the other side the tube thickness's reduction implies higher temperature gradients (and so higher values of the parameters ΔT_{local_disks} and ΔT_{global_disks}) (see figures 3.43 and 3.44), that in any case don't seem to represent a criticality. Taking into consideration increasing values of the wing's width, the parameter ΔT_{local_disks} and ΔT_{global_disks} decreases and increases, respectively: in this scenario w = 30 mm represents the best compromise considering both local and global gradients.

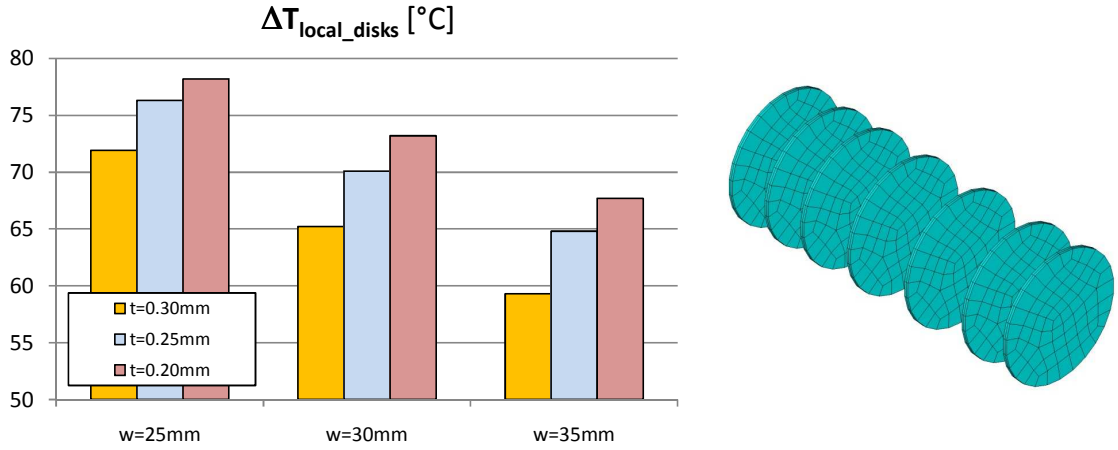

Fig. 3.43. Dependence of ΔT_{local_disks} from the parameters "t" and "w".

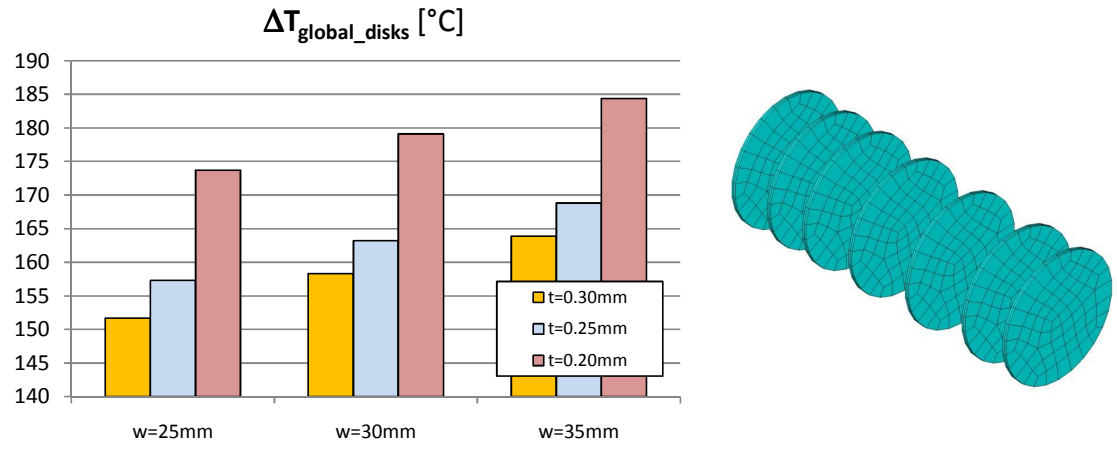

Fig. 3.44. Dependence of ΔT_{global_disks} from the parameters "t" and "w".

On the basis of the aforementioned considerations the design variables "t" (the tube thickness) and "w" (the wing's width) were fixed for the final configuration of the heating system as proposed in the following:

- t = 0.2 mm
- w = 30 mm

The new heating system defined in this way was able to guarantee, considering only the Joule heating thermal load, the maximization of $T_{average\_disks}$, keeping in the same time T_{max_h} and the heating system's potential difference below 2200°C and 10 V, respectively. Figure 3.45 reports the temperature distribution of the new heating system when 1300 A of heating current are applied on it; the correspondent temperature field in the production target is shown in figure 3.46.

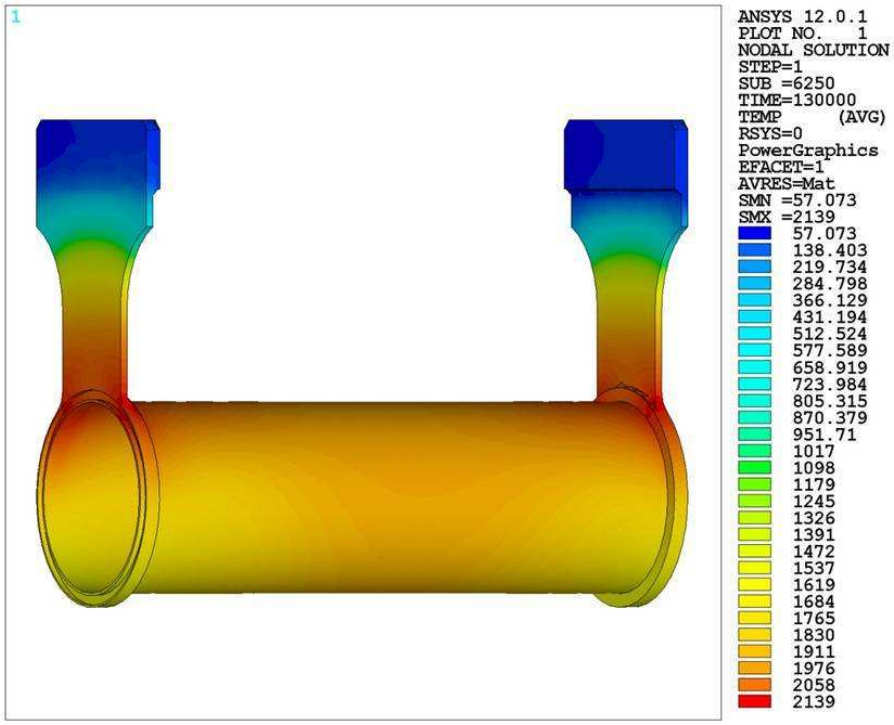

Fig. 3.45. Temperature plot [°C] of the new target heating system correspondent to 1300A of heating current (results from the FE model).

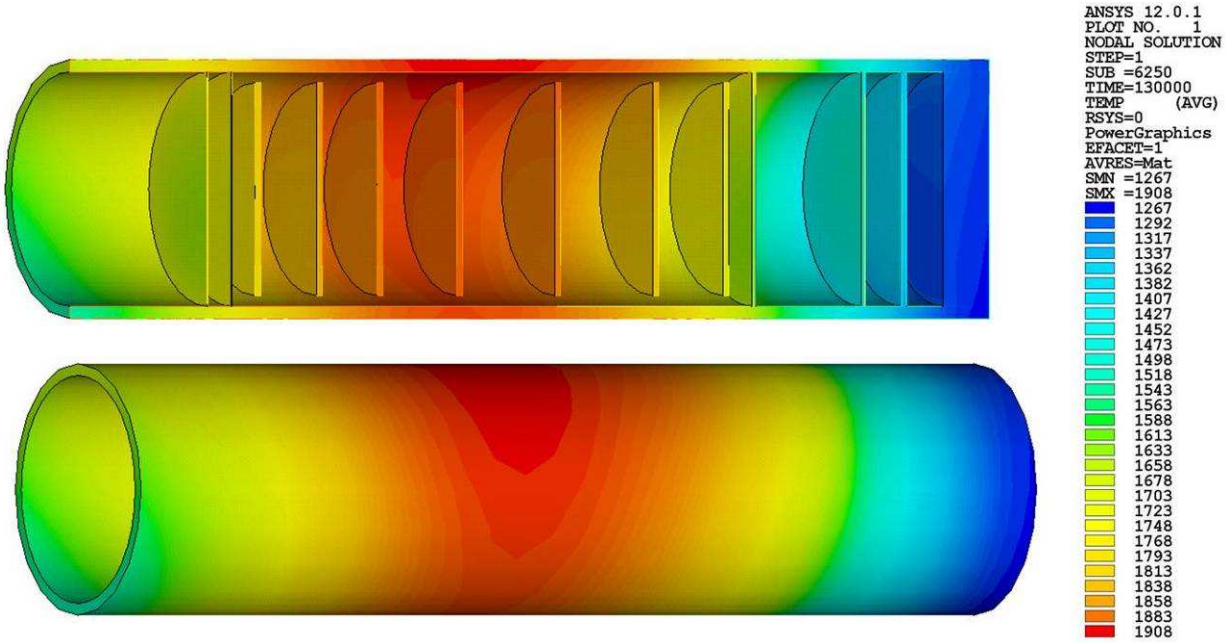

Fig. 3.46. Temperature plot [°C] of the production target (see figure 3.3) correspondent to 1300A of heating current applied on the new target heating system (results from the FE model).

A detailed temperature plot of the uranium carbide disks is then proposed in figure 3.47. It is possible to appreciate the local temperature gradients of disk 1 and disk 7 (see figure 3.31): they are positioned in proximity of the heating system's extremities and are sensitive to the correspondent heating system's temperature gradients (see in figure 3.45 the transition zones between the tube and the wings). Observing figure 3.47 the parameter ΔT_{global_disks} can be easily estimated as difference between the maximum and the minimum temperatures (see figure 3.44).

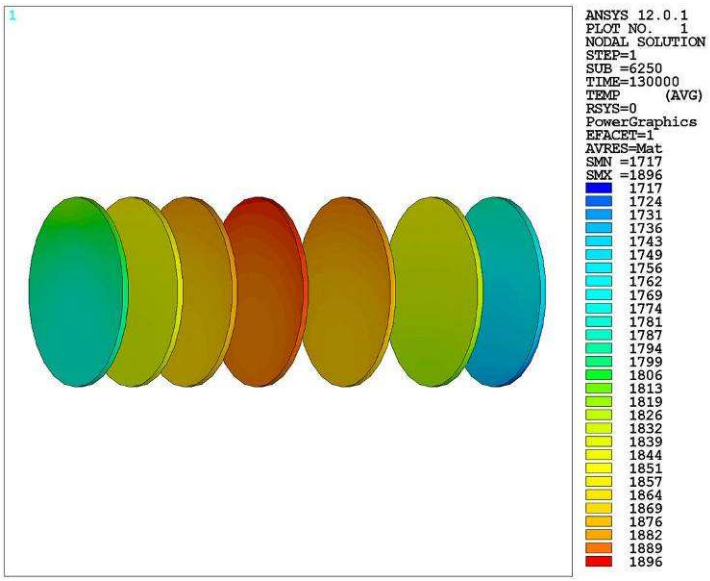

Fig. 3.47. Temperature plot [°C] of the uranium carbide disks (see figure 3.3) correspondent to 1300A of heating current applied on the new target heating system (results from the FE model).

Figures 3.48 clearly demonstrate that the heating system's maximum potential difference is compatible with the power supply adopted (voltage limit equal to 10 V).

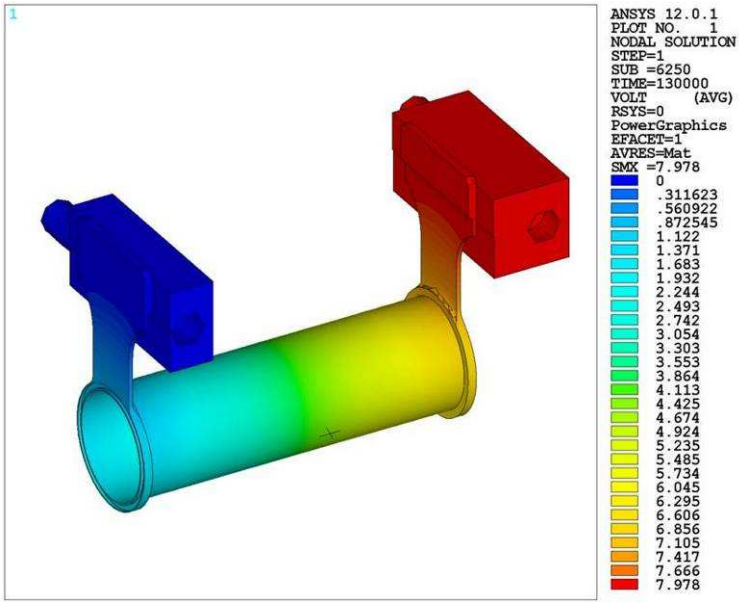

Fig. 3.48. Voltage plot [°C] of the new target heating system correspondent to 1300A of heating current (results from the FE model).

At this point it is important to present some clarifications. First of all, the FE model above described and represented in figure 3.40 was used exclusively to define the geometry of the new target heating system. Then, to study in detail the behavior of the new system a new model was defined, taking into consideration some improvements introduced for the vacuum chamber, the hole on the Ta tube to connect it with the transfer line and a different positioning of the target to go along with the new proton beam's specifications and the ion source encumbrance. Such a model was used to study in detail the effect of both the heating current (with current values ranging from 600 to 1300 A) and the proton beam thermal load. Figure 3.49 clearly shows the new features introduced by the updated FE model.

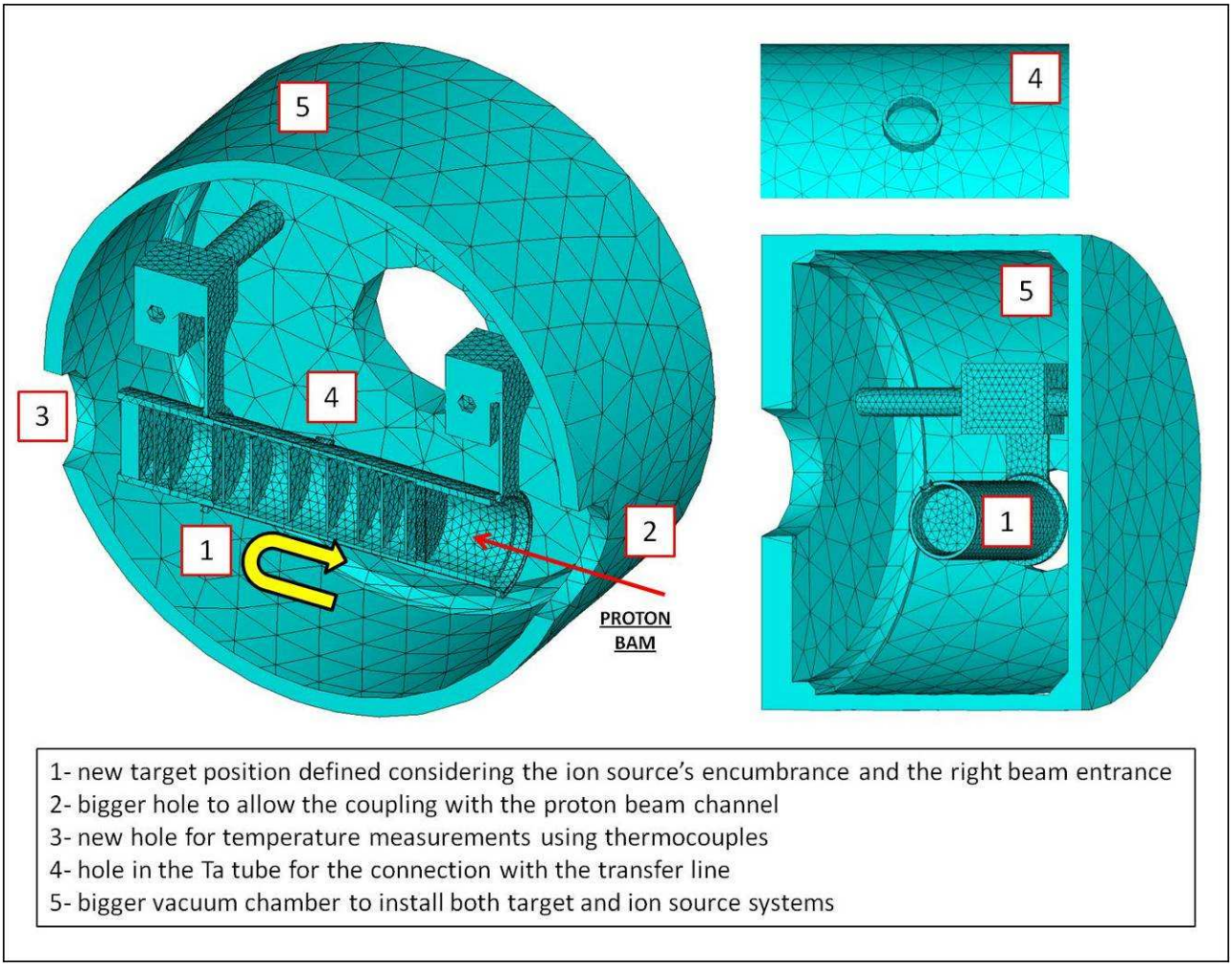

Fig. 3.49. The new features of the upgraded FE model.

Figure 3.50 shows the comparison among the Ta tube temperature (at point P1), the maximum temperature of the new target heating system and the graphite window temperature (at point P2) (see figure 3.51), considering current values ranging from 600 to 1300A; respect to the first heating system prototype (see figure 3.27) the three curves are closer and all staying below the Ta temperature limit of 2200°C. In particular temperature homogeneity was improved and both tube

and window temperatures were increased: this implies also higher temperature levels for the uranium carbide disks, using only the Joule heating thermal load.

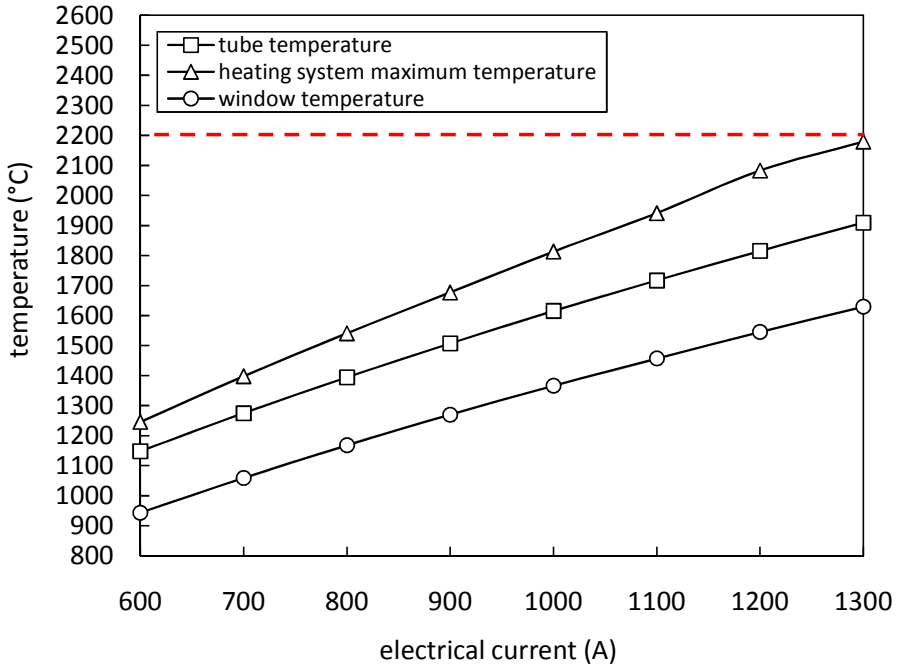

Fig. 3.50. Comparison among the Ta tube temperature, the maximum temperature of the new target heating system and the graphite window temperature (see figure 3.51) (results from the new FE model).

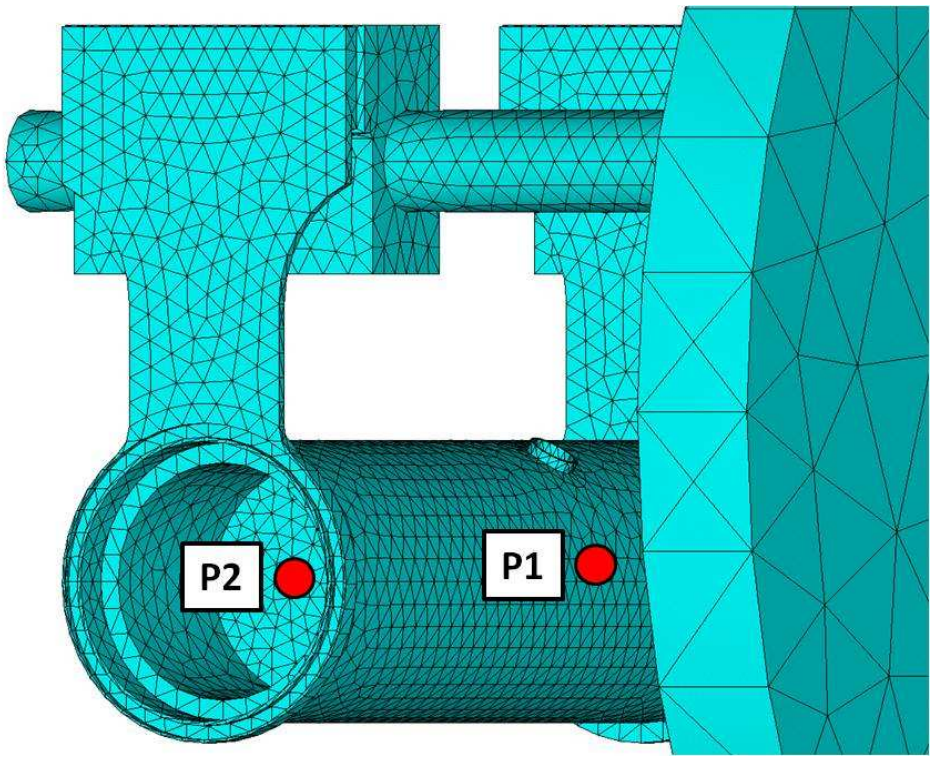

Fig. 3.51. Ta tube (P1) and graphite window (P2) temperature data points.

Figures 3.52 and 3.53 show the temperature distribution of the new heating system and of the production target, respectively, when the heating current is the only thermal load and its intensity is

equal to 1300 A; the two temperature plots were obtained using the new FE model (see figure 3.49) and are obviously similar to the plots obtained with the simpler model used to optimize the heating system's geometry (see figures 3.45 and 3.46).

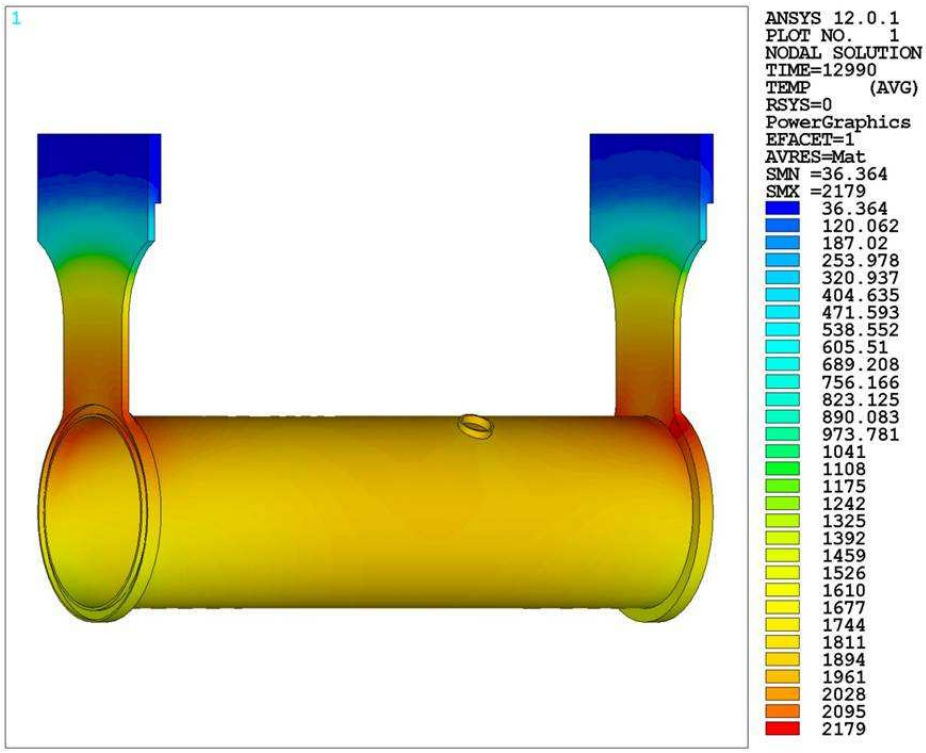

Fig. 3.52. Temperature plot [°C] of the new target heating system correspondent to 1300A of heating current (results from the new FE model).

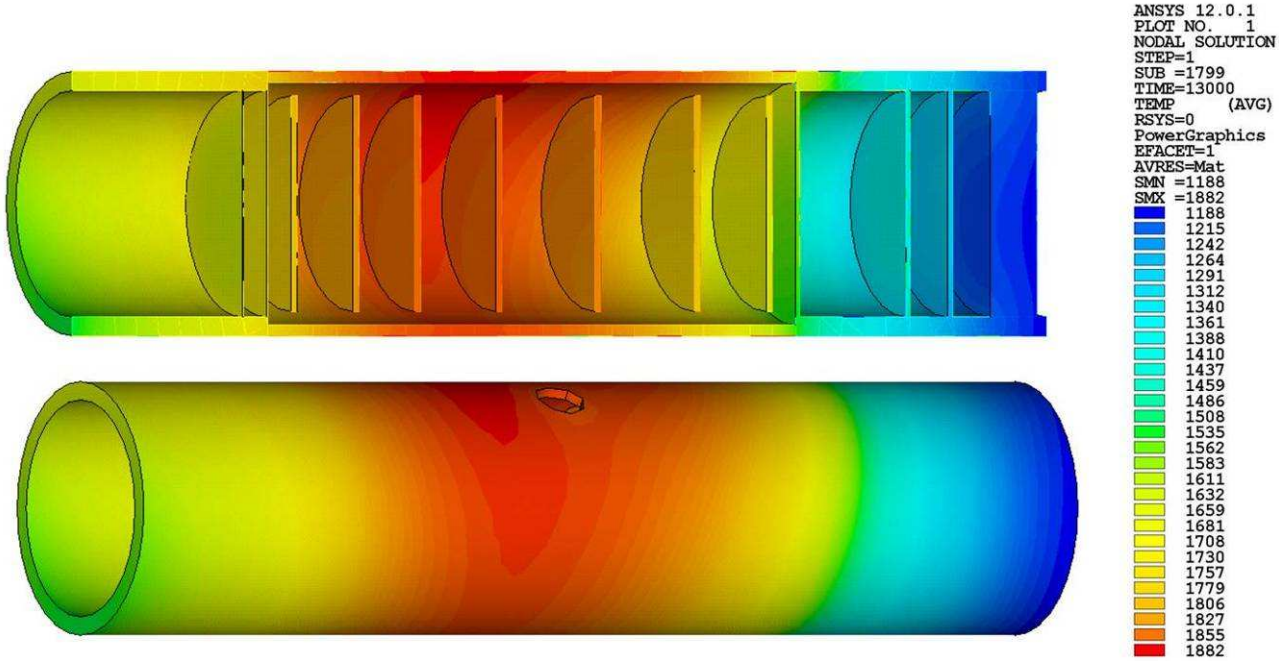

Fig. 3.53. Temperature plot [°C] of the production target correspondent to 1300A of heating current applied on the new target heating system (results from the new FE model).

The minimum, the average and the maximum temperatures of the seven uranium carbide disks are reported in figure 3.54. In general disks from 1 to 5 are characterized by high temperature levels and homogeneous temperature distributions whereas disk 6 and disk 7 present lower temperatures and higher thermal gradients: this can easily be associated to the high cooling capabilities of the box's portion that is not covered by the Ta tube (see figure 3.38). The aforementioned modification is not very useful in this context but as we will see later, it is essential to avoid dangerous hot spots when the proton beam thermal load is active.

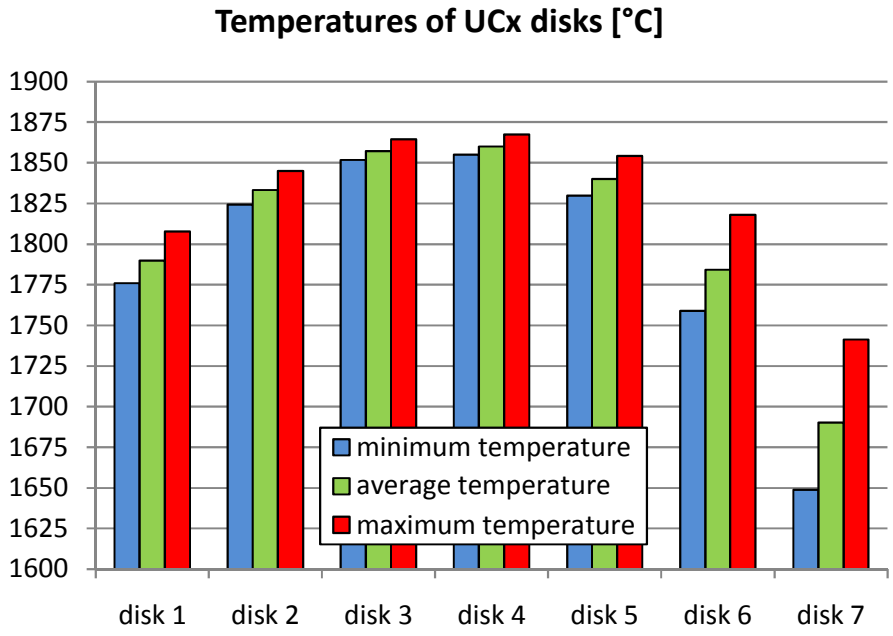

Fig. 3.54. Average, maximum and minimum temperatures of the UC_x disks correspondent to 1300A of heating current (results from the new FE model).

Thanks to figure 3.55 it is possible to observe the temperature distribution of the target heating system due to the proton beam thermal load; contrary to the Joule heating thermal load, the proton beam leads to tube's temperature levels that are higher respect to the wing's ones; the new heating system's maximum temperature is registered in proximity of the zone occupied by the uranium carbide disks and it is abundantly below the temperature limit specified for tantalum (2200°C). In figure 3.56 it is possible to appreciate the temperature plot of the SPES production target due to the primary proton beam. The objects that present the maximum temperature levels are the UC_x disks: in particular the maximum temperature is registered in proximity of disk 3 and is equal to 2266°C, more than 100°C below the melting point of uranium carbide taken as reference in this work (2390°C).

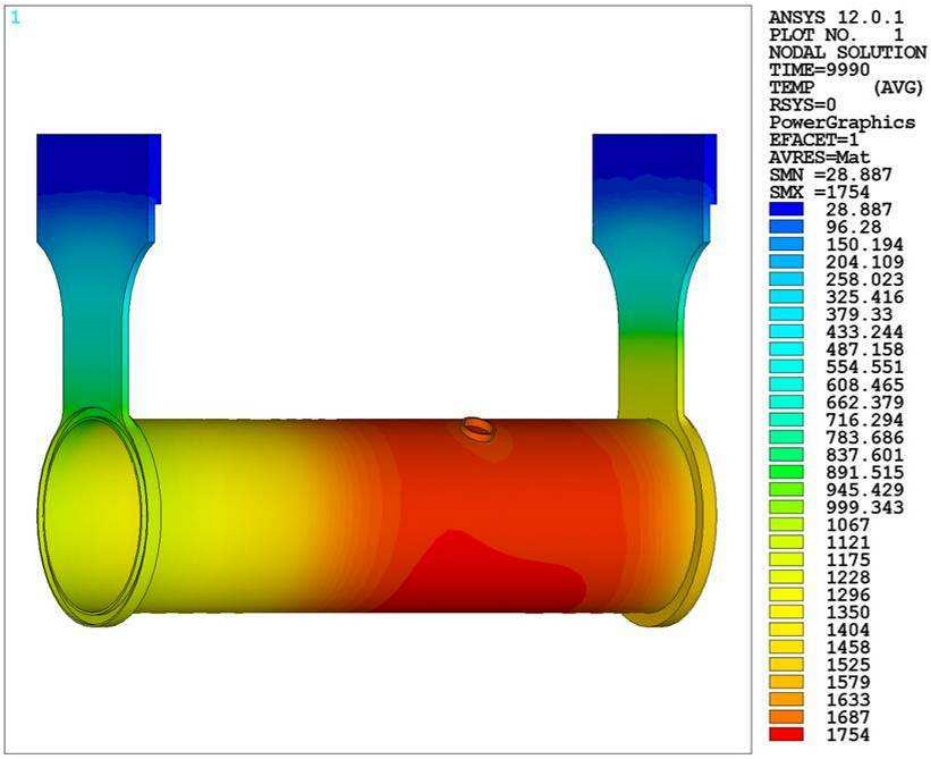

Fig. 3.55. Temperature plot [°C] of the new target heating system correspondent to the proton beam thermal load (results from the new FE model).

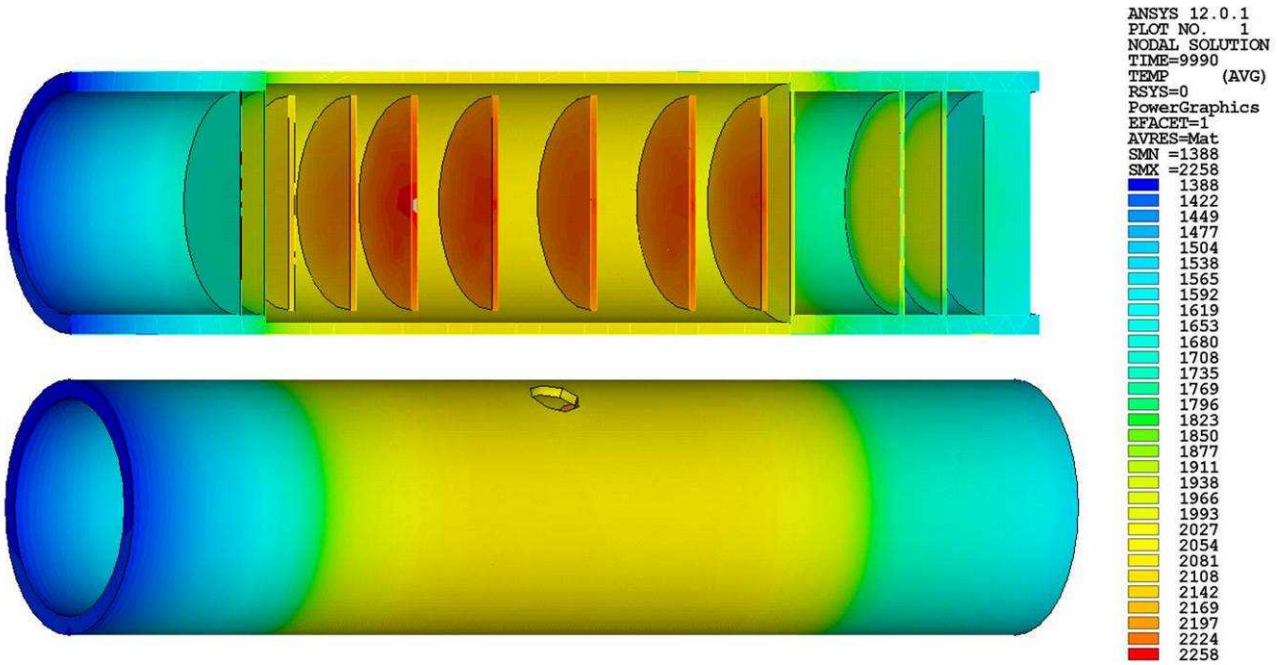

Fig. 3.56. Temperature plot [°C] of the production target correspondent to the proton beam thermal load (results from the new FE model).

In order to have more information about the temperature levels of the uranium carbide disks the following figure has been introduced.

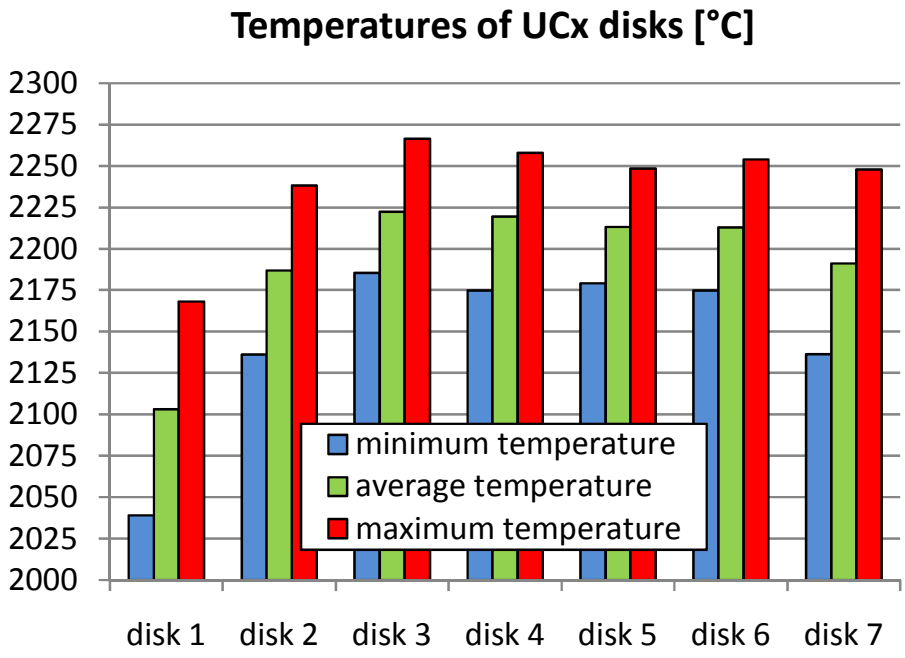

Fig. 3.57. Average, maximum and minimum temperatures of the UCx disks correspondent to the proton beam thermal load (results from the new FE model).

The uranium carbide disks are characterized by similar temperature levels, all except disk 1 which registers lower temperatures and higher thermal gradients: in fact it is positioned close to the region occupied by the graphite windows, where the proton beam power deposition is low (see figure 3.31) and the high emissivity of graphite enhances the cooling process by thermal radiation. Disk 1 presents the maximum T_{MAX} - T_{MIN} value: it is equal to 129°C (see figure 3.58).

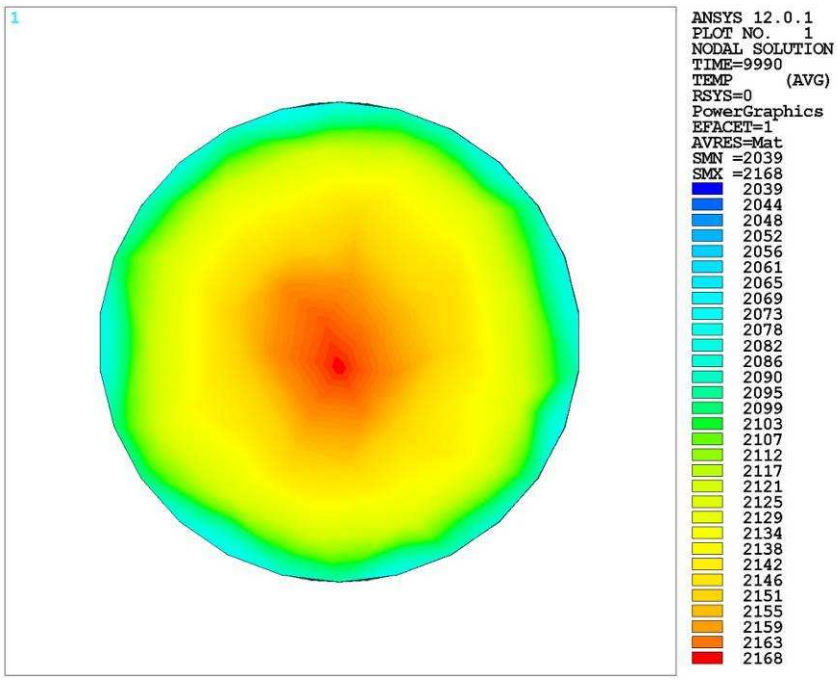

Fig. 3.58. FE temperature plot [°C] of disk 1 correspondent to the proton beam thermal load.

From figure 3.59 it is possible to evaluate the influence of the new heating system when the proton beam thermal load is active: 1000 A of heating current can increase the temperature of the disks of approximately 150°C. With lower current values the influence of the heating system becomes progressively lower, practically negligible when the heating current is less than 400 A.

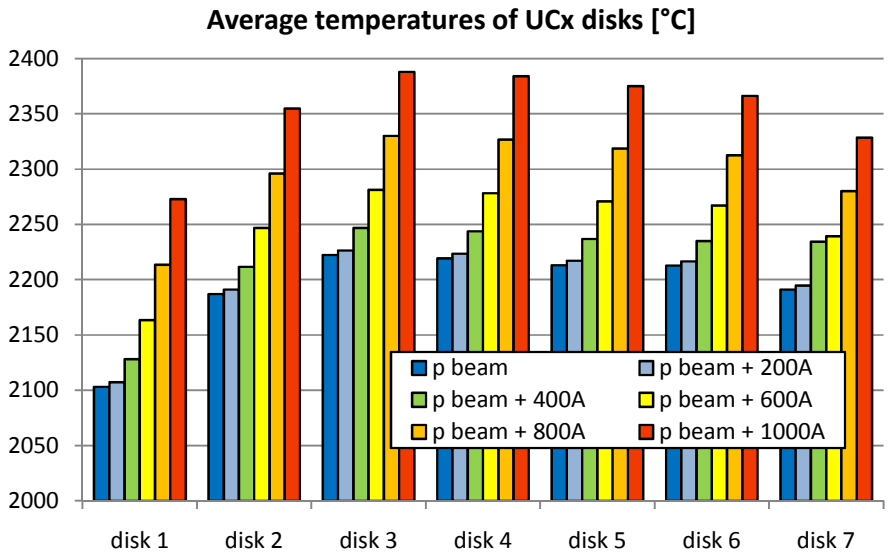

Fig. 3.59. Average temperatures of the UCx disks correspondent to the proton beam thermal load and to different additional current values applied to the new target heating system (results from the new FE model).

With the presence of the proton beam, 1000 A is the maximum electric current value sustainable by the new Ta heating system: figure 3.60 clearly shows how its maximum temperature exceeds the Ta temperature limit (2200°C) when the current values are higher.

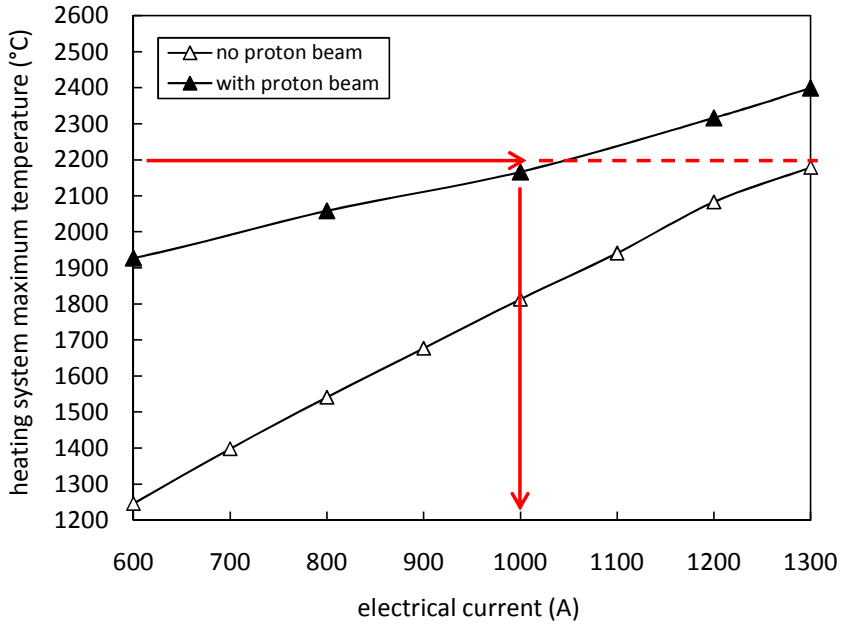

Fig. 3.60. Comparison between the maximum temperature of the target heating system with and without the presence of the proton beam thermal load, considering different values of the heating current (results from the FE model).

3.4.2. Comparison between the old and the new Target prototypes

Once presented and described in detail both the old and the new target heating systems, they were accurately compared considering separately the Joule heating thermal load and the effect of the proton beam.

Figure 3.61 reports the average temperatures of the UC_x disks obtained using the old and the new target heating systems, considering exclusively the Joule heating thermal load and the maximum electrical current values sustainable by the heating systems, that are 1000 A for the old model and 1300 A for the new one. The advantages offered by the new heating system are evident: respect to the old one it is able to heat the disks at higher temperatures, in particular the fourth disk passes from 1507 to 1860°C.

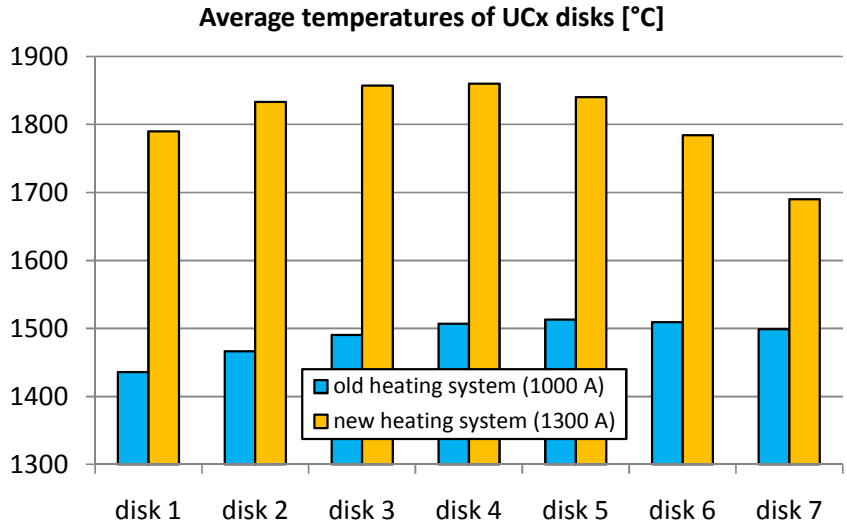

Fig. 3.61. Average temperatures of the UCx disks correspondent to the maximum current values sustainable by the old and the new target heating systems (Joule heating thermal load only) (results from FE calculations).

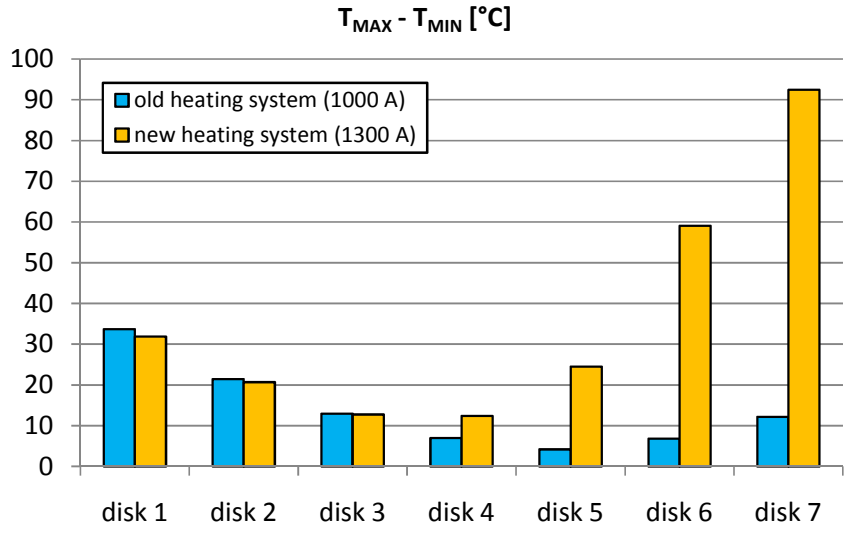

Fig. 3.62. Differences between the maximum and the minimum temperatures of the UCx disks correspondent to the maximum current values sustainable by the old and the new target heating systems (Joule heating thermal load only) (results from FE calculations).

For disk 6 and disk 7 the temperature increment is lower because of the portion of the box that is not covered by the Ta tube (see figure 3.38): the important cooling rate in this zone of the new target prototype leads also to relevant thermal gradients, evidently higher respect to the old target version (see figure 3.62).

If on one hand the new heating system is able to offer higher temperatures when the heating current is the unique thermal load, on the other hand it produces a general cooling down and a temperature homogenization among the disks when solely the proton beam thermal load is applied (see figure 3.63). Also in the latter case the new heating system slightly increases the temperature gradients for the single disks (see figure 3.64).

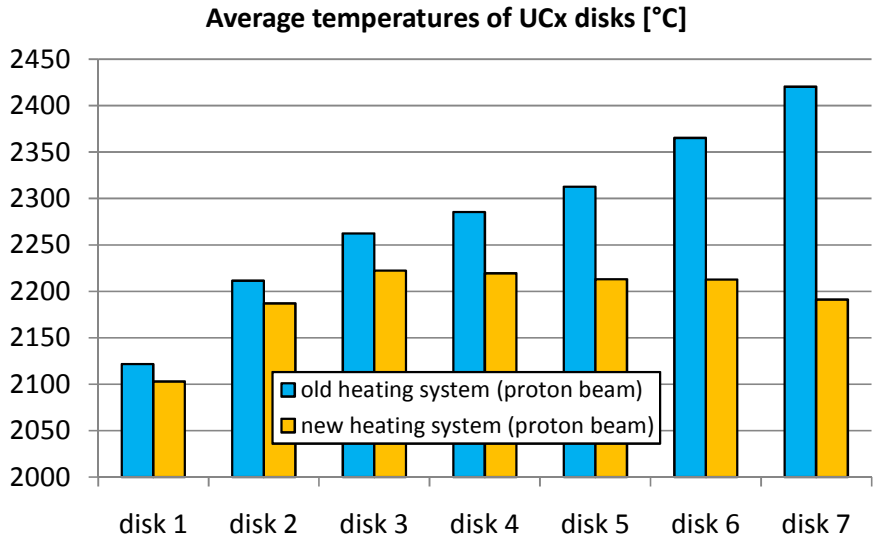

Fig. 3.63. Average temperatures of the UCx disks correspondent to the proton beam thermal load considering both the old and the new heating systems (proton beam thermal load only) (results from FE calculations).

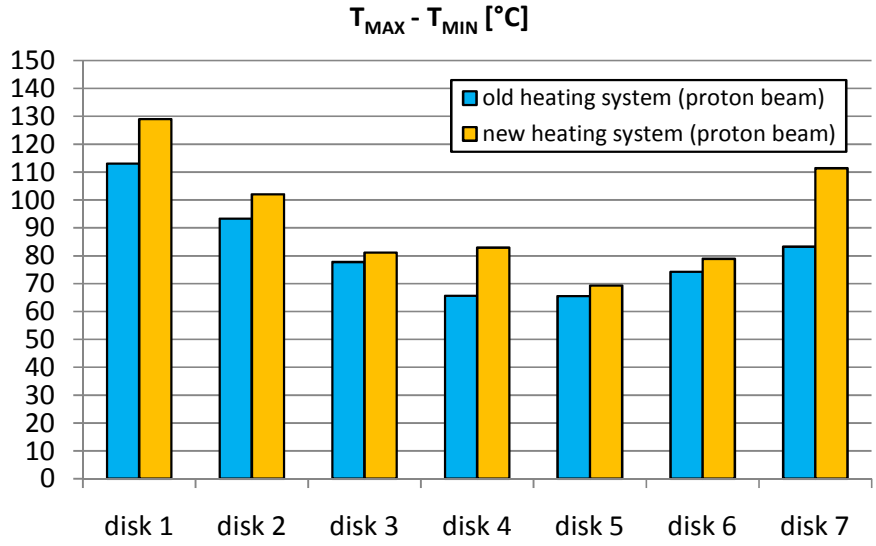

Fig. 3.64. Differences between the maximum and the minimum temperatures of the UCx disks correspondent to the proton beam thermal load considering both the old and the new heating systems (proton beam thermal load only) (results from FE calculations).

3.4.3. Manufacturing of the new Target prototype and experimental tests at LNL

Once approved the geometry of the new heating system it was accurately formalized in a three-dimensional CAD model (see figure 3.65); detailed mechanical drawings were also produced (see figure 3.66) and submitted to the INFN mechanical workshops and to local companies for the manufacturing of the components composing the target and its heating system.

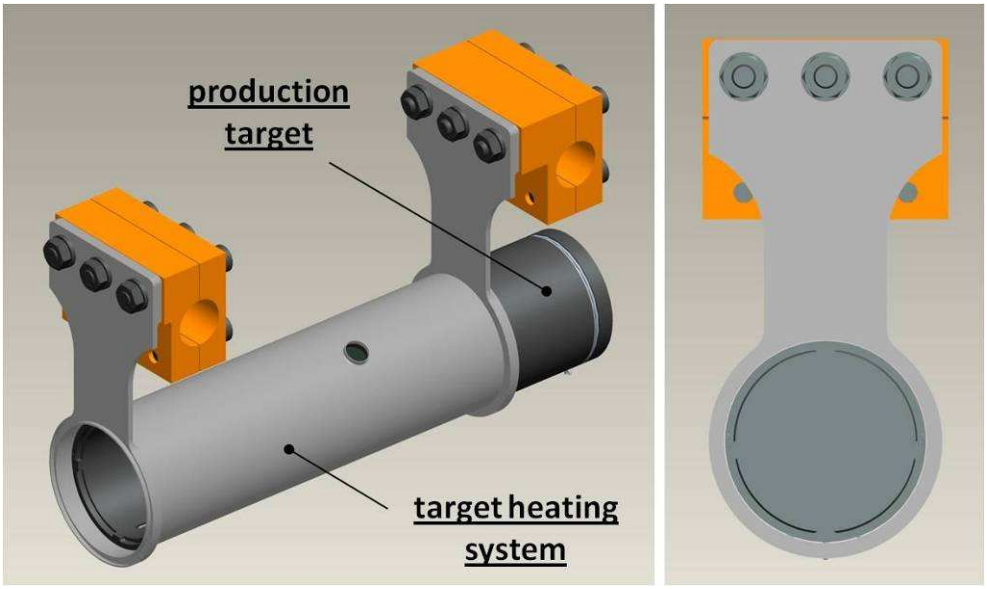

Fig. 3.65. Detailed three-dimensional CAD model of the SPES production target and of its heating system.

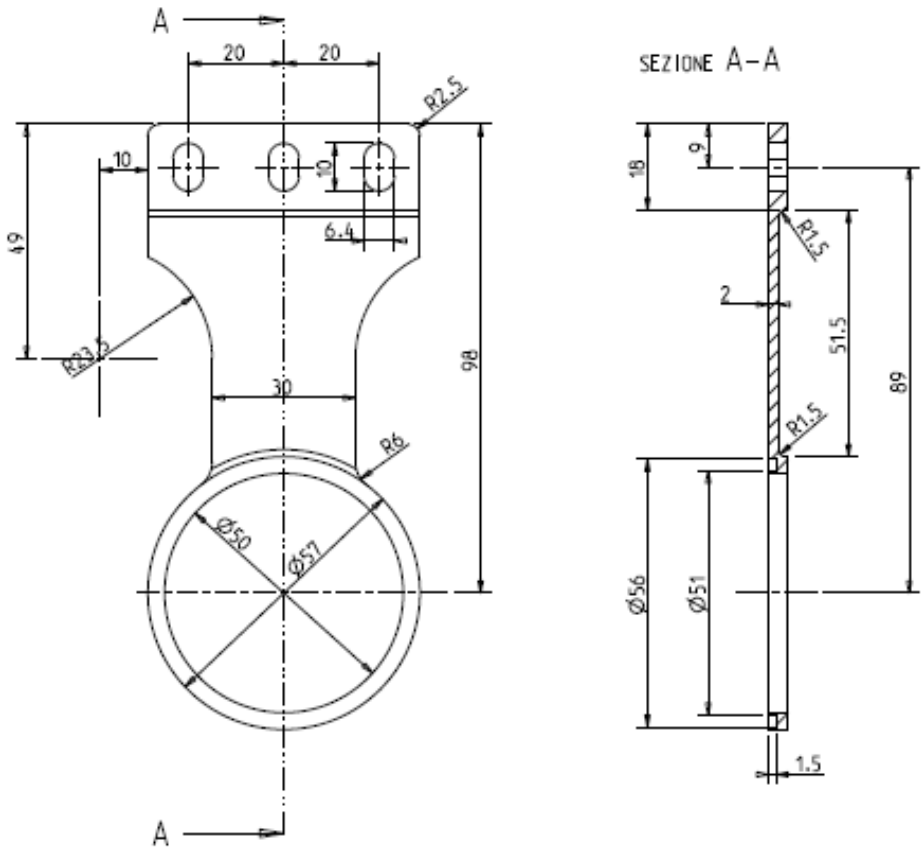

Fig. 3.66. Mechanical drawing taken as reference for the manufacturing of the heating system's wing.

As previously specified one of the main features of the new heating system is the reduced length of the Ta tube containing the target: a portion of the graphite box is now embossed and consequently its architecture has to be changed in order to guarantee the stability and the integrity of the target. With this purpose the original design of the target box, composed of round segments (see figure 3.67), was modified keeping the box's main dimensions unaltered.

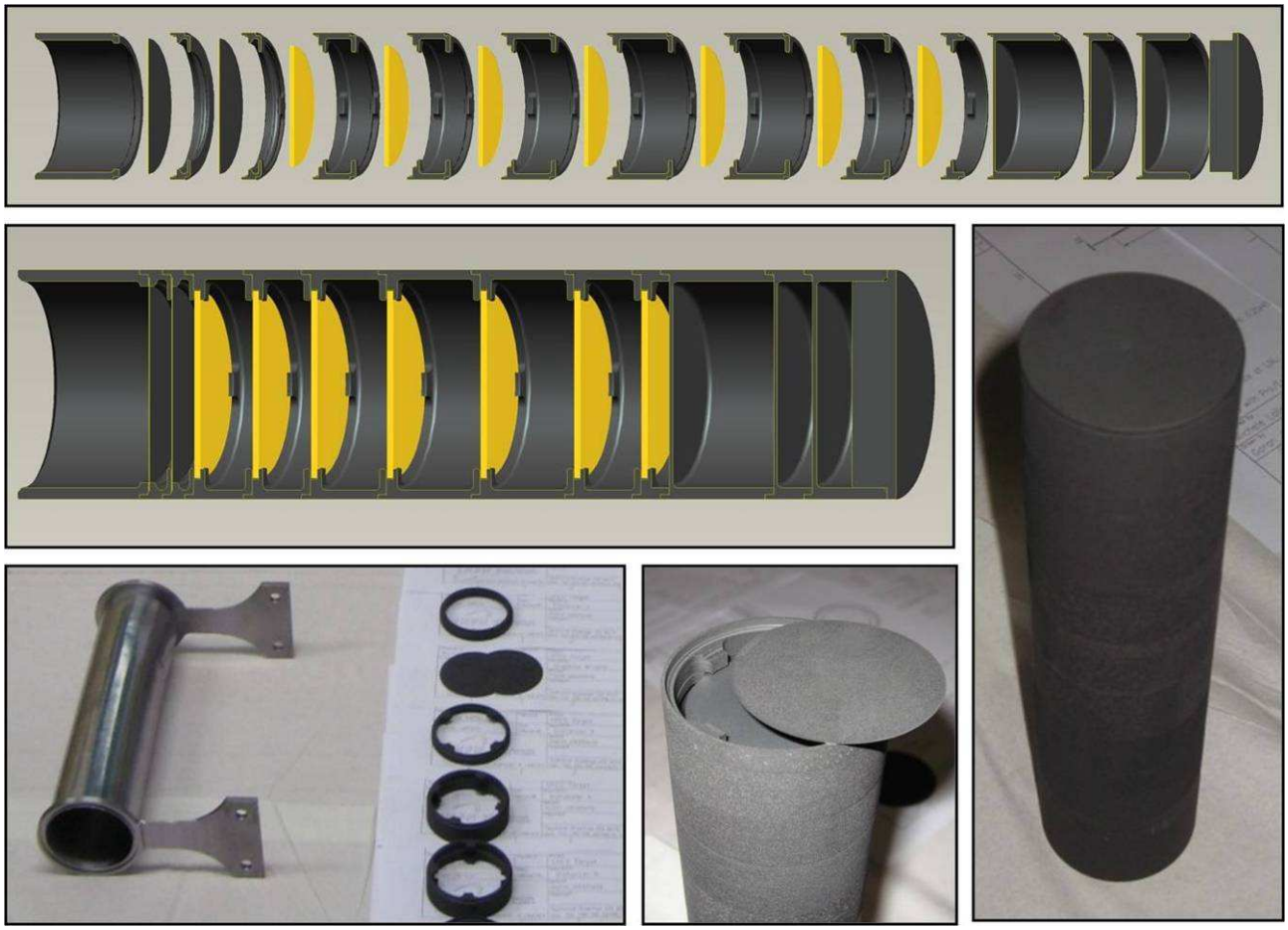

Fig. 3.67. The old design of the graphite box.

As shown in figure 3.68 the new box is constituted by a hollow graphite cylinder divided in two parts according to a cutting plane containing the axis of the cylinder itself; these two long pieces of graphite enclose the two windows, the dumpers and the uranium carbide disks, constituting a unique compact block, that is the SPES production target. The production of the graphite box was not simple and requested an accurate study to fix a reliable manufacturing procedure: turning, milling and wire spark erosion operations were opportunely studied by the INFN technical staff with the contribution of local companies. Figure 3.69 shows a picture of the new target prototype with SiC disks and some details of the new graphite box: the support system used to position and centre the disks and the window zone characterized by a small aperture and two small holes used to fix the box with the heating system (see the following pages).

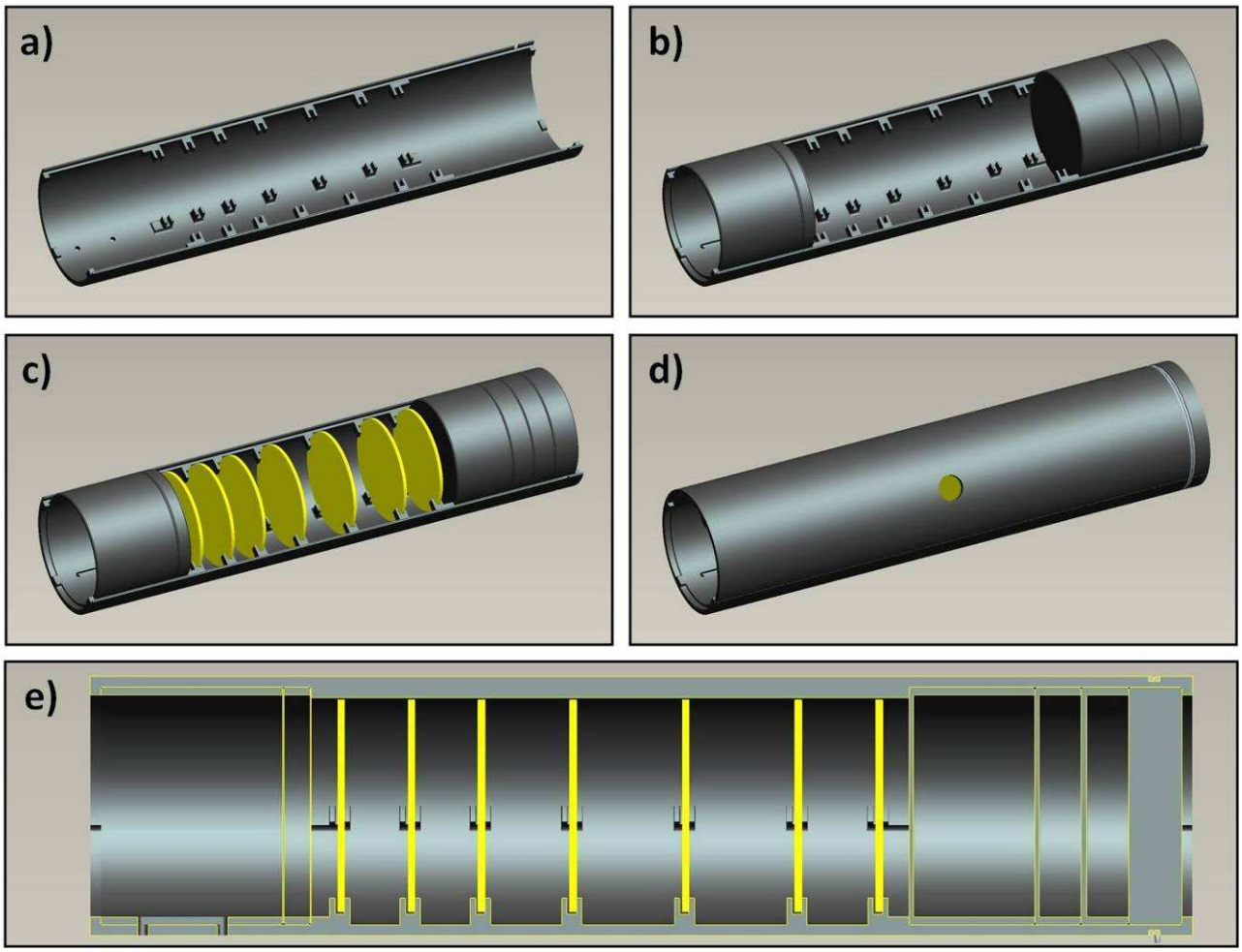

Fig. 3.68. One of the two main graphite parts composing the box (a); installation of windows and dumpers (b); installation of the uranium carbide disks (c); closure of the box (d); section view of the box and of the objects contained inside (e).

Fig. 3.69. The new target prototype with SiC disks and some details of the new graphite box.

The new heating system was entirely manufactured by an external company equipped to perform welding operations with tantalum (these processes need to be performed in a controlled atmosphere inside a prearrange chamber). A particularly difficult step was the realization of the

lateral hole used to connect the heating system with the transfer line: it was accurately extruded in order to respect the dimensional tolerances needed for the coupling and opportunely positioned to respect the alignment constraints with the transfer line.

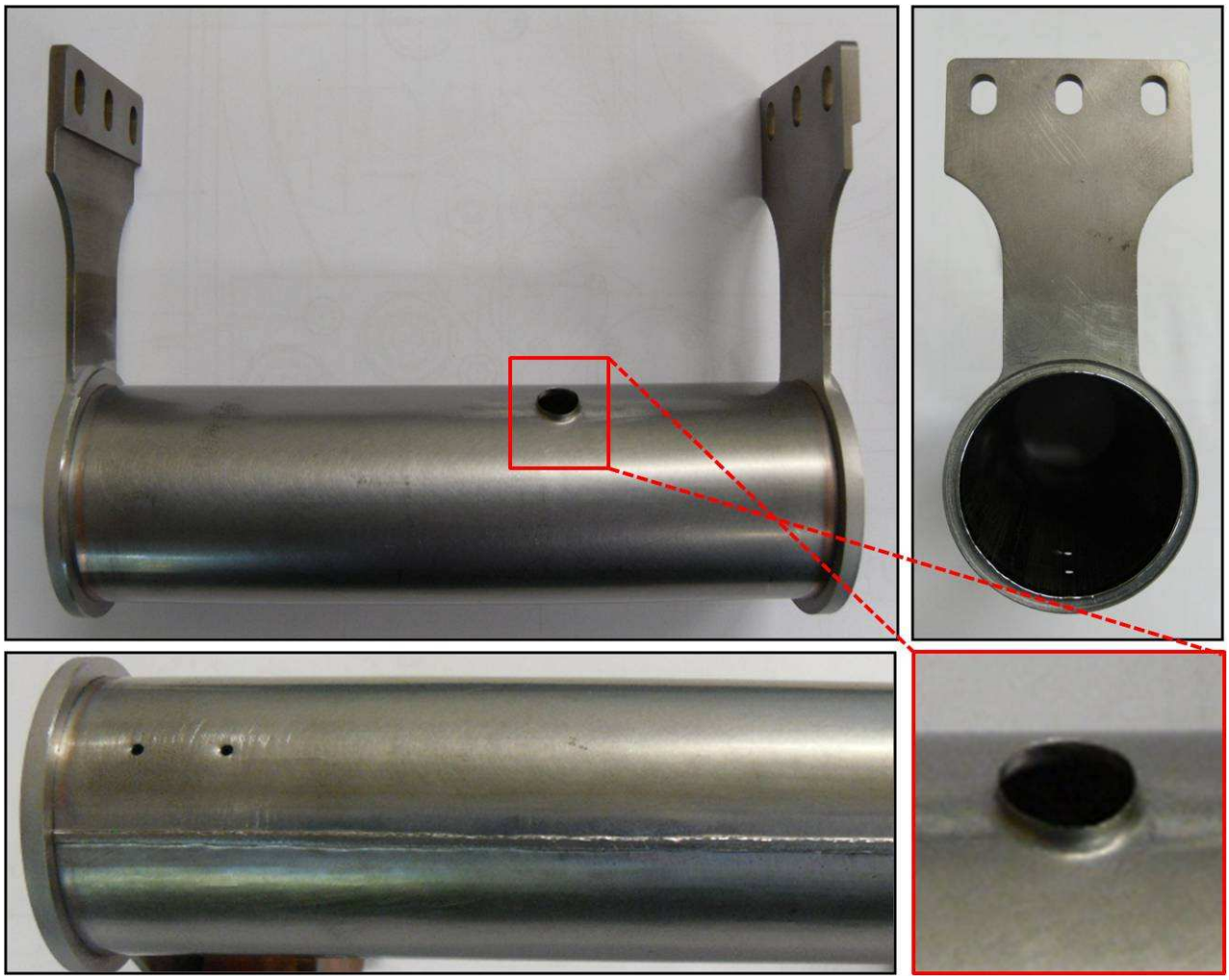

Fig. 3.70. The new heating system.

With the aim to start with the high temperature tests, the heating system was connected with the copper clamps needed to install it on the experimental apparatus (see figure 3.71).

Fig. 3.71. Connection of the heating system with the copper clamps.

Then the production target was accurately inserted in the heating system: two small pieces of Ta wire were used to keep closed the graphite box in proximity of its exposed extremity and to fix the target respect to the heating system (see figure 3.72).

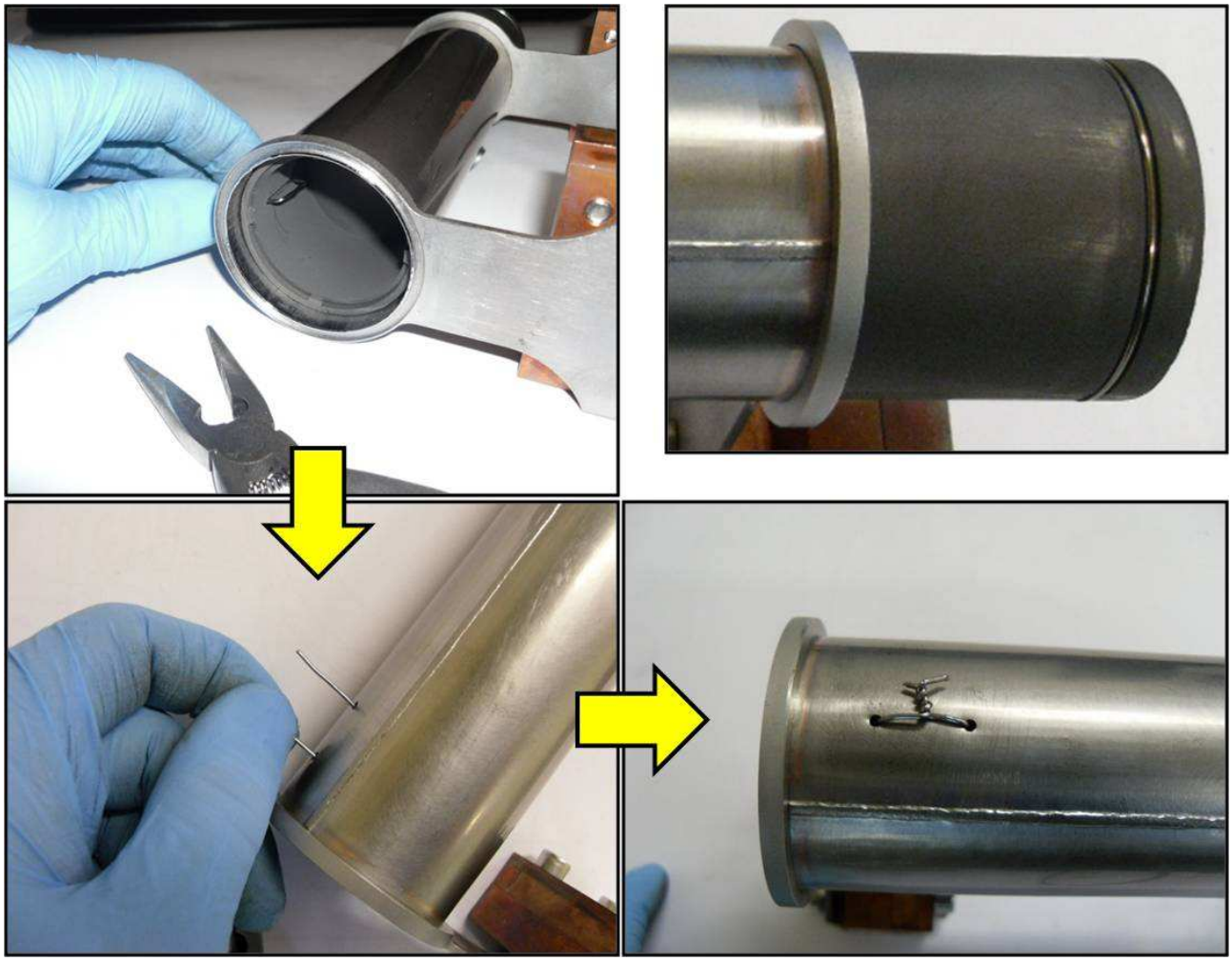

Fig. 3.72. Positioning of the production target inside the heating system.

At this point the target block (i.e. the assembly constituted by the target and the heating system) was installed in the experimental apparatus: copper clamps were opportunely tightened in order to support the high electrical current flux needed to heat the target block at the desired temperature level. The experimental apparatus was upgraded to reach the maximum current value of 1300 A: a new power supply was installed and four standard electrical cables (dimensioned to transport 500 A each) were accurately connected to each one of the two copper clamps (see figure 3.73).

The new water-cooled cover (see chapter 2) was then used to close the vacuum chamber: it is the cover studied for the on-line target station and comprehends an aperture for the proton beam entrance. In particular the target block was positioned and aligned taking into consideration the aforementioned aperture: this procedure allowed to make precise temperature measurements on the target's external graphite window (see figure 3.74).

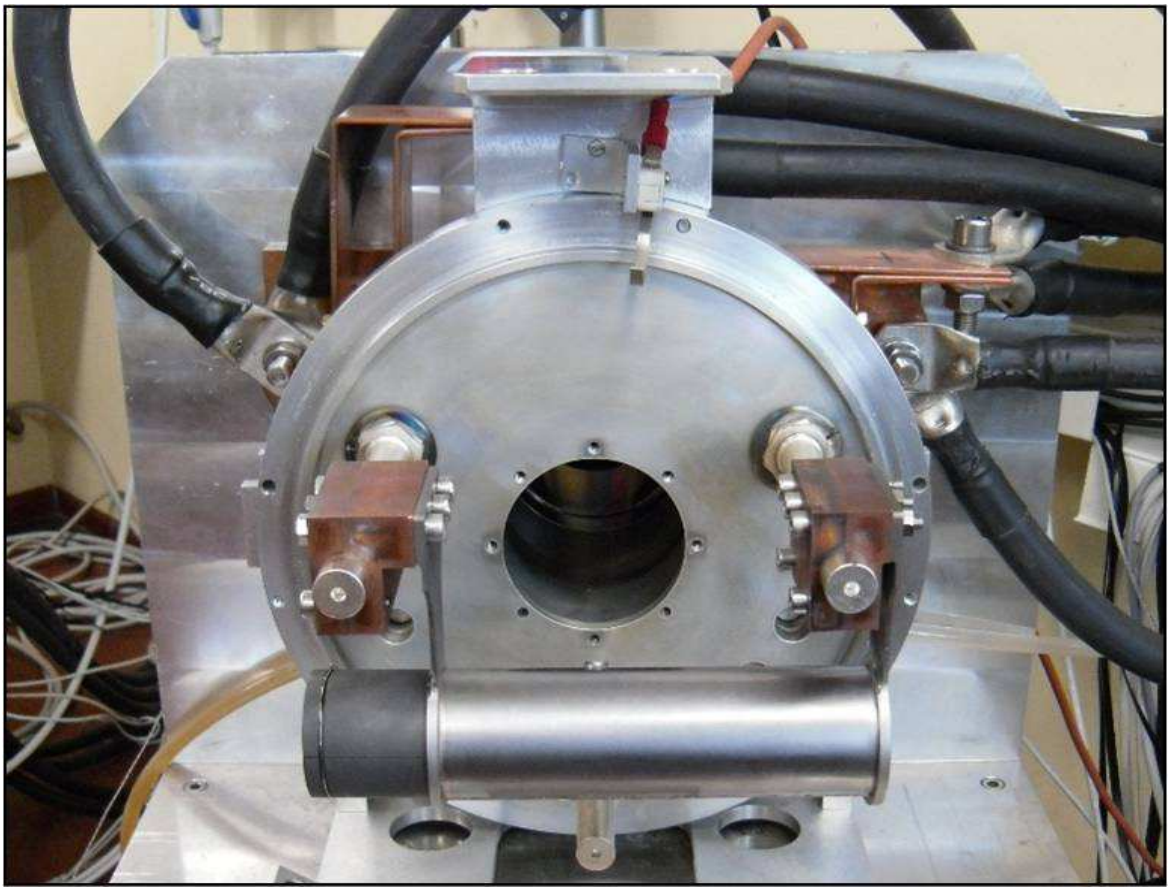

Fig. 3.73. The target block installed in the upgraded experimental apparatus.

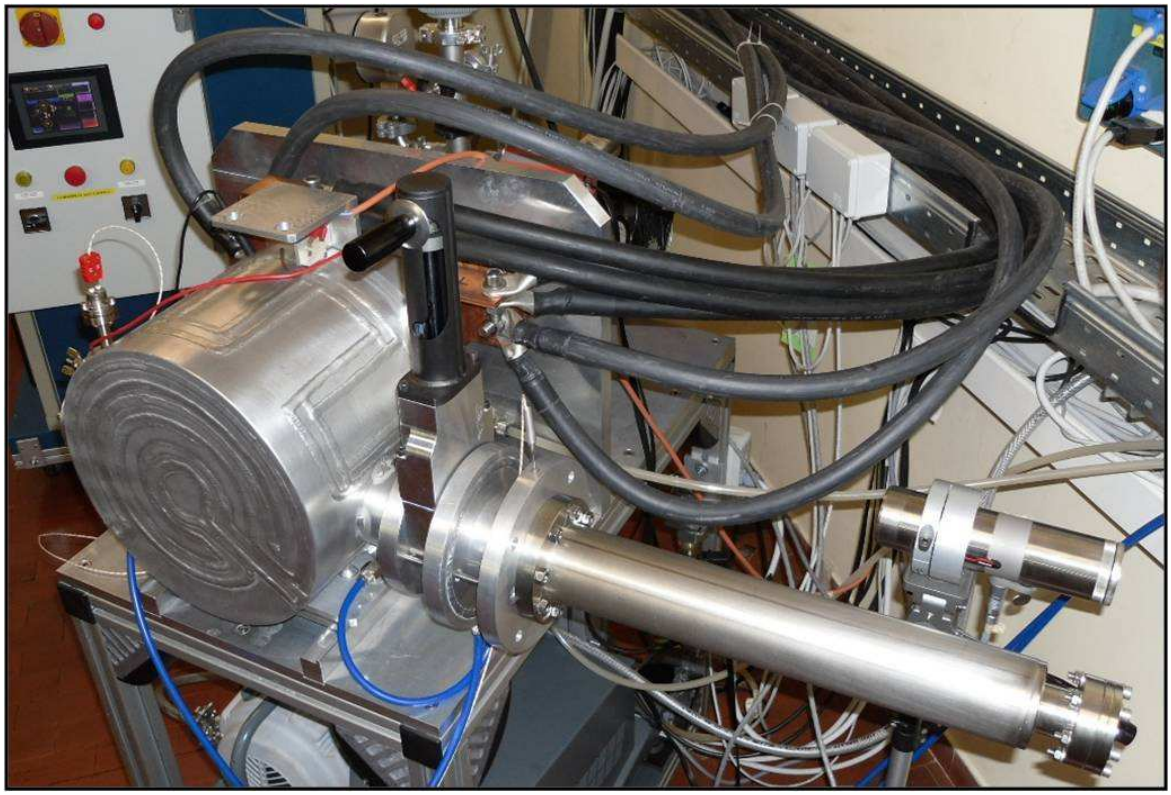

Fig. 3.74. Installation of the water-cooled cover designed for the on-line target station.

Temperature and potential difference measurements were performed as explained in paragraph 3.3.5. Figure 3.75 shows the Ta tube and the graphite window temperatures obtained during test 1, test 2 and test 3; in particular the curves report the average among the three temperature data sets. The correspondent heating system potential difference experimental curve is presented in figure 3.76; also in this case the curve is the average among the three data sets (test 1, 2 and 3).

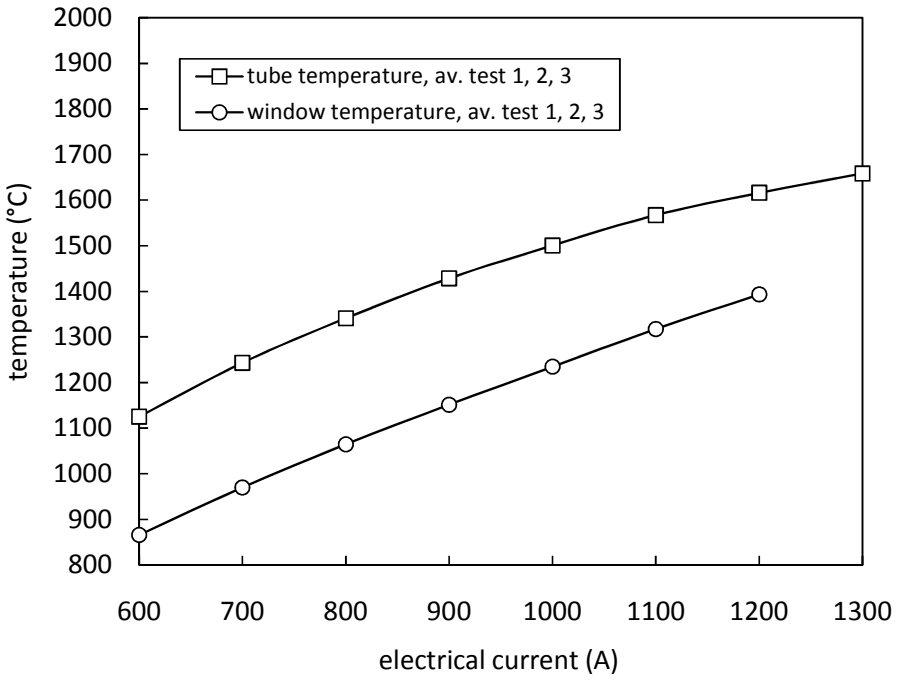

Fig. 3.75. Ta tube and graphite window experimental temperatures: average among three data sets (test 1, 2 and 3).

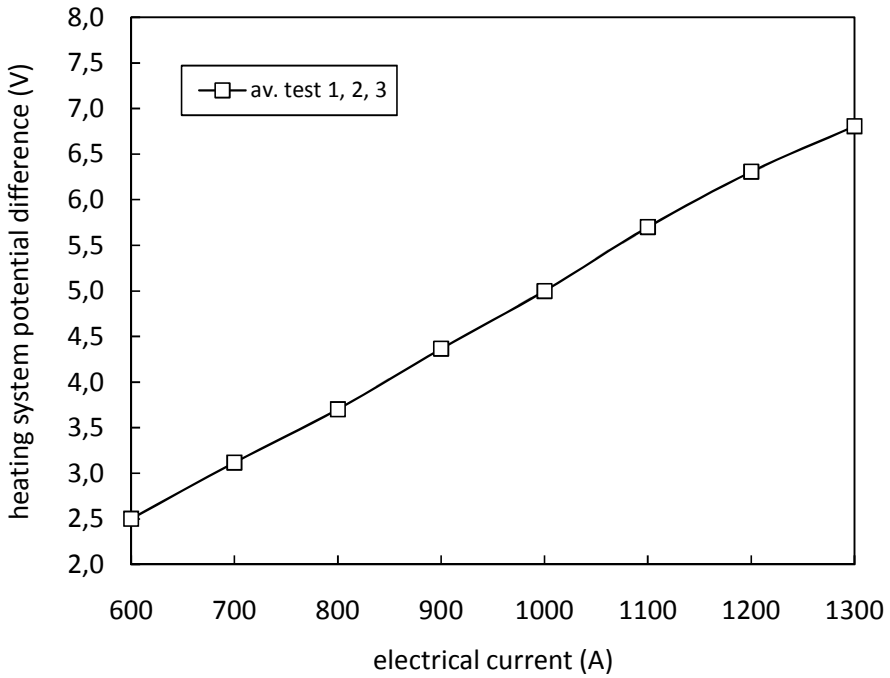

Fig. 3.76. Heating system potential difference experimental data: average among three data sets (test 1, 2 and 3).

Concentrating the attention on the tube's experimental maximum temperature (1658°C), registered when the heating current is equal to 1300 A, it is possible to notice the great difference respect to the correspondent value predicted by the FE model (1909°C) (see figure 3.50). This discrepancy, together with the graphs reported in figures 3.77 and 3.78, led to the suspicion of a parallel electric circuit: in words the heating system's deformations due to thermal expansion seem to cause, especially in proximity of the heating system's wings, some contact points with the graphite box through which a part of the heating current flows. In this way the global electrical resistance decreases and consequently, for the same heating current, the power dissipation goes down too. Figure 3.77 shows the evolution of the tube temperature during test 1, 2 and 3 (the electrical current is kept constant at every time step); it is easy to notice, especially at the higher temperature and current values, the general instability of the heating system. The temperature instabilities noticed in figure 3.77 are faithfully confirmed by figure 3.78 where the correspondent power supply potential difference values are accurately plotted. The parallel circuit in the graphite box is also proved by figure 3.79: once performed the high temperature tests, once extracted the graphite box from the heating system and cleaned it using sandpaper, it was possible to evidence the contact points between the graphite box and the heating system's wings through which the parallel electric current goes in and comes out of the box.

The potential difference values registered automatically from the power supply (see figure 3.78) are in general lower respect to the correspondent values measured directly at the heating system's copper clamps (see figure 3.76): this is obviously due to the power loss through the electrical cables connecting the power supply with the heating system's copper clamps.

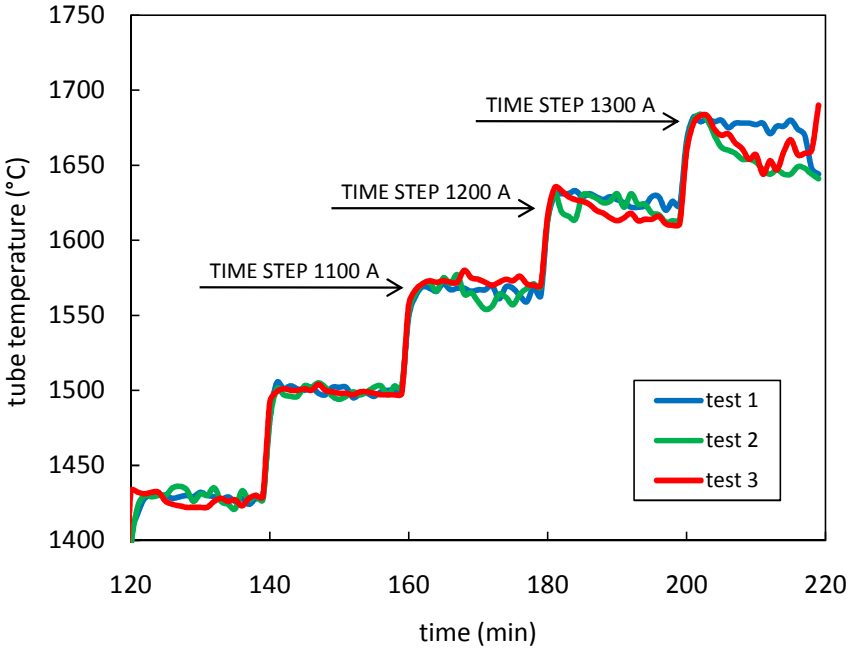

Fig. 3.77. Tube temperature vs time during test 1, test 2 and test 3.

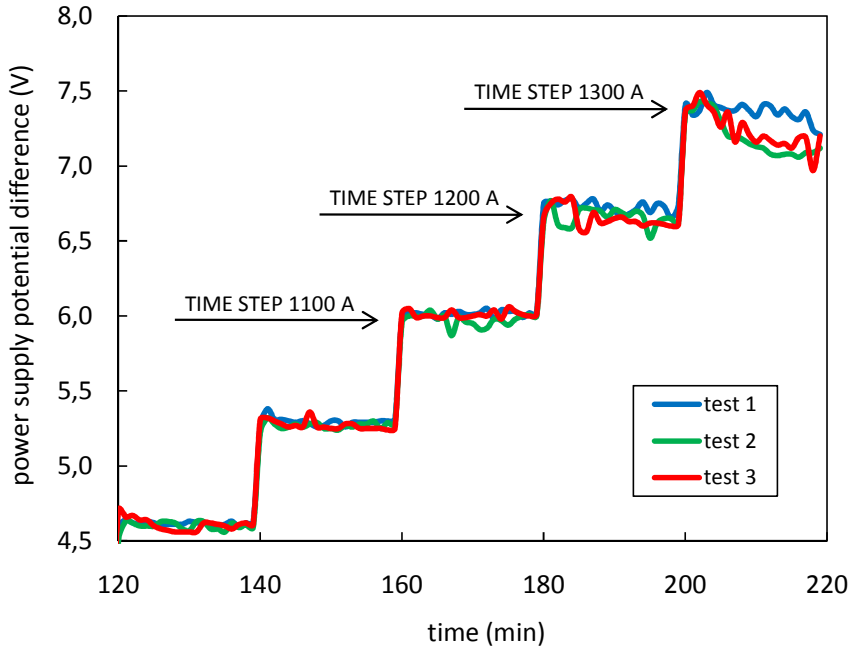

Fig. 3.78. Power supply potential difference vs time during test 1, test 2 and test 3.

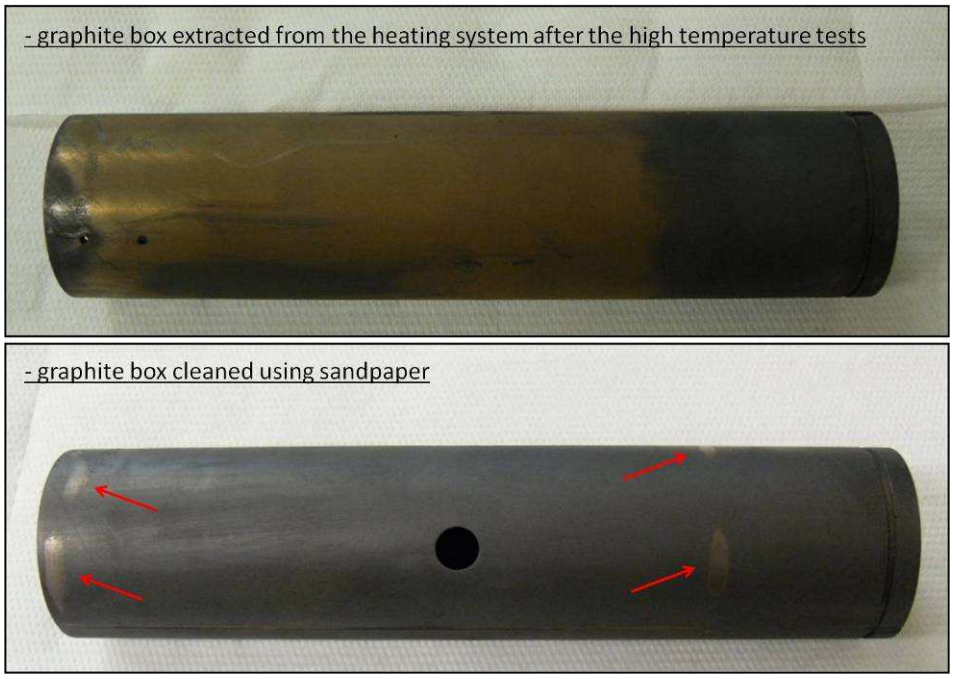

Fig. 3.79. The graphite box extracted from the heating system after the high temperature tests: the evidenced spots were not removed after cleaning with sandpaper and they put clearly in evidence the entry and the exit of the electrical current flowing through the box, constituting a parallel circuit respect to the target heating system.

With the aim to solve the aforementioned problem and consequently to improve the performances of the heating system, the geometry of the graphite box was slightly modified reducing from 49 to 48 mm the external diameter at its extremities (see figure 3.80); in this way it was possible to increase the radial spacing between the box and the Ta tube in proximity of the

heating system's wings, where important deformations due to thermal expansion occur. A new test (test 4) was performed to verify the efficacy of this kind of modification.

Fig. 3.80. Box modified in order to avoid the creation of a parallel circuit.

Figure 3.81 reports the tube temperature levels registered with the new modified box during test 4 and compares it to the tube temperature data obtained during test 3 with the new standard box before the modification described in figure 3.80; the temperature increment is evident and important, but at high temperature and current levels the box's parallel circuit is still active and contributes to decrease significantly the target's temperature levels. Temperature measurements were confirmed and reinforced by the power supply potential difference data (see figure 3.82).

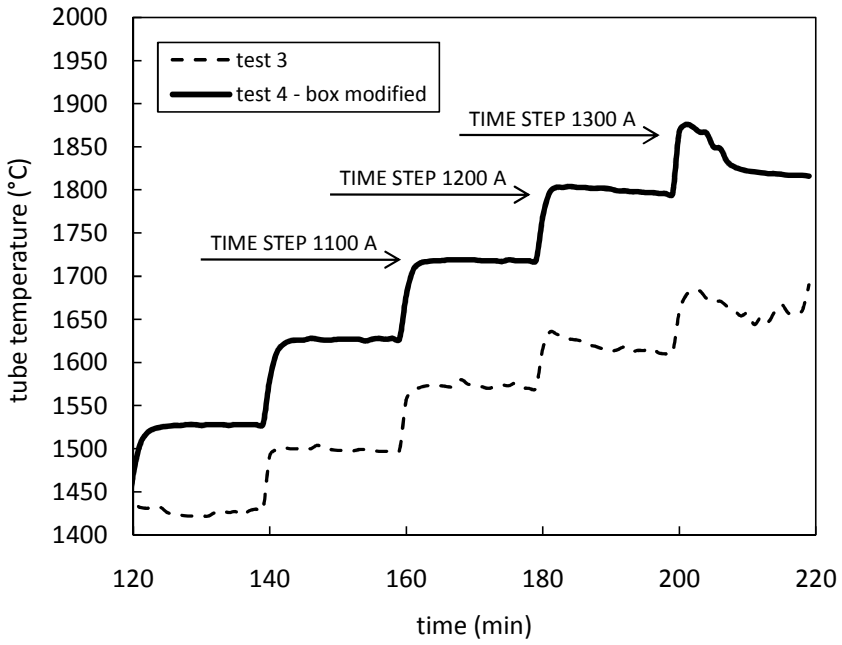

Fig. 3.81. Tube temperature vs time during test 3 and test 4 (with modified box).

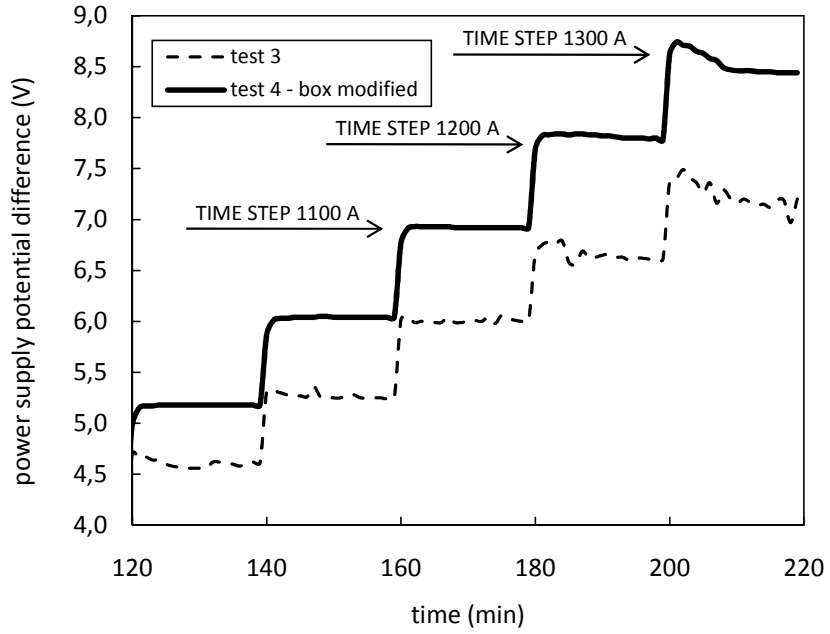

Fig. 3.82. Power supply potential difference vs time during test 3 and test 4 (with modified box).

Figure 3.83 offers the comparison between the standard box and the modified one on both the Ta tube and the graphite window temperatures; the correspondent heating system potential difference values are reported in figure 3.84. It is important to underline that every point reported in figures 3.83 and 3.84 represents the last value of the correspondent time step of figures 3.81 and 3.82, respectively; for every time step the electric current value is constant and, when the heating system behaves in a stable way and the time step is large enough, the last value of the time step is also the higher one (obviously increasing the current value at every time step).

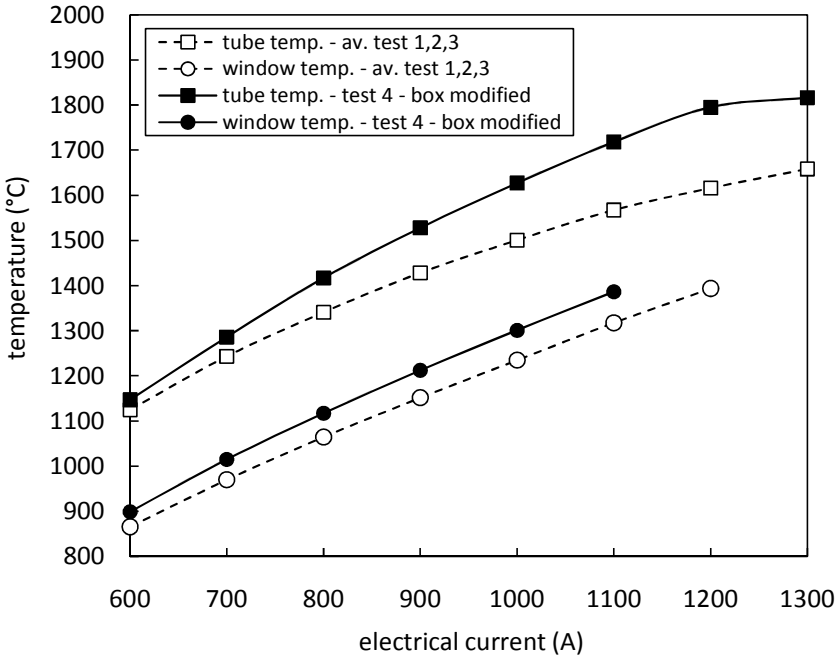

Fig. 3.83. Ta tube and graphite window experimental temperatures: comparison between the standard box and the modified one.

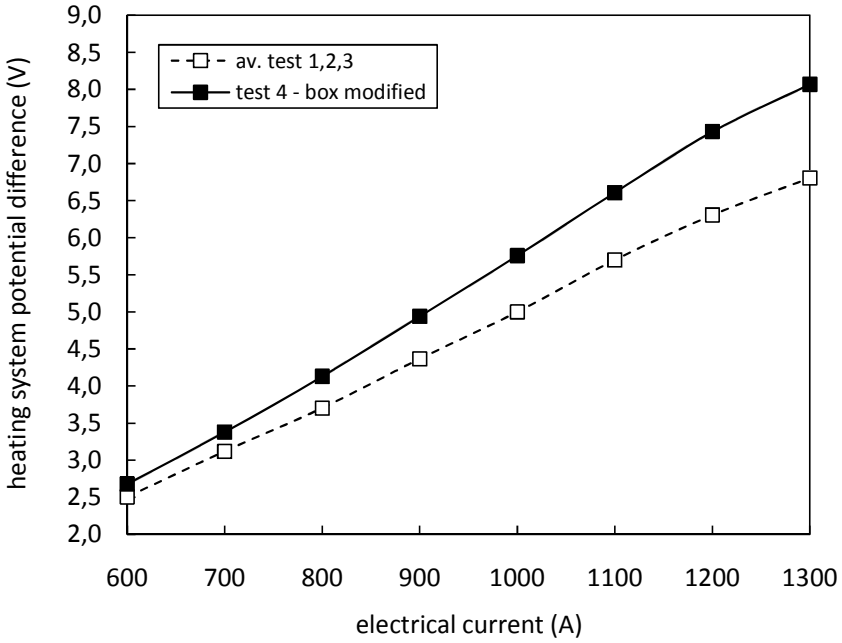

Fig. 3.84. Heating system potential difference experimental data: comparison between the standard box and the modified one.

Unfortunately the box's modifications were not sufficient to delete completely the instabilities of the heating system: in particular they were still present for the time steps correspondent to 1200 A and 1300 A (see figures 3.81 and 3.82); the main consequences are the discontinuities of the curves related to the modified box representing the tube temperature and the heating system potential difference in figures 3.83 and 3.84, respectively.

With the aim to obtain the ideal curves able to represent the target behaviour without instabilities, the higher values instead of the last ones were chosen for the time steps correspondent to 1200 A and 1300 A (see figures 3.81 and 3.82); in this way it was possible to redefine the curves as reported in figures 3.85 and 3.86.

Unfortunately the problem of the box's parallel circuit was not completely solved and a new box prototype is under development: the main idea is to slightly modify its geometry and to produce a more pronounced reduction of its external diameter at the extremities.

Observing figure 3.87 it is possible to observe how, before the modification of the box, the worsening of the heating system's performances was substantially stable. After the box modification the heating system worked in ideal conditions only for current values below 1200 A; once reached 1200 and 1300 A the heating system registered a permanent damage and started a progressive degradation with a substantial stabilization during test 6 and test 7.

In the following paragraph the comparison between FE data and the "ideal" experimental measurements (see figures 3.85 and 3.86) is presented.

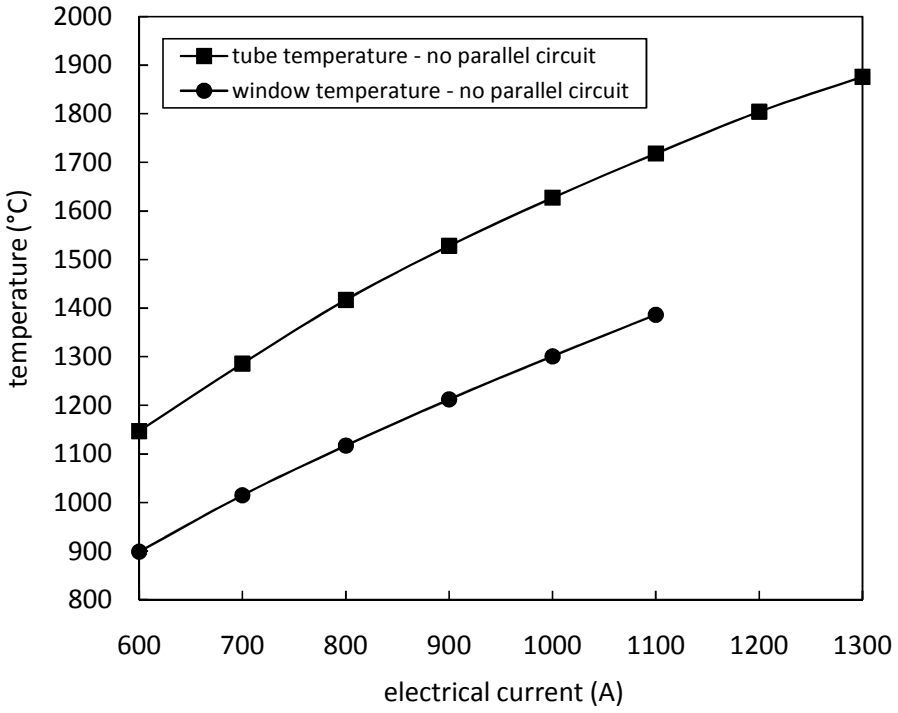

Fig. 3.85. Ta tube and graphite window experimental temperatures: curves obtained considering the maximum temperature values for every time step of test 4 (modified box).

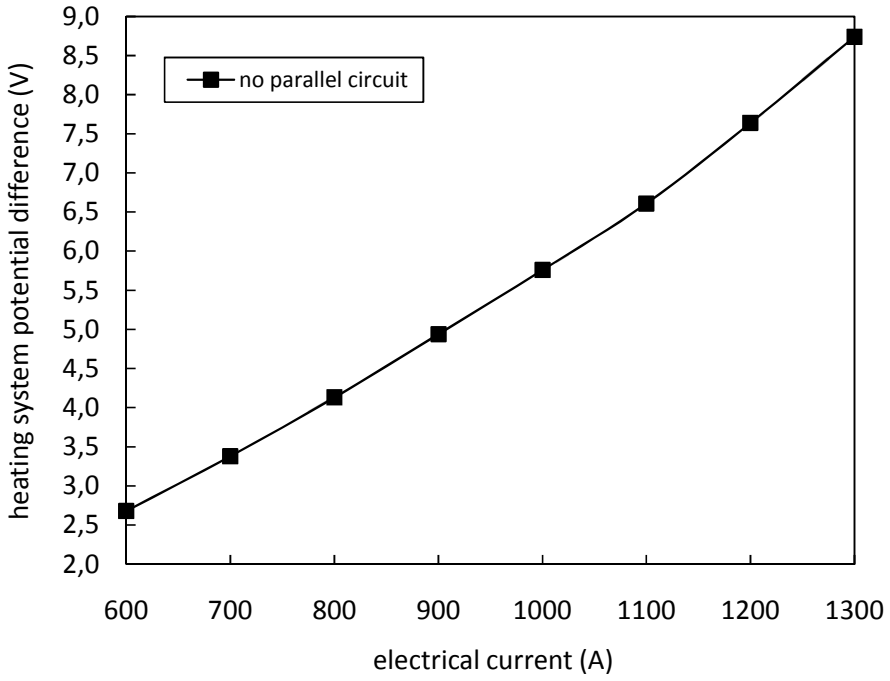

Fig. 3.86. Heating system potential difference experimental data: curve obtained considering the maximum potential difference value for every time step of test 4 (modified box).

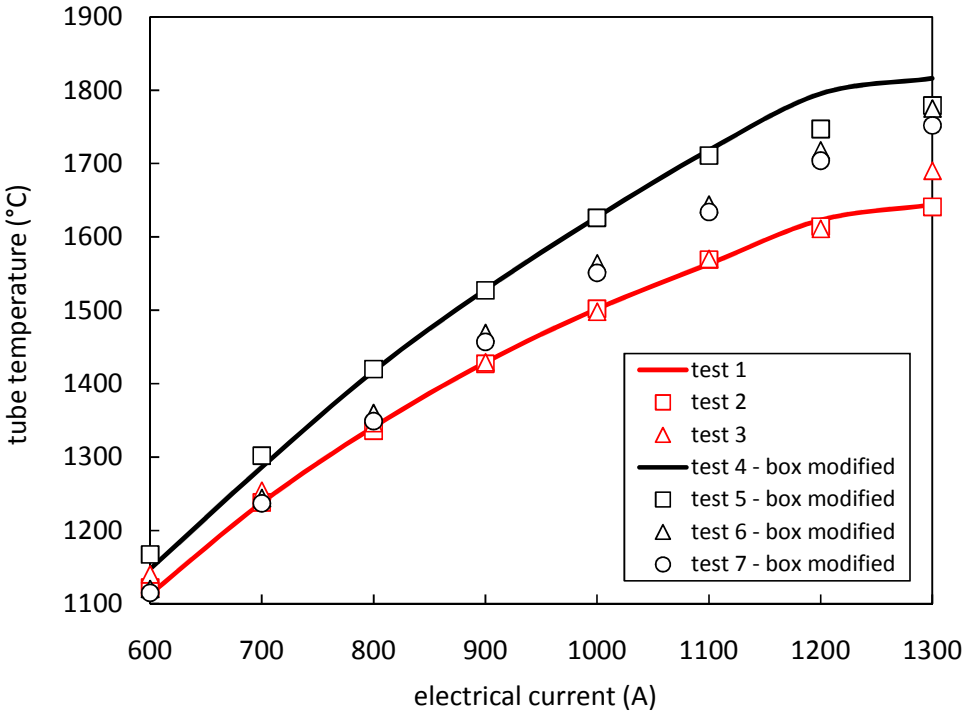

Fig. 3.87. Ta tube experimental temperatures for the seven tests performed.

3.4.4. Comparison between FE and experimental data

Temperature and potential difference values calculated by means of the FE model were compared with experimental data. Figure 3.88 reports a comparison between the FE and the experimental temperatures of the Ta tube, for different values of the electric current.

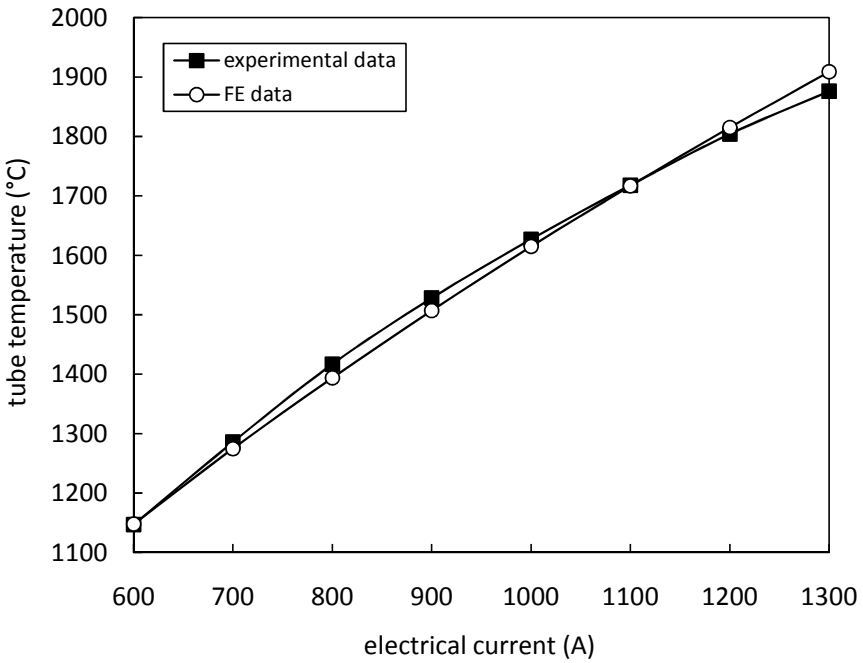

Fig. 3.88. Comparison between FE and experimental Ta tube temperatures. FE and experimental data refer to the point on the outer surface just below the hole for the connection with the transfer line.

The two sets of data are in good agreement and the maximum difference is registered at 1300 A: the FE temperature value is 33°C higher respect to the experimental one.

FE window temperatures are in general higher respect to the correspondent experimental values; the maximum difference is registered at 1100 A and is equal to 71°C.

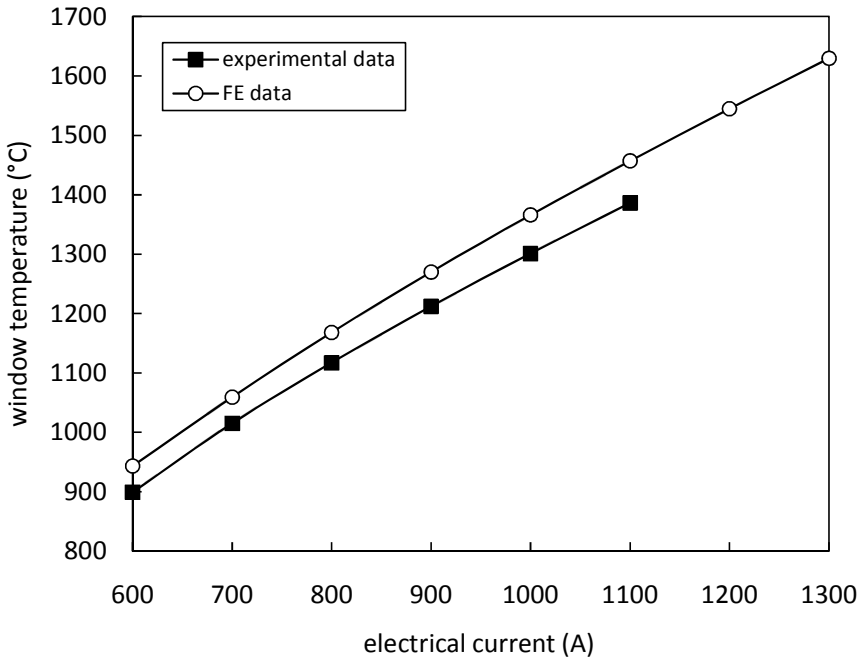

Fig. 3.89. Comparison between FE and experimental window temperatures.

The electric potential difference values detected between the external tips of the Cu clamps are reported in figure 3.90.

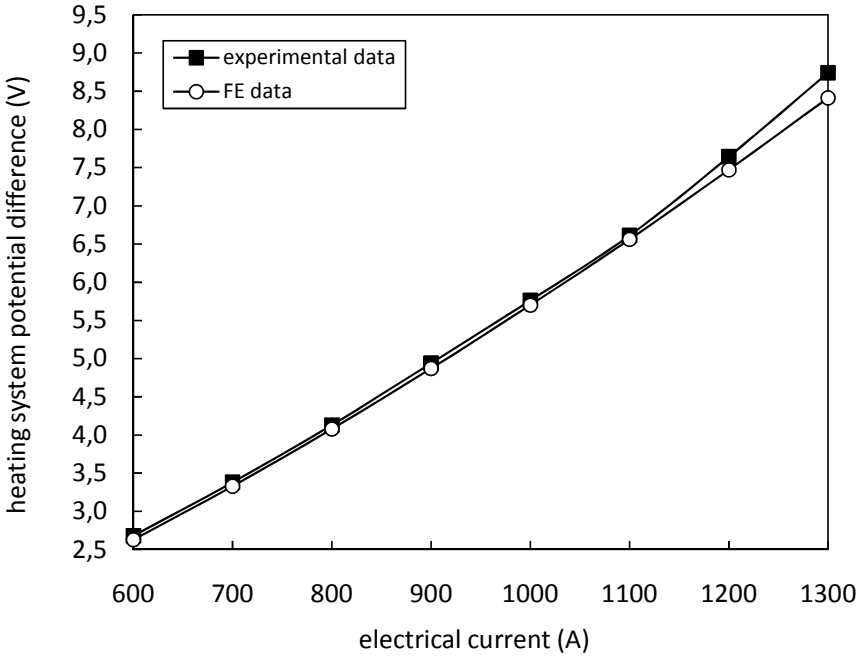

Fig. 3.90. Comparison between FE and experimental heating system potential difference values.

The differences between calculations and measurements can be explained using the same arguments reported in paragraph 3.3.6; the maximum difference is equal to 0.33 V and is registered at high current values, at 1300 A of heating current.

The comparison between the numerical and the experimental approaches was obviously performed taking into account exclusively the Joule heating thermal load: the on-line facility is not ready and consequently there are not experimental data available that consider the proton beam thermal load.

3.5. Detailed thermal-structural analysis of the UC_x disks

Once studied the temperature field of the UC_x disks by a global point of view, the detailed thermal-structural study of the UC_x disks is presented in the following.

The first aspect that is important to underline is the reduction of the physical domain: it includes now only the second window, the first dumper, the seven uranium carbide disks and the portion of the graphite box surrounding them (see figure 3.91).

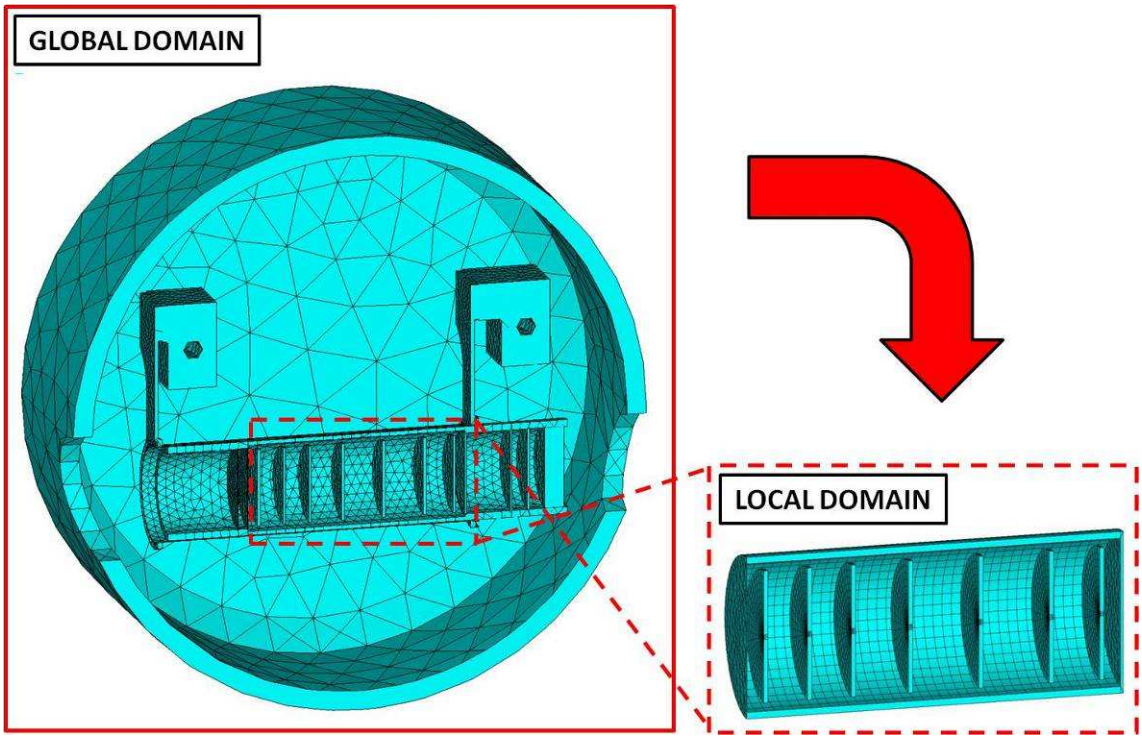

Fig. 3.91. The local domain considered for the detailed thermal-structural study of the UC_x disks.

The definition of this new local domain allowed to improve the quality of the mesh used for the disks and to introduce the proton beam thermal load in a more detailed way. In particular this new mesh is composed exclusively of hexahedral elements and 41 volumes were defined to represent every single disk (5 volumes describe its central core and 4 volumes are needed to model everyone of the 9 rings surrounding it): in this way it was possible to assign ten different power density

values for every disk, allowing to describe in a detailed way the proton beam power deposition, including the variability of power density in the radial direction. Moreover four ordered stratifications of elements were modelled with the aim to reproduce in an accurate way the temperature gradients along the disk's thickness (see figure 3.92).

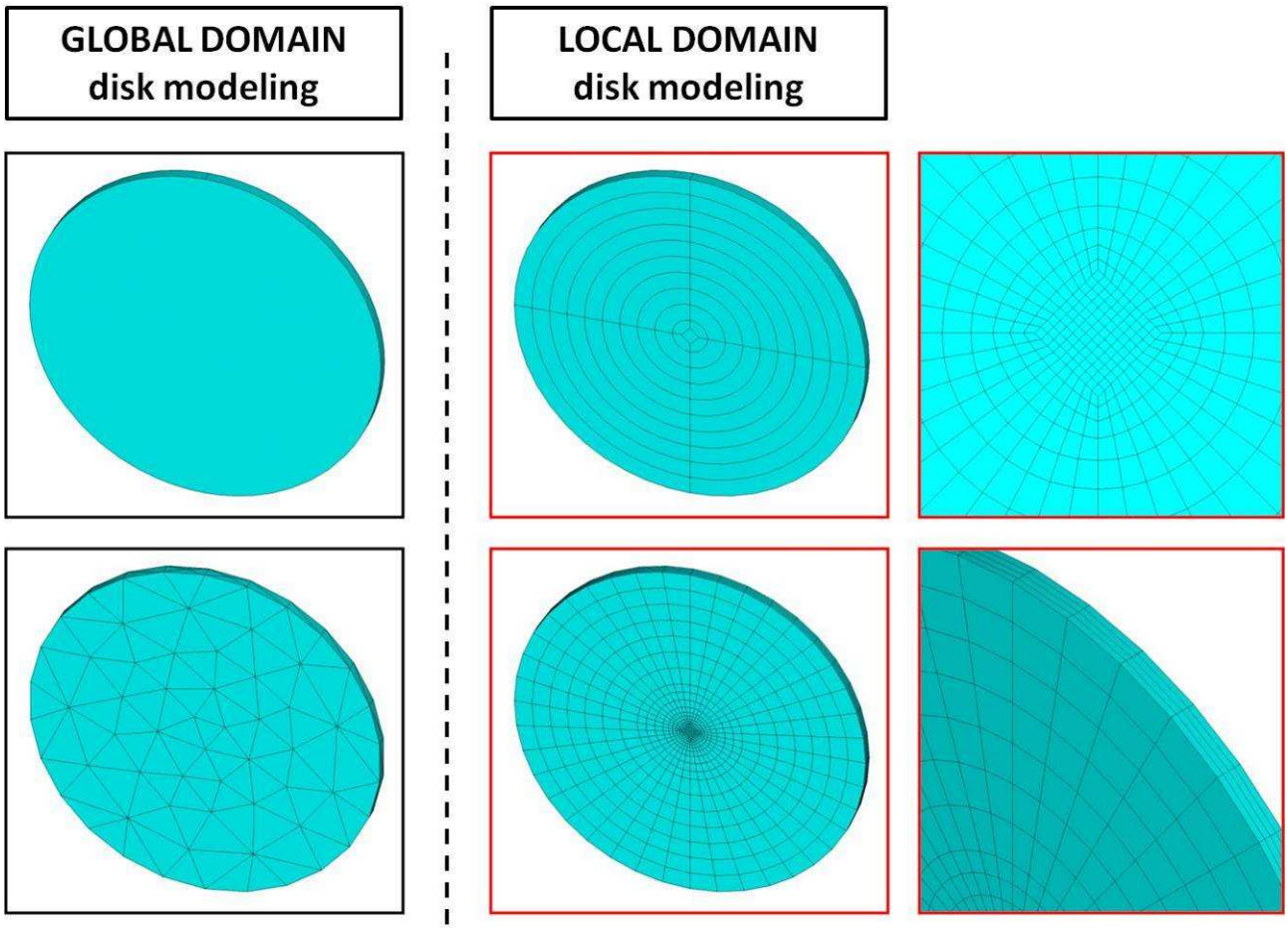

Fig. 3.92. Modelling and discretization of the UCx disks: comparison between global and local models.

Such a mesh allowed to produce a lot of important observations that were not possible to do before because of the bigger amount of components to take into account with the same calculation power available. The same mesh structure was also used to calculate the stress state in the disks induced by thermal gradients.

Before starting to study in detail the effects of the proton beam in the disks (considering a power density variable in the radial direction) and the consequent induced stress state, a comparison with the global mesh was performed considering a single power density value (the average value) for every disk, so the same proton beam thermal load assigned in the previous sets of analyses. In particular the average temperature and the parameter $\Delta T = T_{MAX} - T_{MIN}$ were reported for every disk in figures 3.93 and 3.94, respectively, considering both the global and the local mesh. It is very important to underline that in the local domain, the temperature distributions in the window, in the

dumper and in the portion of box, were assigned as temperature constraints taking as reference the results obtained by means of the global model presented and discussed in the previous paragraphs. The local mesh, importantly refined respect to the global one, produces a general slight temperature increment (see figure 3.93) (the maximum temperature increment is registered at the first disk and is equal to 39.5°C), keeping the parameter $\Delta T = T_{MAX} - T_{MIN}$ substantially unchanged (see figure 3.94) (the maximum ΔT value is equal to 10°C and is associated to disk 4).

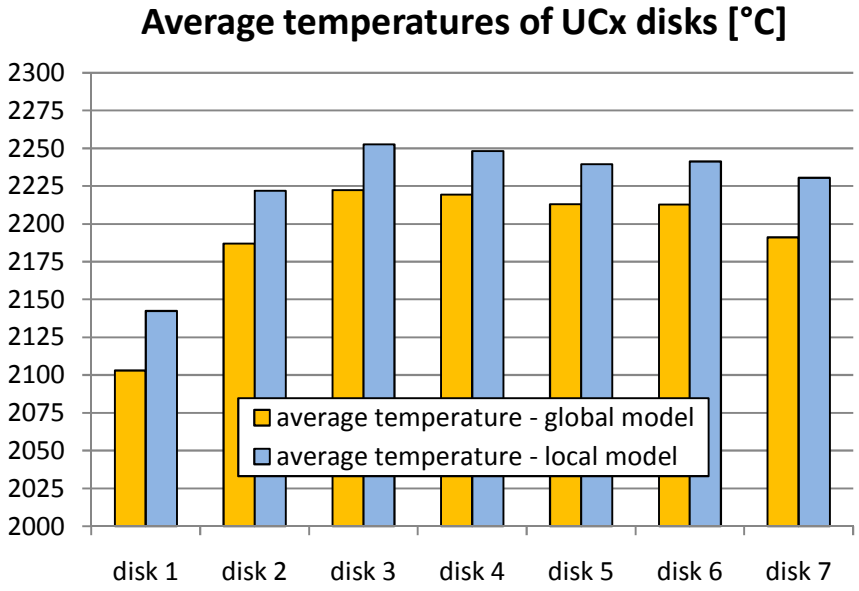

Fig. 3.93. Average temperatures of the UC_x disks: comparison between global and local models.

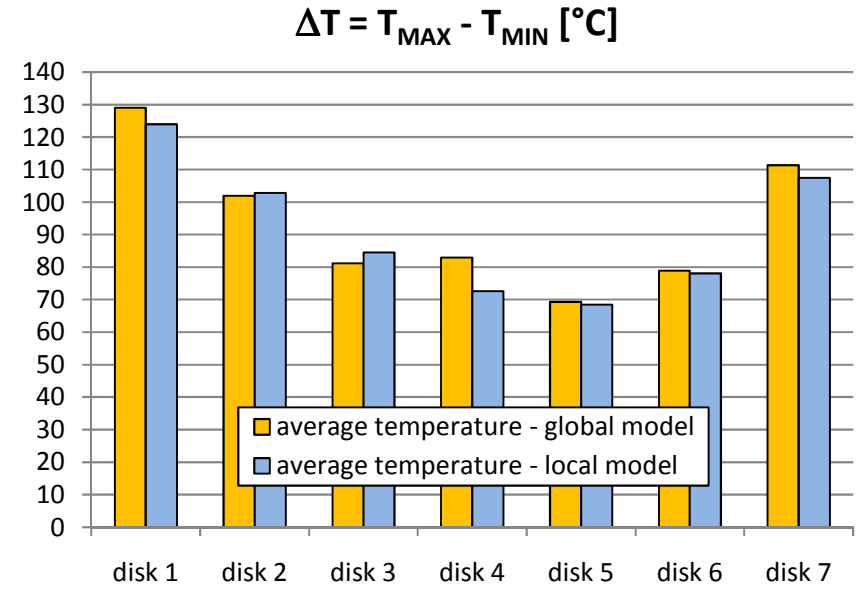

Fig. 3.94. Temperature difference $\Delta T = T_{MAX} - T_{MIN}$ registered for the UCx disks: comparison between global and local models.

At this point, verified the coherence of the local model with the global one, the local model and the fine local mesh are used to study the effect of the proton scattering on the temperature distribution of the disks and the stress state induced on them by thermal gradients.

3.5.1. The effect of the proton scattering on the temperature distribution of the UC_x disks

In the previous paragraph 3.3.8 the power data for the components composing the production target were assigned; in particular thanks to figure 3.31 and table 3.1 it is possible to appreciate the amount of power deposited by the proton beam in each disk.

In the analyses performed until now (using the global model and the global mesh), the power density value assigned to each disk was calculated simply dividing the disk power value by the disk volume value: the power density value obtained in this way was then applied to the single volume constituting the disk.

The main scope of the new local model was the assignment of the beam power deposition using an higher level of accuracy; as explained in the previous paragraph the new local disk model allowed to apply ten different power density values to ten different annular regions of the disk. In this way it was possible to describe the proton scattering and the consequent power density radial profile, that in our case becomes less and less flattened in the last disks. The power density data obtained thanks to the MCNPX numerical code are reported in the following, in table 3.2 and in figure 3.95 [2].

	total power W	**power density** 0 < r < 0,2 cm W/cm^3	**power density** 0,2 < r < 0,4 cm W/cm^3	**power density** 0,4 < r < 0,6 cm W/cm^3	**power density** 0,6 < r < 0,8 cm W/cm^3	**power density** 0,8 < r < 1,0 cm W/cm^3	**power density** 1,0 < r < 1,2 cm W/cm^3	**power density** 1,2 < r < 1,4 cm W/cm^3	**power density** 1,4 < r < 1,6 cm W/cm^3	**power density** 1,6 < r < 1,8 cm W/cm^3	**power density** 1,8 < r < 2,0 cm W/cm^3
disk 1	538	335	332	331	331	331	332	330	330	331	320
disk 2	538	338	344	346	346	344	345	344	343	341	268
disk 3	548	364	373	370	370	372	372	369	364	325	230
disk 4	556	401	403	409	405	403	399	387	356	300	214
disk 5	564	451	452	445	446	434	415	383	339	283	210
disk 6	574	498	490	480	469	445	417	379	335	280	219
disk 7	589	519	516	500	476	453	423	384	340	291	232

TABLE 3.2. Detailed power density data calculated using the MCNPX code.

The effect of the proton scattering is very small for the first disk and the difference between the power density values registered at the centre and at the periphery is approximately equal to 15

W/cm^3; the same difference at the fourth and at the seventh disk is equal to 187 and 287 W/cm^3, respectively, clearly remarking the increasing influence that the proton scattering has passing from the first disk to the seventh one.

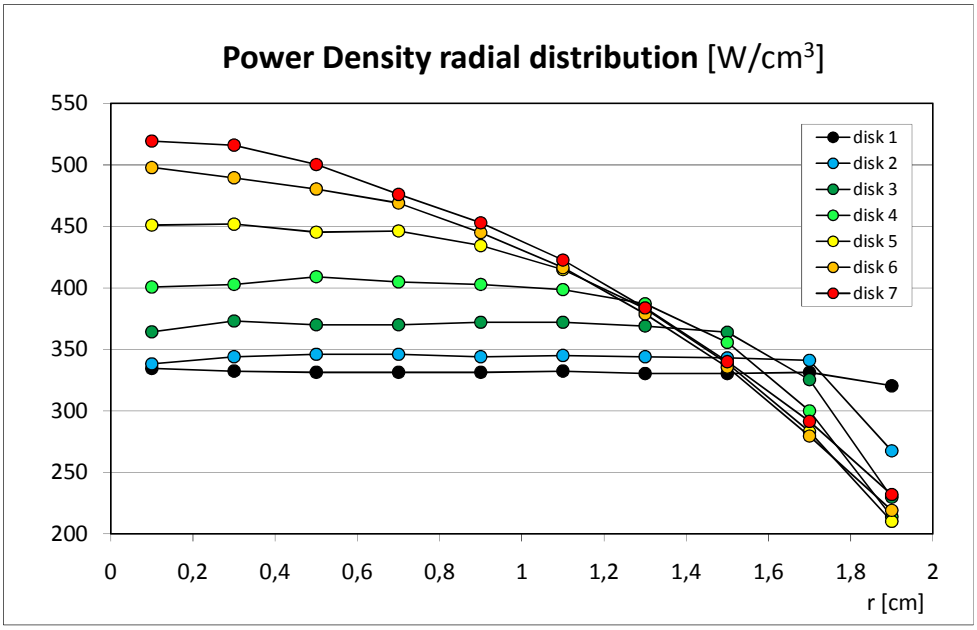

Fig. 3.95. Power density radial distributions for the UCx disks.

The effects of the proton scattering are clearly summarized by figures 3.96 and 3.97; as expected both the average temperature and ΔT register the maximum increment in proximity of the seventh disk: + 23.5°C and + 59.5°C, respectively. The ΔT increment has surely a bigger relative importance (+ 55%) whereas the increment of the average temperature can be considered more or less negligible (+ 1%).

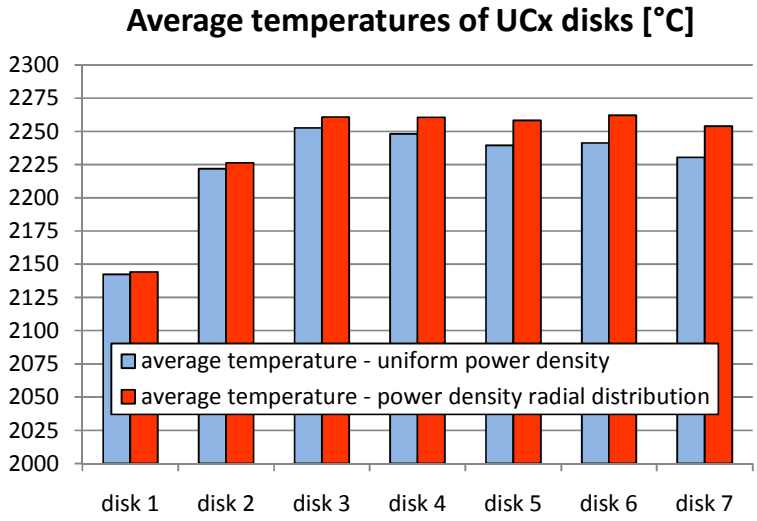

Fig. 3.96. Average temperatures of the UC_x disks: the effect of the power density radial distribution (proton scattering).

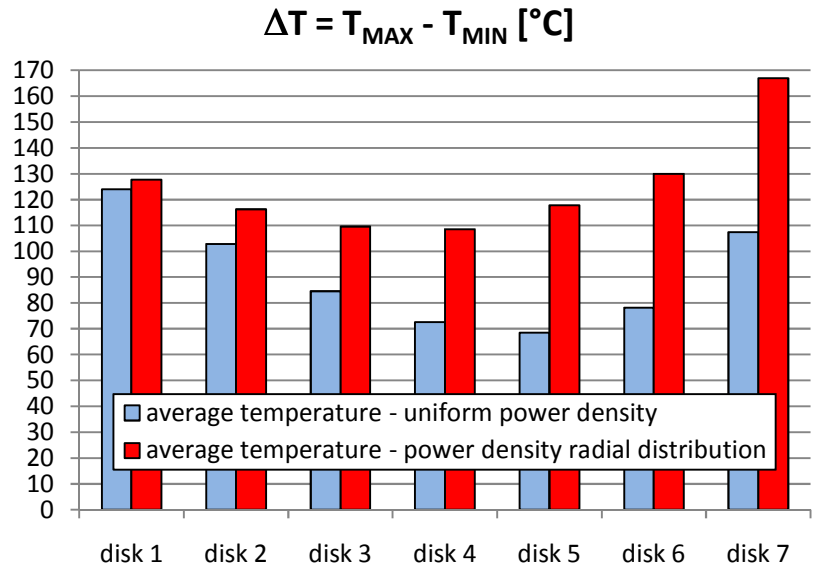

Fig. 3.97. Temperature difference $\Delta T = T_{MAX} - T_{MIN}$ registered for the UCx disks: the effect of the power density radial distribution (proton scattering).

Taking now as reference the temperature field obtained assigning to every disk the correspondent power density radial distribution, some detailed information is given in the following. In particular the minimum, the average and the maximum temperatures of the seven UC_x disks are reported in figure 3.98; the maximum temperature levels are registered in proximity of disk 6 and disk 7 and are equal to 2292°C and 2291, respectively, approximately 100°C below the melting point of uranium carbide (2390°C).

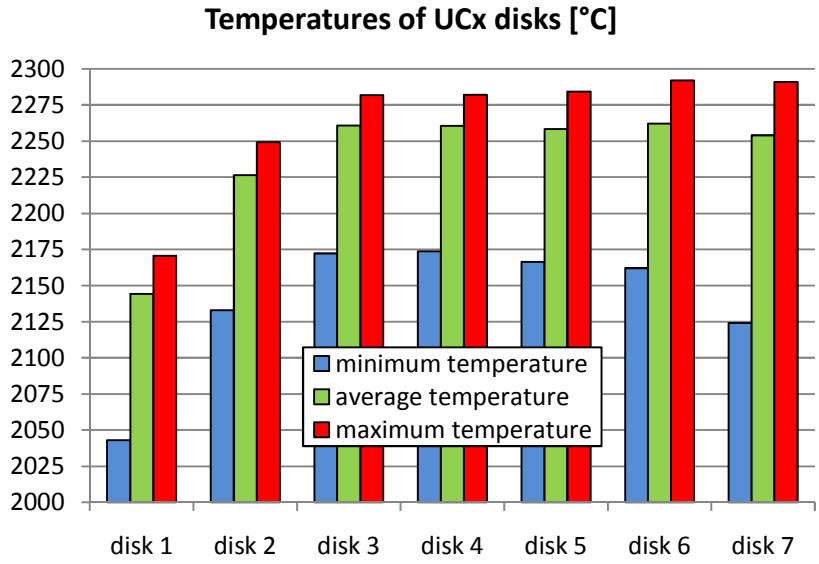

Fig. 3.98. Average, maximum and minimum temperatures of the UCx disks correspondent to the proton beam thermal load (power density radial distribution assigned to every disk).

Figures 3.99 and 3.100 show the radial temperature distribution in the middle plane of every disk and their axial temperature distributions across the thickness, respectively.

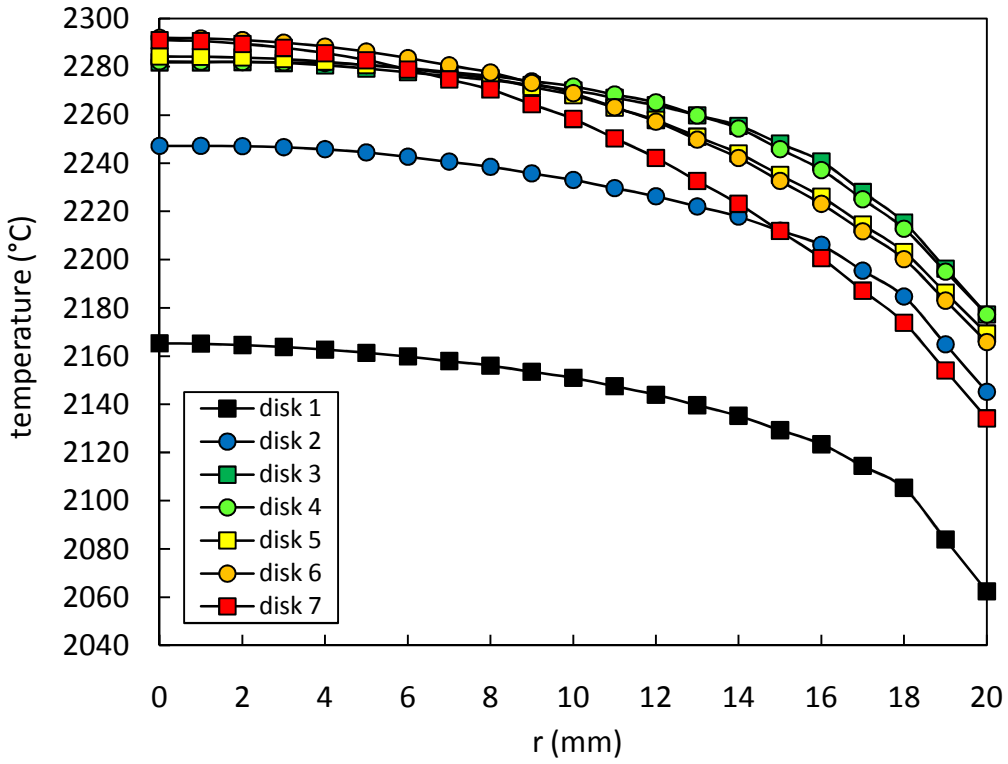

Fig. 3.99. Middle plane radial temperature distribution for the seven UC_x disks.

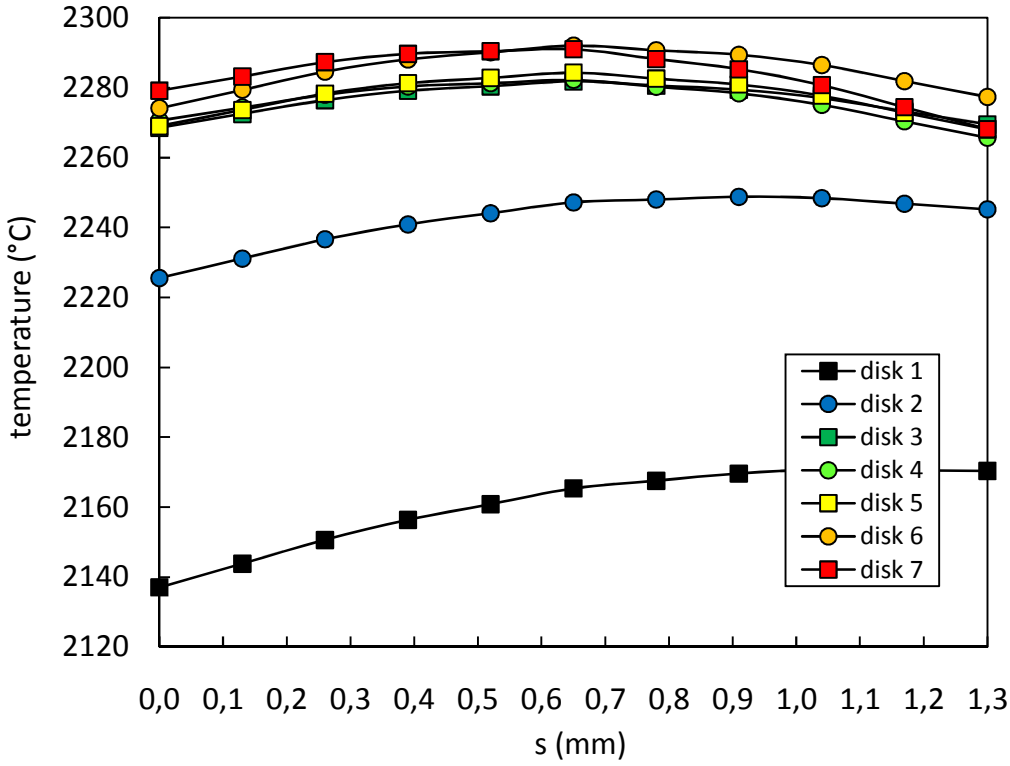

Fig. 3.100. Axial (through the thickness) temperature distribution for the seven UC_x disks (for every disk the coordinates s = 0 and s = 1.3 mm correspond to the proton beam entrance and exit, respectively).

The maximum temperature differences both in radial and in axial direction are accurately reported in table 3.3 for all the seven UC_x disks composing the SPES target; it is very important to

monitor in detail these quantities since they deeply influence the target stress state (see the next paragraph).

	POWER [W]	$\mathbf{T_{MAX}}$ [°C]	$\mathbf{\Delta T_{MAX}}$ in radial direction [°C]	$\mathbf{\Delta T_{MAX}}$ in axial direction [°C]
disk 1	538	2171	103	34
disk 2	538	2249	102	23
disk 3	548	2282	105	13
disk 4	556	2282	105	17
disk 5	564	2284	115	16
disk 6	574	2292	126	18
disk 7	589	2291	157	23

TABLE 3.3. Maximum temperatures and temperature differences both in radial (middle plane) and in axial direction for the seven UCx disks.

The disk that shows the most critic conditions is surely disk 7: it presents a very high maximum temperature (disk 6 is hotter, but with a difference of only 1°C) and very important thermal gradients along both radial and axial direction; as a consequence, before starting to study the stress state induced by thermal gradients, some additional information on the temperature field of disk 7 are given in figure 3.101 and 3.102: the former compares the radial temperature distributions at sections s = 0 (beam entrance plane), s = 0.65 (middle plane) and s = 1.3 mm (beam exit plane) whereas the latter presents the temperature distributions across the thickness in the axial direction, at r = 10 and at r = 20 mm.

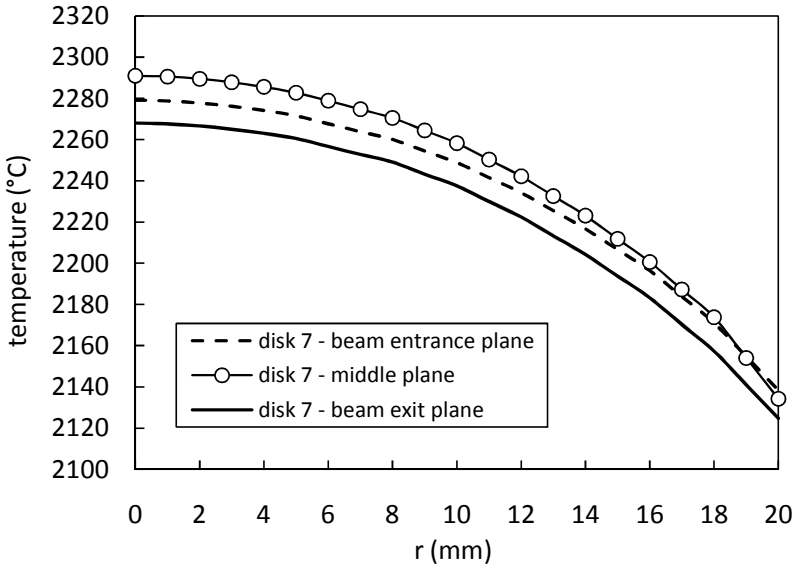

Fig. 3.101. Radial temperature distributions for disk 7 at the beam entrance plane, at the middle plane and at the beam exit plane.

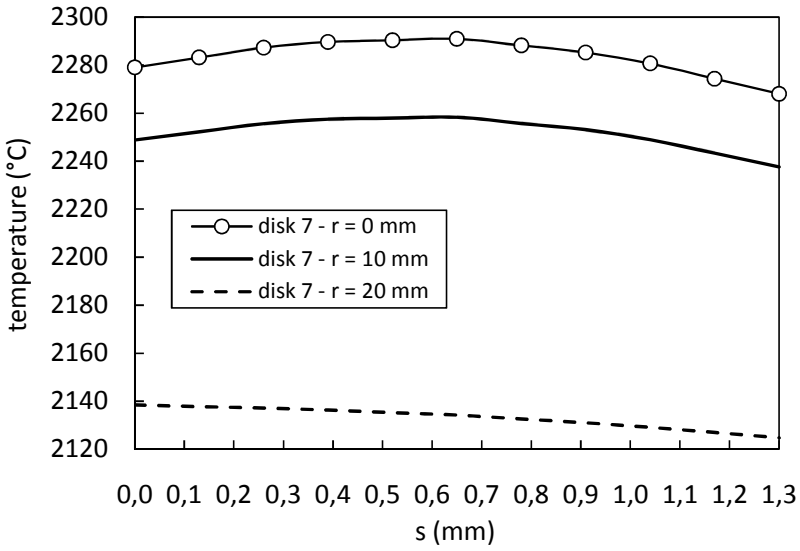

Fig. 3.102. Through the thickness temperature distributions for disk 7 at r = 0, 10 and 20 mm (the coordinates s = 0 and s = 1.3 mm correspond to the proton beam entrance and exit, respectively).

3.5.2. Physical properties of uranium carbide [2]

With the aim to compute the stress state induced by thermal gradients some fundamental properties of uranium carbide are presented in the following.

Considering as reference room temperature, a value suggested for the elastic modulus of uranium carbide is E = 215 GPa, together with the Poisson's ratio value $\nu = 0.269$; the temperature dependence of the elastic modulus is quite pronounced and presents obviously a negative slope. From [30] it is possible to obtain a curve to describe the decrease of E for uranium carbide between room temperature and 1500°C; it has been employed to extrapolate an elastic modulus value at the reference temperature T = 2000°C: the correspondent value is E = 176 GPa, but it is important to remark that the extrapolation from 1500°C to 2000°C is arbitrary and has to be considered with attention. No corrections have been applied to the elastic modulus for the effect of porosity; no corrections have been applied to the Poisson's ratio for the effect of both temperature and porosity.

From [30] it was possible to obtain the mean thermal linear expansion coefficient of uranium carbide at 2000°C: the value adopted $\alpha_m = 12.4 \cdot 10^{-6} °C^{-1}$ was not extrapolated in this case.

Taking into consideration the fracture behavior, uranium carbide is a brittle ceramic material which may be susceptible to catastrophic fracture at low temperature, but a gradual brittle to ductile transition is expected to occur at the temperature range 1100 – 1300°C. This does not mean that the material deforms completely plastically above 1300°C, although, plasticity should assure a certain level of relaxation for thermal stresses. Values of fracture stress are given up to 1300°C only, in particular from [30] it was possible to obtain $\sigma = 200$ MPa.

In this work a linear elastic analytical model and a linear elastic FE numerical model were defined to study the stress state induced by thermal gradients in the UC_x disks (see the next paragraph); in this context the assumption of linearity seems rather adequate up to 1300°C, but it seems more questionable beyond. As a consequence the obtained results must be considered and interpreted paying a particular attention. Further data, analyses and measurements would be needed for definitive results.

3.5.3. The study of thermal stresses

Before starting to present data coming from the detailed 3D FE thermal-structural model of the uranium carbide disks, the two-dimensional model used to obtain preliminary indications on the stress state induced by thermal gradients is described in the following [31].

A disk characterized by the radius "R" and by a very small thickness "s" is isostatically constrained and presents an axisymmetric temperature distribution with the maximum value at the center and the minimum one at the periphery; the temperature gradient in the axial direction is considered negligible. In these conditions it is possible to apply the hypothesis of plane stress according to which only the stress components σ_r and σ_θ are different from zero ($\sigma_z = 0$). It is also supposed that the stress and strain components don't vary across the thickness. As usual a linear elastic, homogeneous and isotropic material is considered. At this point a small portion of the disk, a small element closed among two cylindrical surfaces characterized by the radius "r" and "r + dr" and two radial planes spaced by the angle $d\theta$, is taken into consideration (see figure 3.103).

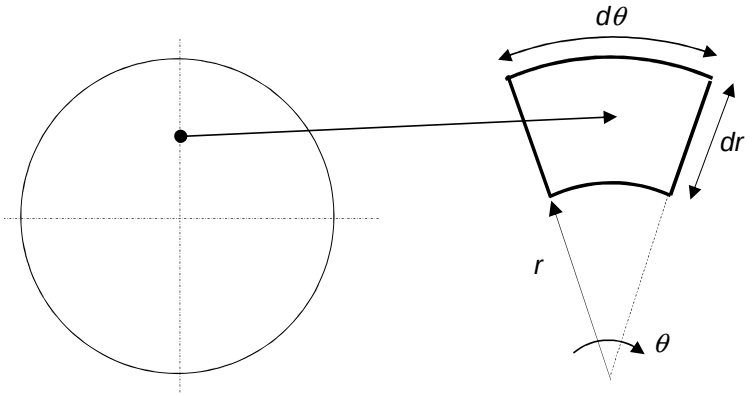

Fig. 3.103. The small element considered to argue the stress state study.

If ε_r and ε_θ are the actual strain components, namely the strain components due to both stress and thermal expansion, it is possible to write the Hooke's law as follows:

$$\varepsilon_r = \frac{1}{E} \cdot (\sigma_r - \nu\sigma_\theta) + \alpha \cdot T \qquad (16.a)$$

$$\varepsilon_\theta = \frac{1}{E} \cdot (\sigma_\theta - \nu\sigma_r) + \alpha \cdot T \qquad (16.b)$$

With the aim to evidence the strain components due to stress only it is possible to rewrite equations (16.a) and (16.b) as proposed in the following:

$$\varepsilon_r - \alpha \cdot T = \frac{1}{E} \cdot \left(\sigma_r - \nu \sigma_\theta\right) \tag{17.a}$$

$$\varepsilon_\theta - \alpha \cdot T = \frac{1}{E} \cdot \left(\sigma_\theta - \nu \sigma_r\right) \tag{17.b}$$

After simple algebraic steps the stress components σ_r and σ_θ can easily be obtained from equations (17.a) and (17.b):

$$\sigma_r = \frac{E}{\left(1-\nu^2\right)} \cdot \left[\varepsilon_r + \nu \varepsilon_\theta - \left(1+\nu\right) \cdot \alpha T\right] \tag{18.a}$$

$$\sigma_\theta = \frac{E}{\left(1-\nu^2\right)} \cdot \left[\varepsilon_\theta + \nu \varepsilon_r - \left(1+\nu\right) \cdot \alpha T\right] \tag{18.b}$$

Choosing arbitrarily two points along the radial direction, the strain components ε_r and ε_θ can be expressed in function of the radial displacement "u" (see figure 3.104). Then:

$$\varepsilon_r = \frac{\left(r_2 + u_2\right) - \left(r_1 + u_1\right) - \left(r_2 - r_1\right)}{\left(r_2 - r_1\right)} = \frac{u_2 - u_1}{r_2 - r_1} = \frac{du}{dr} \tag{19.a}$$

$$\varepsilon_\theta = \frac{2\pi \cdot \left(r + u\right) - 2\pi \cdot r}{2\pi \cdot r} = \frac{u}{r} \tag{19.b}$$

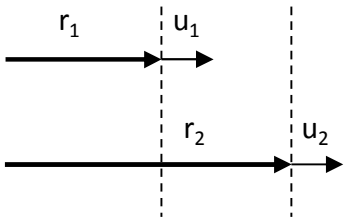

Fig. 3.104. Two arbitrary points along the radial direction.

Without describing the steps needed to obtain it, we report now the equilibrium equation written in polar coordinates:

$$\frac{\partial \sigma_r}{\partial r} + \frac{\sigma_r - \sigma_\theta}{r} + \frac{1}{r} \cdot \frac{\partial \tau_{r\theta}}{\partial \theta} = 0 \tag{20}$$

The shear stress $\tau_{r\theta}$ is zero on account of the symmetry of the deformation and consequently eq. (20) becomes:

$$\frac{d\sigma_r}{dr} + \frac{\sigma_r - \sigma_\theta}{r} = 0 \tag{21}$$

Substituting equations (19.a) and (19.b) in equations (18.a) and (18.b) it is possible to obtain the following expressions:

$$\sigma_r = \frac{E}{\left(1-\nu^2\right)} \cdot \left[\frac{du}{dr} + \nu \frac{u}{r} - \left(1+\nu\right) \cdot \alpha T \right] \tag{22.a}$$

$$\sigma_\theta = \frac{E}{\left(1-\nu^2\right)} \cdot \left[\frac{u}{r} + \nu \frac{du}{dr} - \left(1+\nu\right) \cdot \alpha T \right] \tag{22.b}$$

that substituted in eq.(21) lead to the following differential equation written respect to the function "radial displacement u":

$$\frac{d^2u}{dr^2} + \frac{1}{r} \cdot \frac{du}{dr} - \frac{1}{r^2} \cdot u = \left(1+\nu\right) \cdot \alpha \cdot \frac{dT}{dr} \tag{23}$$

Once performed the integration, the "function u" will allow to define the strain components by means of equations (19) and the stress components thanks to equations (22). The fundamental steps to obtain the exact solution are described in the following.

First of all equation (23) can be rewritten as:

$$\frac{d}{dr}\left[\frac{1}{r} \cdot \frac{d\left(r \cdot u\right)}{dr} \right] = \left(1+\nu\right) \cdot \alpha \cdot \frac{dT}{dr} \tag{24}$$

Integrating the first time respect to "r" it is possible to obtain:

$$\frac{d\left(r \cdot u\right)}{dr} = r \cdot \left(1+\nu\right) \cdot \alpha \cdot T + C_1 \cdot r \tag{25}$$

Integrating the second time the previous equation becomes:

$$u = \left(1+\nu\right) \cdot \alpha \cdot \frac{1}{r} \cdot \int_0^r T \cdot r \cdot dr + C_1 \cdot r + \frac{C_2}{r} \tag{26}$$

Then substituting equation (26) in the expressions (22.a) and (22.b) yields:

$$\sigma_r = -\alpha \cdot E \cdot \frac{1}{r^2} \cdot \int_0^r T \cdot r \cdot dr + \frac{E}{1-\nu^2} \cdot \left[C_1 \cdot \left(1+\nu\right) - C_2 \left(1-\nu\right) \cdot \frac{1}{r^2} \right] \tag{27.a}$$

$$\sigma_\theta = \alpha \cdot E \cdot \frac{1}{r^2} \cdot \int_0^r T \cdot r \cdot dr - \alpha \cdot E \cdot T + \frac{E}{1-\nu^2} \cdot \left[C_1 \cdot \left(1+\nu\right) + C_2 \left(1-\nu\right) \cdot \frac{1}{r^2} \right] \tag{27.b}$$

At this point the constants C_1 and C_2 can be obtained considering the following boundary conditions:

1. $u = 0$ per $r = 0$
2. $\sigma_r = 0$ per $r = R$ (R is the external radius of the disk)

Imposing the first one in the equation (26) and observing that:

$$\lim_{r \to 0} \frac{1}{r} \int_0^r T \cdot r \cdot dr = 0 \tag{28}$$

we obtain that C_2 must be equal to zero ($C_2 = 0$).

The second boundary condition allows to define an expression for C_1 that is:

$$C_1 = (1-\nu) \cdot \frac{\alpha}{R^2} \int_0^R T \cdot r \cdot dr \tag{29}$$

At this point the final expressions for the stress components are:

$$\sigma_r = \alpha \cdot E \cdot \left(\frac{1}{R^2} \int_0^R T \cdot r \cdot dr - \frac{1}{r^2} \int_0^r T \cdot r \cdot dr \right) \tag{30.a}$$

$$\sigma_\theta = \alpha \cdot E \cdot \left(-T + \frac{1}{R^2} \int_0^R T \cdot r \cdot dr + \frac{1}{r^2} \int_0^r T \cdot r \cdot dr \right) \tag{30.b}$$

The stress components σ_r and σ_θ presents finite values for $r = 0$ since:

$$\lim_{r \to 0} \frac{1}{r^2} \int_0^r T \cdot r \cdot dr = \frac{1}{2} \cdot T_0 \tag{31}$$

being T_0 the temperature level at the disk center.

Focusing on the uranium carbide disks, we take now as reference disk 7, that presents the most critical thermal gradient along the radial direction; in particular the radial temperature distribution in the middle plane is considered: as illustrated in figure 3.101 the middle plane is the plane that registers the higher temperature difference between the center and the periphery. Figure 3.105 shows the temperature distribution and the related polynomial interpolating curve; the description of the temperature field by means of a polynomial:

$$T(r) = -0.0104 \cdot r^3 - 0.1314 \cdot r^2 - 1.0014 \cdot r + 2291.8 \tag{32}$$

allows to write the term $\int_0^r T \cdot r \cdot dr$ as:

$$\int_0^r T \cdot r \cdot dr = \int_0^r \left[-0.0104 \cdot r^4 - 0.1314 \cdot r^3 - 1.0014 \cdot r^2 + 2291.8 \cdot r \right] \cdot dr \tag{33}$$

The integral can be solved without approximations leading to the following expression:

$$\int_0^r T \cdot r \cdot dr = -0.0104 \cdot \frac{r^5}{5} - 0.1314 \cdot \frac{r^4}{4} - 1.0014 \cdot \frac{r^3}{3} + 2291.8 \cdot \frac{r^2}{2} \tag{34}$$

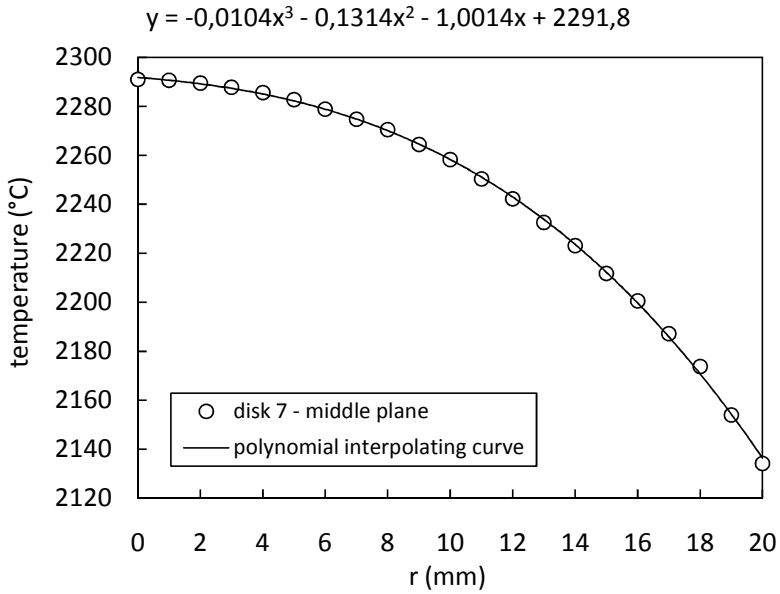

Fig. 3.105. Middle plane radial temperature distribution and the related polynomial interpolating curve.

At this point, with a simple worksheet it is possible to define the radial distribution of the stress components σ_r and σ_θ (see figure 3.106), taking into consideration the material properties needed to pass from the temperature field to the description of the stress state (see equations (30.a)and (30.b)) and the value of the external disk radius:

- E = 176 GPa
- $\alpha = 12.4 \cdot 10^{-6}$ °C^{-1}
- R = 20 mm

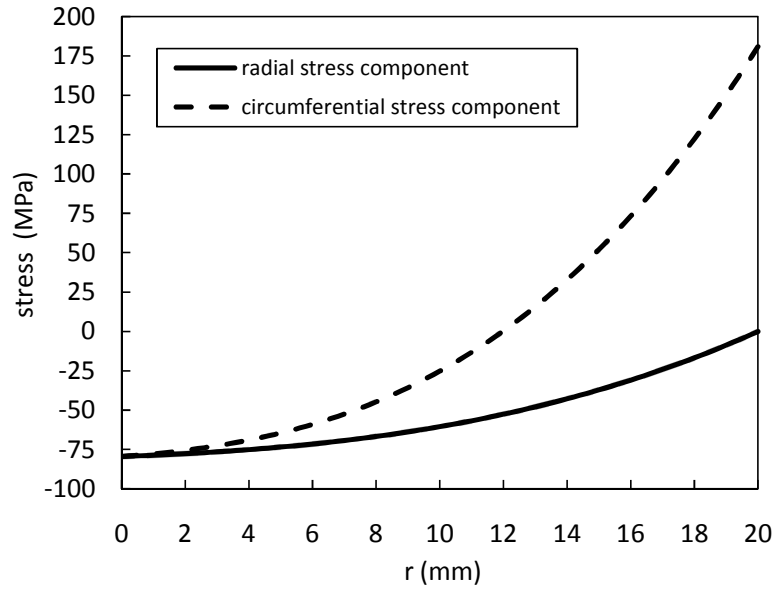

Fig. 3.106. The radial distributions of the stress components σ_r and σ_θ calculated by means of the analytic model in the hypothesis of plane stress.

The radial stress component σ_r is negative (compression) at the disk center (-80 MPa) and reduces gradually its intensity moving from the center to the periphery of the disk where it registers a value equal to zero. Similarly the circumferential stress component σ_θ is negative for "r = 0" (-80 MPa) but becomes gradually positive (tension) for increasing values of "r", reaching the maximum positive value (181 MPa) when "r" is equal to 20 mm. In words, the hotter (high thermal expansion) central part of the disk is compressed and constrained by the colder (low thermal expansion) external ring; on the other side the colder external ring is tensioned by the pushing hotter internal part.

Once performed a preliminary study of the stress state by means of the analytic model, a more accurate estimation of the stress state was produced thanks to a coupled thermal-structural FE model. A coupled-field analysis is a combination of analyses from different engineering disciplines (physics fields) that interact to solve a global engineering problem: in general when the input of one field analysis depends on the results from another analysis, the analyses are coupled. In our case the temperature field introduces thermal strains in the structural field, but the structural strains do not affect the temperature distribution: this is a typical example of one-way coupling but in general the physics fields interact in both directions (two-way coupling).

When the solution of the thermal problem was calculated, volumes and elements belonging to the UC_x disks were selected and the thermal mesh was converted into a structural one: the structural element type SOLID45 (see figure 3.107) was adopted (characterized by three degrees of freedom at each node that are the translations in the nodal x, y, and z directions) and temperatures were input as element body loads at the nodes. The hypotheses of linear elasticity and the material properties reported in paragraph 3.5.2 were adopted.

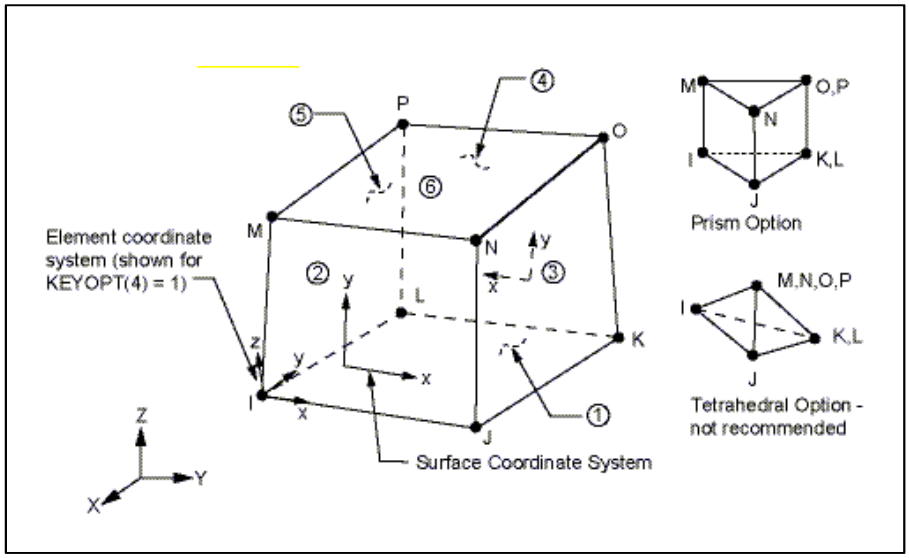

Fig. 3.107. The structural element SOLID45.

Once isostatically constrained the disks as exposed in figure 3.108, the structural solution was calculated: figures 3.109 and 3.110 report the Von Mises stress plot and the first principal stress plot, respectively, putting in evidence the critical conditions of disk 7.

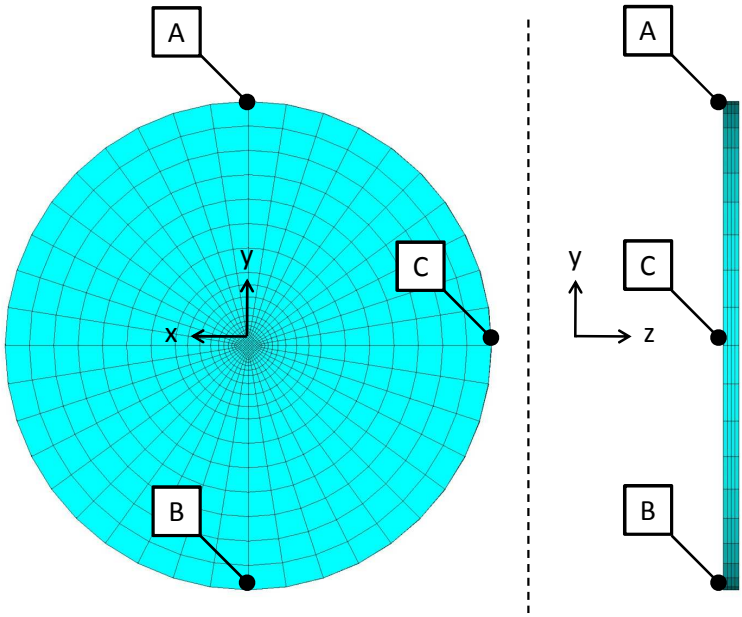

LOCAL CONSTRAINTS	BLOCKED DEGREES OF FREEDOM OF THE RIGID BODY (DISK)
UX_A, UY_A, $UZ_A = 0$	x, y and z displacements
$UZ_B = 0$	x rotation
$UX_B = 0$	z rotation
$UZ_C = 0$	y rotation

Fig. 3.108. The structural constraints assigned to the disks.

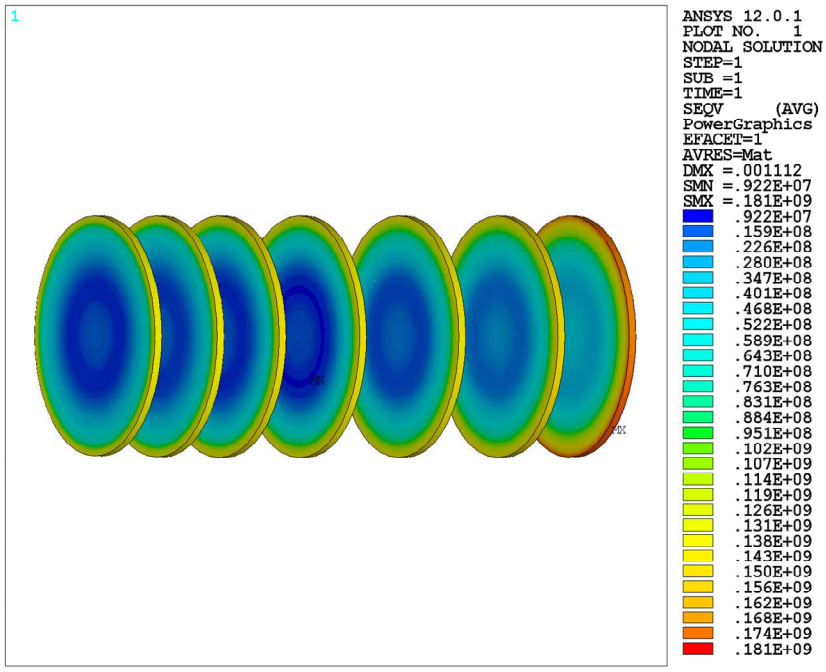

Fig. 3.109. Equivalent Von Mises stress plot [Pa].

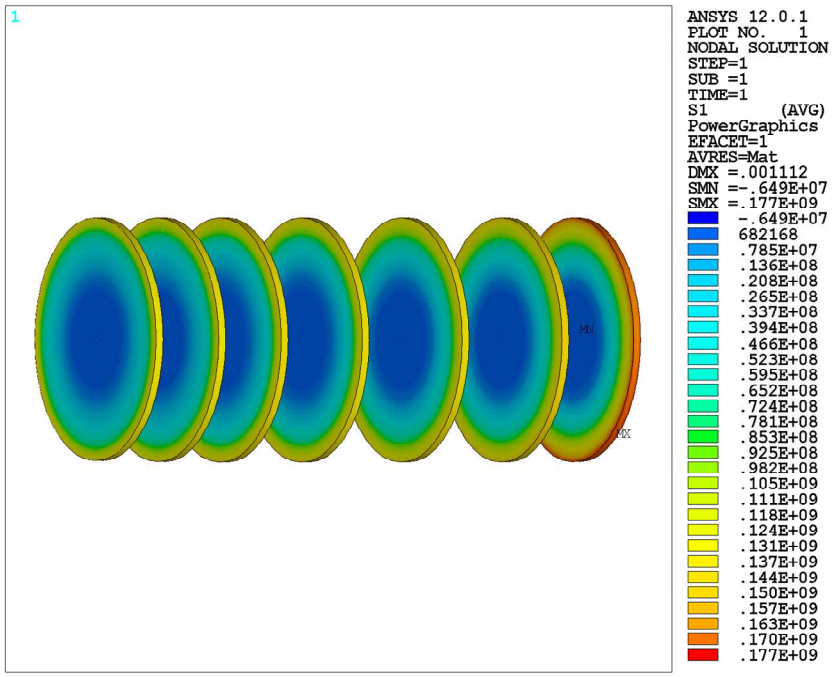

Fig. 3.110. First principal stress plot [Pa].

At this point we concentrate the attention on disk 7, the disk that, as expected, presents the higher stress values. At first it is very interesting to compare the radial stress distributions obtained using the FE model with the correspondent results coming from the aforementioned analytic model. With this aim figure 3.111 shows the comparison between the FE radial stress distribution monitored in the middle plane and the correspondent analytic data: even if results are similar, FE stress values are lower both at the center ($\sigma_{r\text{-}FEM}$ = -98.2 MPa) and at the periphery ($\sigma_{r\text{-}FEM}$ = -11 MPa).

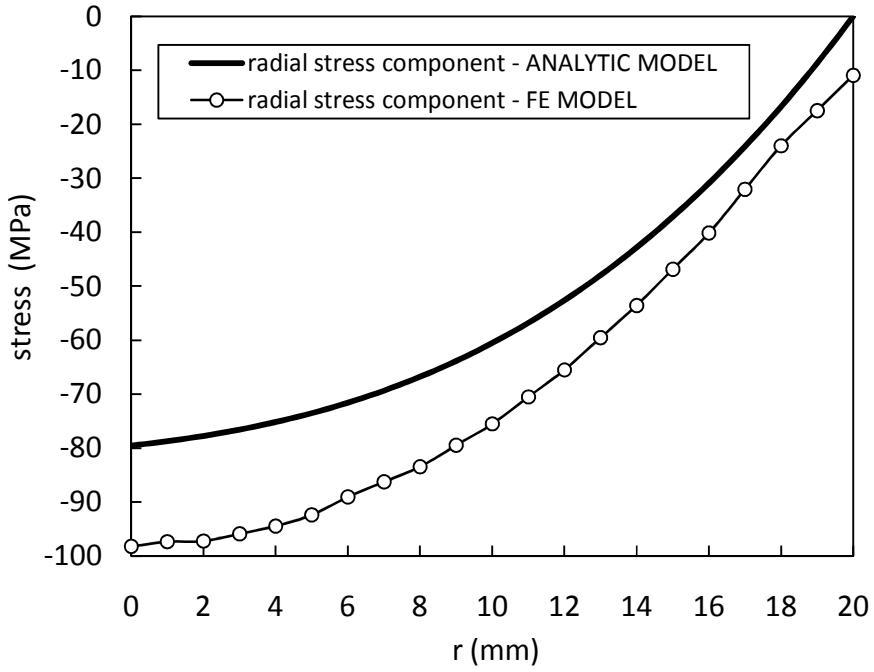

Fig. 3.111. The radial stress component: comparison between analytic and FE model (middle plane).

If on one side the lower value at the center of the disk (r = 0) can be justified by the temperature distribution across the thickness, that is characterized by higher temperatures (high thermal expansion) in the middle plane and lower temperatures (low thermal expansion) at the extremities (see figure 3.102) with a consequent ulterior compression state in the internal part of the disk, on the other side the lower value at the periphery of the disk (r = 20 mm) cannot be justified by similar considerations: here the radial stress component should be equal to zero (no pressure applied to the external surface) but it is not because of the not completely adequate mesh refinement at the periphery. Similar considerations can be done for the circumferential stress component (see figure 3.112): also in this case the agreement between the FE and the analytic model is good and the lower FE stress values can be justified by the compression state in the middle plane induced by the particular through the thickness temperature distribution, that is not considered by the analytic model.

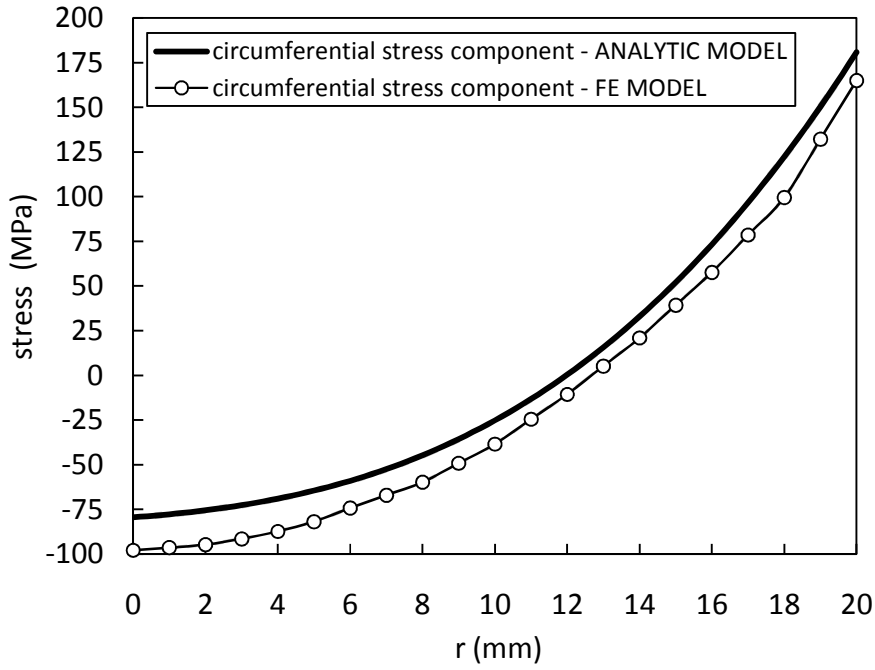

Fig. 3.112. The circumferential stress component: comparison between analytic and FE model (middle plane).

The effects of temperature gradients across the disk's thickness on the stress state of the disks can be appreciated in a more detailed way considering figures 3.113 and 3.114: they compare the stress components monitored in the beam entrance plane, in the middle plane and in the beam exit plane. In both figures the compression effect in the middle plane and the tension effect in the beam entrance and exit planes are evident. Similarly respect to what happens in the radial direction, the hotter (high thermal expansion) middle plane of the disk is compressed and constrained by the colder (low thermal expansion) external planes (beam entrance and exit planes); on the other side the colder external planes are tensioned by the pushing hotter internal part of the disk. The

discontinuities presented by the curves for 0 < r < 2 mm are due to the mesh discontinuity between the central core of the disk and the first ring surrounding it (see figure 3.92) whereas the discontinuities for 18 < r < 20 mm can be justified by the not sufficient mesh refinement at the periphery of the disk.

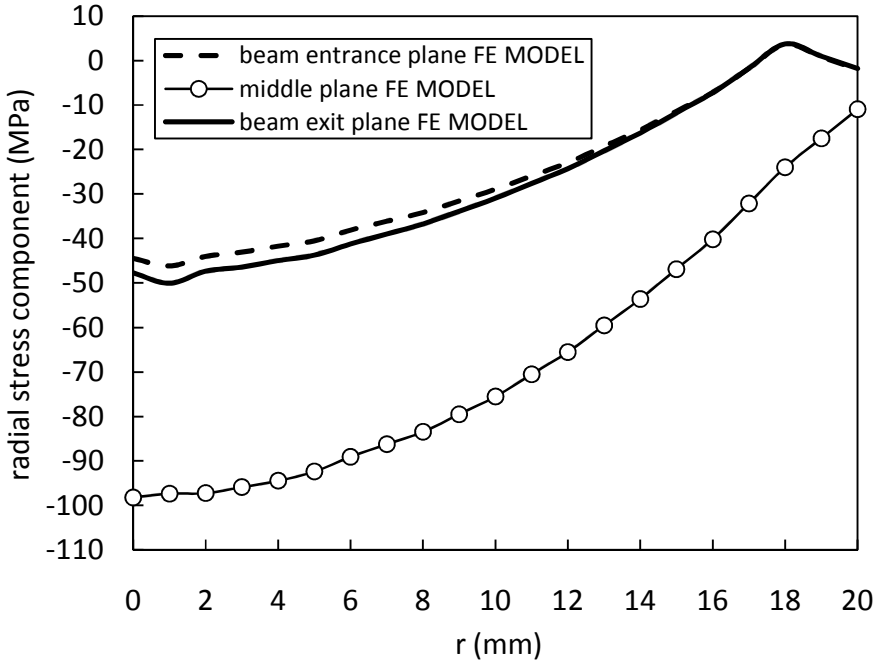

Fig. 3.113. The radial stress component: comparison among the beam entrance plane, the middle plane and the beam exit plane distributions (FE model).

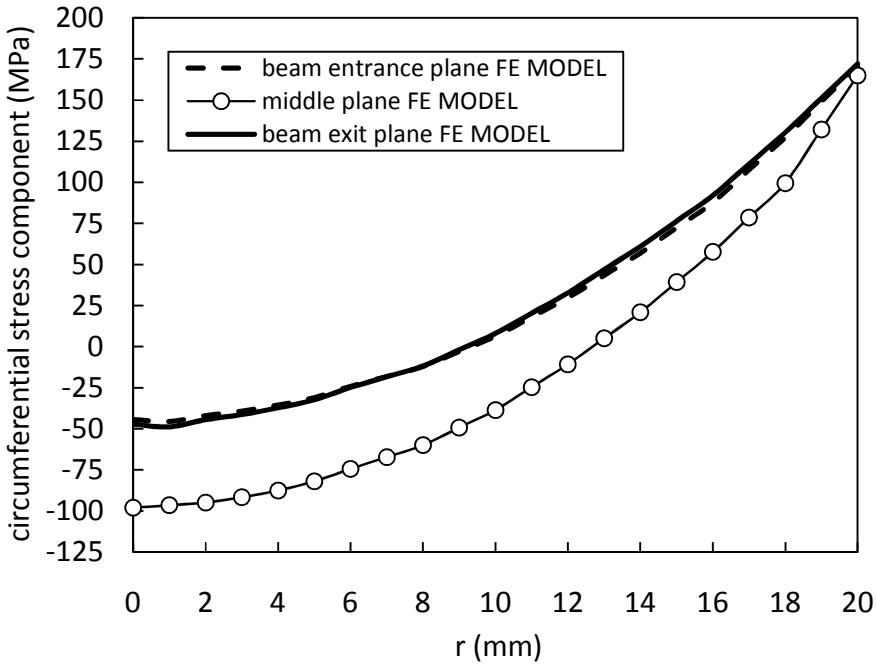

Fig. 3.114. The circumferential stress component: comparison among the beam entrance plane, the middle plane and the beam exit plane distributions (FE model).

Figure 3.115 shows the axial stress component distributions: this stress component is, as expected, close to zero along all the disk radius, for all the planes of interest; the discontinuities revealed at the center of the disk and at its periphery can be easily justified using the aforementioned arguments.

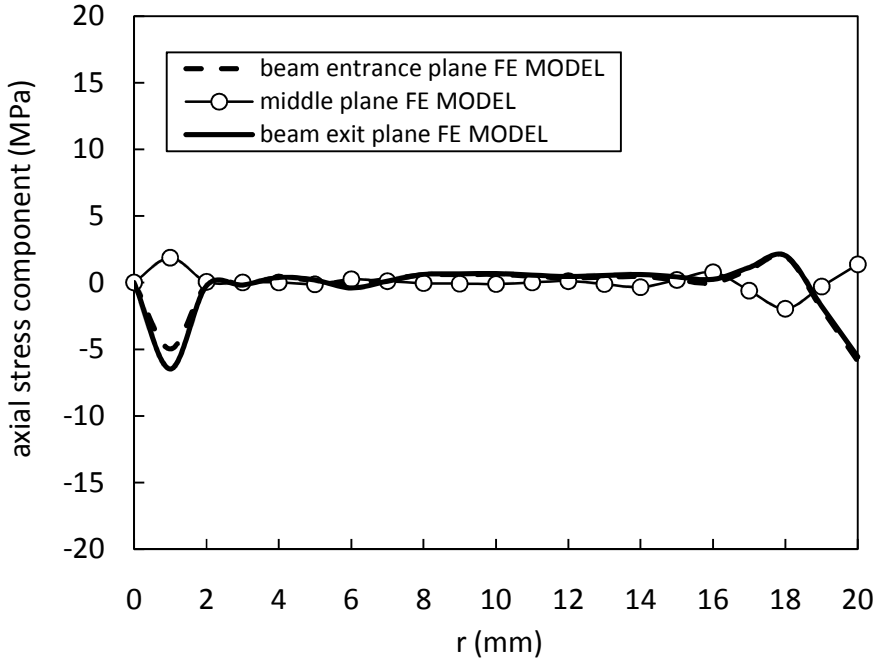

Fig. 3.115. The axial stress component: comparison among the beam entrance plane, the middle plane and the beam exit plane distributions (FE model).

The Von Mises stress and the first principal stress distributions are presented in figures 3.116 and 3.117, respectively. The Von Mises stress is used to verify the stress state in the case of ductile materials whereas the first principal stress is usually adopted to verify the stress state while using brittle materials: we decided to monitor both of them since the behavior of the material is not well known for the working temperatures of the SPES target (~2000°C).

In our case both the maximum Von Mises stress and the maximum first principal stress are lower respect to the fracture stress value of uranium carbide (σ = 200 MPa):

- $\sigma_{VM\text{-}MAX}$ = 176 MPa < $\underline{\sigma = 200\ MPa}$
- $\sigma_{I\text{-}MAX}$ = 172 MPa < $\underline{\sigma = 200\ MPa}$

even if it is important to remark that σ is referred to 1300°C, a temperature level abundantly below 2000°C: it is the only parameter we found [30] to have an idea on the uranium carbide resistance at high temperature.

If on one side the aforementioned fracture stress value will probably decrease for temperature values higher than 1300°C, the expected plasticity of uranium carbide at high temperature should give an important contribution in the attenuation of the stress state.

In any case the results presented and described in this paragraph must be considered and interpreted paying a particular attention: further data, analyses and measurements are needed in order to have more reliable results.

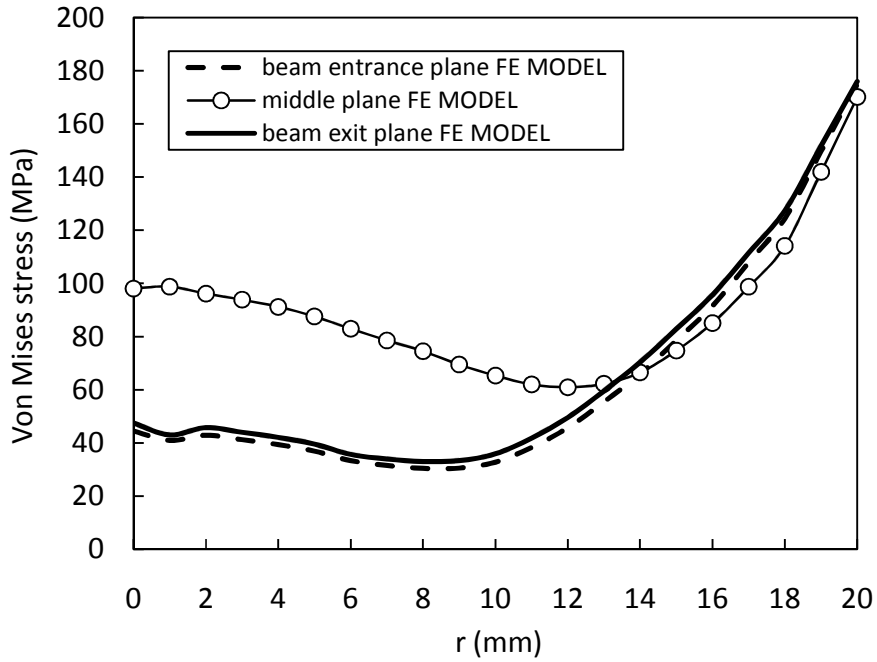

Fig. 3.116. The Von Mises stress: comparison among the beam entrance plane, the middle plane and the beam exit plane distributions (FE model).

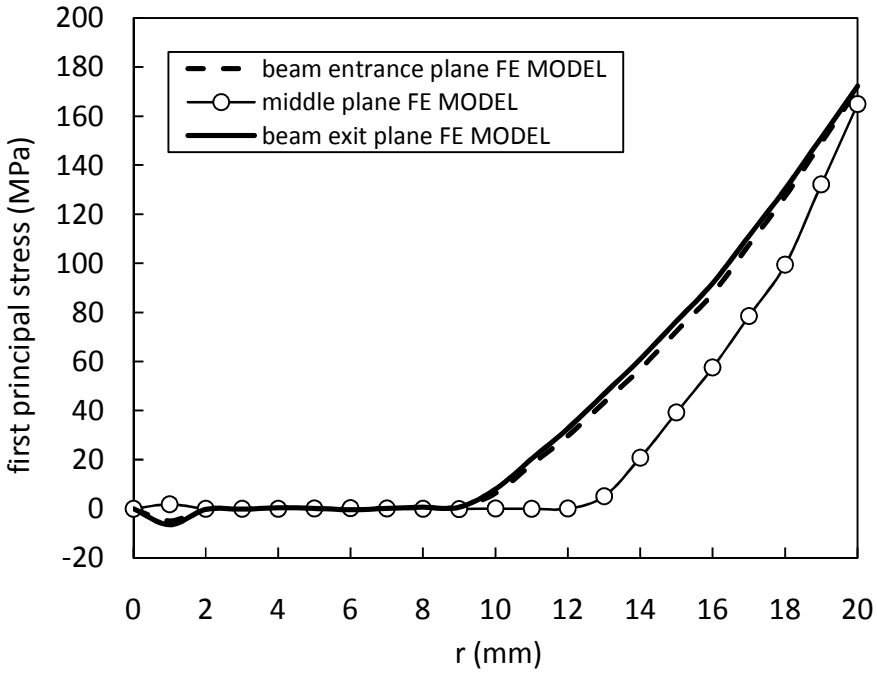

Fig. 3.117. The first principal stress: comparison among the beam entrance plane, the middle plane and the beam exit plane distributions (FE model).

With this aim a new high vacuum furnace and a new crucible (heated by Joule effect) able to reproduce strong thermal gradients in radial direction on disk samples similar to the disks used for the SPES target were recently designed and successfully tested at Legnaro National Laboratories (see figure 3.118): they will be used in the next future to verify off-line the capability of the target disks to sustain the thermal gradients that the proton beam will produce on them during the on-line functioning of the SPES facility.

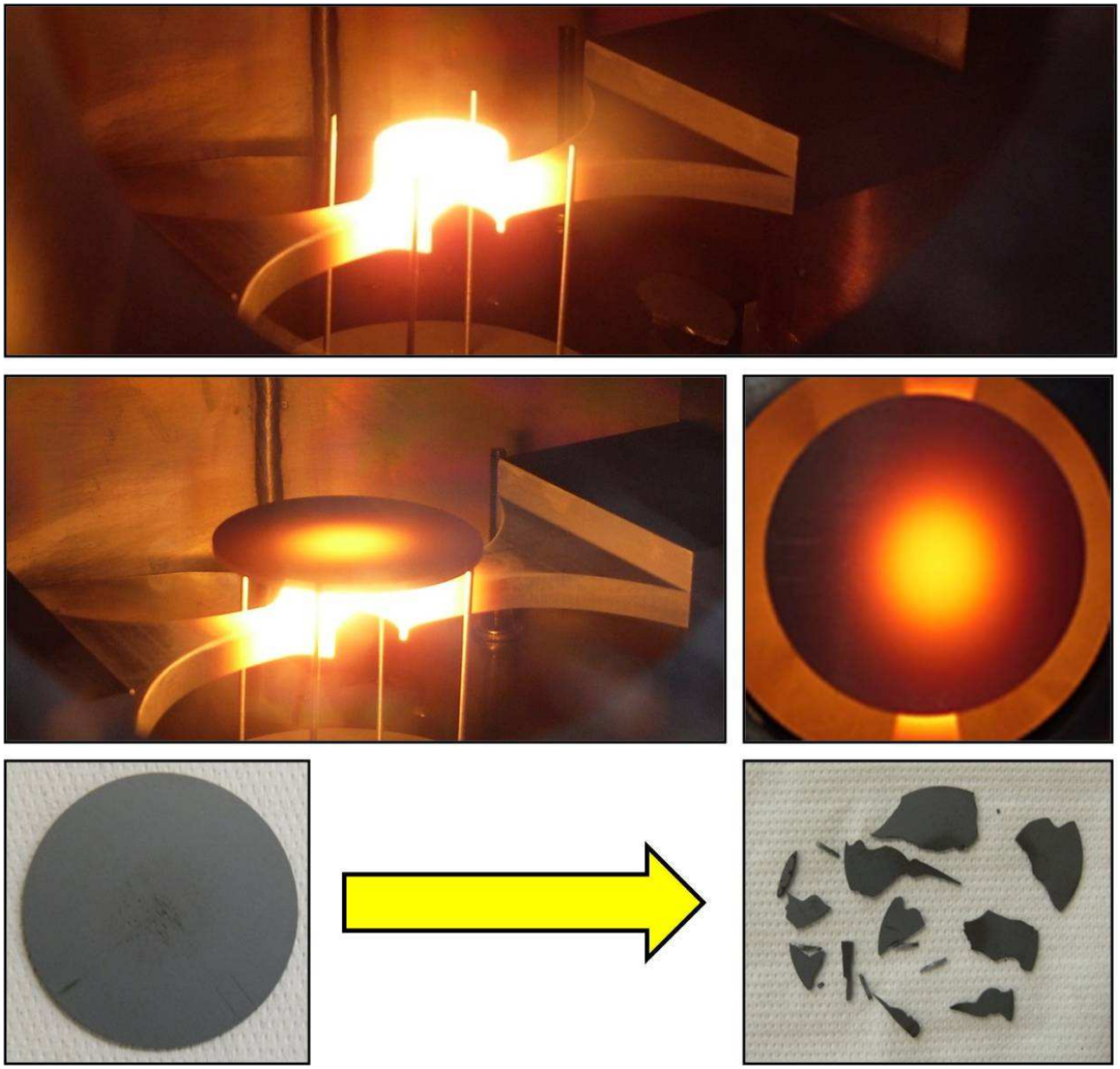

Fig. 3.118. The new high temperature crucible (heated by Joule effect) able to reproduce strong radial thermal gradients on disk samples.

As concluding observation, all the stress components, the Von Mises stress and the first principal stress are reported in the same graph for the beam entrance plane, for the middle plane and for the beam exit plane in figures 3.119, 3.120 and 3.121, respectively.

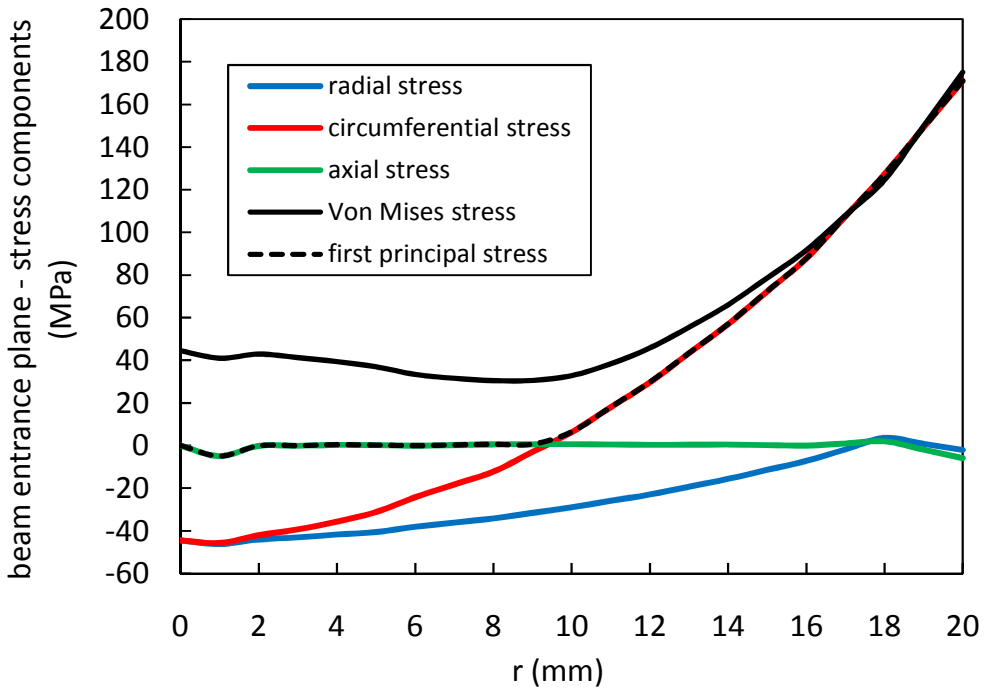

Fig. 3.119. Radial, circumferential, axial stress components, Von Mises stress and first principal stress in the beam entrance plane.

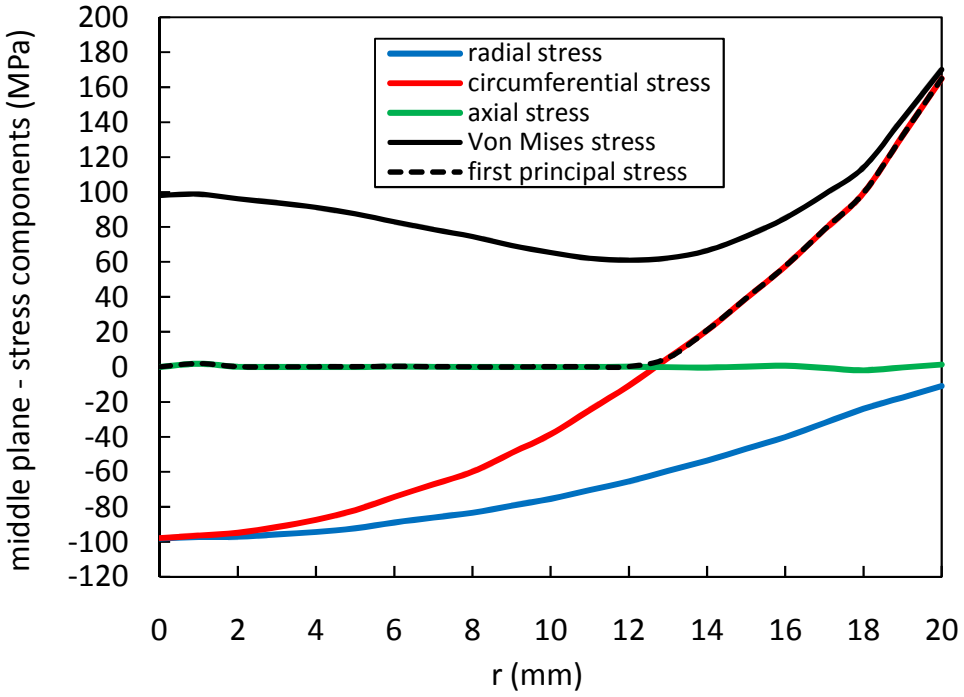

Fig. 3.120. Radial, circumferential, axial stress components, Von Mises stress and first principal stress in the middle plane.

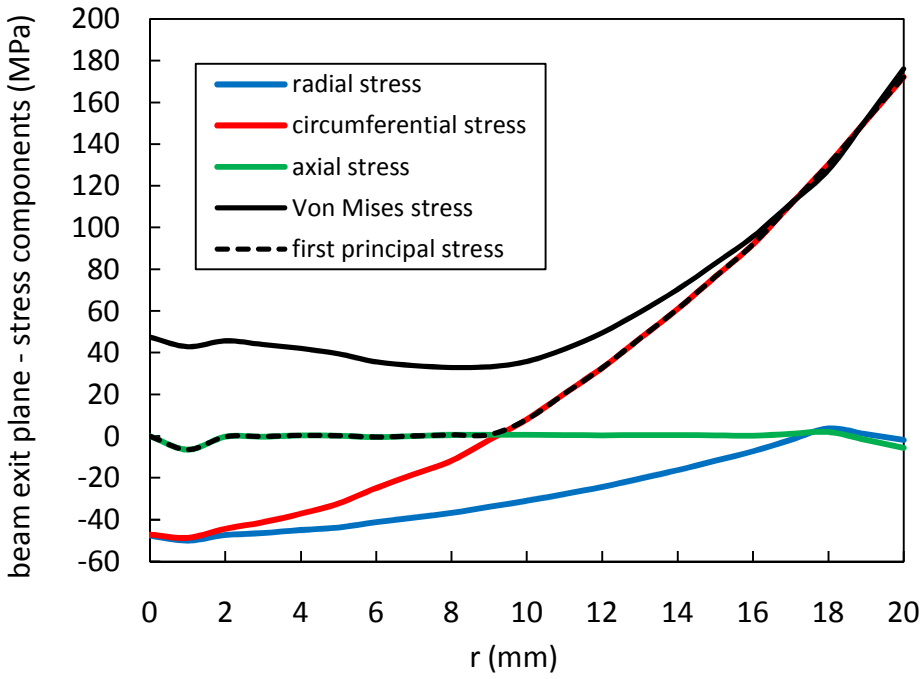

Fig. 3.121. Radial, circumferential, axial stress components, Von Mises stress and first principal stress in the beam exit plane.

3.6. Conclusions

In this chapter the study, the design and the experimental tests performed for the SPES target were presented and discussed in detail. At first the thermal-electric behaviour of the first SPES target prototype was studied by means of both experimental tests and theoretical calculations. Once verified the accuracy of the numerical models and their agreement with experimental data, they were used for the virtual design and the optimization of the new prototype. The new SPES target prototype was produced and tested at Legnaro National Laboratories, confirming the reliability of the correspondent numerical models. The effect of the proton beam on the target temperature field and stress state was studied in detail using a coupled thermal-structural FE model.

REFERENCES

[1] J. Al-Khalili, E. Roeckl, The Euroschool Lectures on Physics with Exotic Beams, vol.2, Springer, Berlin, 2006.

[2] Andrighetto A, Antonucci C M, Cevolani S, Petrovich C, Santana Leitner M. Multifoil UCx target for the SPES project – An update. Eur Phys J A 2006;30:591-601.

[3] Kohl WH. Handbook of materials and techniques for vacuum devices, Woodbury, NY: American Institute of Physics, 1995.

[4] Richard D, Fafard M, Lacroix R, Clery P, Maltais Y. Aluminum reduction cell anode stub hole design using weakly coupled thermo-electro-mechanical finite element models. Finite Elem Anal Des 2001;37:287-304.

[5] Ogasawara T, Hirano Y, Yoshimura A. Coupled thermal-electrical analysis for carbon fiber/epoxy composites exposed to simulated lightning current. Composites Part A 2010;41:973-981.

[6] Abdou G, Tereshkovich W. Performance evaluation of a permanent magnet brushless DC linear drive for high-speed machining using finite element analysis. Finite Elem Anal Des 2000;35:169-188.

[7] Klaassen B. A method for tightly coupled thermal-electrical simulation. Microelectron J 1997;28:239-245.

[8] Binion D, Chen X. Coupled electrothermal-mechanical analysis for MEMS via model order reduction. Finite Elem Anal Des 2010;46:1068-1076.

[9] Wang X, Casolco S R, Xu G, Garay J E. Finite element modeling of electric current-activated sintering: The effect of coupled electrical potential, temperature and stress. Acta Mater 2007;55:3611-3622.

[10] Manzolaro M, Meneghetti G, Andrighetto A. Thermal-electric numerical simulation of a surface ion source for the production of radioactive ion beams. Nucl Instrum Methods Phys Res, Sect A 2010;21:1061-1069.

[11] Meneghetti G, Manzolaro M, Andrighetto A. Thermal-electric numerical simulation of a target for the production of radioactive ion beams. Finite Elem Anal Des, doi:10.1016/j.finel.2011.01.005.

[12] Touloukian YS, DeWitt DP. Thermophysical Properties of Matter vol 7, NY, NY: IFI/Plenum, 1970.

[13] Desai PD, Chu TK, James HM, Ho CY. Electrical Resistivity of Selected Elements. J Phys Ref Data 1984;13:1069-1096.

[14]Chapman AJ. Heat transfer, New York, NY: Macmillan, 1984.

[15] Moliton A. Basic Electromagnetism and Materials, New York, NY: Springer, 2007.

[16] Hogan RE, Gartling DK. Solution strategies for coupled conduction/radiation problems. Commun Numer Meth Engng 2008;24:523-542.

[17] Incropera FP, Dewitt DP, Bergman TL, Lavine AS. Fundamentals of Heat and Mass Transfer 6th edition, NY, NY: Wiley, 2007.

[18] Siegel R, Howell JR. Thermal Radiation Heat Transfer 4th edition, NY, NY: Taylor and Francis, 2002.

[19] Huang TD. An integrated computer model for simulating electrothermomechanical interactions of an exhaust oxygen sensor. Finite Elem Anal Des 2001;37:657-672.

[20] Cohen MF, Greenberg DP. The Hemi-Cube: A Radiosity Solution for Complex Environments. Computer Graphics 1985;19:31-40.

[21] ANSYS Inc. ANSYS® Thermal Analysis Guide, Canonsburg, PA: ANSYS Inc, 2005.

[22] Matula RA. Electrical resistivity of copper, gold, palladium, and silver. J Phys Ref Data 1979;8:1147-1298.

[23] Touloukian YS, Powell RW, Ho CY, Klemens PG. Thermophysical Properties of Matter vol 1, NY, NY: IFI/Plenum, 1970.

[24] Biasetto L, Manzolaro M, Andrighetto A. Emissivity measurements of opaque gray bodies up to 2000°C by a dual-frequency pyrometer. Eur Phys J A 2008;38:167-171.

[25] Taylor RE, Davis FE, Powell RW. Direct heating methods for measuring thermal conductivity of solids at high temperatures. High Temperatures-High Pressures 1969;1:663-673.

[26] Saint-Gobain Ceramics, Structural Ceramics. Thermal Conductivity of Hexoloy® SA Silicon Carbide, Niagara Falls, NY: Saint-Gobain Ceramics, 2003.

[27] Ho CY, Ackerman MW, Wu KY, Oh SG, Havill TN. Thermal conductivity of ten selected binary alloy systems. J Phys Ref Data 1978;7:959-1178.

[28] Modest MF. Radiative Heat Transfer 2nd edition, San Diego, CA: Elsevier Science, 2003.

[29] Greene J P, Levand A, Nolen J, Burtseva T. Uranium carbide fission target R&D for RIA – an update. Nucl Phys A 2004;746:425c-428c.

[30] Hj. Matzke, Science of Advanced LMFBR Fuels, North Holland, 1980.

[31] Timoshenko, Goodier, Theory of Elasticity, McGraw Hill, 1970.

Chapter 4

The SPES Ion Sources: study, design and tests at LNL

4.1. Introduction

As mentioned in chapter 1, depending on the particular requirements, several different ionization mechanisms are used to transform the radioactive atoms coming from the production target into radioactive ions (in general singly charged positive or negative ions are produced, even if in a few cases multiply charged ions are produced as well). In the context of the ISOL facilities, the aforementioned process takes place in particular devices called ion sources, always positioned on a positive (in the case of beams of positively charged ions) or negative (negatively charged ions) high voltage (of typical values between 40 and 60 kV) in order to allow the acceleration/extraction of the radioactive ions.

In this chapter, after a brief overview of the main ionization mechanisms, the ion sources adopted for the SPES facility are presented and described, placing a particular emphasis on their thermal and electric design.

4.2. Ionization Mechanisms [1]

For a specific isotope the **ionization efficiency** (ε_{ion}) is defined as the ratio of the number of ions extracted from the ion source to the number of atoms injected into the ion source. Losses due to leaks in the transfer line between target and ion source and in the ion source itself are included in this number. In order to distinguish this kind of loss from losses due to the radioactive decay, the ionization efficiency is always defined for stable isotopes of a specific element; to take into account losses due to radioactive decay it will be sufficient to multiply ε_{ion} by ε_{delay}.

In the ion sources of ISOL systems, different ionization mechanisms are implemented and their use depends mainly on the ionization potential W_i of the element of interest, the required charge state and the selectivity.

In the next three sections 4.2.1, 4.2.2 and 4.2.3, the three main ionization mechanisms are opportunely described whereas in the rest of chapter the ion sources adopted for the SPES project and the related R&D activities performed at Legnaro National Laboratories are presented and discussed.

4.2.1. Surface Ionization

The most simple way to ionize in ISOL facilities is the surface ionization mechanism. Surface ionization is a physical phenomenon according to which when an atom interacts with a heated surface (the surface ion source) it can lose or gain an electron before leaving the surface as a positive or negative singly charged ion. This technique can be used efficiently for elements with ionization potential (W_i, energy required to remove the outermost electron from an atom or molecule) smaller than 7 eV for the creation of positive ions (positive surface ionization) and with electron affinity (E_A, energy given off when a neutral atom in the gas phase gains an extra electron to form a negatively charged ion) greater than 1.5 eV for the creation of negative ions (negative surface ionization). The ratio n_i/n_0, where n_i and n_0 are the ion density and the neutral density of a certain element, respectively, considering the element's W_i or E_A at a heated surface characterized by the temperature T and the work function φ (the minimum energy needed to remove an electron from a solid to a point immediately outside the solid surface) is given by the Langmuir equation:

$$\frac{n_i^+}{n_0} = \left(\frac{g_i^+}{g_0}\right) \cdot \exp\left[\frac{(\varphi - W_i)}{kT}\right] \tag{4.1}$$

$$\frac{n_i^-}{n_0} = \left(\frac{g_i^-}{g_0}\right) \cdot \exp\left[\frac{(E_A - \varphi)}{kT}\right] \tag{4.2}$$

with g_i and g_0 being the statistical weights of the ionic and atomic ground state and k the Boltzmann's constant. The positive and negative signs indicate positive and negative ions, respectively. At this point the ionization efficiency can be expressed in the following way:

$$\varepsilon_{ion} = \frac{n_i}{n_i + n_0} = \frac{1}{1 + \frac{n_0}{n_i}} \tag{4.3}$$

showing an important dependence on the temperature of the heated surface T and on the difference between the work function of the surface material and the ionization potential of the element (φ - W_i) or between the electron affinity of the element and the work function of the surface material (E_A - φ). Figure 4.1 presents the theoretical surface ionization efficiency versus the difference (φ - W_i) or (E_A - φ): ε_{ion} is high and almost temperature-independent for $W_i < \varphi$ or $E_A > \varphi$ and strongly dependent on temperature and (φ - W_i) or (E_A - φ) for $W_i > \varphi$ or $E_A < \varphi$. To manufacture positive surface ion sources (as we will see later, this is the case of the surface ion source adopted for the SPES project) materials with high work function φ and resistance to high temperatures at high vacuum levels should be used: these are mainly tantalum (φ = 4.19 eV), tungsten (4.53 eV) and rhenium (5.1 eV). On the other hand compounds with low work function like LaB_6 (φ = 2.6 eV) or *BaO* (1.7 eV) are used for negative surface ionization.

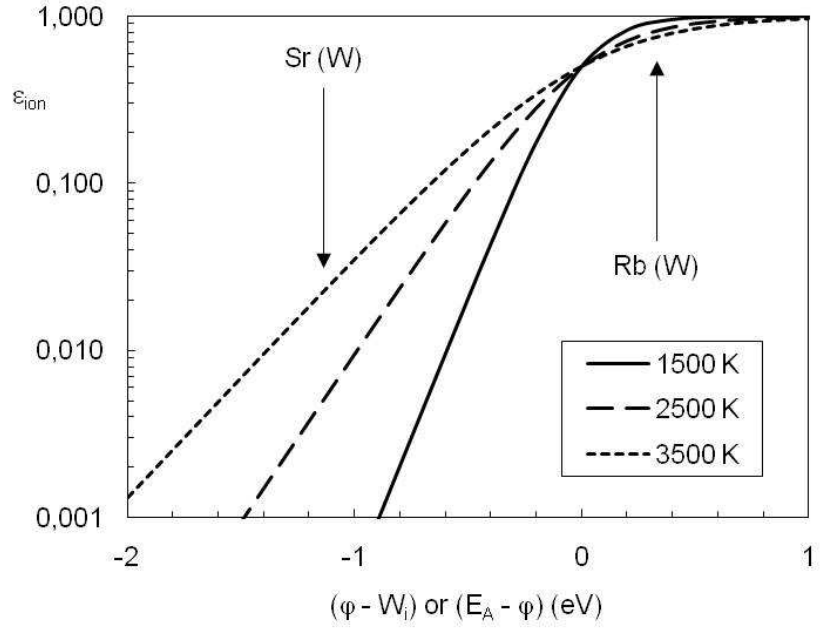

Fig. 4.1. Surface ionization efficiency as a function of (φ - W_i) or (E_A - φ); the values of (φ - W_i) for strontium and rubidium with a tungsten ionizer is indicated. The curves are calculated considering the ratio g_i/g_0 equal to 1. When the ionization potential or the electron affinity equals the work function, the surface ionization efficiency is 50%.

Making use of this ionization mechanism a very high level of selectivity can be reached if the elements of which isotopes are produced in the same nuclear reaction have very different ionization potentials. For instance the neighbouring elements krypton, rubidium and strontium are often produced in the same nuclear reaction: their ionization potentials are very different and equal to 14.0, 4.18 and 5.70 eV, respectively. Using tungsten as surface ionizing material at a temperature of 3000 K leads to ε_{ion} = 0.77 for rubidium whereas ε_{ion} is approximately 80 times smaller for strontium and almost sixteen orders of magnitude smaller for krypton (the ratio g_i/g_0 was assumed equal to 1 for this calculation); in this case a very pure beam of rubidium ions would result. In general all alkali elements (group IA of Mendeljev's table: lithium, sodium, potassium, rubidium, caesium, francium) are very efficiently ionized using positive surface ionization while the halogen elements (group VIIA of Mendeljev's table: fluorine, chlorine, bromine, iodine, astatine) are good candidates for negative ionization.

When surface ionization takes place in a hot-cavity a quasi-neutral plasma in thermal equilibrium can be created under certain conditions of positive surface ionization and electron emission from the walls. Consequently for the reaction of the type [atom $\leftrightarrow$ ion + e^-] the equilibrium constant can be calculated thanks to the Eggert-Saha equation that was originally developed to interpret the spectra from stellar atmospheres:

$$\frac{n_i^+ \cdot n_e}{n_0} = \left(2 \cdot \frac{g_i^+}{g_0} \right) \cdot (2\pi \cdot m_e \cdot kT \cdot h^2)^{3/2} \cdot \exp\left[\frac{-W_i}{kT} \right] \quad (4.4)$$

where n_e is the electron density, m_e the electron mass and h the Planck's constant. The ionization efficiency ε_{ion} can be calculated taking as reference the aforementioned equilibrium constant, evidencing a strong dependence on the ionization potential, the temperature and the pressure of the plasma (= kT ($n_i^+ + n_e + n_0$)). In case of low pressures much higher efficiencies are obtained compared to pure surface ionization. Considering the previous example of rubidium and strontium production and assuming a realistic number for the plasma pressure of $9 \cdot 10^{-5}$ mbar in a tungsten cavity, the efficiency for rubidium is close to 100% while for strontium a value of about 70% is reached. More details about surface ionization can be found in [2].

4.2.2. Electron Impact Ionization

In the case of isotopes of elements characterized by $W_i > 7$ eV and for the creation of multiply charged ions, electron impact ionization is mostly used. The atoms or ions are bombarded by energetic electrons, loosing as a result one or more of their outer electrons. Figure 4.2 presents the cross section for electron impact ionization of argon atoms as a function of electron energy.

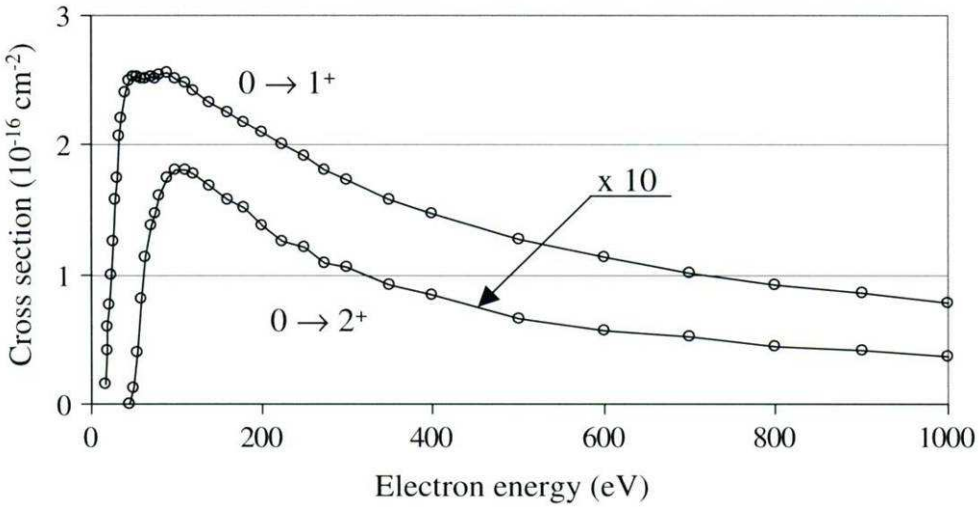

Fig. 4.2. Cross section for electron impact ionization of argon atoms as a function of the electron energy. Data are presented for neutral to singly charged ions ($0 \rightarrow 1^+$) and for neutral to doubly charged ions ($0 \rightarrow 2^+$). It is important to note the different threshold values for the $0 \rightarrow 1^+$ and $0 \rightarrow 2^+$ ionizations. The ionization potential for 1^+ argon ions is 15.75 eV while it is equal to 27.62 eV for 2^+ ions [1].

The differential equation reported below describes the bombardment of atoms by mono-energetic electrons and the related evolution of the atom and ion density as a function of time:

$$\frac{dn_i}{dt} = \left(n_{i-1} \cdot \sigma_{i-1 \rightarrow i} - n_i \cdot \sigma_{i \rightarrow i+1} \right) j_e \quad (4.5)$$

where n_i is the ion density with charge state Q = i, j_e is the electron current density and $\sigma_{i-1\rightarrow i}$ the cross section for impact ionization from charge state (i-1) to i; equation (4.5) is valid for i from 1 to (i_{max}-1). For the neutral atom density (n_0) the first term of the right part of equation (4.5) vanishes, while for the fully stripped ion (ni_{max}) the last term vanishes. It is important to underline that equation (4.5) does not take into account charge exchange, multiple charge ionization or recombination effects.

In figure 4.3 it is possible to appreciate the results of the atom (Q = 0) and ion density as a function of the product of $n_e vt$, with t representing the time the neutral atoms have been bombarded with mono-energetic electrons of density n_e and velocity v. From figure 4.3 it is possible to determine the conditions ($n_e vt$) that are needed to achieve a certain efficiency for a specific charge state. For instance to obtain an argon ionization efficiency $\varepsilon_{ion}(5^+)$ = 30% the neutral atoms have to be bombarded for 6.7 ms with a mono-energetic electron beam of 17 keV and 120 A/cm^2.

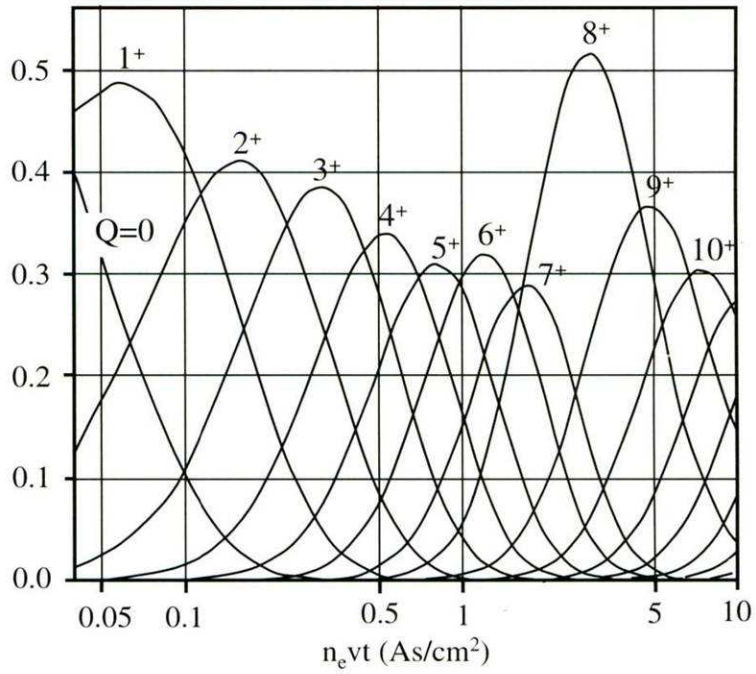

Fig. 4.3. Calculated relative atom (Q = 0) and ion density of argon under bombardment of a mono-energetic 17 keV, 120 A/cm^2 electron beam as a function of $n_e vt$ in As/cm^2. The electron density and velocity is denoted by n_e and v, respectively. At t = 0 the relative atom density was 1 while the ion density was 0. Calculations assume only one-step electron impact ionization. Multi-step electron impact ionization is not taken into account. The cross sections were calculated using [3]. The neon-like properties of Ar^{+8} reduce the cross section for electron impact ionization from the 8^+ to 9^+ compared to 7^+ to 8^+ ionization and create a peak for the 8^+ charge state. This peak is reached after about 17 ms of electron bombardment [1].

Because of the very unselective nature of this ionization process, ion sources based on this principle doesn't offer in general much chemical selectivity.

4.2.3. Laser Ionization

The resonant laser ionization method has recently been implemented successfully at ISOL systems. According to this ionization technique, atoms are stepwise excited by laser photons at precise energy levels, leading finally to the continuum, to auto-ionizing states or to highly excited states close to continuum called Rydberg states. In the latter case ionization can be obtained through infra-red irradiation, an electrical field or atomic collisions. The ionization process typically consists of two or three steps, everyone characterized by a precise energy level (or wavelength λ_i) for the laser photons; because of the resonant nature of most of these steps, resonant laser ionization is very efficient and chemically selective, resulting in an extremely pure ion beam.

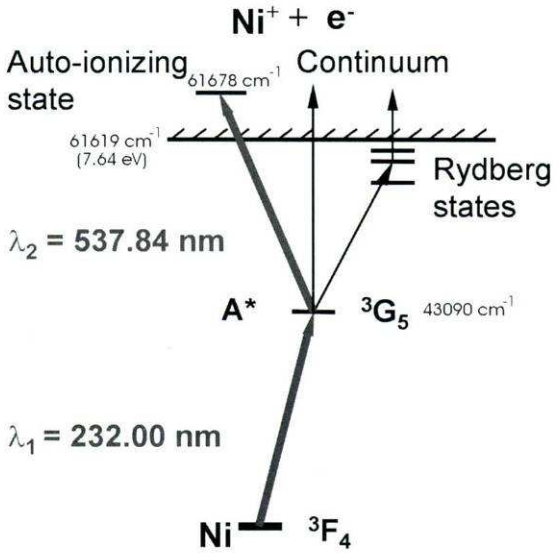

Fig. 4.4. Schematic atomic level scheme showing the principles of resonant photoionization of nickel. Atoms are stepwise excited to the continuum, auto-ionizing states or highly excited, so called Rydberg states from which ionization is achieved by infrared irradiation, electrical fields or gas collisions [1].

The aforementioned ionization technique can be performed using commercially available pulsed lasers like Nd-Yag lasers (typical repetition rate 10 Hz), Excimer lasers (100 Hz), copper vapour lasers (10 kHz) and solid-state lasers (10 kHz). More details on the principles and applications of resonant laser ionization can be found in [4, 5].

4.3. Ion Sources

In the following a brief description of the most commonly used ion source systems at ISOL facilities is presented; the concept of emittance is also explained. A more general and complete overview of ion sources can be found in [6].

4.3.1. Hot-Cavity Ion Sources

This particular type of ion source takes advantage of the aforementioned positive surface ionization mechanism and produce the ionization inside a high temperature closed (except for the extraction hole) tubular volume called hot-cavity, with the effect that atoms have more possibilities (bigger number of wall collisions) of being surface-ionized. High ionization efficiencies are restricted to elements with $W_i < 5.5$ eV, e.g. alkali and alkaline earth elements, using high work function materials for the hot-cavity, such as W, Re or Ta.

4.3.2. High Temperature Plasma Ion Sources

In high temperature plasma ion sources the electron impact ionization mechanism is used to ionize the atoms that are present in the gas phase inside the source; the electron flux is created by a discharge in a low-pressure environment. In this way a plasma is produced in which the ions are confined, preventing them from wall collisions and neutralization. Different types of so-called arc discharge ion sources have been developed [7]; one of the most successfully and widely used sources is the forced-electron beam induced arc-discharge (FEBIAD) ion source: in this model the electrons are extracted from a high temperature cathode and accelerated into a low pressure plasma. Very high efficiency values (in some cases up to 50%) can be reached with this kind of ion source (see figure 4.5).

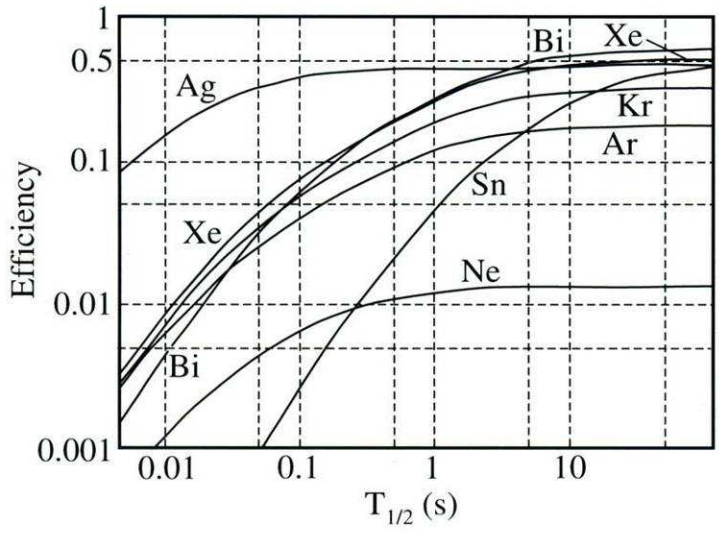

Fig. 4.5. Half-life dependence of the overall efficiency of a series of elements using a FEBIAD type discharge ion source. For large values of the half-life the loss due to the delay is negligible leading to a constant overall efficiency ε_{ion} ε_{trans} that can reach 50% in some cases; every curve corresponds to a series of isotopes of the same element. It is possible to notice the very fast diffusion/effusion of silver (Ag) isotopes: even for isotopes with half lives as short as 100 ms, ε_{delay} is close to 100%; this is in contrast to isotopes of tin (Sn) that exhibit a very long sticking time resulting in an ε_{delay} of only 0.5% for isotopes with a 100 ms half-life. Note the very low efficiency of neon (Ne) which is an inherent property of the ion source used for these measurements [1].

The lightest atoms, for example helium (He) and Neon (Ne) are characterized by lower efficiency as their residence time inside the plasma is short and thus the product $n_e vt$ is too low for efficient ionization (see figure 4.3).

In general, arc discharge ion sources are not selective: the energy spectrum of the electrons is broad and allows ionization of virtually every element. This property is nicely demonstrated in figure 4.5 which clearly shows that the ionization efficiency for the heavy elements like bismuth (Bi), lead (Pb), xenon (Xe), tin (Sn) and silver (Ag) is close to 50% while it is lower for krypton (Kr), argon (Ar) and certainly for neon (Ne) (ionization efficiency just over 1%). At ISOLDE (CERN) the FEBIAD type ion source is coupled with the production target thanks to a transfer tube (called also transfer line); usually the transfer tube is kept at high temperatures but in some particular cases its temperature is decreased in order to improve the system's selectivity: in this way isotopes of less volatile elements adsorb on the transfer tube's walls while isotopes from gaseous elements or gaseous molecules reach the ion source. By means of the aforementioned techniques a very high degree of selectivity can be obtained and pure beams of noble gas isotopes are produced. Another elegant way to improve the system's selectivity was studied at GSI, where a FEBIAD ion source with bunched release was developed. The method is based on the fact that different elements have different enthalphies of adsorption (ΔH_a); the higher the enthalphy of adsorption, the lower is the release efficiency of the respective element from the surface. The principle of this method is as follows. During a certain time all isotopes produced in the reaction are condensed on a cold spot; subsequently the spot undergoes a fast thermal cycle and is heated; as a consequence the isotopes from elements with the lowest enthalphy of adsorption will be released first, followed by the isotopes from the element with the second lowest value and so on. The power of this technique is illustrated in figure 3 of [8] where the time profiles of thallium (ΔH_a = 3.1eV), silver (ΔH_a = 3.4eV) and bismuth (ΔH_a = 3.6eV) beams are shown. During an on line experiment, such cooling-heating cycle are repeated many times, with the time periods for measuring the nuclear properties of interest being optimized with respect to the corresponding release profile.

Another technique used in combination with various ion sources is the so-called "decay release method": it was developed at ISOLDE making use of the pulsed structure of the proton primary beam when investigating neutron-rich nuclei around ^{208}Pb. These nuclei are produced in spallation reactions of uranium which, however, yield contaminants such as francium and radium isotopes, with orders of magnitude higher rates. Fortunately, these isotopes have half-lives in the μs region. Thus, introducing a delay of a few milliseconds after the proton beam impact allowed a suppression of these unwanted isotopes by many orders of magnitude and enabled spectroscopic studies in this region of the nuclear chart [9].

At the end it is important to mention the possibility to obtain very pure beams with the creation of molecular sidebands: this delicate technique has been applied for a very long time. More details on the molecular-ion techniques can be found in [7].

4.3.3. Laser Ion Sources

The laser ionization technique has been implemented in two ways at ISOL systems, namely in a hot-cavity and in a gas cell. A third method based on first condensing the atoms on a cooled surface, subsequently ablating them by a high-intensity laser pulse and finally laser ionizing them has been used for laser spectroscopy purposes but has not yet been installed in an on line target-ion source system. In the following only the hot-cavity laser ionization technique will be described; for more details it is possible to consult [1].

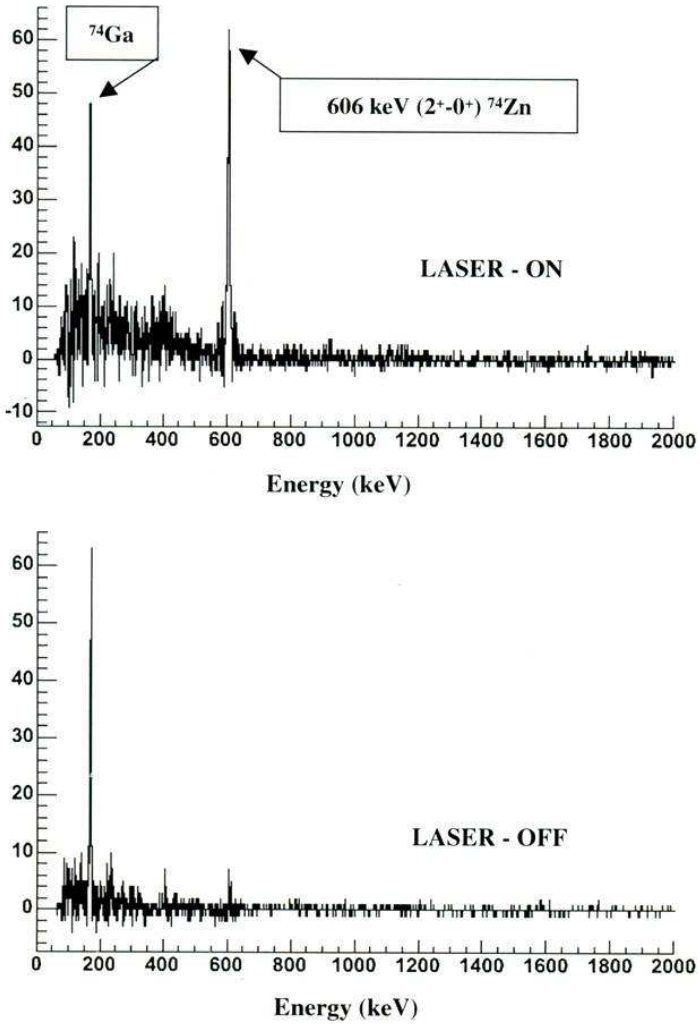

Fig. 4.6. Gamma-ray spectra obtained by a germanium detector from a Coulomb excitation measurement using a post accelerated (2.8 MeV/u) ^{74}Zn beam from ISOLDE. The 2^+-0^+ transition at 606 keV is clearly present in the laser-on spectrum whereas it is completely absent in the laser-off one; the line at 171 keV from Coulomb excitation or a transfer reaction of the contaminant ^{74}Ga is present in both spectra [1].

In the hot-cavity approach the system is in essence identical to a hot-cavity ion source; after diffusion in the target material and effusion towards the cavity, the atoms are kept in the gaseous phase in the cavity and irradiated several times with the laser pulses. Since the residence time inside the hot-cavity is very short (a few hundred μs), lasers with high repetition rate (> 10kHz) are required. Usually copper-vapour lasers are used, but new developments involve solid state lasers as well. Although the selectivity of the photo ionization technique is very high, because of the high temperature of the hot-cavity isotopes of elements characterized by low ionization potential are ionized as well (positive surface ionization mechanism), leading to isobaric contamination. Using this ionization technique efficiency values close to 10% are typically obtained. New cavity materials with lower work function to reduce surface ionization phenomena (and consequently isobaric contamination) are under investigation. More details can be found in [10].

As a concluding remark we observe that the secondary beam purity is a fundamental parameter for ISOL systems and laser ion sources play a crucial role in reducing these contaminations. Figure 4.6 shows the γ-ray spectra with and without lasers from a Coulomb excitation measurement of ^{74}Zn.

4.3.4. Fundamentals of Ion Beam formation [11]

From the point of view of the ion beam formation, an ion source can be considered composed of two parts: a plasma generator that serves as an ion reservoir and an extraction system for accepting ions from the reservoir and forming an ion beam. Both parts of the source may be treated independently as long as the plasma generator provides ions at the required current density and covers the whole area of the extraction system. The extraction system determines the beam properties such as ion current and beam quality in general. The simplest extraction system type is a two electrode (diode) system which is shown schematically in Figure 4.7.

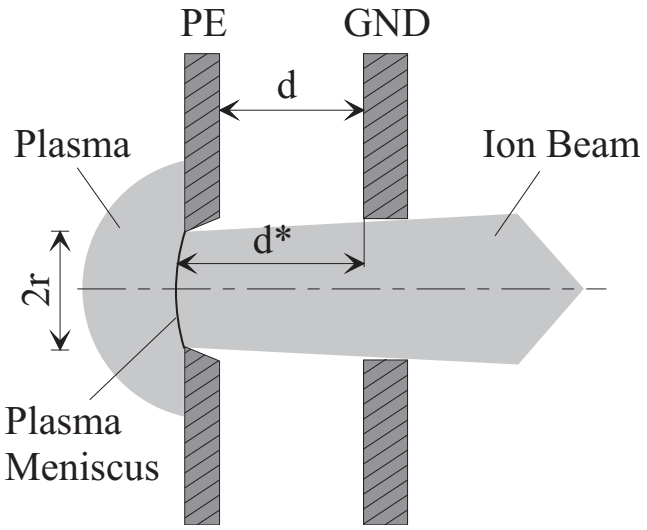

Fig. 4.7. Diode extraction system and beam formation. PE – Plasma electrode; GND – Ground electrode; d – Gap distance; d* – Real gap distance; r – Aperture radius [11].

The extractor consists of a plasma electrode at positive potential and a ground electrode at ground potential. The electric field strength *E* is defined by the voltage *U* and the distance *d* between the plasma electrode and the ground electrode. The emission surface of the ions at the plasma boundary is called the plasma meniscus (see figure 4.7). Electrons coming from the plasma are reflected at this boundary if their energy is less than the potential drop between the two electrodes. Electrons that are generated within the beam channel are accelerated towards the plasma and may change the charge state distribution in the emission region. As a consequence a third electrode, the so-called screening or suppressor electrode, is placed between the plasma electrode and ground electrode, and held at a negative potential; we then have a three-electrode or triode extractor system. This electrode gives rise to a potential hump for these electrons. Electrons generated in the ion beam have energies of few eV up to a few tens of eV, so a potential hump of -100V on the axis is high enough in most cases to screen the electrons. Figure 4.8 shows an AXCEL-INP simulation of the potential lines formed in a triode system with and without ion beam. The applied voltage is 55 kV for the plasma electrode and -6 kV for the screening electrode, the aperture radius of the screening electrode is 5 mm, and the length of the electrode is 4 mm. The minimum voltage on axis is -1708 V without ion beam and -487 V with the ion beam (see figure 4.9).

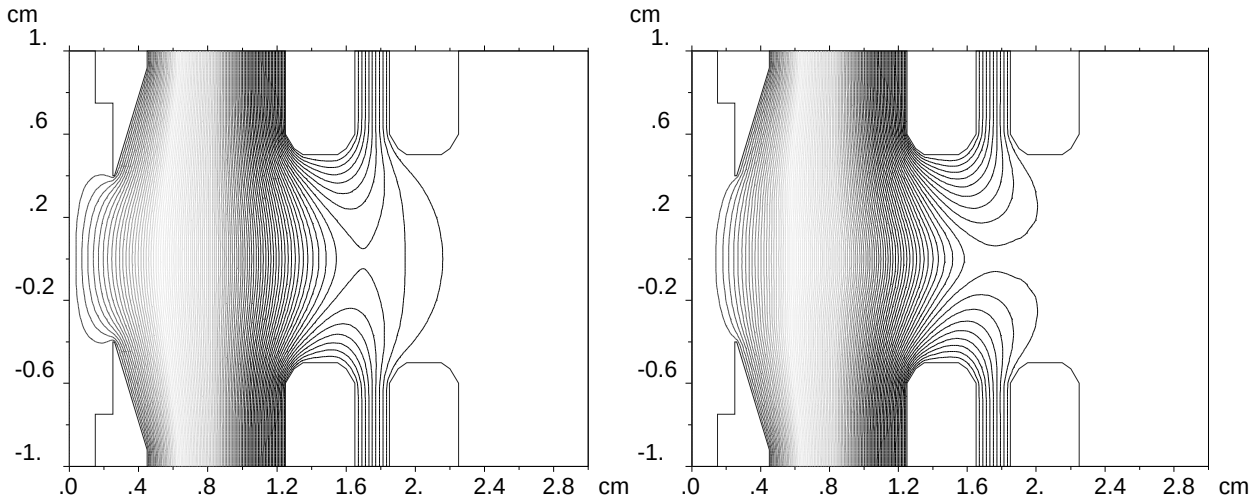

Fig. 4.8. Triode system with potential lines from -6 kV to 55 kV. Electrodes from left to right: Plasma electrode (PE), screening electrode (SE), ground electrode (GND). Left: Potential lines without ion beam. Right: Potential lines with ion beam [11].

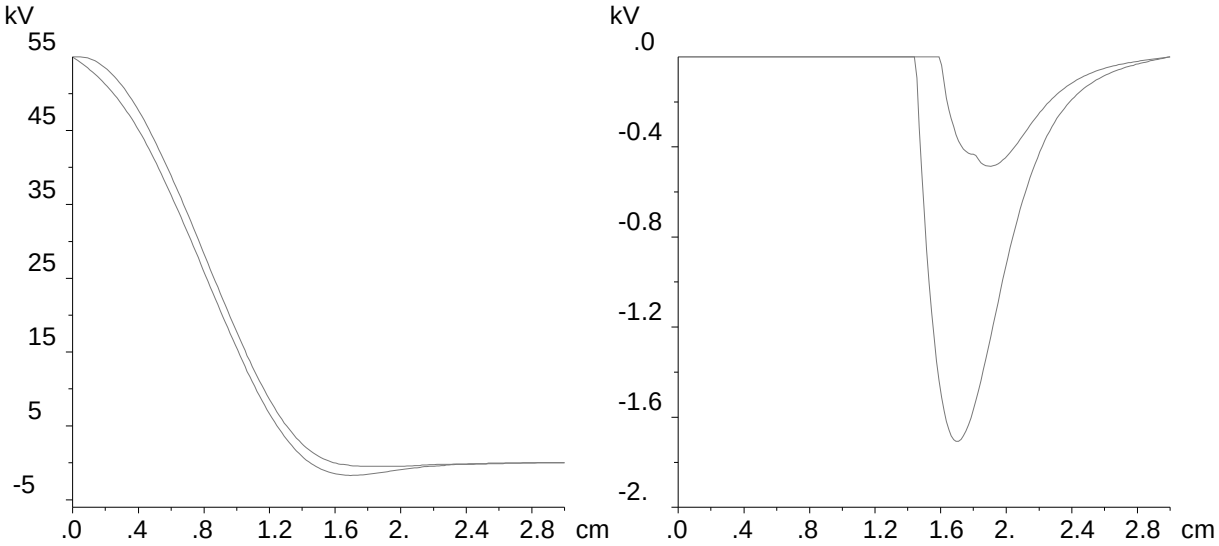

Fig. 4.9. Left: Potential along the z-direction with and without ion beam. Upper curve is the potential line with ion beam. Right: Negative potential along the axis (z-direction) with and without influence of ion beam. The minimum negative potential is -1708 V without ion beam and -487 V with ion beam [11].

4.3.5. Emittance

The emittance is an important property of the ion beam produced by the ion source (and the extraction electrode positioned in front of it): in general the lower the emittance value, the higher the optical quality. To understand the definition of emittance it is important to consider the velocity of the beam in a plane (plane *x*-*y*) perpendicular to the ideal beam direction (direction *z*); instead of the velocity vector profile, one plots the divergence angle in *x* direction as a function of the *x* position ($x' = v_x/v_z$), and similarly for the *y* direction ($y' = v_y/v_z$); this results in a typical plot as presented in figure 4.10. The 95% radial emittance of an ion beam is then defined as the area of the smallest ellipse that contains 95% of the beam intensity (see figure 4.10) divided by π, and this for the *x* and *y* directions:

$$\varepsilon_x = \frac{1}{\pi}\iint dx dx' \tag{4.6}$$

$$\varepsilon_y = \frac{1}{\pi}\iint dy dy' \tag{4.7}$$

The unit of emittance is "π mm mrad". The quantity π resulting from the surface of an ellipse is included in the units: the area of an ellipse with its axis along the main axis would have as surface $x_{max}\, x'_{max}\, \pi$. The measured emittance diagram (see figure 4.10) can have very peculiar shape.

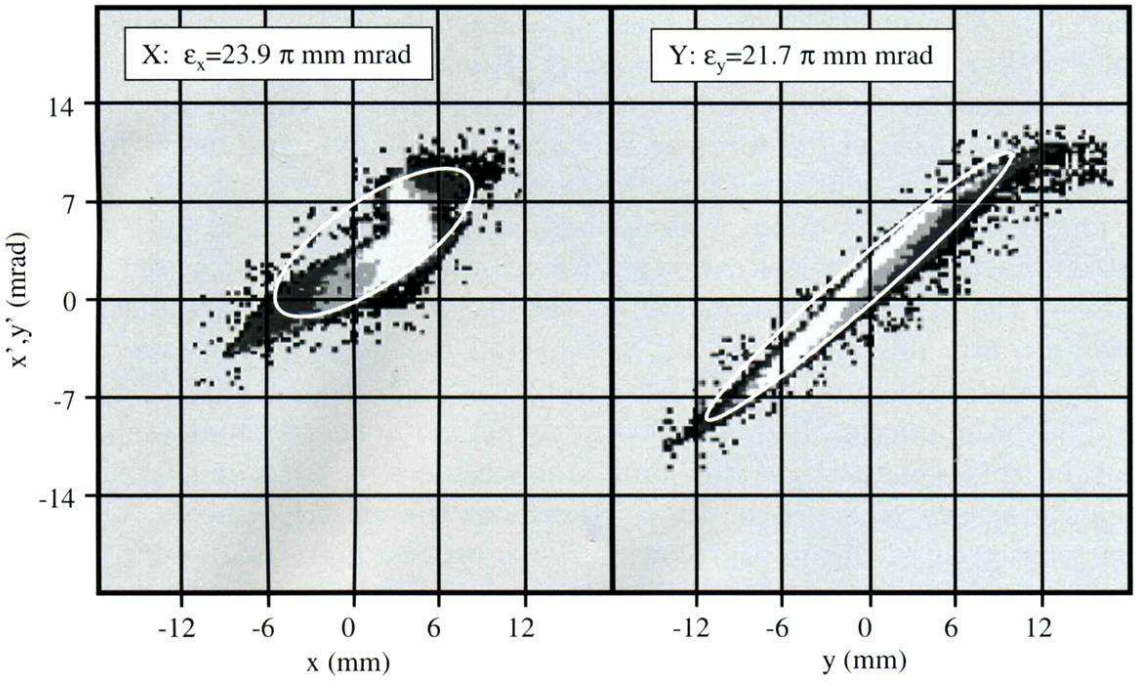

Fig. 4.10. Example of the results of an emittance measurement for a ^{120}Sn beam from the ISOLDE laser ion source; the ellipsoidal contour covers 95% of the beam intensity, the surface of the ellipse representing the final value for the emittance as indicated in the insert. Although the relative difference between ε_x and ε_y is small, the shape of the emittance curves is distinctly different [1].

Still the emittance is related to the surface of the ellipse that includes a specific percentage (in this particular case 95%) of the beam intensity; the latter quantity is generally considered for specifying the emittance as the standard ion-optical elements (lenses, beam pipes, accelerators) have in most cases ellipsoidal acceptance. Ion optical elements like lenses or deflection plates can manipulate an ion beam, thereby turning the ellipse or reshaping it, but the total surface stays constant. The task of focussing an ion beam through a small collimator needs ideally an ellipse with its long axis along the *y*-axis, reducing as a result the spatial spread of the beam. It is easy to understand that after acceleration (increasing of v_z and consequent decreasing of |x'| and of the ellipse area) of the ion beam (higher beam energy) the absolute emittance decreases and the contour plot in figure 4.10 becomes smaller.

To compare emittances at different beam energies it is necessary to normalize the emittance. The normalized emittance is a conserved quantity of the ion beam, defined as:

$$\varepsilon_{nx} = \beta \cdot \varepsilon_x \tag{4.8}$$

with $\beta = v/c$, being v the ion speed and c the speed of light. Along similar lines, to slow down an ion beam needs specific precautions as the emittance will increase, resulting in a larger beam spot.

Apart from the radial emittance, the longitudinal emittance, ε_{long}, is important for example when considering the injection of beam pulses into a trap or accelerator structure. It is defined as the product of the time width of the pulse, Δt, and its energy spread, ΔE:

$$\varepsilon_{long} = \Delta E \cdot \Delta t \tag{4.9}$$

After extraction from the source the ion beam has to be transported, mass analysed and eventually post-accelerated. The transport system, analysing magnets and post-accelerator have limited acceptances. In order to reduce the beam losses to a minimum the radial and longitudinal acceptance of these devices must be equal to or larger than the emittance of the beam. Recently RF-coolers and Penning traps have been developed to cool the ion beam, thus reducing the emittance of an ion beam. These very successful devices allow, among other applications, to slow down ion beams and capture them in ion traps, to softly deposit radioactive ions on surfaces for solid state studies or to adapt the emittance to the acceptance of spectrometers, beam transport systems and accelerators.

Typical emittance values for hot-cavity and laser ion sources are lower than 2 π mm mrad; high temperature plasma ion sources are characterized instead by bigger emittance values, in any case lower than 20 π mm mrad [12].

4.4. The SPES Hot-Cavity Ion Source

In an ISOL facility the pulsing core is the production target followed by the ion source, that are able to convert a stable beam (primary beam) into a RIB (secondary beam).

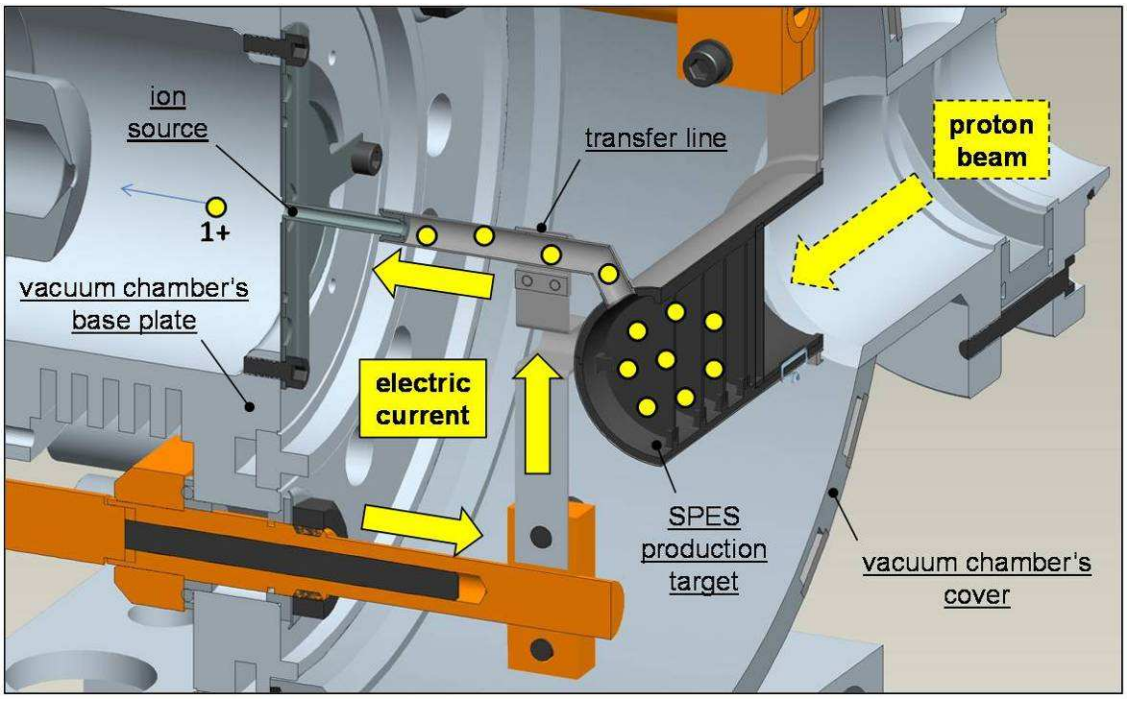

Fig. 4.11. The SPES production target, the transfer line and the ion source (section view).

As mentioned in the previous chapters the SPES production target (see figure 4.11) is made of 7 UC_x co-axial disks (diameter and thickness of 40 and 1.3 mm, respectively) that are impinged by a 40 MeV proton beam (characterized by a current intensity of 0.2 mA), thus generating approximately 10^{13} fissions per second. The radioactive isotopes produced by the ^{238}U fissions are then driven through the transfer line (see figure 4.11) to the ion source: here they acquire a 1+ charge state so that they are able to be accelerated by electrostatic fields.

In the context of the SPES project different ion source types will be used to produce a wide range of beams; in particular, to ionize the isotopes of the elements of the first, second and thirteenth groups a hot-cavity ion source will be used (see figure 4.12).

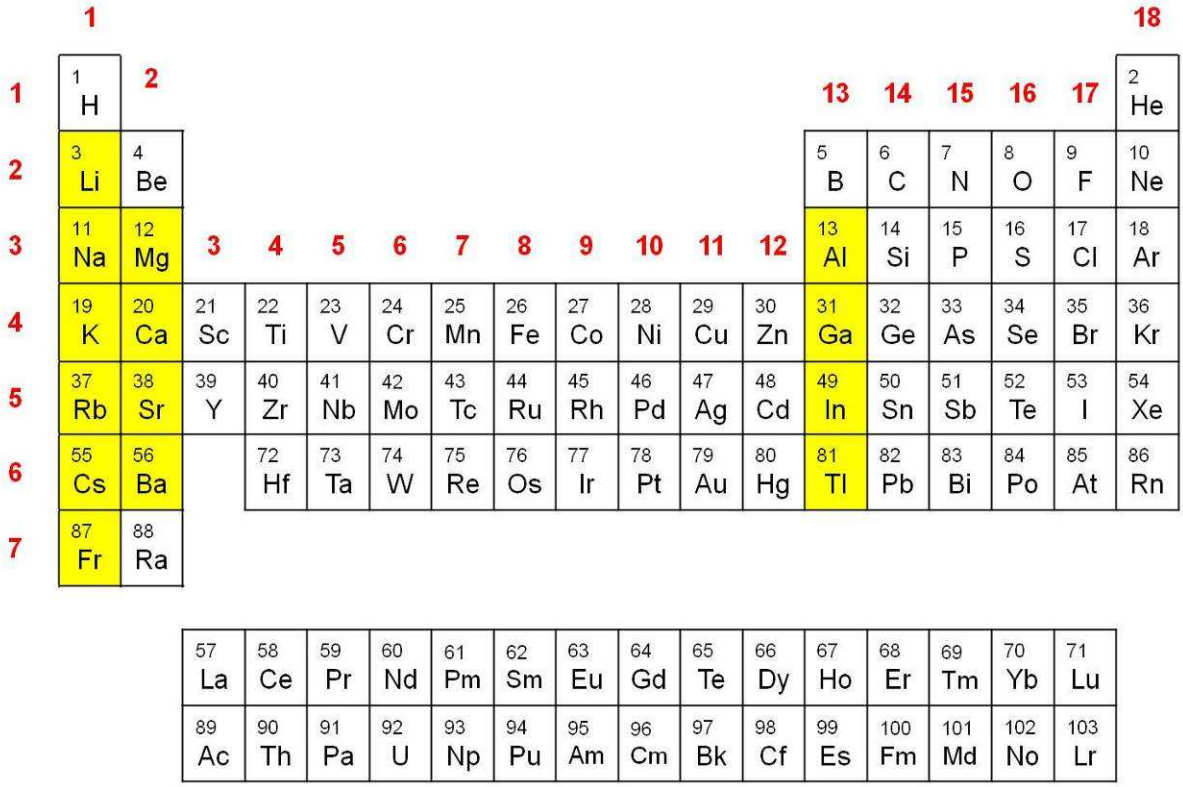

Fig. 4.12. Elements that will be ionized thanks to the Positive Surface Ionization mechanism at SPES.

In the following a detailed presentation of the R&D activities developed at Legnaro National Laboratories on the hot-cavity ion source and transfer line is reported.

4.4.1. Thermal study: theoretical calculations and experimental tests

The surface ion source adopted for the SPES facility is at present the standard MK1 surface ion source [13,14] developed and used at the ISOLDE facility (CERN, Switzerland); it is composed of a tungsten (W) tubular ionizing cavity (length, external diameter and internal diameter equal to 34, 5 and 3.1 mm, respectively) connected on one side to a tantalum (Ta) support (see figure 4.13) and

on the other one to the Ta transfer line by means of a Ta connector; behind the Ta support a Ta screen is positioned.

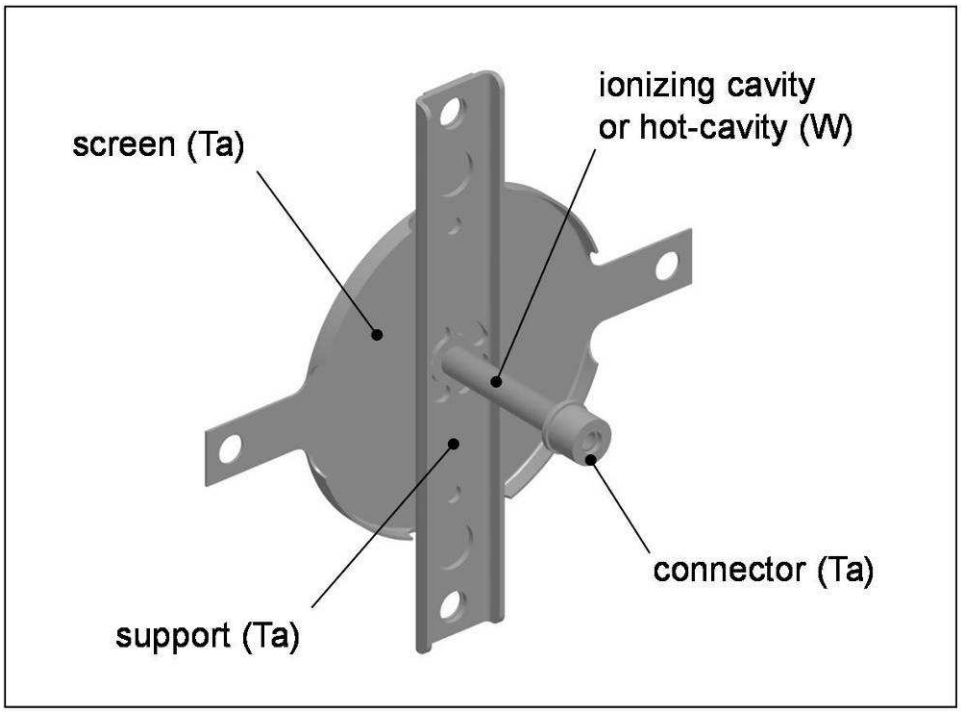

Fig. 4.13. The hot-cavity ion source assembly.

Similarly to the production target, the surface ion source and the transfer line (see figure 4.11) are located under vacuum inside a water-cooled chamber and have to maintain the average temperature of 2000°C and more. Vacuum and high temperature are two essential components to enhance the radioactive isotopes mobility, extraction and ionization. The surface ion source and the transfer line are kept at high temperature thanks to a dedicated and independent 10 kW power supply, able to deliver a maximum electrical current and a maximum potential difference of 1000A and 10V, respectively. The electrical current flows first through Ta transfer line and then through the W tubular ionizing cavity, called also hot-cavity, and dissipates by Joule effect the power which enables the system to reach the desired temperature level. The Ta transfer line consists of a tube with an external and an internal diameter of 9 and 8 mm, respectively, and a length of approximately 38 mm, connected to the W hot-cavity.

In this paragraph the thermal-electric behaviour of the surface ion source and of the transfer line, at present adopted for the SPES project, are studied both from the theoretical and the experimental point of view. In particular Finite Element (FE) numerical models as well as analytic ones were defined first to estimate temperature and potential difference values and then to compare theoretical results with experimental data. The aforementioned two objects were studied independently from the production target, even if preliminary FE simulations showed that the primary beam power deposition in the target might influence the thermal behaviour of the transfer

line and ion source by slightly increasing their temperature level. Anyway such thermal increment can be easily eliminated by reducing the electrical current flowing through the transfer line and ion source themselves.

Similarly to the target heater, it is important to underline that the thermal and the electric problems are coupled, since the thermal load is produced by Joule Effect and the electric resistivities of tantalum and tungsten are temperature dependent. Accordingly, a coupled thermal – electric FE model was defined, in order to study in detail the thermal – electric behaviour of the hot-cavity ion source and of the transfer line and to predict in a virtual environment the effect of some variations in the design variables that could be introduced in the future.

Then, aims of simulations described in the present work are as follows:

- to calculate the heat dissipation by Joule effect in the surface ion source and transfer line;
- to calculate the correspondent temperature distributions;
- to estimate the effects of some material and geometric variations on the temperature distributions.

Before running the numerical simulations, simple, one-dimensional analytic models were defined to estimate the temperature levels of the W hot-cavity and of the Ta transfer line. All theoretical results (both analytical and numerical) were finally compared with thermal and electrical experimental measurements.

Analytic one-dimensional models. Two simple one-dimensional analytic models were defined to easily estimate the temperature levels of the hot-cavity and the transfer line (see figures 4.11 and 4.13). Even if the models do not deliver the complete temperature distributions, but rather a single temperature value, nevertheless the lower accuracy of the analytic models with respect to a computer simulation is acceptable in view of their considerable simplicity, as it will be seen later on. As a general consideration regarding both analytic models, since the hot-cavity and the transfer line working temperatures are on the order of 2000 °C in vacuum, then thermal radiation is dominant with respect to the other heat transfer modes. Moreover in the simplified analytic approach described in the present section, the thermal behaviour of the hot-cavity and the transfer line are assumed as independent from each other. As a consequence, if we take into consideration the external lateral surface of the hot-cavity or of the transfer line (area A_1), the internal surface of the vacuum chamber (total area A_2) and approximate them with equivalent concentric spherical surfaces having areas A_1 and A_2 , the radiative heat flux $q_{1\text{-}2}$ from A_1 to A_2 can be expressed, under the hypothesis of gray-diffuse surfaces, as:

$$q_{1-2} = \frac{A_1 \cdot \sigma_n \cdot \left(T_1^4 - T_2^4\right)}{\frac{1}{\varepsilon_1} + \left(\frac{A_1}{A_2}\right) \cdot \left(\frac{1}{\varepsilon_2} - 1\right)} \tag{4.10}$$

where σ_n is the Stefan-Boltzmann constant , T_1 and T_2 are the absolute temperatures of the two concentric spherical surfaces, ε_1 and ε_2 are the hemispherical total emissivities of surfaces 1 and 2, respectively.

If we consider the heat dissipation due to the electrical current I flowing through the hot-cavity and the transfer line (conductors of uniform cross section S, length L and electric resistivity ρ), and suppose that it is totally dissipated by thermal radiation, then we have:

$$q_{1-2} = \frac{\rho \cdot L}{S} \cdot I^2 \tag{4.11}$$

As a consequence, combining equations (4.10) and (4.11), the temperature T_1 of surface A_1 can be estimated by the following expression:

$$T_1 = \sqrt[4]{T_2^4 + \left(\sigma_n \cdot A_1\right)^{-1} \cdot \left[\frac{1}{\varepsilon_1} + \frac{A_1}{A_2} \cdot \left(\frac{1}{\varepsilon_2} - 1\right)\right] \cdot \frac{\rho \cdot L}{S} \cdot I^2} \tag{4.12}$$

Since $A_2 >> A_1$, eq. (4.12) can be simplified by neglecting the dependence of T_1 from A_2 and ε_2 (in other words, we can consider the surface A_1 irradiating to an infinite environment characterized by the temperature T_2):

$$T_1 = \sqrt[4]{T_2^4 + \left(\sigma_n \cdot A_1 \cdot \varepsilon_1\right)^{-1} \cdot \frac{\rho \cdot L}{S} \cdot I^2} \tag{4.13}$$

Eq. (4.13) can be used to study the temperature dependence of the hot-cavity and transfer line, respectively, from the electrical current flowing through them. It has to be solved numerically, since the electrical resistivity ρ and the emissivity ε_1 are temperature T_1 dependent. Concerning the hot-cavity, the temperature dependence of emissivity and resistivity of tungsten is reported in figures 4.14 and 4.15, respectively. Concerning the transfer line, the electrical resistivity and emissivity of tantalum were considered temperature dependent according to the data found in [15,16].

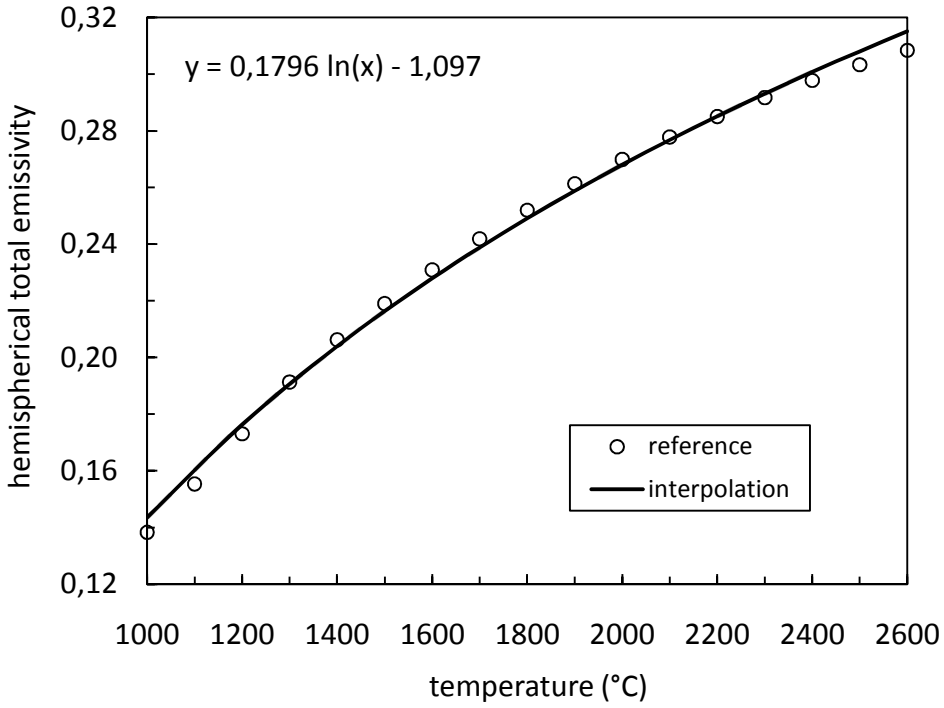

Fig. 4.14. Temperature dependence of the hemispherical total emissivity of Tungsten [15] and interpolating function adopted in the analytic model.

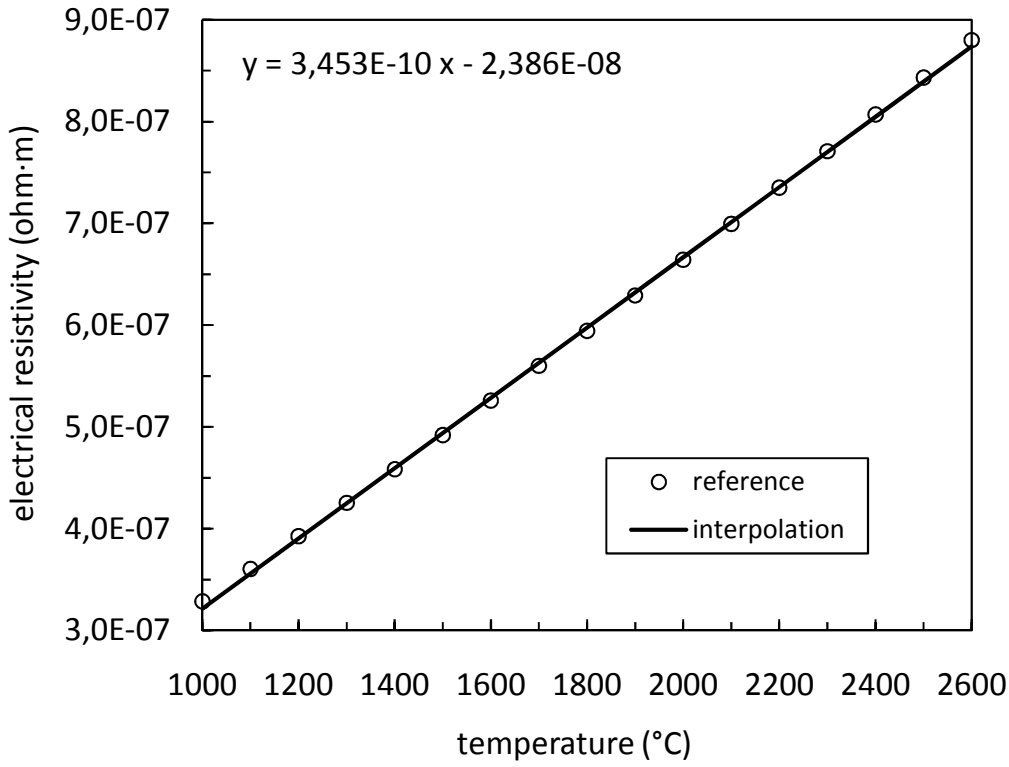

Fig. 4.15. Temperature dependence of the electrical resistivity of Tungsten [16] and interpolating function adopted in the analytic model.

Numerical model. In order to limit the complexity of the numerical model, the geometry of the system studied in this work was simplified as shown in figure 4.16. First of all, the vacuum chamber was not modelled since its internal area is much larger than the overall external area of the objects contained inside and consequently it is not able to influence their thermal behaviour. Then the ion source, the transfer line and the other components contained inside the vacuum chamber were assumed to exchange heat by thermal radiation with an infinite environment characterized by the same temperature of the vacuum chamber. The validity of this hypothesis was verified both analytically and by means of dedicated FE analyses.

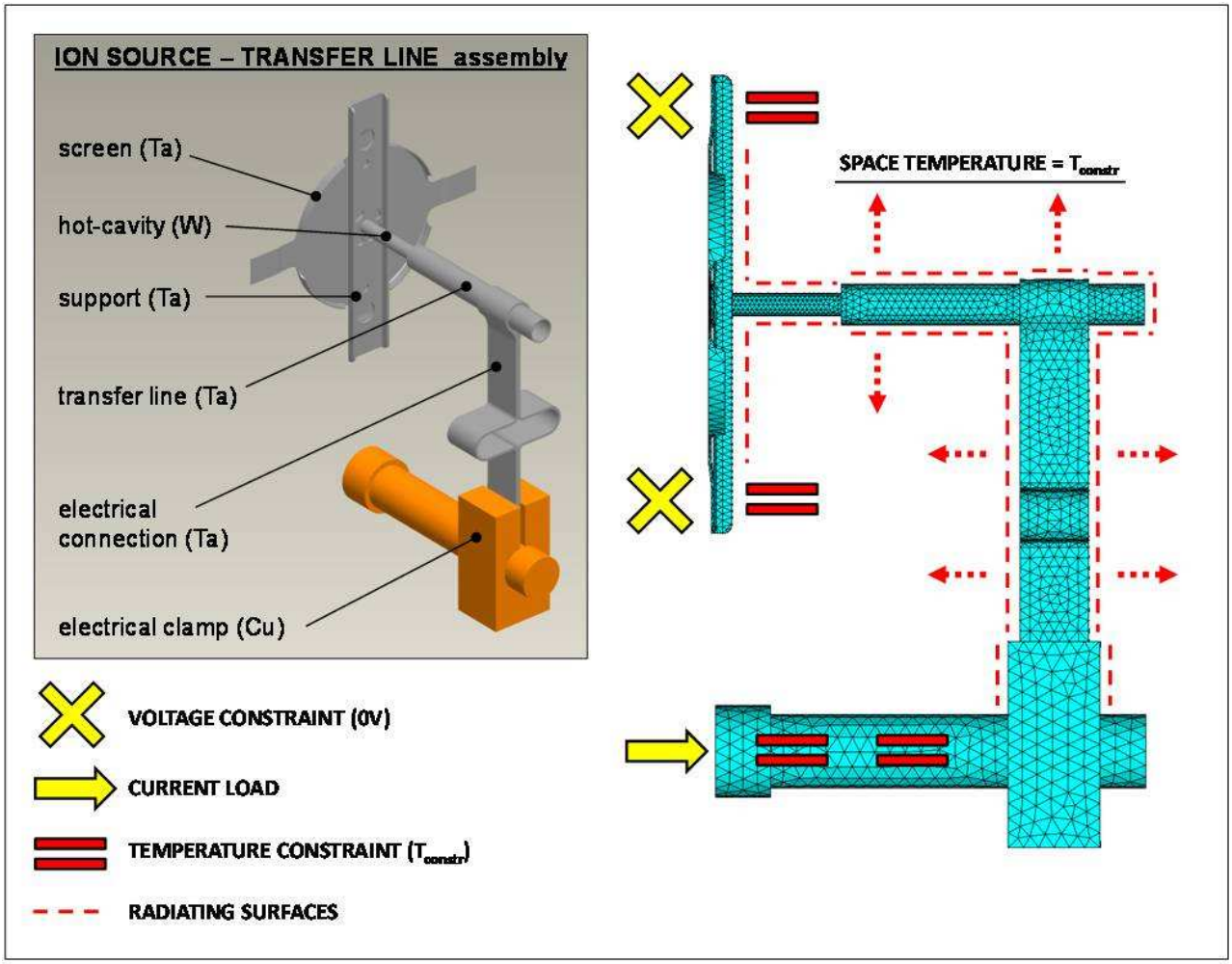

Fig. 4.16. DOF (Degree Of Freedom) constraints and loads applied to the FE thermal-electric model.

A perfect electrical and thermal contact was considered between all modelled components, i.e. between the Ta support, the W hot-cavity, the Ta transfer line, the Ta electrical connection and the Cu electrical clamp. Indeed only the transfer line and the electric connection are joined by means of weldments, which behave with better accuracy as perfect thermal and electrical contacts. Conversely, the electrical connection and the electrical clamp are connected by means of bolts, whereas all the other joints are fitted by mechanical interference: in these cases the assumption of

perfect thermal and electrical contact is less consistent with the real construction detail, as it will be explained in the following paragraphs.

The three-dimensional FE model reported in figure 4.16 was defined in the ANSYS® 12.0 environment and the coupled thermal-electric element SOLID69 was used to consider both the thermal and the electrical problems. Each node of this element has two Degrees Of Freedom (DOF), namely temperature and voltage. As explained with more details in the previous chapters, according to the ANSYS® Radiosity Solver method, that restricts radiation exchange to gray-diffuse surfaces, the conductive problem is solved in conjunction with the radiative one by means of a particular sequential method which considers iteratively the heat diffusion and the radiation equations: radiative heat fluxes (the radiative problem's output) generate boundary conditions for the conductive problem, whereas superficial temperature distributions (the conductive problem's output) provide boundary data for the radiative one. In case of 3-D models, like that analysed in the present paper, the code calculates view factors using the Hemicube method. A single enclosure (i.e. set of surfaces radiating to one another) was defined to compute the radiative heat transfer among the surfaces of the objects and between the surfaces themselves and the surrounding environment characterised by a uniform temperature.

The DOF constraints and loads applied to the FE model are shown again in figure 4.16. Concerning the electrical problem, a constraint of 0 Volt was assigned to the surfaces of the Ta screen that in the real system are in direct contact with the vacuum chamber by means of screw joints (see figures 4.11 and 4.13). Moreover a current load was assigned to the round surface of the electrical clamp’s extremity. Concerning the boundary conditions of the thermal problem, a temperature constraint T_{constr} equal to 25°C was assigned to the same surfaces where a potential of 0V was previously imposed, in order to simulate the presence of the water cooling system. The same temperature T_{constr} was assigned as space temperature to the environment represented by the vacuum chamber, which surrounds the hot-cavity and the transfer line. Due to vacuum, no convective loads are present in the analyses described in this work.

To promote the convergence of the Radiosity Solver method, transient analyses were performed instead of steady state ones [17]; in particular, a stepwise time-dependent current value was assigned to the extreme edge of the Cu clamp, starting from 50A up to the maximum value of 500A, with steps of 50A. At each step, the transient analysis covered a sufficient period of time to let temperatures stabilise.

The materials of the objects included in the FE model are: tungsten, tantalum and copper. As a consequence, to calculate the system’s steady state temperature and voltage distributions, it was necessary to consider their temperature dependent values of electrical resistivity [16,18], emissivity

(hemispherical total emissivity) [15] and thermal conductivity [19]. Conversely temperature independent values of the specific heat and density were considered since such thermo-physical material properties control only the transient thermal behaviour of the system and not the steady state conditions, which in turn were considered at each step of the numerical analysis.

Experimental tests. To perform the off-line tests (i.e. the tests without the presence of the production target shown in Figure 4.11) on the surface ion source and the transfer line, the experimental apparatus presented in figure 4.17 was adopted.

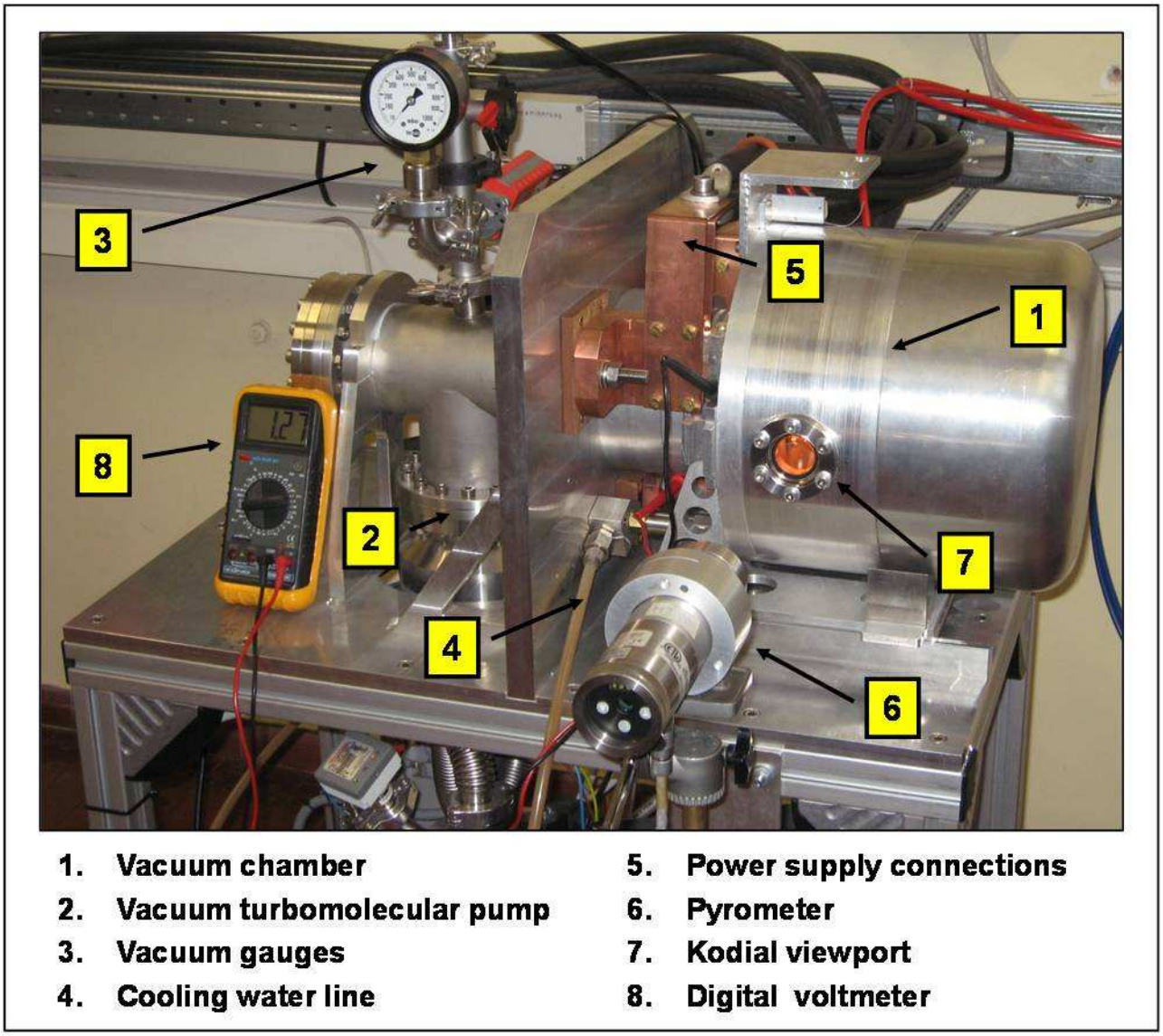

Fig. 4.17. Experimental apparatus.

A 10 kW power supply was electrically connected to the ion source – transfer line loop, causing heat dissipation by Joule effect. A rotary and a turbomolecular pump installed in series provided a vacuum level of 10^{-6} mbar inside the vacuum chamber composed of a round base plate and a cylindrical cover (see figure 4.11). The chamber's base plate and the Cu electrical clamp were

water cooled (water temperature and flow rate equal to 20°C and 400 l/h, respectively) in order to avoid over-temperature problems and damages of the chamber's vacuum gaskets.
Figure 4.18.a shows the surface ion source and the transfer line installed inside the vacuum chamber, while some details of the ion source and of the transfer line are reported in figures 4.18.b and 4.18.c, respectively.

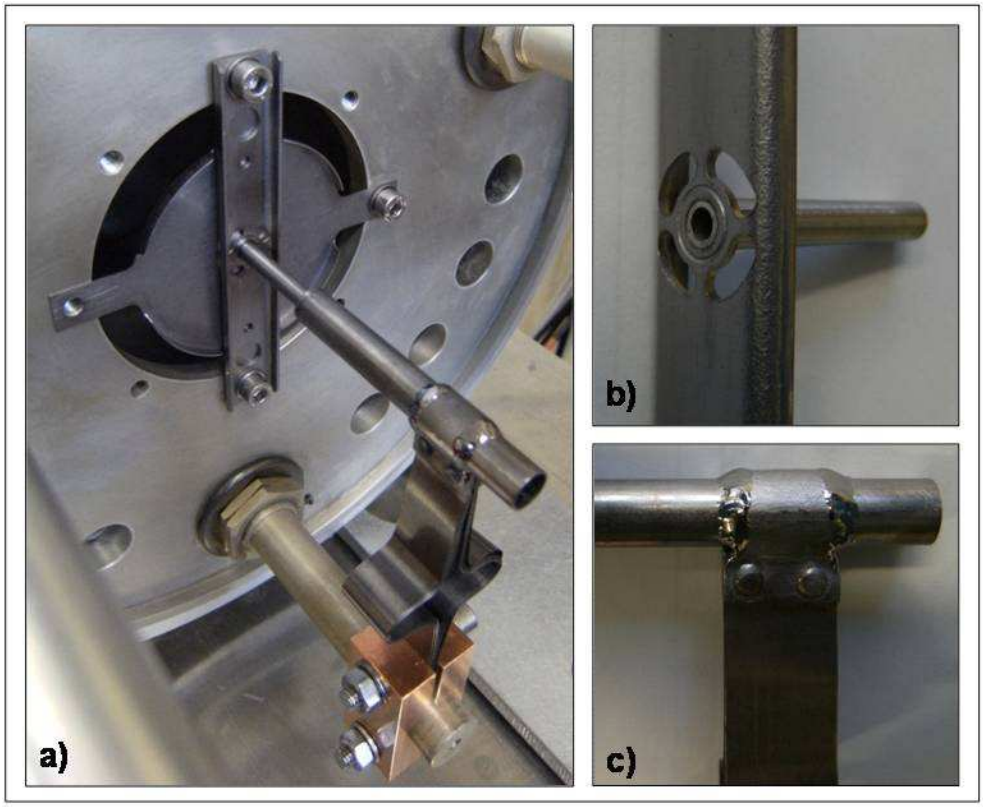

Fig. 4.18. The ion source and the transfer line installed inside the vacuum chamber (a); mechanical (interference) joint between the support and the hot-cavity (b); welded joint between the main tube of the transfer line and the electrical connection (c).

Temperature measurements along the axial extent of both the hot-cavity and the transfer line were performed by means of an infrared two colour pyrometer, able to measure temperatures between 1000 and 3000°C (the blackbody accuracy of the pyrometer was within 0.5% of reading plus 2°C). To measure the temperatures of the objects located inside the vacuum chamber, a borosilicate lass view port (Kodial view port, Torr Scientific Ltd, East Sussex-UK) almost completely transparent to infrared radiation was installed; compressed air flows were used to prevent its local overheating. Experiments were conduced by raising the heating current with steps of 50A, starting from 50A up to 500A, and keeping the current constant for about 20 minutes at each step, in order to let the temperature distribution stabilize. After that, temperature measurements were performed. Electrical potential difference values were measured between the external side of

the Cu clamp and the chamber's base plate by using a digital voltmeter characterized by the measurement range 0-1000V and accuracy equal to 0.1% of reading.

At the end of this paragraph it is important to remark that each value of the experimental data reported in this work is the mean value of three repeated measurements, that in general proved to maintain a very stable behaviour: in particular the difference between one single measurement and the corresponding mean value was always below 2%.

Comparison between theoretical and experimental results. Temperature and potential difference values calculated by means of both the analytic and the FE models were compared with the experimental data obtained by using the apparatus previously described. Figure 4.19 shows the FE temperature distribution corresponding to 300A of applied current and compares the pictures of the real object when heated by the same current level and when kept at room temperature.

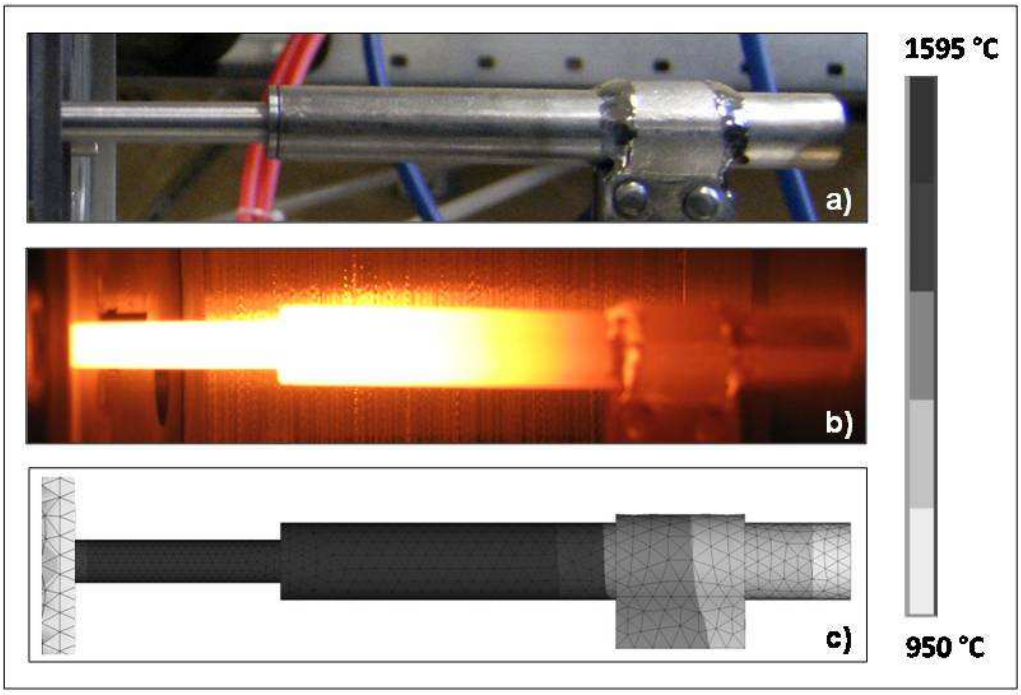

Fig. 4.19. Temperature increments observed experimentally on the hot-cavity and on the transfer line from the initial room temperature (a) to the final regime for 300 A of applied current (b) and comparison with FE results (c).

The points where temperature was experimentally detected were defined considering six representative sections (see figure 4.20): sections s0 and s1 located at the extremities of the hot-cavity, section s2 located at the transition zone between the hot-cavity and the transfer line, sections s3 and s4 that encompass the welding zone between the transfer line and the electrical connection, section s5 at the ending tip of the transfer line. Five measurement points (P1, …, P5) were located at the mid points between two consecutive sections.

Figure 4.20 presents the temperature distributions of the hot-cavity and the transfer line as predicted by the FE model, considering the heating current values of 200, 300, 400 and 500A. FE

temperature values are compared with measured ones at points P1…P5, showing that the FE model is able to accurately reproduce the temperature distribution along the hot-cavity and the transfer line axial direction.

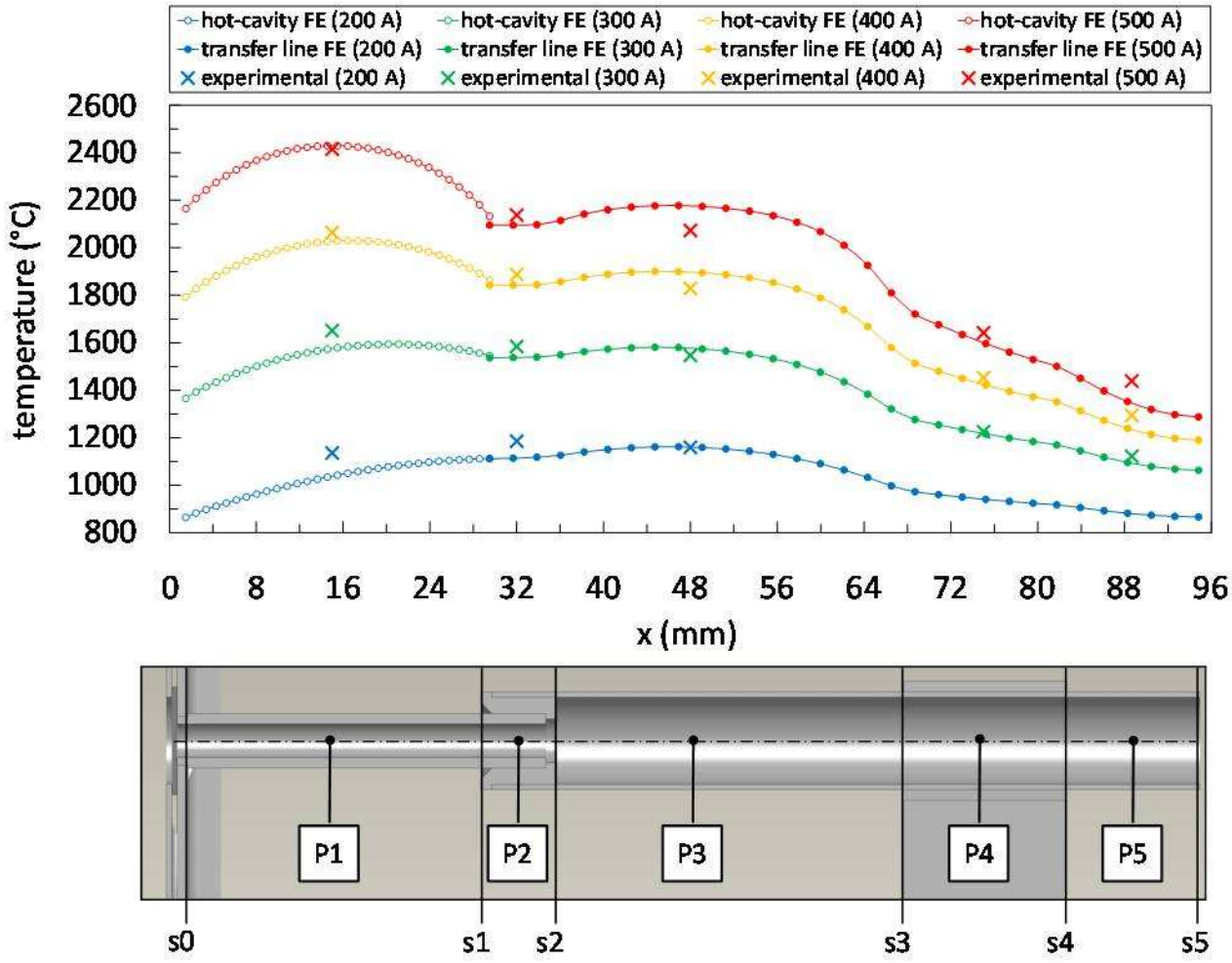

Fig. 4.20. Hot-cavity and transfer line temperature distributions as predicted by the FE analysis for 200, 300, 400, 500A of applied current and comparison with temperature measurements at five points.

Figure 4.21 and 4.22 report a comparison among analytic calculations, FE results and experimental temperatures at point P1 and P3 located at the mid points of the hot-cavity and the transfer line, respectively. The single temperature values delivered by the analytic models are always higher than both FE and experimental data because those models do not consider the additional conductive heat flux towards the more cold extremities of the hot-cavity and transfer line system. Figure 4.21 clearly shows that this effect is weaker at high temperatures, i.e. when the conductive heat transfer mode become more and more negligible with respect to thermal radiation. The FE results show a good agreement with the experimental data. As an example, if we consider the hot-cavity (see figure 4.21), the difference ranges from -101°C (heating current equal to 200 A) to +14°C (heating current equal to 500 A) with respect to the measured temperatures.

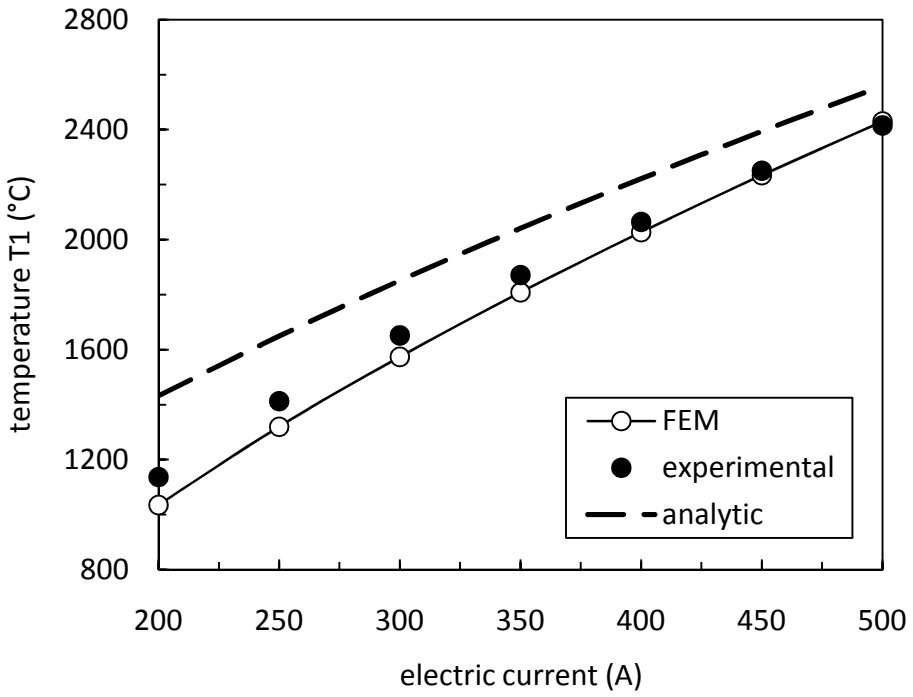

Fig. 4.21. Comparison between theoretical and experimental temperatures at the mid-point of the hot-cavity (point P1 in figure 4.20).

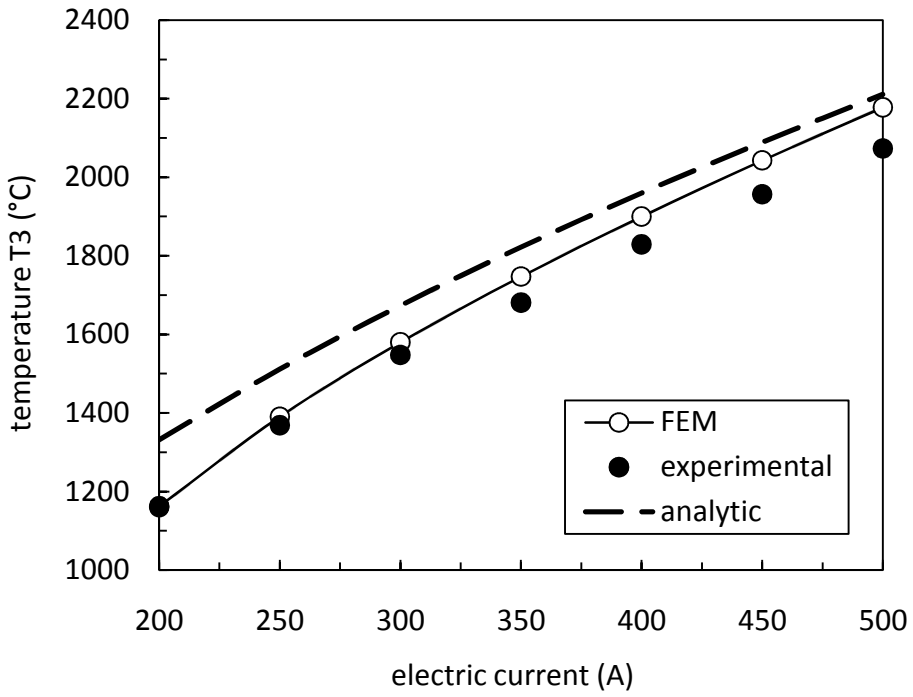

Fig. 4.22. Comparison between theoretical and experimental temperatures at the mid-point of the transfer line (point P3 in figure 4.20).

Table 1 presents the comparison between numerical and experimental temperatures at points P2, P4 and P5. Concerning point P2, calculated temperatures are always lower than experimental ones and the differences range from -71°C for 200A to -41°C for 500A. Concerning points P4 and

P5, the maximum difference of numerical values with respect to experimental ones is seen in both cases when the electric current is 500 A and it is equal to -46°C at point P4 and -86°C at point P5.

Current [A]	$T_{P2\text{-}FE}$ [°C]	$T_{P2\text{-}EXP}$ [°C]	$T_{P4\text{-}FE}$ [°C]	$T_{P4\text{-}EXP}$ [°C]	$T_{P5\text{-}FE}$ [°C]	$T_{P5\text{-}EXP}$ [°C]
200	1115	1186	941	/	882	/
250	1349	1404	1092	1087	1003	1002
300	1538	1584	1216	1226	1096	1122
350	1699	1742	1324	1349	1173	1225
400	1843	1887	1422	1454	1240	1295
450	1974	2016	1512	1545	1299	1358
500	2096	2137	1596	1642	1353	1439

TABLE 4.1. FE and experimental temperature values for points P2, P4 and P5.

The electric potential difference values detected between the external tip of the Cu electrical clamp and the main plate of the vacuum chamber (see figure 4.11) are reported in figure 4.23. The difference between calculations and measurements is probably due to the fact that ideal contacts between components were implemented in the FE model, whereas some electrical contact resistances exist in the real joints above described. In fact the potential difference values calculated by the FE model are always lower than the measured ones for the same applied current. In particular the ratio $\Delta V_{FEM}/\Delta V_{EXP}$ ranges from 0.92 for 200A to 0.90 for 500A.

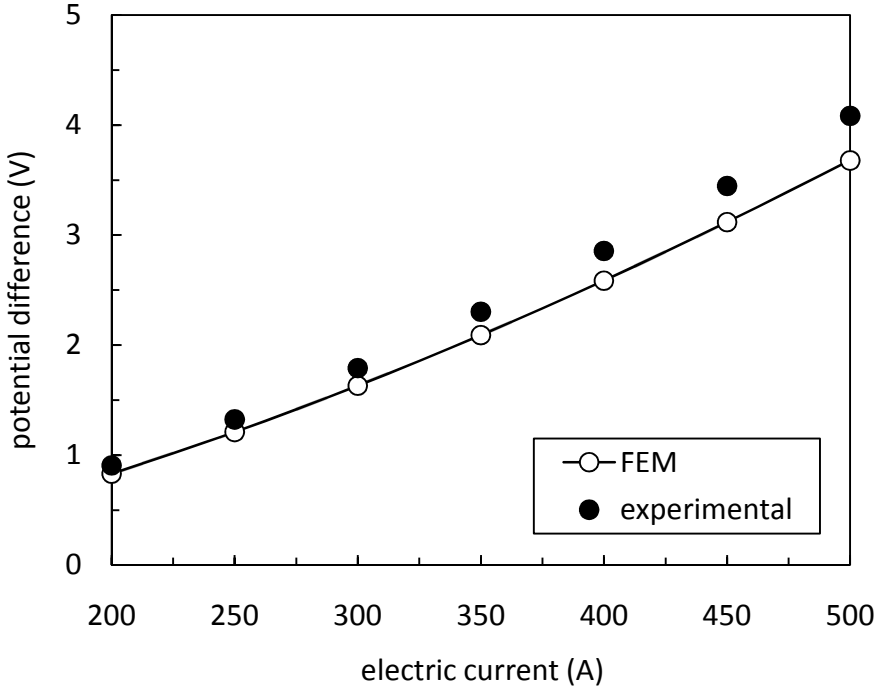

Fig. 4.23. Comparison between numerical and experimental potential difference values.

Sensitivity of the system's working temperature to adopted materials, geometry and boundary conditions. Once the accuracy of the FE thermal – electric model was verified, it was used to study the sensitivity of temperature distributions to some variations of adopted materials, geometry and boundary conditions. In particular, the following design parameters were considered: a) the material of the hot-cavity , b) the external diameter of the transfer line, c) the boundary temperature T_{constr} assigned to the cold surfaces.

a) Influence of the material of the hot-cavity. To manufacture positive surface ion sources, materials characterized by high work function and resistance at high temperatures have to be chosen. In the previous paragraph theoretical results and measured data obtained with the hot-cavity made of tungsten (W) were presented. In this section the hot-cavity and the transfer line temperature distributions calculated by considering the hot-cavity made of tantalum (Ta) or rhenium (Re) are presented, while the transfer line was always supposed made of tantalum. Results of these new numerical analyses are reported in figure 4.24, which highlights that by keeping the same heating current, Ta and Re lead to higher temperatures than W. In particular, considering a Ta hot-cavity, its maximum temperature raises from 2030 to 2272°C for 400A of heating current; in the case of Re, the hot-cavity's maximum temperature increases from 2030 to 2316°C.

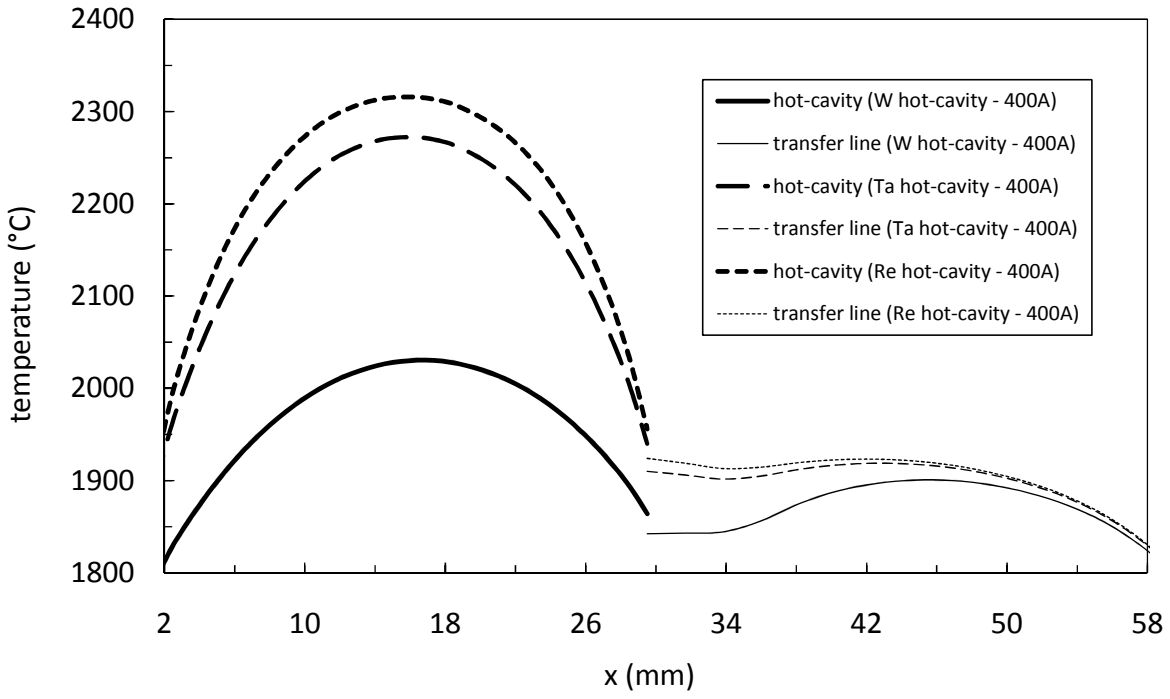

Fig. 4.24. Hot-cavity and transfer line FE temperature distributions for 400A of heating current and for three different materials of the hot-cavity (W, Ta and Re); the material of the transfer line is Ta.

The temperature increments when considering Ta and Re hot-cavities instead of W were well predicted also by the analytic model (figure 4.25). The behaviour described by the numerical as well as by the analytic models is due to the higher electrical resistivity of Ta and Re with respect to

W [16,20], while the emissivity values remains practically unchanged [15,21]. Anyway it should be noted that such temperature increase can be dangerous for material's structural integrity (for instance Ta, in high vacuum environment, shows evident signs of damage when temperatures are above 2200°C) so that lower current values or geometry modifications are needed to avoid damage of the ion source.

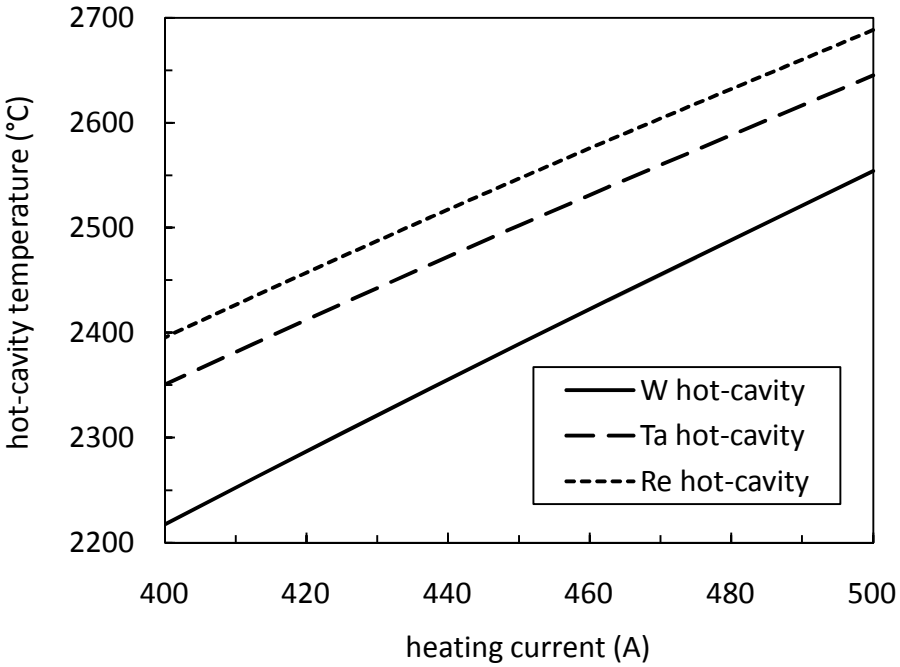

Fig. 4.25. Hot-cavity analytical temperatures versus heating current for three different materials of the hot-cavity (W, Ta and Re).

The transfer line temperature distribution is not heavily influenced by the hot-cavity's material change (see again figure 4.24), but unfortunately the temperature imbalance between hot-cavity and transfer line, already existing in the case of W, worsens with Ta and Re. Usually such thermal imbalance is decreased by wrapping manually the transfer line with foils (thermal screens) made of W, Ta or Mo; either one single material or multiple materials can be used. This technique is characterized by a bad reproducibility and by a bad stability with respect to time: in fact local spot welding phenomena seems to increase gradually, thus changing the resultant electrical resistance and, consequently, the temperature distribution. In the next section an alternative method to smooth away the thermal imbalance between hot-cavity and transfer line is presented.

b) Effect of the external diameter of the transfer line. The simple idea is to reduce the external diameter of the transfer line and consequently its cross section S: in this way its electrical resistance can be increased and, for the same electrical current, its temperature level is expected to increase and approach the hot-cavity's one (see eq. (4.13)); the geometrical configuration remains simple, leading to a high level of reproducibility. Figure 4.26 clearly shows that the reduction of the transfer

line's external diameter from the original value of 9 mm to 8.8 mm leads to a considerable improvement in the temperature balance between the hot-cavity and the transfer line.

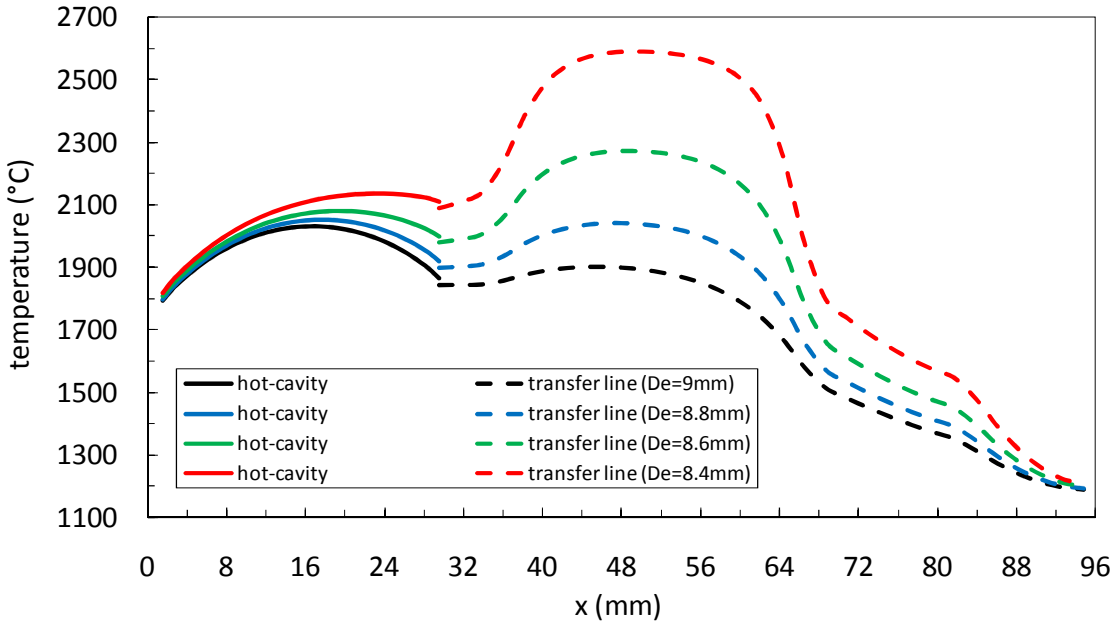

Fig. 4.26. Hot-cavity and transfer line FE temperature distributions for different sizes of the transfer line external diameter (De) considering 400A of heating current.

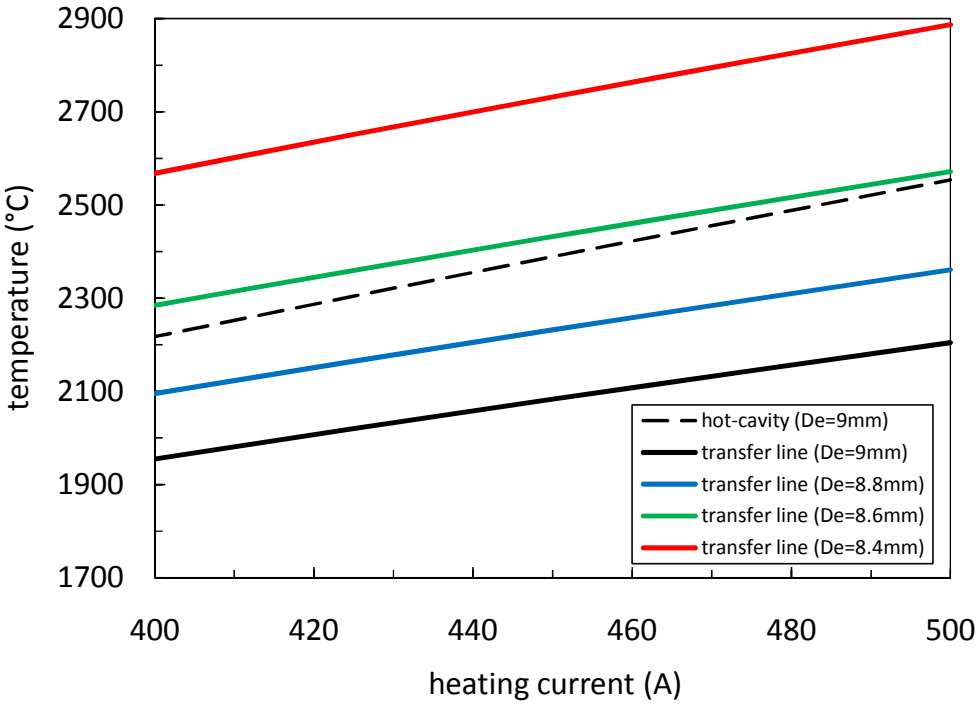

Fig. 4.27. Transfer line analytical temperatures versus heating current for different external diameters (De); as a comparison the W hot-cavity analytical temperature (see figure 4.25) is reported.

For smaller diameters (8.6 and 8.4 mm) the transfer line's temperature increases too much and exceeds the hot-cavity's one. In figure 4.26 the cold point in the proximity of the connector between

the hot-cavity and the transfer line is evident and is due to the wider cross section which decreases the local electrical resistance. The two analytic models of the hot-cavity and the transfer line, respectively, substantially confirm these results, as figure 4.27 demonstrates.

c) Influence of the boundary temperature assigned to the cold surfaces. In the present paragraph, the sensitivity of numerical results to the assigned temperature boundary condition T_{constr} (see figure 4.16) was investigated. In the FE model described in the previous paragraphs T_{constr} was taken equal to 25°C. This is an approximation, especially for the vacuum chamber's cover that, differently from the vacuum chamber's base plate (see figure 4.11) and the electrical clamp, is not directly water cooled and can reach temperature levels close to 150-200°C at the highest applied current values. To verify to which extent this kind of approximation affects the hot-cavity and the transfer line's temperature distributions, a dedicated analysis was performed by imposing T_{constr} equal to 200°C: by so doing the effect of a limit temperature that surely will not be exceeded anywhere in the electrical clamp and in the vacuum chamber was investigated. The results of such analysis were compared with those obtained by keeping T_{constr} equal to 25°C. As shown by figure 4.28, the influence of T_{constr} on the hot-cavity and transfer line temperature distributions is completely negligible due to the dependence of the radiative heat flux on the fouth-power of temperature.

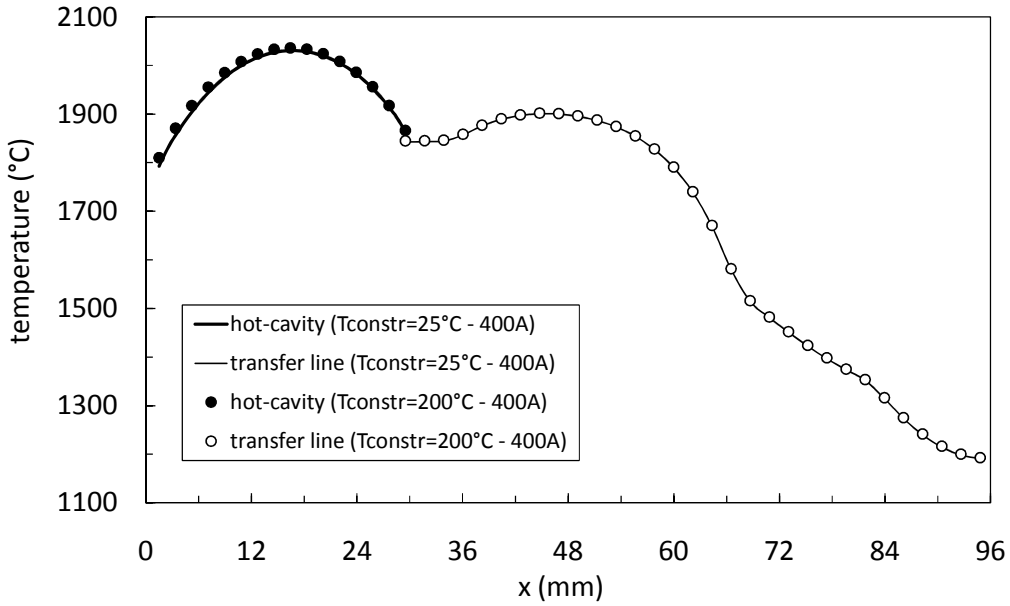

Fig. 4.28. Hot-cavity and transfer line FE temperature distributions for T_{constr} = 25°C and T_{constr} = 200°C (see figure 4.16) considering 400A of heating current.

General observations and remarks. In this study, the thermal-electric behaviour of the SPES (Selective Production of Exotic Species) hot-cavity ion source and transfer line was studied by means of simple one-dimensional analytic models as well as coupled thermal-electric FE analyses. The thermal load was due to the 10 kW electric power dissipated by Joule effect in the ion source

assembly. Theoretical results were compared with experimental data in terms of both temperatures and electric potentials and a good agreement was observed. Once the FE model was validated, additional numerical analyses were performed to investigate the effects of alternative choices concerning some design parameters. In particular the following items were analysed: (i) different materials for the hot-cavity, namely tungsten (W), tantalum (Ta), rhenium (Re), (ii) a reduction of the transfer line's external diameter, and (iii) a variation of the boundary temperature T_{constr} assigned to the cold surfaces. At the end of this study the following conclusions could be drawn:

1) for the same electric current value, hot-cavities made of Ta and Re lead to higher temperature levels respect to the W hot-cavity;

2) the reduction of the transfer line's external diameter from 9 to 8.8 mm leads to a considerable improvement of the temperature balance between the W hot-cavity and the Ta transfer line;

3) the influence of T_{constr} (in the range 0 - 200°C) on the hot-cavity and transfer line temperature distributions is completely negligible.

All these results, along with the FE model validated in the present work were used to optimize the SPES hot-cavity ion source and transfer line; their improved versions will be described in the following paragraphs.

4.4.2. Optimization of the SPES Hot Cavity Ion Source and Transfer Line

The thermal study presented in the previous paragraph puts in evidence an important thermal gradient along the transfer line: in particular the temperature field registers a strong decrease from section s0 to section s5 (see figure 4.20); this is mainly due to the electrical connection's shape, characterized by a thick section (and consequently by a large radiating surface) in proximity of the transfer line (see figure 4.16) and to the transfer line dimensions, not well balanced respect to the hot-cavity's ones.

The solution proposed to solve the aforementioned problems is presented in figure 4.29: a thinner electrical connection increases locally the Joule heating and limits the extension of the radiating surfaces, especially in proximity of the transfer line interface; moreover a small reduction of the transfer line's external diameter (from 9 to 8.8 mm) guarantees a temperature increase along all its axial extension.

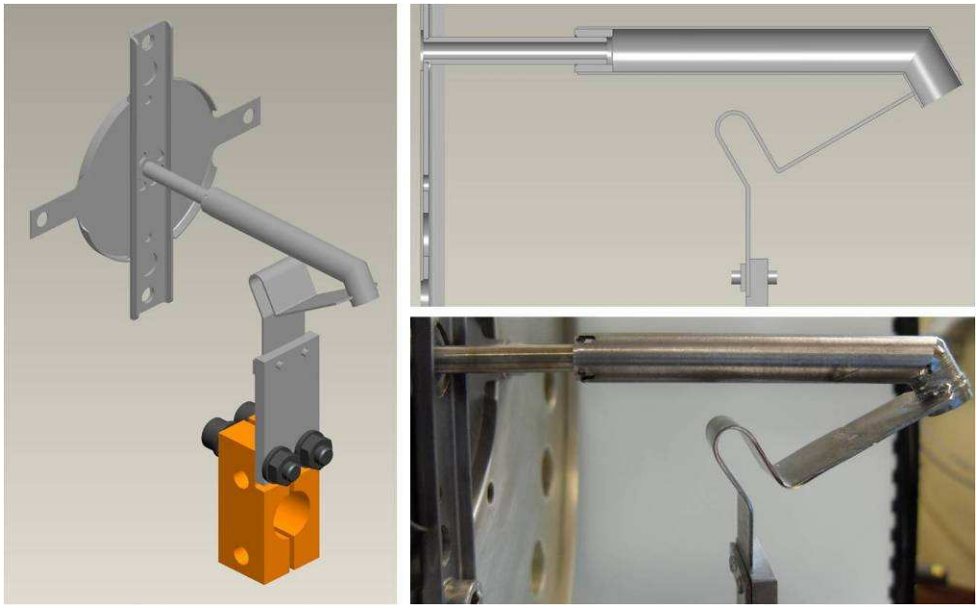

Fig. 4.29. The optimized SPES hot-cavity ion source and transfer line.

Figure 4.30 shows the FE temperature plot and the correspondent picture of the optimized ion source – transfer line system heated by an electrical current of 400A. The temperature distribution along the radioactive isotopes path is homogeneous and does not present cold spot.

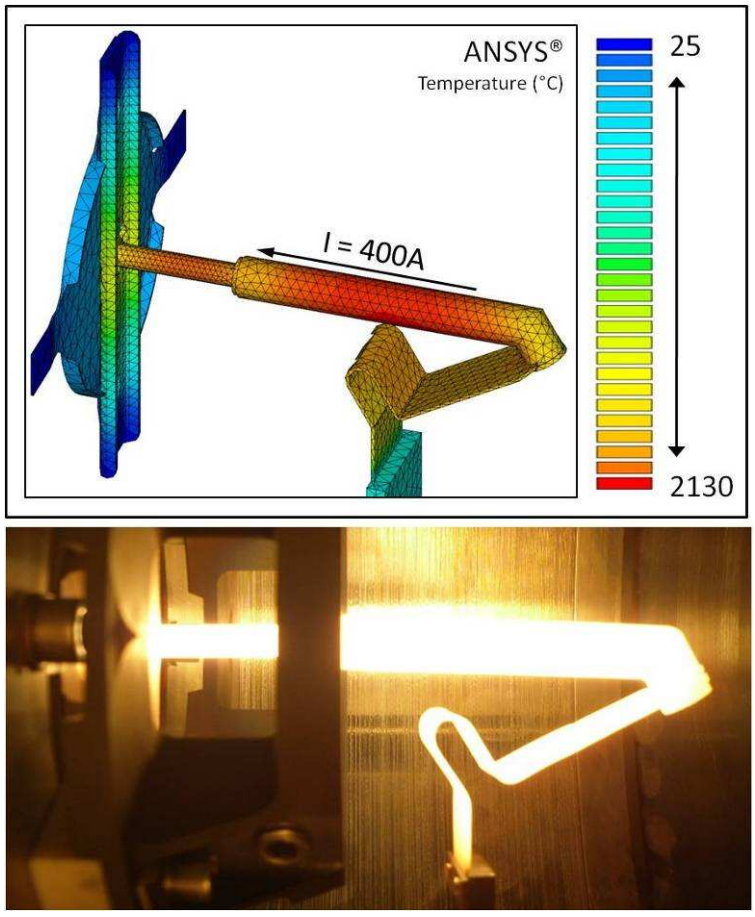

Fig. 4.30. FE temperature plot and correspondent picture of the optimized ion source – transfer line system.

In this case the new ion source – transfer line system was optimized in order to maximize first of all the temperature homogeneity and then the temperature level; in particular the global (related to both hot-cavity and transfer line) maximum temperature level was fixed in proximity of 2200°C, the limiting temperature for tantalum correspondent to the pressure level inside the target – ion source vacuum chamber. Tungsten, the high work function material at present chosen for the hot-cavity, can sustain higher temperatures, close to 2400 – 2500 °C, and it's not excluded in the future a new optimization process in order to maximize separately for the W hot-cavity and for the Ta transfer line both the temperature level and the temperature homogenisation. The following graph presents the temperature profiles along the two components calculated by the FE model for different current values; measured temperature data are also reported, showing a good agreement with theoretical ones. The current value chosen for high temperature functioning is 450A: it allows to reach the maximum temperature homogenization level at the higher sustainable temperature for the hot-cavity and transfer line complex (2200°C).

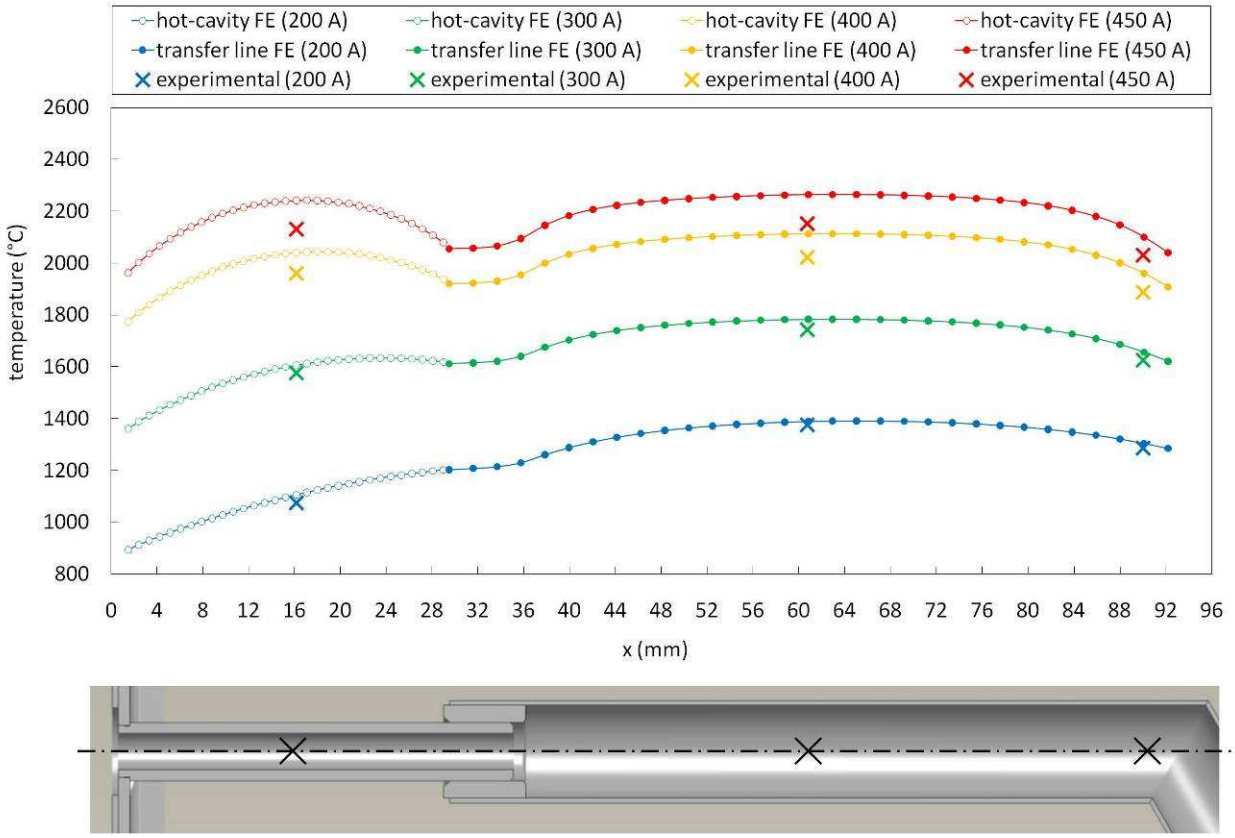

Fig. 4.31. Hot-cavity and transfer line temperature distributions as predicted by the FE analysis for 200, 300, 400, 450A of applied current and comparison with temperature measurements at three points.

Once presented the new hot-cavity and transfer line system it's very interesting to propose a small and brief comparison with its old design in order to underline the improvements and the changes introduced; for this purpose the reader is invited to observe figures 4.32 and 4.33. The

former shows the better temperature balance of the new design and the increased temperature level of the transfer line while the latter puts in evidence the electrical resistance rise introduced by the new thinner electrical connection and transfer line (see figure 4.16 and 4.29).

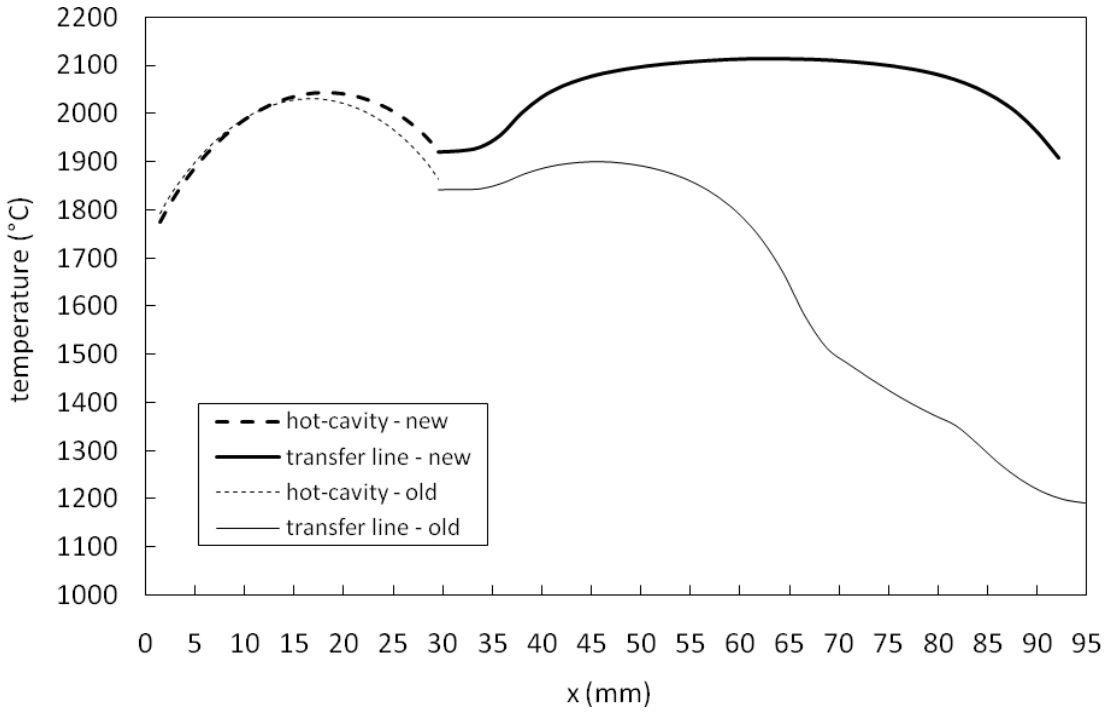

Fig. 4.32. Hot-cavity and transfer line temperature distributions correspondent to the old and the new designs (400 A of heating current).

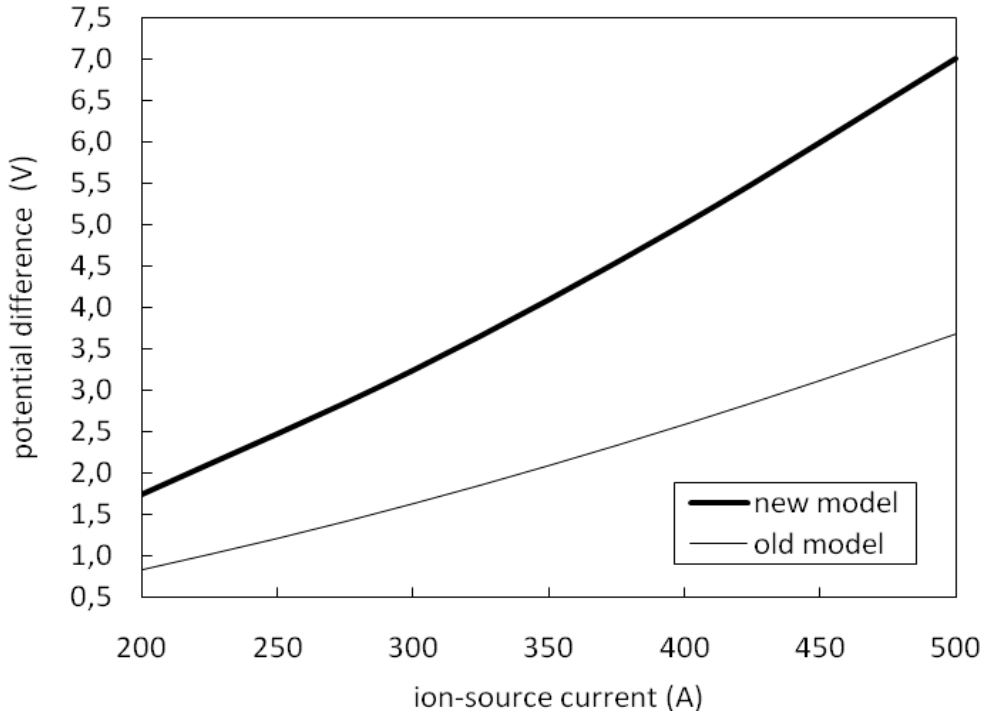

Fig. 4.33. Comparison between the potential difference values of the old and the new configurations.

Another important improvement introduced with the new design of the hot-cavity ion source and transfer line is the capability to limit thermal deformations in proximity of the connection between the Ta support and the W hot-cavity (see figure 4.13). This is the zone of the surface ion source where the beam forms and starts its propagation in the direction of the ground electrode (see figure 4.7): deformations in this zone are able to influence and change the beam emittance and its optical quality and consequently have to be kept under strict control. In the following figure it's possible to appreciate the permanent deformations of the Ta support in proximity of the connection with the W hot-cavity, for the old and the new designs.

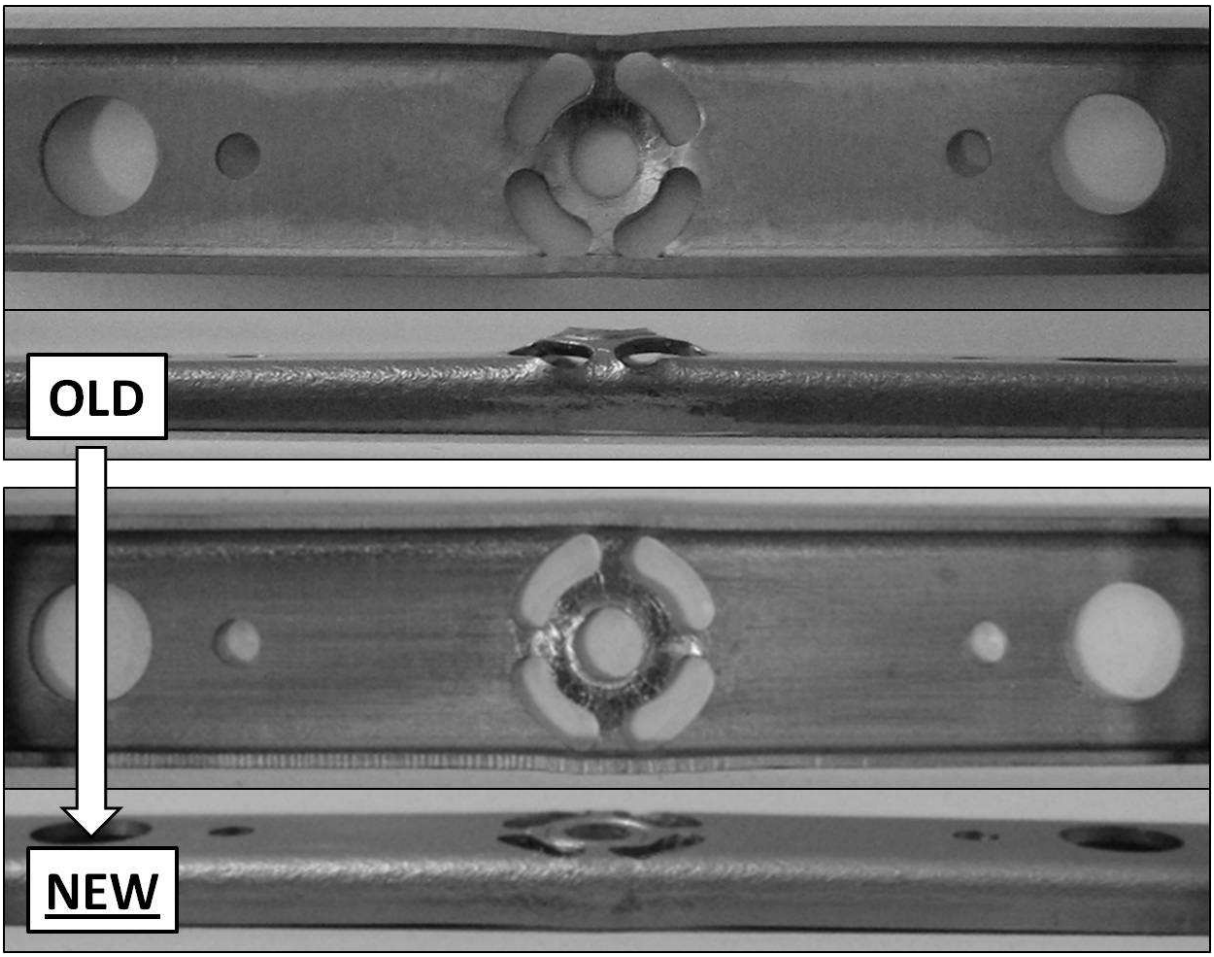

Fig. 4.34. Plastic deformations of the Ta support for the old and the new designs.

This important improvement was reached thanks to a new geometry for the Ta connector placed between the hot-cavity and the transfer line (see figure 4.13): observing figure 4.35 it's possible to notice in the new component the elimination of the internal stopping ring (with internal diameter equal to 4 mm) that in the old design opposed the hot-cavity's thermal dilatation producing a pronounced local plastic deformation at the interface between the hot-cavity and the support.

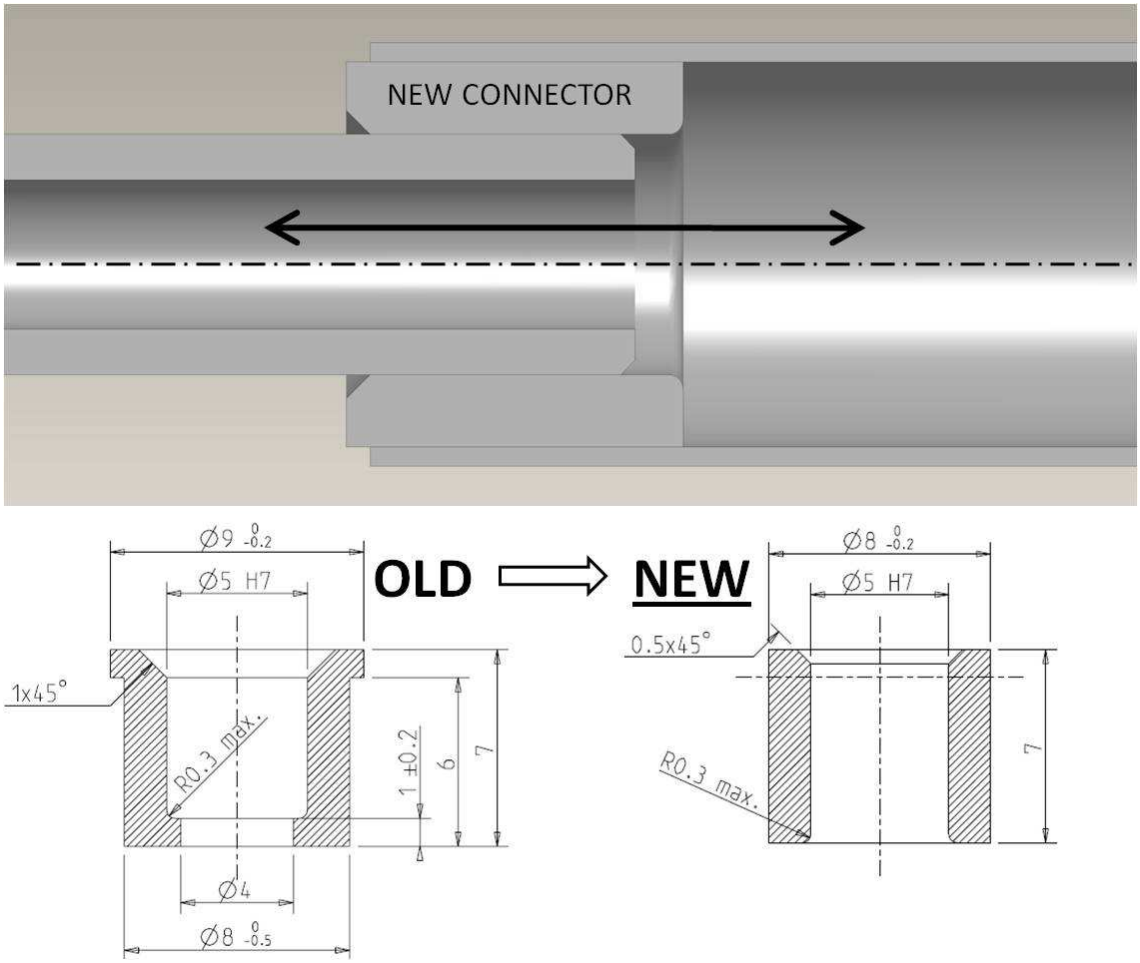

Fig. 4.35. The new connector between the hot-cavity and the transfer line (see figure 4.13).

Another important improvement introduced with the new design is the hot-cavity alignment system. In the previous paragraphs the implementation of the laser ionization technique in a hot-cavity was presented; it was seen that in this approach the system is in essence identical to a hot-cavity surface ion source: after diffusion in the target material and effusion towards the cavity, the atoms are kept in the gaseous phase in the hot-cavity and irradiated several times with the laser pulses. During the irradiation of the cylindrical volume closed inside the hot-cavity it is essential to keep it coaxial respect to the laser beam; at high temperature this is not easy at all and a dedicated alignment system was introduced. It is presented in figure 4.36 and its main components are: a round graphite frame, four centering adjustable tantalum bars and a series of Macor® insulators that sustain the graphite frame and avoid the current flow through the four tantalum bars.

It is important to underline another time that even if the grade of selectivity of photo ionization is very high, because of the high temperature of the hot-cavity isotopes of elements characterized by low ionization potential are ionized as well, leading to contamination; new cavity materials with lower work function to reduce surface ionization phenomena are under investigation; in particular in the previous paragraph the temperature field in the case of a tantalum (lower work function

respect to tungsten) hot-cavity was investigated. A new ion source dedicated to laser ionization will be optimized in the next future using the FE models previously described.

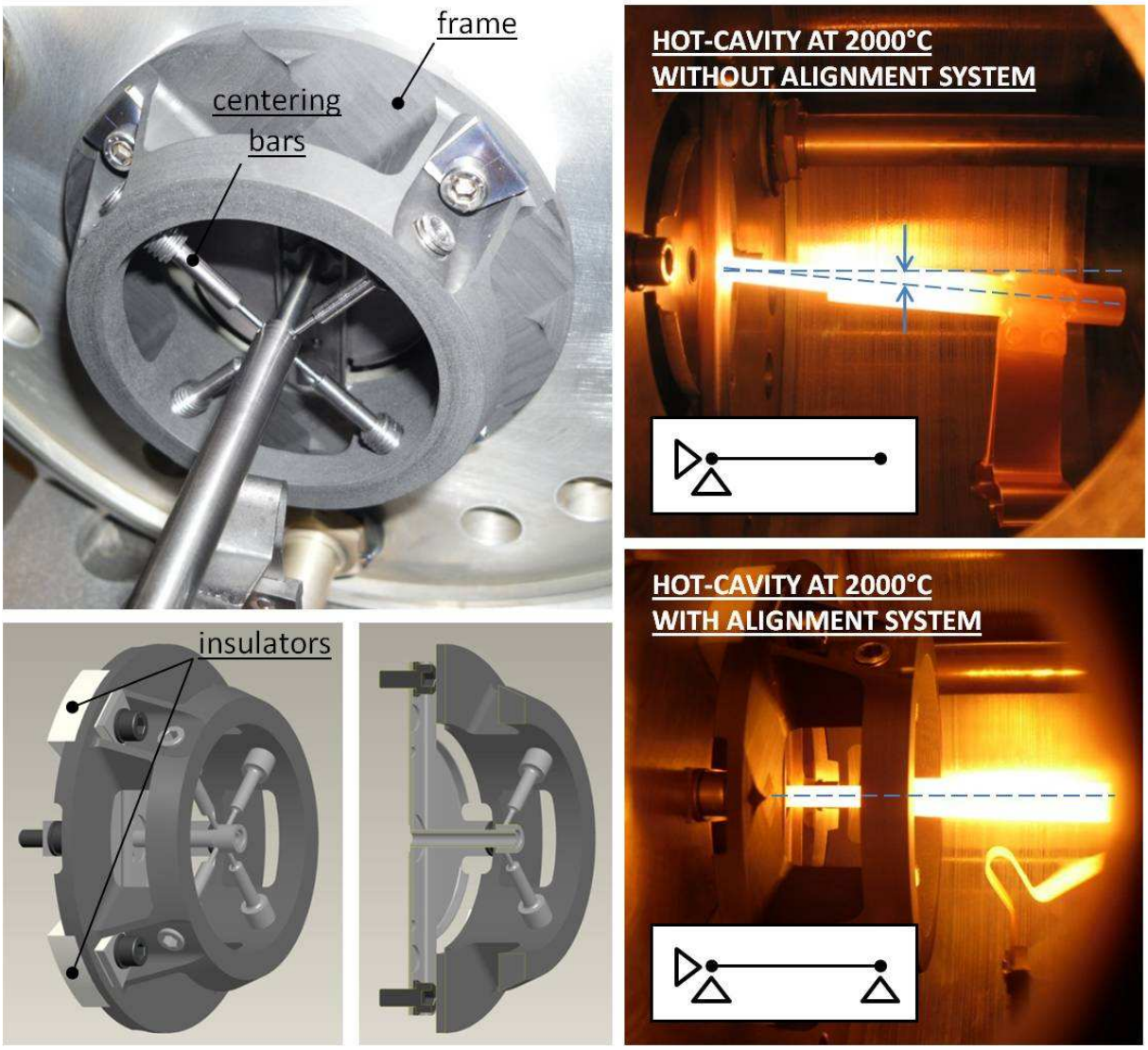

Fig. 4.36. The hot-cavity alignment system and its effect at high temperatures.

4.4.3. Preliminary study of the Ion Beam formation [22]

Once described the thermal and the mechanical study of the SPES hot-cavity ion source, in the present paragraph a preliminary and introductive description of the ion beam formation is presented. As mentioned in the previous paragraphs an ion source can be considered composed of two parts: a plasma generator (in our case the hot-cavity) that serves as an ion reservoir and an extraction system (in our case the extraction electrode) for accepting ions from the reservoir and forming an ion beam (see figure 4.37). In our case (positive surface ionization) the hot-cavity (plasma chamber) is kept at high voltage respect to the extraction electrode: the potential difference ($V_{\text{hot-cavity}} - V_{\text{extraction electrode}}$) fixed between the two aforementioned objects is approximately equal to 60 kV, a value sufficiently high to guarantee a good beam quality.

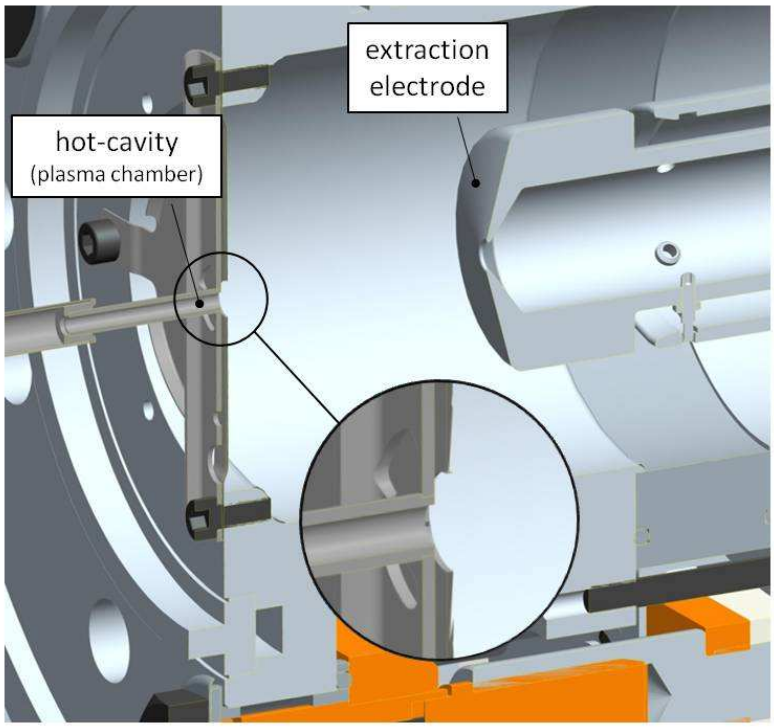

Fig. 4.37. The hot-cavity and the extraction electrode.

The preliminary study of the ion beam formation was realized using ANSYS®, the same FE code used for the thermal analyses described in the previous paragraphs. At first the electrostatic field between the hot-cavity and the extracting electrode was calculated using the element type SOLID123: this is a 3D, 10 node, charge-based electric element characterized by one degree of freedom, voltage, at each node.

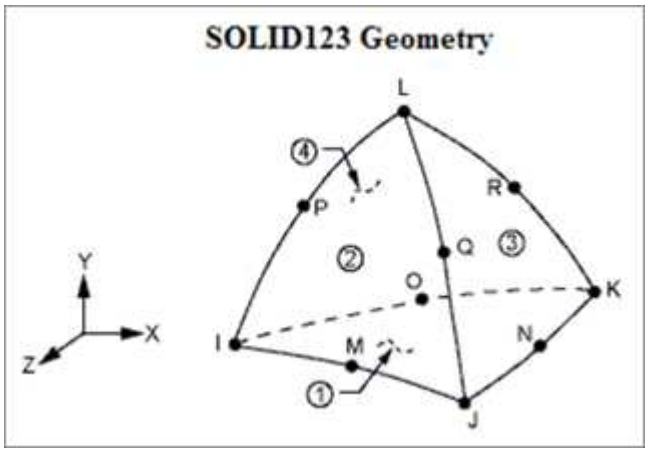

Fig. 4.38. The element type SOLID123.

Then, thanks to the ANSYS® Electromagnetic Particle Tracing [23], the trajectories of the charged particles were defined for different potential difference values. Before describing the main details of

the FE model and the obtained results, a brief presentation of the ANSYS® Electromagnetic Particle Tracing is given in the following.

In the most general case, once the electromagnetic field is computed, particle trajectories can be evaluated by solving the equations of motion:

$$m\{a\} = \{F\} = q(\{E\} + \{v\} \times \{B\}) \tag{4.14}$$

where:

m = mass of particle
q = charge of particle
{E} = electric field vector
{B} = magnetic field vector
{F} = Lorentz force vector
{a} = acceleration vector
{v} = velocity vector

The tracing procedure follows from element to element: the exit point of an old element becomes the entry point of a new element. Once known the entry location and velocity for an element, the exit location and velocity can be obtained by integrating the equation of motion. The ANSYS® Electromagnetic Particle Tracing exploits the following assumptions:

1. No relativistic effects (Velocity is much smaller than speed of light)
2. Pure electric tracing ({B} = {0}), pure magnetic tracing ({E} = {0}), or combined {E-B} tracing
3. Electrostatic and/or magnetostatic analysis
4. Constant {E} and/or {B} within an element
5. Quadrangle, triangle, hexahedron, tetrahedron, wedge or pyramid element shapes bounded by planar surfaces

In the present case pure electric tracing ({B} = {0}) is considered and in the following some details of the FE model used to simulate the beam formation between the hot-cavity and the extraction electrode are presented.

To evaluate the voltage distribution and the electrical field between the hot-cavity and the extraction electrode, their complementary volume (vacuum volume) was defined and modelled thanks to the CAD software Pro/Engineer® Wildfire 4.0 (see figure 4.39). Once defined the volume (the domain of the differential problem) and imported it in the ANSYS® environment, the only

property assigned was the electrical vacuum permittivity $\varepsilon_0 = 8.85\ 10^{-12}\ C^2/Nm^2$. At this point the SOLID123 mesh represented in figure 4.40 was generated.

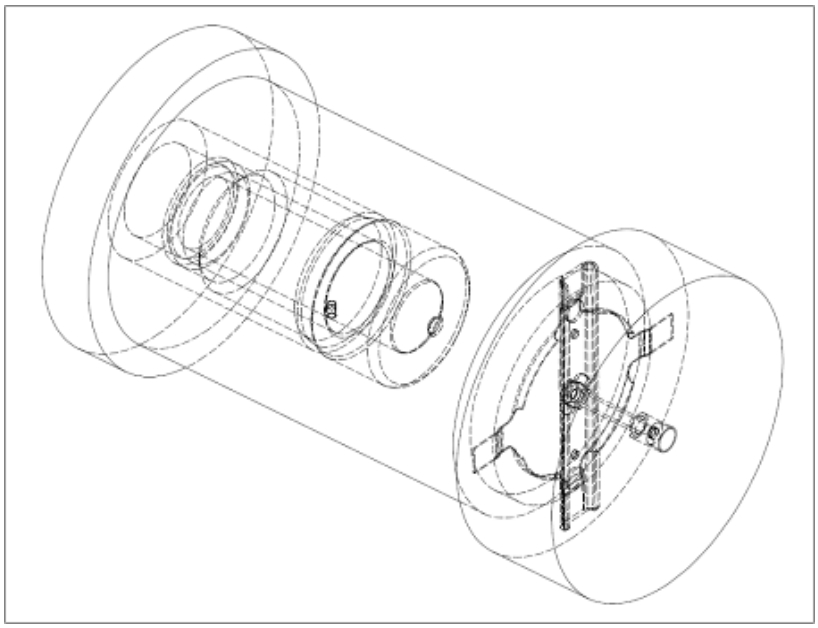

Fig. 4.39. CAD model of the vacuum volume between the hot-cavity and the extraction electrode.

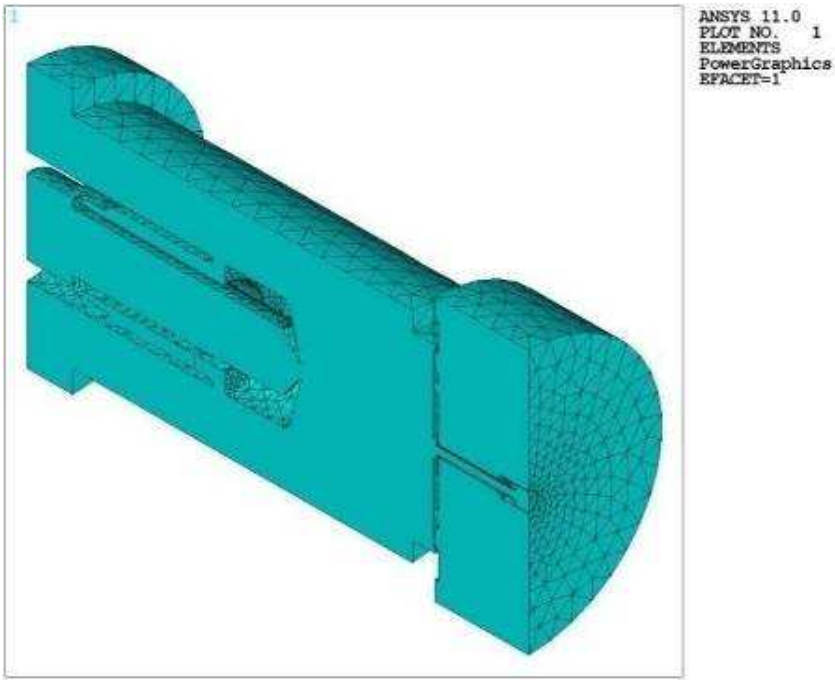

Fig. 4.40. SOLID123 mesh of the vacuum model.

To maintain a continuity with the thermal-electric model of the ion source presented in the previous paragraphs, the nodal voltage constraints in proximity of the ion source's surfaces were assigned considering the results of the analyses described in paragraphs 4.4.1 and 4.4.2. For the extraction electrode the voltage constraint was assigned with steps of 5 kV, with potential difference ($\Delta V = V_{hot\text{-}cavity} - V_{extraction\ electrode}$) values ranging from 5 to 60 kV. Once obtained the

solutions (voltage and electric field distributions) the trajectories of the radioactive isotopes in the vacuum volume were calculated for everyone of the potential difference values imposed; in particular 50 (maximum number of particles that the FE code adopted is able to consider) ^{136}Cs isotopes were introduced in the domain (we remark that in its stable form, caesium has atomic number $Z = 55$ and number of neutrons $N = 78$), with initial positions (X, Y, Z) homogeneously distributed in the volume enveloped by the internal hot-cavity's walls, and with the specification for every isotope of the following important features:

- Initial velocity (V_X, V_Y, V_Z) equal to zero
- Mass equal to $136 \times p = 2.274767416 \cdot 10^{-25}$ *kg* (being the proton mass $p = 1.6726231 \cdot 10^{-27}$ *kg*)
- 1+ charge state, so an electric charge of $1.602 \cdot 10^{-19}$ *C*

The following figures report the results of the performed set of analyses in terms of electrical field (V/m), voltage distribution (V) and isotopes trajectories.

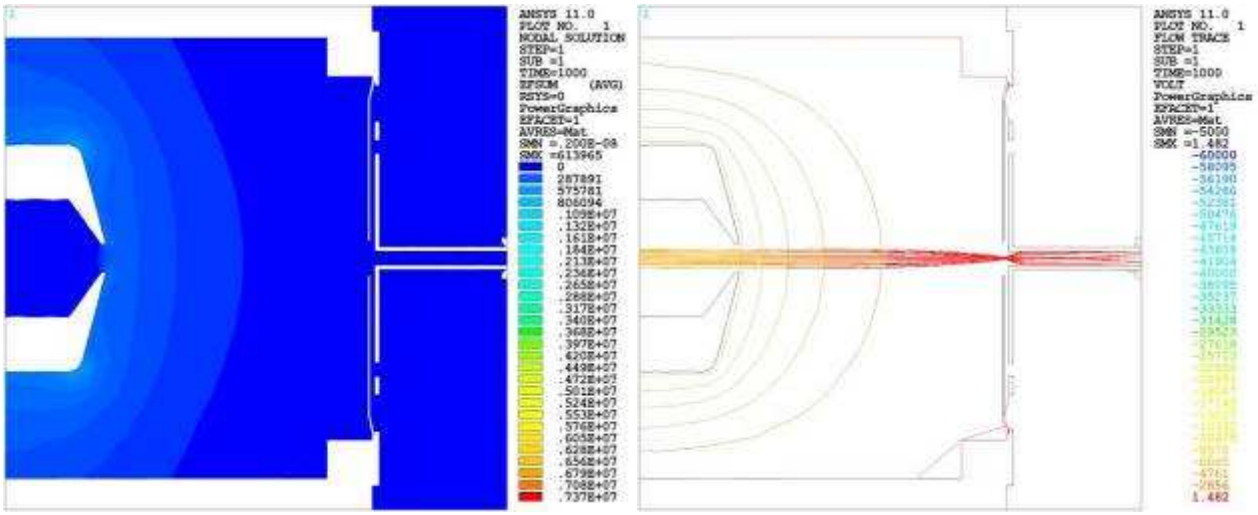

Fig. 4.41. Electrical field (V/m), voltage distribution (V) and isotopes trajectories for ΔV = 5 kV.

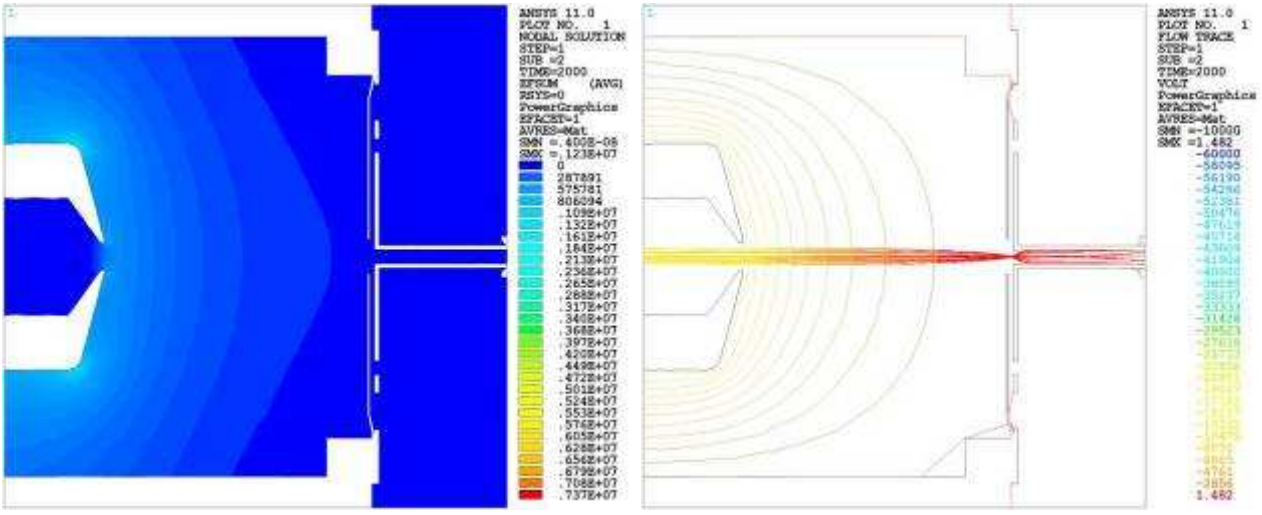

Fig. 4.42. Electrical field (V/m), voltage distribution (V) and isotopes trajectories for ΔV = 10 kV.

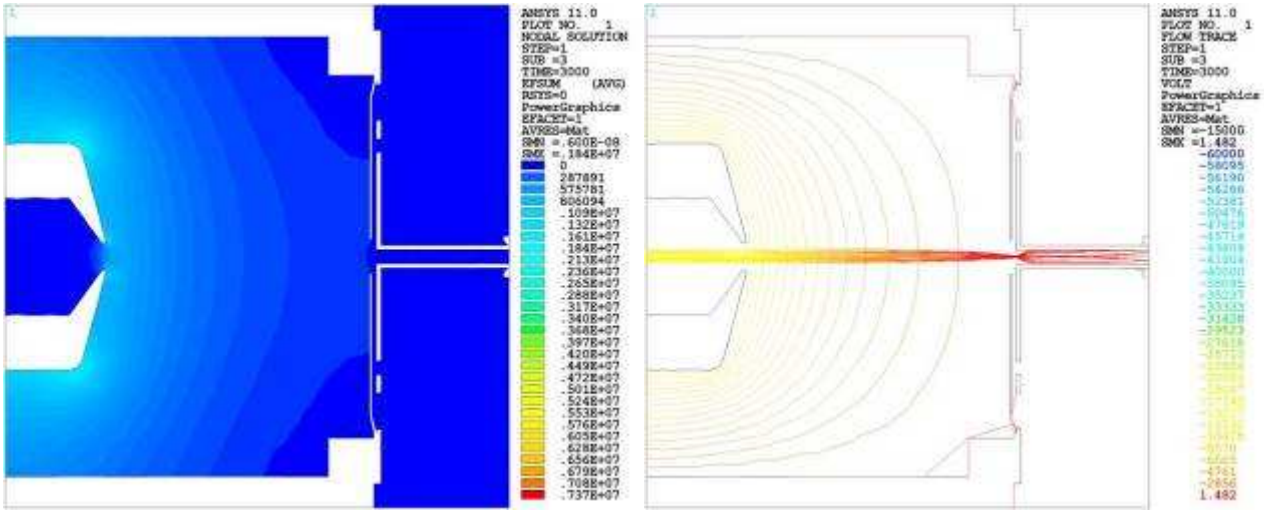

Fig. 4.43. Electrical field (V/m), voltage distribution (V) and isotopes trajectories for ΔV = 15 kV.

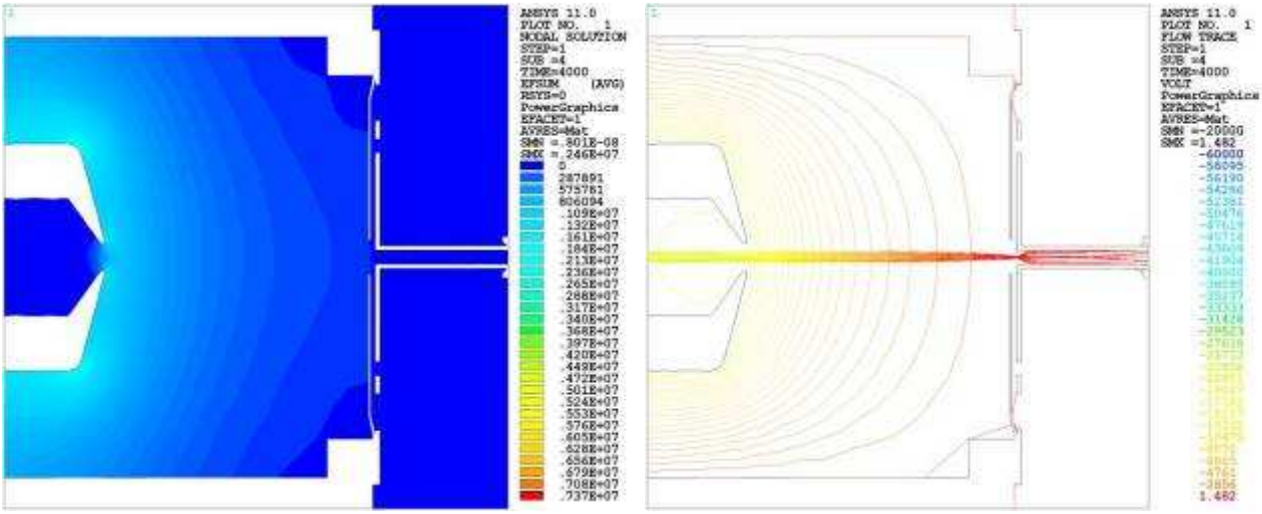

Fig. 4.44. Electrical field (V/m), voltage distribution (V) and isotopes trajectories for ΔV = 20 kV.

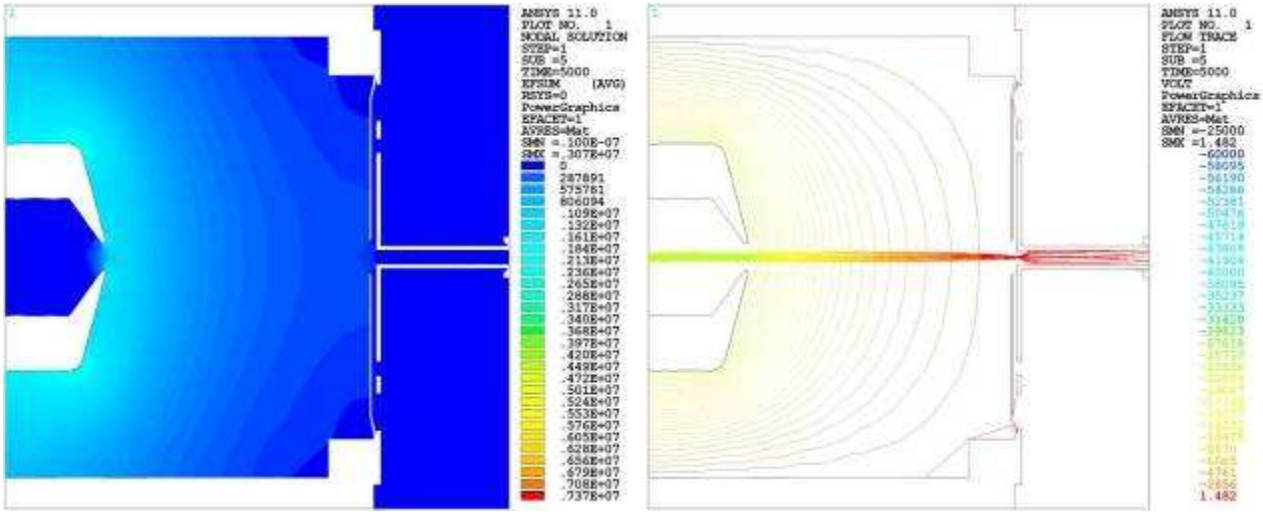

Fig. 4.45. Electrical field (V/m), voltage distribution (V) and isotopes trajectories for ΔV = 25 kV.

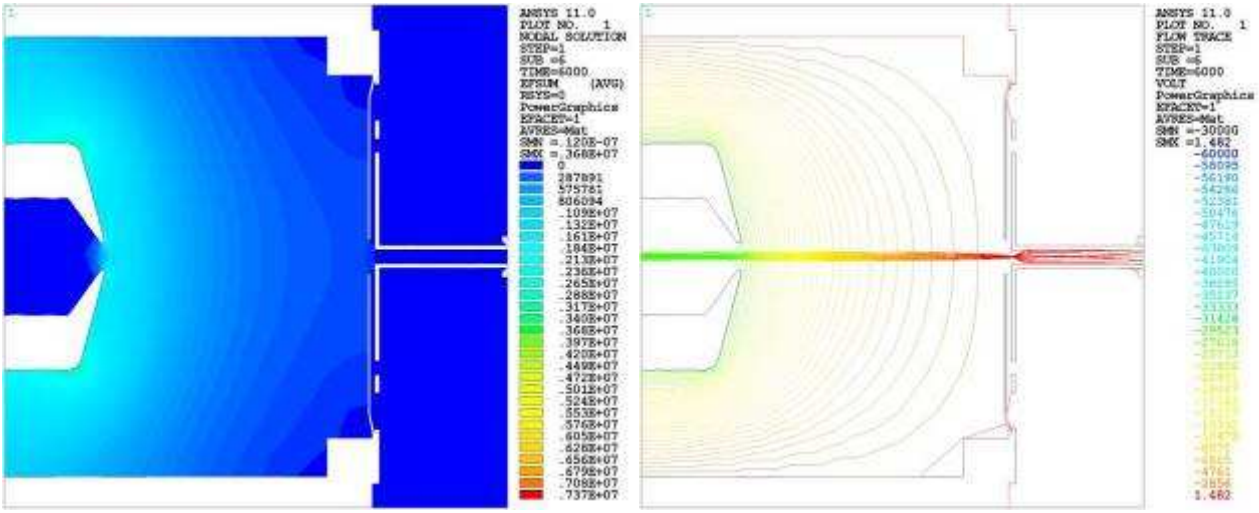

Fig. 4.46. Electrical field (V/m), voltage distribution (V) and isotopes trajectories for ΔV = 30 kV.

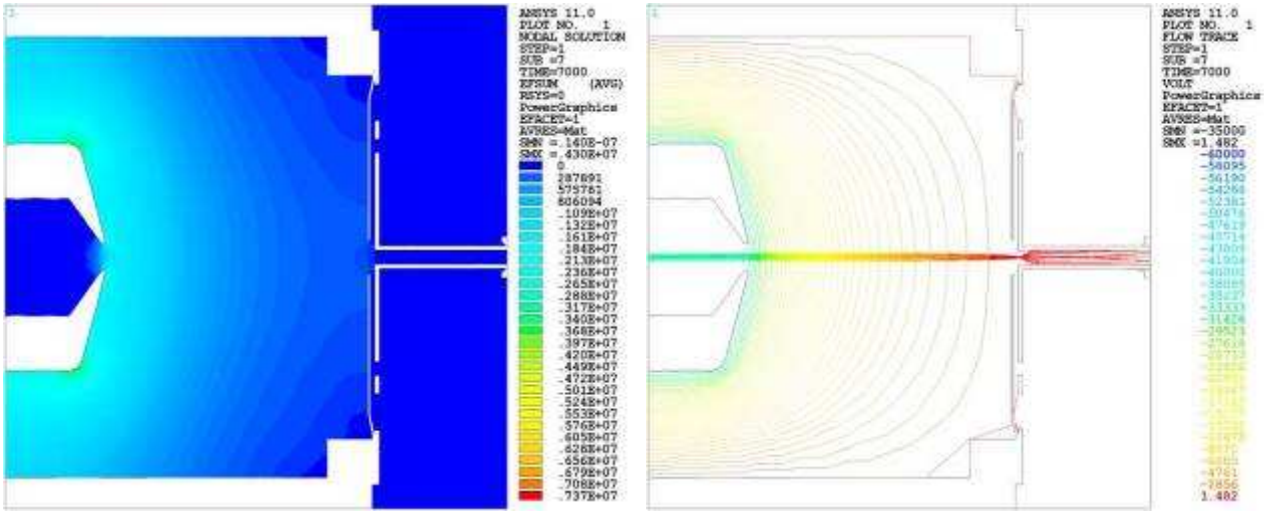

Fig. 4.47. Electrical field (V/m), voltage distribution (V) and isotopes trajectories for ΔV = 35 kV.

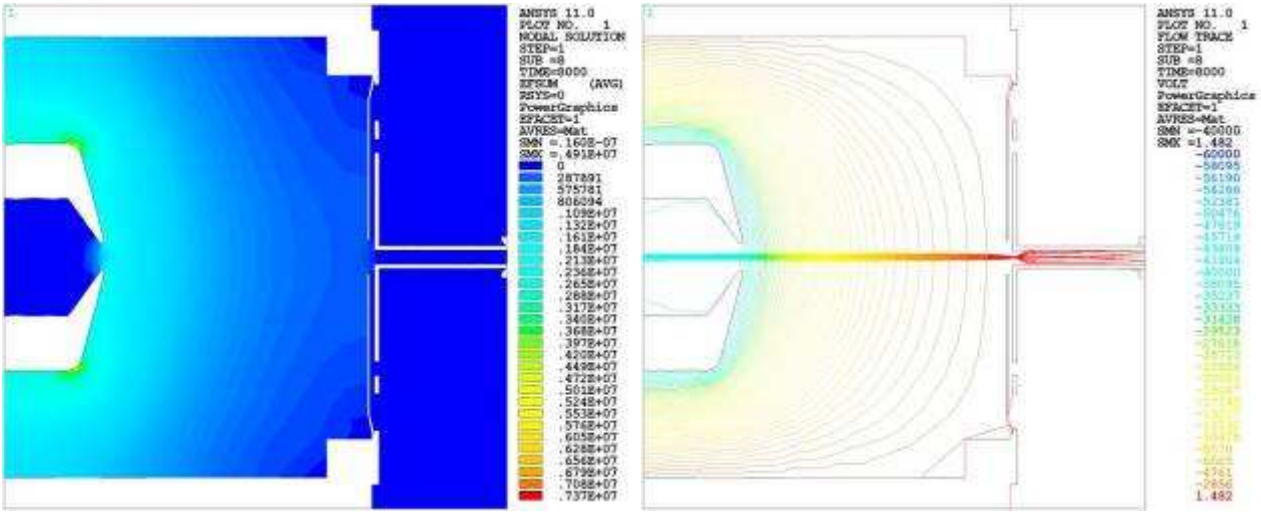

Fig. 4.48. Electrical field (V/m), voltage distribution (V) and isotopes trajectories for ΔV = 40 kV.

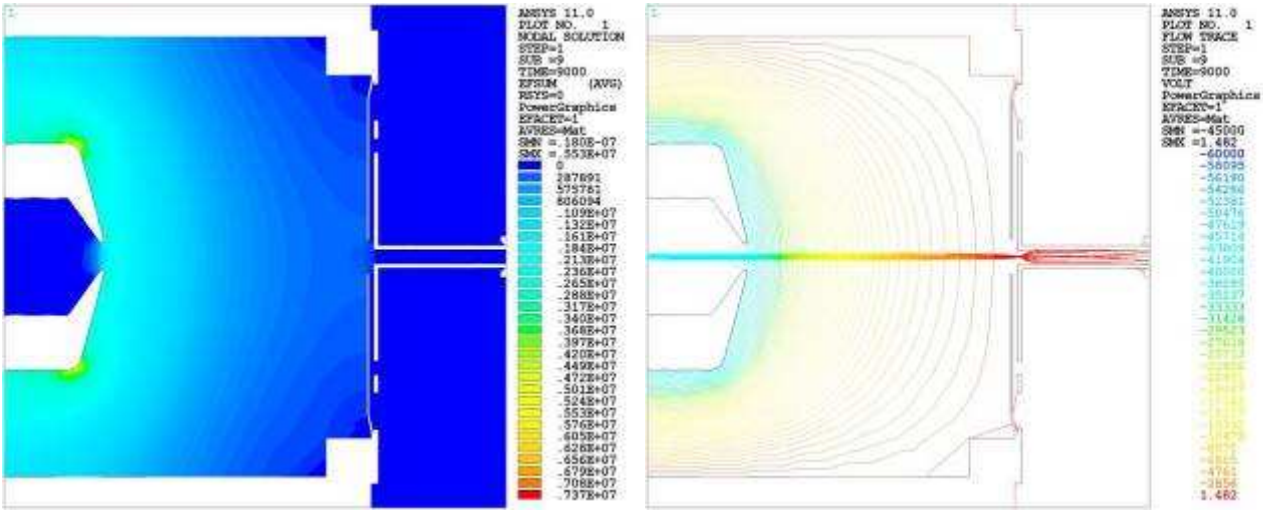

Fig. 4.49. Electrical field (V/m), voltage distribution (V) and isotopes trajectories for ΔV = 45 kV.

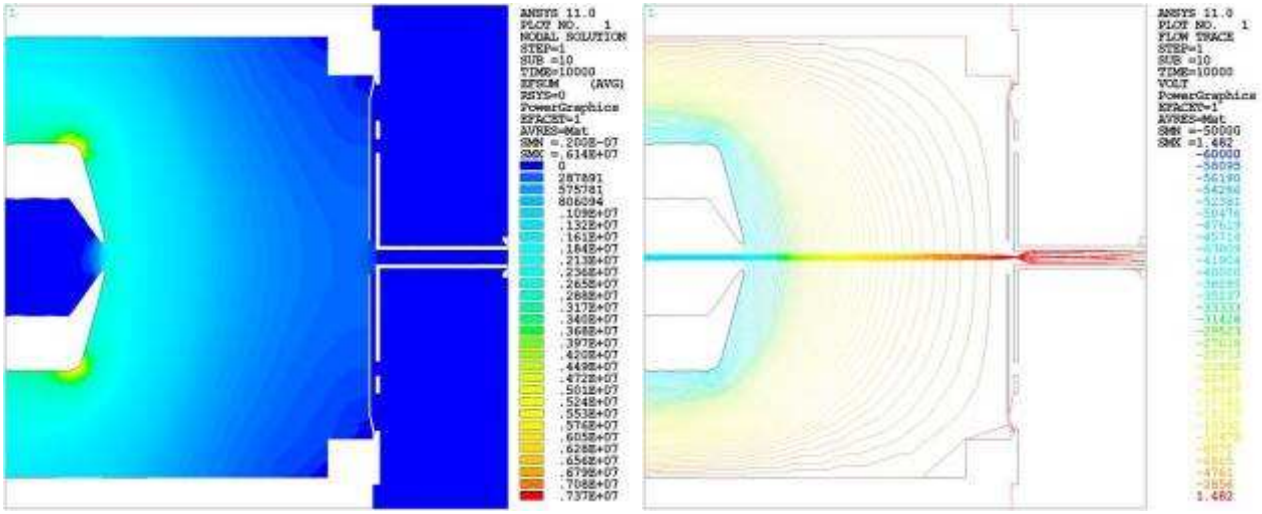

Fig. 4.50. Electrical field (V/m), voltage distribution (V) and isotopes trajectories for ΔV = 50 kV.

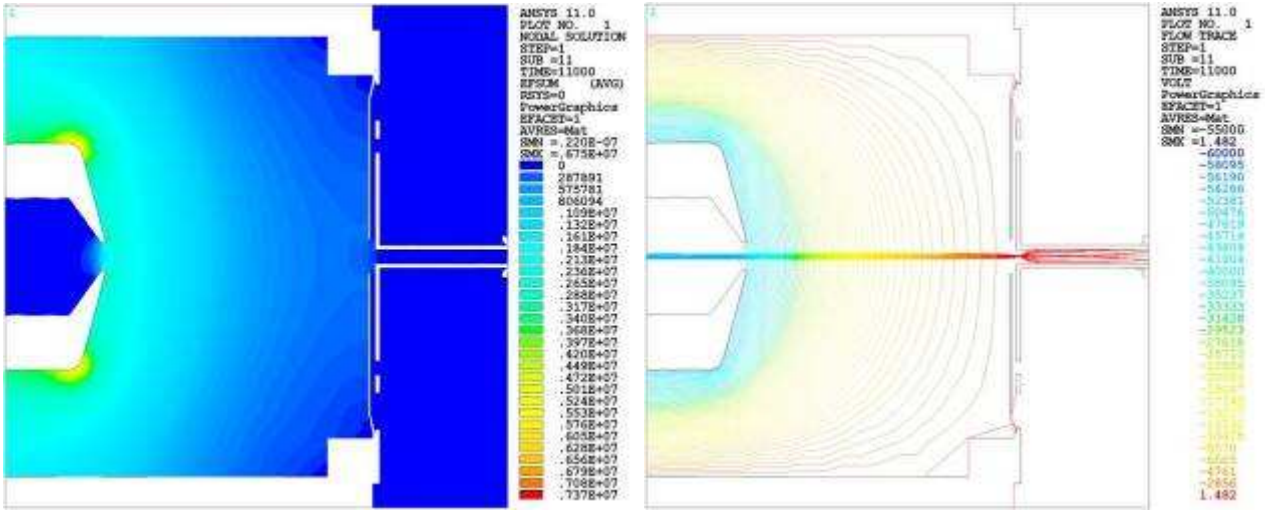

Fig. 4.51. Electrical field (V/m), voltage distribution (V) and isotopes trajectories for ΔV = 55 kV.

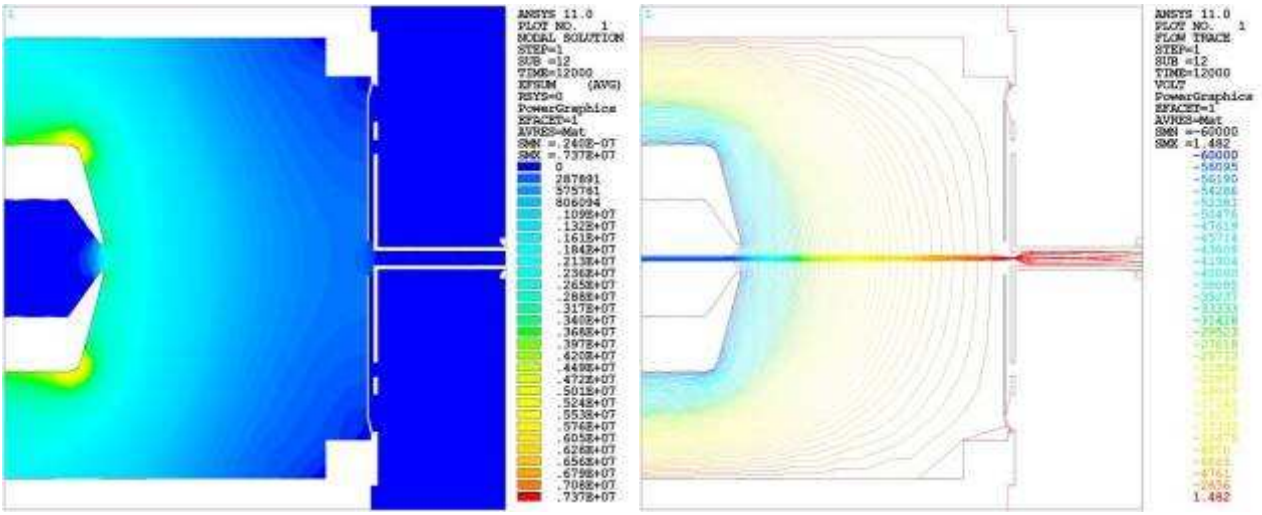

Fig. 4.52. Electrical field (V/m), voltage distribution (V) and isotopes trajectories for ΔV = 60 kV.

Observing the obtained results it is possible to appreciate the increasing of the electric field intensity with the raise of the potential difference $\Delta V = V_{\text{hot-cavity}} - V_{\text{extraction electrode}}$, in particular in proximity of sharp tips; higher ΔV values lead also to a progressive tight compression of particle trajectories and so, to a progressive improvement of beam quality. The ANSYS® code offers also the possibility to monitor the particle's velocity along its trajectory and in principle the beam emittance can be calculated; nevertheless the reliability of such an emittance value is not complete and the main limits are:

- only 50 particles can be included in the numerical model (in the real device the rate of particles that can be accelerated by the extraction electrode is approximately equal to 10^9 particles/s)
- calculations doesn't take into account the effect that the beam has on the electrical field (see figure 4.8 and 4.9)

In the following figures (4.53 and 4.54) a comparison with a finite difference code dedicated to the study of ion sources (Kobra3-INP) is presented: observing figure 4.53 it is possible to appreciate a substantial coherence between Kobra3-INP and ANSYS®, whereas figure 4.54 puts in evidence a lower peak value for the electrical field calculated by Kobra3. It is important to remark that in the Kobra3 model the geometry was considered for simplicity axial symmetric and the set of results was obtained without considering the effect of the beam on the potential distribution and on the electrical field [24].

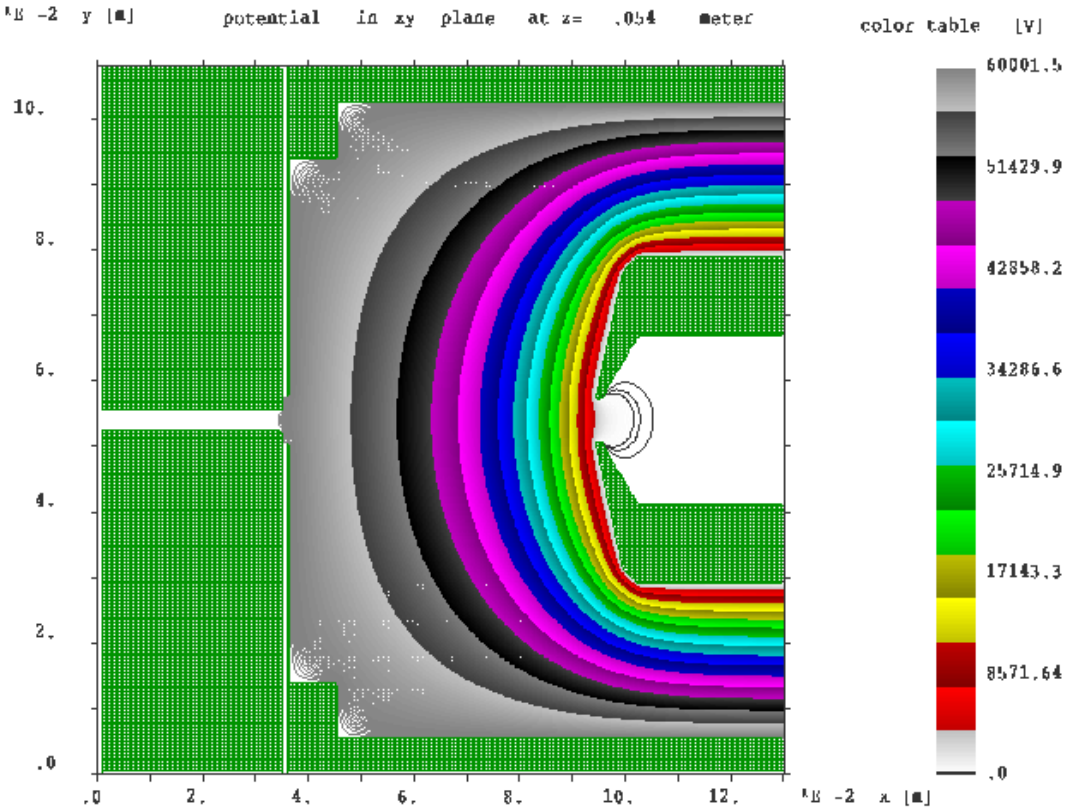

Fig. 4.53. Voltage or Potential distribution (V) for ΔV = 60 kV calculated by Kobra3.

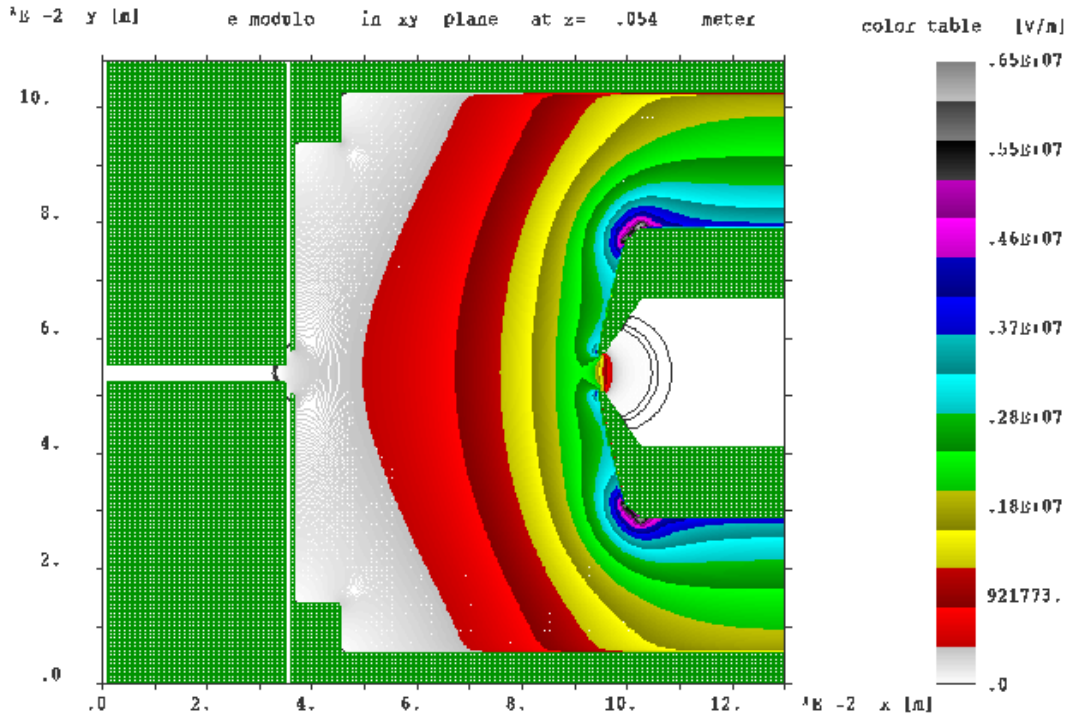

Fig. 4.54. Electrical field (V/m) for ΔV = 60 kV calculated by Kobra3.

In any case the Kobra3 code has a huge number of interesting features to study the behavior of ion sources and beam formation: it is possible for instance to estimate automatically the emittance of a particular beam (see figures 4.55 and 4.56) and the effect of the ion beam on the electric field.

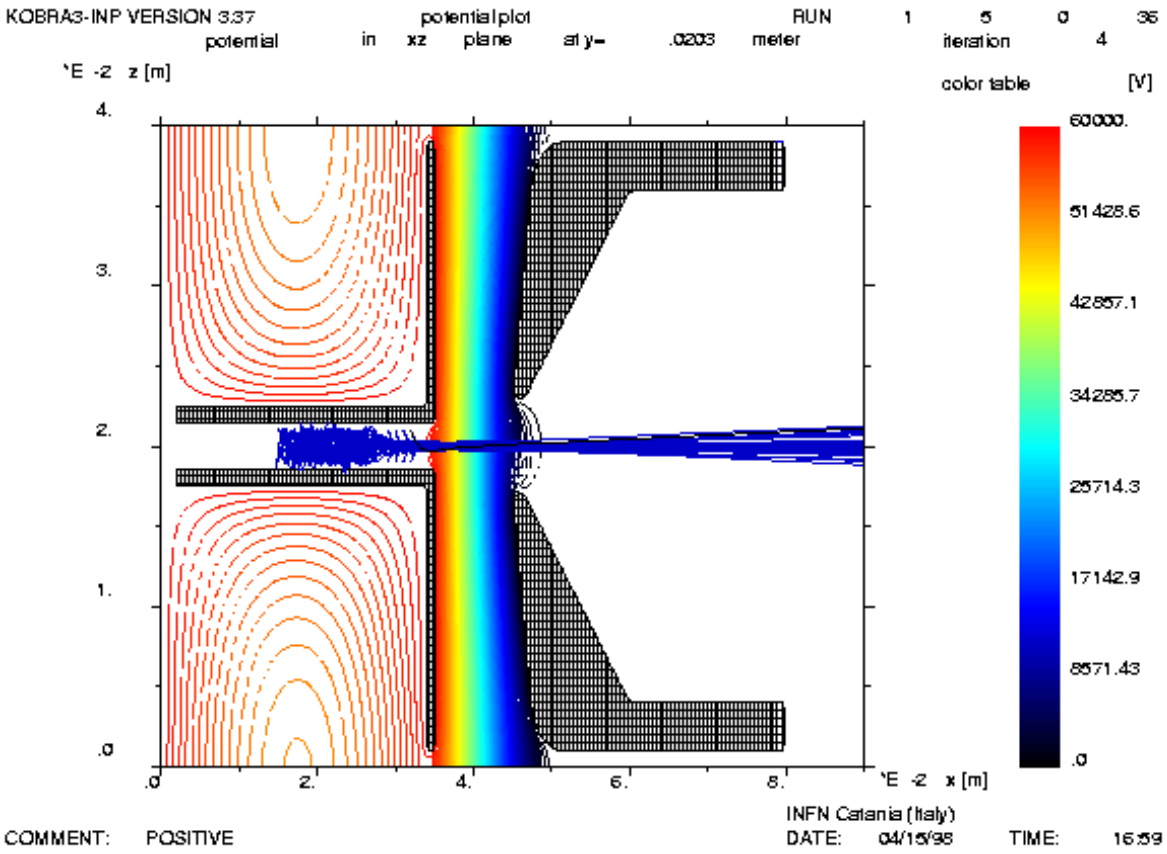

Fig. 4.55. Potential distribution (V) and particle trajectories for ΔV = 60 kV and a ^{21}Na ion beam calculated by Kobra3[25].

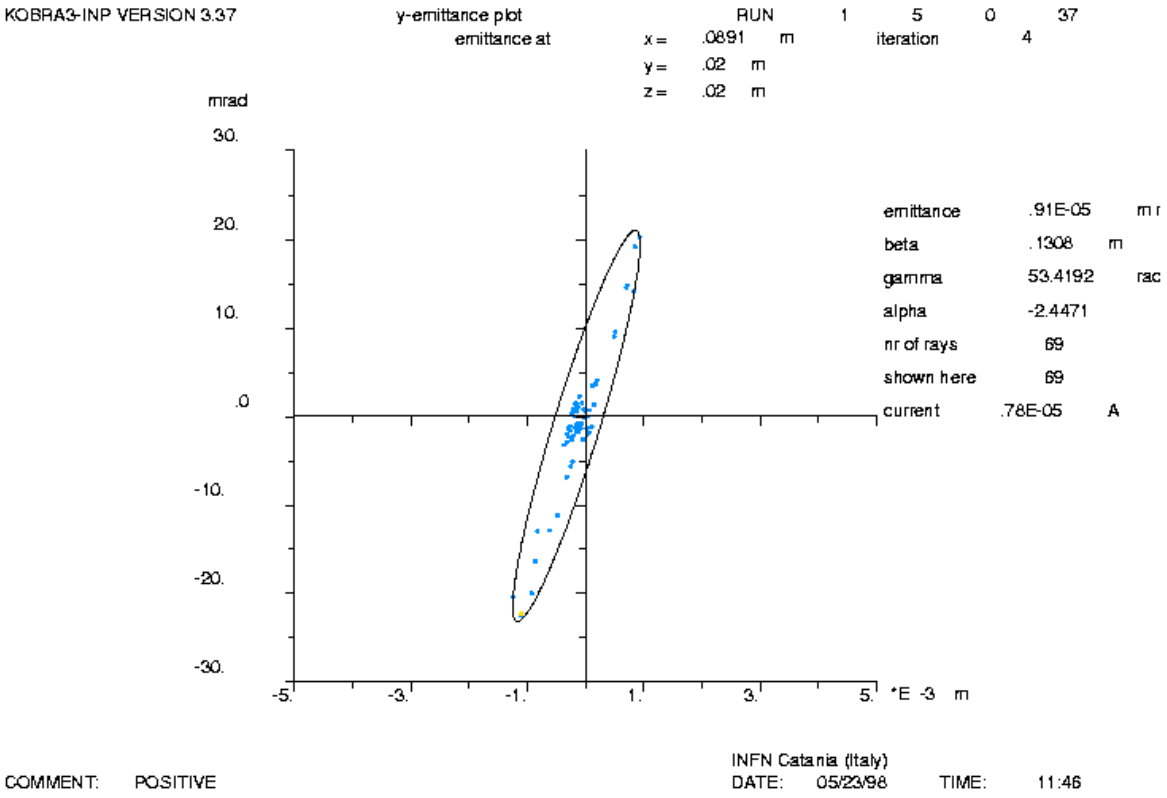

Fig. 4.56. Beam emittance aestimation for ΔV = 60 kV and a ^{21}Na ion beam calculated by Kobra3.

4.5. The SPES High Temperature Plasma Ion Source [26]

As mentioned in paragraph 4.3.2 in high temperature plasma ion sources the electron impact ionization mechanism is used to ionize the atoms that are present in the gas phase inside the ion source; the most successful and widely used High Temperature Plasma Ion Source is the forced-electron beam induced arc-discharge (FEBIAD) ion source. This ionizing device is not selective at all and at ISOLDE (CERN) the transfer line used to connect the production target with the ion source is cooled in order to improve the system's selectivity: in this way isotopes of less volatile elements adsorb on the transfer tube's walls while isotopes from gaseous elements or gaseous molecules reach the ion source. Using this technique very pure beams of noble gas isotopes can be produced. Figure 4.57 presents the beams that can be produced at ISOLDE using a FEBIAD ion source with three different configurations for the transfer line.

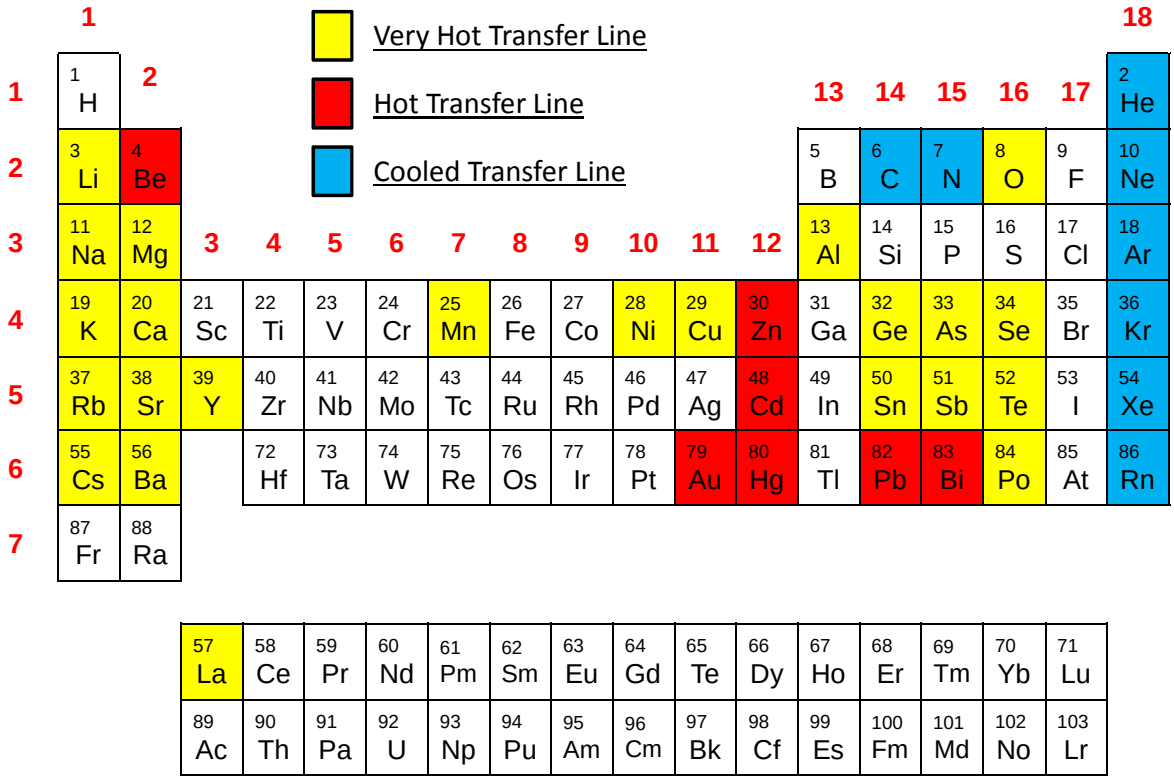

Fig. 4.57. Beams produced at ISOLDE using the FEBIAD ion source: three different transfer line's configurations are available in order to improve the system's selectivity.

At present, the FEBIAD ion source taken as reference for the SPES project is the MK5 ion source developed at ISOLDE; its study is in progress at Legnaro National Laboratories (LNL) and a new version is under discussion considering some features of the FEBIAD ion source used at Holifield Radioactive Ion Beam Facility (HRIBF, USA) and the results of the tests performed at

LNL. In the following a detailed presentation of the R&D activities developed at LNL on FEBIAD ion sources is reported.

4.5.1. The MK5 FEBIAD ion source functioning

Before starting to describe the MK5 source's components and functioning it is important to know its position inside the vacuum chamber: for this purpose it is sufficient to observe figure 4.58. The MK5 ion source is connected to the production target thanks to the transfer line and is positioned within the vacuum chamber's flange, facing the extraction electrode; two Al tapes are wrapped on the external surface of the flange (see figure 4.59) and thanks to the electrical current flowing through them a magnetic field is generated in the zone of the ion source.

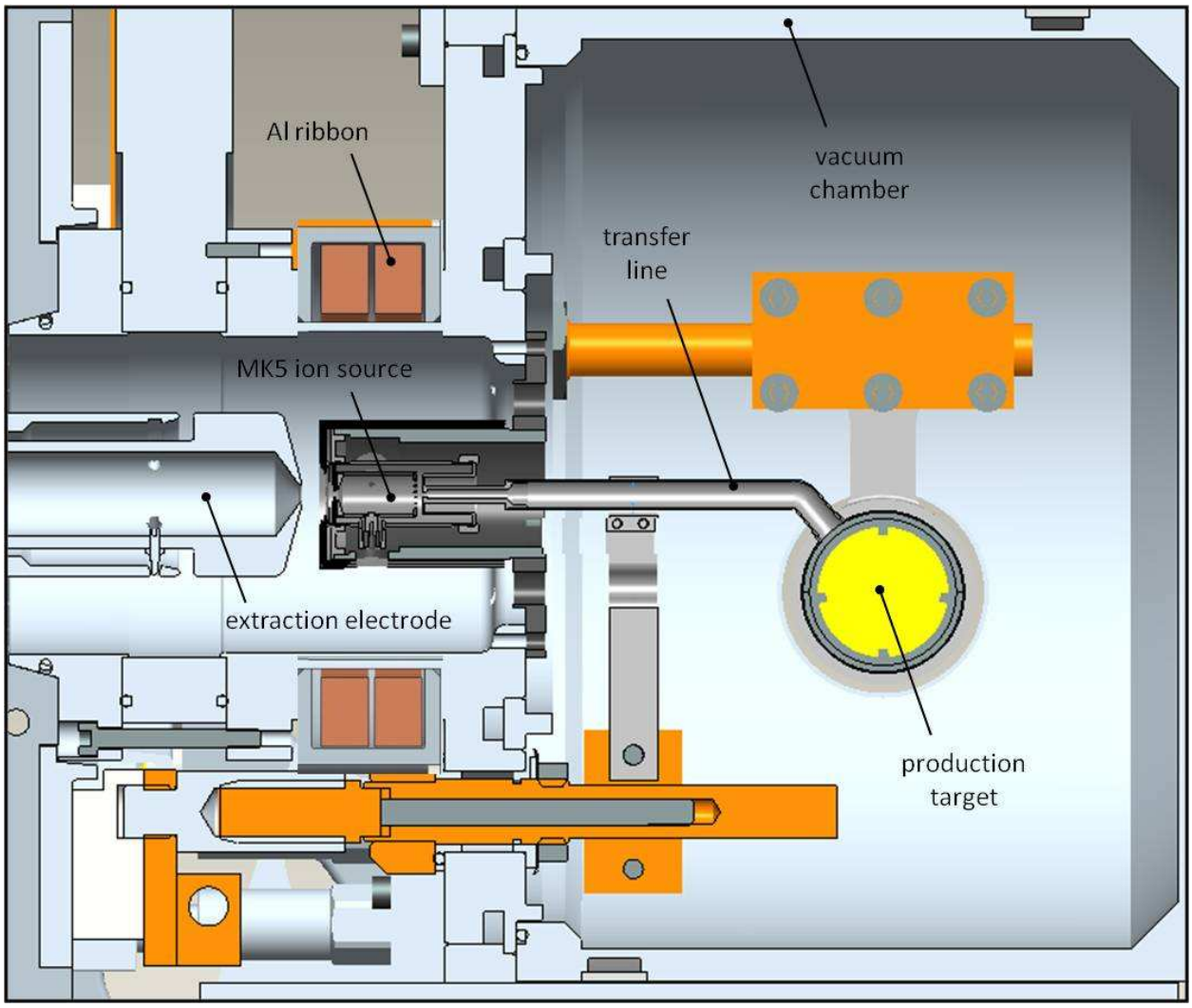

Fig. 4.58. The MK5 ion source and the objects surrounding it.

The MK5 ion source and its main components are presented in figures 4.60 and 4.61. Its functioning is more complex respect to the previously described SPES surface ion source and consequently some considerations are needed to understand how it works and to appreciate the R&D activities below described.

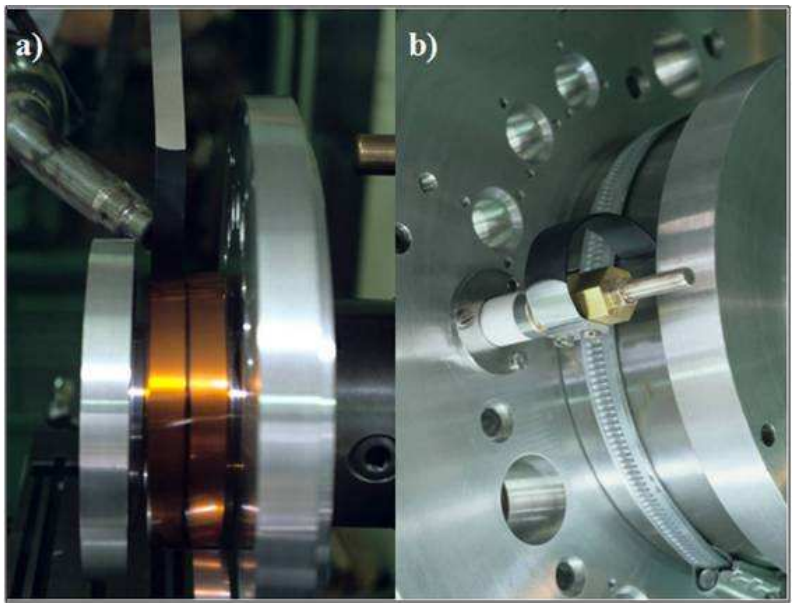

Fig. 4.59. a) The wrapping procedure of the Al ribbon; b) Al ribbons installed on the vacuum chamber's flange and detail of their electrical connection.

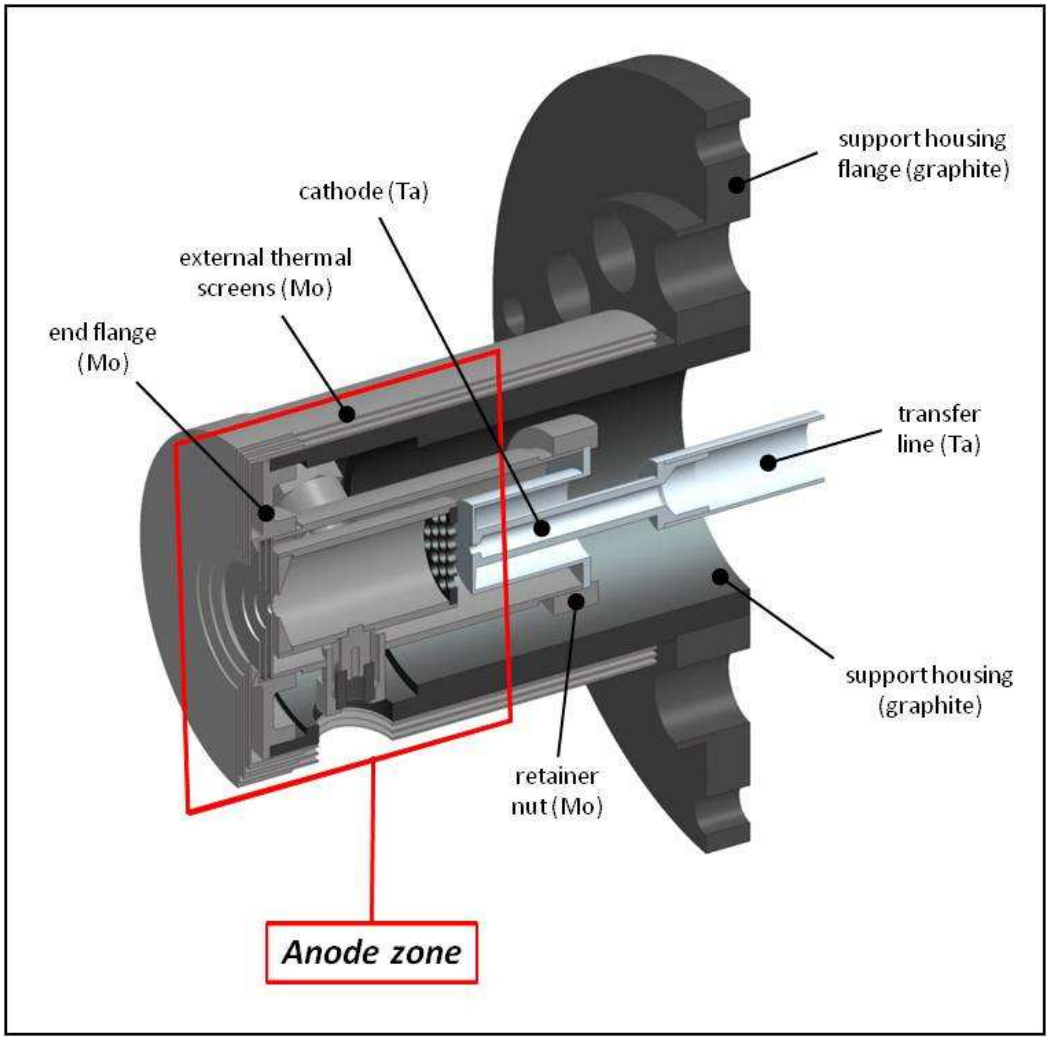

Fig. 4.60. Section view of the FEBIAD MK5 ion source developed at ISOLDE (CERN) and adopted in the context of the SPES project as reference high temperature plasma ion source.

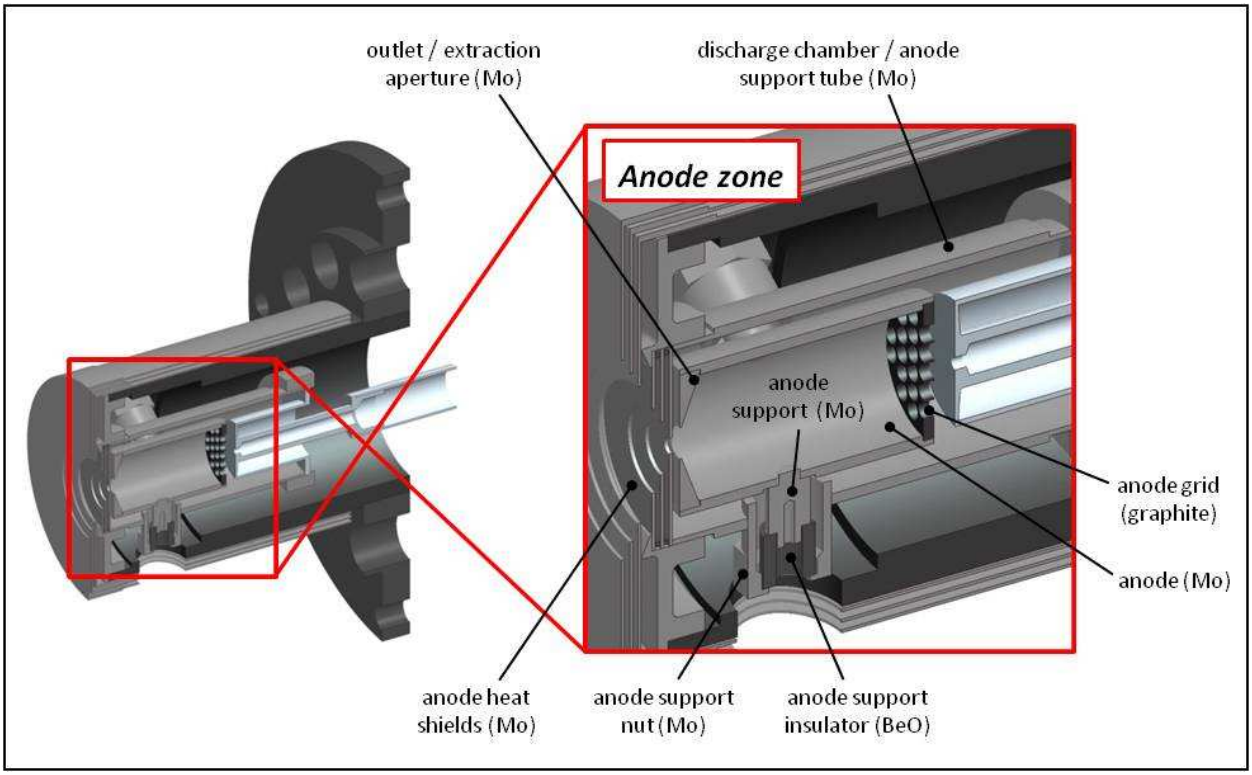

Fig. 4.61. Detailed section view of the “anode zone” of the FEBIAD MK5 ion source.

The first thing to underline and put in evidence is the fact that, like the production target and the surface ion source, also the MK5 ion source is kept at high temperature thanks to Joule effect; in figure 4.62 the schematization of the correspondent electrical loop is presented.

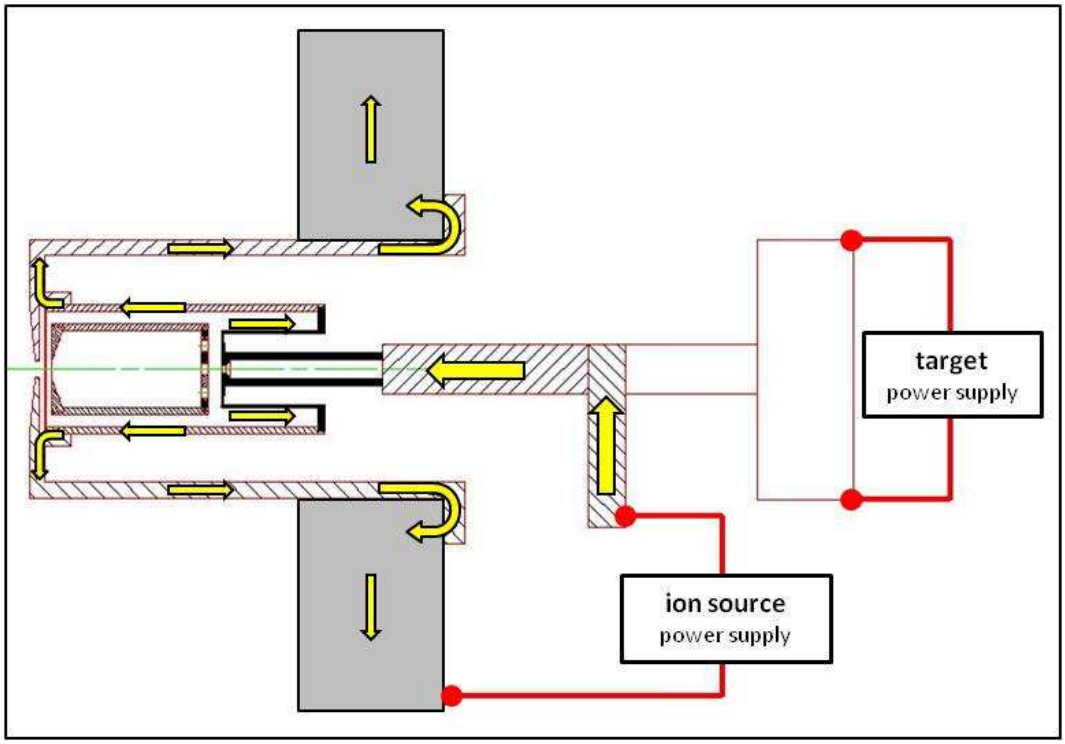

Fig. 4.62. The electrical loop used to heat the MK5 ion source.

When heated at high temperatures the Ta cathode starts to emit electrons (thermionic emission) [27] from the circular surface facing the anode grid. As shown in figure 4.61 the anode assembly is electrically insulated (BeO insulators) respect to the source's components surrounding it and a metallic wire (usually made of tantalum), connecting the anode's bush to an independent and dedicated power supply, maintains the anode assembly at the potential value of + 150 V. In this way the electrons emitted by the cathode are attracted by the anode and the ones that are able to pass through the anode grid enter inside the anode chamber with an energy level approximately equal to 150 eV. The anode chamber is full of radioactive isotopes coming from the production target: they pass through the transfer line and the cathode cavity before entering; once bombarded by the energetic electrons they are ionized according to the aforementioned (paragraph 4.2.2) Electron Impact Ionization mechanism generating the plasma. In front of the anode's Mo outlet (the opposite side of the anode assembly respect to the cathode) an extraction electrode is positioned (see figure 4.58): its negative potential (~ -60 kV) respect to the anode allows the ion beam to originate. As represented in the following figure, the magnetic field produced by the Al ribbons (called also magnets) surrounding the chamber's flange modifies the trajectories of the energetic electrons: the typical helicoidal path improve the interaction with the cloud of isotopes contained in the anode chamber. This high temperature ion source has been used for the production of elements with low vapor pressure values.

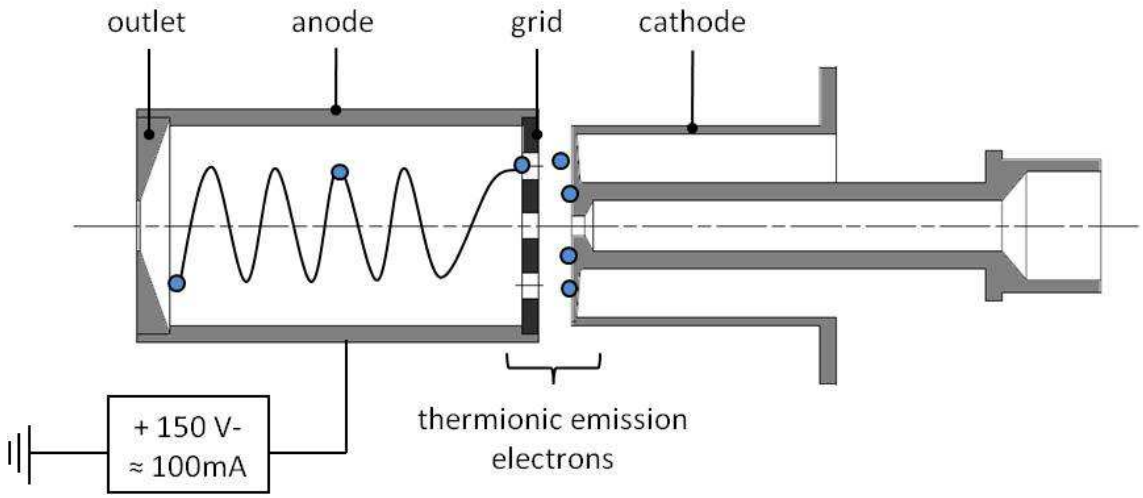

Fig. 4.63. The electrons emitted by the cathode and their path inside the anode chamber.

Even if in this work only the high temperature MK5 ion source is studied and tested, at ISOLDE two further FEBIAD ion source models are used to improve the selectivity of the RIBs production process: the medium temperature MK6 ion source and the low temperature MK7 ion source. They are briefly presented in the following taking as reference a paper written by S. Sundell and H. Ravn in 1992 [28].

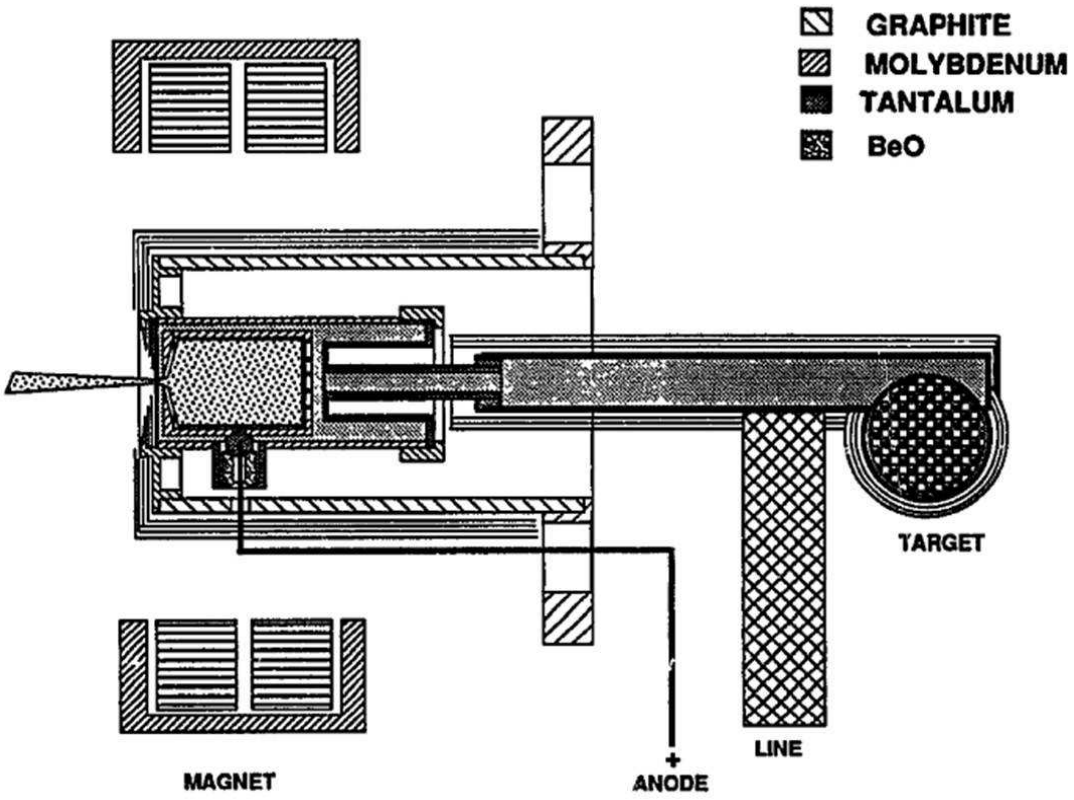

Fig. 4.64. High temperature FEBIAD ion source MK5 (ISOLDE-CERN): maximum working temperature approximately equal to 1900°C [28].

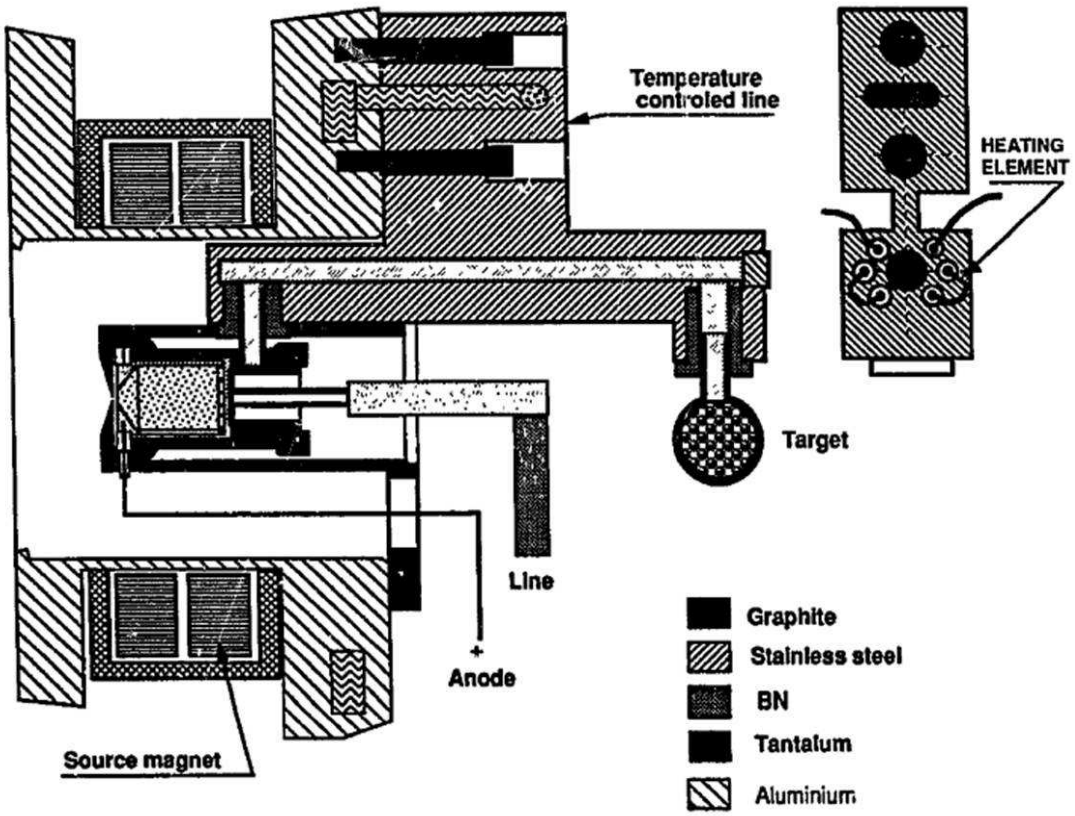

Fig. 4.65. Medium temperature FEBIAD ion source MK6 (ISOLDE-CERN): maximum working temperature approximately equal to 1400°C [28].

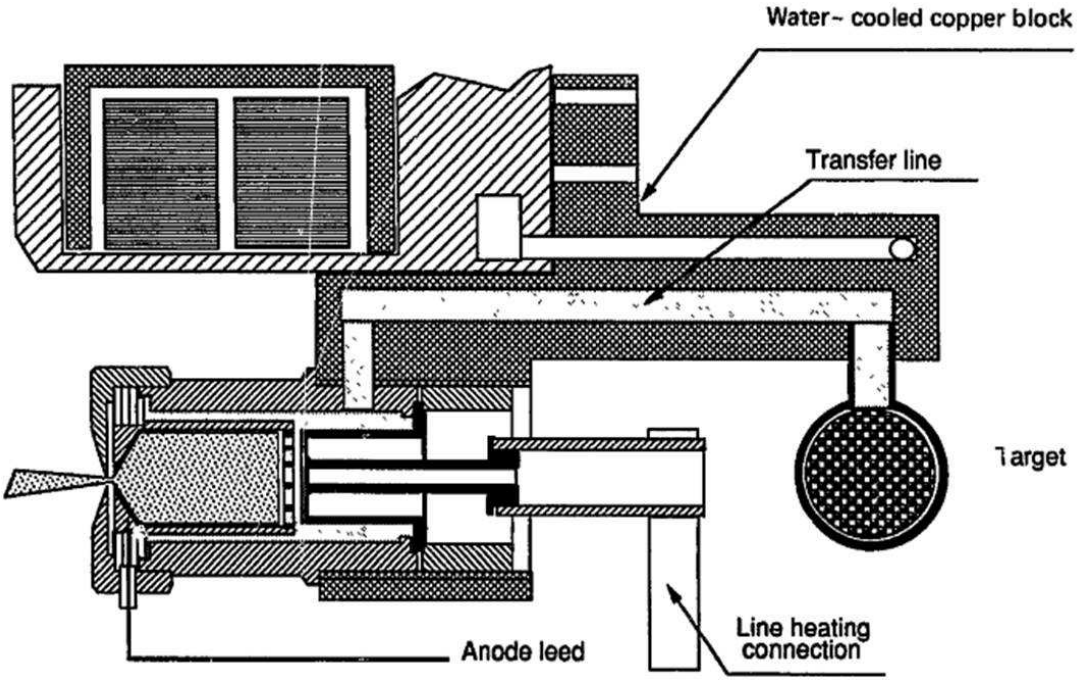

Fig. 4.66. Low temperature (water-cooled) FEBIAD ion source MK7 (ISOLDE-CERN): maximum working temperature approximately equal to 500°C [28].

In the MK6 source the discharge chamber (see figure 4.61) is made of graphite, the anode can be made of molybdenum or graphite and thanks to the lower temperature range respect to the MK5 source, boron nitride (BN) instead of beryllium oxide (BeO) can be used for the insulators. The cathode doesn't present the hole in proximity of the anode interface since the radioactive isotopes pass in this case through the temperature controlled transfer line represented in figure 4.65: it consists of a stainless steel block heated by means of a 0.8 mm Ta wire inserted in its lower part. Using this device the temperature can be varied from 200 to 400°C. This ion source has been used for the production of elements with intermediate to low vapor pressure.

The MK7 source's architecture can be appreciated in figure 4.66; this source is dedicated to noble gases (high vapor pressure) and its design is clearly oriented to keep the temperature as low as possible; also in this case the anode is made of molybdenum and a water-cooled copper block acts as source holder and transfer line. The temperature of the discharge chamber (see figure 4.61) is approximately equal to 500°C and that of the water-cooled transfer line is about 50°C: in this way elements that may be condensed are stopped contributing to purify the RIB of interest. Contrary to MK5 and MK6, the cathode heating current doesn't flow through the discharge chamber, but directly to the copper block.

4.5.2. Thermal study of the MK5 ion source: numerical calculations and experimental tests

Once explained the way the MK5 source works, in this section both the numerical model and the set of experimental tests performed to study the MK5 thermal and electrical behaviour are presented.

The results obtained from the numerical FE model are then compared with thermal and electrical experimental measurements.

Numerical model. With the clear purpose to limit the complexity of the numerical model, the geometry of the MK5 source and of the related auxiliary components were simplified as shown in figure 4.67. For the same reasons presented in the case of the SPES hot-cavity ion source (see paragraph 4.4.1) the vacuum chamber was not modelled and a perfect electrical and thermal contact was considered between all modelled components. Also in this case only the transfer line and the electrical connection are welded to each other and behave similarly to a perfect thermal and electrical contact. All the other joints are realized by means of screws, bolts and mechanical interferences, making less consistent the hypothesis of perfect thermal and electrical contact.

The three-dimensional FE model of the MK5 source was created according to the numerical techniques presented in paragraph 4.4.1 in occasion of the thermal-electric study of the hot-cavity ion source; it is shown in figure 4.67 with a schematic representation of the DOF constraints and loads applied.

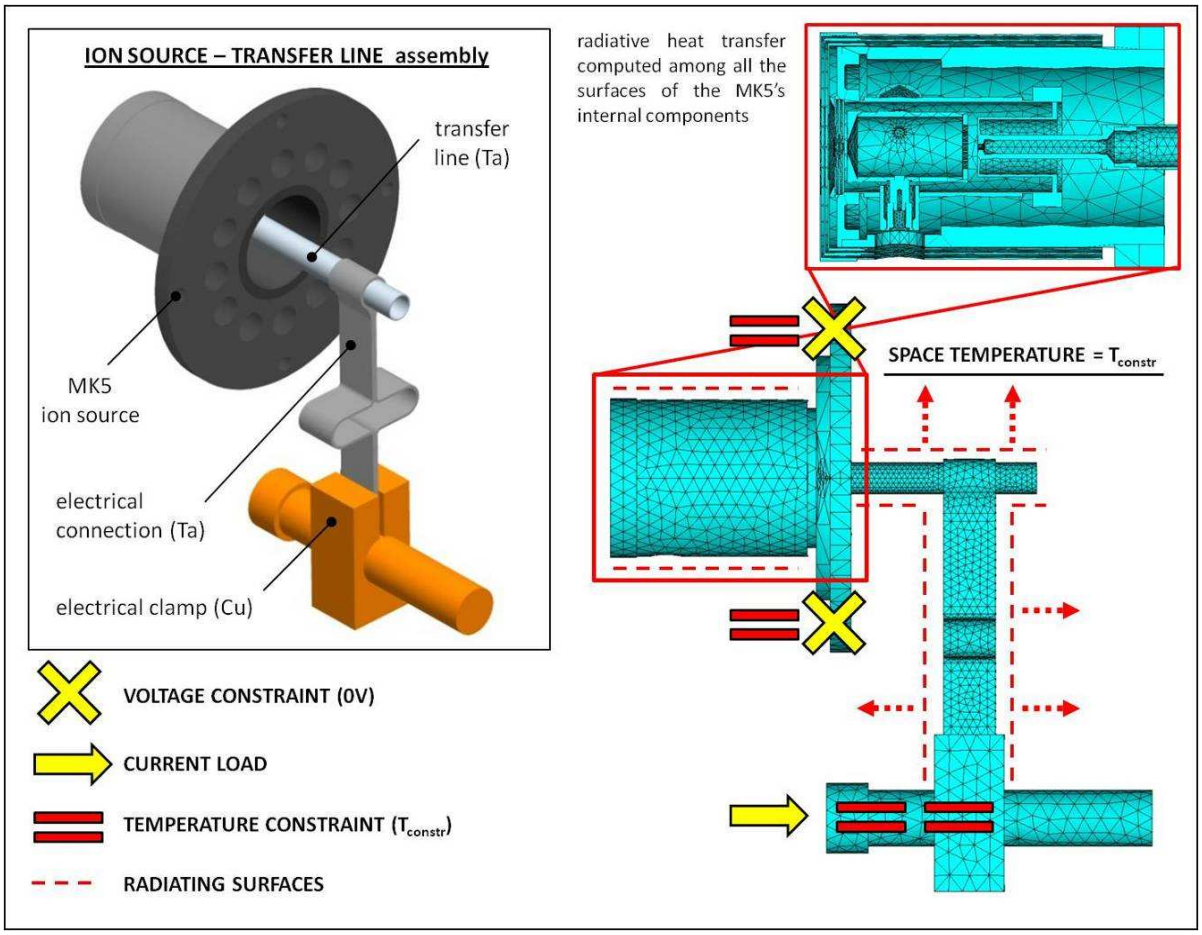

Fig. 4.67. DOF (Degree Of Freedom) constraints and loads applied to the FE thermal-electric model.

Starting with the description of the electric problem, a constraint of 0 V was assigned to the surfaces of the support housing flange (see figures 4.60 and 4.67) in direct contact with the vacuum chamber's baser plate (see figure 4.11) supporting the MK5 source; a current load was assigned to the round surface of the electrical clamp's extremity. Talking about the thermal problem's boundary conditions, a temperature constraint T_{constr} of 25°C was assigned to the same surfaces where a potential of 0V was previously imposed, in order to simulate the presence of the water cooling system that keep under control the temperature of the chamber's base plate. The same temperature T_{constr} was assigned as space temperature to the environment represented by the vacuum chamber which surrounds the hot-cavity and the transfer line. Due to vacuum inside the chamber that contains the MK5 source, no convective loads are present in the analyses described in this work.

As clarified in the following, during the experimental tests performed at LNL to validate the FE model, the MK5 prototype was realized using Ta instead of Mo (for the external thermal screens, the end flange, the retainer nut, the outlet, the discharge chamber, the anode, the anode heat shield, the anode support and the anode support nut) adapting its manufacturing to the Laboratory's material stock; the BeO adopted to produce the anode support insulators was substituted by Al_2O_3, a material characterized by similar thermal and electrical properties but without toxicity problems; a dedicated set of simulations proved the substantial equivalence of the materials from the thermal-electric point of view. As a consequence, with the aim to realize a FE model as close as possible to the correspondent experimental system, Ta components instead of Mo components were modelled; moreover electrical resistivity [29,30], emissivity [31,32] and thermal conductivity [29,33] for tantalum (see paragraph 4.4.1), copper (see paragraph 4.4.1), graphite and Al_2O_3 were accurately implemented considering their temperature dependence. The following figures propose the FE temperature and potential plots correspondent to 300 A of electrical current.

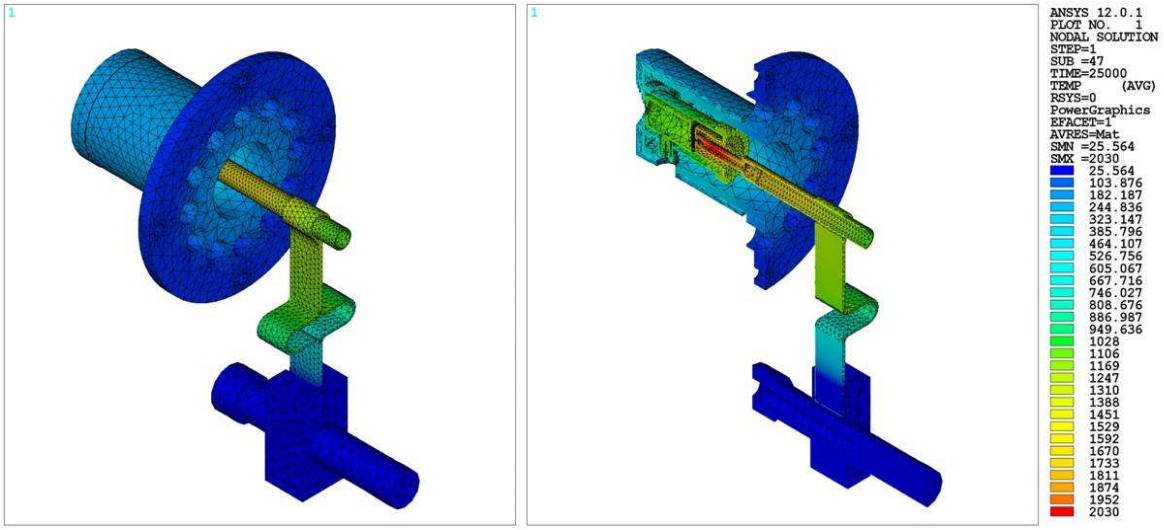

Fig. 4.68. MK5 source's temperature (°C) distribution as predicted by the FE model for 300 A of electrical current.

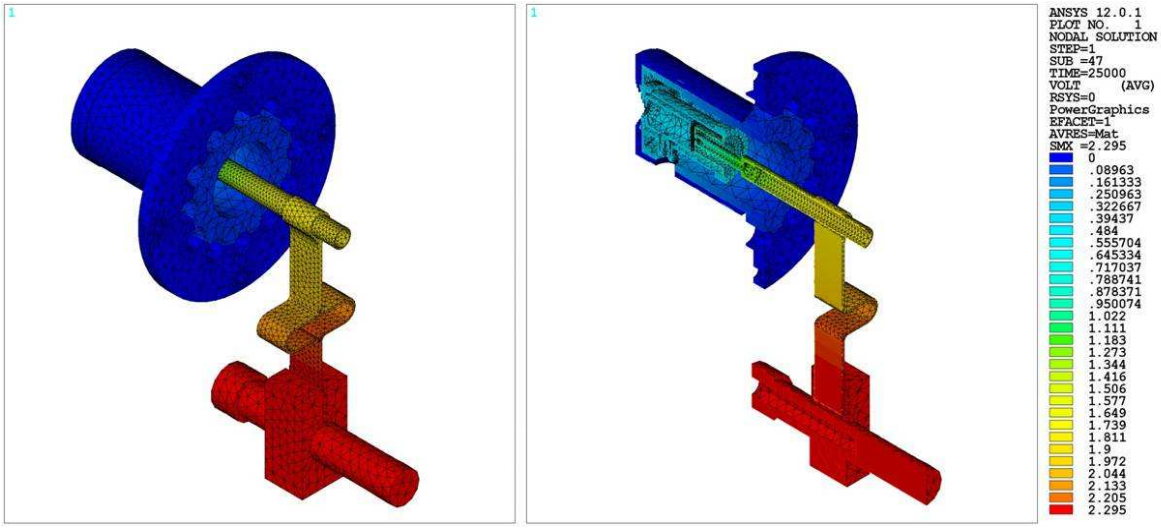

Fig. 4.69. MK5 source's voltage (V) distribution as predicted by the FE model for 300 A of electrical current.

Experimental tests. To perform temperature and potential difference measurements the same experimental apparatus used for the surface ion source's tests was adopted (see figure 4.17). In this case the assembly procedure of the source is more complicated and its main steps are briefly presented below.

First of all the anode, the anode grid and the outlet are connected together to form the anode assembly; the aforementioned components are joined by mechanical interference so in this phase it is very important to handle them softly.

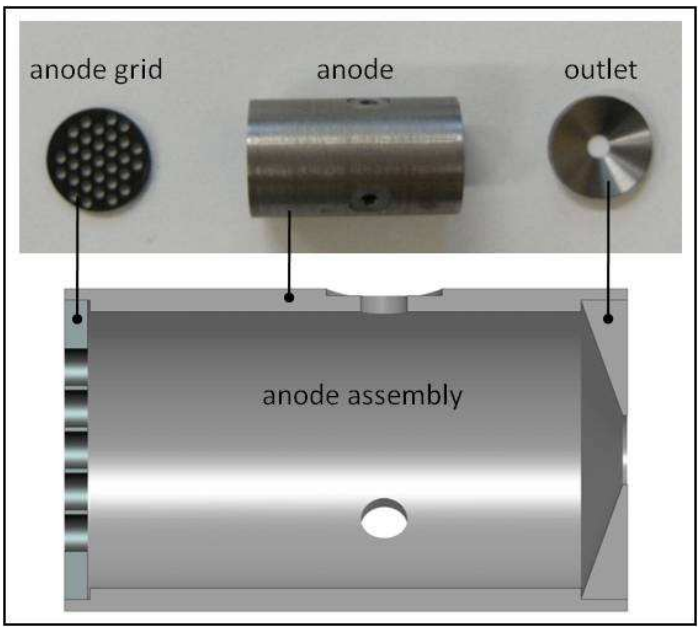

Fig. 4.70. The anode assembly and its components.

Then, using a dedicated tool, the anode assembly and the discharge chamber are aligned as shown in figure 4.71; during this operation it is very important to check the alignment of the three

lateral holes and the orientation of the anode assembly keeping into account that the anode grid will have to face the cathode.

Fig. 4.71. Alignment of the discharge chamber and of the anode assembly.

The next operation is the positioning of the anode supports, of the anode support insulators and of the anode support nuts (see figure 4.61); in this way the anode assembly will be electrically insulated respect to the rest of the ion source. Even if during this test the anode assembly wasn't connected to the anode's power supply, the operation was executed paying a particular attention to the alignment of the discharge chamber respect to the anode assembly.

Fig. 4.72. Positioning of the electrical insulators between the anode assembly and the discharge chamber.

Three anode heat shields are placed inside the circular end flange's cavity (see figures 4.60 and 4.61); they are axially spaced by means of tantalum rings characterized by a thickness of 0.5 mm and a diameter approximately equal to 18 mm; the end flange and the heat shields are then assembled with the rest of the source constituting the assembly shown in figure 4.74.

Fig. 4.73. Positioning of the heat shields inside the end flange's cavity.

Fig. 4.74. The prototype of the MK5 ion source before the cathode's assemblage.

At this point, before starting to connect the cathode it is very important to check the dimensions z_1 and z_2 represented in figure 4.75; the difference between z_1 and z_2 is the anode-cathode gap, so the gap between the graphite anode grid and the larger extremity of the cathode. The dimensions z_1 and z_2 are measured using a digital caliper and varying the measurement position in the circumferential direction (dimensional non-homogeneity due to welded joints). The anode-cathode gap size should always be between 0.9 and 1.4 mm: in particular a value as close as possible to 1.2 mm is recommended. If the gap is less than 0.9 mm, a molybdenum or tantalum spacer is used to increase the anode-cathode gap (spacer positioned between the cathode and the discharge chamber). If the gap is more than 1.4 mm, it is sometimes possible to reduce it by loosening a little bit the

three anode support nuts and by pushing the anode assembly inside the discharge chamber. If the gap is still bigger than 1.4 mm, the anode assembly should not be used.

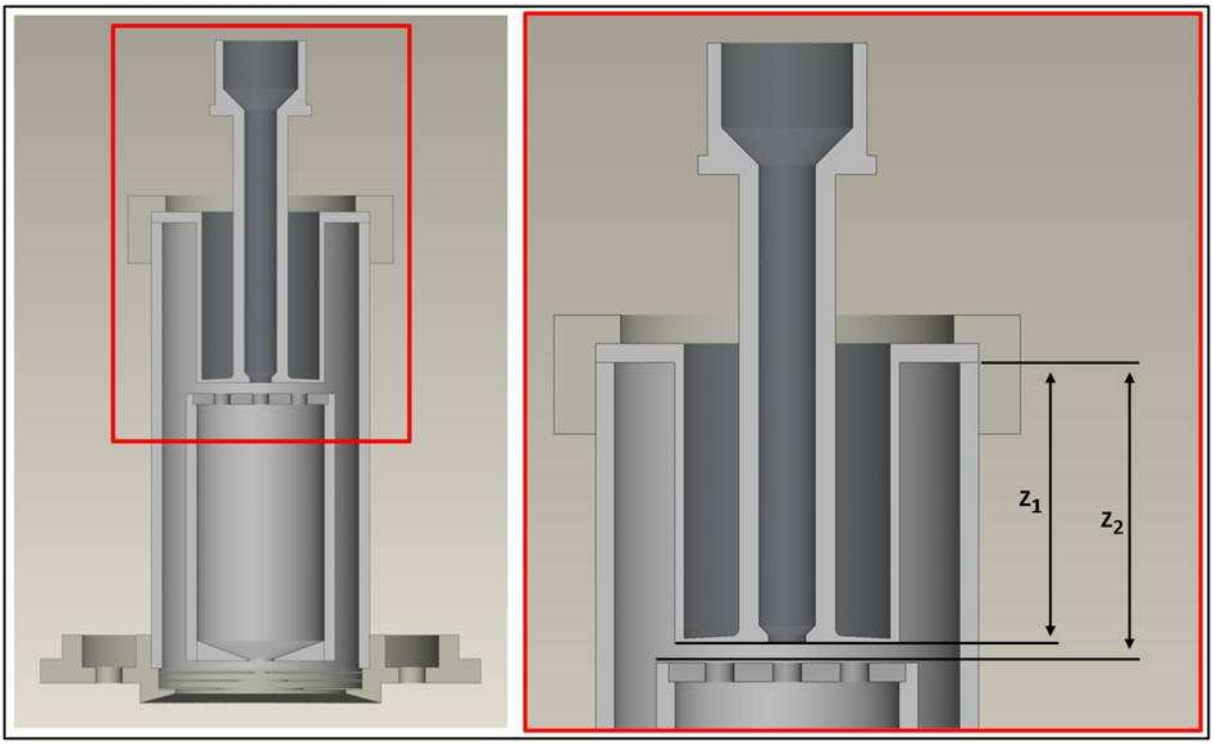

Fig. 4.75. Representation of the dimensions z_1 and z_2.

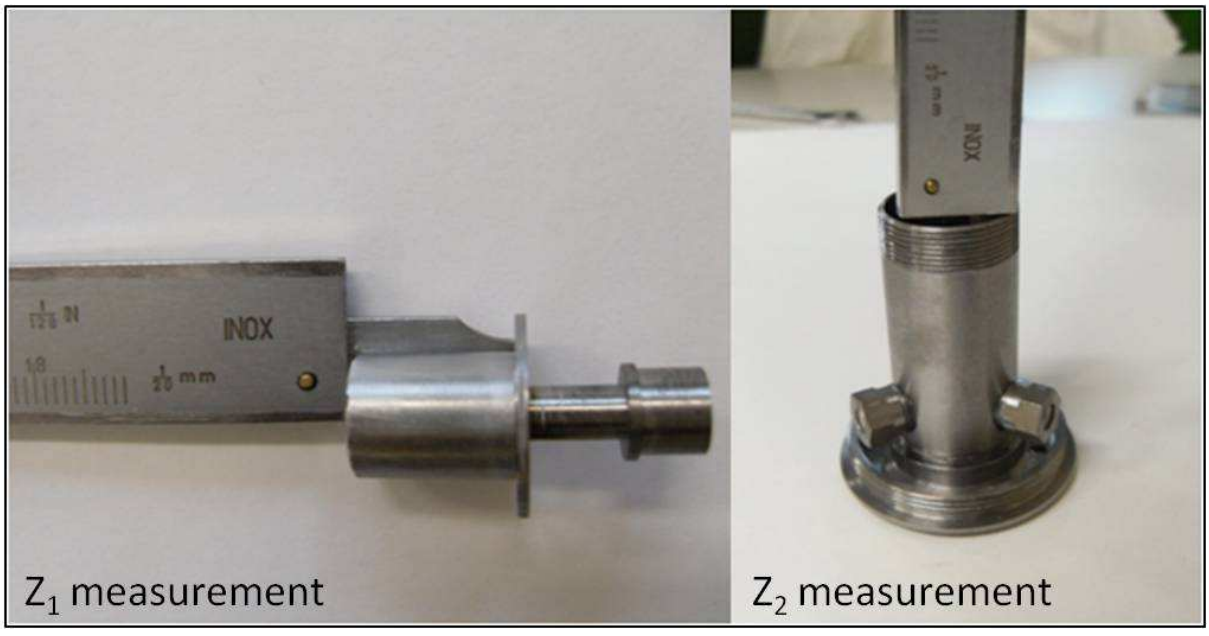

Fig. 4.76. The prototype of the MK5 ion source before the cathode's assemblage.

Once connected the cathode to the main assembly by means of the retainer nut (see figure 4.60), also the support housing, the support housing flange and the external thermal screens are easily assembled and positioned (see figure 4.77).

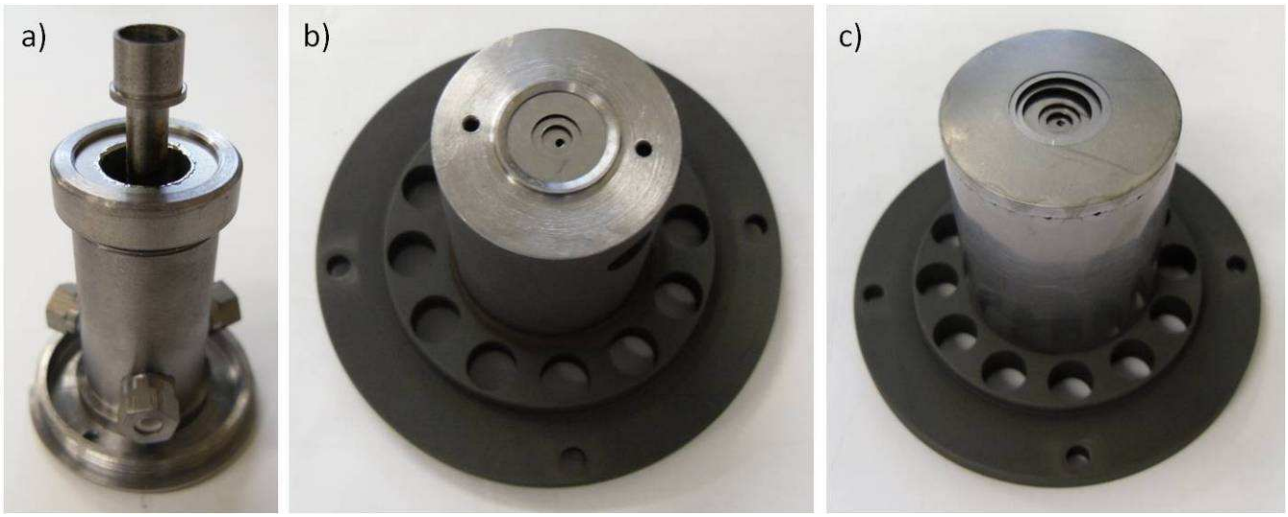

Fig. 4.77. Cathode's connection (a); the graphite support housing and support housing flange assemblage (b); positioning of the external thermal screens (c).

At this point the prototype of the MK5 ion source can be fixed at the vacuum chamber's base plate, ready to be heated by Joule effect.

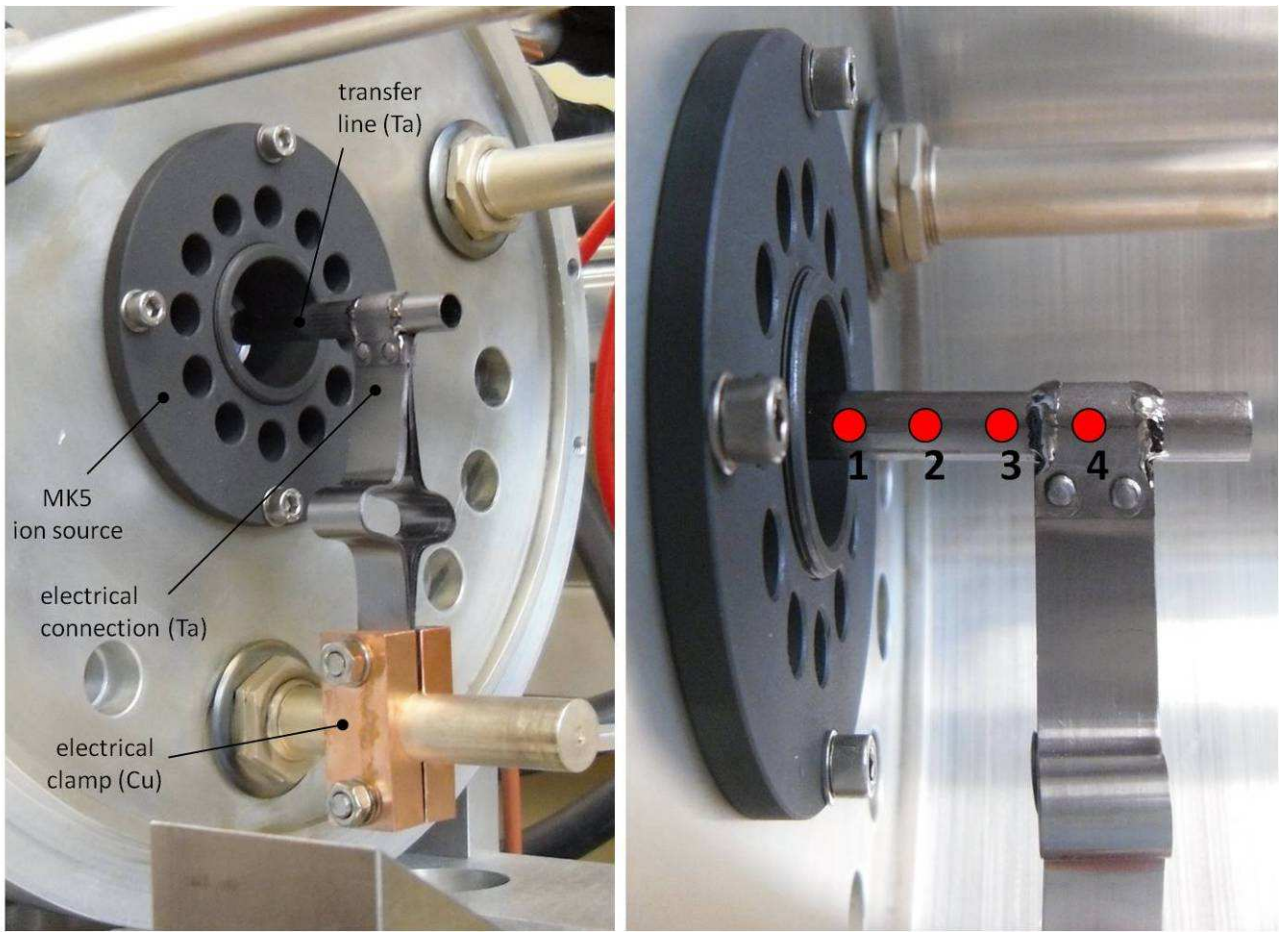

Fig. 4.78. The MK5 ion source installed and the temperature measurement points.

A pair of pictures of the MK5 ion source heated at high temperature are presented in figure 4.79.

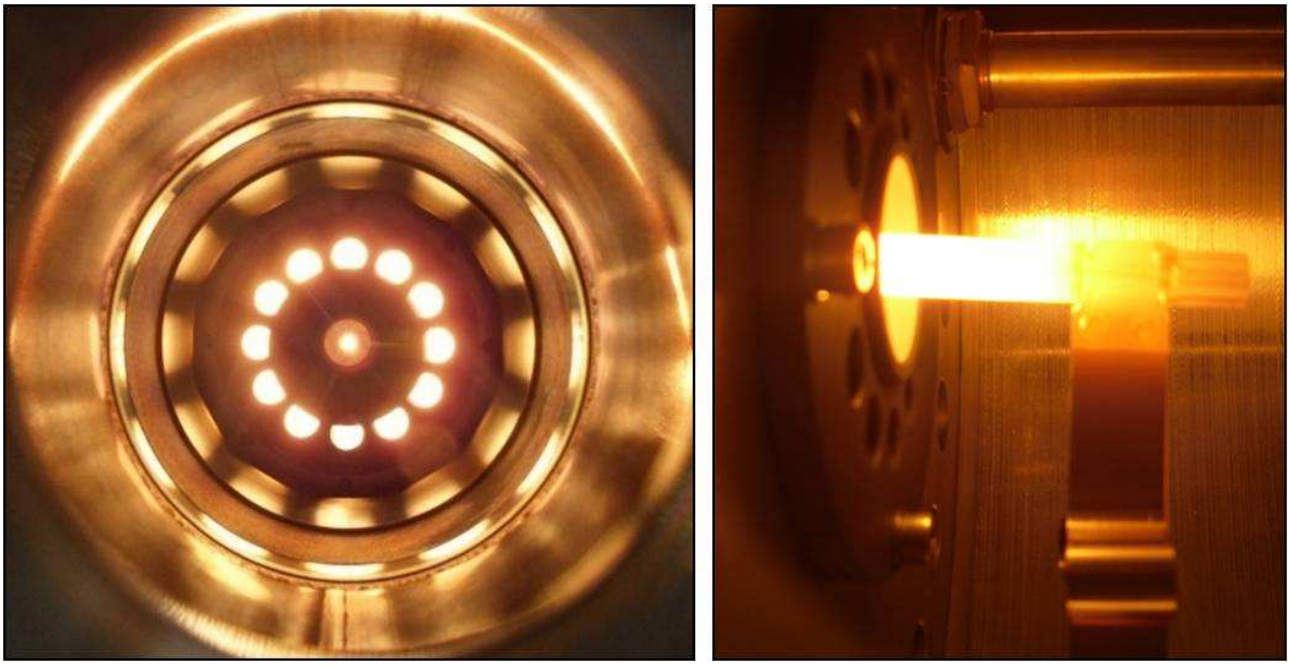

Fig. 4.79. The prototype of the MK5 ion source heated at high temperatures.

A comparison between experimental and numerical data on temperature values at the four points evidenced in figure 4.78 is presented in the following section; the comparison is performed also on the potential difference values adopting the same strategy proposed for the hot-cavity ion source (see paragraph 4.4.1).

Comparison between theoretical and experimental results. Temperature and potential difference values calculated by means of the FE model are now compared with the experimental data obtained by using the apparatus described in the previous section; in particular from figure 4.80 to figure 4.84 the comparison is explicitly presented, showing a substantial convergence between numerical and experimental approaches. If on one hand calculated and measured temperatures are practically coincident, on the other hand experimental potential difference values are always higher respect to the correspondent numerical ones: this is due to the ideal numerical modelling of the contacts between components already described in paragraph 4.4.1.

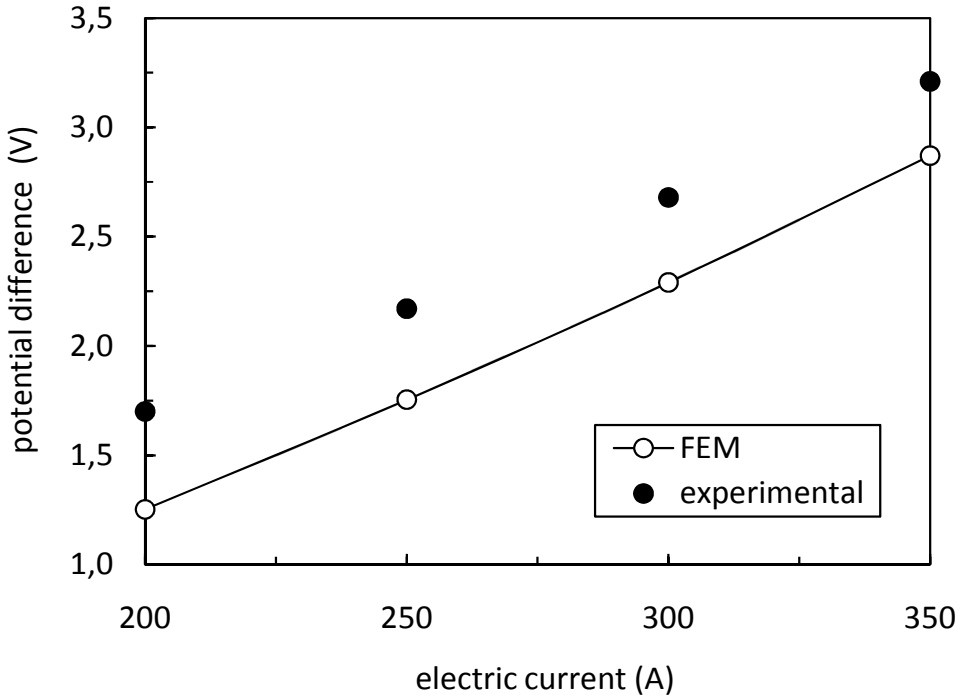

Fig. 4.80. Comparison between numerical and experimental potential difference values.

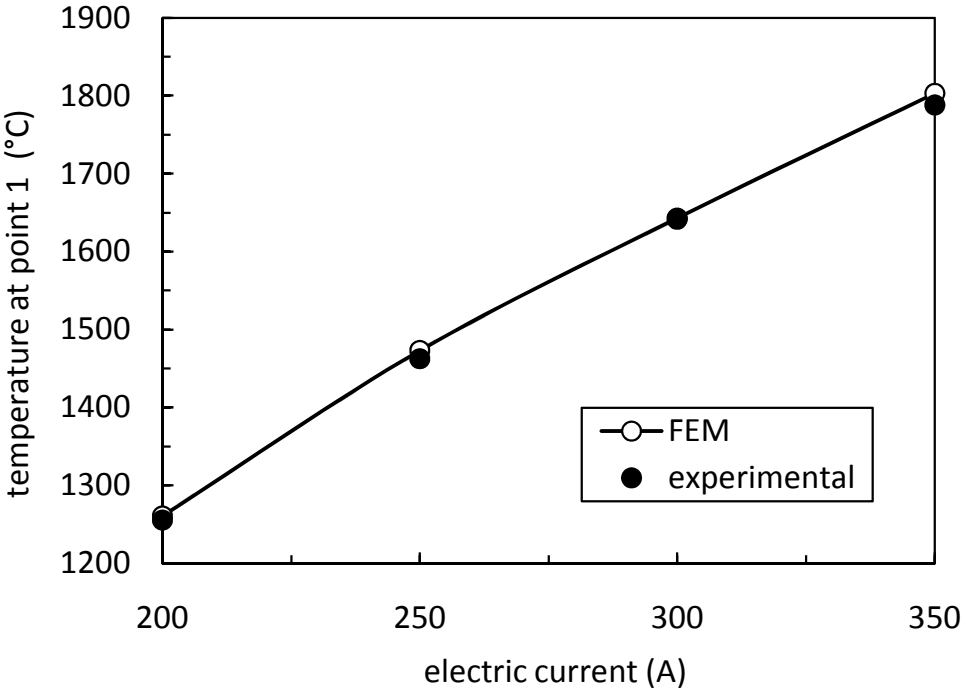

Fig. 4.81. Comparison between numerical and experimental temperatures at point 1 of the transfer line (see figure 4.78).

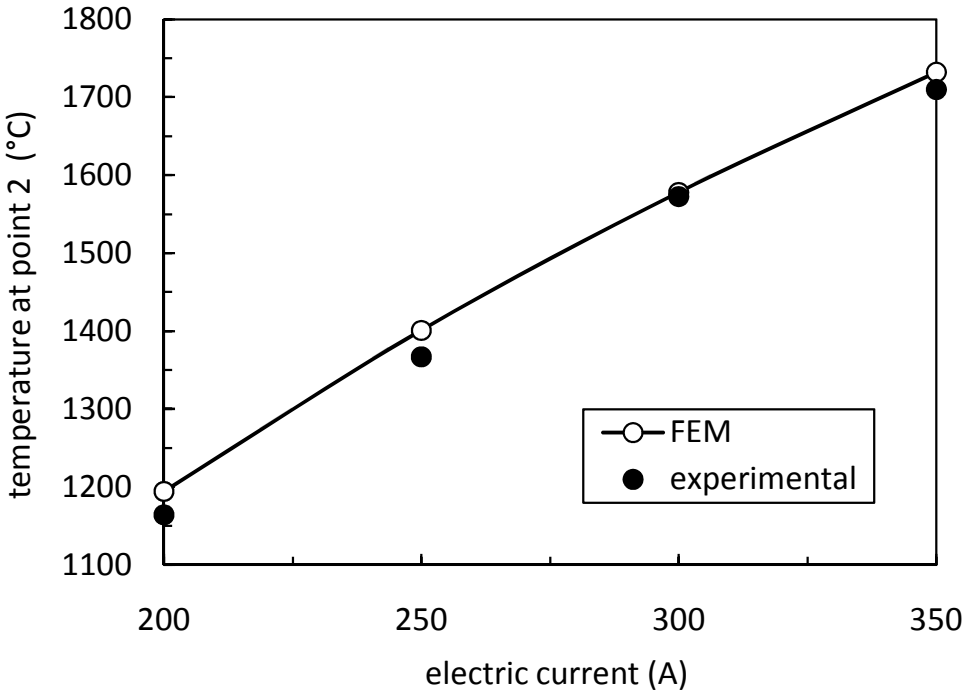

Fig. 4.82. Comparison between numerical and experimental temperatures at point 2 of the transfer line (see figure 4.78).

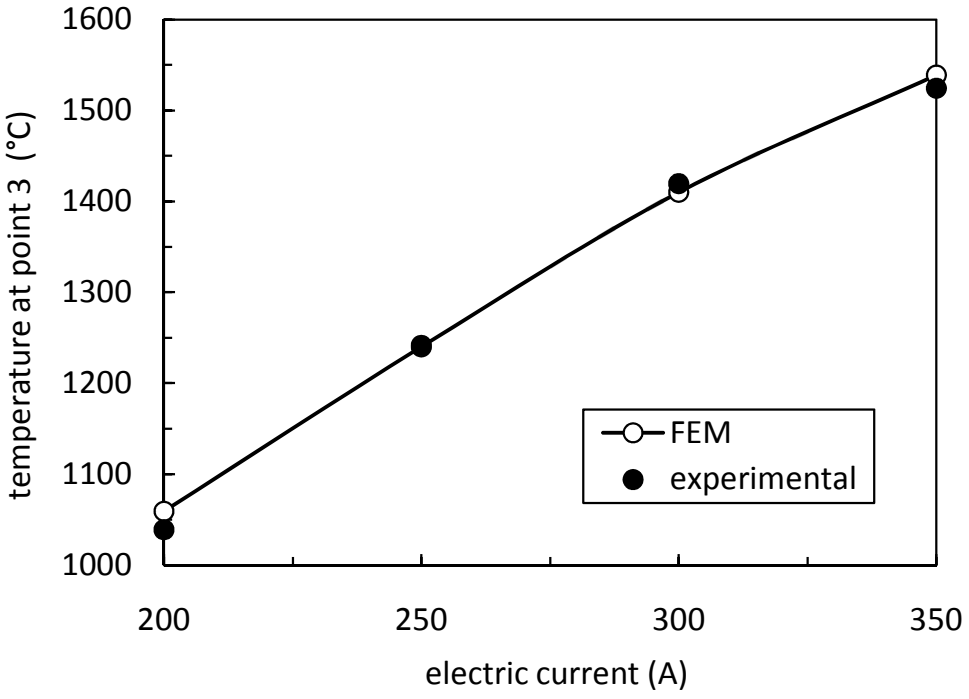

Fig. 4.83. Comparison between numerical and experimental temperatures at point 3 of the transfer line (see figure 4.78).

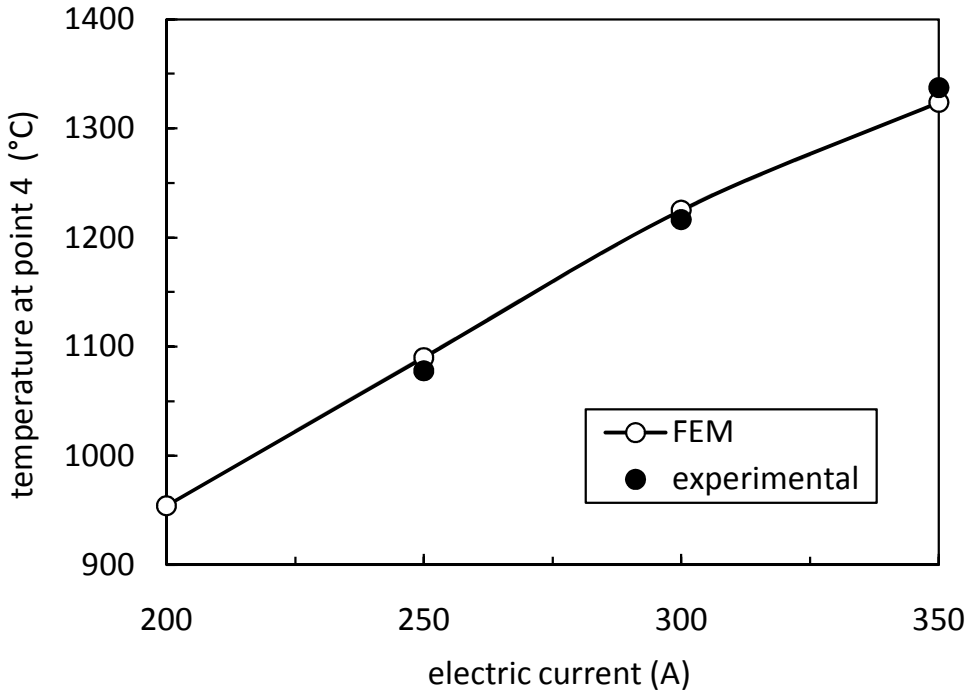

Fig. 4.84. Comparison between numerical and experimental temperatures at point 4 of the transfer line (see figure 4.78).

4.5.3. Preliminary study of the electron trajectories inside the anode chamber

Once explained the way the MK5 ion source (the FEBIAD ion source taken as reference for the SPES project) works and how it is heated at high temperature, an introductive and preliminary study of the electron trajectories inside the anode chamber is now briefly presented. Before starting to introduce the problem it is important to underline that in this case the beam formation is not considered, so the 60 kV of potential difference between the source and the extraction electrode is not applied: the attention is now concentrated on the anode chamber, kept at the potential level of 150 V respect to the rest of the source components (see figure 4.61).

The preliminary study of the electron trajectories inside the anode was realized using the commercial FE code ANSYS®. First of all the electromagnetic field inside the cavities of the source, in particular between the anode and the cathode, and inside the anode chamber, was calculated thanks to the element type SOLID236: it is a 3-D 20-node element with magnetic and electric degrees of freedom (see figure 4.85). Then, thanks to the ANSYS® Electromagnetic Particle Tracing already presented in the previous paragraphs, the trajectories of the electrons produced by the cathode and accelerated in the direction of the anode were calculated considering different magnetic field's intensities and so, different values of the electric current flowing through the Al ribbon wrapped on the vacuum chamber's flange (see figures 4.58 and 4.59). In the present case combined electromagnetic particle tracing ($\{E\} \neq \{0\}$ and $\{B\} \neq \{0\}$) is considered and in the

following some details of the FE model used to simulate the trajectories of the electrons inside the anode chamber are described.

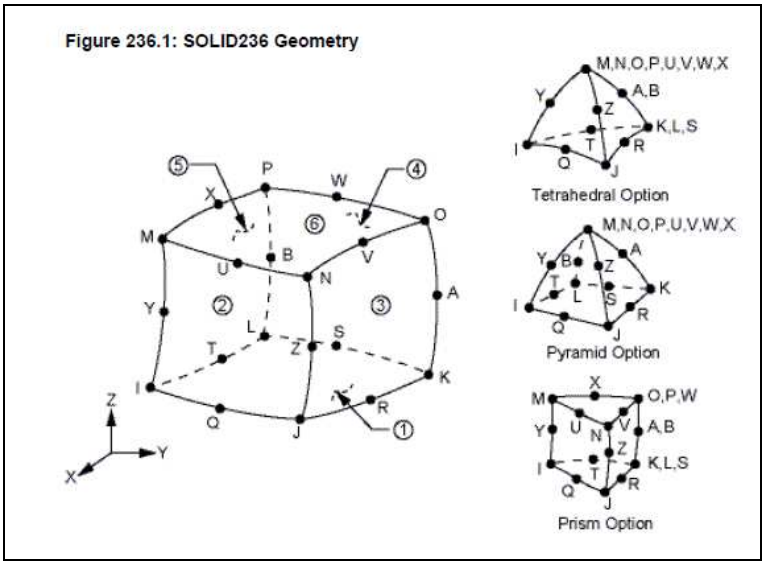

Fig. 4.85. The element type SOLID236.

Figure 4.86 shows the section view of the discretized domain where the electromagnetic field is computed: in particular it includes the gap between the anode and the cathode, and the cavity inside the anode chamber. The electromagnetic properties permittivity $\varepsilon_0=8.85\cdot10^{-12}$ F/m and permeability $\mu_0=1{,}26\cdot10^{-6}$ H/m, both referred to vacuum, were regularly assigned before the creation of the SOLID236 mesh.

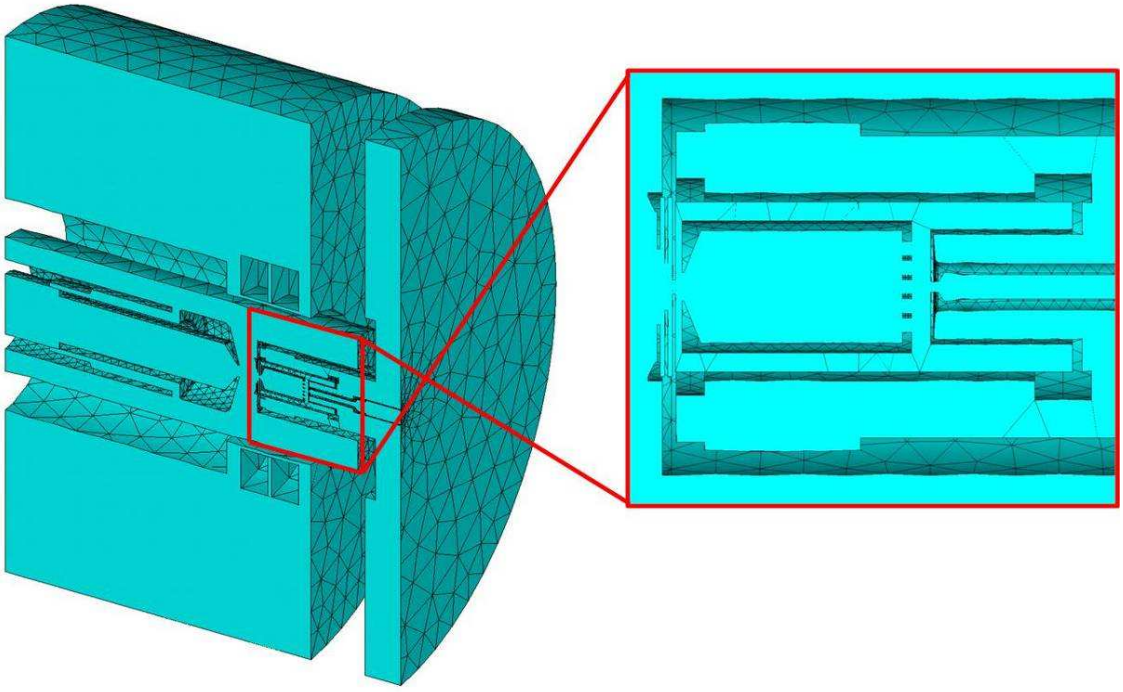

Fig. 4.86. SOLID236 mesh of the domain representing the vacuum zone.

Talking about boundary conditions, a voltage constraint of 150 V was imposed on the surfaces related to the anode, the anode grid and the outlet (see figure 4.61). The effect of the electric current I_{MAGNET} flowing through the Al ribbon was taken into account considering that the Al ribbon is wrapped on the chamber's flange forming two cylindrical blocks (see figure 4.59), each one characterized by 232 stratifications; as a consequence the two correspondent volumes were modelled defining for everyone a cylindrical coordinate system, and the current density assigned to the generic section normal to the circumferential direction was calculated multiplying I_{MAGNET} by 232 and dividing the product by the area of the section itself. Different sets of simulations were performed considering I_{MAGNET} values ranging from 10 to 110 A, with steps of 10 A each. The plots of the voltage, electric field and magnetic field distributions when I_{MAGNET} is imposed equal to 100 A are reported in the following figures.

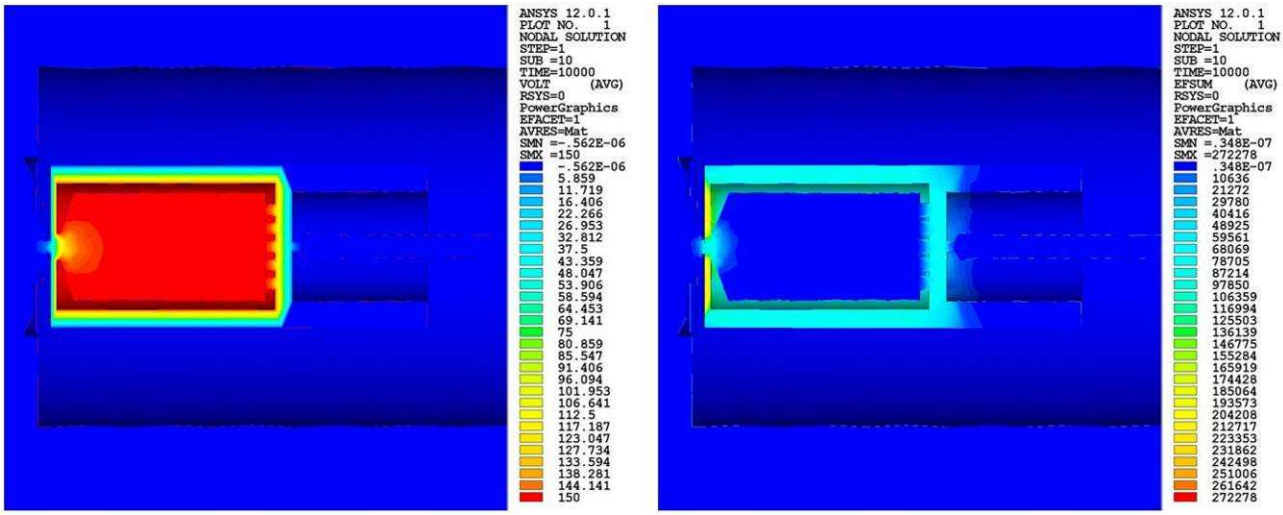

Fig. 4.87. Voltage distribution (V) and electric field (V/m) in proximity of the anode zone (I_{MAGNET} = 100A).

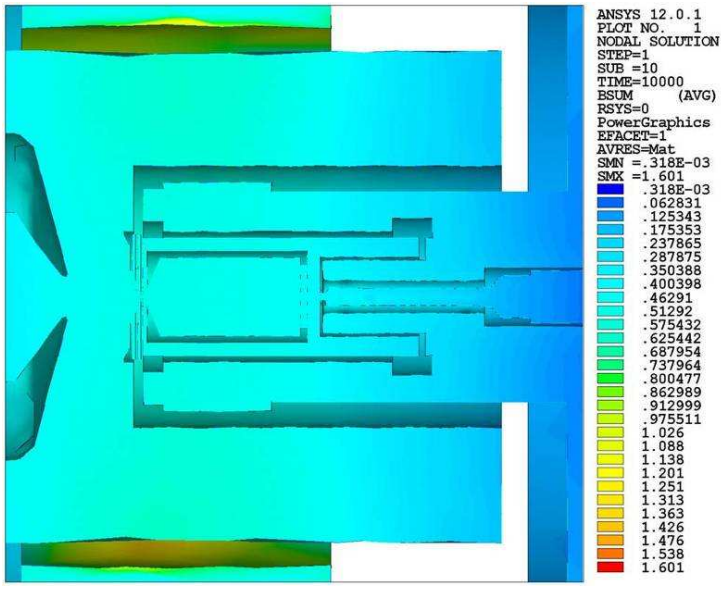

Fig. 4.88. Magnetic field (T) in proximity of the anode zone (I_{MAGNET} = 100A).

Once solved the electro-magnetic problem in the domain presented in figure 4.86, the trajectory of a representative electron inside the anode chamber was computed. First of all the electron's mass ($m_e = 9.11 \cdot 10^{-31} kg$) and charge ($q_e = 1.602 \cdot 10^{-19} C$) were input, then the electron's initial position and velocity were set. In particular the electron's initial position was fixed along the axial direction, inside the anode chamber close to the anode grid (see figure 4.89).

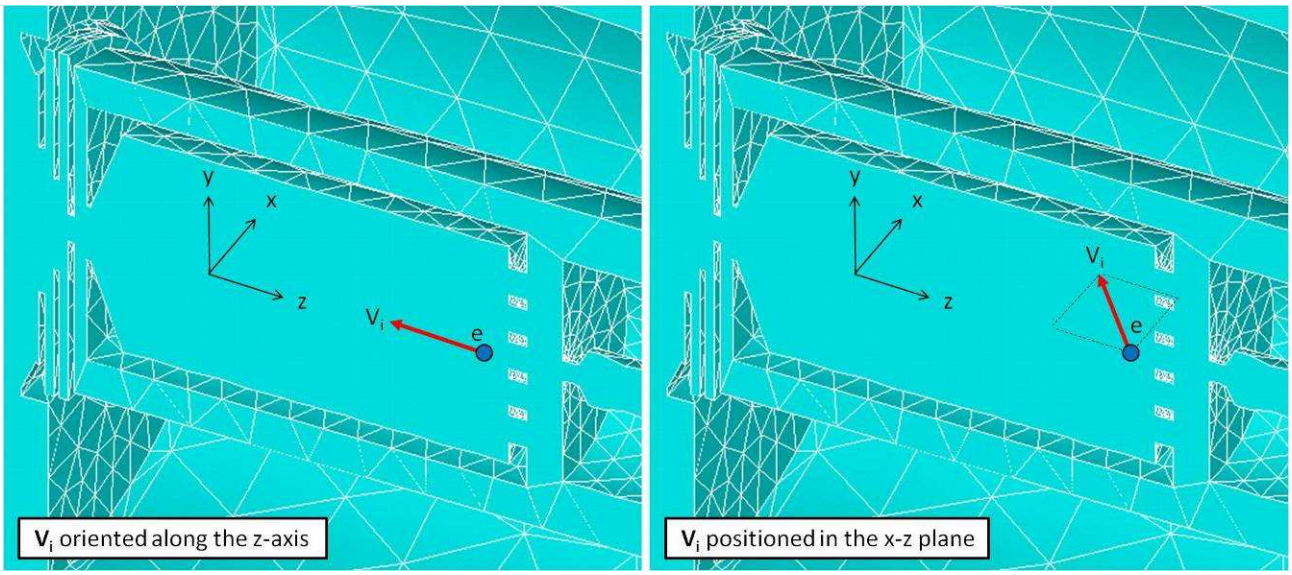

Fig. 4.89. Initial position and velocity of the representative electron.

Its initial velocity was assigned in an approximate way considering the kinetic energy acquired by the electron thanks to the potential difference (of approximately *150V*) between the cathode and the anode grid ($E_k = \Delta V \cdot q_e = 150V \cdot 1.602 \cdot 10^{-19} C = 2.403 \cdot 10^{-17} J$):

$$E_k = \frac{1}{2} \cdot m_e \cdot v_e^2 = \Delta V \cdot q_e = 150V \cdot 1.602 \cdot 10^{-19} C = 2.403 \cdot 10^{-17} J \qquad (4.15)$$

In this way the velocity was easily calculated thanks to the following expression:

$$v_e = \sqrt{2 \cdot \frac{E_k}{m_e}} = 7263278 \cdot \frac{m}{s} \qquad (4.15)$$

In the following figures the trajectories of the representative electron inside the anode chamber are presented taking into consideration I_{MAGNET} = 50A and I_{MAGNET} = 100A; the velocity vector was in one case directed along the z-axis (V_Z = - *7263278 m/s*) and then positioned in the x-z plane at 45° respect to the x-axis (V_X = *5135913 m/s*, V_Z = - *5135913 m/s*) (see figure 4.89); it was possible to appreciate that the magnetic field is able to influence the electron's trajectory only with the presence of a velocity component along the x or y-axis: in this case the magnetic field makes the electron follow an helicoidal path, increasing the ionizing interaction with the isotopes closed inside the anode cavity.

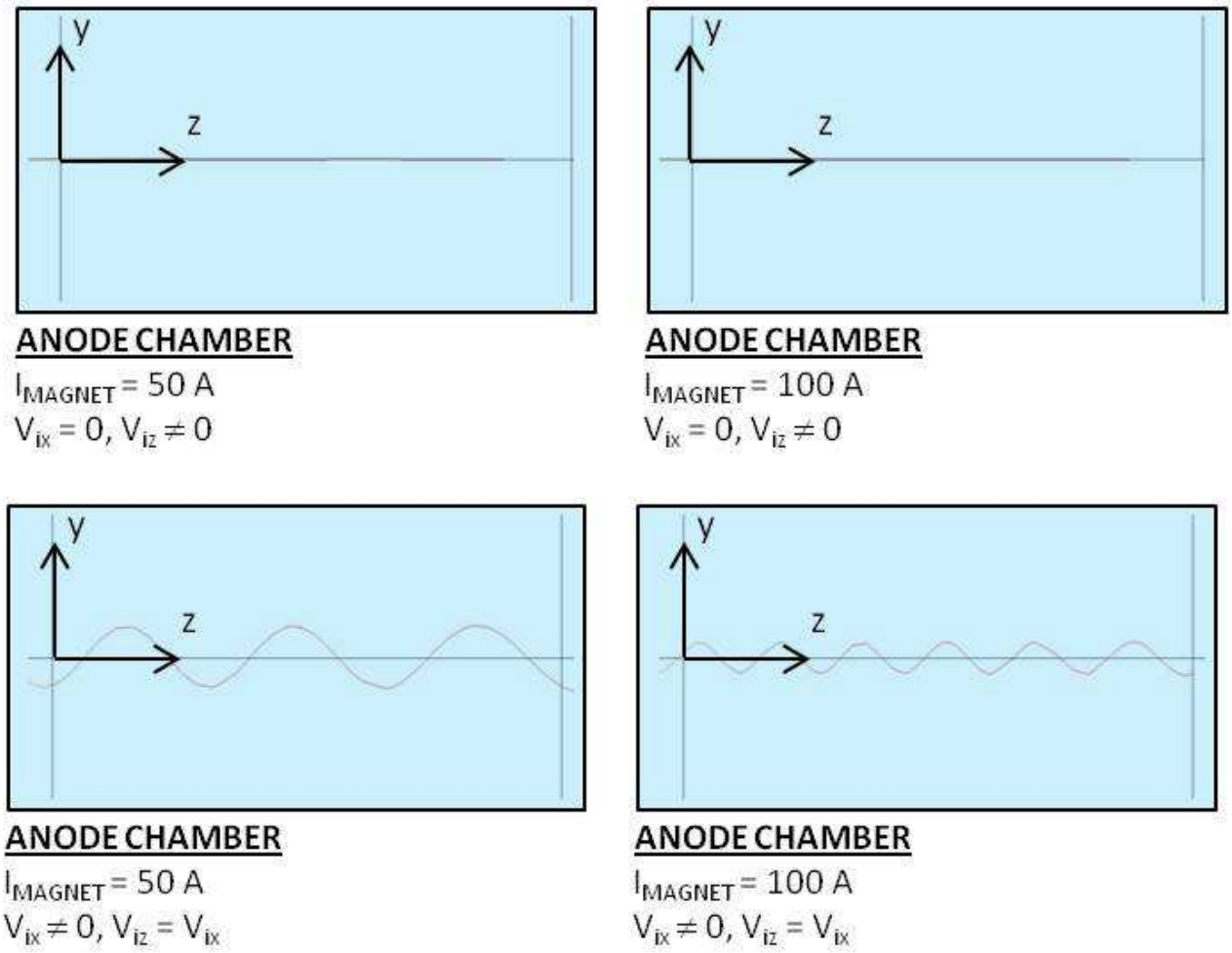

Fig. 4.90. Electron trajectories inside the anode chamber for different combinations of I_{MAGNET}, V_{ix} and V_{iy} (the effect of the magnetic field on the electron's trajectory was opportunely scaled in order to visualize clearly its effect).

It is important to underline that in this first set of simulations the initial velocity of the representative electron was imposed in an approximate way; figure 4.90 evidences the effect of the magnetic field: the higher the magnetic field intensity (I_{MAGNET}), the narrower the helicoidal path. The next step is to simulate the electron's trajectories starting from the cathode's surface facing the anode grid, so to reproduce also the acceleration of the electron due to the potential difference between the cathode and the anode

4.6. Conclusions

In this chapter the ionization mechanisms and the ion sources used in the context of the SPES project were presented and described. Some notions of "ion beam formation" and "ion beam optics" were also included. The thermal behaviour of both the hot-cavity ion source and the high temperature plasma ion source adopted for the SPES facility was studied in detail by means of theoretical models and experimental measurements; a preliminary numerical approach to study the

trajectories of ions and electrons inside the ion source was also introduced. In the next chapter the study, the design and the test of the SPES “production target – hot-cavity ion source” assembly is presented.

REFERENCES

[1] J. Al-Khalili, E. Roeckl, The Euroschool Lectures on Physics with Exotic Beams, vol.2, Springer, Berlin, 2006.

[2] R. Kirchner, Progress in Ion Source development for on-line separators, Nucl. Instrum. Methods 186 (1981) 275-293.

[3] W. Lotz, An Empirical Formula for the Electron-Impact Ionization Cross-Section, Z. Phys. 206 (1967) 205-211.

[4] V.S. Letokhof, Laser Photo Ionization Spectroscopy, Academic Press, Orlando, 1987.

[5] G.S. Hurst, M.G. Payne, Principe and Applications of Resonance Ionization Spectroscopy, Hilger, London, 1988.

[6] B. Wolf, Handbook of Ion Sources, CRC Press, Boca Raton, 1995.

[7] R. Kirchner, Review of ISOL target–ion-source systems, Nucl. Instrum. Methods Phys. Res., Sect. B 204 (2003) 179-190.

[8] R. Kirchner, An Ion Source with bunched beam release, Nucl. Instrum. Methods Phys. Res., Sect. B 26 (1987) 204-212.

[9] P. Van Duppen et al., A new pulsed release method for element selective production of neutron rich isotopes near 208Pb, Nucl. Instrum. Methods Phys. Res., Sect. B 134 (1998) 267-270.

[10] U. Koster et al., On-line yields obtained with the ISOLDE RILIS, Nucl. Instrum. Methods Phys. Res., Sect. B 204 (2003) 347-352.

[11] Ian G. Brown (Editor), The Physics and Technology of Ion Sources, WILEY-VCH, Berkeley - California, 2004.

[12] R. Kirchner, Ion Sources for Radioactive Beams, Particle Accelerators 47 (1994) 127-132.

[13] F. Wenander, J. Lettry, M. Lindroos, Transverse emittance investigation of the ISOLDE target-ion source, Nucl. Instrum. Methods Phys. Res., Sect. B 204 (2003) 261-266.

[14] T. Bjørnstad, E. Hagebø, P. Hoff, O. C. Jonsson, E. Kugler, H. L. Ravn, S. Sundell, B. Vosicki, Recent development of high-temperature metal targets for ISOLDE, Nucl. Instrum. Methods Phys. Res., Sect. B 26 (1987) 174-182.

[15] Y.S. Touloukian, D.P. DeWitt, Thermophysical Properties of Matter, vol.7, IFI/Plenum, New York, 1970.

[16] P.D. Desai, T.K. Chu, H.M. James, C.Y. Ho, Electrical Resistivity of Selected Elements, J. Phys. Chem. Ref. Data 13 (1984) 1069-1096.

[17] ANSYS Inc, ANSYS® Thermal Analysis Guide, ANSYS Inc, Canonsburg, 2005.

[18] R.A. Matula, Electrical resistivity of copper, gold, palladium, and silver, J. Phys. Chem. Ref. Data 8 (1979) 1147-1298.

[19] Y.S. Touloukian, R.W. Powell, C.Y. Ho, P.G. Klemens, Thermophysical Properties of Matter, vol.1, IFI/Plenum, New York, 1970.

[20] G.B. Gaines, C.T. Sims, Electrical resistivity and thermoelectric potential of rhenium metal, Am. Soc. Testing Materials Proc. 57 (1957) 759-769.

[21] V.E. Peletskii, V.P. Druzhinin, The total hemispherical emissivity of tungsten, molybdenum, and rhenium single crystals at high temperatures, High Temp. - High Pressures 2 (1970) 69-74.

[22] M. Libralato, Studio elettro-termo-strutturale del sistema di estrazione e ionizzazione del progetto SPES, Master Degree Thesis in Mechanical Engineering, University of Padua, Italy.

[23] M. Gyimesi, V. Zhulin, and D. Ostergaard, Particle Trajectory Tracing in ANSYS", Fifth International Conference on Charged Particle Optics, Delft University, Netherlands. To be Published in Nuclear Instruments and Methods in Physics Research, Section A. 1998.

[24] A. Galatà, Analisi preliminare della sorgente di ionizzazione superficiale, internal report of Legnaro National Laboratories, March 2009.

[25] http://www.lns.infn.it/excyt/celona/pdf/positive.pdf.

[26] A. Baraldo, Studio elettro-termo-strutturale della sorgente di ionizzazione al plasma del progetto SPES, Master Degree Thesis in Mechanical Engineering, University of Padua, Italy.

[27] http://en.wikipedia.org/wiki/Thermionic_emission

[28] S. Sundell, H. Ravn, Ion source with combined cathode and transfer line heating, Nucl. Instrum. Methods Phys. Res., Sect. B 70 (1992) 160-164.

[29] Taylor RE, Davis FE, Powell RW. Direct heating methods for measuring thermal conductivity of solids at high temperatures. High Temperatures-High Pressures 1969;1:663-673.

[30] http://hypertextbook.com/facts/2006/EuniceHuang.shtml.

[31] Biasetto L, Manzolaro M, Andrighetto A. Emissivity measurements of opaque gray bodies up to 2000°C by a dual-frequency pyrometer. Eur Phys J A 2008;38:167-171.

[32] R.J. Tiernan and J.E. Saunders, Normal emittance measurements by a transient temperature technique, J Appl Phys 64(1988) 459-463.

[33] Y.S. Touloukian, R.W. Powell, C.Y. Ho, P.G. Klemens, Thermophysical Properties of Matter, vol.2, IFI/Plenum, New York, 1970.

Chapter 5

Study, design and test of the SPES "Production Target – Hot-Cavity Ion Source" assembly

5.1. Introduction

In the previous chapters both the production target and the ion source were separately presented and their fundamental roles in the functioning of ISOL facilities [1] were clearly remarked and illustrated in the context of the SPES project. The thermal behaviour of the SPES "production target – hot-cavity ion source" assembly is now studied in detail, dedicating a particular attention to the reciprocal effects between the target and the ion source (see figure 5.1).

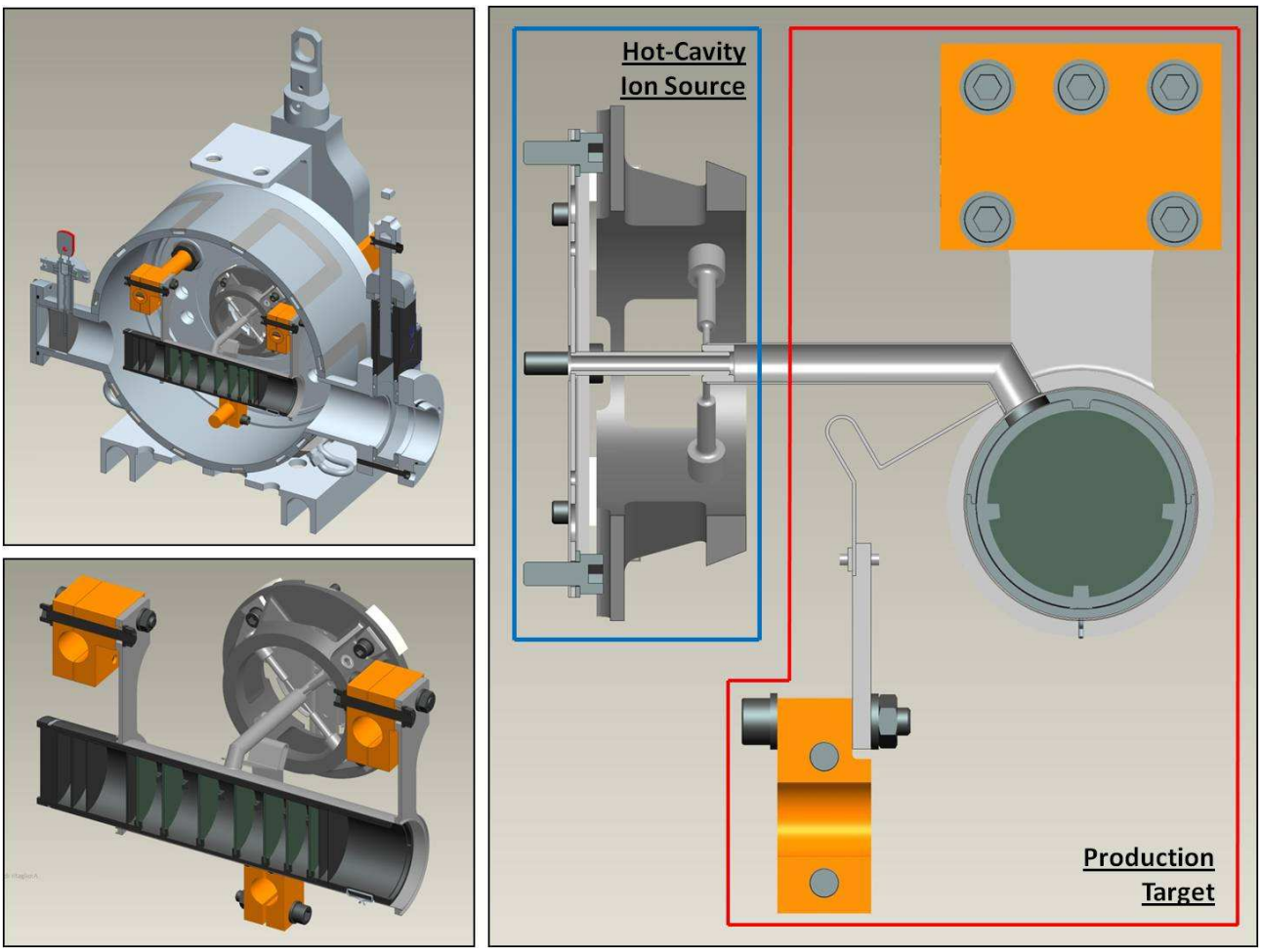

Fig. 5.1. The "production target – hot-cavity ion source" assembly.

The idea to choose the hot-cavity ion source instead of the high temperature plasma ion source was justified by the fact that the former will be used to produce the main part of the radioactive ion

beams planned for the SPES facility, using both the surface ionization and the laser ionization mechanisms. The analogous study performed connecting the target with the high temperature plasma ion source is not included in this work but it could be easily delivered using the same approach.

For the thermal study of the “target – ion source” assembly both the Joule heating and the proton beam thermal loads were considered: in particular the Joule heating thermal loads were implemented taking into consideration both the target heating system current and the ion source current. The two electrical circuits used to heat by Joule effect the target and the ion source are represented in figure 5.2, where it is possible to appreciate also a simple and clear schematization: they are independent and each one is linked to a dedicated power supply.

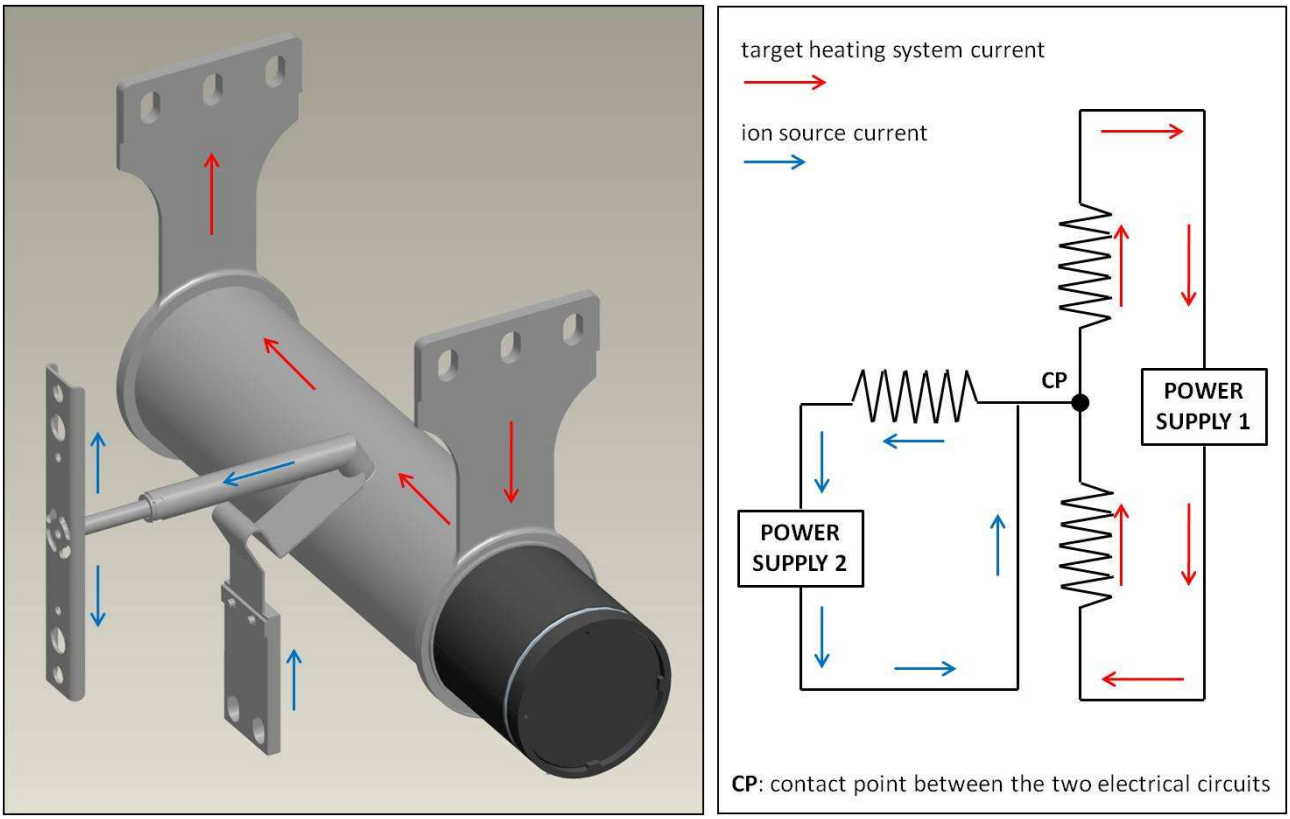

Fig. 5.2. The electrical circuits used to heat by Joule effect both the production target and the ion source.

In the set of analyses presented in the following, Joule heating thermal loads were assigned taking into consideration the electrical current load steps represented in figure 5.3, which were defined observing the heating procedures adopted by similar operative ISOL facilities and the results obtained from the thermal-electric analyses presented in the previous chapters. Usually the ion source is the first object heated at high temperature activating the correspondent electrical circuit; then also the production target is gradually heated by Joule effect. Once stabilized the temperature field, the primary beam is directed to the target to produce the nuclear reactions of interest: when its power is not negligible respect to the heating power produced by Joule effect, the

target heating system current is opportunely decreased in order to keep the temperature field under control and to avoid dangerous hot spots. In the case of the SPES facility (when the production target is linked to the hot-cavity ion source) the ion source electrical circuit is activated before the target circuit, reaching the maximum current value of 400A; then the target heating system current is gradually increased until the value of 1300A.

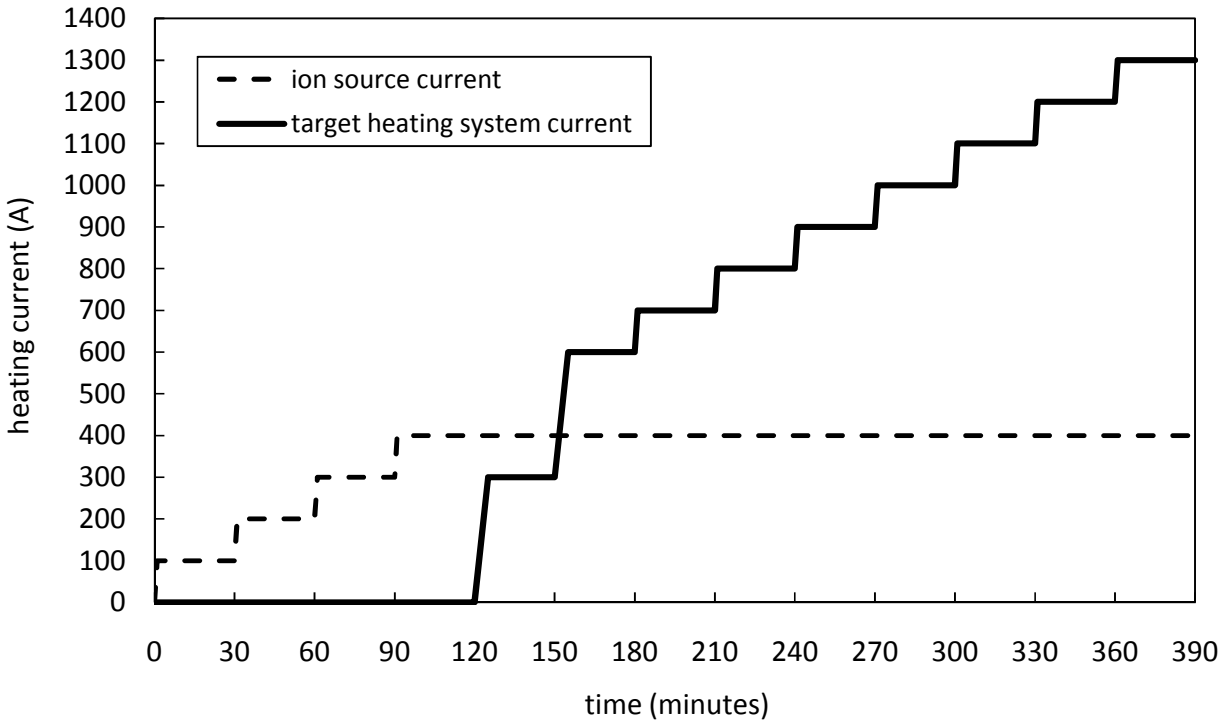

Fig. 5.3. The electrical current load steps used to heat by Joule effect both the production target and the ion source.

At this point, once stabilized the temperature field of the "target – ion source" assembly, the 40 MeV proton beam starts to impinge the SPES target increasing gradually its intensity (beam current) until the working value of 200 μA. In the meantime the target heating system current is gradually reduced to zero with the clear aim to avoid the overheating of the "target – ion source" assembly. So during the ideal working conditions of the SPES facility the ion source current is fixed at 400A, the target heating system current is equal to zero and the intensity of the 40 MeV proton beam is kept at 200 μA. In this context it is important to remark the fundamental role of the target heating system: even if the correspondent electrical current is equal to zero during the facility working conditions, it is essential to heat the target's UC_x disks and to prepare them to receive the proton beam: in fact the thermal gradients caused by the primary beam can be sustained in a better way when the temperature level is high (lower values of the elastic modulus and material plasticity that contribute to decrease the entity of the stress state). Moreover target heating system is always

available to compensate sudden interruptions of the primary beam and so to avoid thermal shocks and high cooling rates that in some cases can seriously damage the target – ion source system.

In the following paragraph the thermal-electric study of the "target – ion source" assembly is presented.

5.2. The SPES "Production Target – Hot-Cavity Ion Source" assembly: thermal-electric study using the FE model

The thermal-electric FE model of the "production target – hot-cavity ion source" assembly was developed using the same techniques presented in chapter 3 for the target and in chapter 4 for the ion source; in the present case both the target and the ion source were included in the same model, and connected by means of the transfer line (see figure 5.4). Ideal thermal and electrical contacts were modelled between the aforementioned objects, in particular between the transfer line and the target heating system. Boundary conditions and thermal loads were assigned exactly as proposed in the previous chapters both for the target and the ion source.

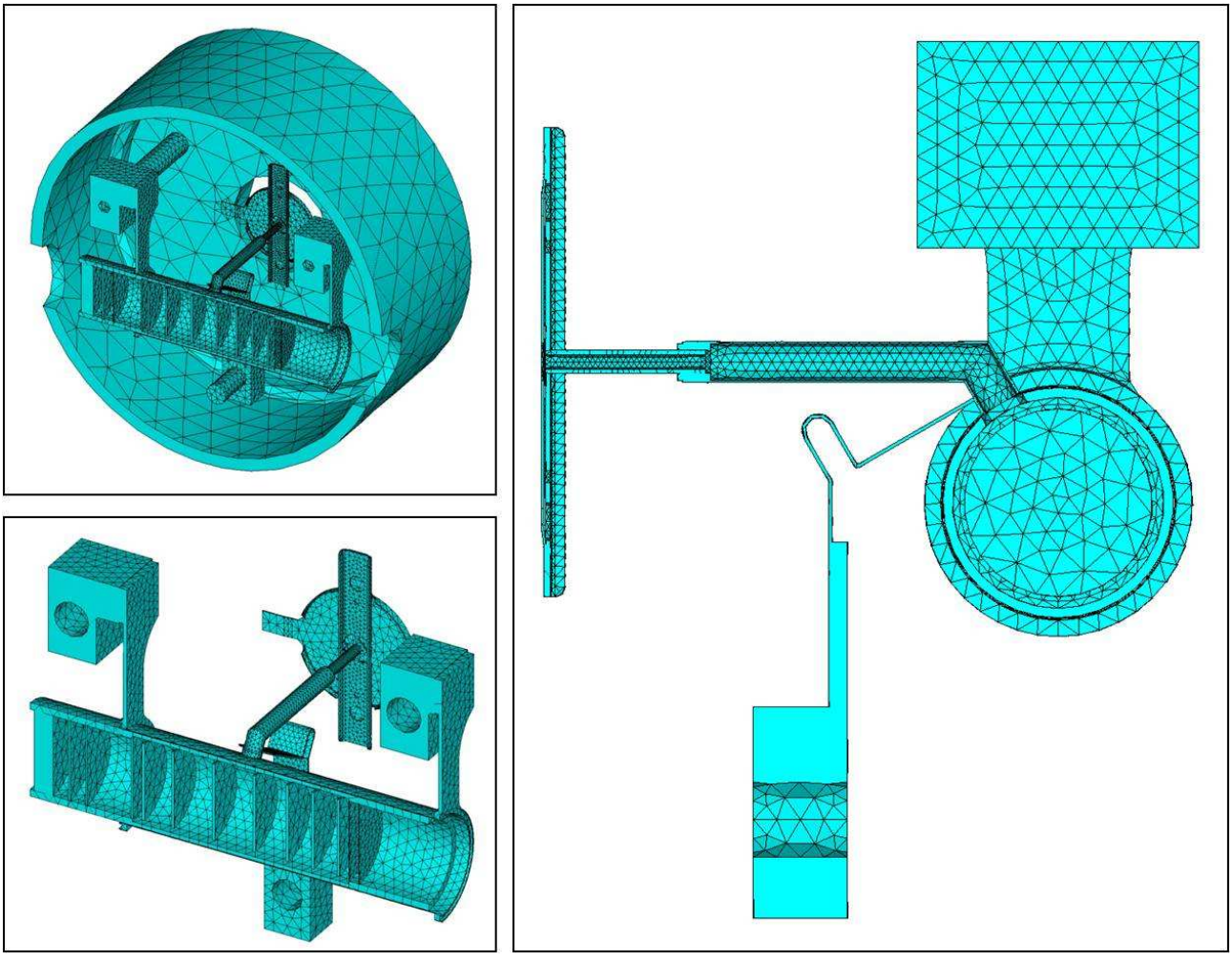

Fig. 5.4. The FE model of the "production target – hot-cavity ion source" assembly.

Data and results obtained thanks to the FE model and imposing the Joule heating thermal loads (see figure 5.3) only (the effect of the proton beam is not considered) are presented in the following.

In figure 5.5 the Ta tube temperature, the maximum temperature of the target heating system and the graphite window temperature (see figure 3.51, chapter 3) obtained with the presence of the ion source and with an ion source current fixed at 400A, are compared to the correspondent temperatures obtained when the ion source is not included in the FE model. The heating effect of the ion source on the production target is evident, especially when the target heating system current is low and in proximity of the connection between the target and the transfer line (the effect on the Ta tube temperature, detected in a point very close to the transfer line, is more pronounced respect to the heating effect produced on the window, positioned far from the connection between the target and the transfer line).

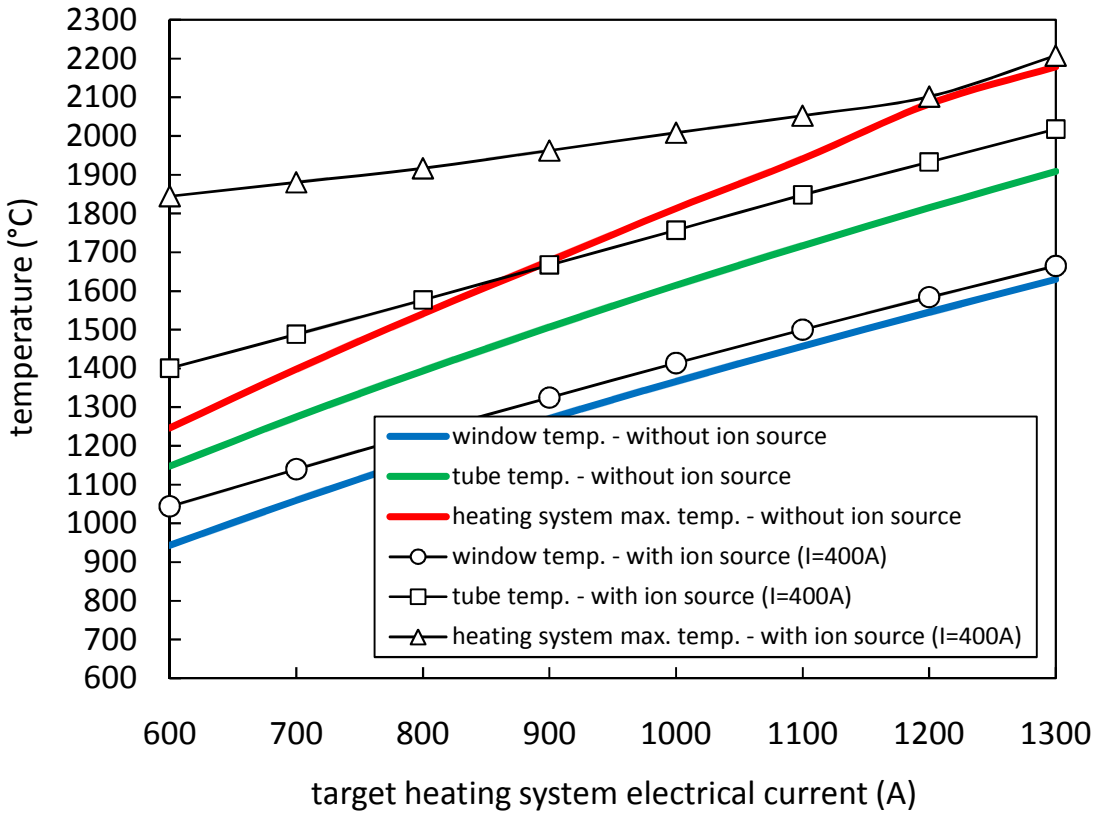

Fig. 5.5. Comparison among the Ta tube temperature, the maximum temperature of the target heating system and the graphite window temperature (see figure 3.51, chapter 3), with and without the presence of the ion source (heated by an electrical current of 400A).

Figure 5.6 shows how the ion source heated by 400A of electrical current can influence the target heating system potential difference. The temperature increment introduced by the presence of the ion source produces the growth of the Ta electrical resistivity, leading to higher potential

difference values for the same current level; however the difference is not very pronounced: the maximum increment is registered for a target heating system current of 600A and is equal to 0.15V.

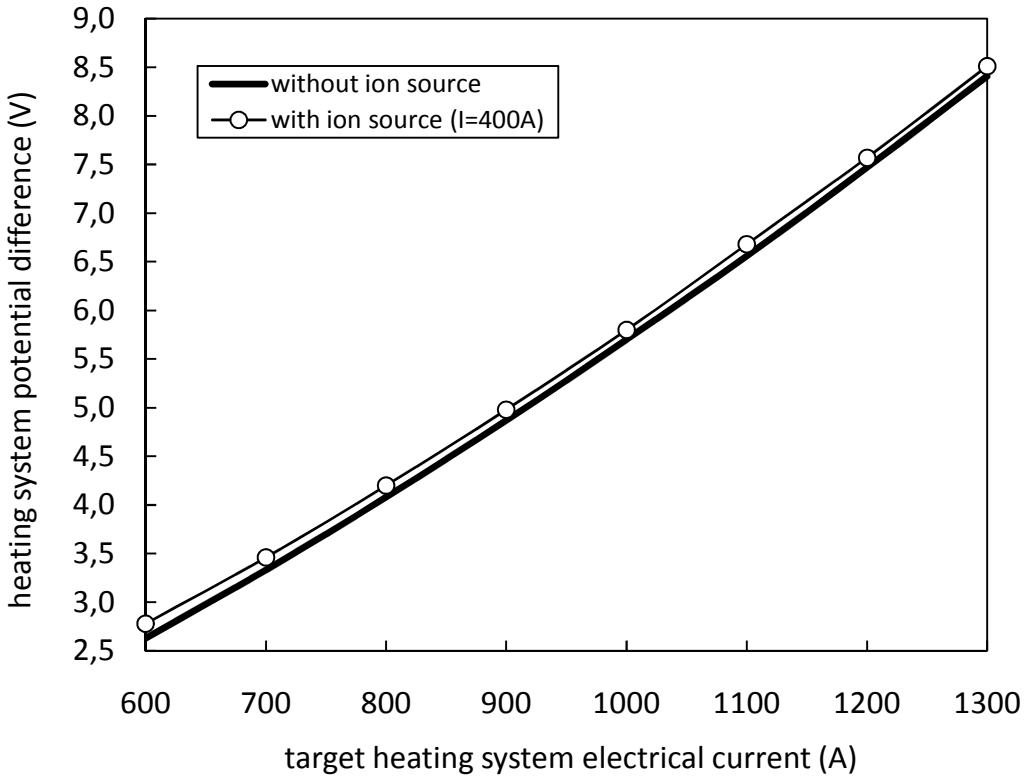

Fig. 5.6. Influence of the ion source (heated by an electrical current of 400A) on the heating system potential difference curve.

Figures 5.7 and 5.8 report the average and the maximum temperatures, respectively, of the UC_x disks correspondent to a target heating system current of 1300A, with and without the presence of the ion source (ion source current fixed at 400A). Disk 5 registers the maximum increment of the average disk temperature: it is equal to 61°C. The lower average disk temperature rise (40°C) is observed in proximity of the first disk, far from the zone of the connection with the transfer line. Disk 4, that with disk 5 occupies the central part of the target (the zone close to the transfer line aperture) presents the maximum increment of the maximum disk temperature due to the presence of the ion source (66°C); also in the case of the maximum disk temperature, the minimum increment (41°C) is monitored in proximity of the first disk.

Figure 5.9 shows the hot-cavity and the transfer line temperature distributions when the ion source heating current is equal to 400A; in particular, the aforementioned temperature distributions are reported considering different cases: the presence of the ion source (and transfer line) only, the presence of both the target and the ion source with the target heating system current equal to zero and the presence of both the objects with the target heating system current fixed at 1300°C.

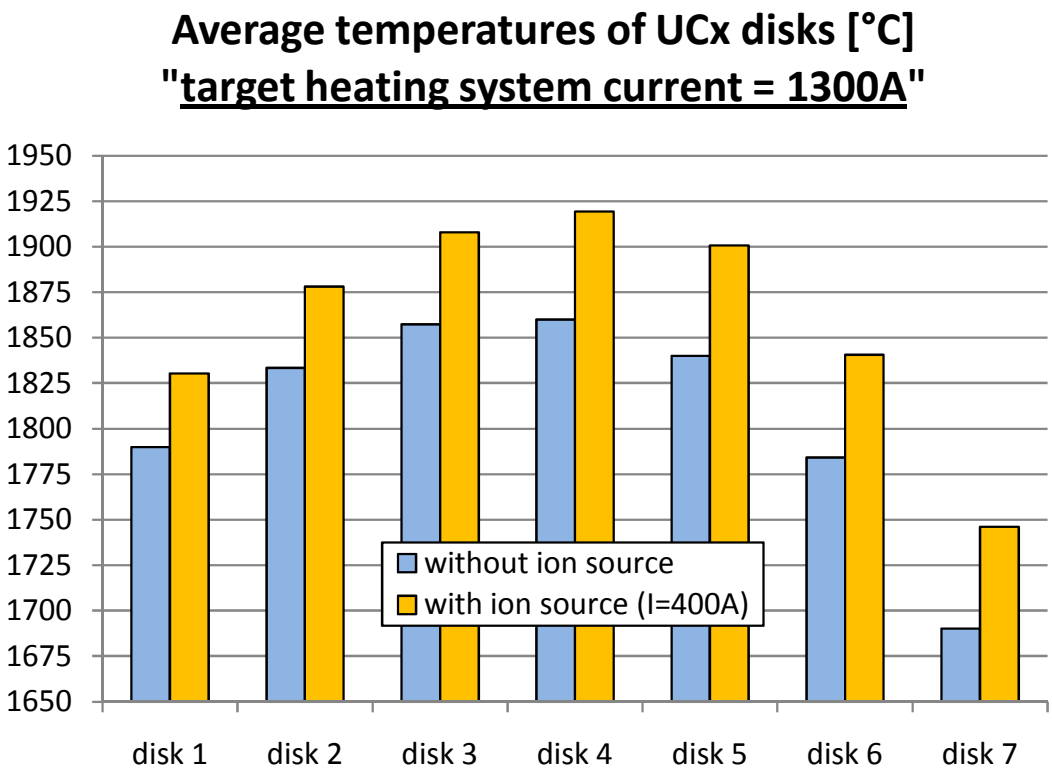

Fig. 5.7. Average temperatures of the UC_x disks correspondent to a target heating system current of 1300A, with and without the presence of the ion source (heated by an electrical current of 400A).

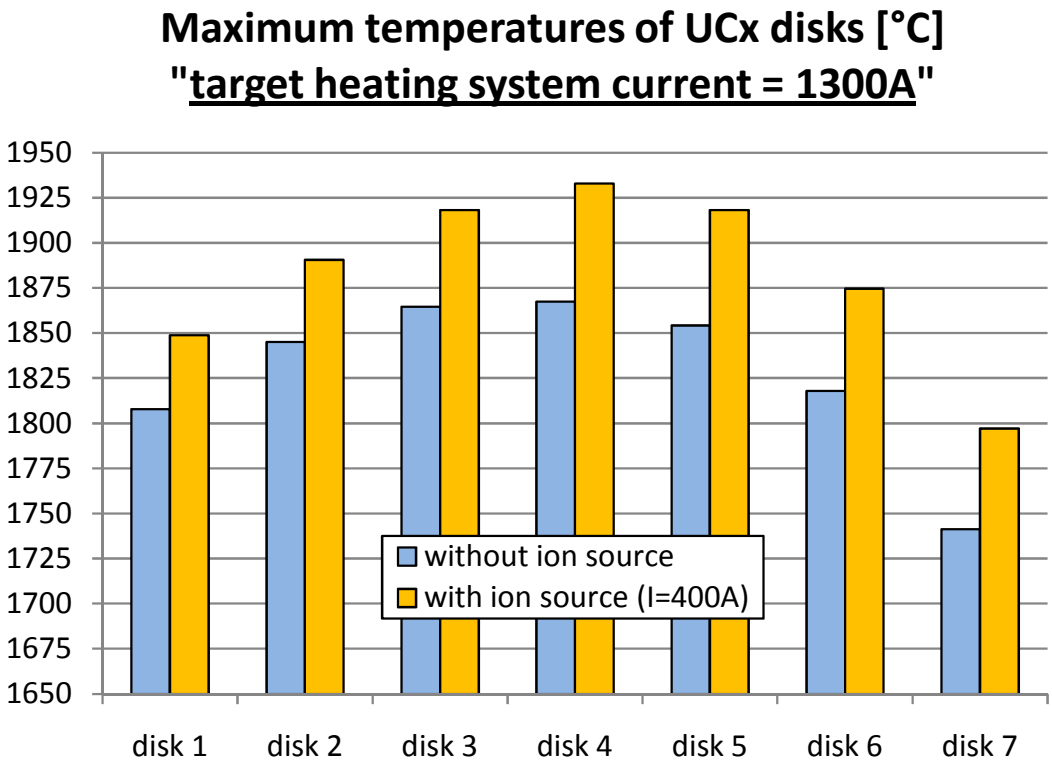

Fig. 5.8. Maximum temperatures of the UC_x disks correspondent to a target heating system current of 1300A, with and without the presence of the ion source (heated by an electrical current of 400A).

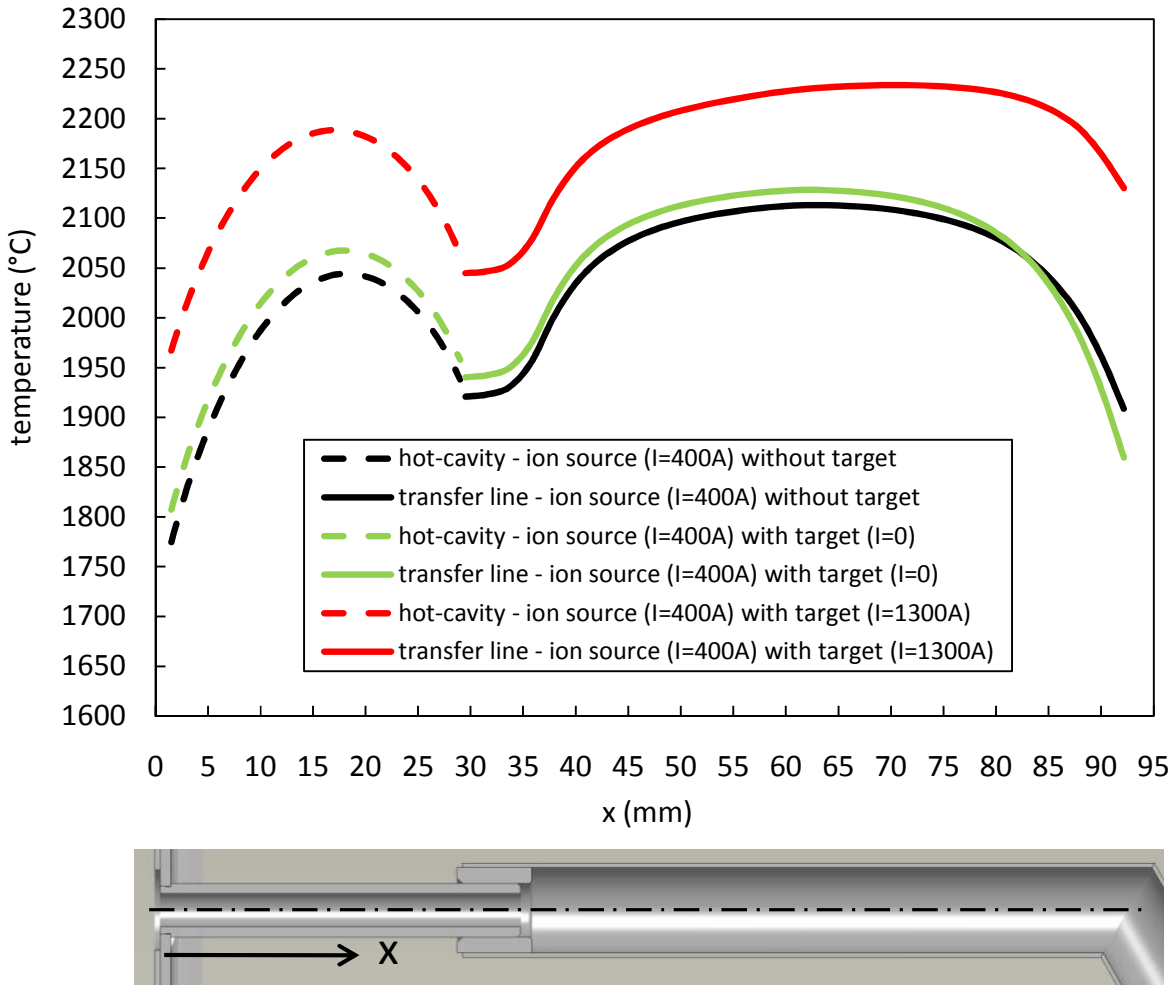

Fig. 5.9. Hot-cavity and transfer line temperature distributions correspondent to 400 A of ion source current: effect of the target system installation with target heating system current values equal to 0 and 1300A.

Respect to the case that considers the presence of the ion source only, the introduction of the production target with the correspondent heating system deactivated produces a general slight temperature increment on both the hot-cavity and the transfer line, mainly due to the radiative flux component reflected back to the aforementioned objects by the Ta tube; only in proximity of the connection between the target and the transfer line the temperature level registers a decrease, caused by the increment of the area available to dissipate heat by thermal radiation. When the target heating system is active and the correspondent heating current is equal to 1300A, both the hot-cavity and the transfer line register an important temperature increase respect to the case of the ion source only, oscillating between 106 and 160°C for the hot-cavity and between 95 and 271°C for the transfer line. It is important to underline that a segment of the transfer line exceeds the temperature limit of tantalum (2200°C, see chapter 3 and 4): as a consequence the maximum ion source current should be slightly reduced or, keeping the same current level, the thickness of the transfer line should be slightly increased.

Granted that the hot-cavity temperature is the temperature of the hot-cavity at the coordinate x=0 (see figure 5.9), in figure 5.10 it is possible to appreciate the hot-cavity temperature curve for ion source current values variable between 100 and 400A; in particular the case of the ion source only is compared to the case characterized by the presence of both the target and the ion source with the target heating system current equal to zero. The two curves are very close: when the ion source current is equal to 100A the presence of the target leads to a small temperature decrease whereas when the heating current reaches 400A a slight temperature increment is registered.

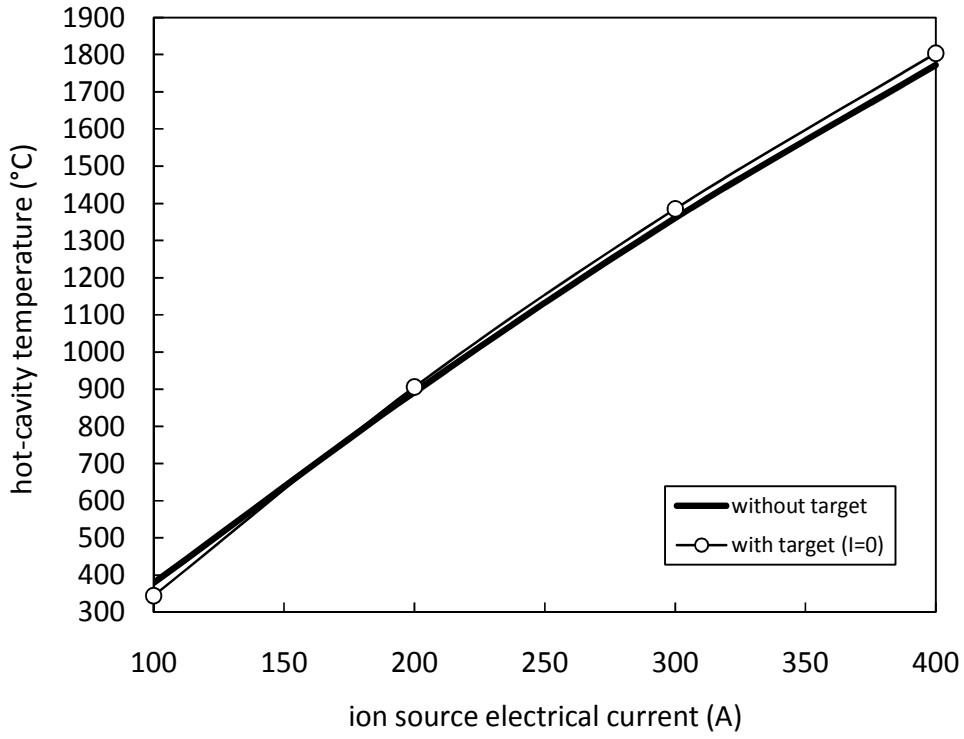

Fig. 5.10. Hot-cavity temperatures for different values of the ion source electrical current: effect of the target system installation with target heating system current equal to zero.

Figure 5.11 shows how the hot-cavity temperature varies when the ion source current is kept constant at 400A and the target heating system current is increased from 600 to 1300A (the complete "production target – hot-cavity ion source" assembly is considered). The gradual temperature increase is evident, in particular the hot-cavity temperature rises from 1830°C to 1963°C changing the heating current value from 600 to 1300A.

Observing figures 5.12 and 5.13 it is possible to appreciate the temperature plot of the target – ion source assembly in the lateral section view and in the frontal section view, respectively. The transfer line is the component that registers the higher temperature levels, exceeding (as mentioned above) the tantalum temperature limit (2200°C) in a portion of its axial extent. As shown in figures 5.7 and 5.8 the temperatures of the UC_x disks are always below 2000°C.

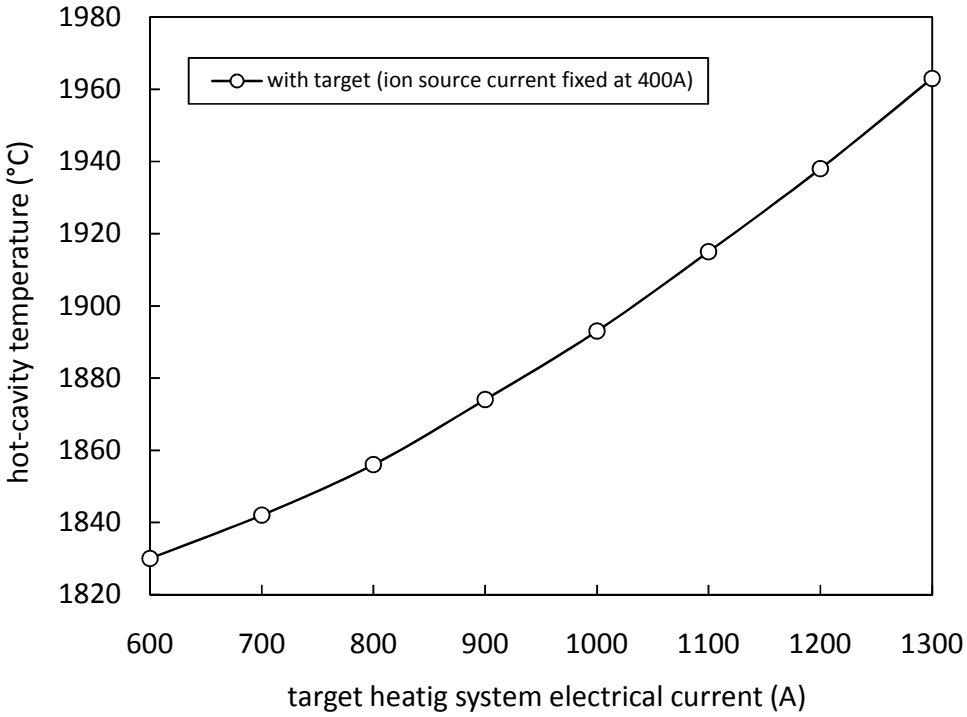

Fig. 5.11. Hot-cavity temperatures for an ion source electrical current fixed at 400A and variable values of the heating system current (the complete "production target – hot-cavity ion source" assembly is considered).

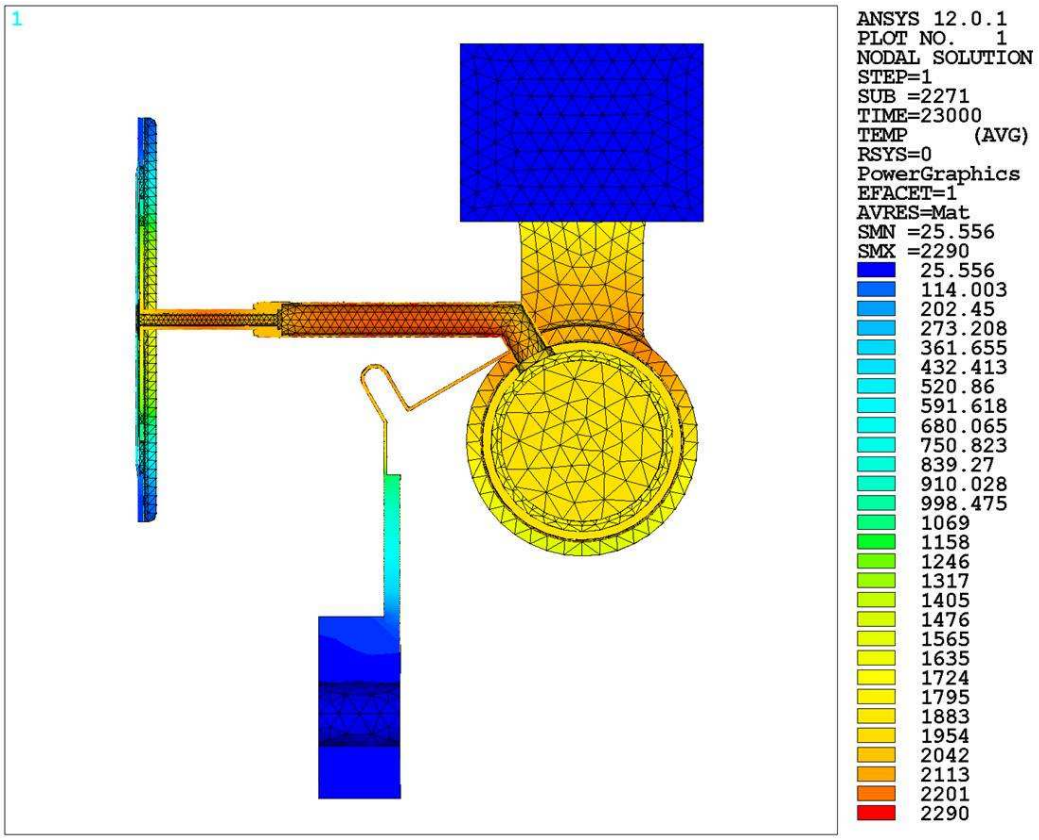

Fig. 5.12. The "production target – hot-cavity ion source" assembly: temperature plot (lateral section view) correspondent to an ion source current and a target heating system current equal to 400 and 1300A, respectively.

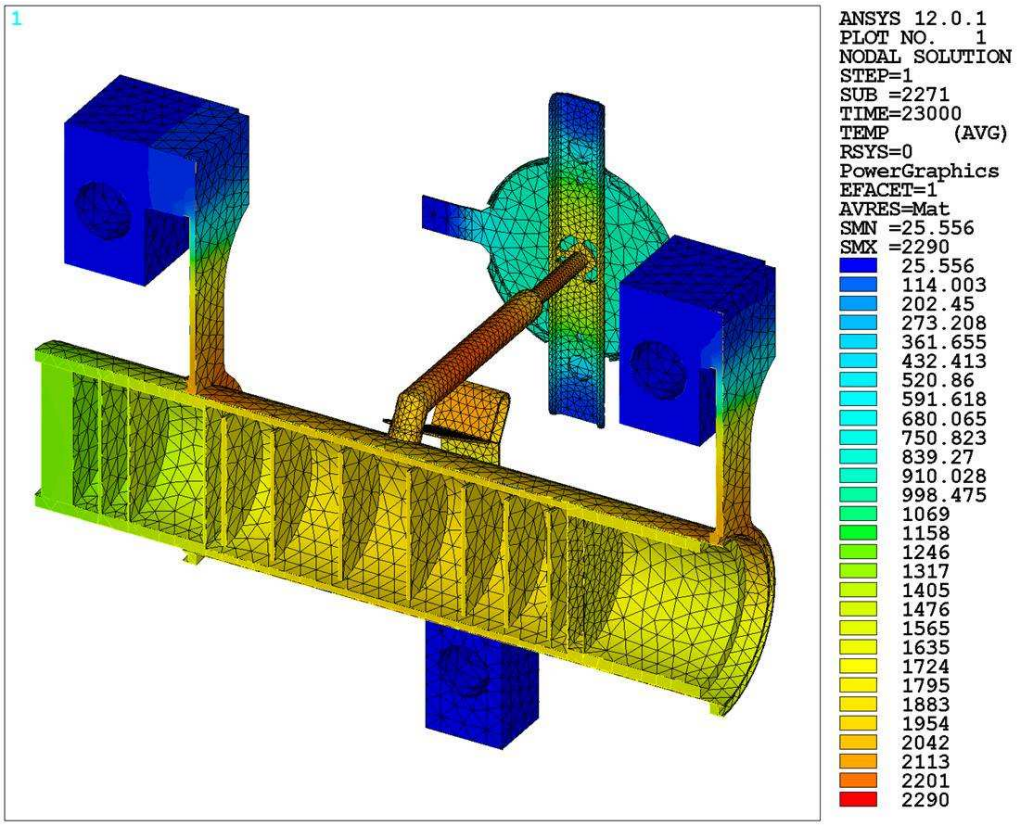

Fig. 5.13. The "production target – hot-cavity ion source" assembly: temperature plot (frontal section view) correspondent to an ion source current and a target heating system current equal to 400 and 1300A, respectively.

At this point we start to present data obtained considering the effect of the proton beam thermal load and of the ion source heating current (fixed at 400A) only (the target heating system current is not taken into consideration): it is very important to underline that the aforementioned set of thermal loads represent the on-line working conditions of the SPES target – ion source assembly. Figures 5.14 and 5.15 report the average and the maximum temperatures, respectively, of the UC_x disks correspondent to the proton beam thermal load, with and without the presence of the ion source (heated by an electrical current of 400A). As expected disks 4 and 5 register the maximum increment of the average disk temperature: for both of them it is equal to 31°C. On the other side the lower average disk temperature increment (20°C) is observed in proximity of disk 1. Similar considerations can be done for the maximum disk temperature: disk 4 and disk 5 (that occupy the central part of the target) present the maximum increment of the maximum disk temperature (30°C) due to the presence of the ion source; the minimum increment is registered in proximity of the first disk (19°C).

Figure 5.16 shows the effect of the proton beam thermal load on the hot-cavity and transfer line temperature distributions when the ion source heating current is fixed at 400A.

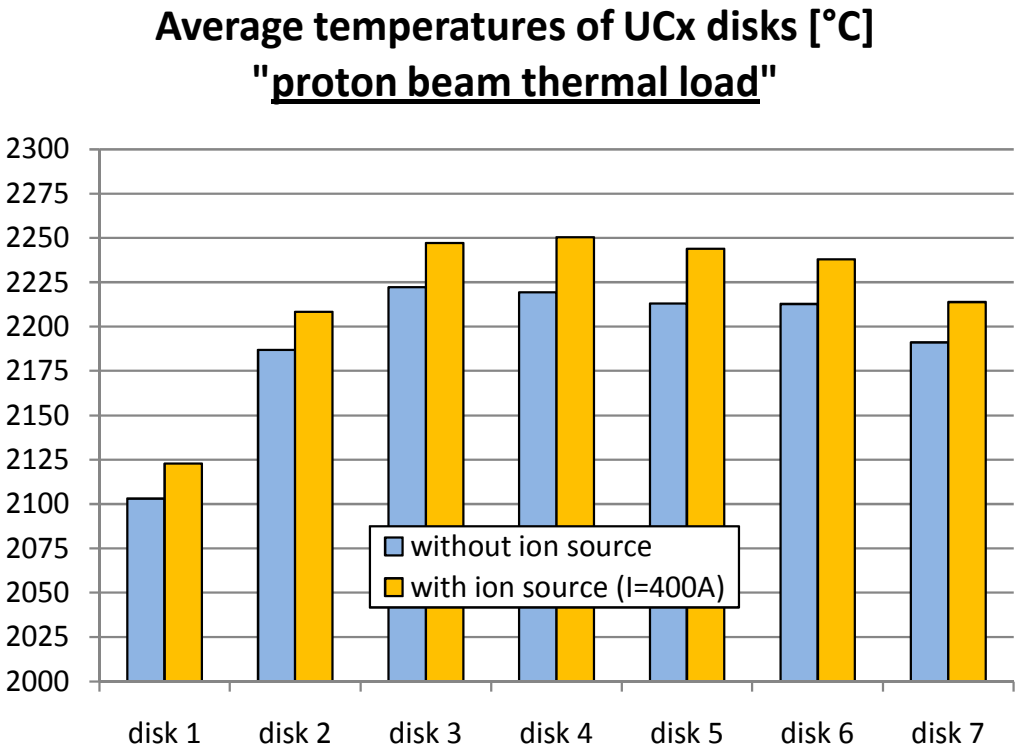

Fig. 5.14. Average temperatures of the UC_x disks correspondent to the proton beam thermal load, with and without the presence of the ion source (heated by an electrical current of 400A).

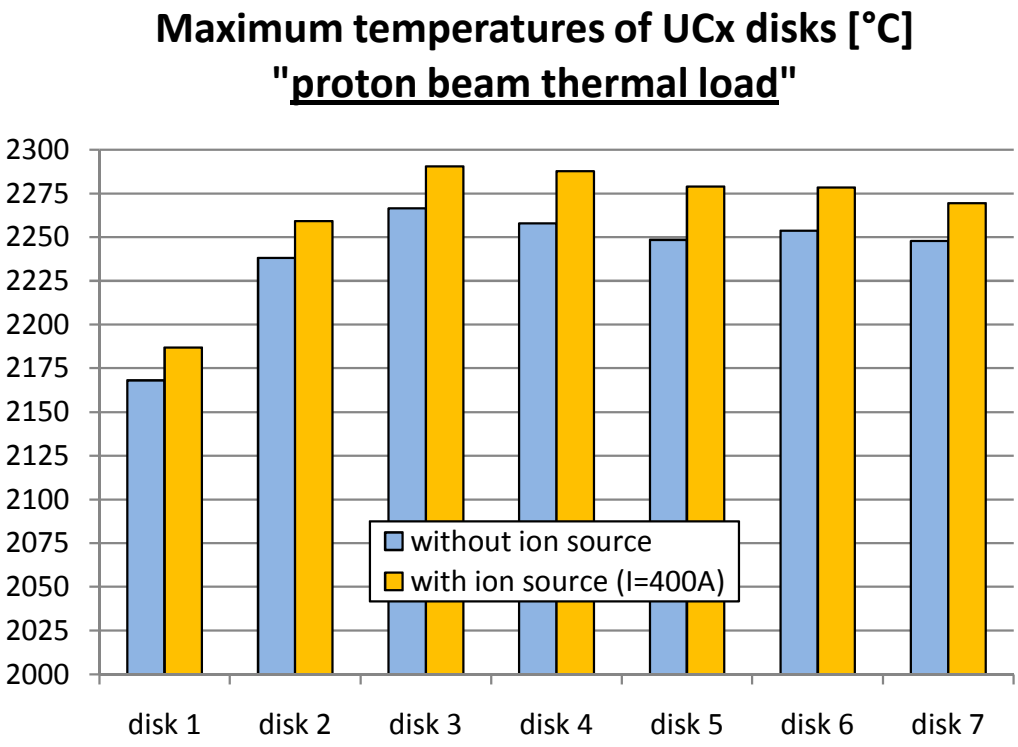

Fig. 5.15. Maximum temperatures of the UCx disks correspondent to the proton beam thermal load, with and without the presence of the ion source (heated by an electrical current of 400A).

In particular, both the hot-cavity and the transfer line temperature distributions are reported considering different cases: the presence of the ion source (and transfer line) only, the presence of both the target and the ion source without thermal loads applied to the target and the presence of both the objects with the effect of the proton beam thermal load. Respect to the case that considers the presence of the ion source only, the introduction of the production target without thermal loads was discussed above while commenting figure 5.9. With the introduction of the production target and the application of the proton beam thermal load, both the hot-cavity and the transfer line register an important temperature increase respect to the case of the ion source only, oscillating between 88 and 134°C for the hot-cavity and between 80 and 234°C for the transfer line. Also in the case of the on-line working conditions a segment of the transfer line slightly exceeds the temperature limit fixed for tantalum (2200°C).

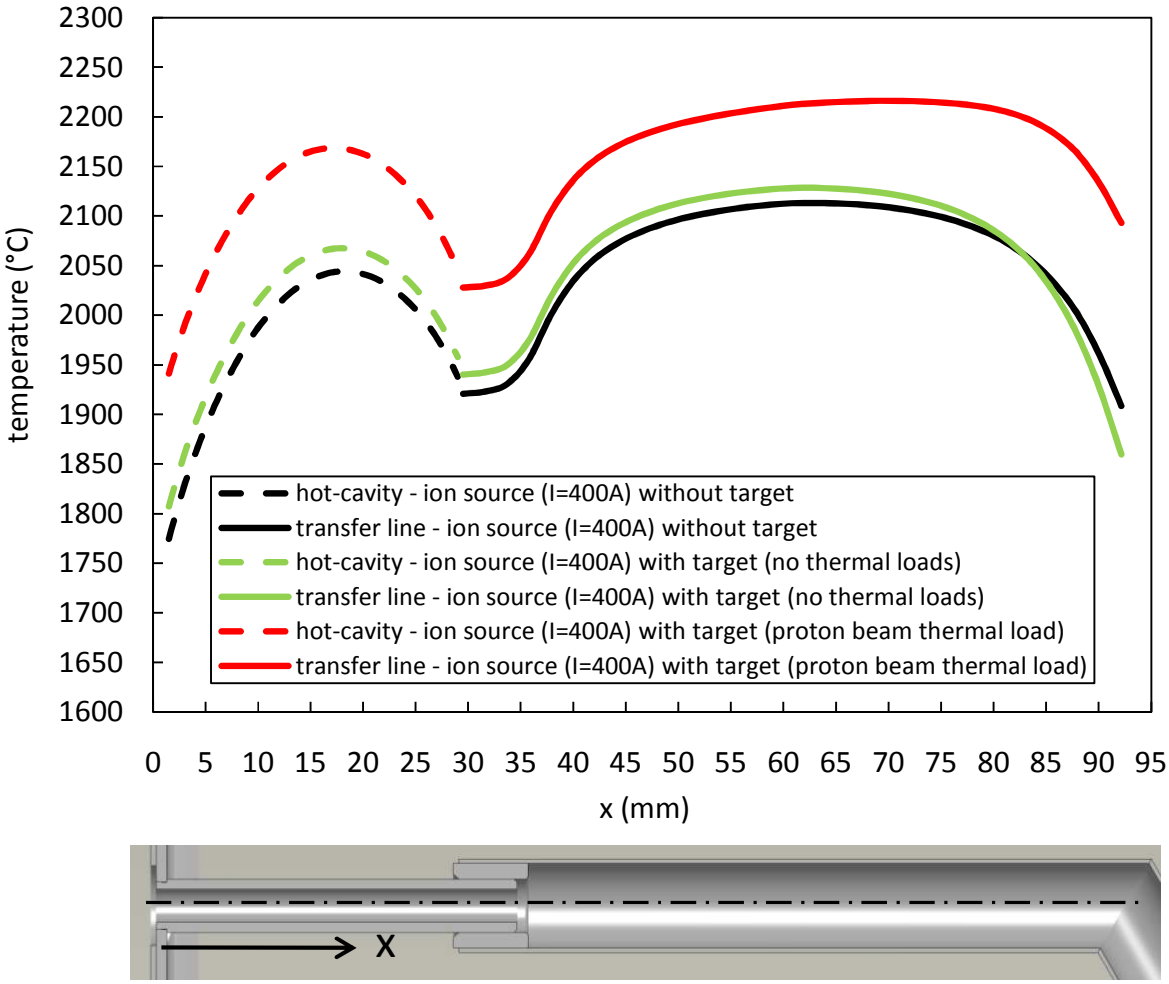

Fig. 5.16. Hot-cavity and transfer line temperature distributions correspondent to 400 A of ion source current: effect of the target system installation with and without the application of the proton beam thermal load.

Figures 5.17 and 5.18 propose the temperature plot of the target – ion source assembly (for the on-line load condition) in the lateral section view and in the frontal section view, respectively.

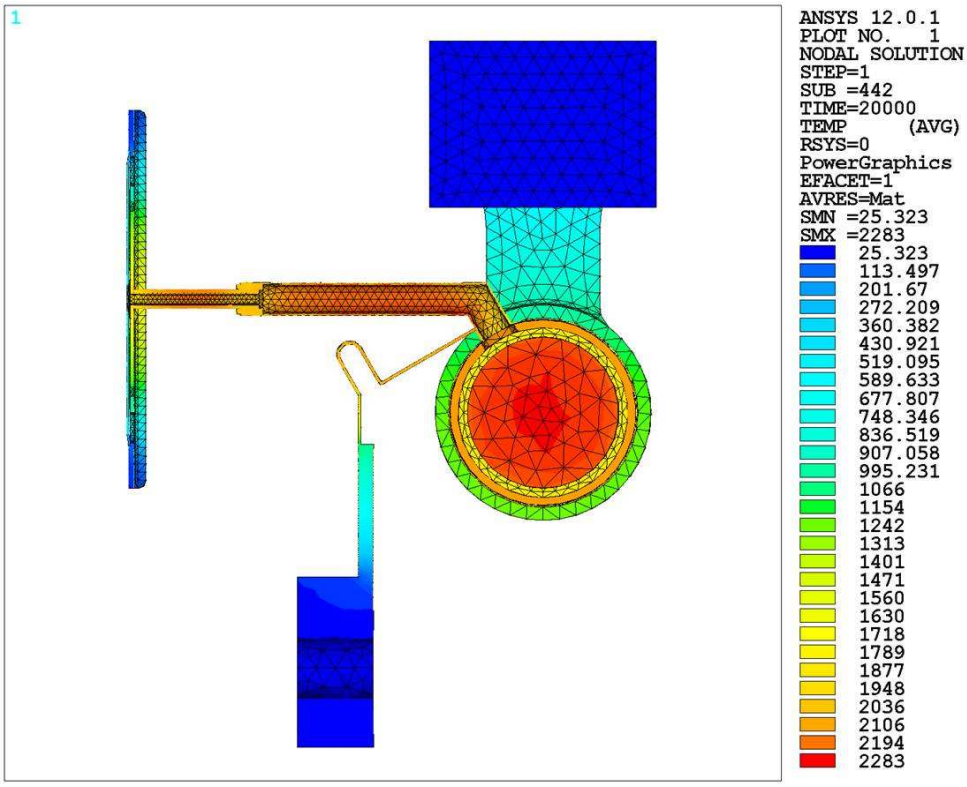

Fig. 5.17. The "production target – hot-cavity ion source" assembly: temperature plot (lateral section view) correspondent to an ion source current fixed at 400A with the presence of the proton beam thermal load.

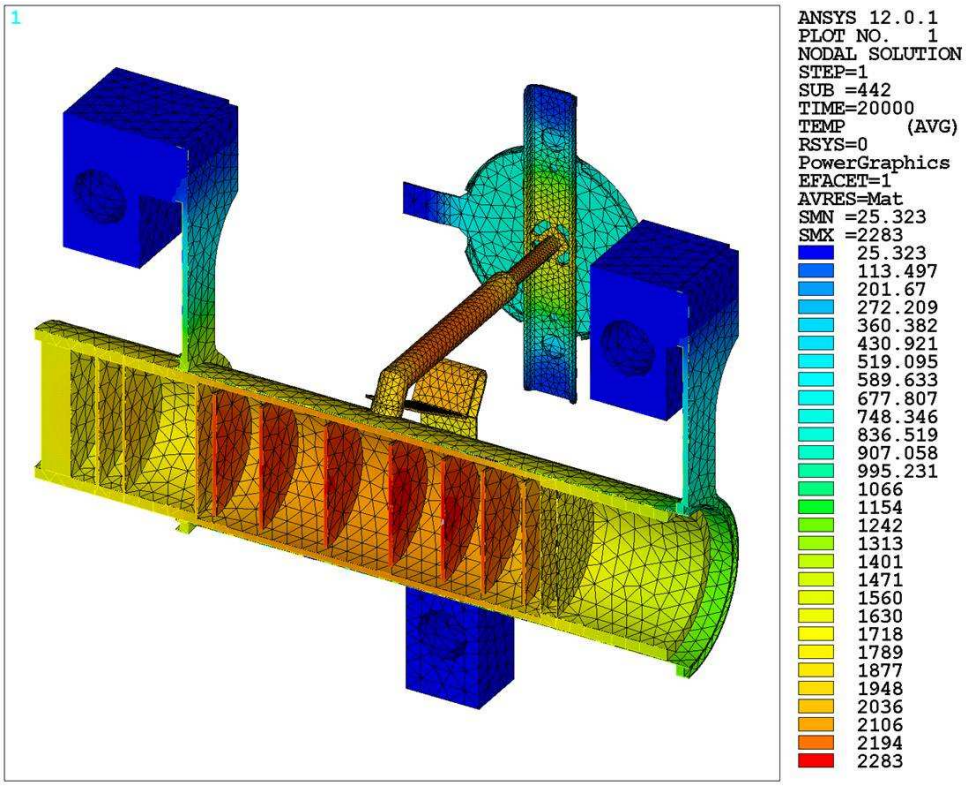

Fig. 5.18. The "production target – hot-cavity ion source" assembly: temperature plot (frontal section view) correspondent to an ion source current fixed at 400A with the presence of the proton beam thermal load.

As expected the maximum temperature value is observed in proximity of the UC_x disks (desk 3): it is equal to 2291°C, more or less 100°C below the melting point of uranium carbide taken as reference in this work (2390°C). Very high temperature levels, close to 2200°C, are registered also all along the hot-cavity and the transfer line (see figure 5.16).

In the next paragraph the off-line tests of the target – ion source assembly performed at Legnaro National Laboratories are illustrated and experimental data are compared to results obtained by means of the FE model above described.

5.3. Experimental tests and comparison with numerical data

In this paragraph the experimental tests on the target – ion source assembly are presented and discussed in detail; temperature and potential difference measurements are then compared to numerical data obtained thanks to the FE thermal-electric model described in the previous paragraphs.

Figure 5.19 shows the assemblage of the hot-cavity ion source complex: in particular the installation of the main part of the hot-cavity ion source is presented in figure 5.19.a and the positioning of the transfer line is reported in figure 5.19.b.

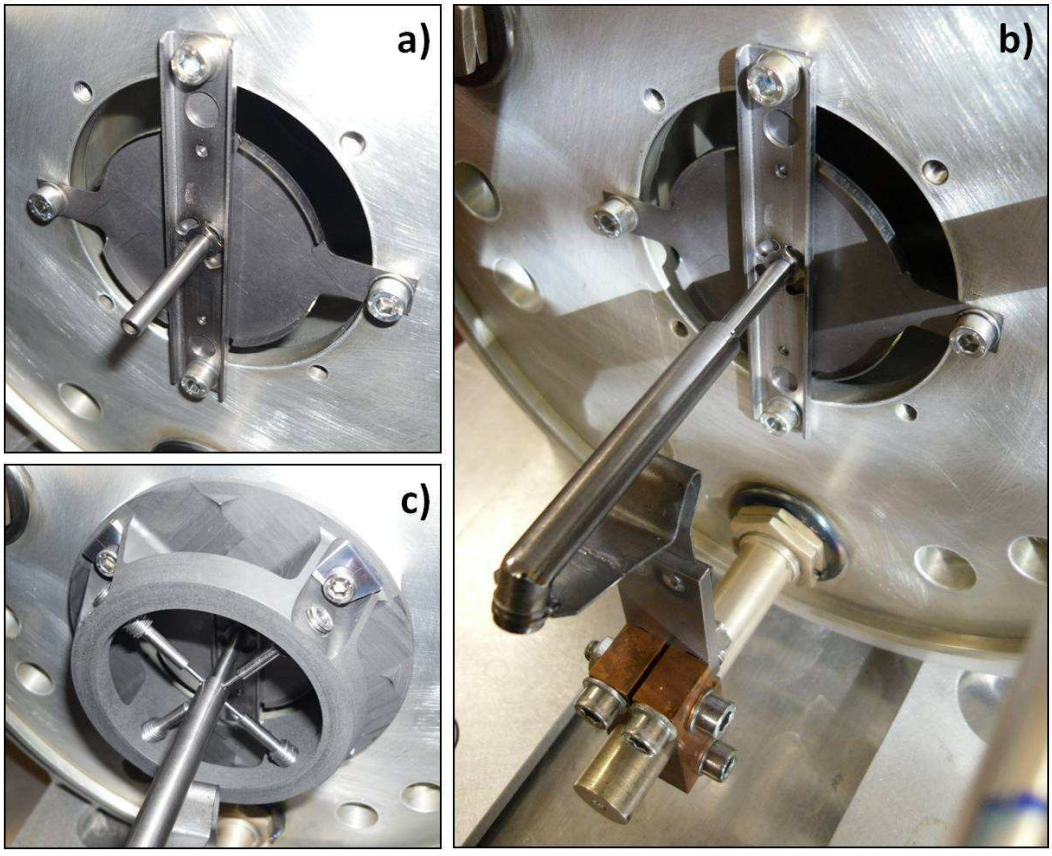

Fig. 5.19. Installation of the hot-cavity ion source (a); positioning of the transfer line (b); preliminary installation of the hot-cavity alignment system (c).

Figure 5.19.c illustrates also the preliminary installation of the hot-cavity alignment system: we remember that this device is used to guarantee a correct penetration of the laser beam inside the hot-cavity when the hot-cavity ion source is used for laser ionization processes but in general it is useful to avoid large deformations and deflection in proximity of the interface between the hot-cavity's external extremity and the extraction electrode, where the ion beam originates: bad deformations in this zone can cause important worsening of the ion beam emittance and so of the ion beam quality.

Once assembled the main part of the hot-cavity ion source, the transfer line and the alignment system, the production target was installed and accurately fixed verifying its alignment respect to the primary beam channel (the channel in the target vacuum chamber used to allow the proton beam entrance) and to the transfer line; a particular attention was dedicated to connect the transfer line to the Ta tube of the target heating system. At this point the hot-cavity was permanently aligned using the centering screwed bars of the hot-cavity alignment system (see figure 5.20).

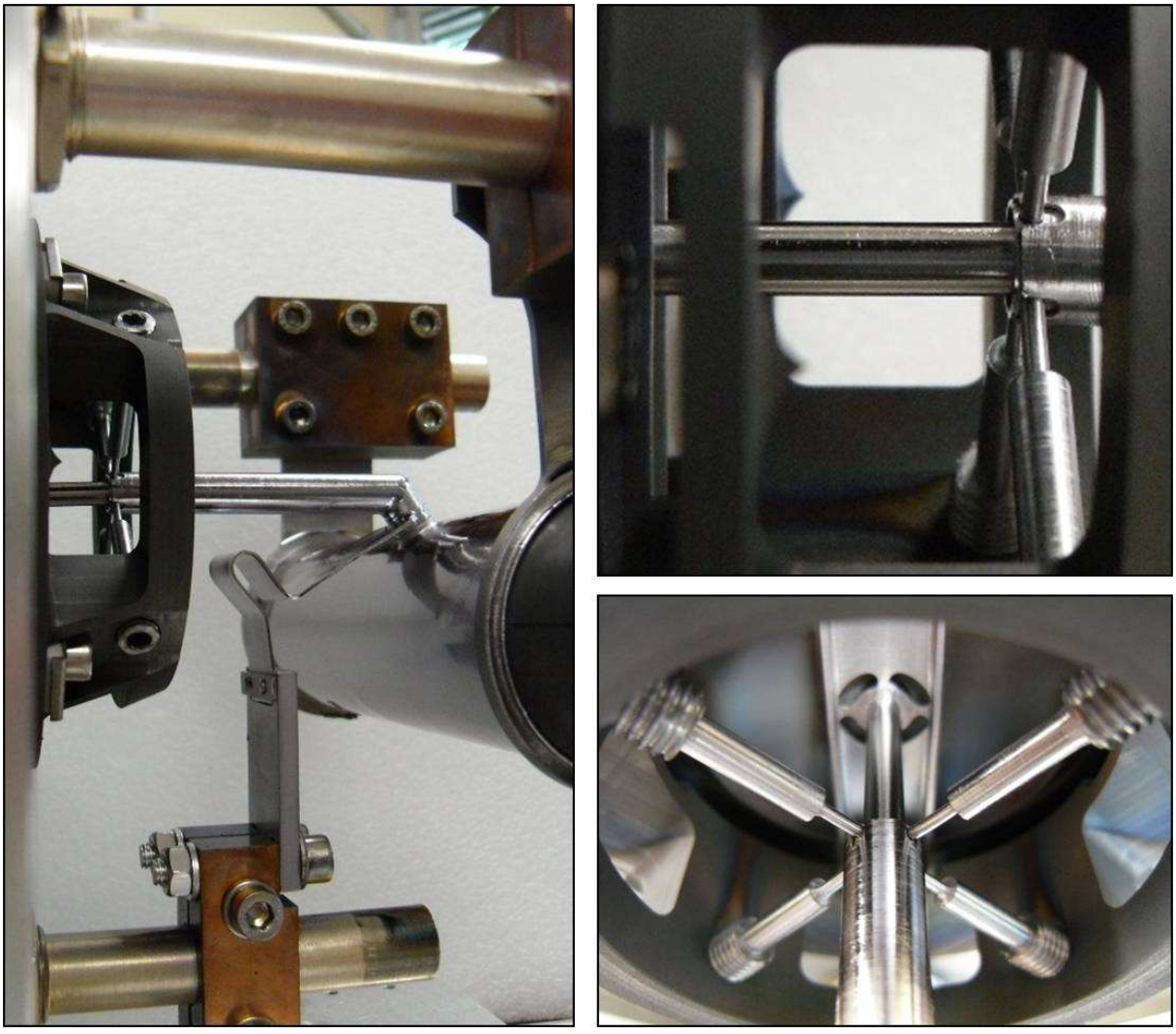

Fig. 5.20. Installation of the production target, transfer line fixing and alignment of the hot-cavity using the centering screwed bars of the hot-cavity alignment system (see paragraph 4.4.2, chapter 4).

A detailed picture of the “production target – hot-cavity ion source” assembly installed at Legnaro National laboratories is presented in figure 5.21; it is important to notice that the FE model proposed in the previous paragraphs did not include the alignment system: this detail introduced an approximation but its entity was surely not very important since the contact points with the four centering bars are very small (low conductive thermal fluxes and consequently low influence on the local temperature field) (see figure 5.20) and the graphite frame is light and characterized by four big lateral apertures (low interaction with the radiative heat transfer phenomena) (see figure 5.19, 5.20 and 5.21).

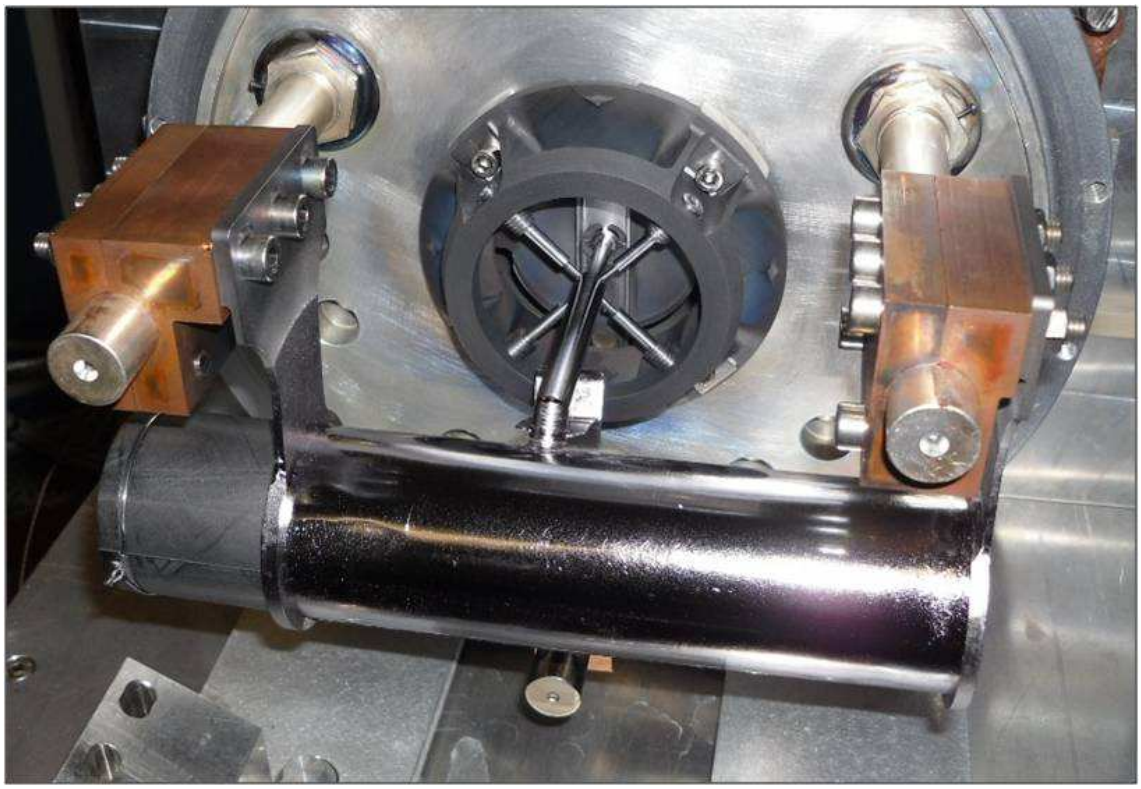

Fig. 5.21. The “production target – hot-cavity ion source” assembly.

An important detail to remark is that the production target assembled for this set of measurements was the same target prototype used in the tests described in chapter 3; in particular the tests related to the present chapter are subsequent to test 7 described in paragraph 3.4.3 (see figure 3.87): this means that the target heating system did not work at the maximum of its capabilities because of the problem of the box’s parallel circuit (see chapter 3).

The target vacuum chamber used for this measurement set was the same chamber described in chapter 3 and used during the experimental tests of the new production target prototype; in the present case it allowed to monitor two temperature points: the window temperature and the hot-cavity temperature (we remember that the hot-cavity temperature is the temperature of the hot-cavity at the coordinate x=0, see figure 5.9). Two different power supplies were used to feed the

target heating system circuit and the ion source circuit: both of them were characterized by the maximum current and the maximum potential difference values of 1000A and 10V, respectively. The potential difference values related to the target heating system and to the ion source electrical circuits were monitored as proposed in chapters 3 and 4.

During the experimental tests current loads were assigned as proposed in figure 5.3; the only difference was the maximum value of the target heating system current that in the present case was equal to 900A because of the limitations of the power supply adopted.

Figure 5.22 shows the comparison between FE and experimental window temperatures for different heating system current values and ion source current fixed at 400A; as expected experimental values are lower respect to FE ones: in fact during the experimental tests it was not possible to make the target heating system work in ideal conditions because of the problem of the box's parallel circuit described in chapter 3. For heating system current values equal to 600 and 900A, the temperature differences registered are equal to 135 and 123°C, respectively. Observing figure 5.23 it is possible to appreciate the correspondent heating system potential difference values: usually experimental data are higher respect to numerical ones (because of ideal thermal and electrical contacts implemented in the FE model, and not ideal contacts that characterize the real object) but in this case the two curves are practically coincident thanks to the reduction of the heating system equivalent electrical resistance (the aforementioned reduction is due to the box's parallel circuit, see chapter 3).

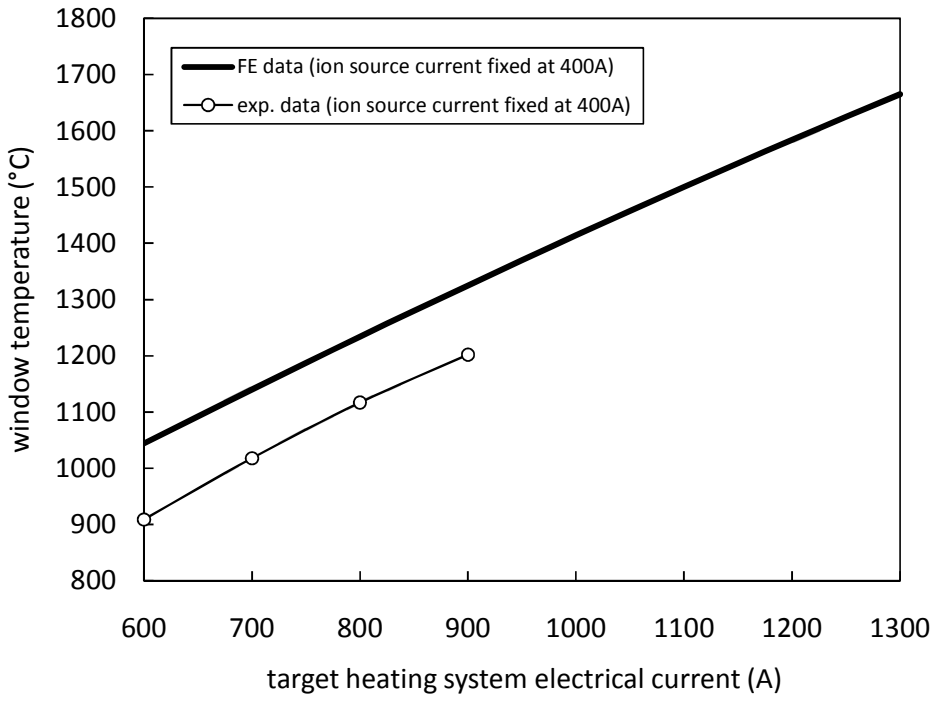

Fig. 5.22. Window temperatures for different heating system current values and ion source current fixed at 400A: comparison between FE and experimental data.

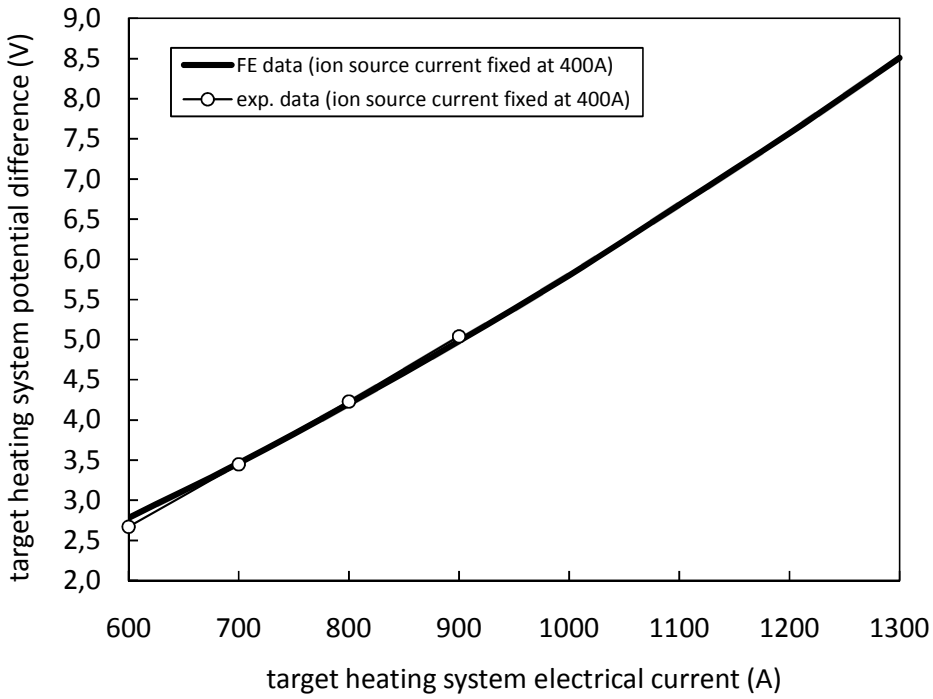

Fig. 5.23. Target heating system potential difference values for an heating system current ranging from 600 to 1300A and an ion source current fixed at 400A: comparison between FE and experimental data.

Figures 5.24 and 5.25 report the hot-cavity temperature and the ion source potential difference curves, respectively, for different ion source current values and target heating system current equal to zero.

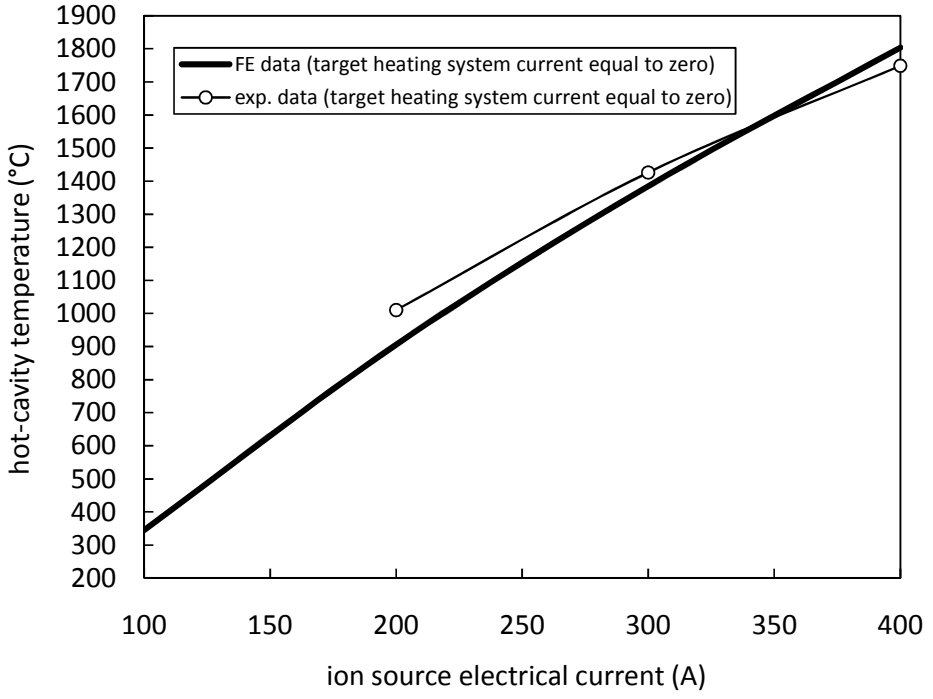

Fig. 5.24. Hot-cavity temperatures for different ion source current values (target heating system current equal to zero): comparison between FE and experimental data.

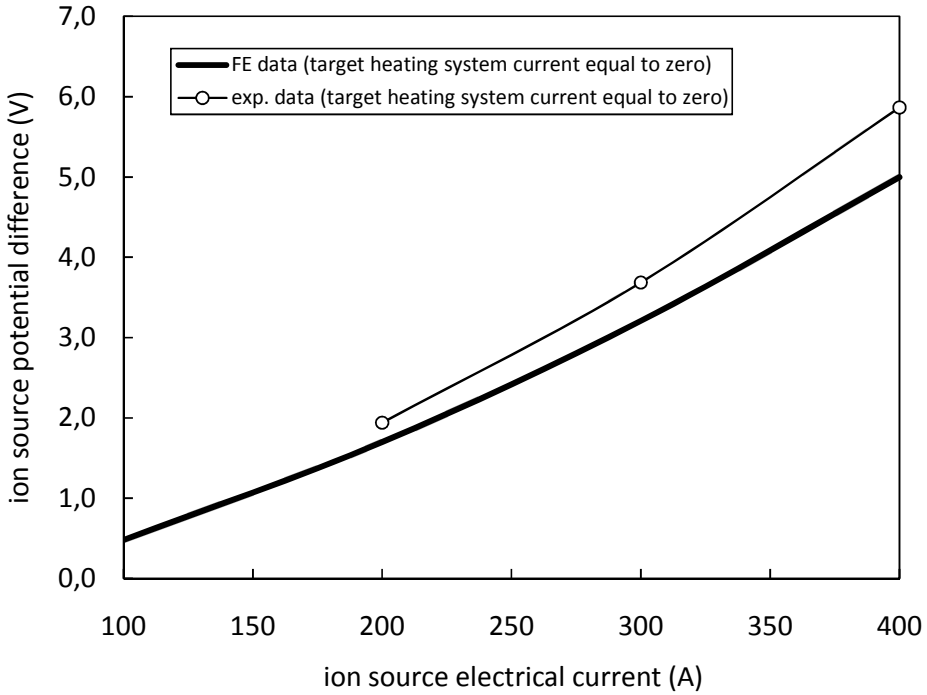

Fig. 5.25. Ion source potential difference values correspondent to ion source currents ranging from 100 to 400A (target heating system current equal to zero): comparison between FE and experimental data.

In the case of the hot-cavity temperature curves, experimental values are above the correspondent numerical ones for low ion source currents, whereas the experimental curve is below the numerical one for high current values: in particular the differences between experimental and numerical hot-cavity temperatures are equal to 105 and 55°C for current values of 200 and 400A, respectively (see figure 5.24). Concerning the ion source potential difference values, the experimental curve is constantly above the numerical one and rapidly diverges from it for high current values, mainly because of thermal and electrical contact phenomena just described in the previous chapters: the difference between the two curves ranges from 0.24 to 0.87V passing from 200 to 400A of current.

Figure 5.26 reports the hot-cavity temperature values obtained keeping the ion source current fixed at 400A and increasing the heating system current from 600 to 1300A; the mismatch between the numerical model and the experimental data is evident: numerical temperatures increase gradually with the heating system current whereas numerical temperature values are approximately constant. The same discrepancy can be observed in the correspondent ion source potential difference curves (see figure 5.27): also in this case numerical potential difference values increase gradually with current whereas experimental values remain approximately constant. The aforementioned anomaly can be explained observing figures 5.28, 5.29 and 5.30: these figures, reporting some pictures of the real target – ion source assembly heated by different values of heating system and ion source currents, show the substantial thermal (and consequently electrical)

discontinuity between the transfer line and the tantalum tube. If on the one hand the real objects (target and ion source) seem to be practically decoupled, on the other hand the FE model defines a perfect thermal and electrical continuity between the transfer line and the tantalum tube.

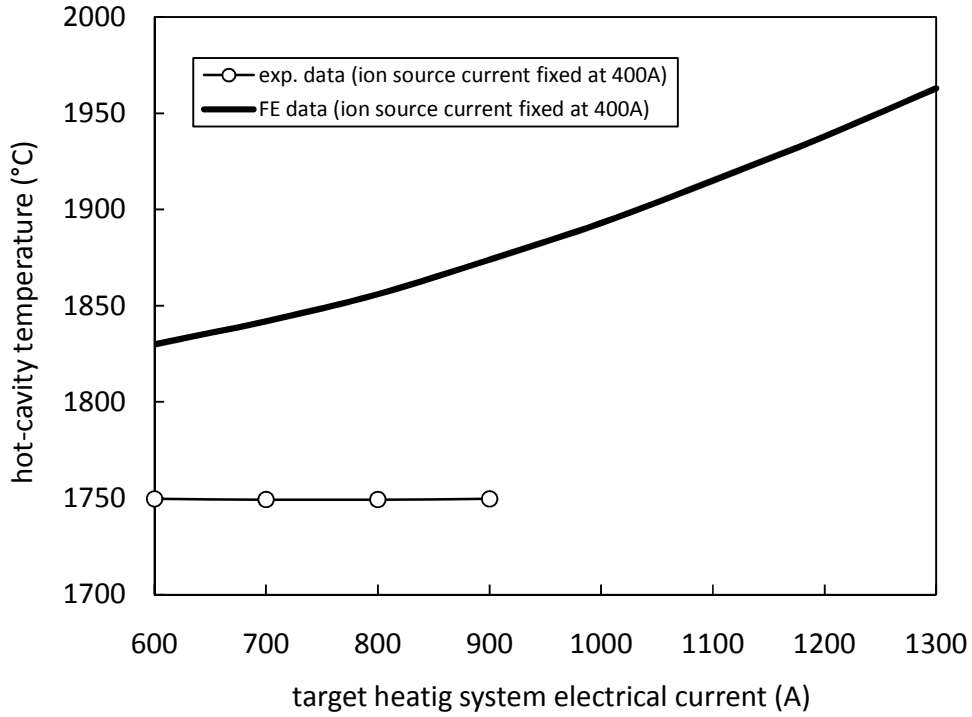

Fig. 5.26. Hot-cavity temperatures for different target heating system current values (ion source current fixed at 400A): comparison between FE and experimental data.

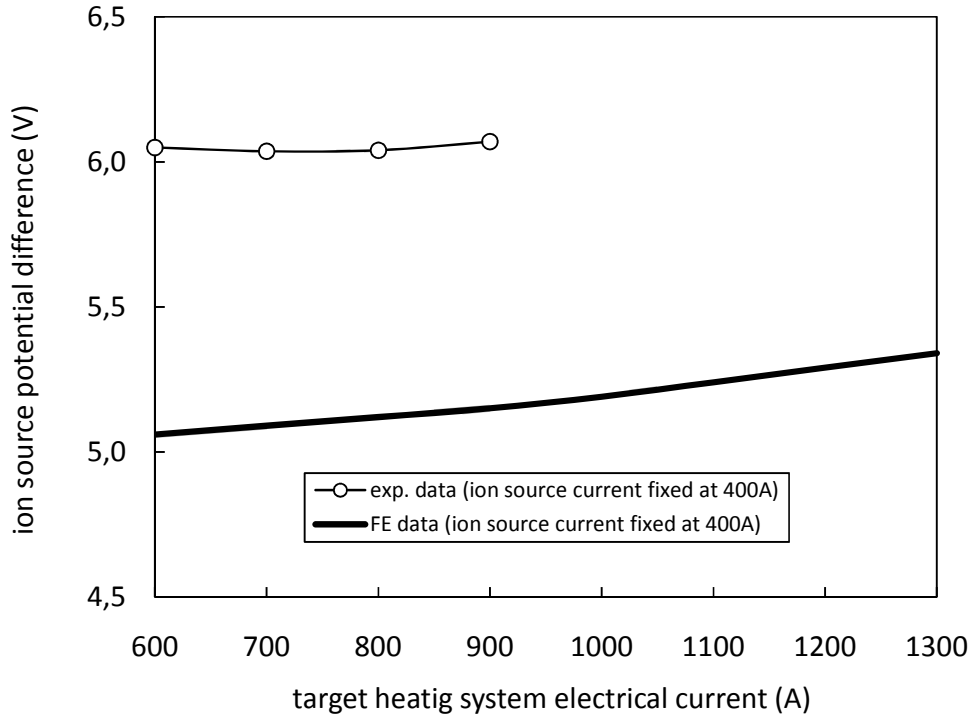

Fig. 5.27. Ion source potential difference values correspondent to target heating system currents ranging from 600 to 1300A (ion source current fixed at 400A): comparison between FE and experimental data.

As a consequence it is possible to justify the fact that both the hot-cavity temperature and the ion source potential difference experimental curves are not influenced by the target (in particular by the target heating system electrical current) and the dependence of the correspondent numerical curves from the heating system current (see figures 5.26 and 5.27).

By means of a special vacuum chamber's cover (see figures 4.11 and 4.17, chapter 4), characterized by a lateral viewport but without cooling system, it was possible to observe, with some limitations for the maximum heating currents assigned, both the ion source and the target (connected by means of the transfer line) heated at high temperatures. In particular figure 5.28 shows the target – ion source assembly heated by an ion source current of 200A: the temperature discontinuity between the tantalum tube of the target heating system and the transfer line is evident. The aforementioned discontinuity is clearly visible also in figure 5.29 where only the target heating system (with 700A of heating current) contributes to heat the target – ion source assembly. The two objects seem to be separated, independent: the transfer line's extremity is connected to the Ta tube's hole by mechanical interference that, respect to a welded joint, does not allow to create a perfect material continuity, even if the interference is very tight. Figure 5.30 report an image of the target – ion source assembly heated by both the heating system current (700A) and the ion source current (200A): also in this case the discontinuity at the transfer line – Ta tube connection is evident.

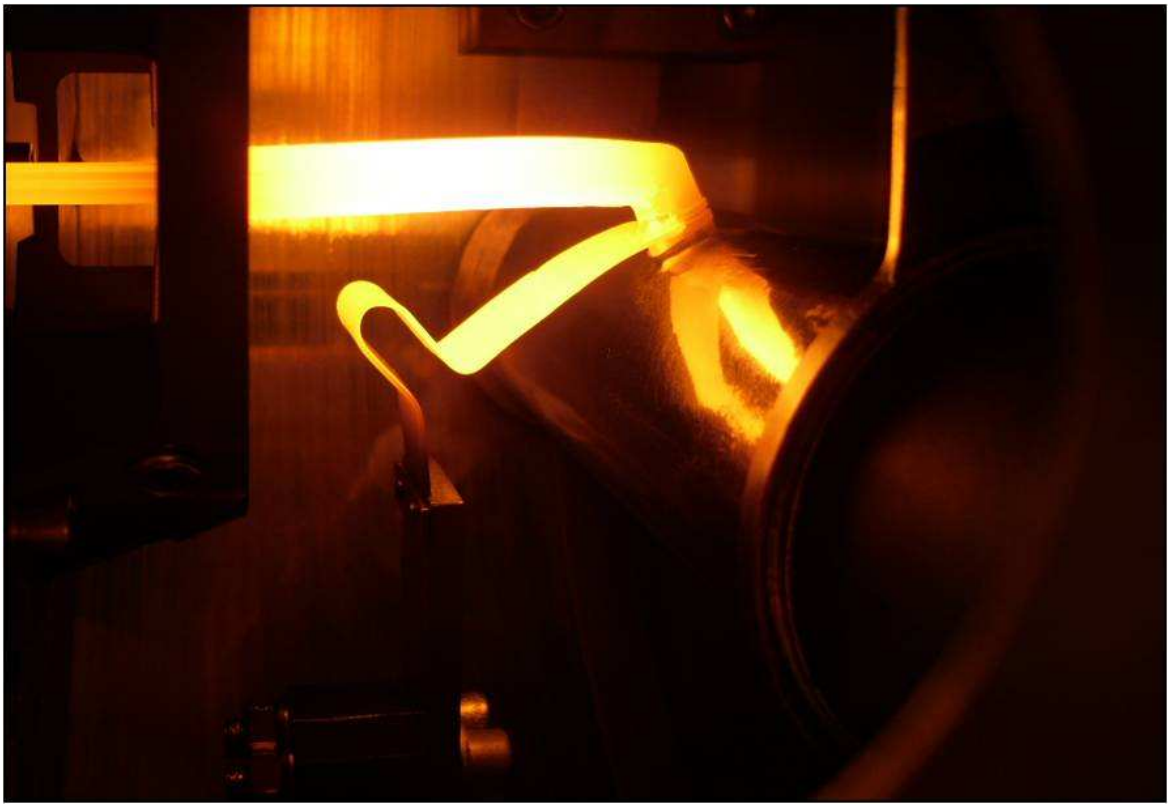

Fig. 5.28. Picture of the "production target – hot-cavity ion source" assembly heated by an ion source current equal to 200A.

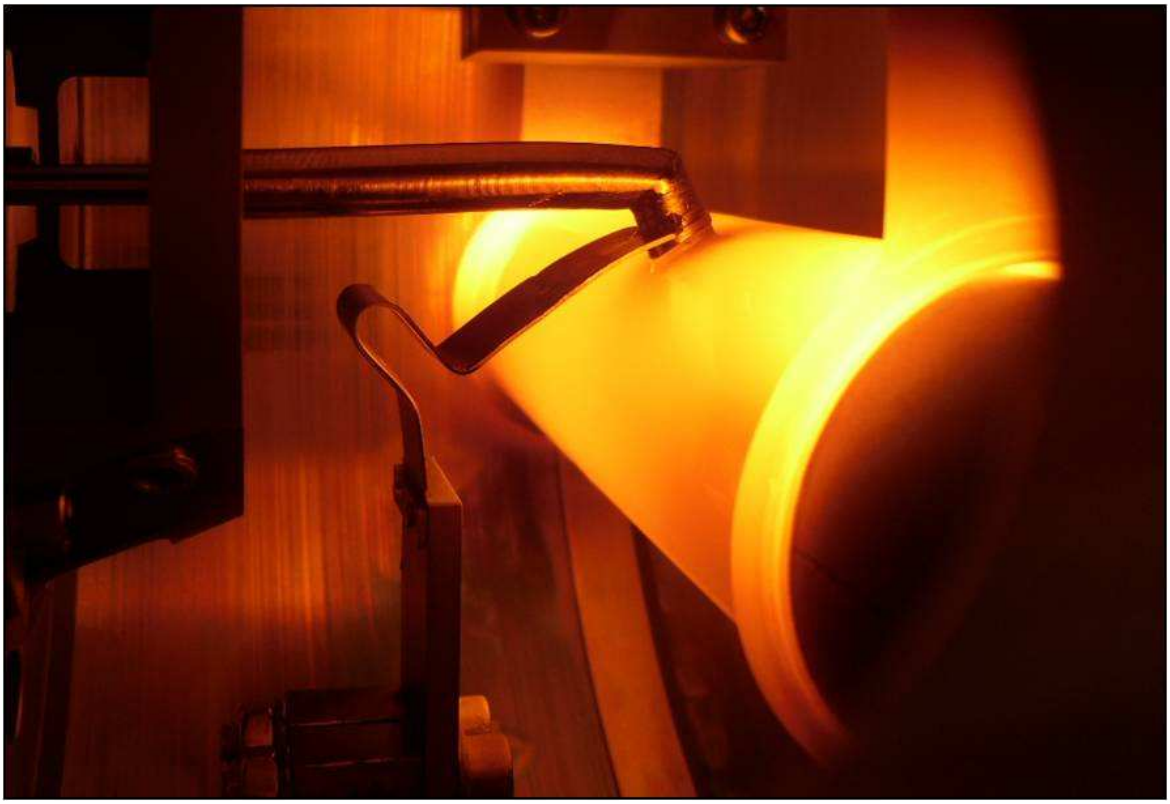

Fig. 5.29. Picture of the “production target – hot-cavity ion source” assembly heated by a target heating system current equal to 700A.

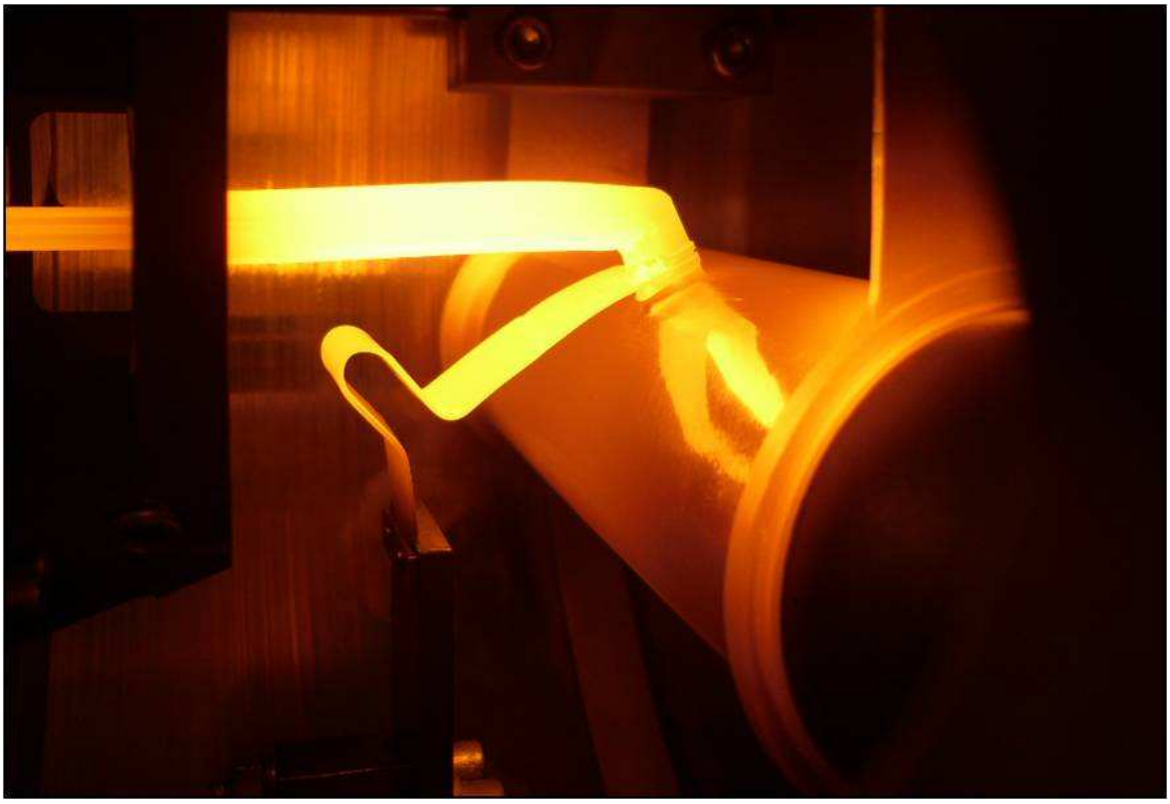

Fig. 5.30. Picture of the “production target – hot-cavity ion source” assembly heated by a target heating system current and an ion source current equal to 700 and 200A, respectively.

At the end of this paragraph figure 5.31 shows a picture of the ion source heated at high temperature by a current of 400A. The picture was taken through the secondary beam channel: it is easy to recognize the hot-cavity at the center, the main round frame of the alignment system and a small portion of the four centering bars used to keep the hot-cavity aligned.

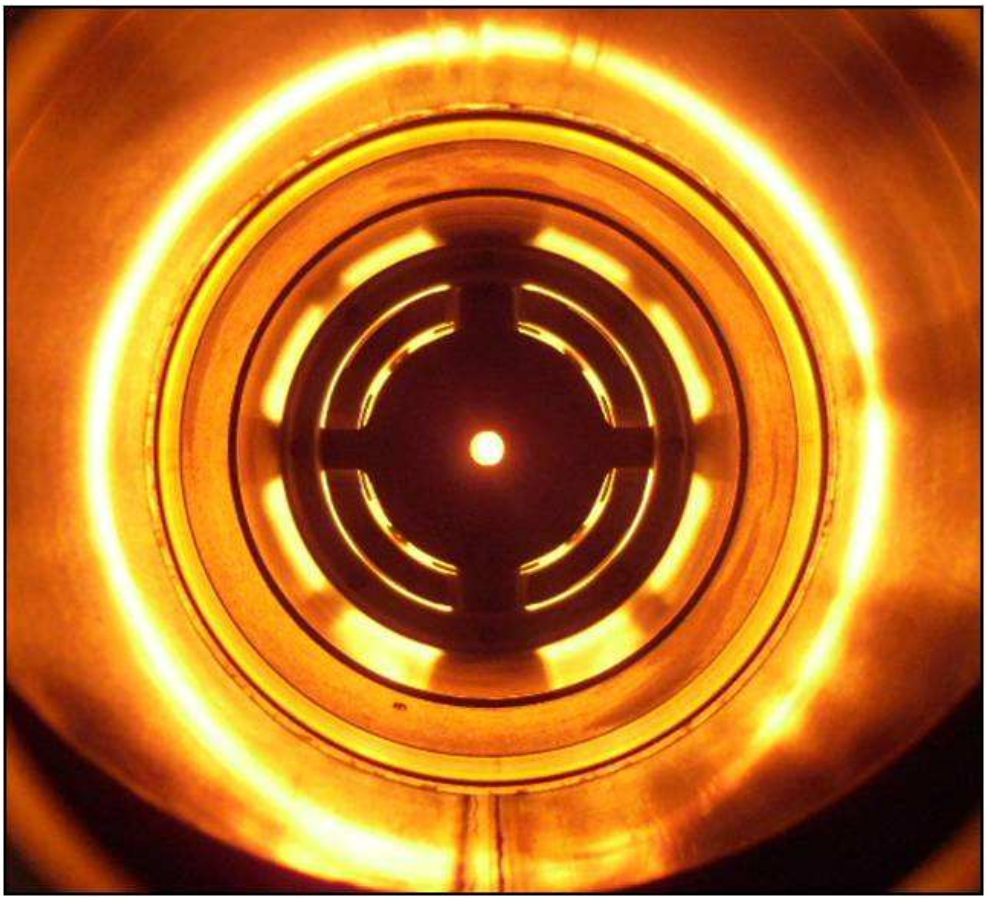

Fig. 5.31. Picture of the rear side of the hot-cavity ion source heated by an ion source current equal 400A (target heating system current equal to zero).

5.4. Conclusions

In this chapter a detailed study of the SPES “production target – hot-cavity ion source” assembly was presented and discussed. At first the thermal-electric behaviour of the assembly was studied using a numerical FE model, then the obtained results were compared to temperature and potential difference values measured at Legnaro National Laboratories during dedicated experimental off-line tests. Analogies and discrepancies between numerical and experimental data were discussed in detail.

REFERENCES

[1] J. Al-Khalili, E. Roeckl, The Euroschool Lectures on Physics with Exotic Beams, vol.2, Springer, Berlin, 2006.

Chapter 6

On-line tests of the scaled SPES Target prototype at the Oak Ridge National Laboratories (US Department Of Energy)

6.1. Introduction [1]

As widely exposed in the previous chapters, the main intent of the SPES (Selective Production of Exotic Species) project is the study and construction of an ISOL facility at Legnaro National Laboratories (INFN, Italy) for the production of neutron-rich radioactive ion beams in the mass range from 80 to 160 amu. The nuclei of interest will be produced by means of a 40 MeV, 200 μA proton beam, directly impinging on seven separate thin disks made of uranium carbide (namely UC_x). The core of the SPES facility is surely the target – ion source complex; in particular the production target is characterized by an original concept: with the aim to optimize the dissipation by thermal radiation of the power deposited by the proton beam, a careful design of the geometry was performed which resulted into the one presented here and consisting in seven thin disks (with thickness and diameter equal to 1.3 and 40 mm, respectively) accurately spaced in the axial direction. This approach can optimize the power dissipation and favour diffusion and effusion of the produced isotopes towards the ionization chamber. Theoretical calculations and simulations done in Legnaro [2] show that this target is a possible solution, in terms of both composition and layout, to produce exotic nuclei from uranium fission with rates up to 10^{13} fission/sec. In addition a series of tests using a SiC target prototype made in 2007 at HRIBF (ORNL) [3] show that the SPES target architecture can sustain very high proton beam currents (higher respect to the one-piece target usually adopted) without over-heating, and allows for easy fission product diffusion towards the ionization chamber. The Holifield Radioactive Ion Beam Facility (HRIBF) is a first generation national user facility for nuclear physics and nuclear astrophysics research [1]. With its 40 MeV primary proton beam, HRIBF is the closest of the ISOL facilities worldwide to the final SPES facility in terms of layout and power. Due to the common interests and features, an active collaboration between the SPES project at Legnaro National Laboratories and HRIBF started some years ago. The aim of this collaboration is to investigate, develop and test new target materials and new configurations for both targets and ion sources. In this chapter the first results on a UC_x SPES target prototype tested at HRIBF will be presented. In particular this work is based on the measurements performed using a scaled version of the UC_x SPES target, with discs of 13 mm diameter instead of 40 mm. The aforementioned prototype was developed in the SPES laboratories,

adjusted to fit the HRIBF target holder and then sent to the Oak Ridge National Laboratories (ORNL) for on-line measurements. This scaled version of the SPES target was found to be fully operative and functional. By scaling the production rate in the target and considering the release data collected in this work, it is possible to predict the radioactive beam intensities that will be available from the full scale target when installed in the SPES facility. By means of these on-line tests it is also possible to compare, in terms of release efficiency and other parameters of interest, the SPES target performance to that of other targets presented in the literature. In order to check the dependence of the isotope yields as a function of the target temperature, three sets of yield measurements were performed, at 1600°C, 1800°C and 2000°C. In this chapter only the results at the higher temperature (2000°C, the SPES target working temperature) are presented.

6.2. The SPES target prototype and the target – ion source system used at HRIBF

The architecture of the SPES target prototype is shown in figure 6.1: seven uranium carbide disks characterized by a diameter of 13±0.1 mm and a thickness of 1±0.1 mm are contained inside a cylindrical graphite box closed at its extremities by a graphite window (where the proton beam enters the target) and three dumpers (in proximity of the target zone where the beam is stopped). The porous uranium carbide disks were prepared in a dedicated chemistry laboratory, sited in the Department of Chemical Sciences of Padua University, following a particular carbothermal route [1]. The dimension scale factor of the prototype was fixed taking into consideration the geometrical constraints of the standard HRIBF target holder and the idea to conserve the heat flux density value (measured in [W/m^2]) (associated to the power deposited by the proton beam) on the external surfaces of the uranium carbide disks during the on-line operations [4]. With this aim the total external area of the disks was reduced by a factor of 10 (approximately), considering the characteristics of the cyclotron installed at HRIBF that, opportunely configured, could be able to provide a 800 W (40 MeV, 20 μA) primary proton beam, 10 times less powerful respect to the 8 kW (40 MeV, 200 μA) proton beam that will be used for the SPES facility. Table 6.1 reports a set of data useful to understand the dimension scale of the SPES target prototype.

SPES target	proton beam characteristics	beam power ***q***	disk's main dimensions	tot. ext. area of the disks ***A***	heat flux density ***q/A***
full scale	40 MeV, 200 μA	8000 W	ϕ=40 mm, t=1.3 mm	18736 mm^2	0.43 W/mm^2
prototype	40 MeV, 20 μA	800 W	ϕ=13 mm, t=1 mm	2144 mm^2	0,37 W/mm^2

TABLE 6.1. Comparison between the full scale SPES target and the SPES target prototype on thermal loads and geometry.

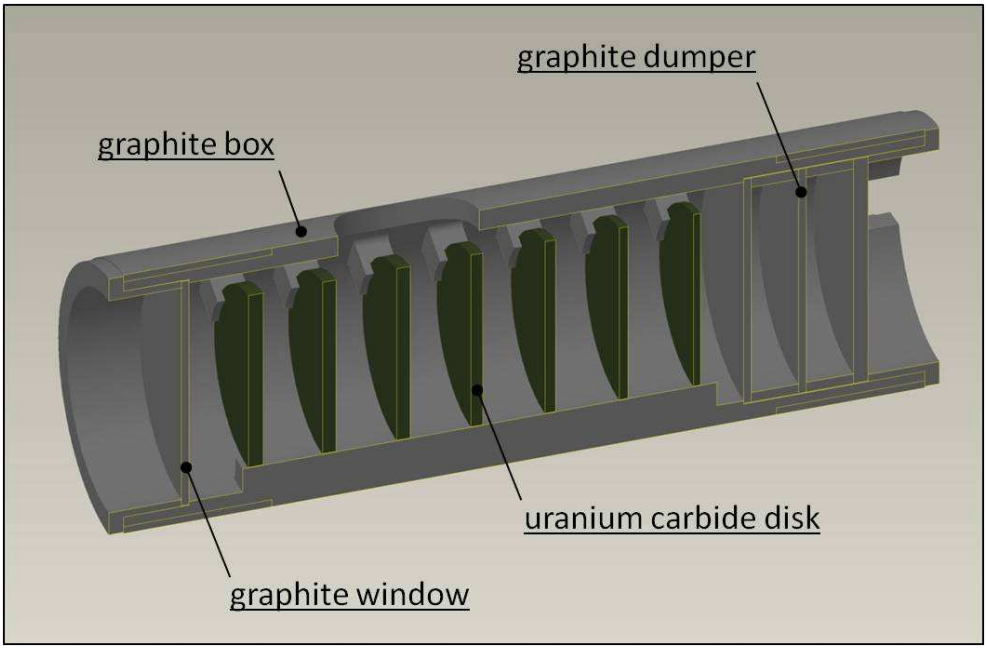

Fig. 6.1. The SPES target prototype: section view showing the uranium carbide disks, the window, the dumpers and the box made of graphite.

A couple of pictures of the SPES target prototype prepared before the installation in the HRIBF tantalum holder are reported in figure 6.2.

Fig. 6.2. The SPES target prototype: picture of the real object assembled at HRIBF.

Figure 6.3 shows the SPES target prototype installed in the standard HRIBF tantalum holder, fixed and closed at one extremity by a screwed graphite cap: in particular the two pictures report the target installation before and after the closure with the cap. The holder is directly connected to the transfer line (by means of a welding) and positioned inside a coaxial cylindrical tantalum heater which can heat the target at very high temperatures thanks to high electrical currents passing through it (see figure 6.5); the heater is surrounded by a coaxial tantalum screen that gives an important contribution in keeping the target temperature at very high levels.

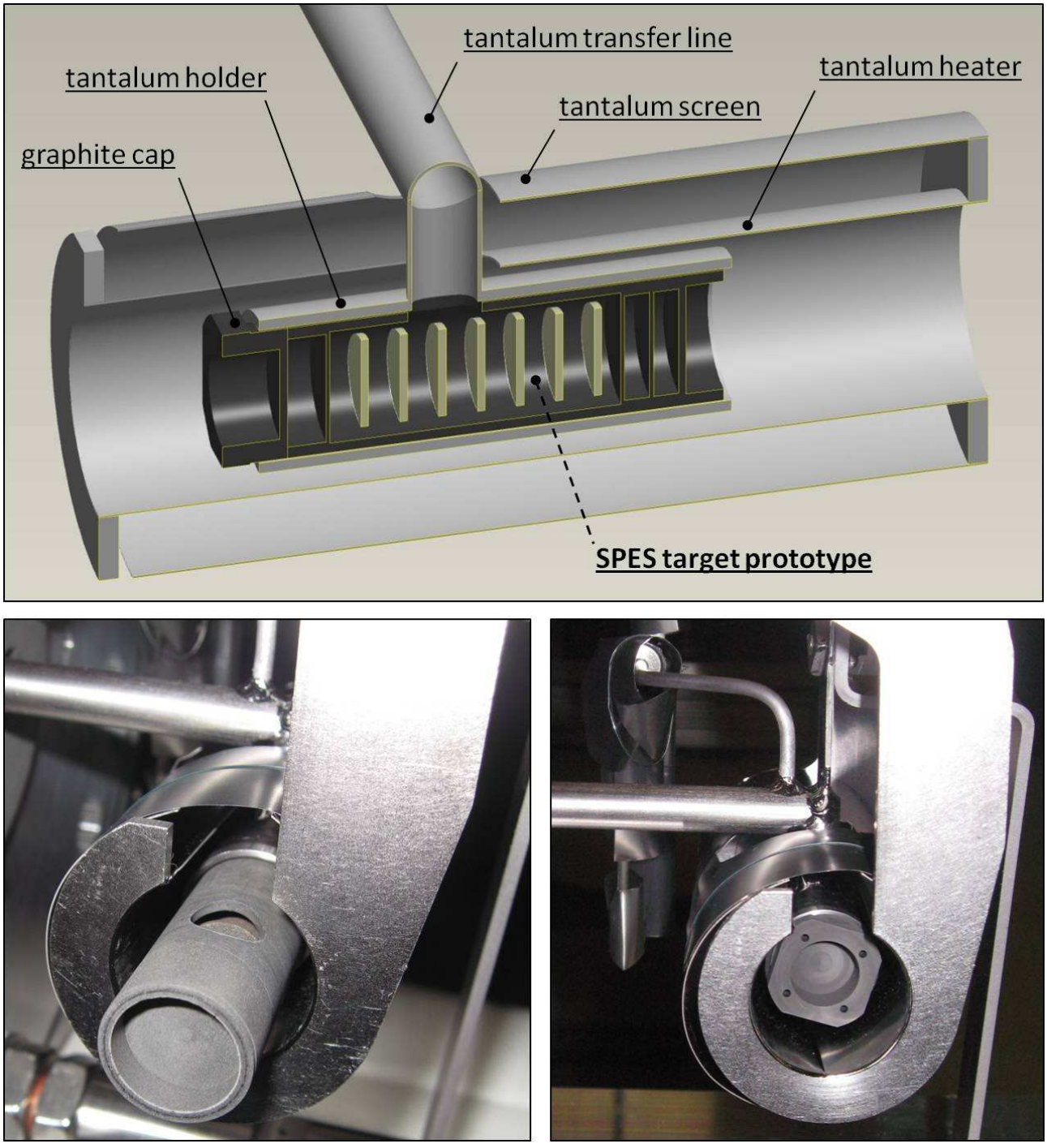

Fig. 6.3. The SPES target prototype installed in the HRIBF target – ion source system.

The aforementioned transfer line is connected on one side to the target holder and on the other side to the standard FEBIAD ion source (see chapter 4, paragraph 4.5.1) used at HRIBF, called EBPIS (Electron Beam Plasma Ion Source); it is very similar to the MK5 ion source described in chapter 4 and the way it works is exactly the same: the EBPIS plasma ion source and its main components are illustrated in figure 6.4 (schematic representation, the anode supports are not reported, for further details see appendix A).

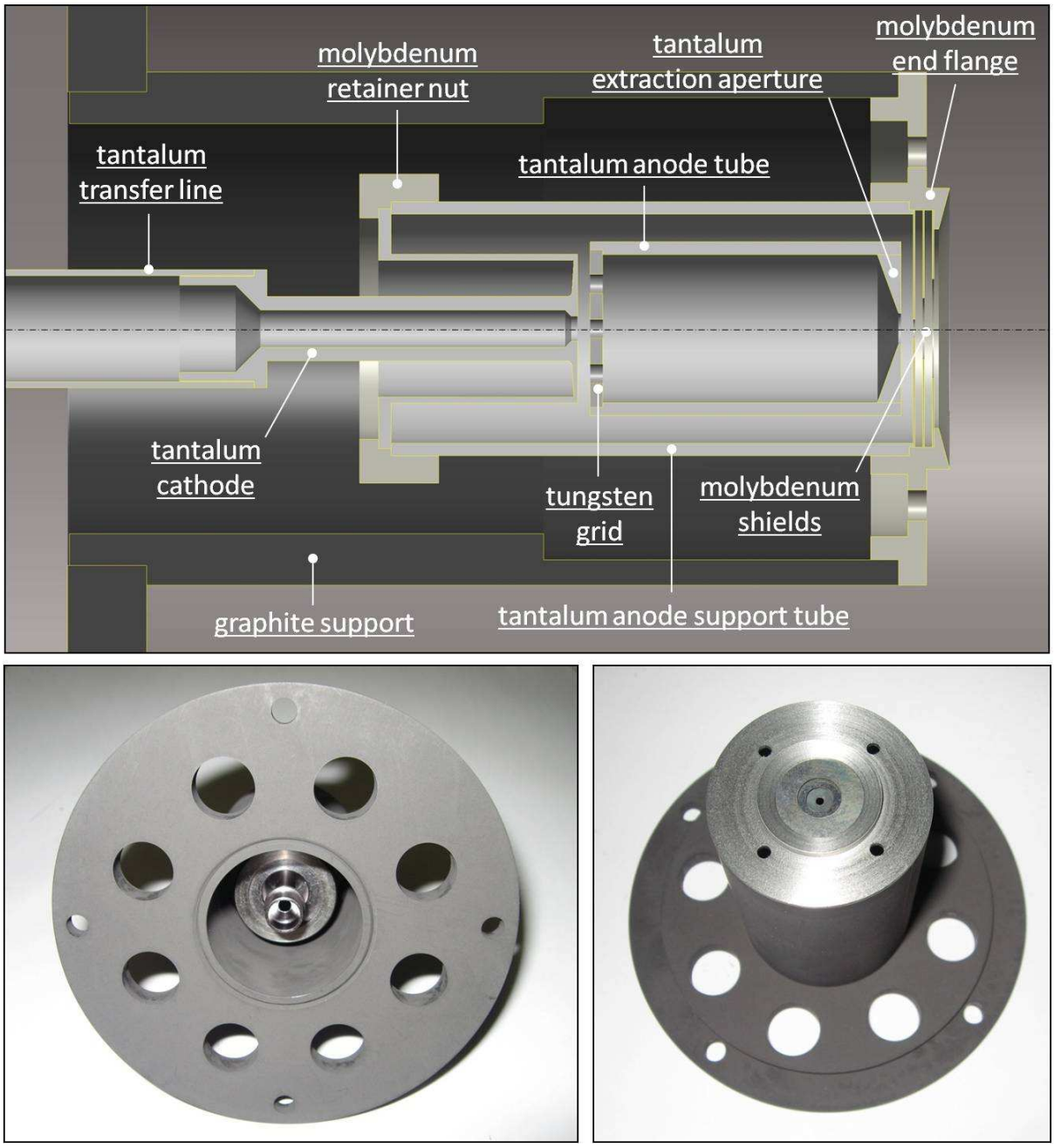

Fig. 6.4. The EBPIS high temperature plasma ion source and its main components.

At this point it is important to underline that during the experimental on-line tests reported in this work, the maximum intensity of the 40 MeV proton beam was fixed at 50 nA and consequently the correspondent thermal load could be considered completely negligible for the target, respect to

the thermal loads due to the heating currents flowing through the target heating system and the ion source. Even if experimental on-line tests with higher proton beam intensities are planned for the next future, the numerical thermal simulations presented in this chapter took into consideration only the Joule heating thermal loads, reproducing in this way the same set of thermal loads assigned during the performed experimental on-line tests (the power deposited by the 40 MeV, 50 nA proton beam can be considered negligible). New sets of numerical thermal simulations considering both the effect of the heating currents and the effect of the proton beam (with intensities close to 20 μA) will be performed soon.

The two electrical circuits used to heat by Joule effect the target and the ion source are represented in figure 6.5, where it is possible to appreciate also a simple and clear schematization: they are independent and each one is linked to a dedicated power supply.

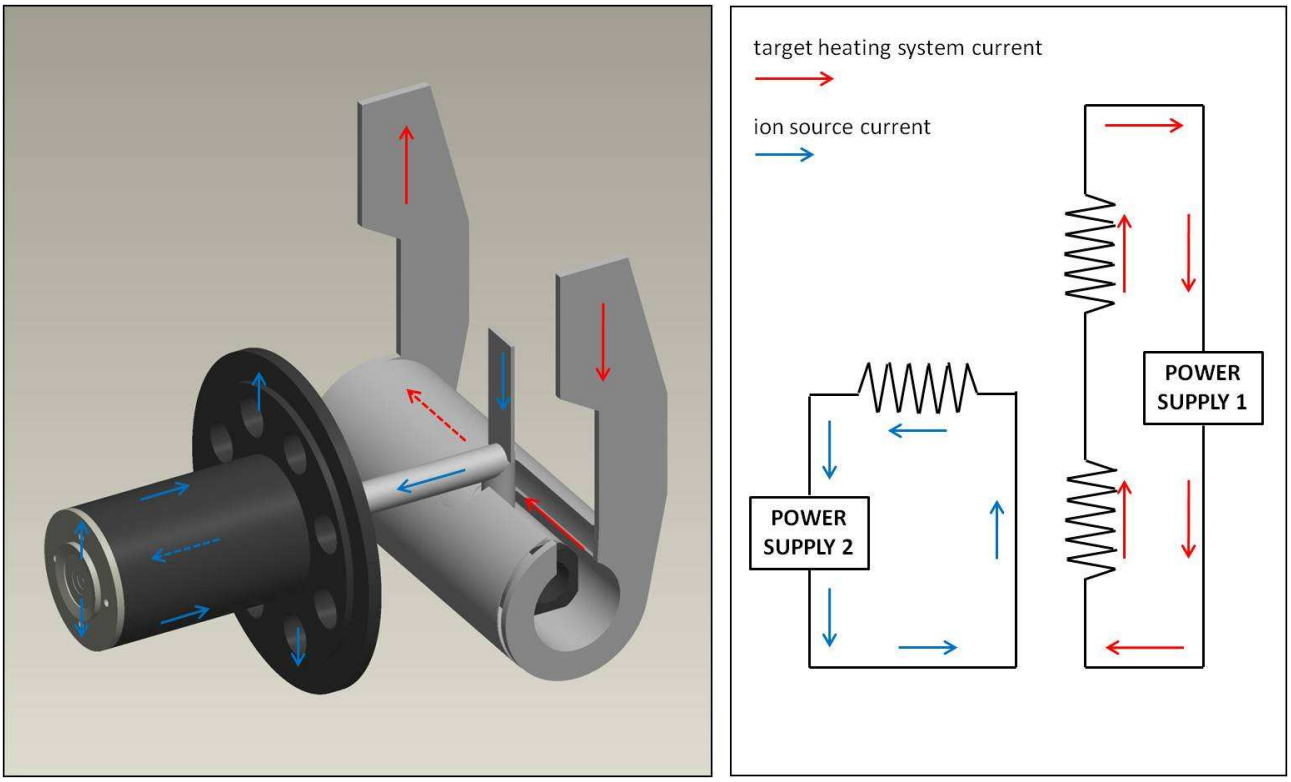

Fig. 6.5. The electrical circuits used to heat (by Joule effect) the production target and the ion source.

In the set of analyses presented in the following paragraphs, Joule heating thermal loads were assigned taking into consideration the electrical current load steps represented in figure 6.6, which were defined taking as reference the off-line heating procedure adopted during the preparation of the target – ion source system for the on-line tests described in this chapter. Obviously during the experimental tests the current levels were increased in a more gradual way (ramps instead of steps) and current values were kept constant for a bigger amount of time in order to allow temperature measurements and monitoring after reaching steady state conditions.

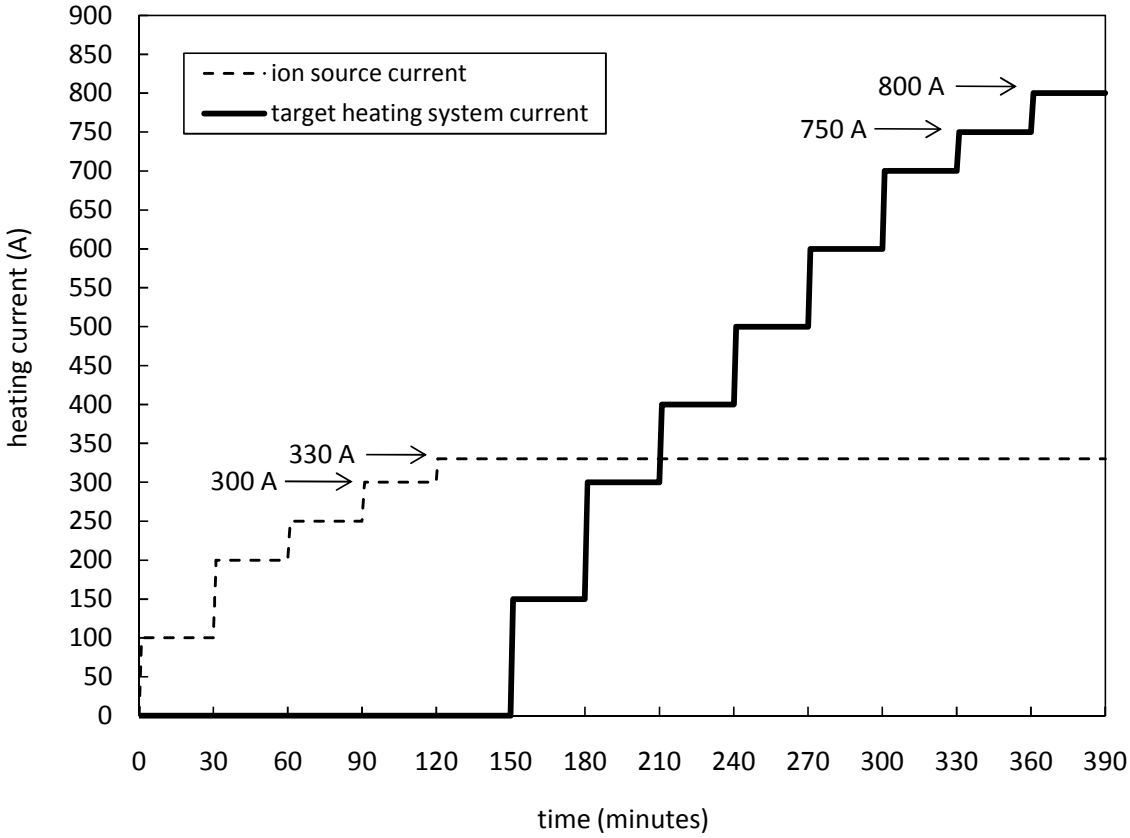

Fig. 6.6. The electrical current load steps used to heat by Joule effect both the production target and the ion source.

In the next paragraph the FE (Finite Element) model developed to study the thermal behaviour of the SPES target prototype and of the HRIBF target – ion source system is presented.

6.3. The SPES target prototype installed in the HRIBF target – ion source system: thermal-electric study using the FE model

The thermal-electric FE model of the SPES target prototype installed in the HRIBF target – ion source system (see figure 6.7) was defined using the same techniques presented in the previous chapter for the SPES "production target – hot-cavity ion source" assembly. Boundary conditions and thermal loads were assigned in a similar way, taking into consideration the electrical circuits illustrated in figure 6.5 and the electrical current load steps reported in figure 6.6. As explained in the previous chapter the effect of the proton beam was not introduced (proton beam power negligible for the on-line tests performed until now on the SPES target prototype) and only the Joule heating thermal loads were assigned; in particular figures 6.8 and 6.9 report the temperature plot correspondent to an ion source current and a target heating system current equal to 330 and 800A, respectively.

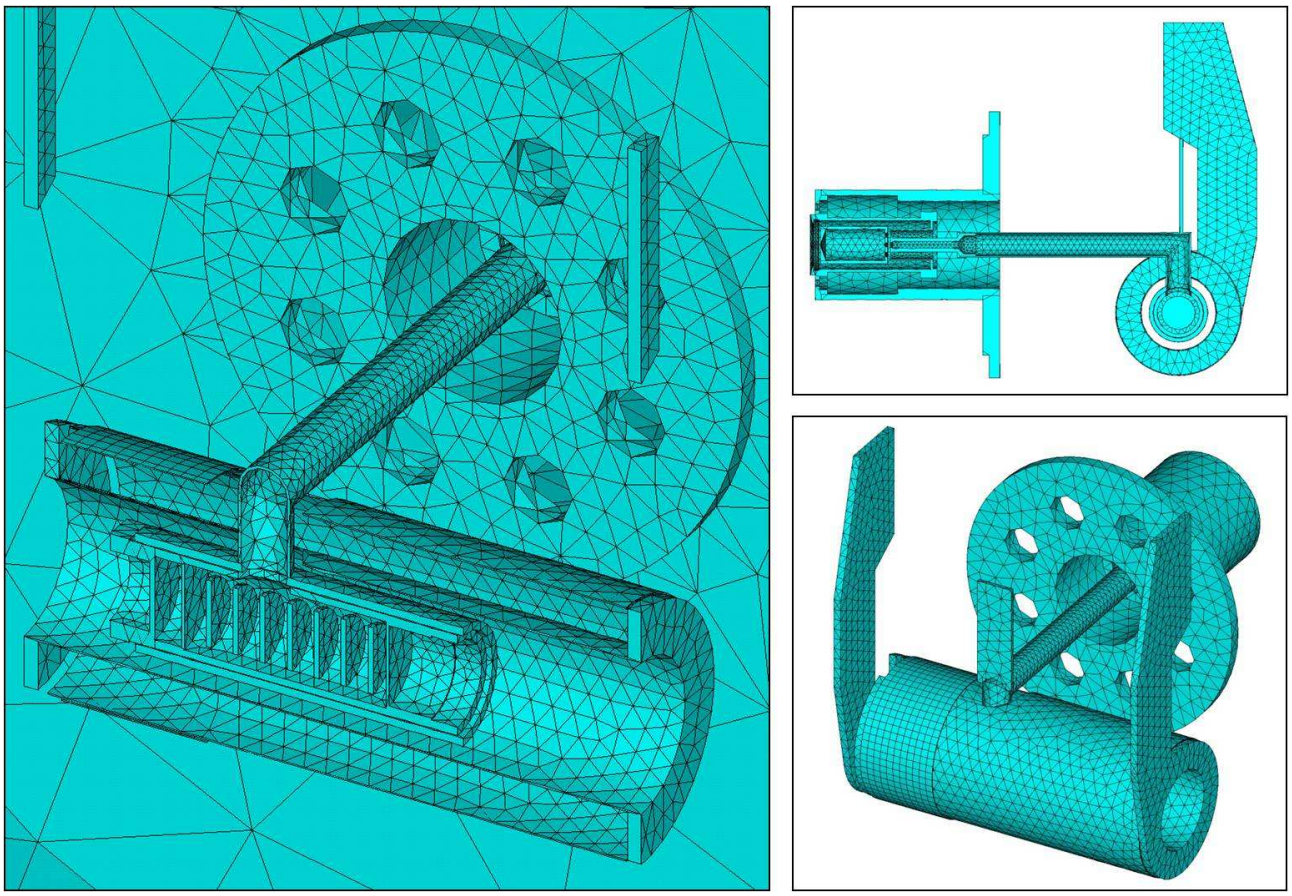

Fig. 6.7. The FE model of the SPES target prototype installed in the HRIBF target – ion source system.

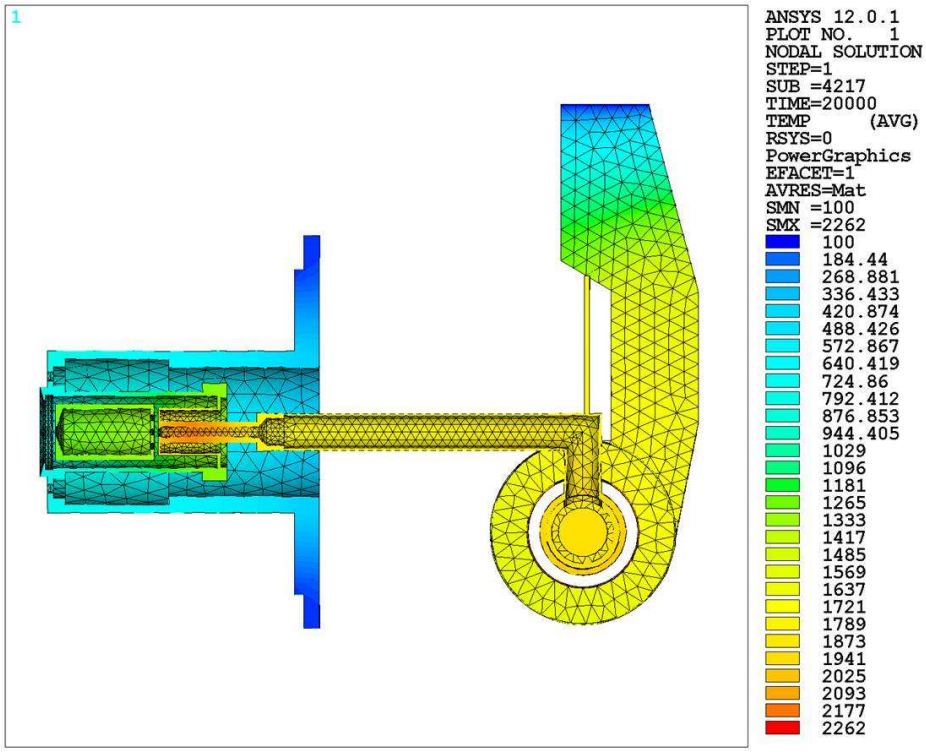

Fig. 6.8. The SPES target prototype installed in the HRIBF target – ion source system: temperature plot (lateral section view) correspondent to an ion source current and a target heating system current equal to 330 and 800A, respectively.

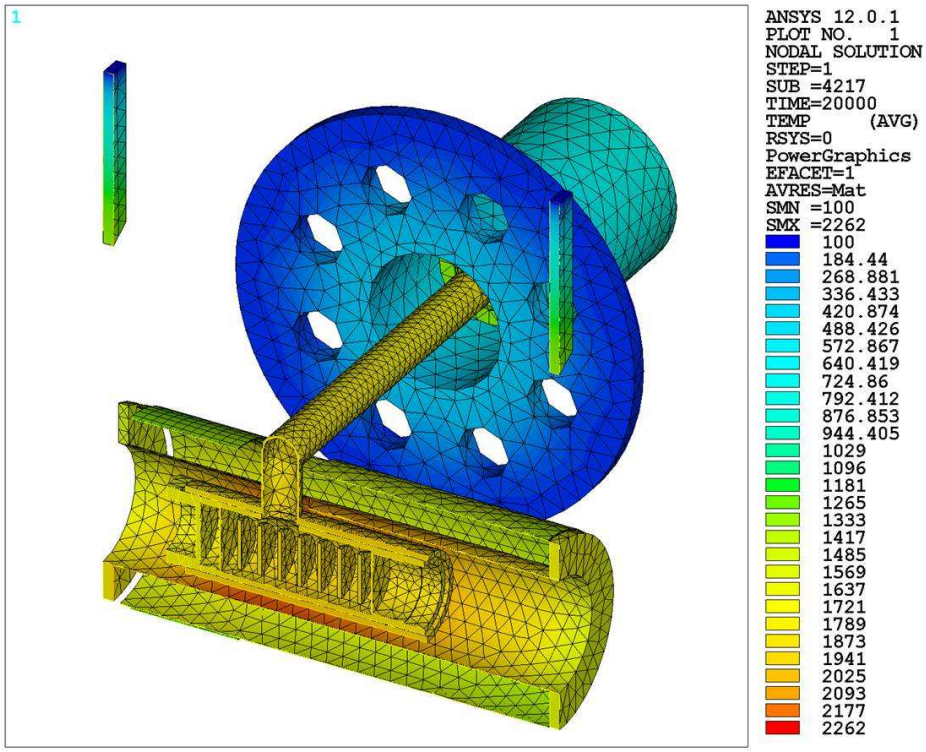

Fig. 6.9. The SPES target prototype installed in the HRIBF target – ion source system: temperature plot (frontal section view) correspondent to an ion source current and a target heating system current equal to 330 and 800A, respectively.

The advantages that such model can offer are evident: one is surely the possibility to know the temperature field not only on the external surfaces of the target – ion source system but also in the internal zones, where experimental measurements are not possible: in the disks, in the graphite box, in the cathode, in the anode tube et cetera. Figure 6.10 presents the points where, in the next paragraphs, we will propose a direct comparison between FE and experimental data.

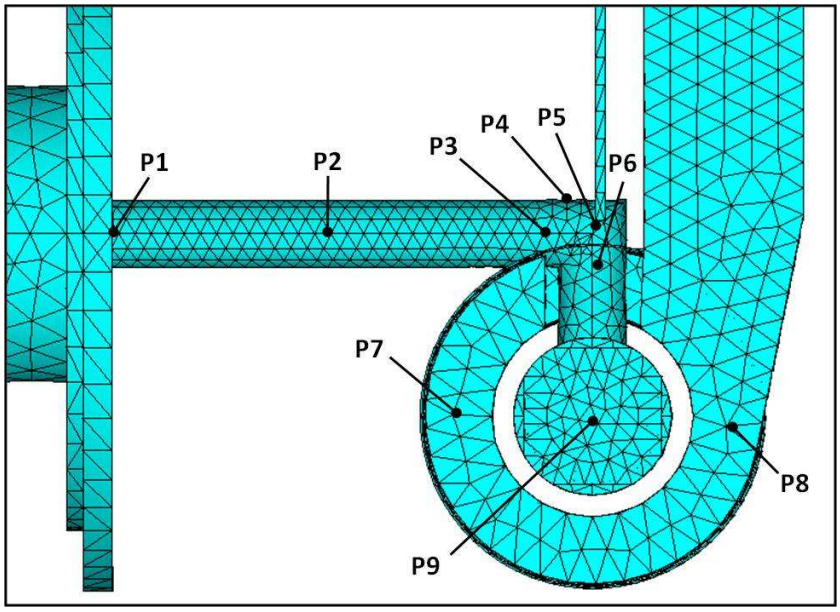

Fig. 6.10. The points taken into consideration for the comparison between FE and experimental temperature data.

Taking as reference the aforementioned set of points we could obtain the correspondent temperature values performing dedicated sets of experimental measurements and FE analyses, obviously without the presence of the primary proton beam. At this point, once verified the correspondence between experimental and numerical data we could use the FE model to study the temperature fields in the internal zones of the target – ion source system, where there are not experimental temperature data available. Both numerical and experimental results could be considered reliable also to describe the temperature filed of the system during the on-line tests described in this chapter, where the intensity of the 40 MeV proton beam is very low, close to 50 nA (deposited power approximately equal to 2 W).

Once validated off-line the FE model as described above, the main advantage that it can offer is surely the possibility to estimate the on-line temperature field of the target – ion source system with the presence of an high intensity proton beam, once opportunely introduced the correspondent thermal loads: in this case the information coming from the numerical model is particularly precious since experimental measurements with an high intensity proton beam are very difficult, often impossible.

Figure 6.11 shows the average temperatures of the cap and of the disks, obtained thanks to the FE model, considering an ion source current and a target heating system current equal to 330 and 800A, respectively (proton beam thermal load not introduced); as we will see in the next paragraphs only the cap' temperature could be compared to the correspondent experimental value: the average temperatures of the disks could be estimated only numerically.

During the on-line tests it is very important to know and to keep under control the temperature field of the target, in particular of its disks: for this purpose the FE model represents an extremely powerful tool.

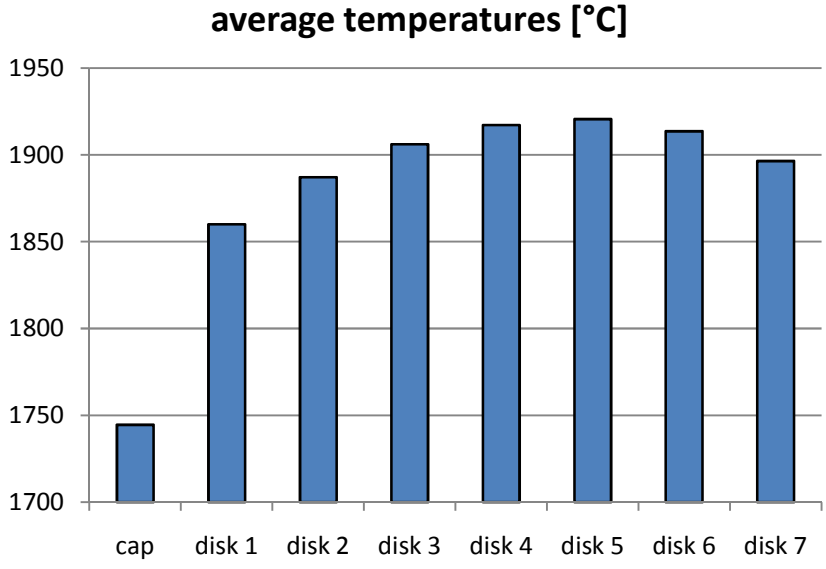

Fig. 6.11. FE average temperatures for the cap and the uranium carbide disks.

6.4. The On-Line Test Facility (OLTF) at HRIBF: preliminary temperature measurements and production of radioactive ion beams using the SPES target

At HRIBF, the On-Line Test Facility (OLTF), formerly known as UNiversity Isotope Separator at Oak Ridge (UNISOR), is used to develop and optimize targets and ion sources for the production of radioactive ion beams (see figure 6.12). The OLTF is composed of a target – ion source station that receives the primary proton beam from the 25 MV tandem accelerator, which is capable of delivering a proton beam with energy up to 50 MeV (see figure 6.13). This analogy with the SPES primary beam energy makes the OLTF an ideal facility where to perform on-line tests on the SPES target prototypes.

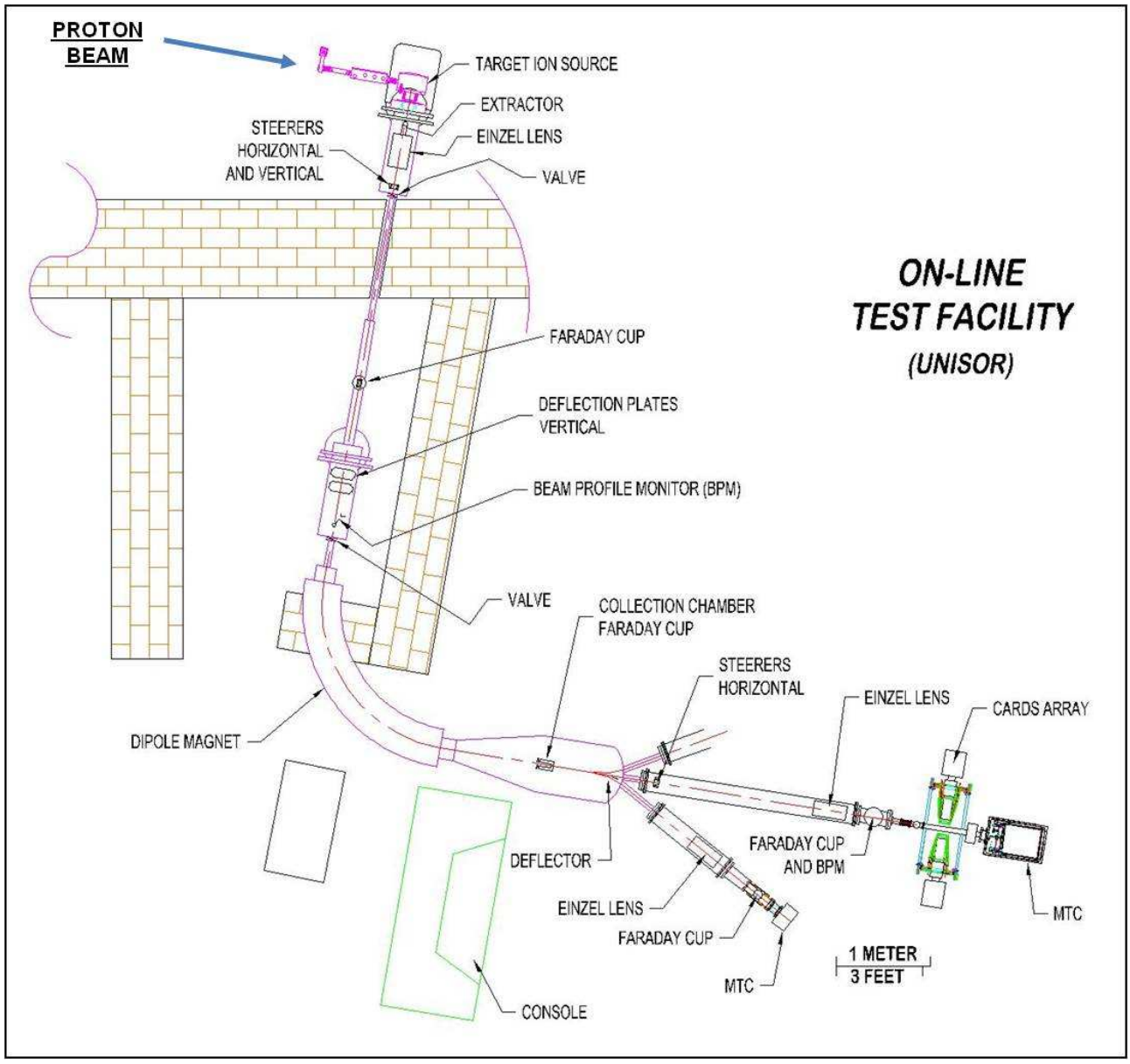

Fig. 6.12. Layout of the On-Line Test Facility (OLTF) at HRIBF.

Fig. 6.13. The HRIBF 25 MV tandem accelerator used to provide the 40 MeV, 50 nA primary proton beam during the on-line tests of the SPES target prototype [5].

Figure 6.14.a shows the target – ion source system (prepared for the test of the SPES target prototype) installed in the standard HRIBF target chamber, whereas figures 6.14.b and 6.14.c present the target chamber positioned in the OLTF target – ion source station without the cover and with the water-cooled cover connected to the proton beam channel, respectively.

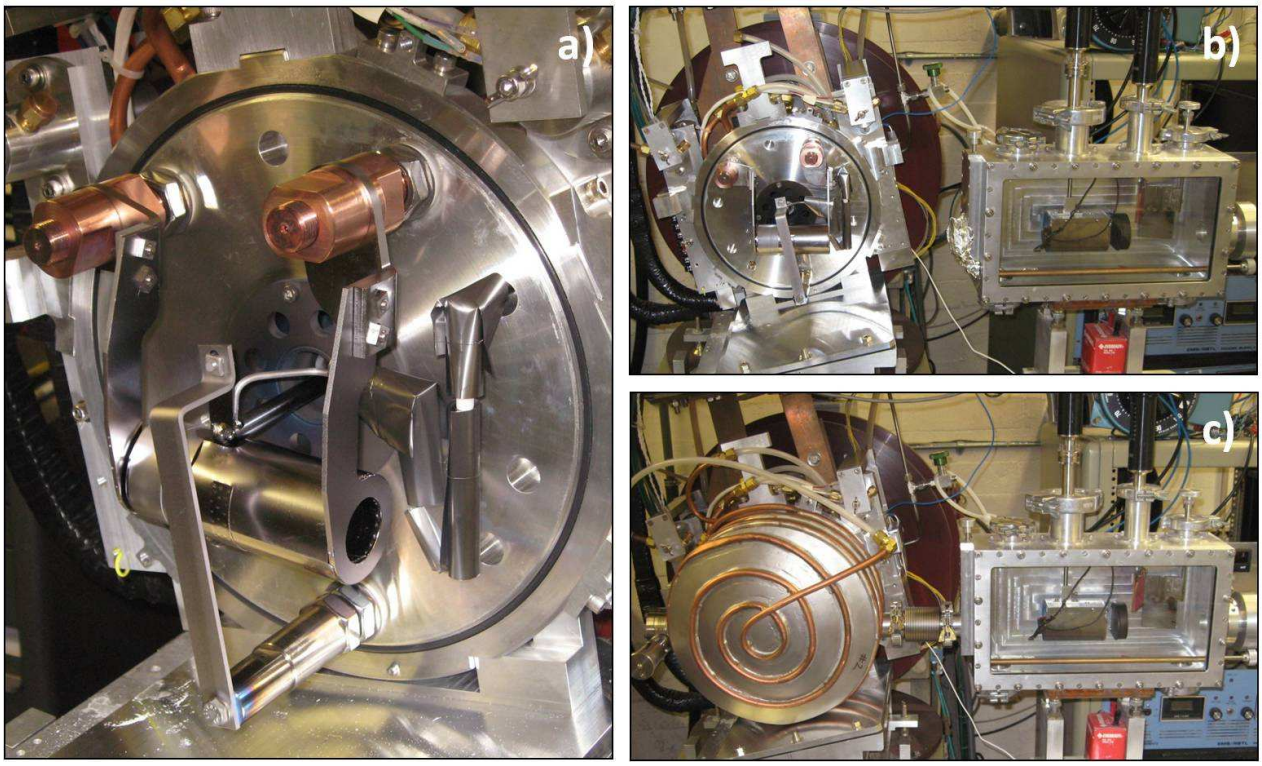

Fig. 6.14. Housing of the target – ion source system in the target chamber (a); target chamber without cover positioned in the OLTF facility (b); target chamber with water-cooled cover connected to the primary proton beam channel (c).

The first week of tests was entirely dedicated to the off-line thermal characterization of the target – ion source system; figure 6.15 shows the view used to take temperature measurements by means of an optical pyrometer: temperature levels were measured on the same points indicated in figure 6.10. They will be compared to FE data in the next chapter. Both the target and the ion source were heated taking as reference the same current values reported in figure 6.6.

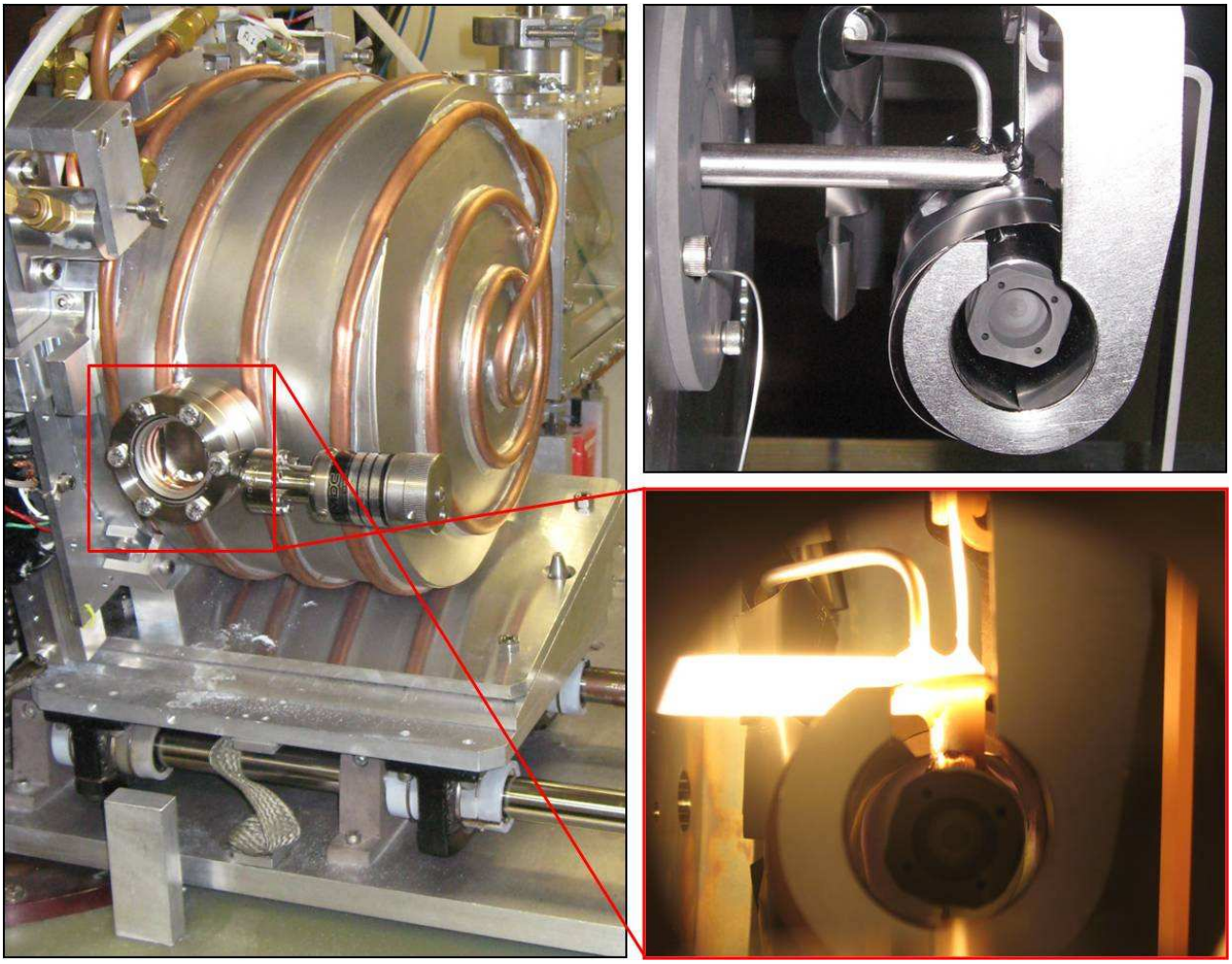

Fig. 6.15. The view of the target – ion source system adopted to take temperature measurements by means of an optical pyrometer: the same points shown in figure 6.10 were taken into consideration as measurement points.

Thermal characterization was done before the on-line tests, in order to collect useful data and measurements to study the thermal-electric behavior of the target – ion source system and to out-gas the target and the ion source in a gradual way following the standard OLTF procedure. Thanks to the thermal treatments previously described, the out-gassing from the target was always small during the subsequent on-line tests allowing the target chamber pressure to be always around the value of 10^{-4} Pa. Once completed the thermal characterization of the target – ion source system, the target temperature was risen to 2000°C and the uranium carbide disks were irradiated by a 40 MeV, 50 nA beam of protons. Fission products were ionized by means of the Electron Beam Plasma Ion

Source (EBPIS) whose working principle (FEBIAD ion source) was widely discussed in chapter 4: it is represented in figure 6.4. The EBPIS was equipped with standard Xe and Kr leaks that serve to monitor the performance of the ion source during on-line operations. Once ionized the fission products were extracted from the ion source thanks to a potential difference of 50 kV and mass-selected by means of a 90 degrees mass separator magnet (see figure 6.12). A Faraday cup was used to measure beam currents after mass analysis. After calibration the user could chose the desired mass and measure the fission fragment yields by detecting γ-rays from the decay of the isotope, using a moving tape system connected to a Ge detector. The layout of the test facility is shown in figure 6.12.

In the set of on-line measurements described in this chapter the yields of 36 masses ranging from 72 to 141 amu were measured. For every mass of interest, after fine tuning of the mass separator magnet (by maximization of the Faraday cup current), a γ-decay measurement was done using the moving tape system and the Ge detector. The calculation of the yields of the different isotopes was carried out by analyzing the gamma-ray spectra obtained from the Ge detector coupled to a multi-channel analyzer (MCA) [1]. Once stopped data collection for all scheduled masses, after a week of cooling time, a visual inspection on the target was done and no significant structural changes or breakdown were observed (see figure 6.16).

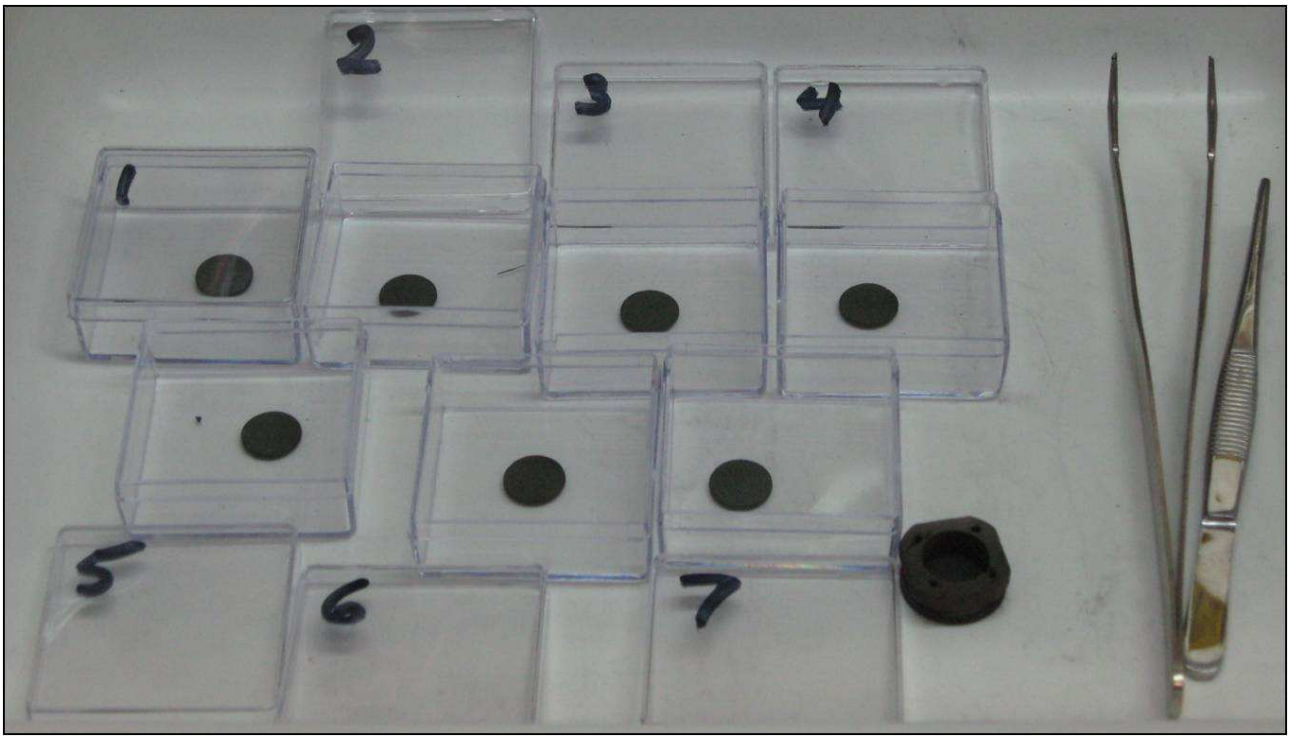

Fig. 6.16. The seven uranium carbide disks after online tests.

6.5. Thermal study of the SPES target prototype installed in the HRIBF target – ion source system: comparison between FE and experimental data

In the previous paragraphs the SPES target prototype and the HRIBF target – ion source system used for the low intensity on-line experimental tests reported in this work were presented in detail; in particular paragraph 6.3 offers a detailed description of the FE model used to study the thermal-electric behavior of the target – ion source system and in the following it is possible to verify its reliability comparing numerical data to the correspondent experimental temperature measurements performed during the preparation/conditioning of the target before the on-line tests.

First of all, keeping equal to zero the target heating system current, the transfer line temperature field was studied increasing gradually the ion source current up to 330A: figure 6.17 reports the points where experimental temperature values were compared to numerical ones.

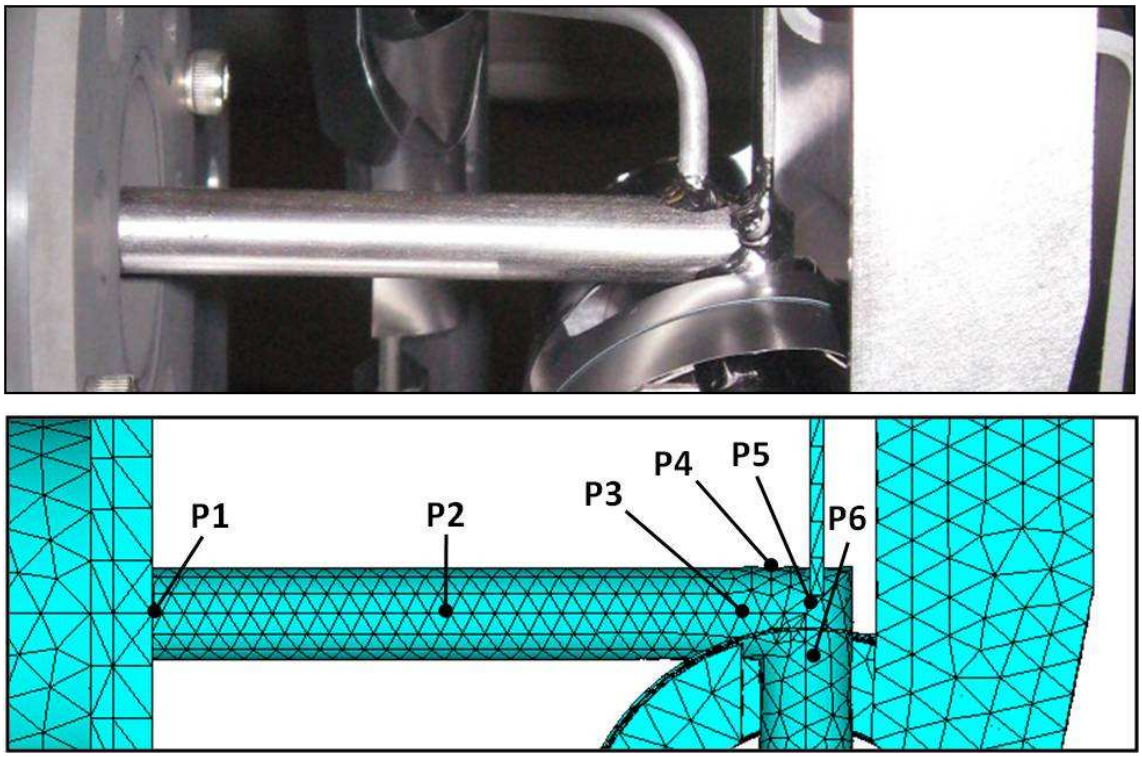

Fig. 6.17. Study of the transfer line temperature field: comparison between numerical and experimental data at points P1, P2, P3, P4, P5 and P6.

Figures 6.18 and 6.19 show the comparison between numerical and experimental data at points P1 and P2, respectively. The FE model is able to reproduce in a good way the thermal behavior of the transfer line in proximity of these points; in particular the maximum differences between FE and experimental temperatures were noticed in both cases for an ion source current of 330A: they were equal to 23 and 40°C at points P1 and P2, respectively.

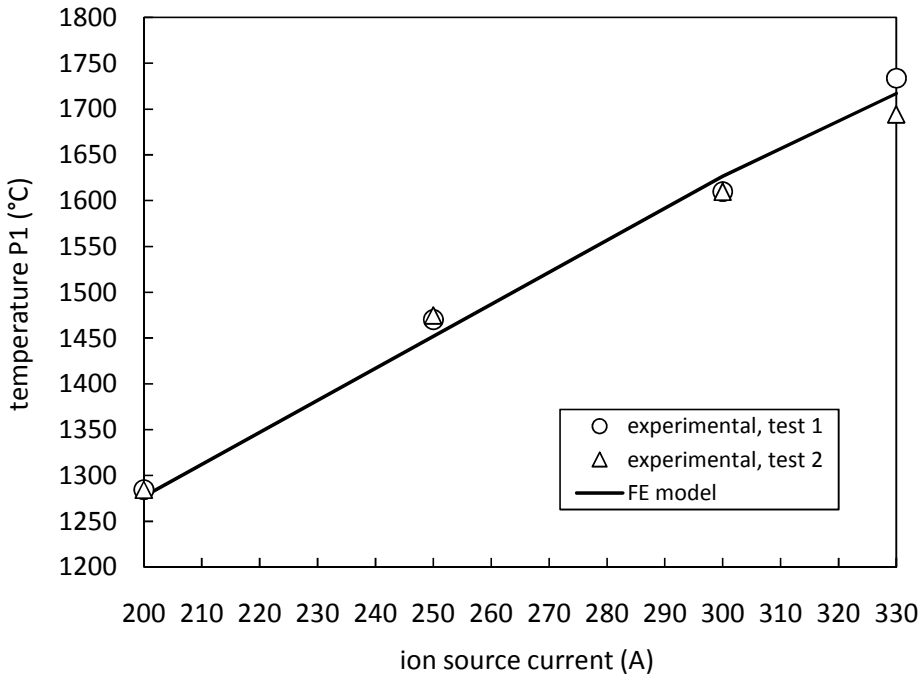

Fig. 6.18. Transfer line thermal study: comparison between experimental and numerical temperature data at point P1 (target heating system current equal to zero).

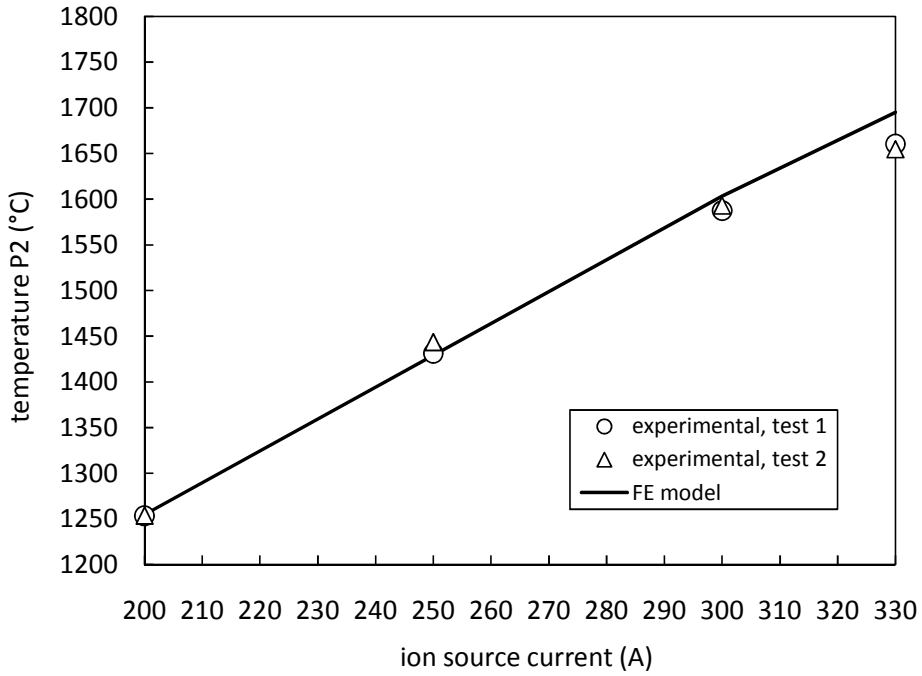

Fig. 6.19. Transfer line thermal study: comparison between experimental and numerical temperature data at point P2 (target heating system current equal to zero).

In proximity of point P3 thermal gradients start to be more pronounced and consequently a minimum difference on the pyrometer pointing between two subsequent temperature measurements at point P3 can lead to important differences on the detected temperature values. Observing figure 6.20 it is possible to observe how all temperature measurements are in general positioned around

the FE model curve but in some cases with relevant gaps: the bigger one is equal to 81°C and was registered for an ion source current equal to 250A.

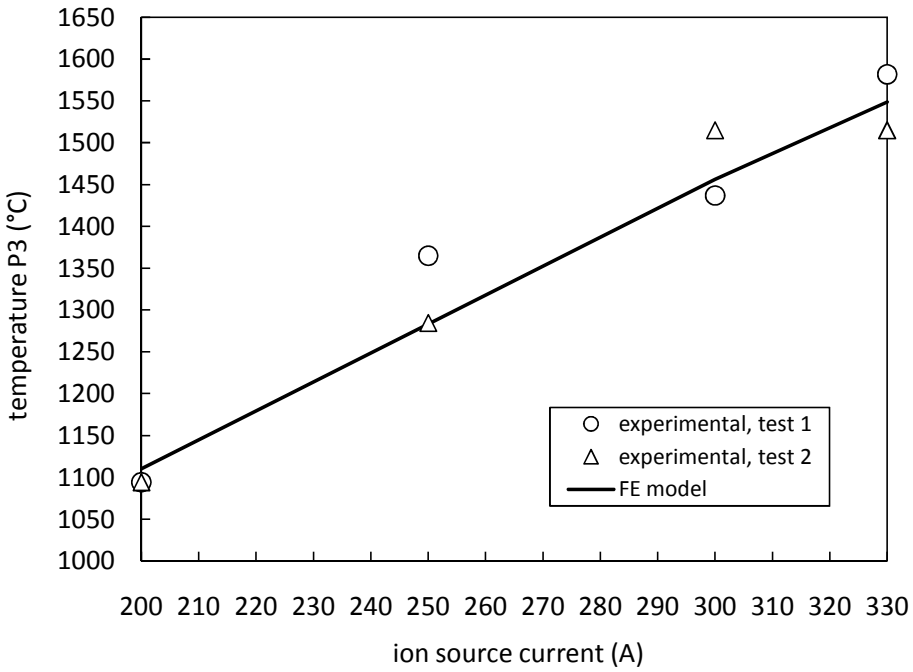

Fig. 6.20. Transfer line thermal study: comparison between experimental and numerical temperature data at point P3 (target heating system current equal to zero).

Figure 6.21 shows the comparison between experimental and numerical data in proximity of point P4; FE temperature values are always higher respect to measured ones: the bigger temperature difference, equal to 119°C, was registered for an ion source current equal to 330A.

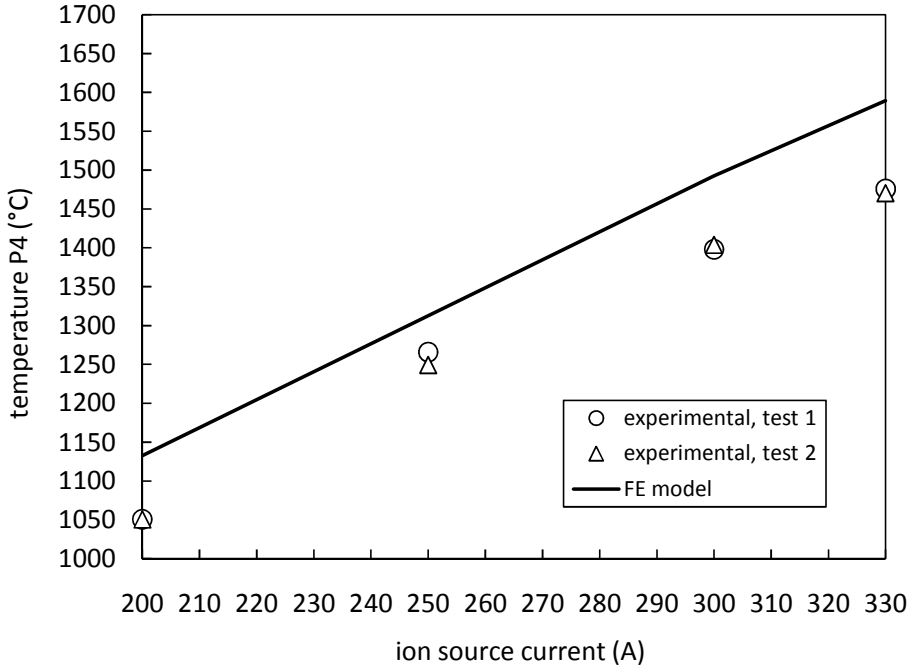

Fig. 6.21. Transfer line thermal study: comparison between experimental and numerical temperature data at point P4 (target heating system current equal to zero).

This important difference is due to the fact that the detail of the gas tube connection was not included in the FE model; in the real target – ion source system it cools down locally the transfer line increasing in proximity of point P4 the radiating area (see figure 6.22).

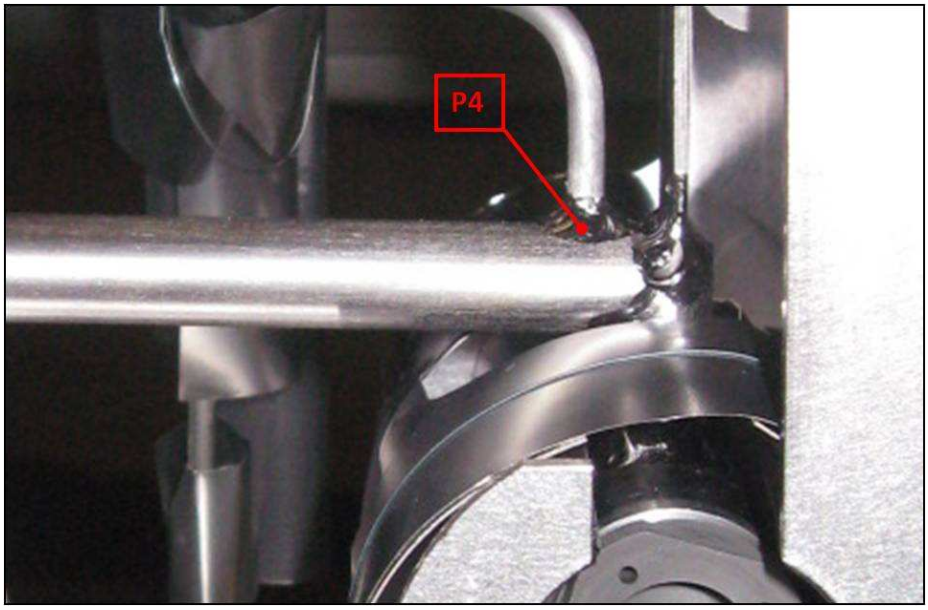

Fig. 6.22. Gas tube connection to the transfer line in proximity of point P4.

Similar considerations can be done for point P5 (see figure 6.23): in this case the effect of the gas tube connection is less pronounced and the maximum temperature difference between experimental and numerical data is equal to 47°C (ion source current equal to 330A).

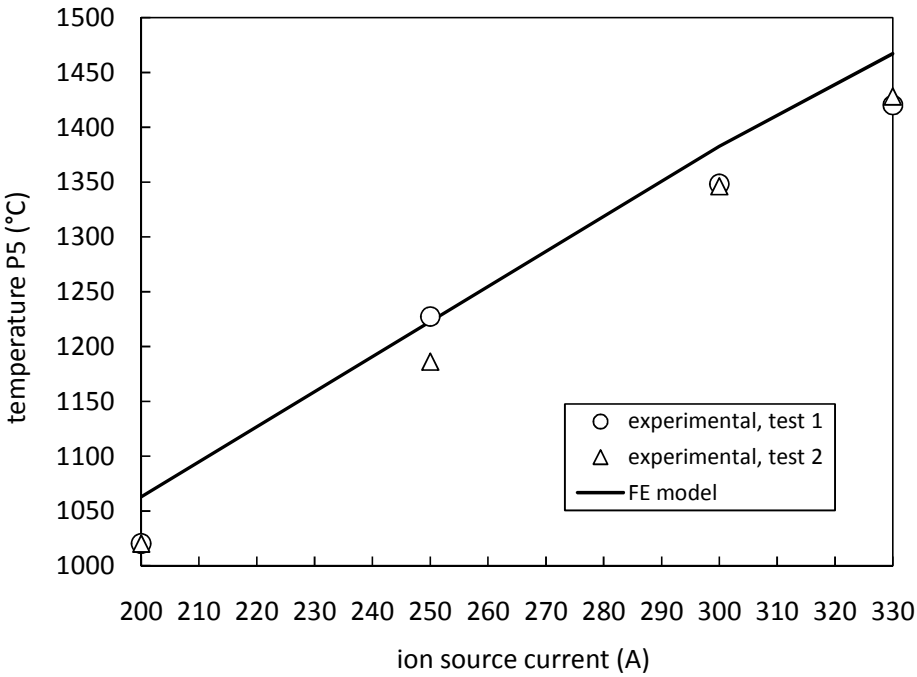

Fig. 6.23. Transfer line thermal study: comparison between experimental and numerical temperature data at point P5 (target heating system current equal to zero).

Figure 6.24 shows the comparison between experimental and numerical data at point P6; the maximum gap was registered for an ion source current of 300A: it was equal to 98°C and was mainly due to the very high temperature gradient existing in proximity of point P6 (see figure 6.25). In fact in this zone, as previously exposed for point P3, a small difference on the pyrometer pointing between two subsequent measurements can lead to relevant differences on the detected temperature values.

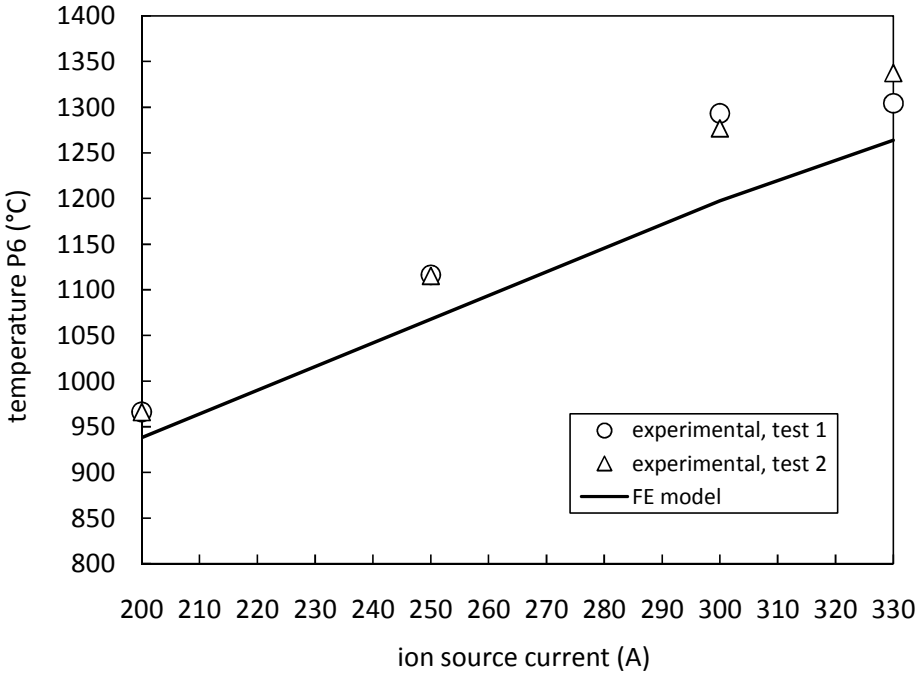

Fig. 6.24. Transfer line thermal study: comparison between experimental and numerical temperature data at point P6 (target heating system current equal to zero).

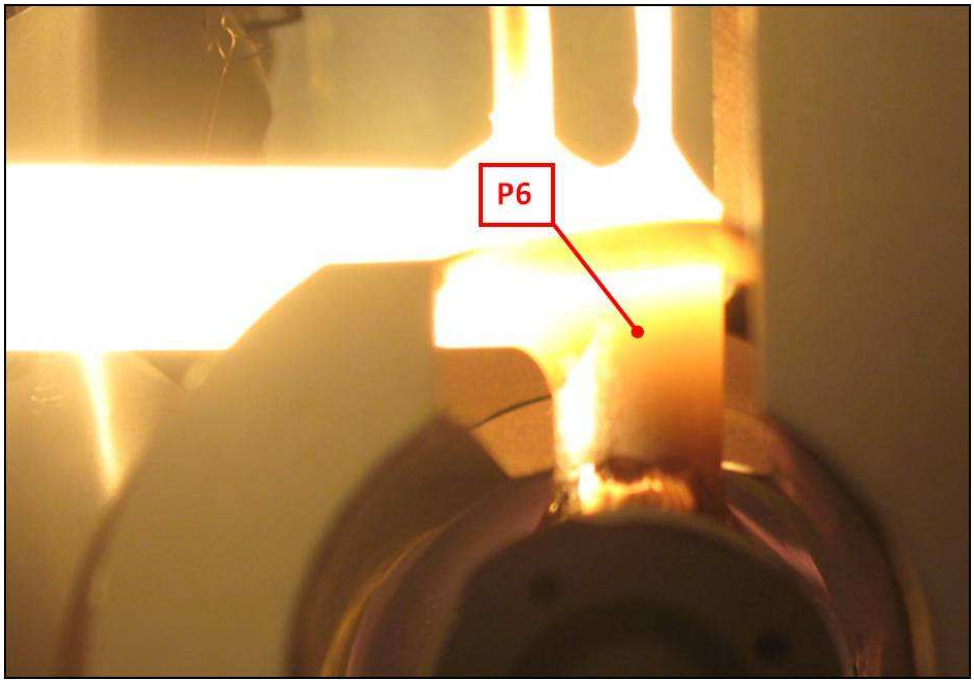

Fig. 6.25. Picture reporting the important temperature gradient in proximity of point 6.

At this point, once completed the transfer line thermal-electric characterization, the ion source current was fixed at 330A; then the thermal study of the whole target – ion source system started, gradually increasing the target heating system current up to 800A (see figure 6.6). The thermal-electric characterization of the target – ion source system was performed in two steps: at first considering the naked system presented in figure 6.3 and then adding a set of thin tantalum thermal screens on the transfer line and at the extremities of the target heating system (see figure 6.26). The aforementioned set of screens is usually installed on HRIBF target – ion source systems during high temperature on-line tests.

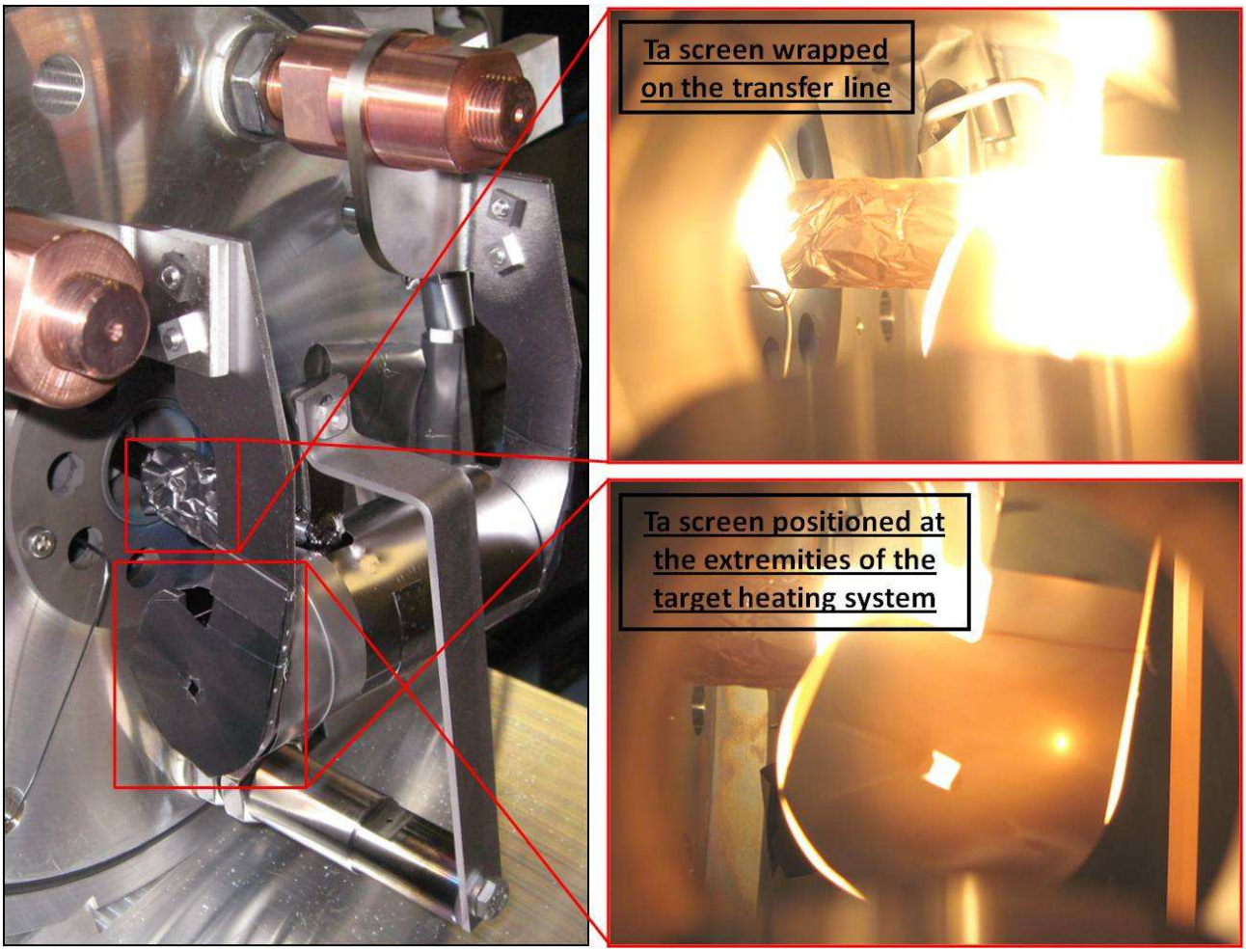

Fig. 6.26. The tantalum thermal screens wrapped around the transfer line and positioned at the extremities of the target heating system.

Figure 6.27 shows the comparison between experimental and FE data at point P1 for the target – ion source system configurations without and with screens; in the first case a very good correspondence between measured and numerical temperature values was registered whereas in the second one the FE model produced always higher temperatures respect to experimental measurements: this was mainly due to the way the tantalum screen wrapped around the transfer line was modeled. In the numerical model it was positioned without contact points, coaxially respect to

the transfer line, whereas the real screen was rested directly on the transfer line, in contact with it and producing an electric parallel resistance, leading to a global decreasing of the power deposited by Joule effect by the same electric current (see figure 6.28). With thermal screens, the maximum difference between experimental and numerical temperatures, equal to 102°C, was registered for a target heating system current of 400A.

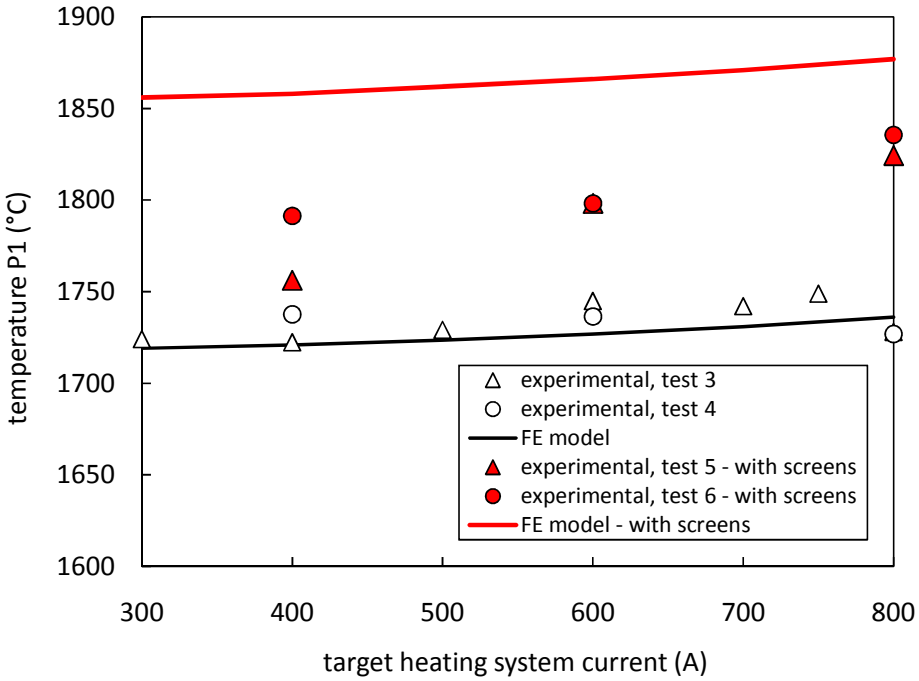

Fig. 6.27. Thermal study of the target – ion source system: comparison between experimental and numerical temperature data at point P1 (ion source current fixed at 330A).

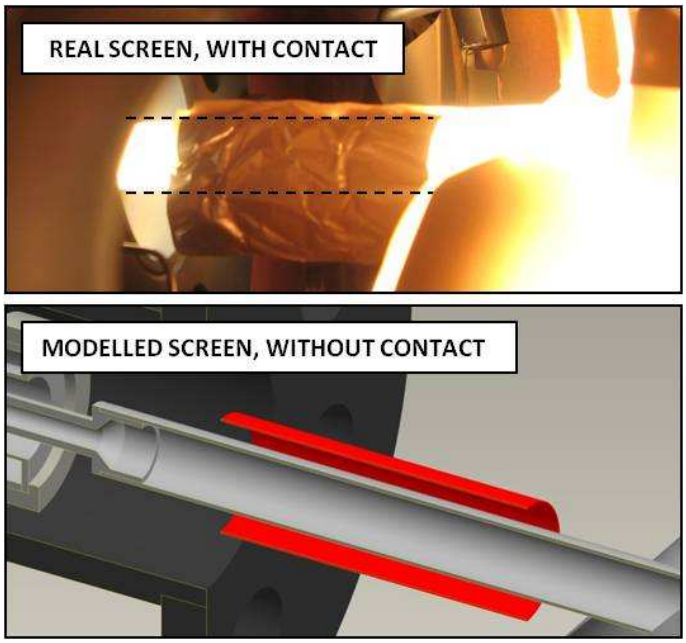

Fig. 6.28. The tantalum thermal screen wrapped around the transfer line: experimental observations and modellization.

At point P2 temperatures were measured only without thermal screens (once positioned the screens, it was not possible to point directly with the pyrometer the transfer line section where point P2 is located): experimental data showed a good agreement with FE calculations. A FE temperature curve was also introduced to estimate virtually the effect of the thermal screen wrapped on the transfer line (see figure 6.29).

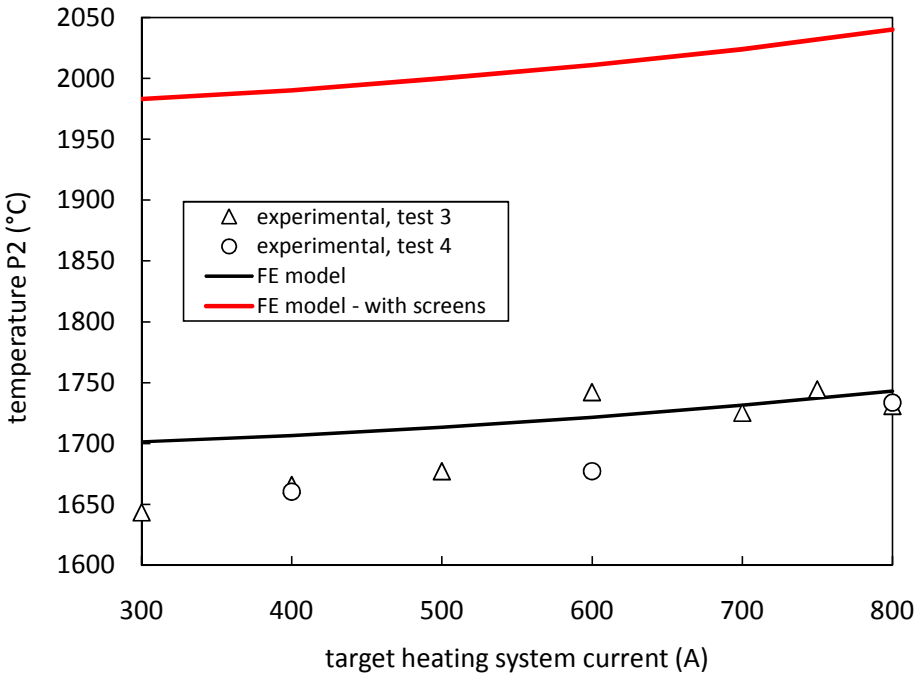

Fig. 6.29. Thermal study of the target – ion source system: comparison between experimental and numerical temperature data at point P2 (ion source current fixed at 330A).

As shown in figure 6.30, points P3, P4 and P5 are located in proximity of the gas tube connection; in particular point P4 is positioned directly on the welding between the gas tube and the transfer line whereas points P3 and P5 are slightly shifted respect to it.

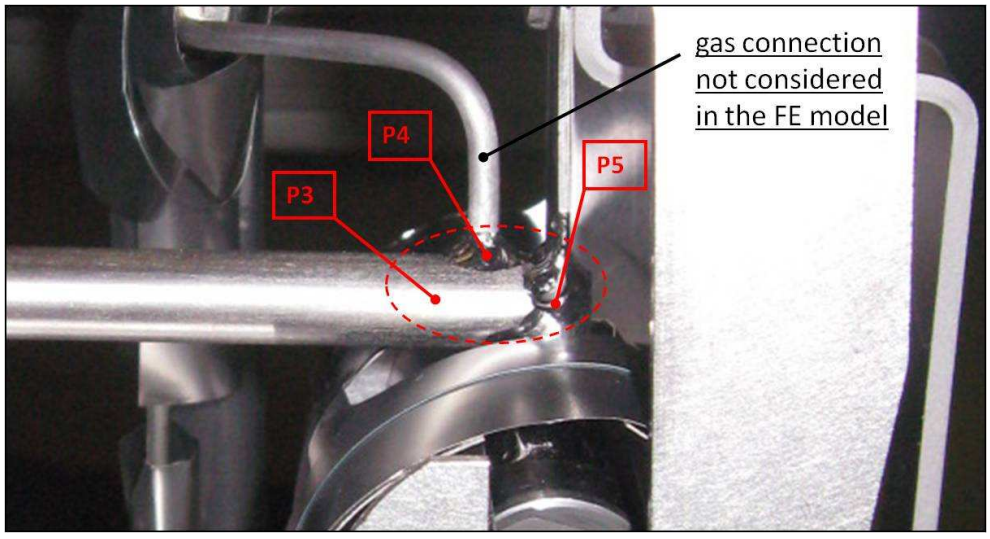

Fig. 6.30. The test points P3, P4 and P5 positioned in proximity of the gas tube connection.

As explained above, the gas tube was not included in the FE model mainly because of the need to limit the model size and consequently to obtain the numerical solution in a reasonable amount of time. The tube represents a passive element (it is not heated by an electric current) and cools locally the transfer line: its effect is very important at point P4 (big translation of the FE curves respect to the correspondent experimental ones, see figure 6.32) and less pronounced at points P3 and P5 (see figures 6.31 and 6.33).

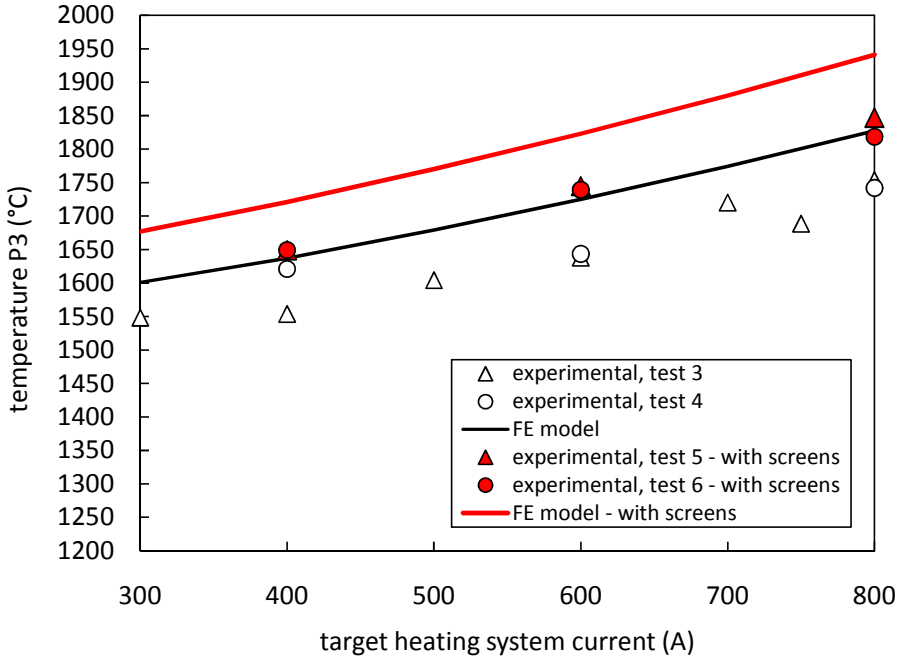

Fig. 6.31. Thermal study of the target – ion source system: comparison between experimental and numerical temperature data at point P3 (ion source current fixed at 330A).

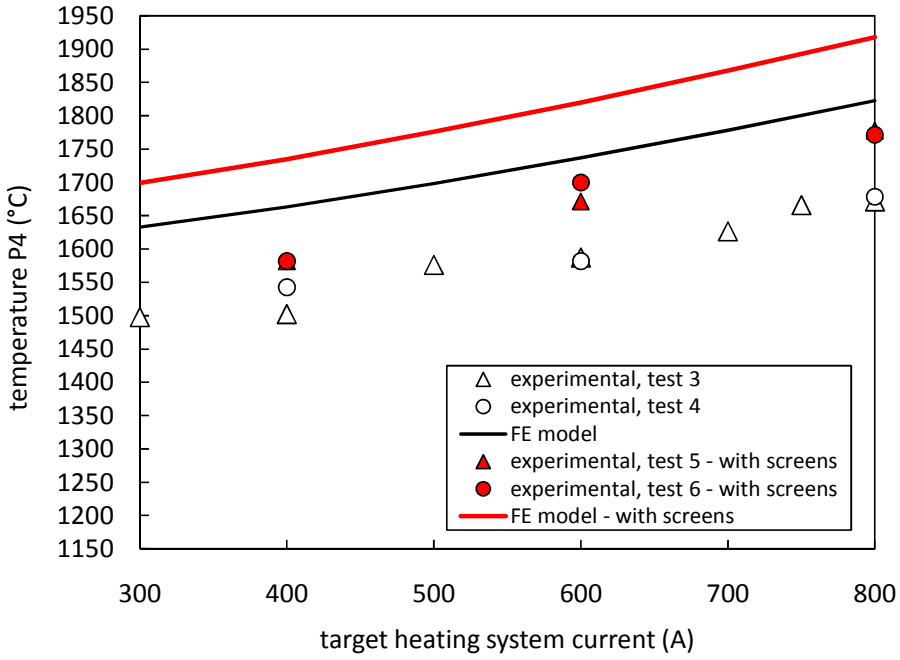

Fig. 6.32. Thermal study of the target – ion source system: comparison between experimental and numerical temperature data at point P4 (ion source current fixed at 330A).

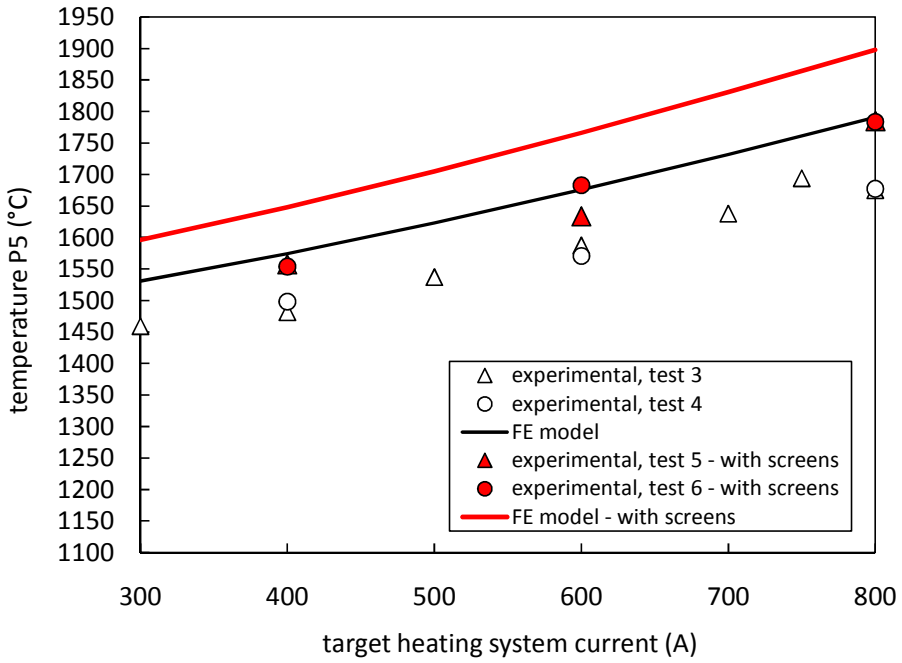

Fig. 6.33. Thermal study of the target – ion source system: comparison between experimental and numerical temperature data at point P5 (ion source current fixed at 330A).

At pint P6 the correspondence between the numerical and the experimental data is good both with and without the presence of the thermal screens (see figure 6.34).

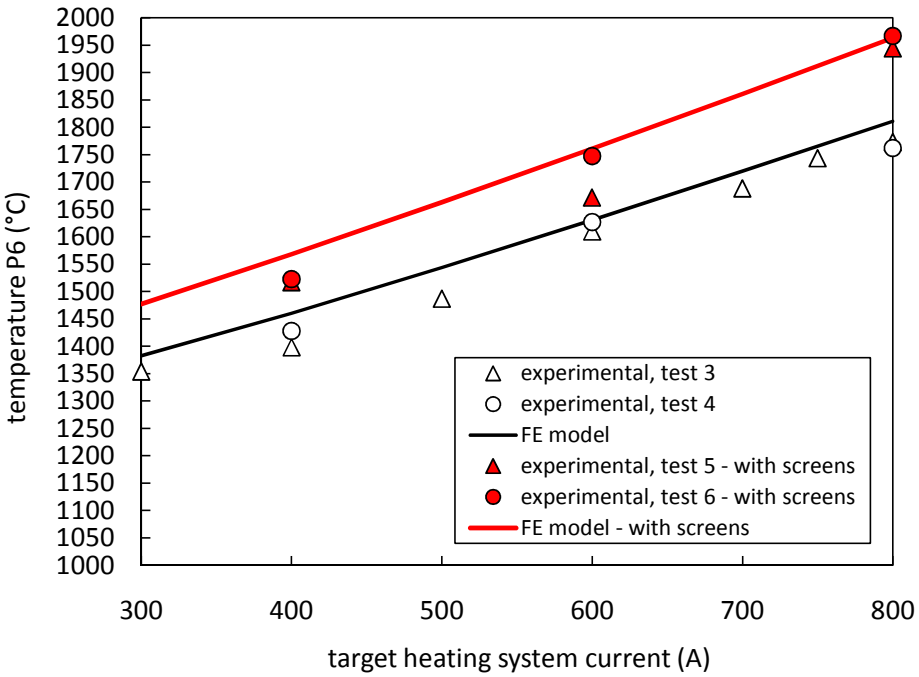

Fig. 6.34. Thermal study of the target – ion source system: comparison between experimental and numerical temperature data at point P6 (ion source current fixed at 330A).

Also at points P7 and P8 the FE model is able to predict in a reliable way the experimental data (see figures 6.35 and 6.36, respectively) but in this case it was possible to make the comparison

between FE and experimental temperatures only with the naked (without screens) target – ion source system: in fact the tantalum thermal screens placed at the extremities of the target heating system cover completely the zones in proximity of points P7 and P8 (see figures 6.10 and 6.26) and make temperature measurements by means of pyrometer impossible. Anyway FE curves allow to appreciate the temperature increments (for points P7 and P8) due to the introduction of the screening system.

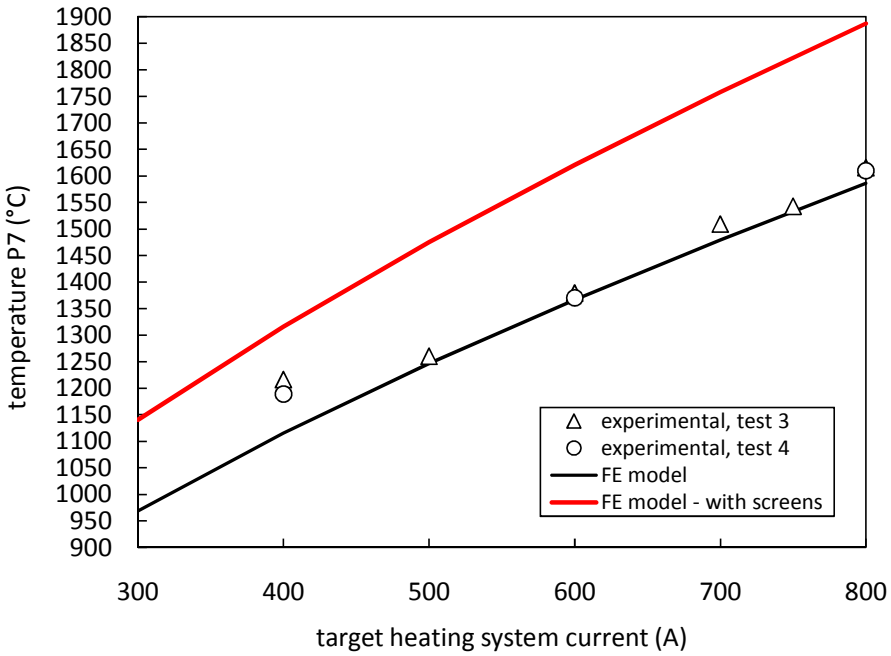

Fig. 6.35. Thermal study of the target – ion source system: comparison between experimental and numerical temperature data at point P7 (ion source current fixed at 330A).

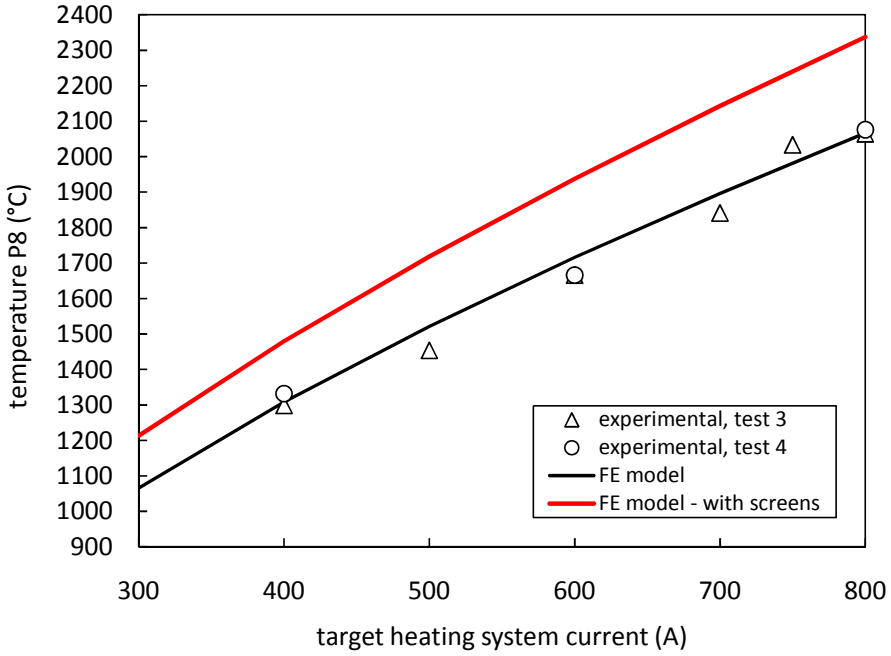

Fig. 6.36. Thermal study of the target – ion source system: comparison between experimental and numerical temperature data at point P8 (ion source current fixed at 330A).

Point P9 is the most important one since it represents the SPES target prototype; it is positioned at the center of the external round surface of the graphite cap (see figure 6.10). For point P9 temperature measurements were performed both without and with thermal screens: in the latter case a small hole was produced in the thin screen in order to allow temperature measurements on the graphite cap using the optical pyrometer. The correspondence between numerical and experimental data is satisfactory (see figure 6.37); for the configurations without and with thermal screens, the maximum differences between experimental and FE temperatures were equal to 117°C (heating system current equal to 800A) and 107°C (heating system current equal to 600A), respectively.

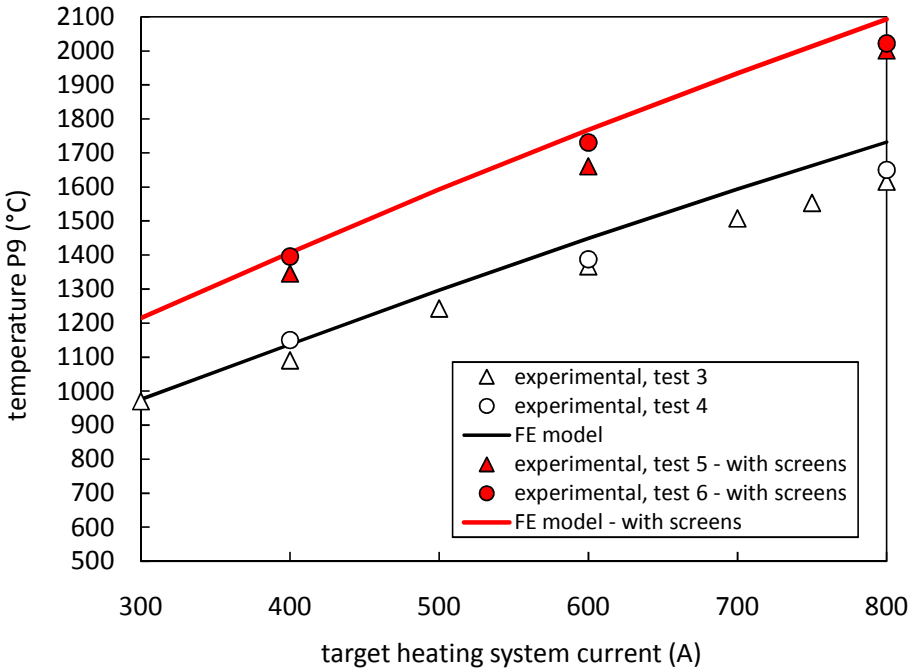

Fig. 6.37. Thermal study of the target – ion source system: comparison between experimental and numerical temperature data at point P9 (ion source current fixed at 330A).

The FE model above described was validated by means of experimental temperature measurements, with the presence of Joule heating thermal loads only. At this point it is ready to be used to study in a virtual environment the effect of an high intensity primary beam, in particular the 40 MeV, 20 μA primary proton beam discussed in the previous paragraphs: the power density values to assign to the various components impinged by the beam (window, disks and dumpers) will be previously calculated thanks to dedicated numerical codes. A complete set of FE simulations dedicated to the study of the proton beam thermal effect will be performed soon, in the next future.

6.6. Production of radioactive ion beams using the SPES target prototype: data analysis and results

As exposed in paragraph 6.4, once completed the thermal characterization of the target – ion source system and stabilized the target temperature at 2000°C, the uranium carbide disks were impinged by

a 40 MeV, 50 nA proton beam. After ionization the fission products were extracted from the ion source and mass-selected thanks to a mass separator magnet (see figure 6.12). A Faraday cup was used to measure beam currents after mass analysis and the yields of the fission fragments were obtained detecting the γ-rays from the decay of the radioactive isotopes, using a moving tape system connected to a Ge detector [1] (see table 6.2). The yield, measured in "ions/s·μA", is a parameter used to quantify the production rate of a particular isotope, relating the correspondent beam current (measured in "ions/s") to the current of the primary beam (measured in "μA").

Isotope	**$T_{1/2}$**	**Yield** (ions/s·μA)	**ΔYield** (ions/s·μA)
^{121}Ag	0.78s	$5.53\cdot10^{6}$	$1.44\cdot10^{5}$
^{81}Ga	1.22s	$2.20\cdot10^{5}$	$6.55\cdot10^{3}$
^{120g}Ag	1.23s	$1.52\cdot10^{7}$	$4.32\cdot10^{5}$
^{124}Cd	1.29s	$8.24\cdot10^{6}$	$1.63\cdot10^{5}$
^{78}Zn	1.47s	$1.22\cdot10^{5}$	$3.62\cdot10^{3}$
^{123m}Cd	1.82s	$1.08\cdot10^{7}$	$1.60\cdot10^{5}$
^{92}Kr	1.84s	$1.55\cdot10^{6}$	$2.42\cdot10^{4}$
^{90}Br	1.91s	$9.94\cdot10^{5}$	$4.01\cdot10^{4}$
^{119}Ag	2.10s	$2.96\cdot10^{7}$	$2.47\cdot10^{5}$
^{93}Rb	5.80s	$3.25\cdot10^{5}$	$1.03\cdot10^{4}$
^{123g}In	5.98s	$1.22\cdot10^{8}$	$2.03\cdot10^{6}$
^{72}Cu	6.60s	$2.19\cdot10^{5}$	$4.30\cdot10^{3}$
^{133m}I	9.00s	$1.04\cdot10^{7}$	$1.54\cdot10^{5}$
^{88}Br	16.30s	$1.15\cdot10^{7}$	$2.31\cdot10^{5}$
^{79g}Ge	19.00s	$1.31\cdot10^{6}$	$4.05\cdot10^{4}$
^{81}As	34.00s	$7.15\cdot10^{5}$	$1.59\cdot10^{4}$
^{132}Sn	39.70s	$2.14\cdot10^{6}$	$2.80\cdot10^{4}$
^{120m}In	47.30s	$4.23\cdot10^{7}$	$1.02\cdot10^{6}$
^{140}Cs	1.06m	$1.44\cdot10^{6}$	$4.85\cdot10^{4}$
^{94}Sr	1.23m	$6.30\cdot10^{6}$	$1.91\cdot10^{5}$
^{133}Sb	2.50m	$9.77\cdot10^{6}$	$3.72\cdot10^{5}$
^{137}Xe	3.83m	$4.58\cdot10^{7}$	$2.88\cdot10^{6}$
^{93}Sr	7.45m	$1.10\cdot10^{7}$	$1.12\cdot10^{5}$
^{95}Y	10.30m	$2.05\cdot10^{6}$	$6.66\cdot10^{4}$
^{141}Ba	18.30m	$2.48\cdot10^{6}$	$3.24\cdot10^{5}$
^{83g}Se	22.40m	$3.30\cdot10^{6}$	$3.23\cdot10^{4}$
^{134}Te	41.80m	$4.90\cdot10^{7}$	$7.70\cdot10^{6}$
^{134g}I	52.50m	$1.40\cdot10^{8}$	$2.77\cdot10^{7}$
^{87}Kr	1.27h	$1.09\cdot10^{7}$	$1.04\cdot10^{6}$

TABLE 6.2. Yields of the selected group of the isotopes produced and analyzed.

Table 6.2 reports the yields of the selected group of the 77 isotopes produced and analyzed during the on-line tests described in this chapter. These values were obtained by averaging, for each isotope, the yield calculated from each characteristic γ-ray peak present in the spectra. The uncertainties Δyield listed in table 6.2 were calculated taking into account both statistical and systematic errors.

The yields reported in table 6.2 show that the SPES uranium carbide target is suitable for the production of isotopes with half-lives of ~ 1 second or greater, where the half-life ($T_{1/2}$) is the period of time it takes for a particular isotope undergoing decay to decrease by half. This represents a promising result, even if not conclusive, about the release characteristics of this target for many elements. A more complete representation of the isotopes produced, ionized and analyzed during the on-line measurements with the target at 2000°C is shown in figure 6.38, in which the order of magnitude of yield at the tape system for each isotope is reported. The analysis of data obtained with the target at 1600°C and 1800°C is in progress: results will be compared soon with data at 2000°C presented in this chapter.

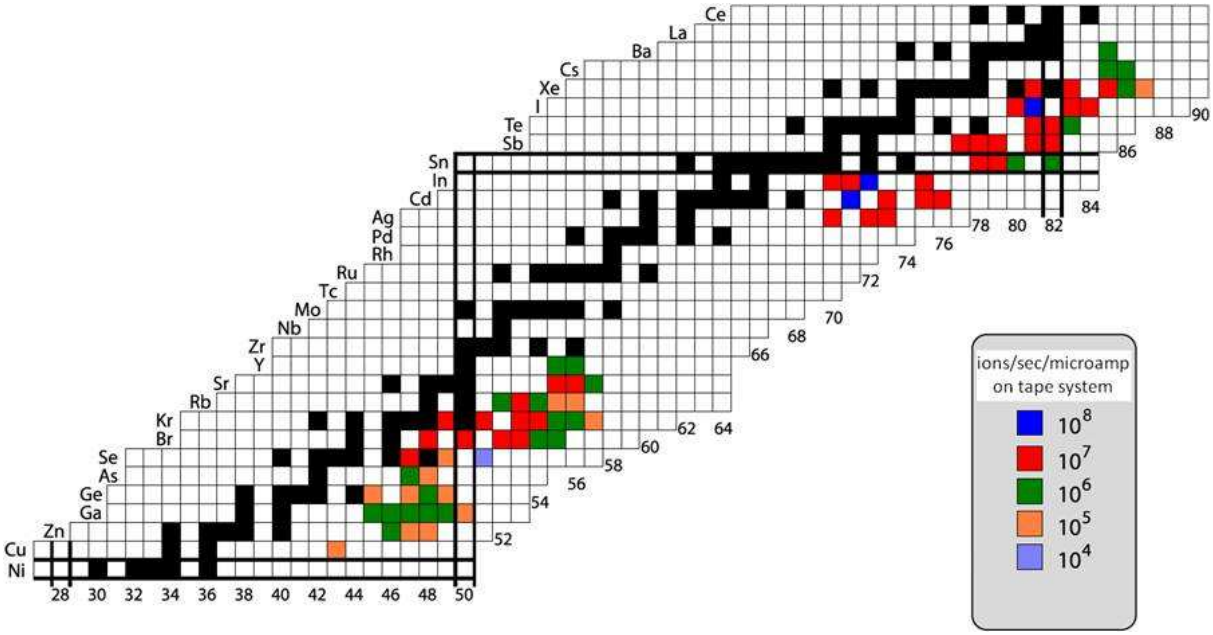

Fig. 6.38. Representation of the radioactive ion beams extracted (with the reference temperature of 2000°C for the target) and indication of the relative intensities.

The total number of isotopes extracted with enough intensity to be accurately measured is clearly limited by the use of a relatively low proton beam current. For this reason, yields of very neutron-rich isotopes, which are produced via fission within the uranium carbide SPES target, have not been measured. Further experiments, involving higher proton beam current values (about 10 μA) on the same target configuration, are planed with the aim to evaluate the release efficiency of a target array of neutron-rich isotopes.

6.7. Conclusions

The on-line test of the uranium carbide SPES target prototype was carried out at the HRIBF facility (ORNL) using a 40 MeV proton beam with intensity values of approximately 50 nA. Before starting the on-line test the target was heated at high temperatures (approximately 2000°C) by Joule effect: temperature measurements on the target – ion source system were performed, allowing to validate the thermal-electric FE model defined to study in detail the temperature field of the target – ion source complex. During the on-line test we measured the beam intensities of 20 elements and 77 isotopes. On-line measurements indicated that the SPES target prototype was able to work as well as lower density targets presently in use at HRIBF; moreover the SPES target material and shaping demonstrated to be a feasible solution to produce exotic ions in the context of ISOL facilities, in particular for the SPES facility that is expected to run the first radioactive ion beam in 2015.

REFERENCES

[1] D. Scarpa et al., Neutron rich isotope production using the uranium carbide multi-foil SPES target prototype, Eur. Phys. J. A, under review.

[2] Andrighetto A, Antonucci C M, Cevolani S, Petrovich C, Santana Leitner M. Multifoil UCx target for the SPES project – An update. Eur Phys J A 2006;30:591-601.

[3] M. Barbui et al., Calculations and first results obtained with a SiC prototype of the SPES direct target, Nucl. Instrum. Methods Phys. Res., Sect. B 266 (2008) 4289–4293.

[4] M. Manzolaro, Analisi termica e strutturale del bersaglio diretto per la produzione di fasci radioattivi per il progetto SPES, Master Degree Thesis in Mechanical Engineering, University of Padua, Italy

[5] http://www.phy.ornl.gov/hribf/accelerator/tandemweb/

Conclusions

At the end of this work a new version of the target – ion source system has been proposed, studying and designing modifications with the aim to optimize the electrical, the thermal and the structural functioning of both the target and the ion source. Taking as reference the organization of the chapters constituting the thesis, a series of concluding remarks is reported in the following.

In the first chapter a general overview of the SPES project and its scientific context was presented. Some aspects of research in nuclear physics with radioactive ion beams were illustrated, together with some important applications of exotic beams in solid-state physics and nuclear medicine. A detailed description of the main components constituting an ISOL facility was also furnished and a parallel general presentation of the main components of the SPES facility was reported at the end of the chapter.

With the second chapter the macro-components belonging to the SPES production area were presented; in particular the front end and the target chamber containing the target – ion source system were described including a large number of details.

In chapter 3 the study, the design and the experimental tests performed for the SPES target were presented and discussed in detail. At first the thermal-electric behaviour of the first SPES target prototype was studied by means of both experimental tests and theoretical calculations. Once verified the accuracy of the numerical models and their agreement with experimental data, they were used for the virtual design and the optimization of the new prototype. The new SPES target prototype was produced and tested at Legnaro National Laboratories, confirming the reliability of the correspondent numerical models. The effect of the proton beam on the target temperature field and stress state was studied in detail using a coupled thermal-structural FE model.

In chapter 4 the ionization mechanisms and the ion sources used in the context of the SPES project were presented and described. Some notions of “ion beam formation” and “ion beam optics” were also included. The thermal behaviour of both the hot-cavity ion source and the high temperature plasma ion source adopted for the SPES facility was studied in detail by means of theoretical models and experimental measurements; a preliminary numerical approach to study the trajectories of ions and electrons inside the ion source was also introduced.

In chapter 5 a detailed study of the SPES “production target – hot-cavity ion source” assembly was presented and discussed. At first the thermal-electric behaviour of the assembly was studied

using a numerical FE model, then the obtained results were compared to temperature and potential difference values measured at Legnaro National Laboratories during dedicated experimental off-line tests. Analogies and discrepancies between numerical and experimental data were discussed in detail.

The on-line test of the uranium carbide SPES target prototype was carried out at the HRIBF facility (ORNL) using a 40 MeV proton beam with intensity values of approximately 50 nA; its description was accurately reported in the sixth chapter of the thesis. Before starting the on-line test the target was heated at high temperatures (approximately 2000°C) by Joule effect: temperature measurements on the target – ion source system were performed, allowing to validate the thermal-electric FE model defined to study in detail the temperature field of the target – ion source complex. During the on-line test we measured the beam intensities of 20 elements and 77 isotopes. On-line measurements indicated that the SPES target prototype was able to work as well as lower density targets presently in use at HRIBF; moreover the SPES target material and shaping demonstrated to be a feasible solution to produce exotic ions in the context of ISOL facilities, in particular for the SPES facility that is expected to run the first radioactive ion beam in 2015.

In the next future an intense set of ionization tests will be performed at Legnaro National Laboratories with the aim to study in detail the global functioning of the ion sources adopted for the SPES facility and to improve and optimize them according to the specific needs of the project.

Appendix A

Procedure for the assemblage of the target – ion source system at HRIBF (ORNL)

1. Introduction

In this appendix the assemblage and the preparation of the Electron-Beam-Plasma-Ion-Source (EBPIS) and of the target heating system used to test on-line the SPES target prototype at HRIBF (ORNL) are presented. A step by step description of the assemblage procedure is reported together with some important notes and observations on the HRIBF target – ion source system. All the objects presented in the following paragraphs were developed and built at ORNL, with the exception of the SPES target prototype (cylindrical graphite box containing seven axially spaced uranium carbide disks, see chapter 6), designed and produced at Legnaro National Laboratories: as specified in chapter 6, it was developed in order to fit with the standard HRIBF target heating system.

2. Step by step assembly procedure of the EBPIS and of the target heating system

In the following the main steps needed to assembly the EBPIS and the HRIBF target heating system are described.

STEP 1: preliminary remarks

Obtain the complete list of the parts composing the EBPIS and the target heating system; obtain also the mechanical drawing of the target – ion source assembly.

Item	Material	Part No.	Quantity	Cost Ea.	Vendor	Vendor Part No.
Target & Transfer Line						
target holder	carbon		1			
target holder cap	carbon		1			
target tube	Ta		1			
Transfer line-assembly						
vertical transfer line	Ta		1			
horizontal transfer line	Ta		1			
1/8" gas feed line	Ta		1			
current strap	Ta		1			

Item	Material	Part No.	Quantity	Cost Ea.	Vendor	Vendor Part No.
1/8" gas feed tube	Ta		1			
Transfer line heat shield	Ta		1			
1/8"-1/8" union elbow	SS		2			
1/8" cryogenic/current break	SS		1		Insulator Seal Inc.	9611003
current lead	Ta(2.5%W)		1			
buss extension	SS		1			
3/4-16 nut	SS		1			
#10-32 threaded rod	Ta		1			
#10-32 nut	Ta		2			
1/4-20 hex bolt	SS		1			
1/4" washer	SS		1			
CATHODE						
body sub-assembly		TIS-101-01				
cathode body	Ta	(A)	1			
cathode sleeve	Ta	(B)	1			
cathode ring	Ta	(C)	1			
support nut	Mo	TIS-106-01	1			
ANODE						
anode sub-assembly		TIS-201-02				
anode tube	Ta	(A)	1			
extract aperture	Ta	(B)	1			
grid	W	(C)	1			
support tube	Ta	TIS-202-01	1			
anode support nut	Mo	TIS-203-01	3			
anode support insulator	Al_2O_3	TIS-204-01	3			
anode support	Mo	TIS-205-01	3			
anode heat shield set	Mo	TIS-206-01	1			
heat shield spacer wire	Mo		2			
anode wire	Mo		1			
anode push-on connector	BeCu		1		Insulator Seal Inc.	9924003
TIS SUPPORT						
head flange	C	TIS-301-03	1			
outer tube	C	TIS-302-01	1			
end flange	Mo	TIS-303-01	1			
#10-32 socket head screw	SS		4			
#10 washer	SS		4			
filament	Ta(2.5%W)		1			
heat shield (fixed)	Ta(2.5%W)		1			
heat shield (loose)	Ta		1			
heater bracket - left	Nb		1			
heater bracket - right	Nb		1			
#10-32 threaded rod	Ta		4			
#10-32 nut	Ta		8			
buss nut	Cu		4			

TABLE 1. The complete list of the parts composing the target heating system and the EBPIS.

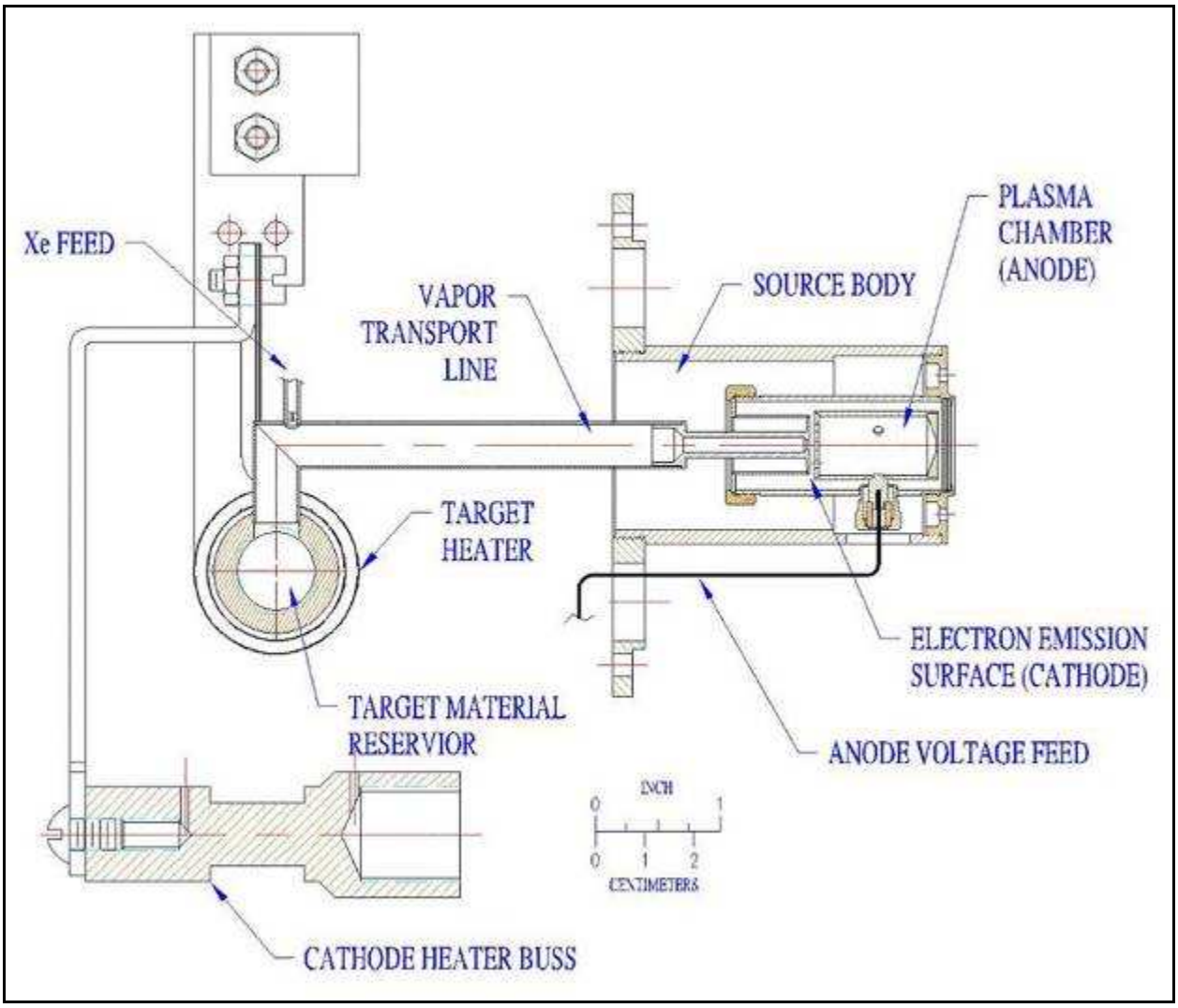

Fig. 1. Mechanical drawing of the EBPIS's assembly.

STEP 2: preparation of the EBPIS's parts

Collect all the EBPIS's parts listed in table 1 (only CATHODE, ANODE and TIS SUPPORT) and reported in figure 2; clean them (with the exception of the support housing and the support housing flange, made of graphite) using alcohol and an ultrasonic cleaner, as shown in figure 3. After cleaning the parts handle them using latex gloves and avoiding contacts with other dirty objects: parts cleanliness is a fundamental prerequisite for the correct functioning of the EBPIS.

STEP 3: preparation of the tools

Collect all the tools necessary for the EBPIS's assembly (see figure 4). Also in this case, they must be clean; if not use alcohol to prepare them.

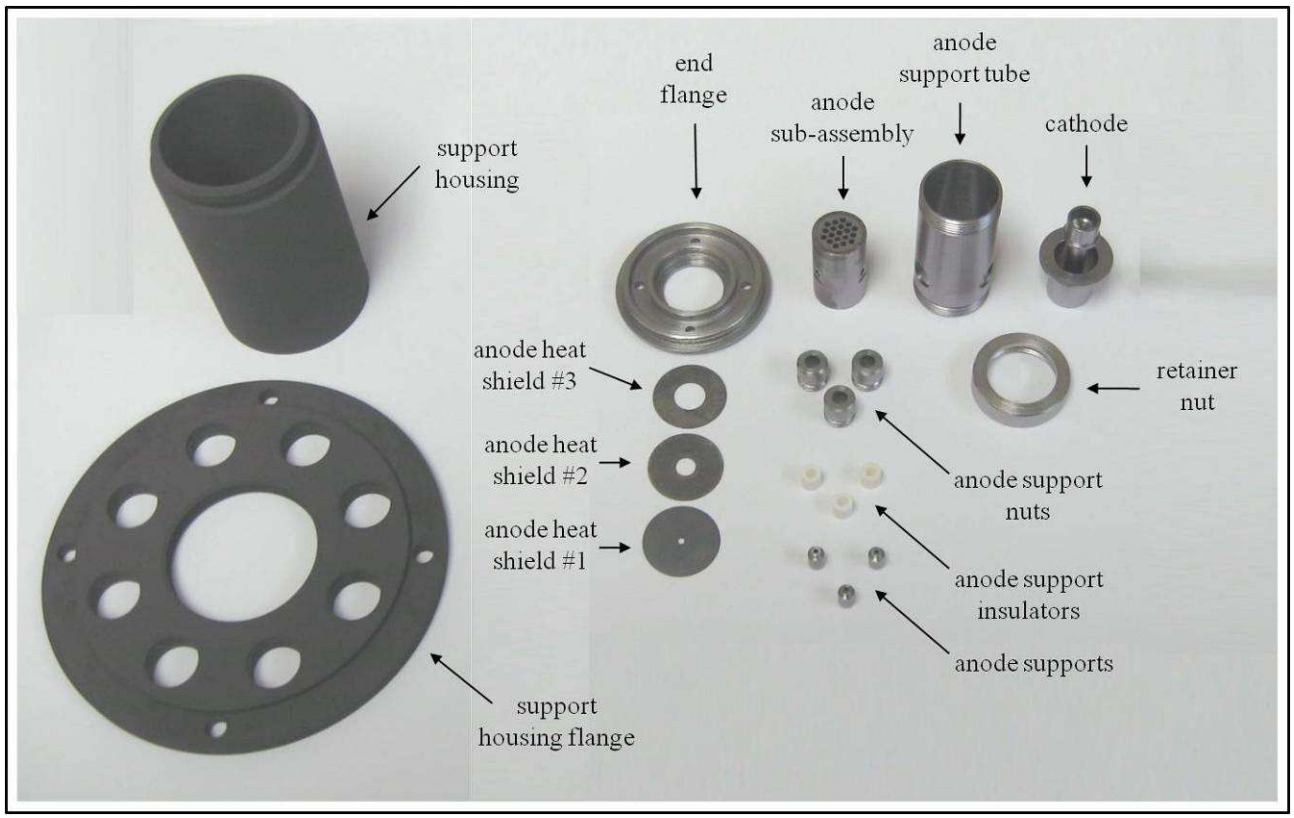

Fig. 2. The EBPIS's main parts.

Fig. 3. EBPIS's main parts ultrasonic cleaning.

Fig. 4. Tools used during the assembly of the EBPIS [1].

STEP 4: anode assembly

A) Take the alignment tool represented in figure 5 and put the *anode sub-assembly* inside its cavity (previously cleaned with alcohol), facing the bottom of the cavity with the Tungsten grid.

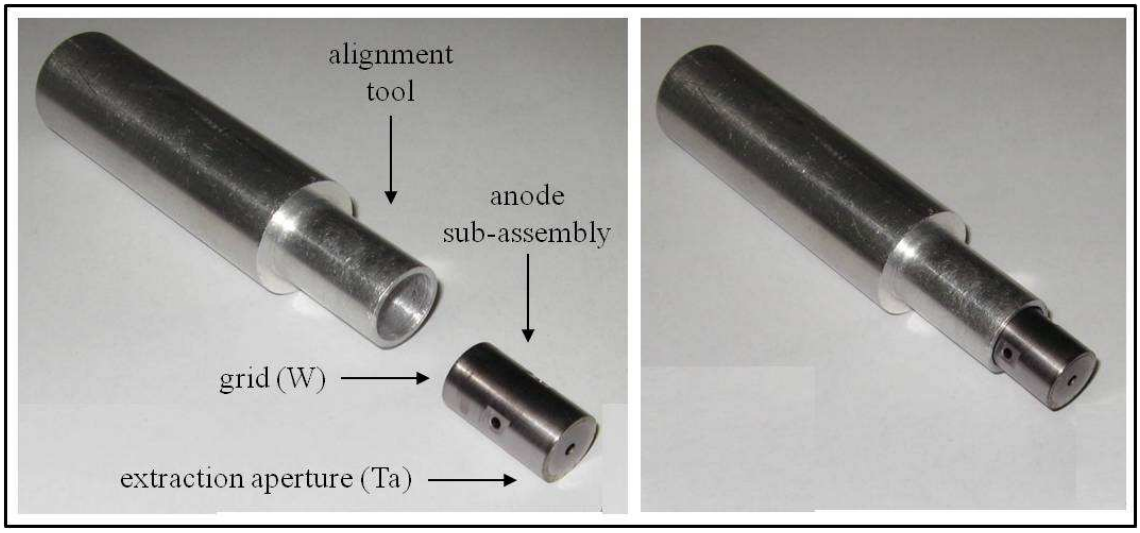

Fig. 5. Positioning of the *anode sub-assembly*.

B) Insert the *anode support tube* in the alignment tool as represented in figure 6 and rotate it so that its holes are aligned respect to the holes in the *anode sub-assembly*. The circular extremity of the *anode sub-assembly* more distant respect to the three radial holes must face the alignment tool.

Fig. 6. Positioning of the *anode support tube.*

C) Insert one of the three *anode supports* on one of the three holes of the *anode sub-assembly* (see figure 7 and 7.a); then position on the *anode support* one of the three *anode support insulators*, as shown in figure 7.b. At the end place one of the three *anode support nuts* onto the *anode support insulator* and screw it into the *anode support tube* (see figure 7.c). Repeat the operations listed above for the other two supports of the EBPIS.

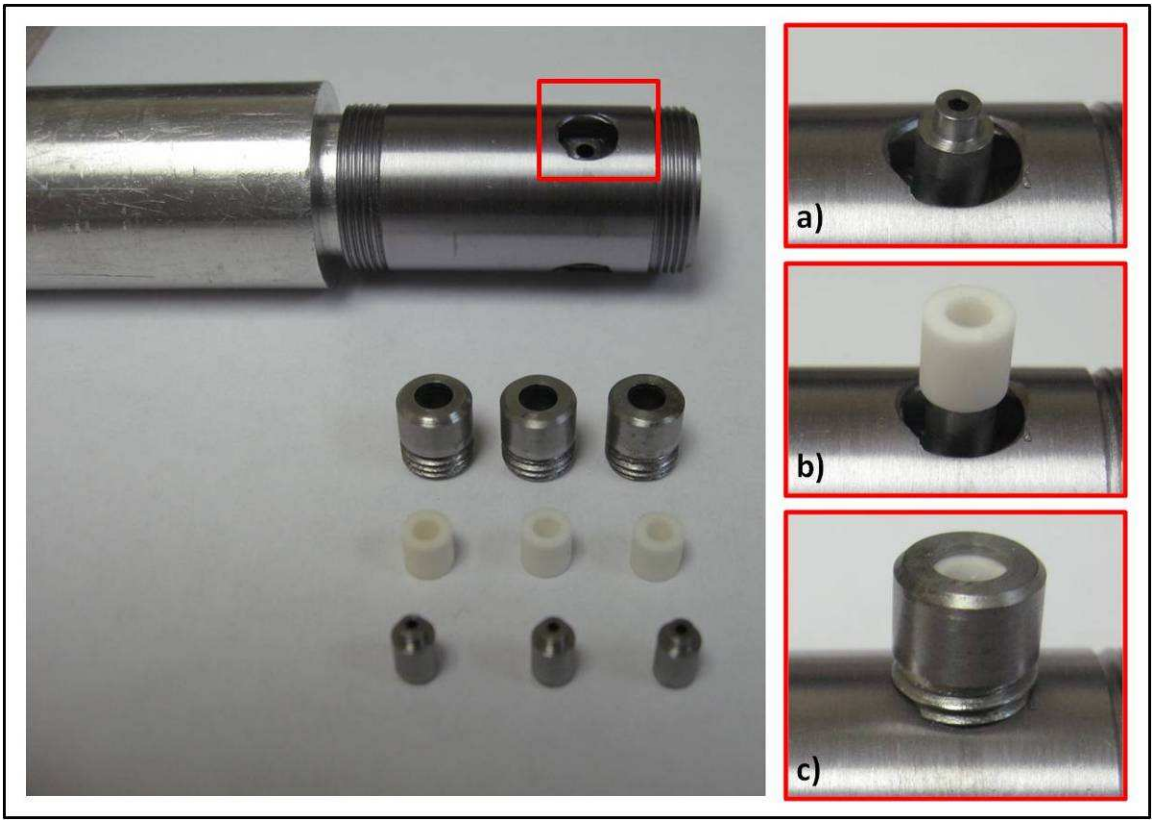

Fig. 7. Anode supports assembly: positioning of the *anode support* (a), of the *anode support insulator* (b) and of the *anode support nut* (c).

D) Check the alignment of the *anode sub-assembly* within the *anode support tube* by inserting the alignment tool on both ends of the assembly and looking at the gaps: it is very important to maintain the radial spacing between the *anode sub-assembly* and the *anode support tube* constant along the circumferential direction. Some small adjustments are usually necessary to reach a good positioning accuracy (see figure 8).

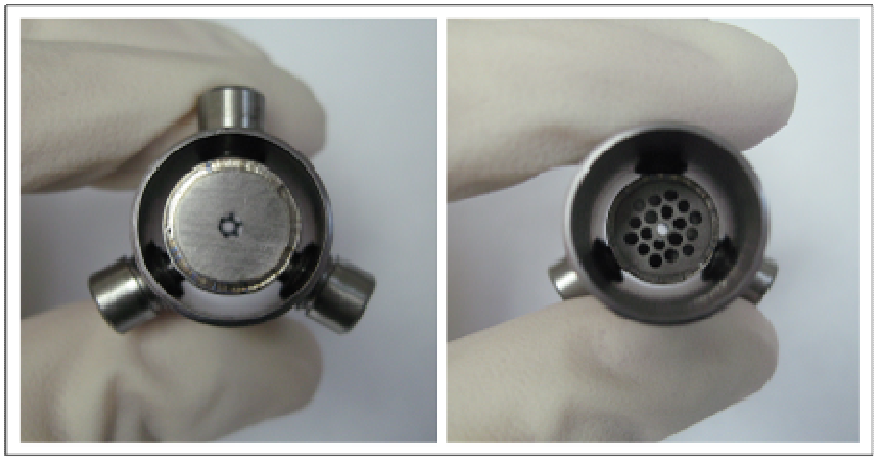

Fig. 8. Positioning check of the *anode sub-assembly*.

E) Take the *end flange*, the three *anode heat shields* (#1, #2 and #3) and prepare two annular spacers (see figure 9) starting from a piece of Niobium (Nb) wire (diameter of 0.025'' = 0.635 mm) and forming it into a solid cylindrical support with a diameter of approximately 0.69'' = 17.5 mm; check that the circular formed wires lie flat and that they are large enough so that if they move they don't obstruct the center holes of the *anode heat shields*.

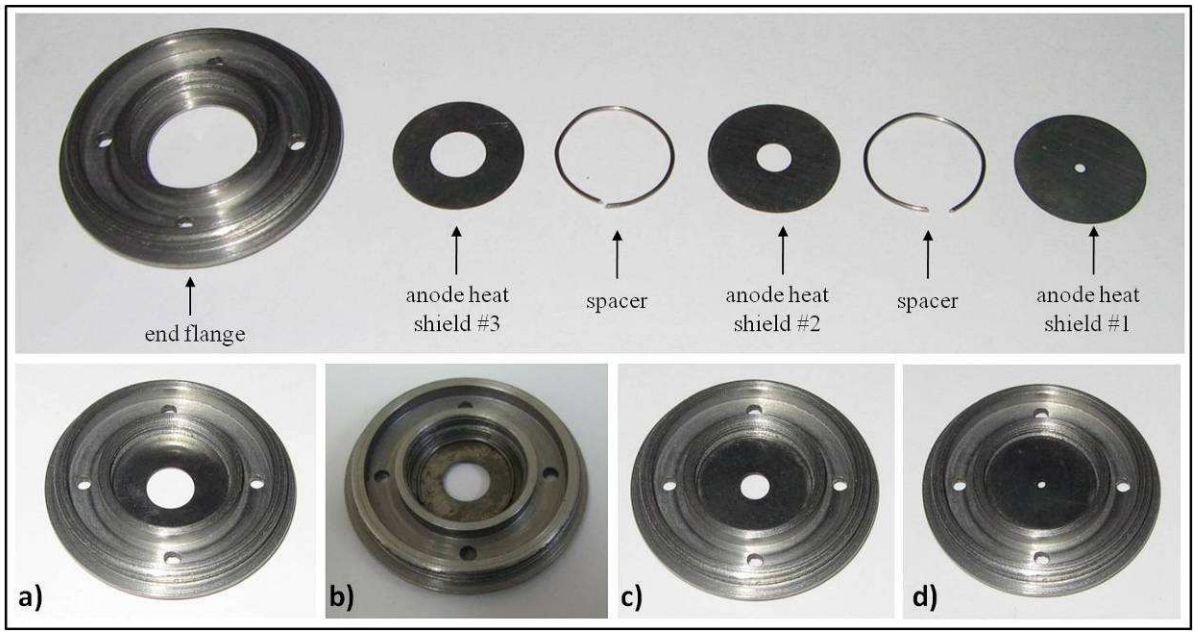

Fig. 9. The *end flange*, the *anode heat shields* and the spacers; details of the positioning of the *anode heat shield #3* (a), of the first spacer (b), of the *anode heat shield # 2* (c); the complete assembly of the three *anode heat shields* on the *end flange* (d).

F) Screw the *end flange* onto the *anode support tube* keeping the *anode heat shields* centered and correctly positioned inside the *end flange*; the anode assembly is at this point ready (see figure 10).

Fig. 10. The anode assembly.

STEP 5: check of the anode-cathode gap

Before starting to connect the *cathode* to the anode assembly it is very important to check the dimensions z_1 and z_2 represented in figure 11; the difference between z_1 and z_2 is the anode-cathode gap, so the gap between the Tungsten anode grid of the *anode sub-assembly* and the extremity of the *cathode* opposite respect to the transfer line.

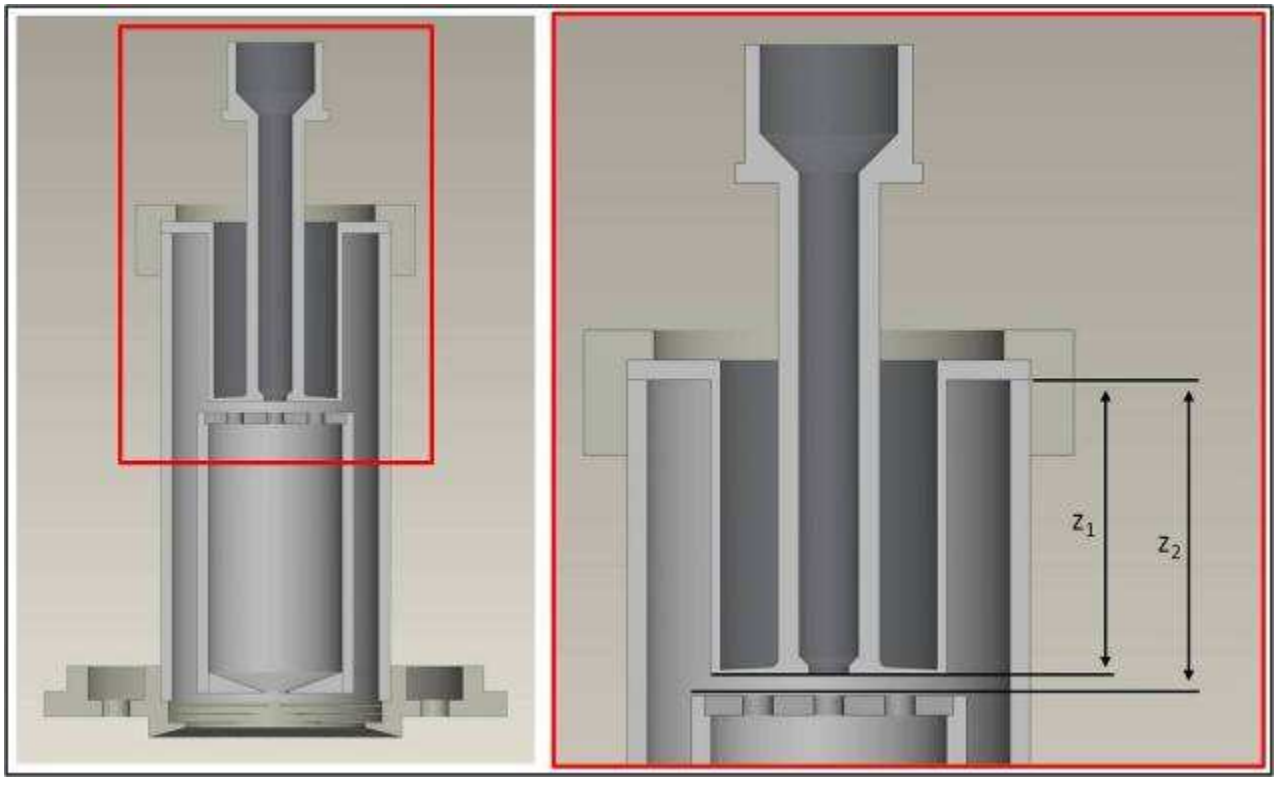

Fig. 11. The dimensions z_1 and z_2.

Measure the dimensions z_1 and z_2 using a digital caliper and varying the measurement position in the circumferential direction (dimensional non-homogeneity due to welded joints). In the present example (see figure 12) three measurements (z_1 = 14.97, 14.96, 14.98 mm, medium value equal to *14.97*) for the *cathode* and six (z_2 = 15.97, 15.94, 15.99, 15.95, 15.98, 15.98 mm, medium value equal to *15.97*) for the anode grid were collected. Usually more measurements are needed for z_2 respect to z_1 mainly because of the different type of welding used for the cathode and the anode grid: for the cathode (z_1) the Electron Beam Welding technique (refined welding surface) is used whereas the anode grid (z_2) is welded to the rest of the *anode sub-assembly* by means of Laser Welding Technique (less refined welding surface).

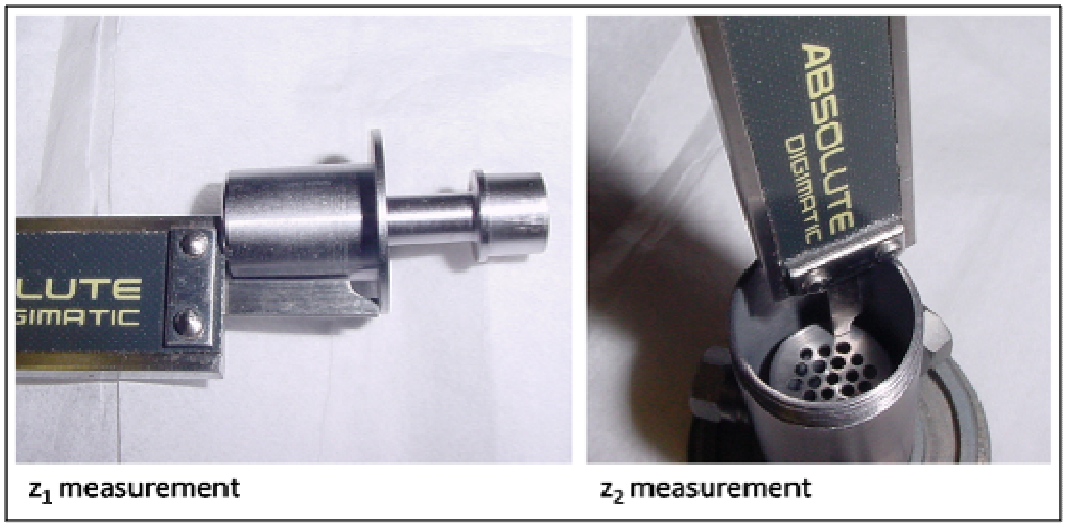

Fig. 12. Measurements of the dimensions z_1 and z_2 [1].

As exposed before, the difference between z_1 and z_2 represents the anode-cathode gap: in this case z_2 - z_1 = 15.97 mm – 14.97 mm = 1 mm. The anode-cathode gap size should always be between 0.9 and 1.4 mm: in particular a value as close as possible to 1.2 mm is recommended. If the gap is less than 0.9 mm, a Molybdenum spacer is used to increase the anode-cathode gap (spacer positioned between the *cathode* and the *anode support tube*). If the gap is more than 1.4 mm, it is sometimes possible to reduce it by loosening a little bit the three *anode support nuts* and by pushing the *anode sub-assembly* inside the *anode support tube*. If the gap is still bigger than 1.4 mm, the anode assembly should not be used. In the present example the anode-cathode gap is equal to 1 mm and a 0.2 mm spacer was used to increase the gap value from 1 to 1.2 mm, the optimal value.

STEP 6: connection between the cathode and the anode assembly

Once checked the anode-cathode gap, position the *cathode* on the *anode support tube* (with the spacer interposed if necessary) and block it by screwing the *retainer nut* into the *anode support tube* (see figure 13). While fixing the *retainer nut* check that the *cathode* is well centered respect to the

anode support tube. To facilitate this operation try to pull the *cathode* in the axial direction while screwing the *retainer nut*: it will be centered and will find its final position respect to the *retainer nut* (thanks to one of its geometrical feature) and so (once the *retainer nut* is completely screwed) to the *anode support tube*.

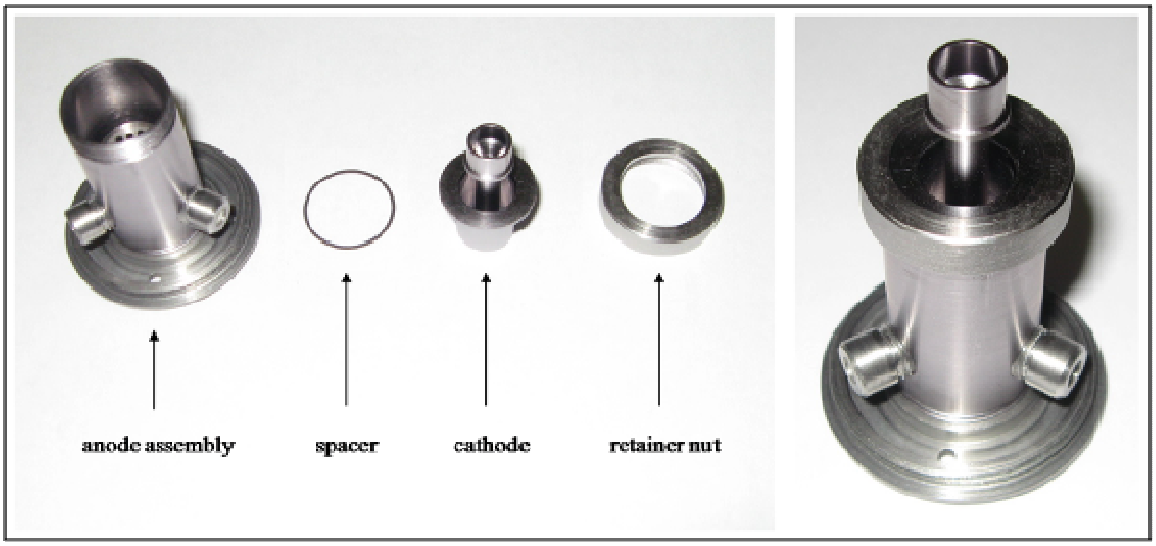

Fig. 13. Connection between the *cathode* and the *anode assembly*.

STEP 7: preliminary assembly of the support housing and of the support housing flange for the determination of the anode wire connection hole

A) Screw the cathode-anode assembly into the *support housing* and then into the *support housing flange*, as shown in figure 14; fix the objects but don't force too much to avoid to brake the brittle graphite parts.

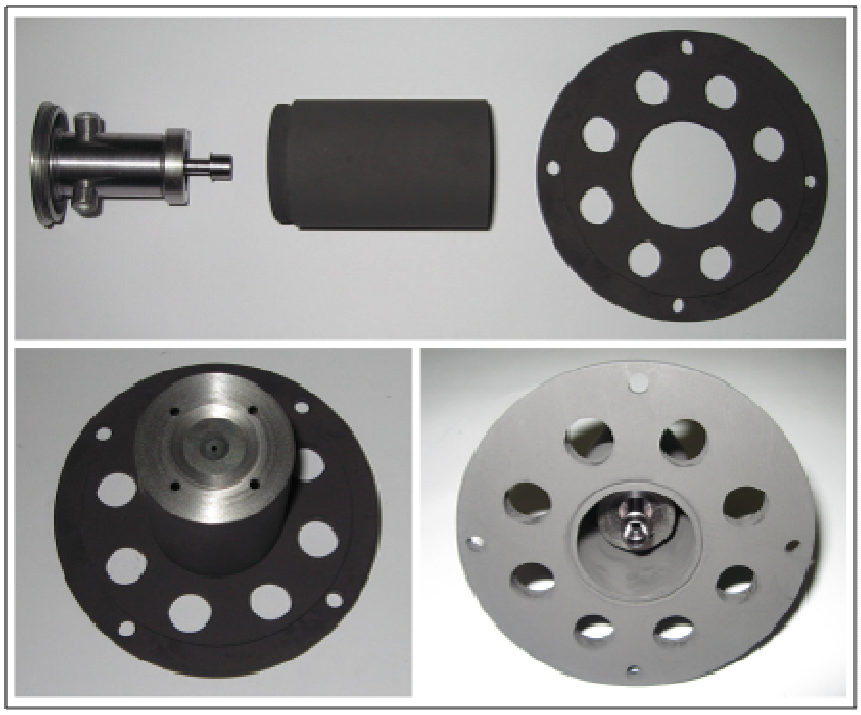

Fig. 14. Preliminary assembly of the *support housing* and of the *support housing flange*.

B) At this point mark the frontal part of the *support housing* to identify the circumferential position of the hole to execute on its lateral surface for the connection of the anode wire. Taking as reference figure 15, there are three possible places for the hole to be drilled, corresponding to the three *anode sub-assembly* supports. Orient the *support housing flange* so that one of the four mounting holes is straight up (see the red line of figure 15 at Position 1) and examine the positions of the three *anode sub-assembly* supports. Rotate the assembly of 90° and inspect again (figure 15, position 2). Repeat the inspection rotating the assembly of 90° for other two times (figure 15, positions 3 and 4). Now chose the position where one of the three *anode sub-assembly* supports falls closest to the '8 o'clock' position (position 4, for the present example) and mark with a sharp pointed tool the frontal side of the *support housing* in correspondence of this position (see the yellow line of figure 15). The reason why the '8 o'clock' position is preferred is due to the position of the anode feed through on the Al alloy main plate of the vacuum chamber in which the EBPIS will be installed (see figure 15).

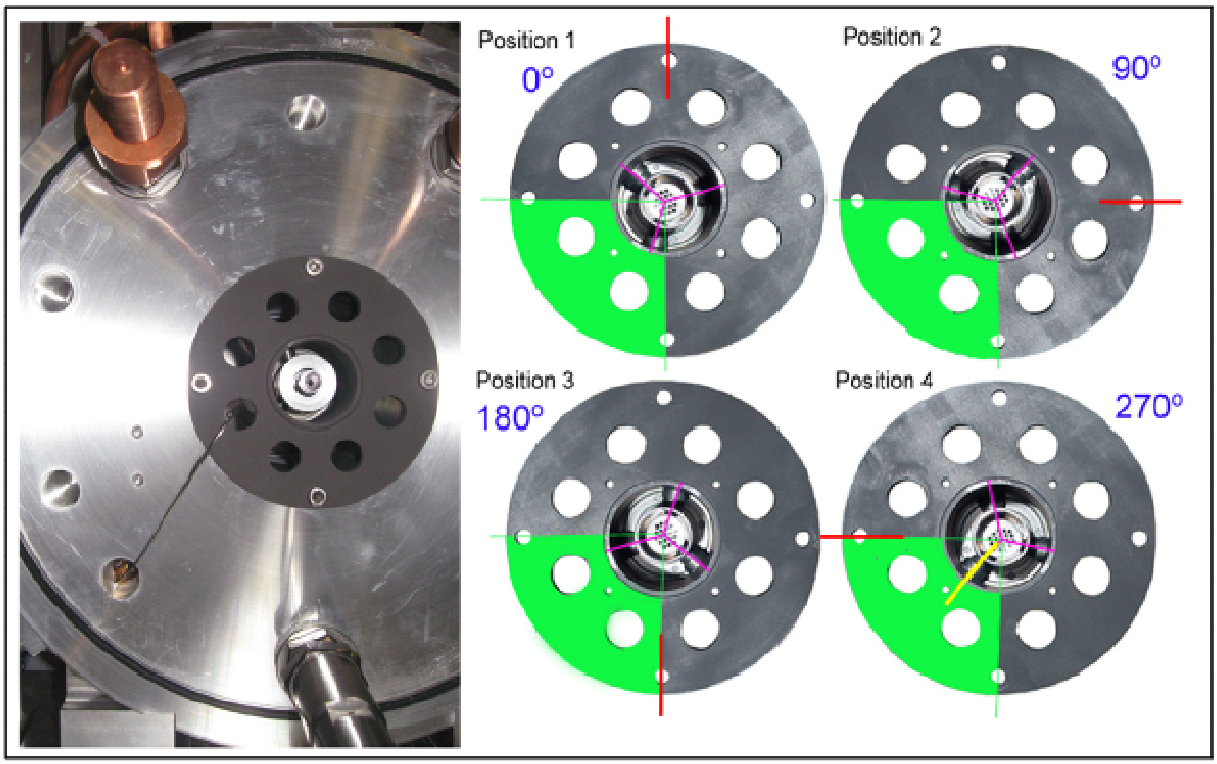

Fig. 15. Definition of the circumferential position of the anode wire connection hole [1].

C) As shown in figure 16, transport the circumferential reference for the anode wire connection hole from the frontal side of the *support housing* to its lateral surface, as close as possible respect to the support axial position. Even if the anode wire connection hole will have a reasonably large diameter, it is very important in this phase to maintain a discrete level of accuracy while marking the lateral surface of the *support housing*.

Fig. 16. Transportation of the circumferential reference for the anode wire connection hole on the lateral surface of the *support housing*.

D) Disassemble the *support housing*, measure the distance in the axial direction of the *anode sub-assembly* supports respect to the frontal extremity of the *end flange* and reproduce the correspondent reference on the external surface of the *support housing*. At this point the references for the anode wire connection hole are univocally defined (see figure 17).

Fig. 17. Definition of the axial reference for the anode wire connection hole on the lateral surface of the *support housing*.

STEP 8: drilling of the support housing and definitive assembly of the EBPIS

A) Drill the *support housing*'s lateral surface (see figure 18.a) producing a hole characterized by a diameter of 0.400'' (10.16 mm); act in a delicate way in order to avoid to damage the brittle

graphite *support housing*. Reassembly the *support housing* and verify the centering of the anode wire connection hole respect to the *anode sub-assembly* support (see figure 18.b).

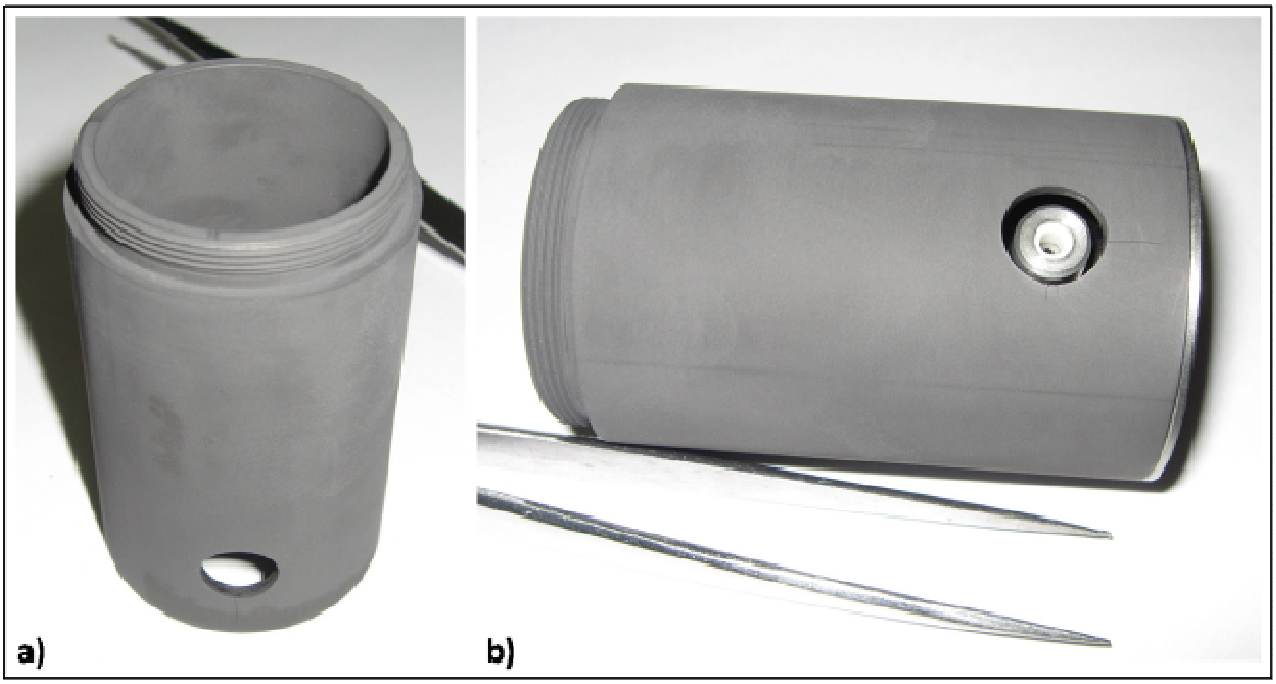

Fig. 18. The anode wire connection hole on the lateral surface of the *support housing* (a) and its alignment check respect to the *anode sub-assembly* support (b).

B) Reassembly now the *support housing flange*; cut a piece of Molybdenum wire with a length and a diameter of 10'' (250 mm) and 0.040'' (1 mm), respectively: it will be used as anode wire. File one end of the wire until it fits snugly into the *anode sub-assembly* support. Wash the wire with alcohol. At approximately 0.8'' (20 mm) in radial direction from the external surface of the *support housing* make a 90° bend in the anode wire and pass it through one of the holes in the *support housing flange* (see figure 19). Additional shaping of the wire will be done in the later step.

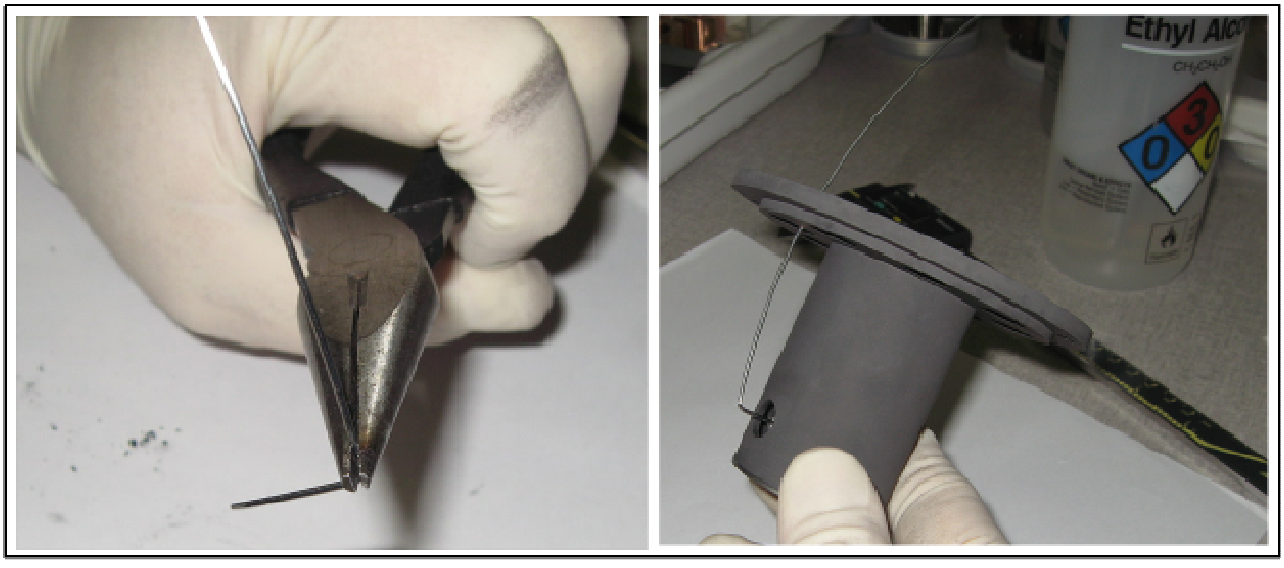

Fig. 19. Preparation of the anode wire and connection with the *anode sub-assembly* support.

STEP 9: positioning of the EBPIS into the vacuum chamber and anode connection

A) Using four appropriate screws fix the EBPIS respect to the main plate of the vacuum chamber, paying attention on the right positioning of the anode wire (see figure 20).

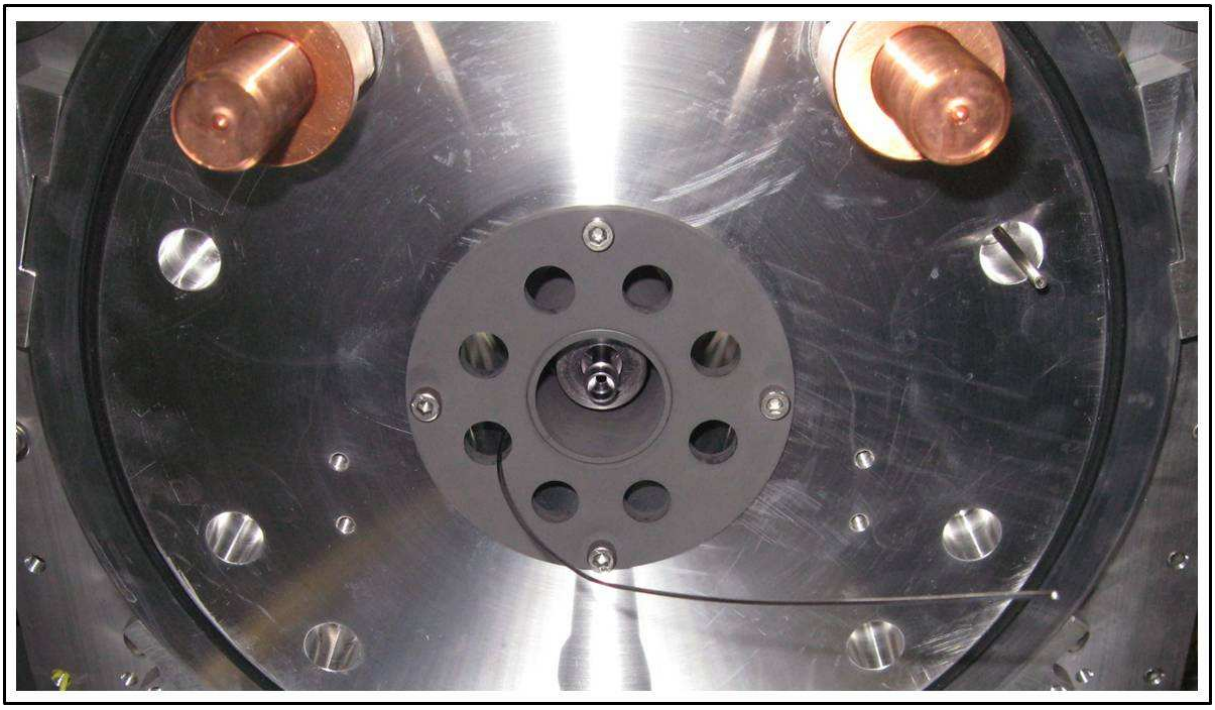

Fig. 20. Positioning of the EBPIS inside the vacuum chamber.

B) Once identified the position of the anode feed through on the main plate of the vacuum chamber, bend and cut appropriately the anode wire (see figure 21).

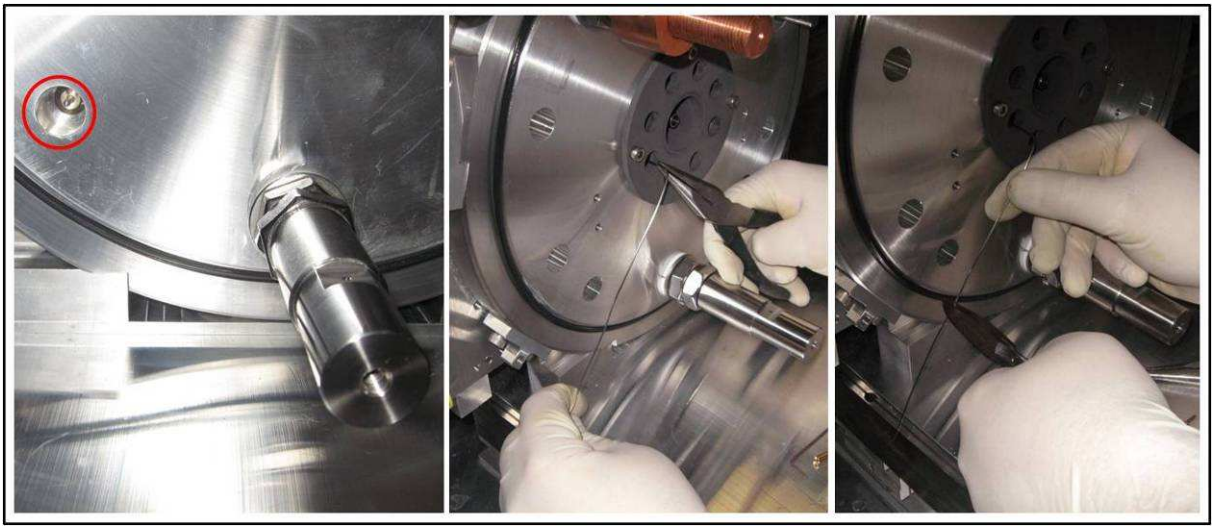

Fig. 21. Positioning of the EBPIS inside the vacuum chamber.

C) Position the anode wire inside the Copper transition, fix the transition's screw and connect in this way the anode wire with the anode feed through (see figure 22).

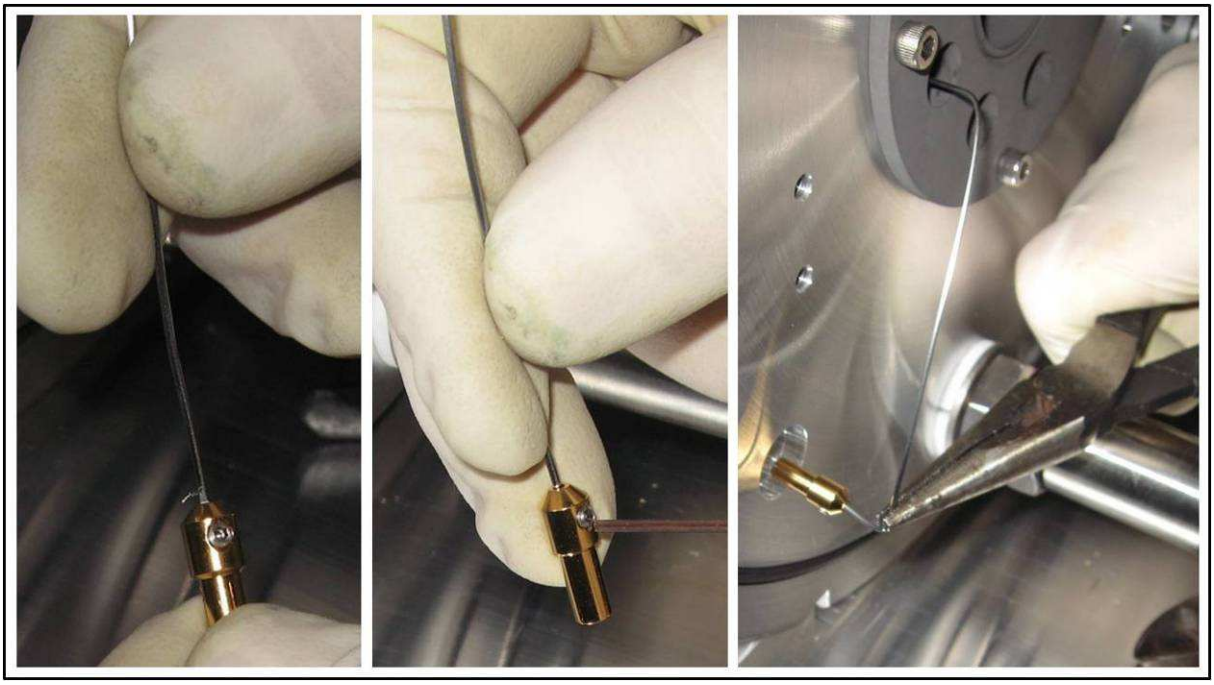

Fig. 22. Connection of the anode wire with the anode feed through.

D) The EBPIS is now completely assembled and prepared inside the vacuum chamber (see figure 23).

Fig. 23. The EBPIS assembled and prepared inside the vacuum chamber.

E) As last point, check visually and by means of a digital voltmeter that there are not electrical contacts between the anode wire and the support housing flange and between the anode wire and the vacuum chamber (see figure 24).

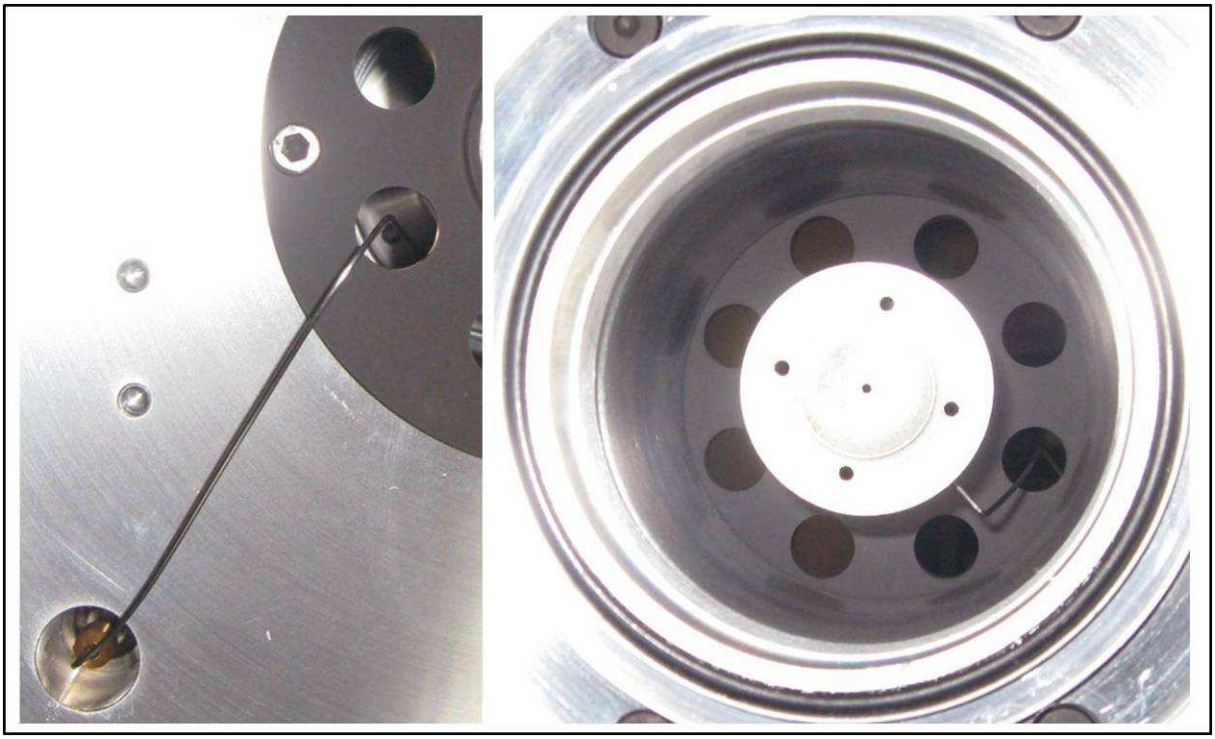

Fig. 24. Checks to avoid electrical contacts

STEP 10: preparation of the parts composing the target heating system

Collect all the parts composing the target heating system (see figure 2) and clean them using alcohol. After cleaning the parts handle them using always latex gloves.

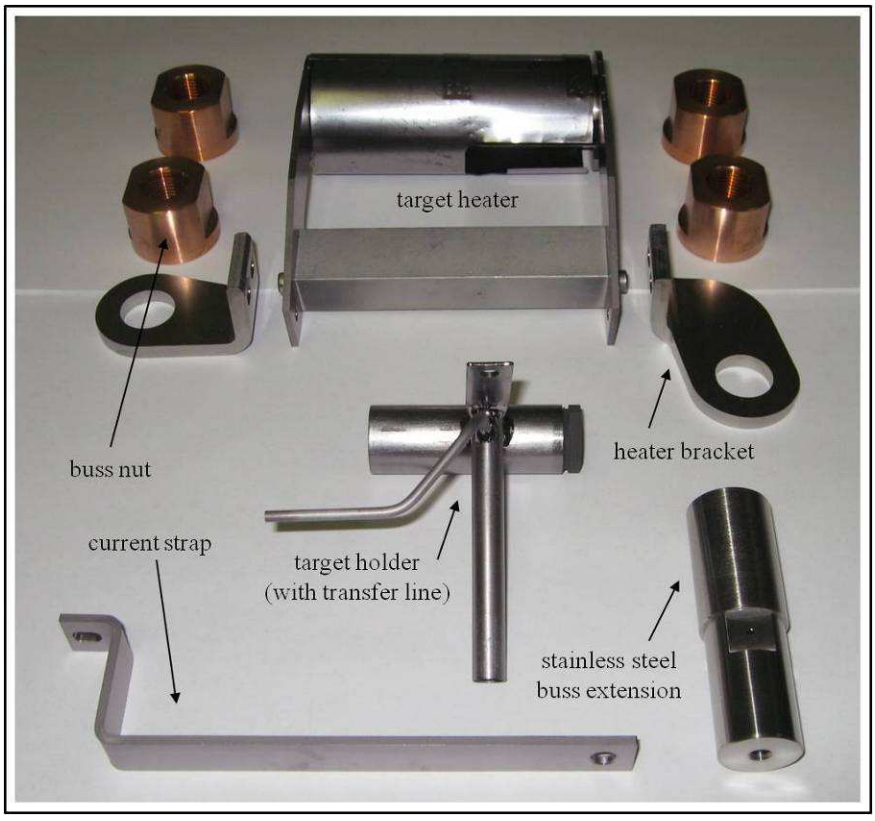

Fig. 25. The parts composing the target heating system.

STEP 11: positioning and pre-alignment of the target holder

At this point install the buss extension on the electrical clamp that provides the electrical current needed to heat the transfer line and the ion source; then position the target holder (comprehending the transfer line) and pre-align it using a cross laser (see figure 26).

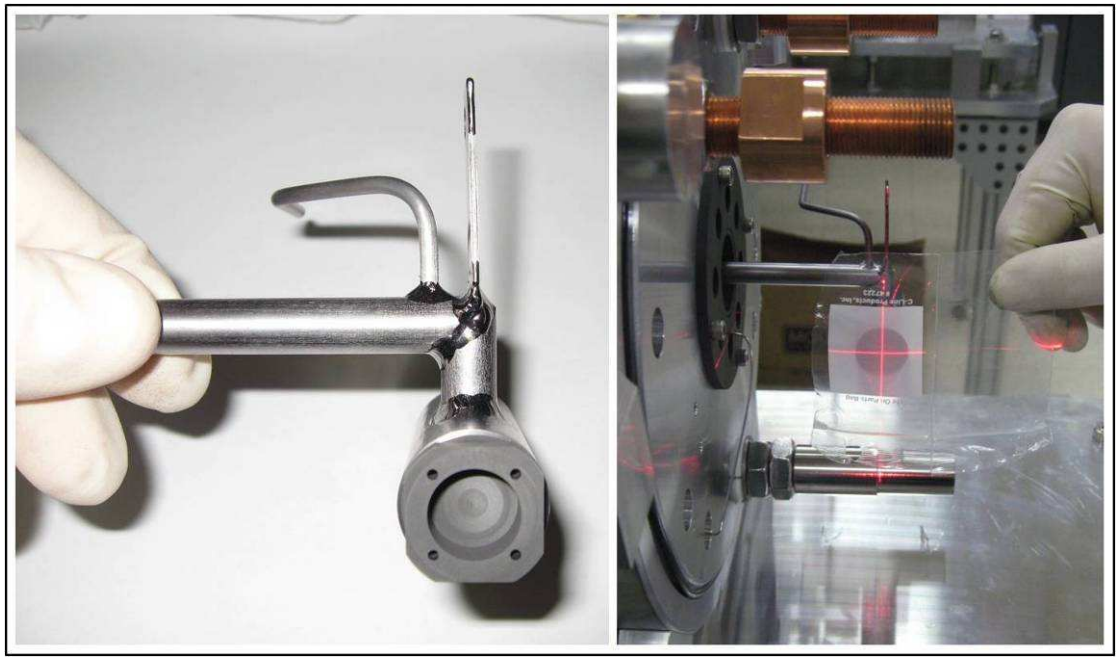

Fig. 26. Positioning and pre-alignment of the target holder; the buss extension installed on the electrical clamp.

STEP 12: installation of the target heater

Position the target heater and align it with the target holder by means of the buss nuts and the heater brackets (see figure 27); connect the transfer line (target holder) to the buss extension installing the tantalum current strap reported in figure 25.

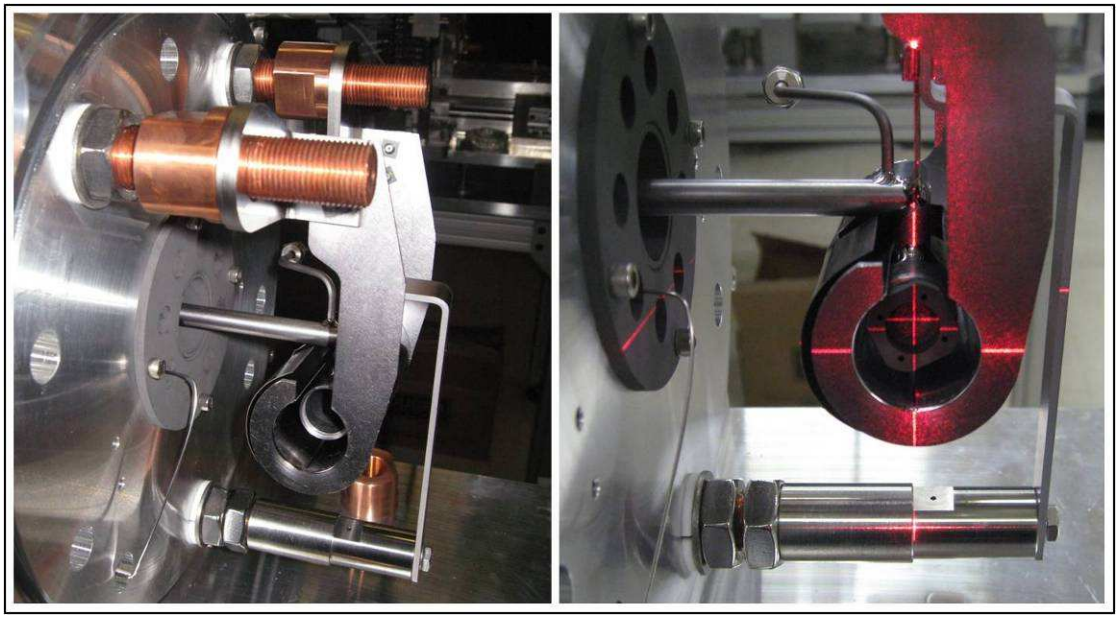

Fig. 27. Installation of the target heater.

STEP 13: gas connection

A) Prepare the current break and the Swagelok gas fittings reported in figure 28.

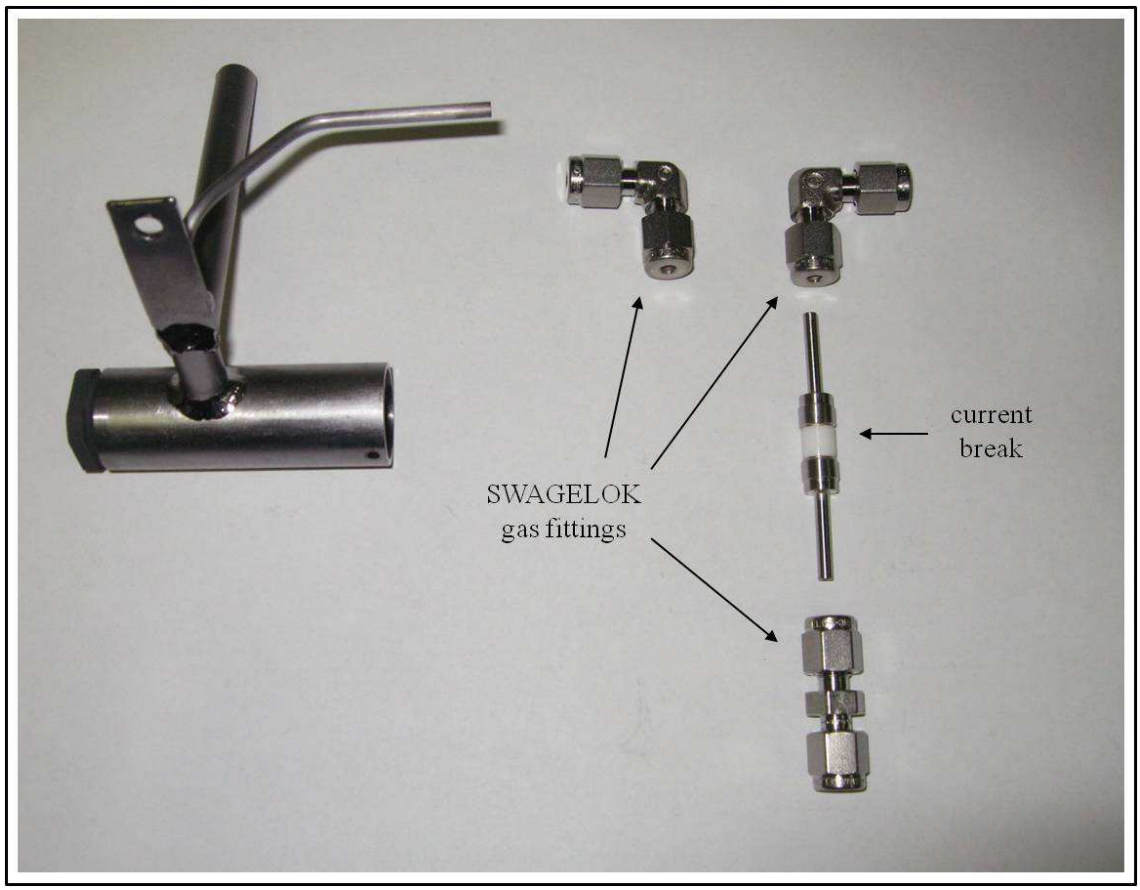

Fig. 28. The current break and the gas fittings.

B) Connect the gas fittings to the transfer line's gas tube and to the chamber's gas inlet as reported in figure 29; install then the current break and the bended stainless tube that allows to close the gas loop (see the right side of figure 29).

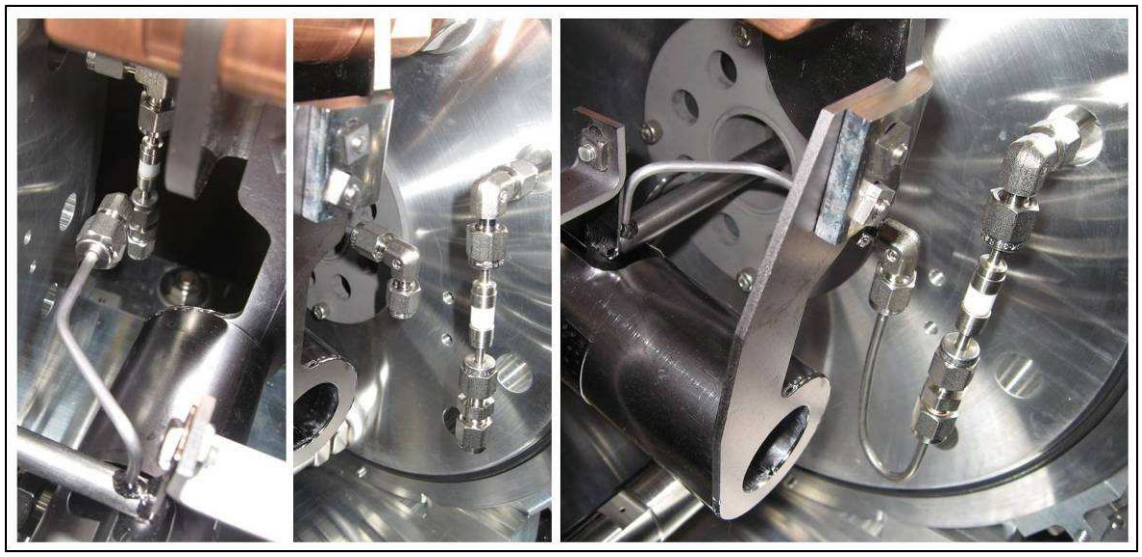

Fig. 29. Installation of the gas loop.

STEP 14: thermal screens

Position around the gas tubes and on the frontal part of the target heating system a series of thin Ta foils (opportunely shaped) and fix them with Ta wire as reported in figure 30; keep under control the electrical insulation of the gas loop.

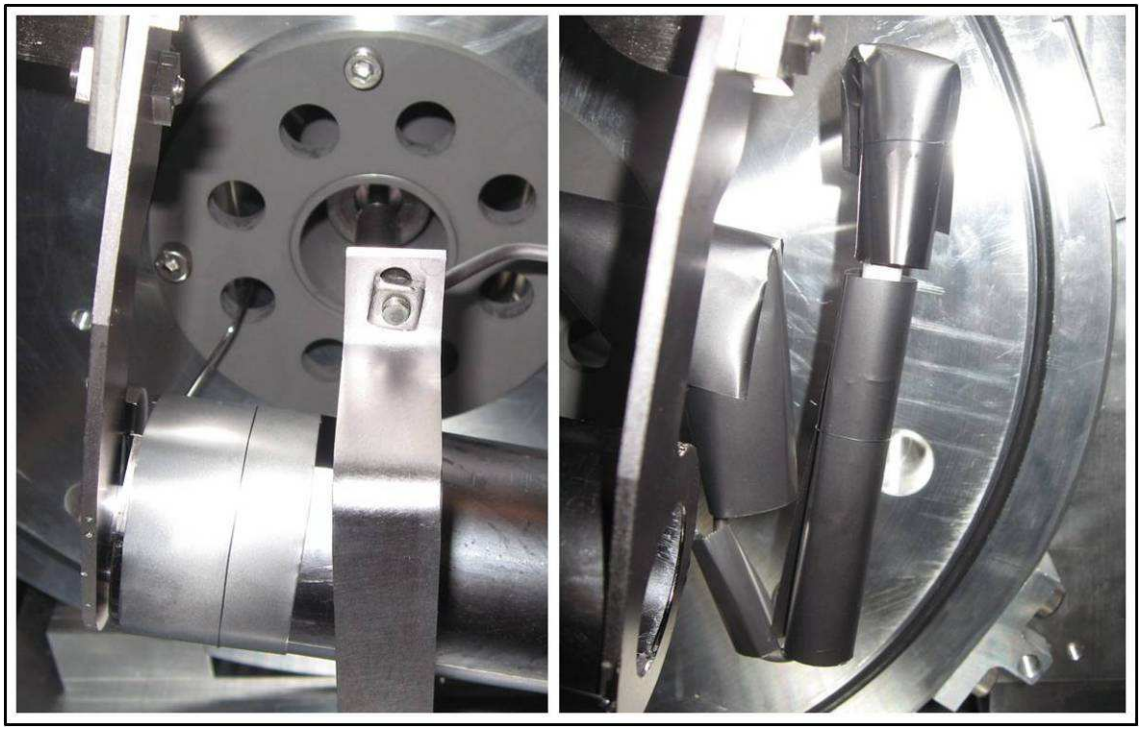

Fig. 30. The thermal screens installed around the gas tubes and on the frontal part of the target heater.

STEP 15: preparation of the SPES target prototype and installation in the HRIBF target heating system

A) Prepare the seven uranium carbide disks, the graphite box, the window and the dumpers on a clean container; assemble them handling the UC_x disks carefully in order to prevent contamination.

Fig. 31. The SPES target prototype assembly.

B) Insert carefully the SPES target prototype inside the HRIBF target heating system (see figure 32) and check the radioactivity level using a Geiger counter (see figure 33).

Fig. 32. The SPES target prototype inserted inside the target heating system.

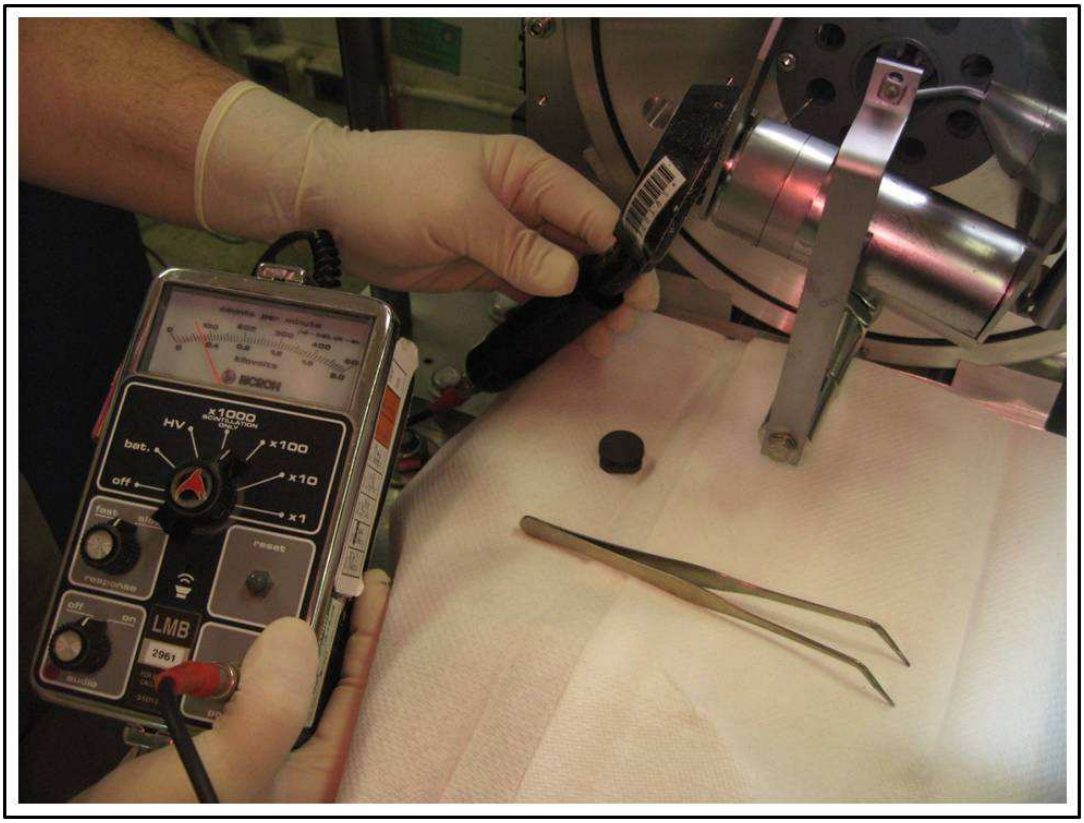

Fig. 33. Checking the radioactivity level by means of the Geiger counter.

C) At this point the target can be fixed inside the holder using the graphite cap and, once produced high vacuum inside the target chamber, it is finally ready to be heated at high temperatures and to be impinged by the proton beam.

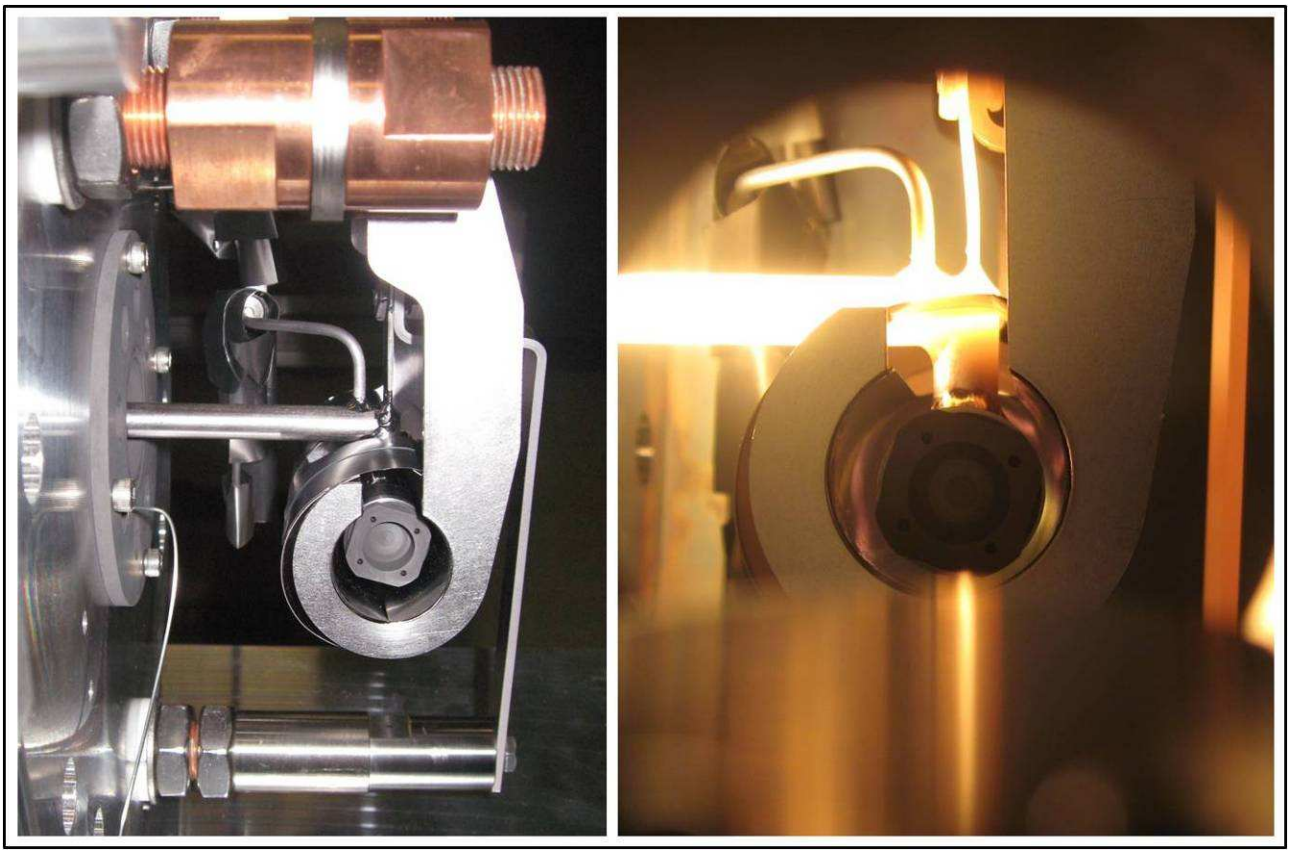

Fig. 34. The target – ion source system ready to be heated at high temperatures and to be impinged by the primary proton beam.

REFERENCES

[1] D. Stracener, GUIDELINE FOR ASSEMBLY of Electron-Beam-Plasma Ion Source, internal report, HRIBF, ORNL (US Department Of Energy).